

Ionic Materials for Photoelectrochemical Solar Cells

Marie Josephe Vanessa Armel

(MSc, Hons)

Sponsored by



A thesis presented for the degree

“Doctor of Philosophy”

In the School of Chemistry at Monash University



To my parents
and in memory of my grandmother

“The road to success is always under construction”

Larry Wall and Kathleen Russell



Contents

Abstract	XIV
Declaration	XVIII
Acknowledgments	XIX
Structures and abbreviations	XX
1 Introduction	1
References	5
2 Background and literature review	
Chapter overview	7
2.1 History of photovoltaic effect	8
2.2 Solid state solar cells	9
2.2.1 Intrinsic and extrinsic semiconductors	9
2.2.2 Homojunctions	11
2.2.3 Heterojunctions	13
2.2.4 Metal-semiconductor junction	13
2.3 Photovoltaic devices: conventional solar cells, emerging technology and commercialization	15
2.4 Photoelectrochemical cells	17

2.4.1 The electrolyte	17
2.4.2 Semiconductor-Electrolyte junction	19
2.4.3 Dye sensitised solar cells	21
2.4.4 Functioning of DSSCs	22
2.4.4.1 Working principle	22
2.4.4.2 Kinetics of DSSCs	24
2.4.4.3 Loss mechanisms and limiting factor	25
2.4.5 Photovoltaic performance	26
2.4.6 Materials in DSSCs	28
2.4.6.1 Substrates	29
2.4.6.2 Semiconductors	29
2.4.6.2.1 N-type semiconductors	29
2.4.6.2.2 P-type semiconductors	33
2.4.6.3 Sensitisers	34
2.4.6.3.1 Dyes for N-type semiconductors	34
2.4.6.3.2 Dyes for P-type semiconductors	37
2.4.6.4 Counter electrodes	37
2.4.6.5 Redox couples	39
2.4.7 Types of DSSC devices	42
2.4.7.1 Sandwich and monolithic dye sensitized solar cells	42
2.4.7.2 Tandem devices	44

2.5 Ionic Liquids	46
2.5.1 Brief history	46
2.5.2 Application of ionic liquids	47
2.5.2.1 Pharmaceutical ionic liquids	48
2.5.2.2 Solvents and catalysts	48
2.5.2.3 The energy industry	49
2.6 Ultimate aim	53
References	54

3 Experimental

Chapter overview	61
3.1 Characterisation techniques: Structural analysis	62
3.1.1 Nuclear magnetic resonance spectroscopy (NMR)	62
3.1.2 Electrospray ionisation spectrometry (ESI)	62
3.1.3 Single crystal x-ray diffraction	63
3.2 Thermal analysis	65
3.2.1 Differential Scanning Calorimetry (DSC)	65
3.2.2 Thermogravimetry analysis (TGA)	66
3.2.3 Accelerated Rate Calorimetry (ARC)	66
3.2.3.1 Self heat rate vs. temperature	68
3.2.3.2 Temperature vs. Time	68
3.2.3.3 Pressure vs. time/temperature	68

3.2 Physico-Chemical properties	69
3.2.1 Density	69
3.2.2 Viscosity	69
3.2 Electrochemical methods	71
3.2.1 Water Content Determination - Coulometric Karl Fischer	71
3.2.2 Ion selective electrode	73
3.2.3 A.C. Conductivity	73
3.2.4 Basic electrochemistry	76
3.2.4.1 Experimental set up	76
3.2.4.2 Electrodes used to study redox reactions	77
3.2.4.3 Transport properties of ions	77
3.2.4.4 Cyclic voltammetry	78
3.2.5 Diffusion NMR spectroscopy	82
References	83

4 Device fabrication and characterisation

Chapter overview	85
4.1 Materials	86
4.1.1 TCO coated glass	86
4.1.2 Dense TiO ₂ layer	87
4.1.3 Nanocrystalline TiO ₂ layer	87
4.1.4 Scattering TiO ₂ paste	87

4.1.5 Dyes	88
4.1.6 Counter electrodes	88
4.1.7 Cell sealing	89
4.1.8 Electrolytes	89
4.1.9 Chemicals and solvents	89
4.2 Device fabrication	90
4.3 Characterisation and measurement	95
4.3.1 Current-Voltage characterisation	95
4.3.2 Incident photon-to-current conversion efficiency (IPCE)	96
4.3.3 Absorbed photon-to-current conversion efficiency (APCE)	97
4.3.4 UV/Vis spectroscopy	98
4.3.5 Scanning Electron Microscopy	98
4.3.6 Profilometer	98
4.3.7 BET analysis	98
4.3.8 Error analysis	99
References	100

5 Synthesis of low viscous phosphonium ionic liquids

Chapter overview	101
5.1 Introduction	102
5.1.1 Synthetic routes to phosphonium based ionic liquids	102
5.1.1.1 Metathesis route	102

5.1.1.2 Halide free route	103
5.1.2 Applications of phosphonium based ionic liquids	103
5.1.3 Transport properties of phosphonium based ionic liquids	105
5.1.3.1 Method for assessing the formation of aggregates in an ionic liquid: the Walden plot	106
5.1.3.2 Method of assessing ion pairs in ionic liquids: Stokes-Einstein equation and Nernst-Einstein equation	108
5.1.4 The effect of different cations and anions	109
5.1.5 Aims of this chapter	110
5.2 Experimental	112
5.2.1 Analysis	112
5.2.2 Synthesis of phosphonium based ionic liquids	113
5.3 Results and discussions	120
5.3.1 Thermal properties	120
5.3.2 Transport properties	132
5.3.2.1 Viscosity	132
5.3.2.2 Ionic conductivity	134
5.3.2.3 The Walden plot	139
5.3.2.4 Diffusion measurements of neat phosphonium ionic liquids	140
5.3.3 Electrochemical window	147
5.4 Conclusions	150
References	151

6 Effect of ionic liquid on the flatband potential of n-type semiconductor (Titania)

Chapter overview	157
6.1 Introduction	158
6.1.1 General Overview	158
6.2 Aim of this work	161
6.3 Experimental	161
6.3.1 Electrochemical measurement of flatband potential	161
6.3.2 Materials and Ionic liquids	162
6.3.3 ATR-FTIR	163
6.3.4 UV spectroscopy	163
6.4 Results and discussions	164
6.4.1 Determination of flatband potential of TiO ₂ in aqueous medium using UV-Spectroscopy and Mott-Schottky measurement	164
6.4.2 Determination of E _{fb} in non aqueous medium using Mott Schottky method	168
6.4.2.1 Neat ionic liquids	168
6.4.2.2 Effect on V _{fb} of the addition of water to C ₂ mimNTf ₂	175
6.4.2.3 Addition of bases and acids in different ionic liquids	177
6.4.2.4 Addition of lithium iodide and then 4-tert-butylpyridine to C ₃ mpyrNTf ₂	179
6.4.2.5 Base and Acid treatment of TiO ₂ film	180

6.5 Conclusions	182
References	183

7 Ionic liquids in dithienothiophene based organic dye sensitised solar cells

Chapter Overview	187
7.1 Introduction	188
7.1.1 Sensitisers for DSSCs	188
7.1.1.1 Ruthenium based sensitisers	188
7.1.1.2 Metal free Organic sensitisers	191
7.1.2 Aim of work	193
7.2 Experimental	193
7.2.1 UV-Vis	195
7.2.2 Cyclic voltammetry	196
7.2.3 Preparation of the dye sensitised solar cells	196
7.2.4 Evaluation of the DSSC	196
7.3 Results and discussions	197
7.3.1 UV spectroscopy	197
7.3.2 Determination of the redox potential of organic sensitisers	199
7.3.3 Electrolytes	202
7.3.3.1 Ionic liquid electrolytes	203
7.3.4 Current-Voltage measurements	210

7.3.4.1 Effect of solvents for the sensitization of electrodes	
using THD1 dye	210
7.3.4.2 The effect of chenodeoxycholic acid and film thickness	
using standard THDn electrolyte	217
7.3.4.3 Photovoltaic performance in phosphonium ionic liquids	
containing solar cells	222
7.3.4.3.1 Phosphonium ionic liquid electrolytes with	
Z907 and N719	222
7.3.4.3.2 The P ₂₂₂₍₂₀₁₎ NTf ₂ electrolyte with THD3 as	
sensitisers in DSSCs	237
7.3.4.3.3 Different phosphonium ionic liquid electrolytes	
in DSSCs with various organic sensitisers	243
7.3.4.3.4 Effect of scattering layer on the performance	
of DSSCs with organic sensitisers	248
7.3.4.3.5 The effect of different ionic liquid anions and	
cations on device performance	251
7.4 Conclusions	258
References	259

8 Ionic liquids with porphyrin dye sensitised solar cells

Chapter overview	263
8.1 Introduction	264
8.1.1 Porphyrin chromophores for dye sensitised solar cells	264

8.2 Aim	265
8.3 Experimental	267
8.3.1 Transient adsorption spectroscopy	267
8.3.2 Ionic liquids	267
8.3.3 Preparation of electrolytes	269
8.4 Results and discussion	270
8.4.1 Physical and chemical properties of ionic liquids	270
8.4.2 Photovoltaic characterisation	274
8.4.2.1 Different porphyrin sensitisers	274
8.4.2.2 The effect of adding chenodeoxycholic acid and increasing the concentration of 4-tert-butylpyridine in GD2-based DSSCs	276
8.4.2.3 Ionic liquids electrolytes with Porphyrin sensitisers	281
8.4.2.3.1 Binary ionic liquids with the P159 sensitiser	281
8.4.2.3.2 Ternary ionic liquids mixtures with porphyrin sensitisers GD2, GD3 and P159	284
8.4.2.3.3 Transient light absorption spectroscopy of DSSCs with the P159 dye	290
8.5 Conclusions	294
References	295

9 Solid state materials with dye sensitised solar cells

Chapter overview	297
9.1 Introduction	298
9.1.1 Organic ionic plastic crystals	298
9.2 Types of solid state electrolyte already studied in DSSCs	301
9.2.1 Molecular plastic crystals	301
9.2.2 Inorganic P-type semiconductor	302
9.2.3 Organic p-type semiconductor	303
9.2.4 Solid polymer electrolytes and polymer gel electrolytes	305
9.3 Experimental	306
9.3.1 Synthesis of organic ionic plastic crystals	307
9.4 Results and discussions	308
9.4.1 Molecular plastic crystals: Succinonitrile	308
9.4.1.1 Thermal analysis	309
9.4.1.2 Conductivity measurement	311
9.4.1.3 Electrochemical measurement	312
9.4.1.4 Photovoltaic measurement	314
9.4.2 Organic ionic plastic crystals	319
9.4.2.1 Thermal analysis	319
9.4.2.2 Conductivity measurement	323
9.4.2.3 Electrochemical analysis	326

9.4.2.4 Photovoltaic performance of OIPC using ruthenium dye	328
9.5 Conclusions	330
References	331
10 Conclusions and Future work	
10.1 Conclusions	335
10.2 Synthesis of novel phosphonium ionic liquids	336
10.3 The effect of the ionic liquid on the flatband potential of n-type semiconductors	338
10.4 Phosphonium based ionic liquids with dithienothiophene sensitisers	337
10.5 Ionic materials for porphyrin dye sensitised solar cells	337
10.6 Solid state materials in dye sensitised solar cells	338
10.7 Future work	339
Appendix	
A.1 Time-Temperature profile	341
A.2 VTF behaviour of ionic liquids	342
A.2.1 Viscosity	342
A.2.2 Ionic conductivity	347
A.3 Cyclic voltammetry of NTf₂⁻ anion	353
A.4 UV spectroscopy and ATR-FTIR	353
A.4.1 UV spectroscopy	353

A.4.2 ATR-FTIR of untreated TiO ₂ film and treated TiO ₂ film	355
A.5 Crystal structure determination of the iodide and triiodide salts	356
A.6 Electron Kinetic measurement	361
A.7 UV-Vis spectra of the effect of chenodeoxycholic acid with porphyrin sensitisers	362
A.8 Thermal analysis of neat pyrrolidinium ionic liquids	363
A.9 Diagram of equivalent circuit for a symmetrical cell	363
A.10 Publications	364

Abstract

The pressure on governments to find alternative energy sources which are cheaper, sustainable and also less polluting, has triggered a significant amount of research into solar cells. Conventional solar cells are mainly based on silicon, but the cost of production and materials of these types of devices is high. Dye sensitised solar cells (DSSCs) are an alternative type of solar cell that uses cheaper components. Since their discovery in 1991, many research groups across the world have investigated this type of device in an attempt to understand and optimise their operation. There are several factors that limit the performance of these devices, such as corrosion of the counter electrode, leakage of the commonly used molecular liquid electrolyte and insufficient light absorption by the sensitisers.

The aim of this research was to synthesise and characterise novel ionic liquids for use as the electrolyte in dye sensitised solar cells, and also understand the behaviour of commonly used ionic liquids, such as the imidazolium-based family, when in contact with the TiO₂ photoanode layer.

New phosphonium ionic liquids were synthesised for use as electrolytes in DSSCs. Different anions such as tetrafluoroborate, hexafluorophosphate, dicyanamide, bis(trifluoromethanesulfonyl)amide, thiocyanate and bis(fluorosulfonyl)imide, combined with different asymmetric phosphonium cations, were used to prepare either ionic liquids, or solids that show plastic crystal behaviour. The chemical and physical properties of these phosphonium ionic liquids were measured and they all show relatively good thermal stability, except for the bis(fluorosulfonyl)imide series. They also exhibit good ionic conductivity and are considered to be “good” ionic liquids according to their position on the Walden plot.

These new phosphonium ionic liquids were utilised as electrolytes in dye sensitised solar cells using dithienothiophene organic dyes, and the results compared to those obtained using the common ruthenium-based dyes. The effect of film thickness, scattering layer and particle size were investigated with the organic sensitisers. With these new dithienothiophene sensitisers, a thin (2 μm) transparent TiO₂ layer with a scattering layer of ~ 6 μm is the optimum for the device to perform well. The addition of chenodeoxycholic acid in the dye bath showed an improvement in device efficiency.

Addition of small amounts of solvent such as water, valeronitrile or tetraglyme are also discussed.

These novel phosphonium ionic liquids show promising behaviour in these cells. The best device performance was achieved with the least viscous phosphonium ionic liquids containing the methoxy group on one of the alkyl chains. The power conversion efficiencies using these dithienothiophene dyes were all > 5 % under full sun and > 6 % at low sun intensity.

In order to understand the behaviour of ionic liquids in dye sensitised solar cells, the effect of this class of material in contact with the semiconductor was investigated by measurement of flatband potentials. Depending on the “acidity” or “basicity” of the neat ionic liquids, the position of the conduction band edge of the semiconductor is shifted. The purity of the ionic liquid is also a very important factor as it can affect the position of the flatband potential of the TiO₂-ionic liquid junction. For example, C₂mimBF₄ gives two different flatband potentials depending on the quality of the ionic liquid from the supplier. The effects of acid treatment and the addition of additives such as lithium iodide and N-methylbenzimidazole to the ionic liquid were also investigated. As expected, addition of small ions such as Li⁺ or H⁺ shift the flatband potential towards more positive values, whereas the presence of basic materials such as 4-tert-butylpyridine or N-methylbenzimidazole gives more negative potentials. These additives as well as the ionic liquids play an important role in dye sensitised solar cells, especially on the open circuit voltage.

The use of imidazolium, ammonium and phosphonium based ionic liquid electrolytes was also investigated with porphyrin sensitisers and transient spectroscopy measurements were performed to elucidate the influence of the ionic liquid on the device performance.

Another interesting class of materials, which are related to the family of ionic liquids studied here, are the organic ionic plastic crystals. These were investigated as potential solid electrolytes in dye sensitised solar cells. It is the first time that these materials have been successfully used in DSSCs. Relatively good performance was obtained with an electrolyte based on the organic ionic plastic crystal, C₁mpyrN(CN)₂. Performance of > 5 % was obtained with Ruthenium as the sensitiser under full sun intensity.

Finally, the use of another type of solid electrolyte based on succinonitrile was investigated with both the porphyrin sensitiser (P159) and with a ruthenium based sensitiser (N719). Over 5 % efficiency was achieved at low sun intensity with the porphyrin dye. This is the first time that such a good performance has been obtained with a solid electrolyte in porphyrin based DSSCs.

Under the Copyright Act 1968, this thesis must be used only under the normal conditions of scholarly fair dealing. In particular no results or conclusions should be extracted from it, nor should it be copied or closely paraphrased in whole or in part without the written consent of the author. Proper written acknowledgement should be made for any assistance obtained from this thesis.

I certify that I have made all reasonable efforts to secure copyright permissions for third-party content included in this thesis and have not knowingly added copyright content to my work without the owner's permission.

Declaration

This thesis, composed by myself, is submitted to Monash University for fulfilment of the requirements for a Doctor in Philosophy in Chemistry at Monash University. The research was carried out by myself, except where acknowledged, in the School of Chemistry (Monash University). It is wholly original, except where due reference is given, and has not been submitted for any previous degree.

Acknowledgments

First of all, I would like to thank Professor Doug MacFarlane, Professor Maria Forsyth, Professor David Officer and Dr. Jenny Pringle for giving me the opportunity to do my PhD, for all their ongoing support, guidance and valuable discussions. I couldn't ask for such excellent mentors.

A special thanks to Dr. Peter Newman for his exceptional help and contribution to my study at Monash, especially for the correction of my thesis before submission, and also for sharing his experiences and knowledge.

I would also like to thank Dr. Bjørn Winther-Jensen and Dr. Patrick Howlett for their valuable help and constant discussion in electrochemistry.

Thank you to all the members of the MacFarlane/Forsyth research group that I have the gotten the possibility to know and work with: Youssef, Orawan, Pam, Kevin, Kylie, Radha, Mega, Vijay, Aleksey, Ekaterina, Tristan, Paul and Martin. A special thanks to the solar group for having me around.

Jelena, I appreciate your friendship, help and constant support, during all the happy and sad times that we have had. I express my deepest gratitude to Gary and Huy, for their general support, especially helping me with the odd question now and again, and for being patient, understanding and caring. To all those I have forgotten to mention, I greatly thank you for your contribution and support.

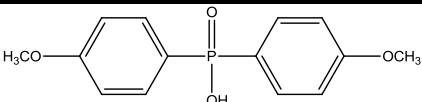
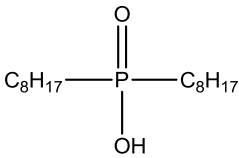
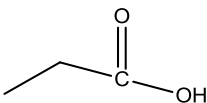
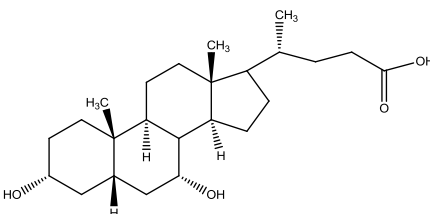
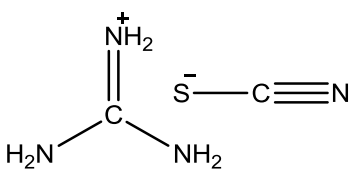
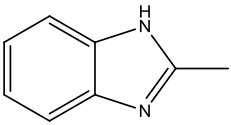
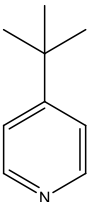
Tim, what can I say, thank you for making me laugh and always being in a good frame of mind, and well spirited, no matter the occasion. By the way, feel free to translate the French section if you dare; I am sure that you will think that it directly concerns you and become extremely paranoid until you finally translate it.

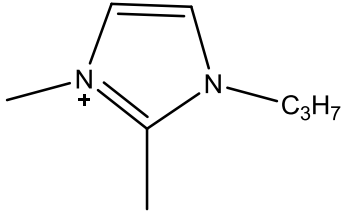
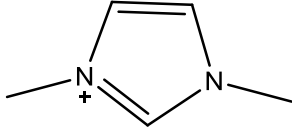
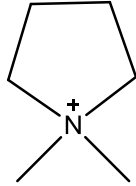
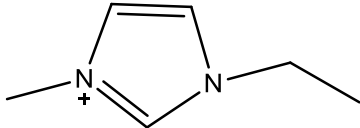
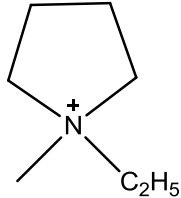
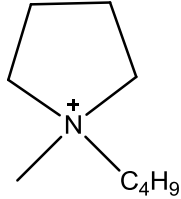
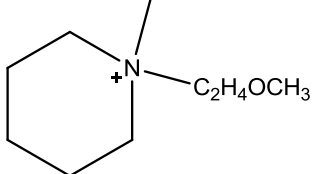
Finalemnt, je voudrais remercier mes parents pour leur support, aide, encouragement et leur amour à chaque étapes de ma vie. A ma soeur ainée et sa famille pour m'avoir héberger et aider dans les moments difficiles. A ma petite soeur pour son aide précieuse. Un grand remerciement à ma mamie Liselle pour avoir été toujours présente dans ma vie. Finalemnt à mes grandparents pour leur encouragement.

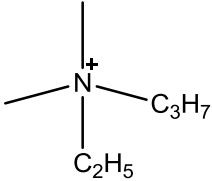
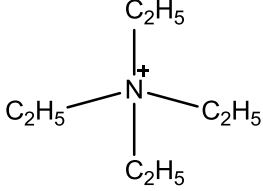
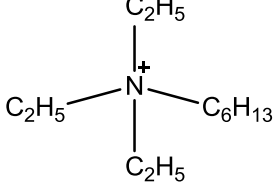
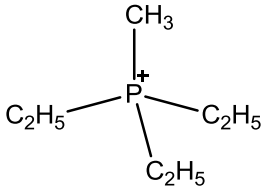
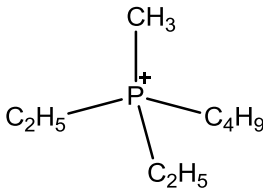
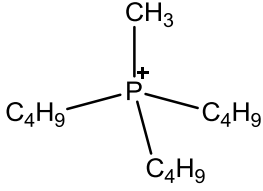
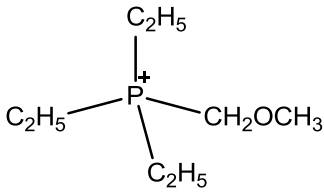
Structures and Abbreviations

Abbreviation	Full name
¹ H NMR	Proton Nuclear Magnetic Resonance
AM	Air Mass
APCE	Absorbed-Photon-to-Current Efficiency
ARC	Accelerated Rate Calorimetry
BET	Brunauer-Emmett-Teller
Btu	British thermal unit
CB	Conduction band
CE	Counter electrode
CIGS	Copper-Indium-gallium-selenide
CNTs	Carbon nanotubes
CV	Cyclic voltammetry
dcbpy	Dicarboxylic bipyridine
DSC	Differential Scanning Calorimetry
DSSC	Dye sensitised solar cells
EIS	Electrochemical Impedance Spectroscopy
EPFL	École polytechnique fédéral de Lausanne
eV	Electron volt
<i>ff</i>	Fill factor
FTIR	Fourier Transform Infra-Red Spectroscopy
FTO	Fluorine doped tin oxide
HOMO	Highest occupied molecular orbital
HTM	Hole transporting material
ILs	Ionic liquids
IMPS	Intensity Modulated Photocurrent Spectroscopy
IMVS	Intensity Modulated Photovoltage Spectroscopy
IPCE	Incident Photon-to-Current Efficiency
I_{sc}	Short circuit current density
ISE	Ion-Selective Electrode
ITO	Tin doped indium oxide

IV	Current-Voltage
LiI	Lithium iodide
LUMO	Lowest unoccupied molecular orbital
MS	Mass Spectrometry
NHE	Normal hydrogen electrode
OIPC	Organic ionic plastic crystals
OMPC	Ordered multimodal porous carbon
PEDOT	Poly(3,4-ethylene dioxythiophene)
PEMFC	Proton exchange membrane fuel cells
PEN	Polyethylene naphthalate
PET	polyethylene
PGSTE	Pulsed-Field-Gradient Stimulated Echo
PILs	Protic ionic liquids
PV	Photovoltaic
Redox	Reduction-oxidation
SEM	Scanning Electron Microscopy
SWCNT	Single walled carbon nanotubes
TCO	Transparent conductive oxide
TGA	Thermogravimetric Analysis
TiO ₂	Titanium dioxide
TMFDS	Tetramethylformaninium disulphide
TMTU	Tetramethylthiourea
TW	TeraWatts
UV-Vis	Ultraviolet-Visible Spectroscopy
VB	Valence band
V _{oc}	Open circuit voltage

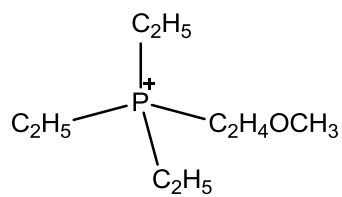
Abbreviation	Full name	Structure
	Bis-(4-methoxyphenyl)phosphinic acid	
	Diisooctylphosphinic acid	
	Propanoic acid	
DCA	Chenodeoxycholic acid	
GSCN	Guanidinium thiocyanate	
NMB	N-methylbenzimidazole	
TBP	4-tertbutylpyridine	

C_1dmim^+	1-propyl-dimethylimidazolium	
C_1mim^+	Dimethylimidazolium	
C_1mpyr^+	N,N-dimethylpyrrolidinium	
C_2mim^+	1-ethyl-3-methylimidazolium	
C_2mpyr^+	N-ethyl-N-methylpyrrolidinium	
C_4mpyr^+	N-butyl-N-methylpyrrolidinium	
$MOEMPIP^+$	1-(2-methoxyethyl)-1-methylpiperidinium	

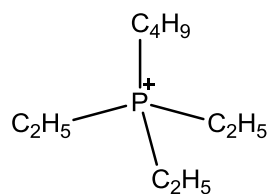
N_{1123}^+	Dimethylethylbutylammonium	
N_{2222}^+	Tetraethylammonium	
N_{2226}^+	Triethylhexylammonium	
P_{1222}^+	Methyl(triethyl)phosphonium	
P_{1224}^+	Diethylmethyl(isobutyl)phosphonium	
P_{1444}^+	Butyl(triethyl)phosphonium	
$P_{222(101)}^+$	Triethyl(methoxymethyl)phosphonium	

$P_{222(201)}^+$

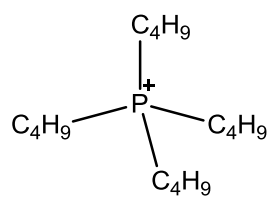
Triethyl(methoxyethyl)phosphonium

 P_{2224}^+

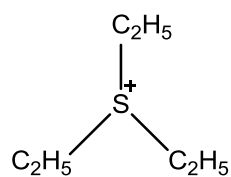
Butyl(triethyl)phosphonium

 P_{4444}^+

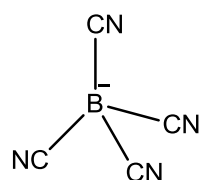
Tetrabutylphosphonium

 S_{222}^+

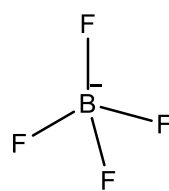
Triethylsulphonium

 $B(CN)_4^-$

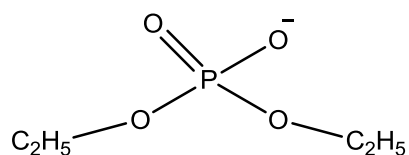
Tetracyanoborate

 BF_4^-

Tetrafluoroborate

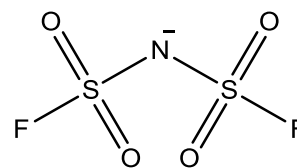
DEP⁻

Diethylphosphate



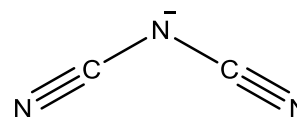
FSI⁻

Bis(fluorosulfonyl)imide



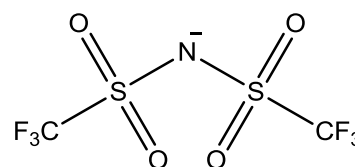
N(CN)₂⁻

Dicyanamide



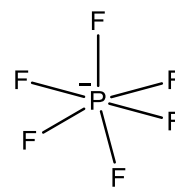
NTf₂⁻

Bis(trifluoromethanesulfonyl)amide



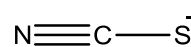
PF₆⁻

Hexafluorophosphate



SCN⁻

Thiocyanate



Chapter 1

Introduction

Today, with population growth expected to double by 2050,¹⁻³ the future global economy is likely to consume even more energy due to rising energy demand, especially from developing countries. Fossil fuels are our primary energy source. The impact of using such sources of energy has been linked to an increase in global CO₂ emissions at a projected rate of 1.8 % per year.¹ CO₂ emissions are having a negative impact on the world climate, causing global warming (an increase of average temperature by 0.8 °C since 1880⁴) leading to side effects such as an increase in sea level, intensified hurricane activity and drought.⁵

The total utilisation of all energy sources is shown in Figure 1.1. The consumption of fuels is predicted to increase by 50 to 100 % by 2030. At present, fossil fuels are the largest supply of energy worldwide, providing for 86 % of the world's energy consumption and this is predicted to decrease by 3 % by the year 2030.⁶ The use of renewable energy technologies are expected to continually grow.

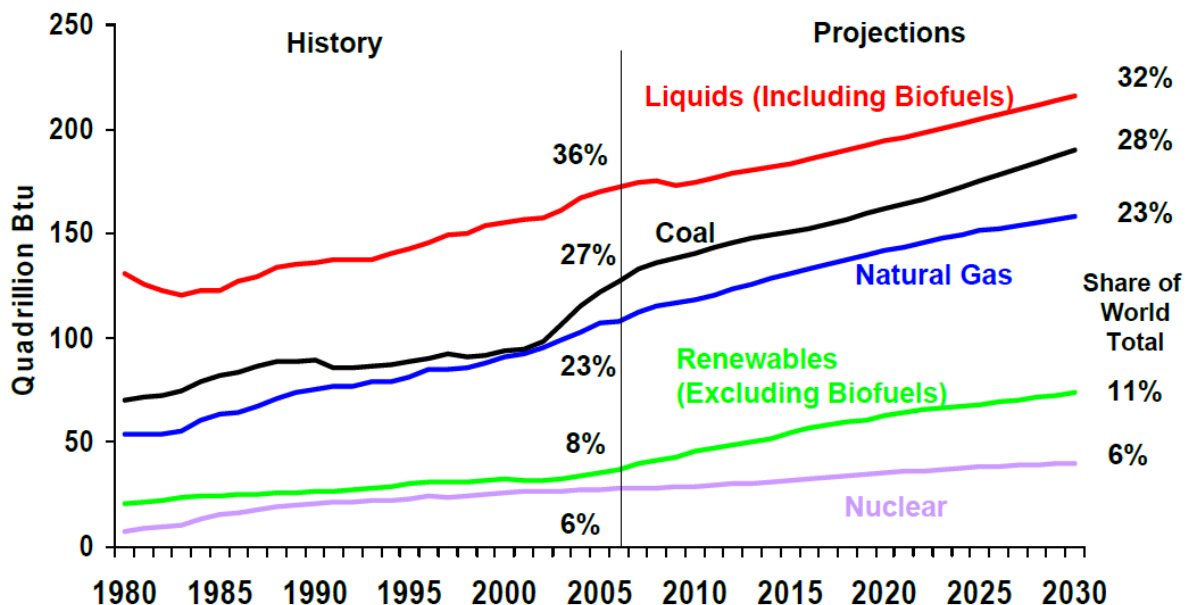


Figure 1.1: World energy demand by fuel, 1980-2030 (Btu –British thermal unit)⁶

1. Introduction

At present, the world energy demand is around 14 TW (TeraWatts) and is expected to go up to 28 TW by 2050.⁷ Our society's predominant reliance on fossil fuels is causing a huge impact on the environment. Alternative means of producing energy that are more environmental friendly, cheaper and accessible, are desperately needed.

If we want to accommodate for the rising energy demand, nuclear energy is one such solution. Nuclear energy in itself provides 15 % of the world's electricity. In Europe alone, nuclear is a primary mean of supplying electricity, with France being the highest consumer at 78 %.⁸ Nuclear energy in the short term can reduce the amount of CO₂ emitted, but at a considerable cost. The radioactive by-product formed and its disposal is a huge burden, not only in terms of disposal, but also lifetime of the waste. Aside from these negative aspects, there are ongoing costs for the maintenance of the nuclear reactor.

Renewable energy is thus an important way forward. Solar energy (photovoltaic) is one such technology which offers a simple alternative to both nuclear and fossil fuels. The existing photovoltaic technology is quite expensive. To reduce its cost, further research and development is required in this field to make this technology viable for the public as well as industry.

Other types of renewable energy which can supply the remaining demand include wind, biomass, geothermal, tidal and hydroelectric. These technologies have a minor impact on the environment, but the power output produced is quite low and can be variable.

Silicon photovoltaic cells are well known but the production costs of these devices remains a barrier to their widespread use. One attractive and well known alternative photovoltaic device is the dye sensitised solar cell (DSSC). It was developed by Professor Grätzel at EPFL in 1991.⁹⁻¹⁰ The DSSC is composed of five main components: the substrate (transparent conductive glass), the photoelectrode (semi conductor film), the dye, the electrolyte and the cathode. The full description of this technology is given in Chapters 2 and 4. An impressive solar light-to-current conversion efficiency of 11 % was recently obtained using a DSSC with a liquid based electrolyte.¹¹ The attractive aspects of these types of devices are that the materials are cheap and the fabrication costs are low when compared to conventional silicon solar cells.

Silicon solar cells require highly pure and crystalline materials; any trace of impurities or defect will drastically lower the performance of such devices. The capital cost of building plant to manufacture silicon based devices is thus very high.

The dye sensitised solar cell technology has greatly progressed in the last couple of years and DSSCs with an efficiency of 8 % are being commercialised by Dyesol¹² and other Japanese¹³ and European¹⁴ companies.

Even though an impressive 11 % efficiency was recently obtained, there are still many problems associated with the organic solvent electrolyte, especially in terms of long term stability at elevated temperatures. The liquid electrolyte causes technological issues such as the desorption of the dye and degradation of the cell. There are also other factors that limit the performance of the DSSC, such as corrosion of the counter electrode by the iodide/triiodide redox couple, leakage of the electrolyte, and insufficient light absorption by the sensitizers.

To resolve some of the above problems, alternative electrolytes need to be found to replace the liquid one. Thus, the objective of this work is to investigate new electrolytes for dye sensitized solar cells. This thesis concerns the preparation and characterization of organic salts which form ionic liquids and organic ionic plastic crystals; these electrolyte materials are then tested in various DSSC cell types.

In Chapter 2, a brief description concerning the development of photovoltaic devices will be provided as well as a commentary on the progress and the “discovery” of newer technologies such as DSSCs. Ionic liquids are another field which has attracted the attention of a broader segment of the scientific community and the application of these “new” class of materials in electrochemical devices will be discussed.

Chapter 3 concerns the analytical methods used to characterise the synthesised ionic liquids. A full description of equipment used will also be given.

In Chapter 4, the assembly of the DSSC at a laboratory level will be described. The techniques used to evaluate the performance, as well as understanding function, will also be described.

1. Introduction

Chapter 5 will focus on trying to understand the effect of ionic liquid at the semiconductor-electrolyte interface. Electrochemical techniques, such as electrochemical impedance spectroscopy, are used to determine the flatband potential of the TiO₂ in contact with the ionic liquid. UV-spectroscopy is another method that has been used to determine the flatband potential. How the flatband potential of the TiO₂ is affected by addition of “impurities” is also investigated.

Chapter 6 concerns the synthesis of novel low viscous phosphonium ionic liquids. The physical properties of these ionic liquids that were characterised using various analytical methods will be discussed.

Chapter 7 concerns the use of these novel phosphonium ionic liquids with new dithienothiophene dyes in dye sensitised solar cells. For the first time, a phosphonium ionic liquid is shown to provide very high performance in a DSSC.

Chapter 8 investigates the use of imidazolium based ionic liquids with porphyrin sensitisers in DSSCs. The effect of different anions was investigated, as well as the effect of acid treatment.

Chapter 9 investigates the use of a new type of solid state electrolyte based on an organic ionic plastic crystal. The performance is examined in the dye sensitised solar cells with these novel electrolytes.

References

1. F. Birol, World Energy Outlook 2000, <http://www.iea.org/textbase/nppdf/free/2000/weo2000.pdf>, Last accessed 24th April 2010.
2. N. Lior, *Energy Convers. Manage.*, 2001, **42**, 1769-1805.
3. H. Zlotnik, World Population Prospects The 2008 Revision, http://esa.un.org/unpd/wpp2008/pdf/WPP2008_Executive-Summary_Edited_6-Oct-2009.pdf, Last accessed 24th April 2010.
4. R. Gutro, http://www.nasa.gov/vision/earth/environment/2005_warmest.html, Last accessed 24th April 2010.
5. K. Emanuel, *Nature*, 2005, **436**, 686-688.
6. E. I. Administration, International Energy Outlook, <http://www.eia.doe.gov/oiaf/ieo/pdf/0484%282009%29.pdf>, Last accessed 24th April 2010.
7. N. S. Lewis, in *Energy and Transportation*, National Academy Press, 2003, pp. 33-39.
8. I. A. E. Agency, *Energy, Electricity and Nuclear Power: Developments and Projections*, 2007.
9. M. Grätzel, *J. Photochem. Photobiol. C*, 2003, **4**, 145-153.
10. B. O'Regan and M. Grätzel, *Nature*, 1991, **353**, 737-740.
11. Y. Chiba, A. Islam, Y. Watanabe, R. Komiya, N. Koide and L. Han, *Jpn. J. Appl. Phys.*, 2006, **45**, L638-L640.
12. <http://www.dyesol.com>, Last accessed 24th April 2010
13. <http://www.aisin.com/csr/environment/development/>, Last accessed 24th April 2010
14. <http://www.g24i.com>, Last accessed 24th April 2010

Chapter 2

Background and literature review

Chapter overview

In the first part of this chapter, a brief description of the band structure and properties of semiconductors will be discussed, followed by the photovoltaic effects produced by different junctions. A brief history of the photovoltaic effect will also be given, before the introduction of photoelectrochemical cells. The main focus will be on dye sensitized solar cells. The second part will look at ionic liquids; a brief history will be given, followed by applications of these materials in different electrochemical devices. The last part will focus on the literature concerning the use of ionic liquids with dye sensitised solar cells.

2. Background and literature review

2.1 History of the photovoltaic effect

The photovoltaic effect (PV) which converts sunlight into electricity was first recognised in 1839 by French physicist Alexandre-Edmond Becquerel.¹ His experiment consisted of illuminating one of the two platinum electrodes immersed in a metal halide solution. He discovered that this gave rise to a current when the cell was illuminated. The research that followed this discovery on the photovoltaic effect was mainly focused towards the development in photography. In 1837, Louis Daguerre created the first photographic image using silver iodide, and at the same time, William Henry Fox Talbot was working on the calotype process. It was not until 1938, that a coherent and satisfactory explanation on the photographic effect was given by Gurney and Mott, giving rise to the Gurney-Mott theory, which is now widely accepted.

Willoughby Smith discovered the photovoltaic effect in selenium in 1873.² In 1876, William G. Adams discovered that illuminating a junction between selenium and platinum produced a photovoltaic effect.³ However, it was not until 1883, that the first solar cell was built, by Charles Fritts,⁴ who coated the semiconductor selenium with an extremely thin layer of gold to form the junctions. The device was only around 1 % efficient. Russell Ohl patented the concept of the modern solar cell in 1946.⁵

Albert Einstein gave a comprehensive theoretical description on the photovoltaic effect in 1904. He was awarded the Nobel Prize for describing the mechanism behind the photoelectric effect and his theoretical explanation was verified by Robert Millikan in 1916.

The modern age of solar power technology arrived in 1954 when Bell Laboratories,⁶ experimenting with semiconductors, accidentally found that silicon doped with certain impurities was extremely sensitive to light. This resulted in the production of the first practical solar cells, with a sunlight energy conversion efficiency of around 6 %.⁶ This milestone created interest in producing and launching a geostationary communications satellite by providing a viable power supply. Russia launched the first artificial satellite in 1957, and the United States' first artificial satellite was launched in 1958.⁷ Russian Sputnik 3, launched on May 15th, 1957, was the first satellite to use solar arrays. This was a crucial development that diverted funding from several governments into research for improved solar cells.

In the 1970s, the oil crisis experienced by various countries dependent on these materials led to the development of alternative sources of energy. Photovoltaic devices were the subject of intense research during this period, and a range of different methods of producing efficient and cost effective devices were explored.

Today, silicon solar cells dominate the photovoltaic markets and the record efficiency for a laboratory cell is 24.7 %.⁸ The efficiency of the commercial silicon solar panels can reach 15 %.⁹

2.2 Solid state solar cells

In this section, the photovoltaic effect that arises at different junctions will be briefly described. Firstly, the different types of semiconductors are described, followed by the traditional semiconductor based materials that produce the PV effect. In the second part, the photochemical cell is introduced, with a focus on dye sensitized solar cells. The operating systems and development of the DSSC device will also be described.

2.2.1 Intrinsic and extrinsic semiconductors

Semiconductors are a class of materials with a band gap in the range of 0.5 to 3 eV (electron volt).⁴ Semiconductors can either be intrinsic or extrinsic.¹⁰ Intrinsic semiconductors are mainly pure materials with a perfect crystal structure. Under thermal excitation, electrons in the valence band (VB) (the highest occupied band) are excited to the lowest unoccupied band called the conduction band (CB). Electronic transition across the energy gap to the CB creates a hole in the VB. During the process of electron-hole pair generation, the concentration of electrons in the CB is equal to the concentration of holes in the VB.

When an electric field is applied the electrons and holes flow in opposite directions, with a certain velocity, and a net current density is produced. Figure 2.1 shows a schematic diagram of an energy band structure of an intrinsic semiconductor. The best known semiconductor is silicon (Figure 2.1 (b)).¹¹

On the other hand, a semiconductor in which an impurity is deliberately introduced is called an extrinsic semiconductor. The process of adding an impurity is called doping. There is more interest in extrinsic semiconductors due to better conductivity compared to

2. Background and literature review

intrinsic semiconductor, and the properties of these materials are such that they are essential components in many electrical devices.

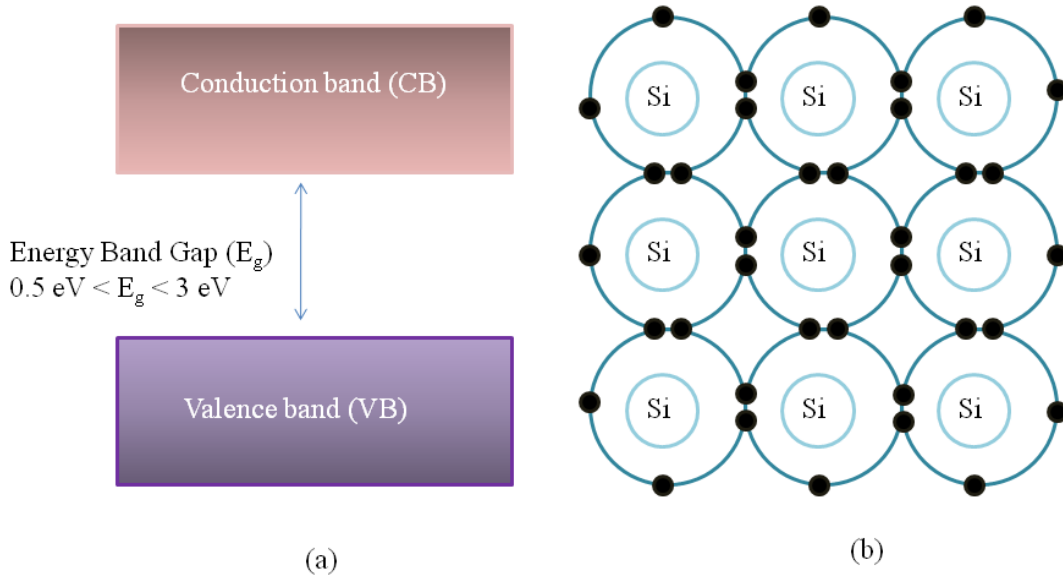


Figure 2.1: Schematic band structure of an intrinsic semiconductor (a) and Silicon (b)⁴

There are two main types of extrinsic semiconductors. A semiconductor which has been doped to increase the electron concentration relative to hole concentration is called an N-type semiconductor. N-type semiconductors are produced by doping an intrinsic semiconductor with five coordinated atoms such as phosphorus. Impurities that contribute electrons to the conduction band are called donors. On the other hand, a semiconductor that is doped to increase the concentration of positive charge carrier relative to the negative is called a P-type semiconductor. P-type semiconductors are produced by replacing some of the atoms in the crystal structure with acceptor impurity atoms such as boron.

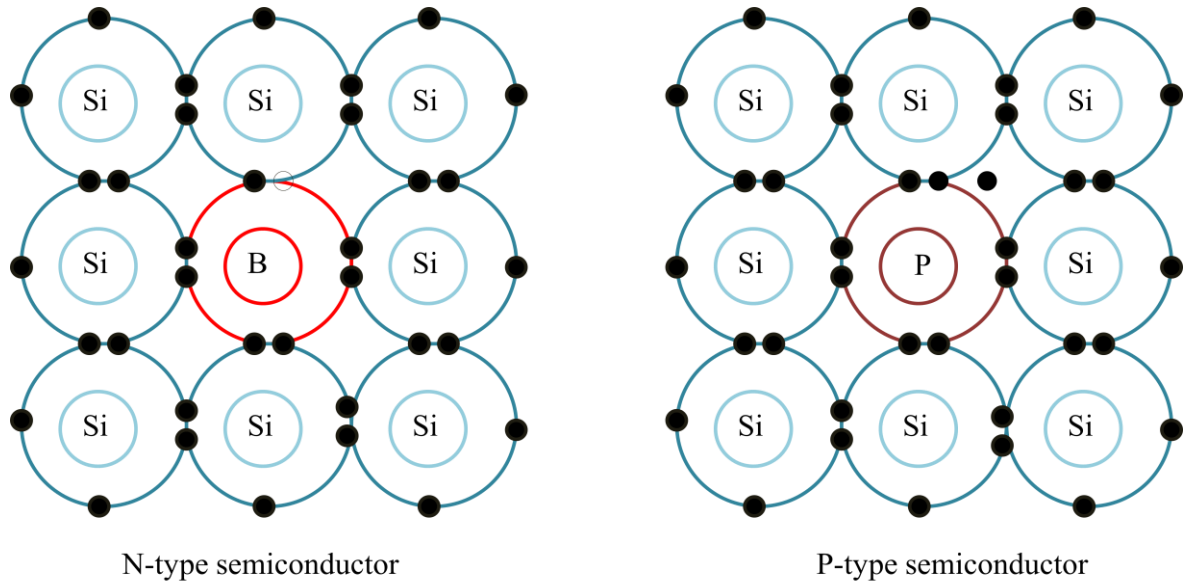


Figure 2.2: Schematic diagram of N-type and P-type semiconductors⁴

The function of these elements within an intrinsic semiconductor is to raise or lower the Fermi level (E_f) as shown in Figure 2.3.¹²

The Fermi–Dirac distribution function, $f(E)$, provides the probability of an energy level E being occupied by an electron:

$$f(E) = \frac{1}{1 + e^{(E-E_F)/k_B T}} \quad (\text{Eq 2.1})$$

Where E_F is the Fermi energy, k_B is the Boltzmann constant and T is the absolute temperature. The Fermi energy is the electrochemical potential of the electrons in a solid, also described as the energy level, where the probability of being occupied by an electron is $1/2$.¹¹

2.2.2 Homojunctions

A homojunction⁴ is composed of a junction using one material but with different doping; one doped n-type and the other doped p-type. By joining p-type and n-type semiconductors a p-n junction is formed, as shown in Figure 2.3. Important parameters such as the energy level of the vacuum (E_{vac}), the energy level of the conduction band (E_C) and valence band (E_V), the Fermi level (E_F), the band gap (E_g), the work function ($e\Phi$), the electron affinity (E_A) and ionization energy (E_I) are also labelled in the diagram.

2. Background and literature review

When the two materials are brought into contact, electrons start to diffuse from the n-type material to the p-type material, which is the same process that occurs for holes coming from the p-type material. The flow of carriers builds up an electric field that starts to hinder further diffusion until equilibrium is reached. The energy band structure is shown in Figure 2.3.⁴

When the p-n junction is illuminated with an energy $h\nu > E_g$, a photon is absorbed and an electron-hole pair is generated. The charge density of the electron and hole are enhanced above their equilibrium values and their quasi Fermi levels are separated. Due to the field at the junction, the increase of excess carriers start to flow and can be delivered to the external circuit.⁴

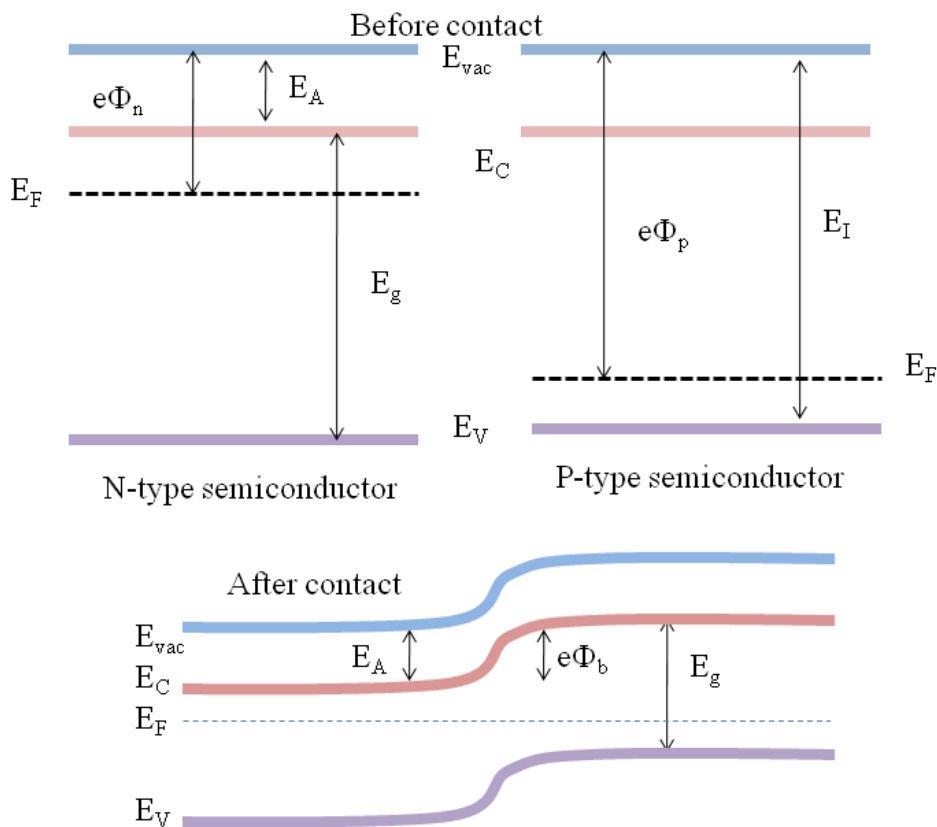


Figure 2.3: Illustration of the p-n junction between an n-type semiconductor and a p-type semiconductor⁴

The first form of solar energy technology to produce useful efficiencies and become commercialised and commonly used is pn-silicon. As of today, this still dominates other semiconductors, holding 95 % of the international solar cell market.

2.2.3 Heterojunctions

The heterojunction⁴ is in principle similar to homojunctions except that two different semiconductors of different band gaps are used. This photovoltaic design offers an opportunity to prepare efficient solar cells from highly absorbing thin-film materials without substantial losses through electron-hole recombination at the surface. CdS/CdTe¹³ and CdS/CIGS¹³ solar cells are examples of such a structure. Heterojunction semiconductors are also used in lasers, for the conversion of nuclear energy into electrical power and batteries.¹⁴ Figure 2.4 shows a typical band diagram for a p-n junction between a wide band gap n-type semiconductor and a p-type semiconductor.

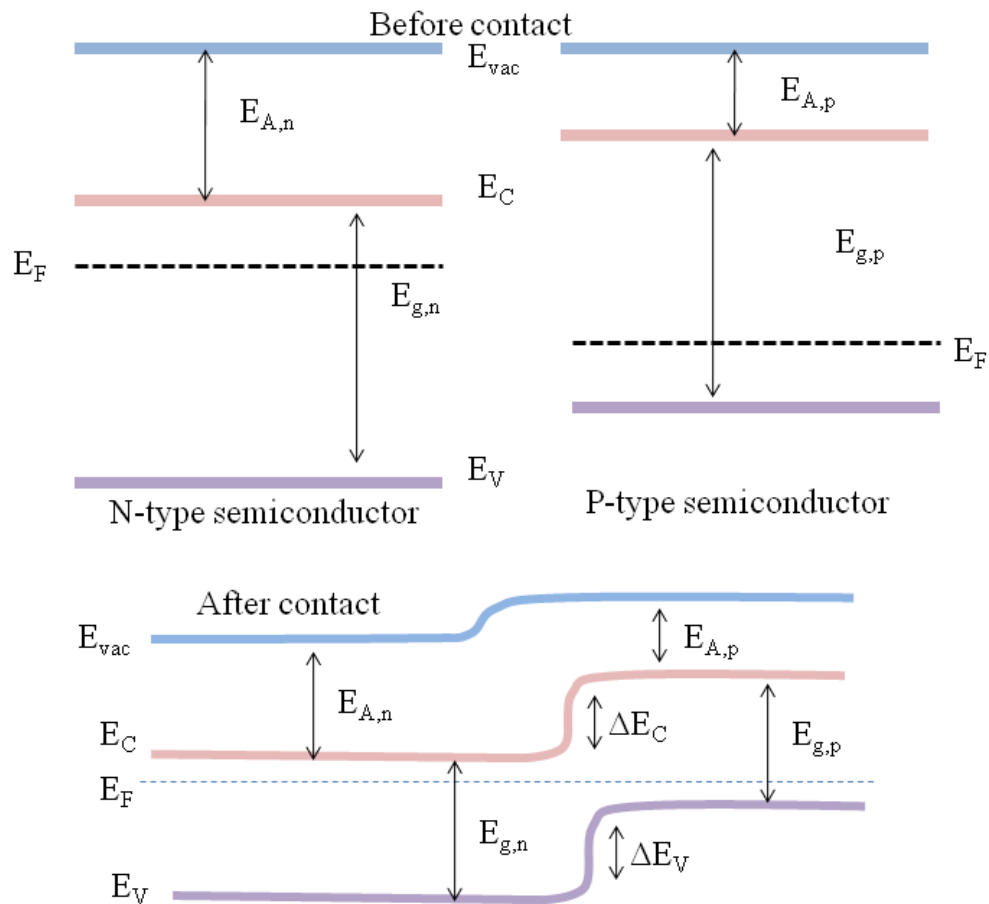


Figure 2.4: Illustration of a p-n heterojunction between two semiconductors with different energy band gaps⁴

2.2.4 Metal-semiconductor junction

The metal-semiconductor^{15, 16} junction is of great importance as it is present in many semiconductor devices. It can form either an ohmic or Schottky barrier depending on the

2. Background and literature review

position of the Fermi level. When the n-type semiconductor is brought into contact with a metal of larger work function, an electric field is set up close to the interface. This electric field will drive electrons from the semiconductor to the metal and holes will thus remain in the semiconductor. Because the metal has a larger charge carrier density, band bending can only occur in the semiconductor. The depleted space charge region is often called the depletion region.

A typical band diagram is shown in Figure 2.5, showing the difference in Fermi level, where the work function of the metal is larger than the work function of the semiconductor.

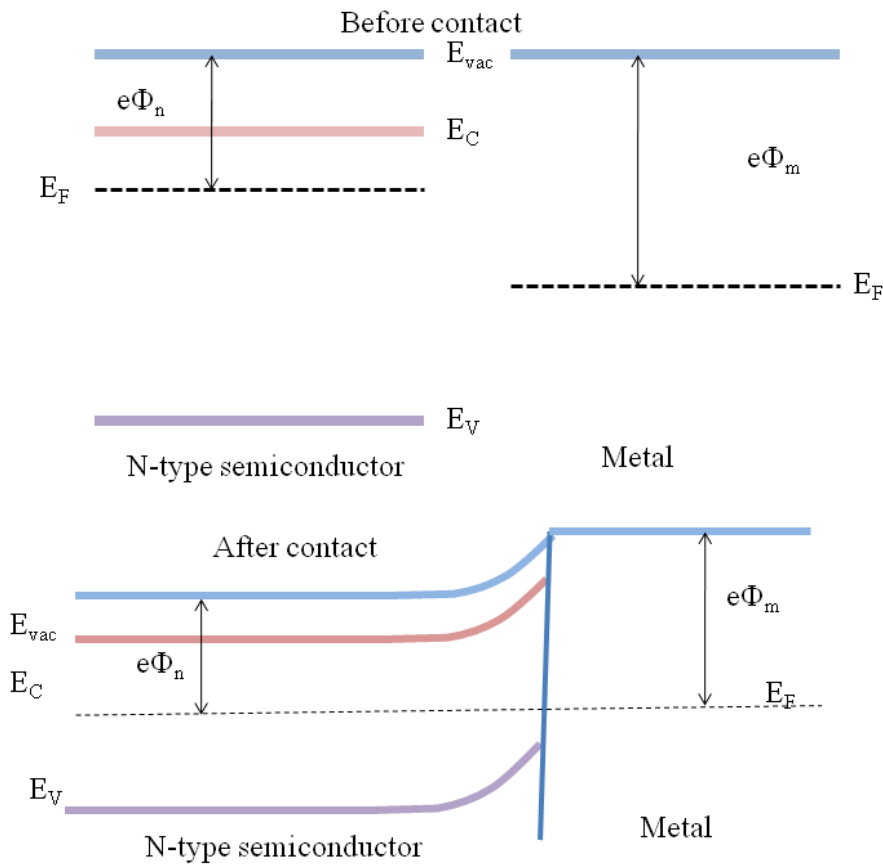


Figure 2.5: Illustration of the Schottky barrier between an n-type semiconductor and a metal

An ohmic barrier occurs at the metal-semiconductor junction when the Schottky barrier is low enough to allow the carriers to move freely in and out the semiconductor, thus creating only a very low resistance across the junction.

2.3 Photovoltaic devices: conventional solar cells, emerging technology and commercialization

The aim of photovoltaic solar research and development is not only to reduce the cost of PV cells and modules, but also to make them more efficient and competitive than conventional ways of generating power. One way to achieve this is to increase the conversion efficiency of the PV devices. In order to increase the efficiency, semiconductor materials with appropriate band gap energies should be developed. Their optical, structural and electrical properties should be properly engineered to match the solar spectrum so that they can effectively collect charge and better utilize the solar spectrum.

Silicon is the most widely used light absorbing semiconductor and crystalline silicon is used to manufacture solar panels. They are classified as first generation solar cells. These devices delivered high efficiency but at a high cost. Even though they are expensive, they still dominate the solar market with an 89 % market share. Crystalline silicon can be divided into two types: single-crystal silicon and polycrystalline silicon. In single crystalline silicon, efficiency of the order of 15 to 25 % can be achieved.¹⁷

Another category of photovoltaic devices using the same operating principal as silicon-based PV is the III-V solar cells. GaAs¹⁸ is an example of this type of semiconductor and its electronic properties are much better than pn-Si. GaAs has a band gap of 1.4 eV,¹⁹ which is near ideal for single junction solar cells. This semiconductor can be doped with aluminum, indium and antimony to achieve higher performance. GaAs can achieve performances of 29 % under concentrated light, compared to silicon which only reaches an efficiency of 27 %, and this is close to the maximum theoretical efficiency that can be achieved of 31 %.^{17, 20, 21} However, even though GaAs is more effective than Silicon, the cost of production is much greater.

Second generation solar cells have lower efficiency but are cheaper to manufacture.²² Thin film solar cells are classified as second generation solar cells as they required minimum material and involve a cheaper fabrication procedure. The most successful thin film solar cell is CdTe, with an efficiency of 18 %.²²

Other semiconductors that can be used in thin film solar cells are amorphous silicon, cadmium telluride, copper sulphide-cadmium telluride and copper indium diselenide. These semiconductors can be easily deposited onto inexpensive substrates such as glass,

2. Background and literature review

flexible plastic or stainless steel. Even though these types of solar devices seem very interesting and cost effective, the main issue is the long term stability of the device. For instance, the main issue of $\text{Cu}_2\text{S}/\text{CdS}$ cell is the migration of copper ions, which can short-circuit the device. Another important issue is the toxicity of the materials. Dye sensitised solar cells are considered to be second generation solar cells, as the cost of production is not expensive, and the efficiency for the moment is still low as compared to first generation solar cells.²³

The term ‘third generation solar cells’ is ambiguous as it uses the concepts of the first and second generation solar cells in other devices, such as hot carrier devices, polymer devices and tandem cells. At Monash University, work is being done on tandem devices and an improvement in device efficiencies was achieved.²⁴ Even though only a modest performance is obtainable with these types of devices, there is a possibility of further increasing the conversion efficiency, by carefully engineering each part of the device. The first type of third generation solar cells to attain popular recognition were multi-junction devices based on a triple junction $\text{GaInP}/\text{GaInAs}/\text{Ge}$, with a record performance of 40.7%.²⁵ Figure 2.6 shows the development of photovoltaic devices throughout the years. It is important to have an understanding of the field of DSSC with respect to the recent progress of other solar technologies.

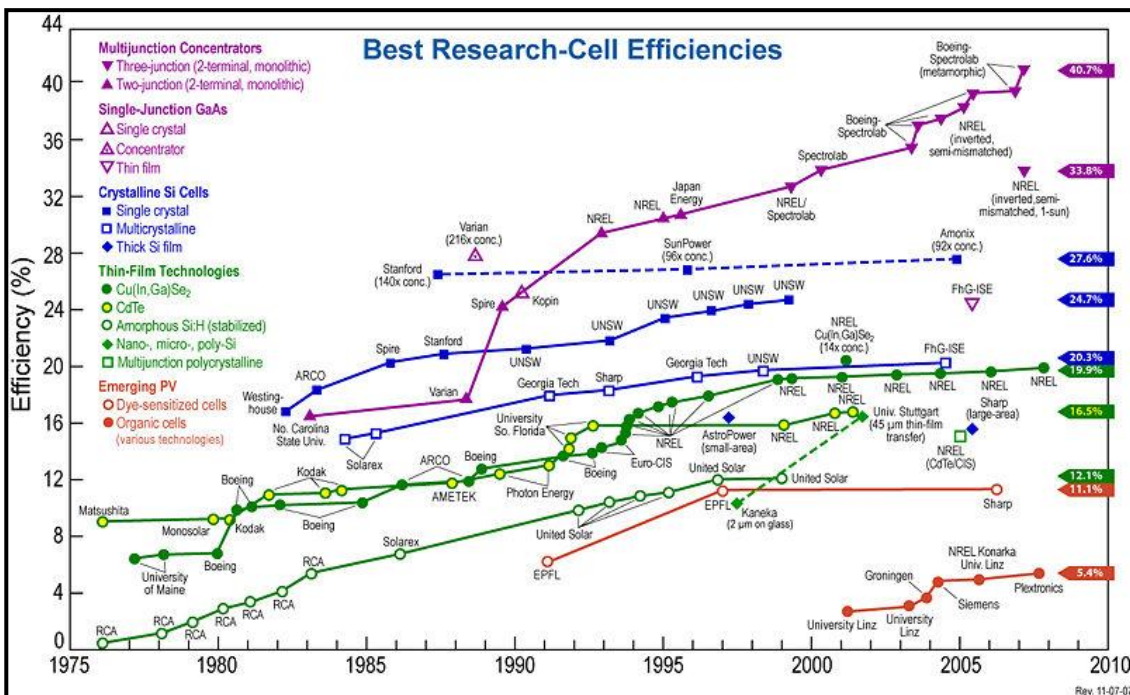


Figure 2.6: Development of photovoltaic devices from 1975 to 2010²⁷

Figure 2.7 depicts the cost and the efficiencies of the different generations of photovoltaics. The first generation data is mainly based on actual products. Single junction silicon cells are approaching the theoretical limit efficiency of 33 %, and can reach cost parity with energy derived from fossil fuels.¹⁷ The second generation is based on a combination of actual and speculative products. As previously stated, dye sensitised solar cells form part of the second generation materials, and they can offer significantly lower production costs, thus there is potential for commercializing these products. Finally, the third generation data is mostly speculative. It is aimed at enhancing the poor performance of the second generation solar cells technologies, while retaining the low production costs. Nevertheless, from the chart, it is clear that photovoltaic devices have the potential to be viable, and that the cost of solar electricity has the potential to be much lower than fossil fuels.²⁶

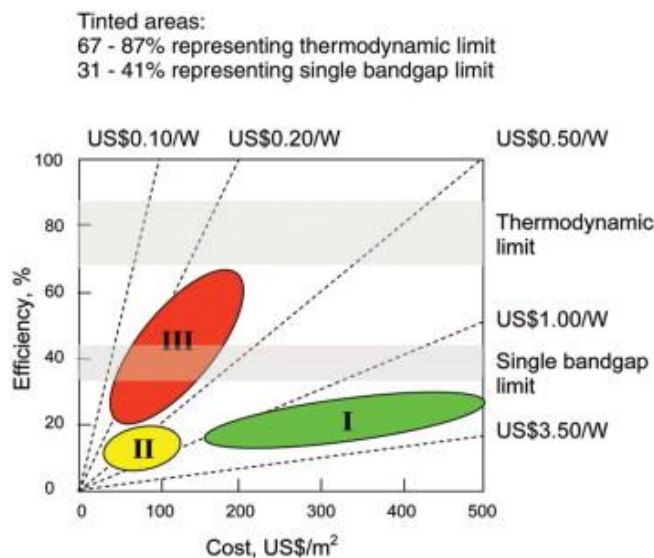


Figure 2.7: Schematic representation of estimated efficiencies and costs²⁷

2.4 Photoelectrochemical cells

2.4.1 The electrolyte

The electrolyte in a photoelectrochemical cell usually consists of cations, anions and a redox couple. When describing the electrolyte in contact with a semiconductor, it is important to describe it in the same terms as the semiconductor; i.e. in terms of energy levels.²⁸ The energy level of ions in solution reflects the tendency of the electroactive species to donate or receive electrons when it reaches the electrode. The energy level model for an electrolyte is quite complicated because the polar solvent around the ions has

2. Background and literature review

a great impact on their energy level. The potential distribution of the ion is affected by both the solvent and thermal fluctuations.¹¹

The probability that the energy of the ion of the redox couple has changed to another level due to thermal fluctuations in the electrolyte is given by the function $W(E)$. The intersection of the distribution of the oxidized and reduced species in the electrolyte (as shown in Figure 2.8), assuming equal concentration, can be interpreted by the electrochemical potential E_{redox} or the Fermi level of the electron in the liquid phase,²⁹ where:

$$E_{Redox} = \frac{(E_{Ox} + E_{Red})}{2} \quad (\text{Eq 2.2})$$

The electrochemical potential of electrons in the redox electrolyte is given by the Nernst equation:²⁹

$$E_{Redox} = E_{Redox}^{\circ} + \frac{R_g T}{nF} \ln\left(\frac{C_{Ox}}{C_{Red}}\right) \quad (\text{Ox} + ne \rightarrow \text{Red}) \quad (\text{Eq 2.3})$$

Where E_{Redox}° is the standard redox potential, R_g is the common gas constant, T is the temperature, n is the number of electrons transferred, F is the Faraday constant, C_{ox} is the concentration of the oxidised species and C_{red} is the concentration of the reduced species. Electrochemists traditionally used the standard hydrogen electrode as a reference point, whereas in the semiconductor solid state physics community, the vacuum level is taken as the zero point reference.³⁰

The redox potential can be easily expressed versus the vacuum level using the following equation:³⁰

$$E_{F, Redox} = -4.5 \text{ eV} - e E_{Redox} \quad (\text{Eq 2.4})$$

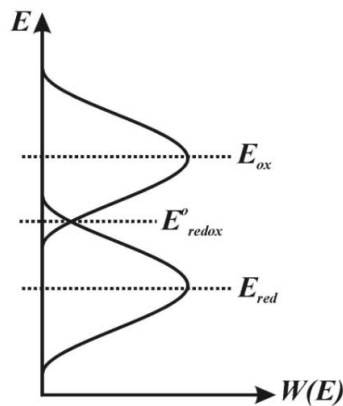


Figure 2.8: The energy levels of a redox couple in a solvent

2.4.2 Semiconductor-Electrolyte junction

A semiconductor-electrolyte junction is equivalent to the metal-semiconductor junction but uses a liquid electrolyte containing a redox couple rather than an electronic conductor to form the junction. During the illumination of the semiconductor-electrolyte junction, photoelectrochemical reactions can occur. A photoelectrochemical cell consists of a working electrode (semiconductor attached to a conducting substrate), a counter electrode and an electrolyte between the two electrodes. The electrodes are interconnected via an external circuit.

The theory of the semiconductor-electrolyte junction was first formulated by Gerischers.³¹ According to this theory, when an n-type semiconductor is brought into contact with an electrolyte containing a redox couple, electrons start to flow from the semiconductor into the electrolyte until the Fermi levels equalize, creating a positive space charge layer in the semiconductor. Charge carriers generated by band gap excitation of the semiconductor are separated by the electric field in the space charge region. The major carriers move to the bulk while the minor carriers (holes) move towards the surface where they react with the redox couple in the electrolyte. Hence, a photovoltage is built up within the semiconductor phase that may drive an electric current through an external circuit. For the current to flow through the external circuit, the oxidized species must be able to recover an electron from the counter electrode and regenerate the reduced form.

This electrochemical junction has the advantage that the field is established spontaneously when the semiconductor is immersed into an electrolyte solution. An example of photoelectrochemical cells is the dye sensitized solar cells, also known as the “Grätzel cell” after the inventor.

Figure 2.9 illustrates the schematic energy diagram of the semiconductor-electrolyte junction under different bias situations: (a) before contact, (b) under a flatband condition, (c) under a depletion situation at equilibrium and (d) under accumulation at equilibrium for an n-type semiconductor.

2. Background and literature review

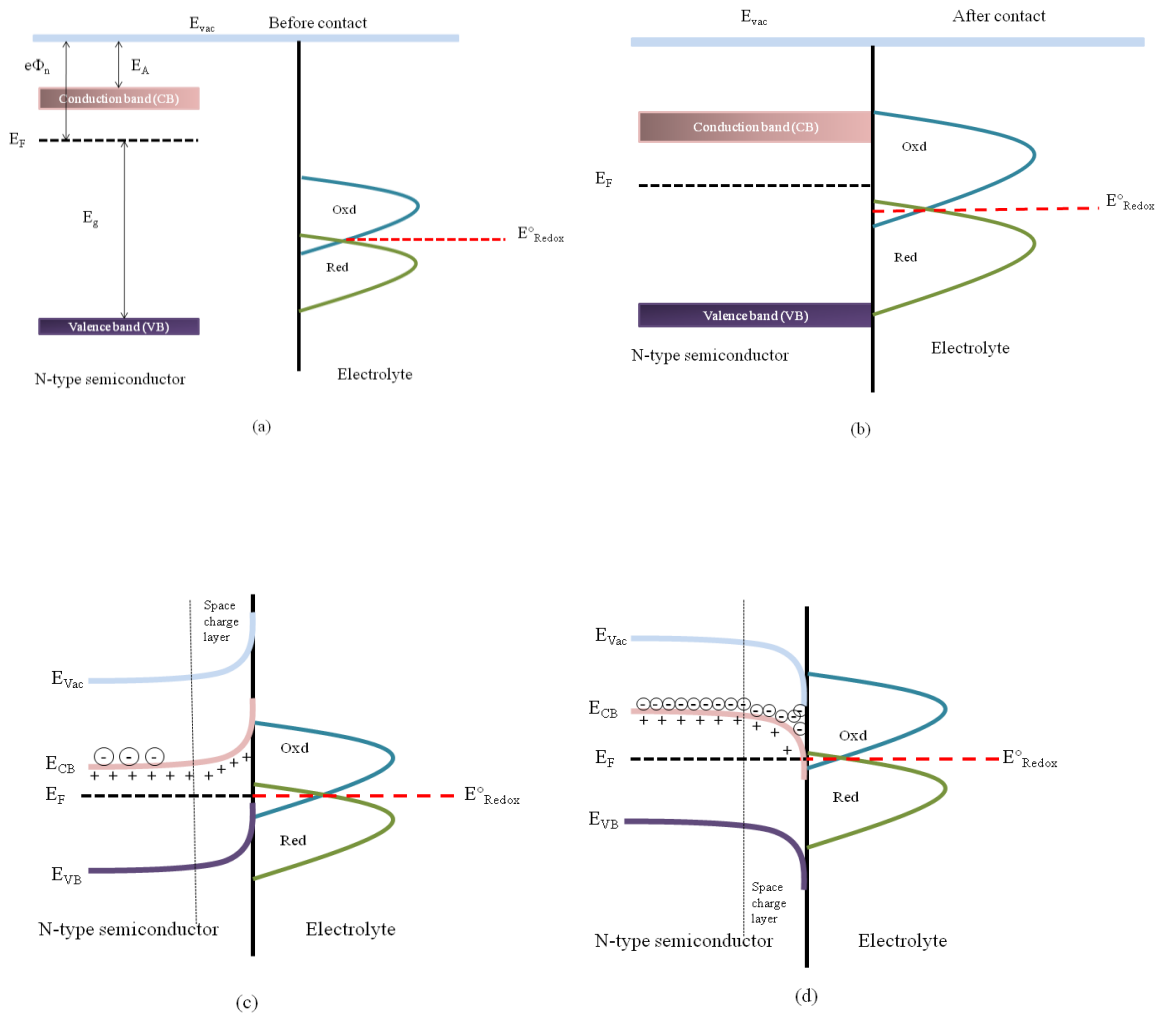


Figure 2.9: (a) Before contact, (b) flatband potential condition, (c) depletion and (d) accumulation situation under equilibrium conditions for an n-type semiconductor⁴

For an n-type semiconductor, if $E_F > E^{\circ}_{Redox}$, electron transfer occurs from the conduction band of the semiconductor into the electrolyte causing a deficit of the majority charge carrier, and then a depletion layer is established in the semiconductor. The reverse situation happens when $E_F < E^{\circ}_{Redox}$, whereby the electrolyte in this case injects electrons into the conduction band of the semiconductor causing an excess of the major charge carriers and therefore an accumulation layer is established in the semiconductor. The thickness of the space charge layer varies between 10^{-4} and 10^{-6} cm.³²

The flatband potential is defined as the potential at which the semiconductor bands are flat i.e. there is zero space charge in the semiconductor and no band bending, as shown in Figure 2.9 (b). The flatband potential is usually measured with respect to a reference electrode and several methods can be used to establish the flatband potential of a semiconductor. Chapter 5 gives a full description of the methods used to determine this important parameter and also the effect of impurities.

2.4.3 Dye sensitised solar cells

The biggest breakthrough in the development of dye sensitised photoelectrochemical technology was almost undoubtedly in 1991, with the incorporation of nanoparticles with very large surface areas; cells with efficiencies of 7 % were reported. Importantly, this value is based on pan-chromatic light (simulated AM 1.5 sunlight).³³ This type of cell has since been further improved, with Chiba *et al.* reporting an efficiency of 11 %.³⁴ Unfortunately, the enhancement in device efficiency has been relatively slow in recent years. 10 % efficient cells were realised in 1993, using a ruthenium sensitizer (N3) with a thick titania film.³⁵ With the improvement in ruthenium based dyes, only 1 % has been added to this efficiency in the 13 years since.

A number of different strategies have progressed in order to try and improve the efficiency of these cells. For instance, core-shell treatment extended sensitisation range with new dyes or cocktail dyeing,^{36, 37} alternate redox couples (detailed later),^{38, 39} by altering the particle morphology or using other semiconductors as detailed further in the next section,^{40, 41} by treating the semiconductor with acid (which is investigated in Chapter 8) or addition of a co-adsorbent into the dye solution. Recently, a further increase in device performance was obtained by Chen *et al.*,⁴² by addition of di-n-hexyl bis-(3,3-dimethyl-butyl)-phosphonic acid in a modified high molar extinction coefficient ruthenium dye coded CYC-B11. By incorporating electron rich thiophene derivatives as an extended ligand, an increase in extinction molar coefficient was achieved. This makes it interesting for use with solid state electrolytes, where a thin film is required for the cell to perform better without any significant loss in photocurrent. The use of this sensitizer with a volatile electrolyte yields a photocurrent density of 20.05 mA cm⁻², a V_{oc} of 743 mV, a fill factor of 0.77 and an efficiency of 11.5 %.⁴²

2. Background and literature review

The incident-photon-to-current-conversion efficiency (IPCE) spectrum shows a broad adsorption range from 460 nm to 685 nm, with a maximum of 95 % at 580 nm. So far, this is the highest efficiency ever achieved. As stated earlier, various methods have been used in order to improve the device performance. In the following section the different components of the DSSCs are discussed.

2.4.4 Functioning of DSSCs

2.4.4.1 Working principle

A schematic presentation of the operating system of the DSSC is shown in Figure 2.10. The basic element of a DSSC is a nanostructured material composed of titanium dioxide (TiO_2) that is sintered on a transparent conductive oxide (TCO) glass. This electrode is soaked in a dye solution so that the dye is anchored to the surface of the film.⁴³ If the dye has ground and excited states in an appropriate energetic position (see Figure 2.10), this excitation of the dye can lead to charge injection into the semiconductor and, importantly, the dye is then restored via charge transfer from a redox couple in the electrolyte.

Under illumination, electrons are excited within the dye, giving them enough energy to be injected into the conductive band of the TiO_2 (as shown in Equations 2.5 and 2.6). The electrons flow through the TiO_2 onto the electrodes, through an external circuit and then to the counter electrode (CE). The original state of the dye is restored by electron donation from the redox couple in the electrolyte. For efficient restoration of the dye, the redox couple should be more positive than the ground state of the dye. Typically, the redox couple consists of iodide/triiodide in an organic solvent (such as acetonitrile, methoxypropionitrile).^{33, 44} The circuit is completed by the redox shuttle, which is oxidised by the photoexcited dye and is regenerated at the counter electrode with the assistance of a catalyst. Typically, both electrodes are made on transparent conductive substrates, allowing some light to be transmitted; one of the main commercial appeals of the technology used in dye sensitised solar cells.

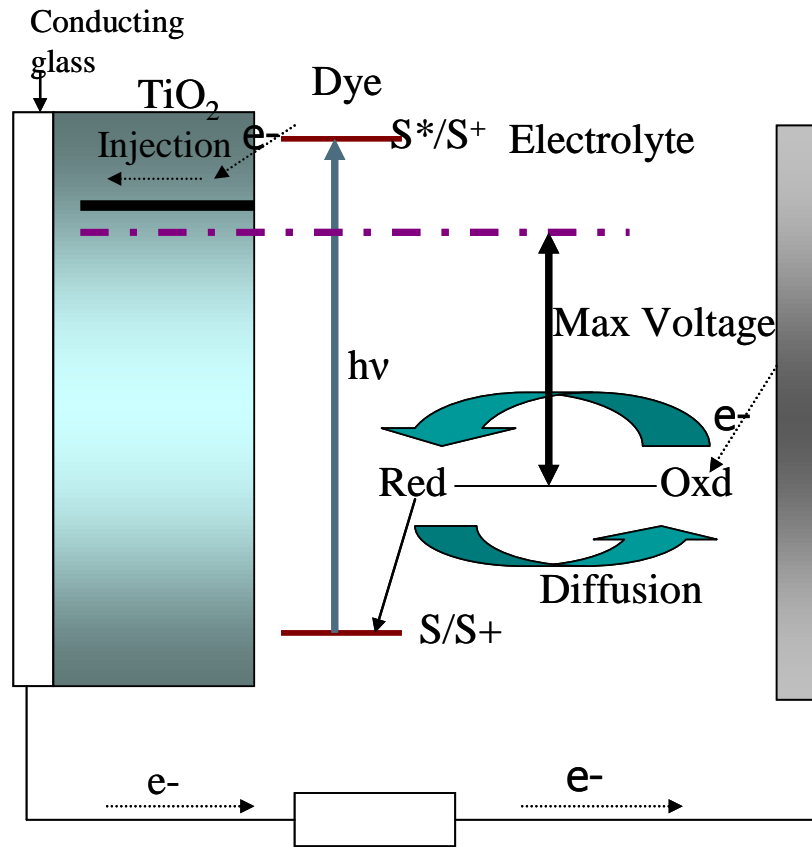


Figure 2.10: Schematic diagram of a dye sensitised solar cells



2. Background and literature review

2.4.4.2 Kinetics of DSSCs

The electron transfer kinetics in a DSSC are an important factor in understanding the working principles of the photoelectrochemical solar cell and its limitations.

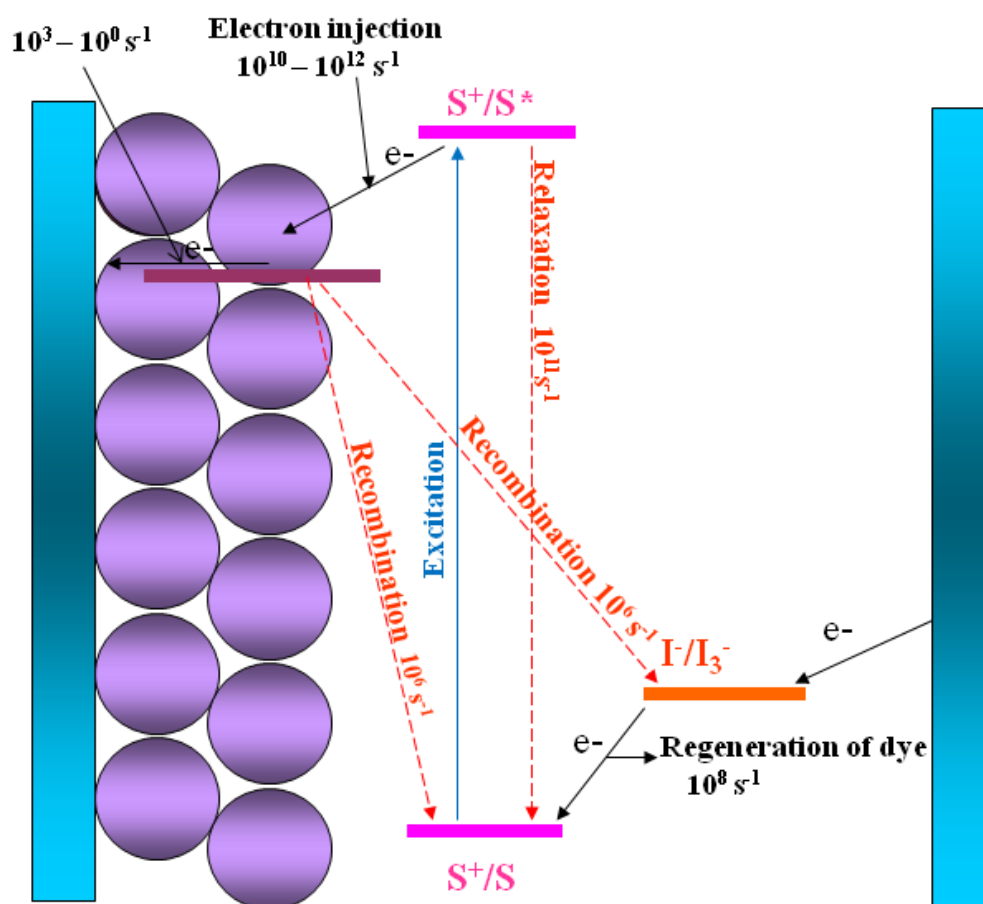


Figure 2.11: Schematic diagram showing the kinetics of a dye sensitised solar cell

Figure 2.11 shows the different kinetics of the processes that occur in a DSSC. Upon illumination, the dye is excited to a higher energy level in the time domain of femtoseconds,⁴⁵ resulting in the formation of an electron hole pair. The electron is injected into the TiO₂ within 1 picosecond and this is the fastest chemical process occurring in the DSSC. The electron can then either percolate to the back contact of the TCO, or can be lost due to recombination with either the oxidized dye, or with the triiodide in the electrolyte solution.

These two recombination processes occurs within the microsecond timescale.⁴⁶ The recombination reaction (Table 2.1) is very critical and can limit the performance of the DSSC. The other desirable reaction, the regeneration of the dye by iodide, is also a fast reaction, occurring in the tens of nanoseconds.⁴⁷ Table 2.1 summarises the different electron processes and the time domain in which they occur.

Table 2.1: Summary of the kinetics in a dye sensitised solar cell

	Reaction		Time domain
1	$S + hv \rightarrow S^*$	excitation	fs
2	$S^* \rightarrow S^+ + e^- (TiO_2)$	injection	fs-ps
3	$S^* \rightarrow S + hv$	relaxation	ps
4	$S^+ + I^- \rightarrow S + I_3^-$	regeneration	ps-ns
5	$S^+ + e^- (TiO_2) \rightarrow S$	recombination	μs
6	$I_3^- + 2e^- (TiO_2) \rightarrow 3I^-$	recombination	μs

2.4.4.3 Loss mechanisms and limiting factors

There are several factors that can limit the performance of the DSSC with molecular liquid electrolytes such as corrosion, leakage, degradation and evaporation. Thus, alternatives for these electrolytes are sought, such as organic ionic plastic crystals (OIPCs) and ionic liquids. These salt-based electrolytes have a very low vapour pressure, which should resolve the evaporation problem of the liquid electrolytes.

Other limiting factors include the relatively high loss of energy in the system due to the large difference in redox potentials. Other losses are due to device resistance, reflection and adsorption of the TCO glass and bad contact between the nanoparticles of the TiO_2 . The cell is further limited by the solar light harvesting, which is related to the amount of dye on the surface of the TiO_2 and also the properties of the dye itself.

2. Background and literature review

2.4.5 Photovoltaic performance

A solar cell can be represented by a current source connected in parallel with a diode, as shown in Figure 2.12.

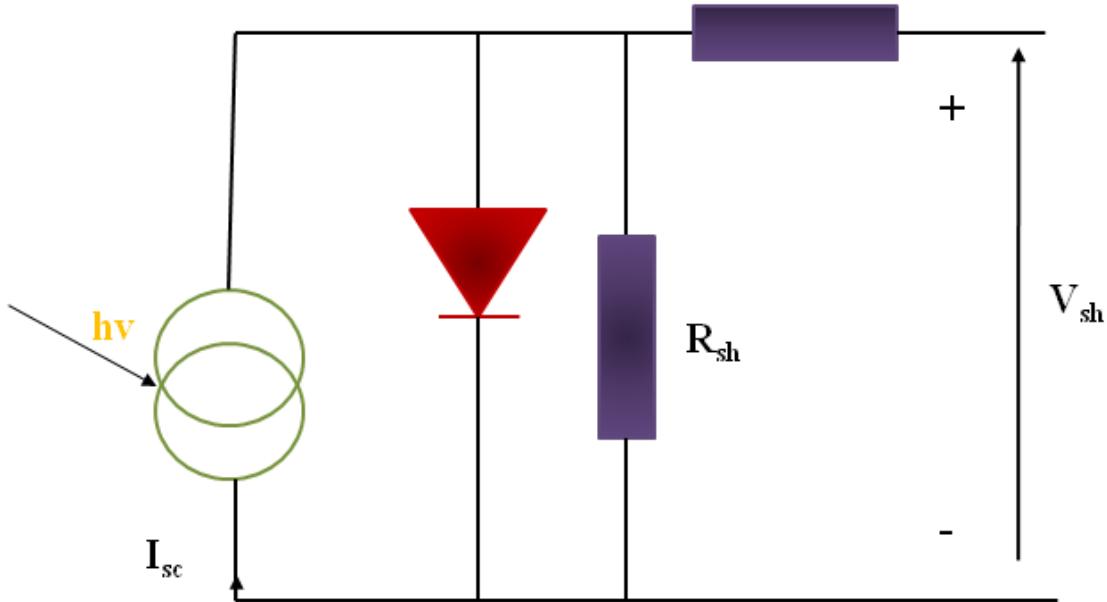


Figure 2.12: Equivalent circuit of a solar cell

The important property of a p-n junction is the current-voltage characteristics. A derivation requires discussion of diffusion and recombination of carriers. The result is:

$$I = I_0 \left(e^{\frac{eE}{k_B T}} - 1 \right) \quad (\text{Eq 2.10})$$

where k_B is the Boltzmann constant, T is the absolute temperature, e is the electron charge, E is the potential at the terminals of the cell and I_0 is the saturation current of the junction.⁴

The short circuit, I_{sc} is the current obtained when there is no potential across the cell, as shown in Figure 2.12. I_{sc} is dependent on the incident light.

The open-circuit voltage, V_{oc} , is the maximum voltage available from a solar cell, and this occurs at zero current. The open-circuit voltage corresponds to the amount of forward bias on the solar cell due to the bias of the solar cell junction with the light-generated current.⁴ The open-circuit voltage is shown on the current-voltage (IV) curve below.

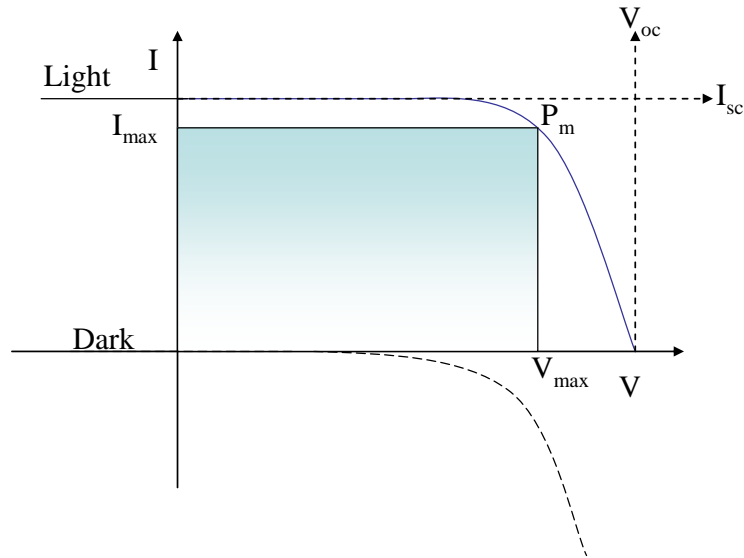


Figure 2.13: Schematic IV curve of a solar cell showing open circuit voltage (V_{oc}) and short circuit current (I_{sc})

A solar cell can function over a wide range of voltages and currents. By increasing the voltage of the cell from zero to V_{oc} , a maximum output electrical power is obtained.⁴

$$P_m = I_{max} \times V_{max} \quad (\text{Eq 2.11})$$

Another important characteristic of the solar cell performance is the fill factor. This is the ratio of maximum power output divided by V_{oc} and I_{sc} .⁴

$$FF = \frac{V_{max} I_{max}}{V_{oc} I_{sc}} \quad (\text{Eq 2.12})$$

The solar cell efficiency (η) is defined as the ratio of the maximum power output to the energy of the incident irradiant solar light.⁴

$$\eta = \frac{P_{MAX}}{P_{light}} = \frac{V_{max} I_{max}}{P_{light}} = \frac{FF \times V_{max} I_{max}}{P_{light}} \quad (\text{Eq 2.13})$$

The efficiency of the solar cell depends on the temperature of the cell, the light intensity and the spectral distribution of the light intensity (Figure 2.13).

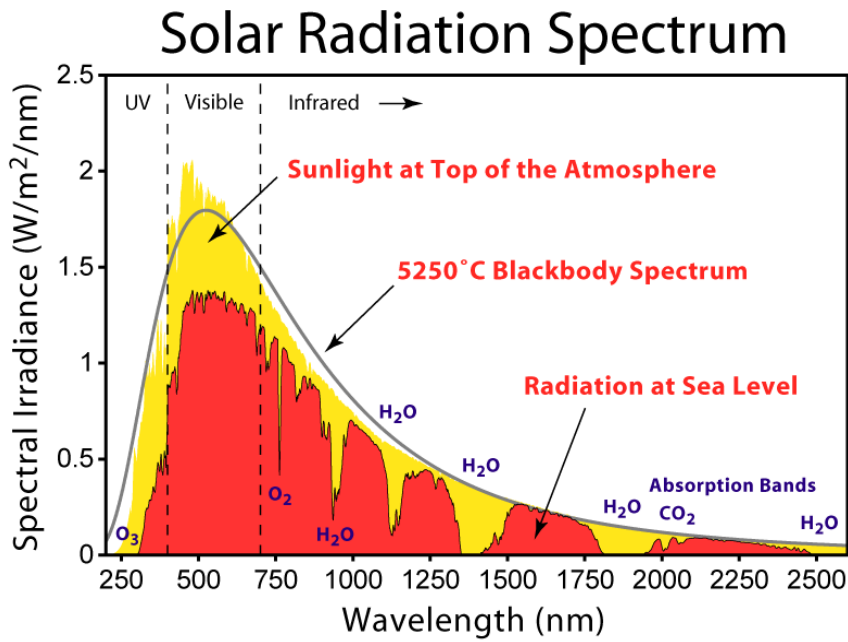


Figure 2.14: The solar spectrum⁴⁸

In standard testing conditions, the light intensity is 1000 W m^{-2} , the spectral distribution is that of AM 1.5 global standard solar spectrum and temperature is $25 \text{ }^\circ\text{C}$.⁴⁹

These four quantities, I_{sc} , V_{oc} , ff and η are the key parameters characteristic of a solar cell.

The incident monochromatic photon-to-current conversion efficiency (IPCE) value is the ratio of the observed photocurrent divided by the incident photon flux, uncorrected for reflective losses for optical excitation through the conducting glass electrode.

$$IPCE = \frac{125 \times \text{photocurrent density}}{\text{wavelength} \times \text{photon flux}} \quad (\text{Eq 2.14})$$

2.4.6 Materials in DSSCs

As already stated, the DSSC is composed of five main components. In order to improve the performance, stability and cost of the device, researchers have looked at each individual component. One thing to keep in mind with this strategy is that when changing one aspect of the DSSC, the relationship to the other parts must not be underestimated. The challenge for all researchers is to look at the device as a whole, as well as at the individual components, when trying to make further improvements.

2.4.6.1 Substrates

Electrodes for DSSCs are mainly produced on TCO glass, with a transparent layer of the semiconductor coated on top. Other flexible substrates have been employed, such as TCO coated polymers (notably PEN and PET) which are better for commercialisation as they are more flexible.⁵⁰ Metal sheets have also been used for one half, as long as the substrate is resistant to the redox mediator, although TCO glass is by far the most popular choice.⁵¹⁻
53

The most commonly used TCO glasses in solar and other applications (electrochromic devices or flat panel) are fluorine doped tin oxide (FTO) and tin doped indium oxide (ITO). FTO is preferred as it is more thermally stable compared to ITO. ITO is mainly used on flexible substrates due to its low toxicity and easy deposition. Also, in a non-annealed state, it has a dramatically lower sheet resistance than FTO; i.e. the heat treatment is less substantial.⁵⁴

2.4.6.2 Semiconductors

As discussed in the previous section, there are two types of semiconductors; n-type and p-type. The most common semiconductor used in “Grätzel cells” is an n-type semiconductor. For tandem devices, a p-type semiconductor is preferred. In this section, a brief summary of the different n-type and p-type semiconductors used in the dye sensitised solar cells field will be described.

2.4.6.2.1 N-type semiconductors

The semiconductor in conventional solar cells acts as a means to harvest the light, resulting in charge separation and transport. In DSSCs, light harvesting is mainly performed by the sensitiser adsorbed on the semiconductor, thus the role of the semiconductor is primarily that of charge transport. Because the semiconductor is not the main light harvester, a wide band gap semiconductor can be used. Metal oxides are commonly used due to the fact that the dye can adsorb directly onto their surface, through a number of suitable binding groups.

Since the semiconductor is the host of the dye, it must have a large surface area, high mechanical stability and good electrical connectivity in order to better facilitate light harvesting as well as charge extraction. Controlling the morphology of the film is therefore

2. Background and literature review

critical. It is vital to understand and consider the properties of the semiconductor from the perspective of a dye sensitized solar cell. Properties such as charge carrier density and charge mobility should also be considered. Highly doped semiconductors can be problematic as this increases the probability of the recombination process between the semiconductor and the redox couple, reducing the performance of the device.

Titania is the most widely studied semiconductor in DSSCs. It exists in three crystalline forms, as either brookite, anatase or rutile. The last two are the most important. The anatase phase is usually preferred, as it gives films that are fundamentally transparent and colorless. TiO_2 is considered as an n-type semiconductor and it has excellent mechanical, optical and chemical properties. Titania has a band gap of 3.2 eV, which corresponds to 388 nm, meaning that it can only absorb limited amounts of direct sunlight. Because of the large scale production of TiO_2 , this material is cheaper than silicon and is easily available from different industrial sources.

A number of other metal oxide semiconductors have also been considered for the production of functional DSSCs. For example, CdO, ZnO, SnO_2 , ZrO_2 , Nb_2O_5 , Fe_2O_3 , WO_3 and Ta_2O_5 have all been used as the photoelectrode in DSSCs. Mane and co-workers demonstrated that CdO can be used as a photoelectrode in DSSCs.⁵⁵ CdO has been widely used in other applications such as diodes, sensors and electronic devices. This material shows high transparency in the visible region of the solar spectrum, making it an interesting candidate as a photoelectrode. Unfortunately, as demonstrated by Mane and co-workers, only a very modest performance was obtained for CdO coated with N3 dye. The device achieved only 2.95 % efficiency, with poor fill factor the main limiting factor. Efforts are being made in order to enhance the fill factor, which may substantially increase the device performance. ZnO has also been considered as an alternative photoelectrode due to the similarity in band gap energy to that of TiO_2 .⁵⁶ The use of ZnO as a photoelectrode has some advantages, such as the ease in which it is produced in different forms, and the fact that it has a high electron mobility of $115\text{-}155 \text{ cm}^2 \text{ V}^{-1} \text{ s}^{-1}$, compared to $10^{-5} \text{ cm}^2 \text{ V}^{-1} \text{ s}^{-1}$ for TiO_2 .^{57, 58} Also, according to Hagfeldt and co-workers, the carrier lifetime in ZnO is longer than that in TiO_2 , and it possesses low trap density, making the electrons move faster.⁵⁹ In the past few years, ZnO has been used in DSSCs, but the conversion efficiency of the devices was quite poor.⁶⁰ An improvement in device performance was recently obtained by Zhang *et al.*, by using lithium salts to grow the ZnO aggregates. Devices made

with this Li-ZnO film, with N3 as the sensitizer and a liquid electrolyte, gives an efficiency of 6.1 %, which is the highest performance ever obtained with ZnO.⁵⁶ This enhancement is due to the presence of lithium ions, which has an effect on the growth of the ZnO aggregates, and thereby affects the morphology of the film. In the past, conversion efficiencies varying between 0.35 to 5.0 % were achieved with this photoelectrodes.⁶¹⁻⁶³ The poor performance of the ZnO comes from the stability of ZnO in acidic conditions. The proton from the Ruthenium sensitizers makes the dye solution relatively acidic, which partially dissolves the ZnO to form Zn^{2+} dye aggregates. In order to solve this problem, ZnO should be immersed in an ethanol solution under reflux.⁶⁴

The best performance achieved by SnO_2 is 5.0 %. Recently, Wang *et al.* demonstrated that the use of a hierarchical structure of SnO_2 enhanced the performance of the device.⁶⁵ An efficiency of 6.4 % was obtained with a film thickness of 13.2 μm , which gave a photocurrent of 14.4 $mA\ cm^{-2}$ and a V_{oc} of 763 mV. This enhancement is mainly due to the efficient light scattering effect of the hierarchical structure.

In order to enhance the performance of metal oxide photoelectrodes, some have been mixed with other metal oxides. Ito and colleagues have investigated the binary SnO_2/ZnO electrodes for dye sensitised solar cells, giving efficiencies of 6.34 %.⁶⁶ Tennakone *et al.* have been able to achieve a performance of 8 % using the same composite photoelectrode (SnO_2/ZnO) with good stability.⁶⁷ However, there is still a long way to go before any other metal oxides can reach the performance obtained by TiO_2 . Nb_2O_5 , WO_3 , Ta_2O_5 , ZrO and many other n-type semiconductors have been considered as photoelectrodes for dye sensitised solar cells, but they are not very competitive due to poor performance. Nevertheless, they have been used as core-shell or binary composites with TiO_2 in order to decrease the recombination process that occurs when TiO_2 is in contact with the electrolyte, which primarily is the V_{oc} . An increase of 21 % in photocurrent and 8.1 % in photovoltage of the DSSCs were obtained when a thin layer of TiO_2-WO_3 composite was spin coated onto the transparent layer of TiO_2 .⁶⁸ Recently Saito *et al.* reported the use of WO_3 as energy storage electrodes.⁶⁹ They demonstrated that the device has a discharge capacity of 4.57 C after 10 h of photocharge, with the only limiting factor being the high resistivity of the membrane. Optimization of the membrane thickness as well as cell structure is still under investigation for further improvement.

2. Background and literature review

Nb₂O₅ has been used as a core shell material and as a composite with TiO₂ in an attempt to modify the electrical transport properties of TiO₂ and to increase the V_{oc}. Ahn *et al.*⁷⁰ reported that a Nb₂O₅ thin film on the TiO₂ film forms an energy barrier at the semiconductor-liquid interface leading to an increase in diffusion length from 17.3 μm (no coreshell) to 23.8 μm. They demonstrated that with a TiO₂ film thickness of 25 μm with Nb₂O₅ the increase in device performance is more significant. Other metal oxides such as MgO, SrTiO₃, CaCO₃ and Al₂O₃ have also been used in a core-shell structure to reduce recombination reactions. One should keep in mind, however, that this type of treatment only has an effect on devices that initially show poor performance. On moderately or highly efficient devices, no significant effect is observed. This is presumably because the degree of recombination occurring in high performing devices is minimal and only charge injection is affected. Furthermore, producing a good core shell structure is not trivial.

Another approach to improving the device performance is by doping the semiconductor with “impurities”. ZrO₂ is a well known metal oxide, usually used as a scattering layer to improve the capturing of light.⁷¹ Park *et al.* recently demonstrated that ZrO₂ nanofibers can also be used as a doping material for TiO₂.⁷² On increasing the amount of ZrO₂, an improvement in photocurrent density and efficiency are observed even though a decrease in fill factor and V_{oc}. The best conversion efficiency was obtained with 7 wt% ZrO₂, with a short circuit current density of 24.7 mA cm⁻², an open circuit voltage of 670 mV, a fill factor of 0.51 and an overall performance of 8.3 %. This is the first time that such high photocurrents have been obtained in a DSSC using a liquid electrolyte. If the V_{oc} and fill factor can be further improved, then the device performance could potentially surpass the current 11.5 % record for efficiency. The maximum theoretical V_{oc} that can be obtained for TiO₂-based DSSCs, with a typical I⁻/I₃⁻ redox couple, is 950 mV.⁷³ Typical experimental V_{oc} obtained with a ruthenium sensitizer and I⁻/I₃⁻ in a liquid electrolyte is 700-800 mV, due to the recombination processes occurring during the operation of the device. In an attempt to increase the V_{oc}, Feng and co-workers intentionally incorporated Tantalum into the TiO₂ and they obtained a V_{oc} of 870 mV.⁷⁴ They attributed the increase mainly due to the shift in the flatband potential of the doped TiO₂.

Another strategy used in an attempt to enhance the device performance is to control the morphology of the TiO₂ nanoparticles. The use of nanostructures such as nanowires,⁷⁵ nanorods,^{76, 77} and nanofibers⁷⁸ have been used in DSSCs. These nanostructures are more

favorable for ionic liquid-based electrolytes than the mesoporous structures.⁷⁹ A 9.3 % efficiency was obtained for DSSCs using single crystals like anatase nanowires with liquid electrolyte.⁸⁰ DSSCs fabricated using a single film of mesoporous TiO₂ beads gave an efficiency of 10.6 %, with a derivative of a ruthenium sensitizer using a liquid molecular solvent.⁸¹ This is the first time that such a performance has been obtained with a mesoporous TiO₂ film without using a scattering layer. Efforts are also underway to improve the TiO₂ semiconductor to realise high efficiency DSSCs for use with a non volatile electrolyte. The mesoporous TiO₂ beads are made up of sub micrometer sized beads. The particles are monodisperse, with a spherical morphology and an 830 nm diameter. The bigger size of the beads gives the film the ability to scatter light and also permits high dye loading.⁸²

The efficiency of DSSCs depends significantly on the properties of the semiconductor. To build up a high performing device, it is important to control the morphology and interfacial properties of the TiO₂. The surface area will affect the amount of dye adsorbed, the pore size distribution will affect the diffusion of ions through the TiO₂ network, the particle size distribution determines the optical properties of the TiO₂ and the electron diffusion depends on the interconnection of the TiO₂ particles. All of these properties should be considered for the optimization of the semiconductor.

2.4.6.2.2 P-type semiconductors

Unlike n-type semiconductors, there are relatively few p-type semiconductors investigated for dye sensitised solar cell technologies. The most common ones are NiO and CuO. CuSCN and boron doped diamond have also been investigated, and they showed quite considerable efficiencies.⁸³⁻⁸⁵ P-type semiconductors have also been used as hole conductors to replace the liquid electrolytes, and this is fully discussed in Chapter 9. NiO is presently the most common and efficient p-type semiconductor used in solar cells and is also widely used in applications such as electrochromic devices, super-capacitors and gas sensors.⁸⁶ Quite good performance has been recently achieved with this oxide in tandem photovoltaic devices.^{24, 87} The highest reported values of DSSCs using NiO is 0.41 %, with a V_{oc} of 218 mV and a I_{sc} of 5 mA cm⁻². CuO is another p-type material that has been used in DSSCs and the best performance was obtained after annealing the oxides at 300 °C, yielding an efficiency of 0.011 %.⁸⁸

2. Background and literature review

2.4.6.3 Sensitisers

The sensitiser is another key element that needs to be carefully engineered for a high performing device. Metal complex sensitisers are usually made up of anchoring ligands and ancillary ligands. The anchoring ligands are responsible for the attachment on the TiO₂ surface, while the ancillary ligands can be engineered to give better overall conversion efficiencies.

2.4.6.3.1 Dyes for N-type semiconductors

Thousand of dyes have been synthesised and tested in DSSCs. The best performing chromophores so far are based on ruthenium sensitisers. In order to have a viable dye, it should be able to inject electrons into the conduction band of the semiconductor with a high quantum efficiency. Ideally, it should be able to absorb in the whole solar spectrum (400 to 900 nm) so that a greater number of photons can be harvested to do efficient work. A primary requirement is that the dye should be very stable for a long period of time. High performing dyes should be able to shield the semiconductor surface from the electrolyte to prohibit the back reaction process between the electrolyte and the semiconductor. The dye should also be able to bind onto the surface of the TiO₂. If the dyes are not attached properly to the TiO₂, they can be easily dissolved into the electrolyte, thus reducing the stability as well as the overall performance of the device. Dyes with large molar extinction coefficients can harvest the photon efficiency with a shorter light absorption length which can potentially reduce the need for thick TiO₂ films. The use of a thin film will shorten the distance of electron transport and decrease transport losses, thus potentially augmenting the conversion efficiency as well as increasing the open circuit voltage. In this regard, many ruthenium sensitisers have been synthesised with high molar extinction coefficients. In designing novel sensitisers, high efficiency and high temperature stability should be taken into consideration, especially for commercial applications. In an attempt to increase the absorption range and molar extinction coefficient of a ruthenium dye, Kim *et al.* have replaced one of the 4,4'-dicarboxylic acid-2,2'-bipyridine (dcbpy) ligands of the N3 dye with a highly conjugated ancillary ligand, a dipyrindylamine derivative, and extended the ligand with thiophene units.⁸⁹

The photovoltaic results obtained with the new ruthenium complexes, JK-85 and JK-86, showed a conversion efficiency of 7.66 % and 9.03 % respectively, compared to N719 which gave a performance of 8.88 %.

A similar strategy was employed by Jin *et al.*, replacing the dcbpy ligand with triarylamine moieties that act as electron donors and are known to give high efficiencies.⁹⁰ They obtained similar performances to N719 sensitisers with un-optimised devices. A multifunctionalised ruthenium based sensitiser developed by Chen *et al.* also showed better performance, with the same fabrication and measuring conditions, than N3.⁹¹ In their case, they incorporated an alkyl-substituted carbazole moiety into the thiophene-substituted bipyridine ligand. This unit not only enhanced the light harvesting capacity, but also created a more hydrophobic environment. Many other varieties of ruthenium based sensitisers, such as Z907, C102, K19, K8, K77 and C104, have also been prepared and they all showed very good stability, but unfortunately all of these dyes exhibit lower performance than the classical ruthenium sensitisers (structure shown in Chapter 7 in Figure 7.1). Figure 2.15 shows the structure of ruthenium sensitisers that have high molar extinction coefficients and are more thermally stable than the common and commercially available sensitisers. Recently, Gao *et al.* sensitised a ruthenium complex bearing alkylthiophene blocks conjugated with bipyridine ligands, named C101, and this newly developed dye shows good efficiencies with a volatile electrolyte, and also very good performance with solid state electrolytes.⁹²

2. Background and literature review

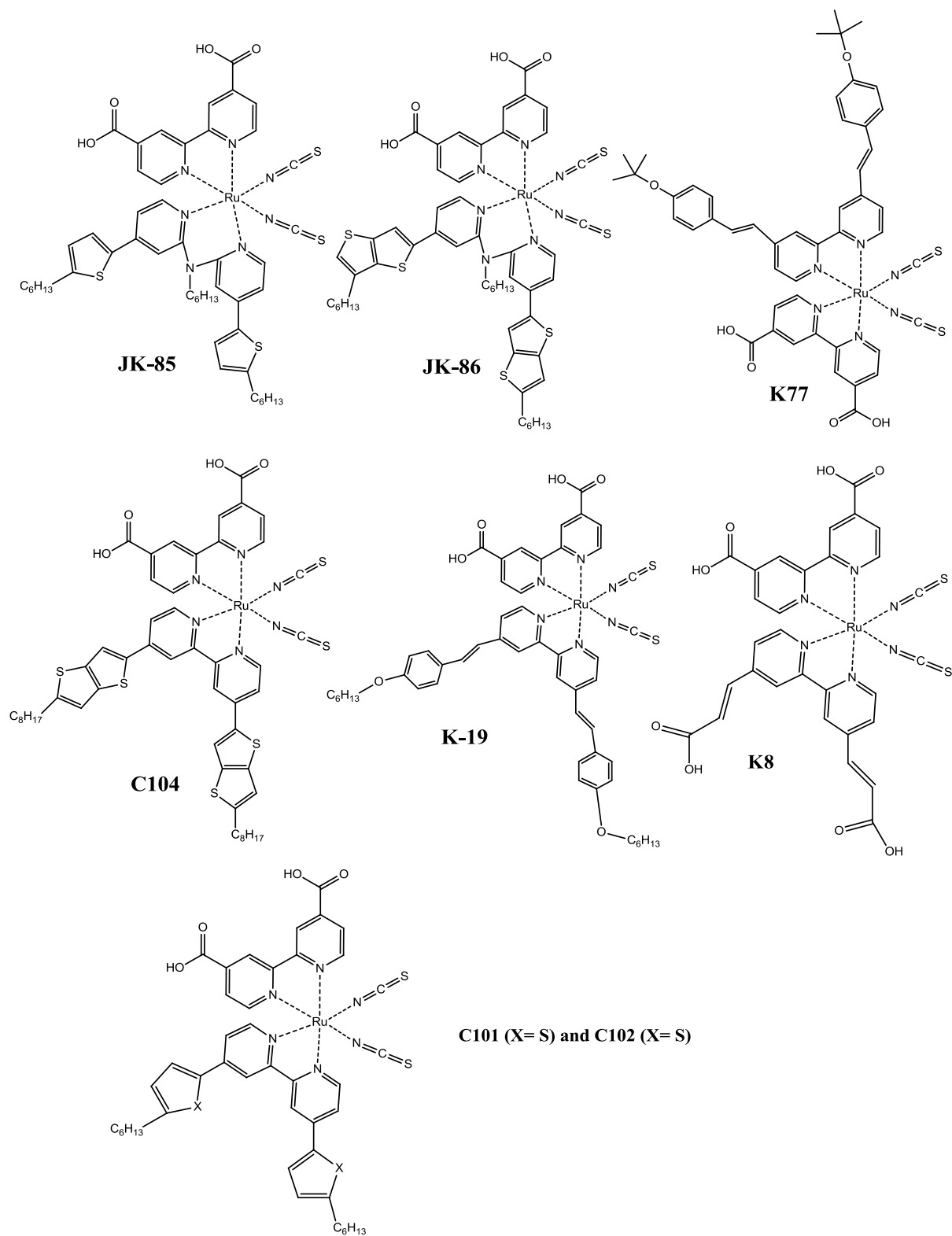


Figure 2.15: The structure of high molar extinction coefficient ruthenium sensitizers

2.4.6.3.2 Dyes for P-type semiconductors

Much of the research on sensitisers has been focused on n-type semiconductors, while very few dyes are available for p-type semiconductors. Sensitisers for p-type semiconductors should have very high molar extinction coefficients as it is quite difficult to make thick layers of NiO. Coumarin 343 is one of the few sensitisers that have shown a reasonable performance with NiO. Other coumarin sensitisers, such as NKX-2587 and NKX-2677, have also been investigated (structure shown in Chapter 7 in Figure 7.2). Cyanine dyes such as NK-3628 and NK-2612 have been used by Simukura and co-workers.⁸⁸ Figure 2.16 shows the structure of dyes used for sensitising p-type semiconductors.

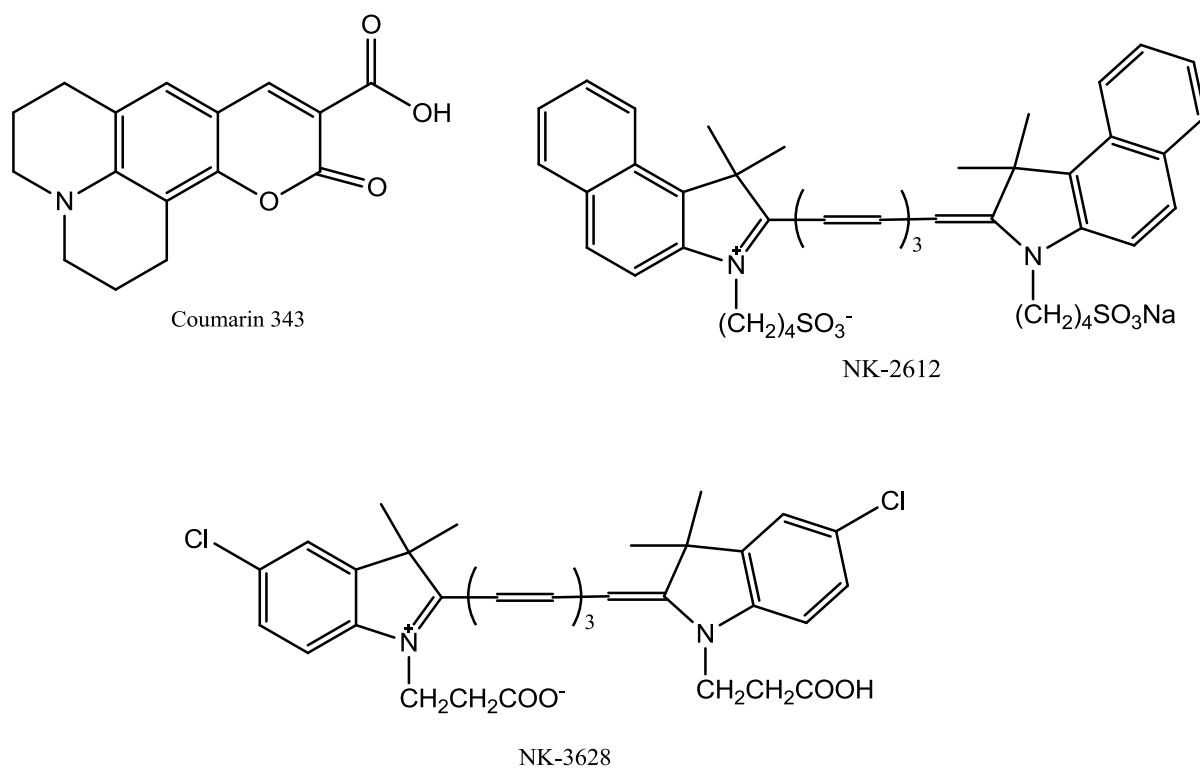


Figure 2.16: Dyes for used in p-type dye sensitised solar cells

2.4.6.4 Counter electrodes

The counter electrode is another important element in DSSCs. Platinum is usually used as the catalyst for the regeneration of iodide, although other noble metals such as gold have also been used.⁹³ These metals showed fast regeneration kinetics, thus forming high performing devices. Unfortunately, the high cost of these materials inhibits them for large scale applications. Conversely, carbon, which is abundantly present in nature, is a potential

2. Background and literature review

candidate as a catalyst to reduce the tri-iodide back to iodide. Various forms of carbon materials have been used as counter electrodes for DSSCs. For example, single wall carbon nanotubes,^{94, 95} graphite,⁹⁶ graphene,⁹⁷ carbon black,⁹⁸ and mesoporous carbon⁹⁹ have all been investigated. The limiting factors of these type of materials are the high charge transfer resistance and the slow diffusion of the electrolyte in the carbon matrix.¹⁰⁰ In order to improve these limiting factors, a better catalytic activity and more porous structures of the carbon are required. Fan and colleagues have developed an ordered multimodal porous carbon electrode for dye sensitized solar cells and quantum dot solar cells.¹⁰¹ They demonstrated quite good performances with the use of the ordered multimodal porous carbon (OMPC) counter electrode, obtaining an efficiency of 8.7 % for OMPC and 9.3 % with Pt. Nam *et al.* obtained better performances with multi-wall carbon nanotubes (CNTs) grown by chemical vapour deposition.¹⁰⁰ They have been able to achieve an efficiency of 10.04 % with CNT counter electrodes, which is better than their device incorporating Pt counter electrodes (8.8 %). Highly ordered carbon materials are required for this application, as high conductivity is necessary for the efficient regeneration of the tri-iodide. Jiang and co-workers recently demonstrated the use of natural wood as counter electrodes.¹⁰² They showed that bamboo and oak can be prepared as highly ordered carbon arrays with a large surface area, high conductivity and well connected microstructure. The best performance was obtained with oak mesoporous carbon arrays as counter electrodes, reaching an efficiency of 7.98 % compared to the 7.93 % obtained with Pt. Thus, with a good design and by improving the catalytic activity of the carbon materials, they can be used as counter electrodes.

Recently, Grätzel and co-workers demonstrated the use of CoS as a replacement for Pt. They successfully deposited CoS on a flexible substrate and showed excellent stability under prolonged light soaking, retaining 85 % of its performance.¹⁰³ The iodide-triiodide redox couple showed good reversibility with this new catalyst, and the use of this material has the potential to considerably lower the cost of the DSSCs. Wang and colleagues showed that titanium plate can also be used as counter electrodes.¹⁰⁴ The advantage of this material is the low sheet resistance, high resistance to corrosion, low density and good mechanical properties. The titanium plate showed high conversion efficiencies compared to Pt, measured under similar conditions, due to the better fill factor and high short circuit current density. Another interesting material used as counter electrodes is a nitride-nickel bifunctional foil. A conversion efficiency of 8.31 % was obtained, compared to 7.93 %

with FTO/Pt.¹⁰⁵ Conducting polymers have also been widely used as a counter electrode in DSSCs and good performance were achieved with these materials.^{106, 107} All of these studies were performed with the aim of lowering the cost of the DSSCs for commercial applications, and also to prolong the lifetime of the DSSCs, as these novels materials are more resistant to corrosion. Further, certain redox couples are more reversible using PEDOT electrodes, as discussed in the next section. For instance, the tetramethylthiourea/tetramethylformanium disulphide TMTU/TMFDS²⁺ couple does not work on gold electrodes, and is quite irreversible on a glassy carbon electrode, but behaves better on a PEDOT counter electrode. (Figure 2.17)

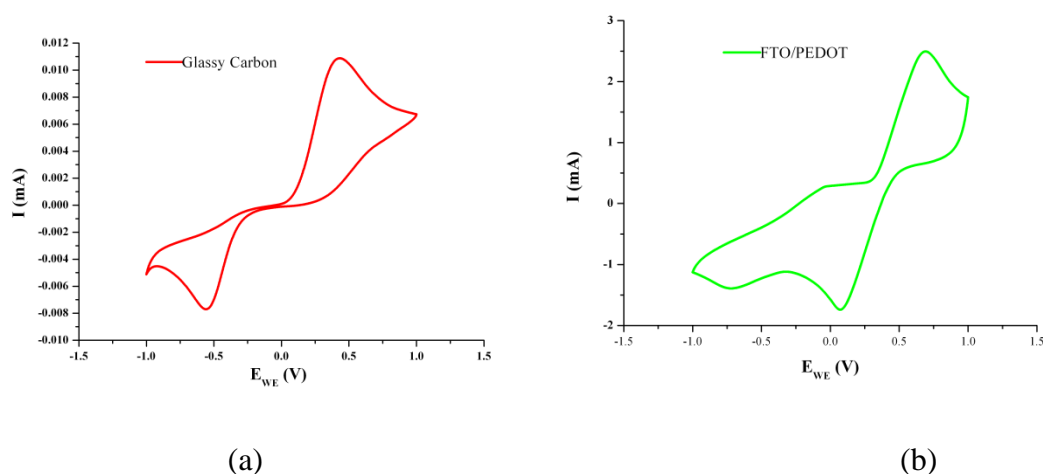


Figure 2.17: CV of TMTU/TMFDS²⁺ with (a) glassy carbon as the working electrode and (b) PEDOT as the working electrode, in a one compartment set up with Pt as the counter electrode, and a non aqueous saturated calomel electrode as the reference electrode. Scan rate of 10 mV s⁻¹

2.4.6.5 Redox couples

Another essential element in DSSCs is the mediator in the electrolyte solution, which can either be a volatile solvent, an ionic liquid or an organic ionic plastic crystal. According to Wolfbauer *et al.*,¹⁰⁸ there are a number of characteristics necessary for the ideal mediator for use in DSSCs. First, the redox potential of the couple must be thermodynamically favorable with respect to the HOMO and LUMO level of the sensitiser; i.e. it should be below the LUMO level of the hole injecting dye and above the HOMO level of the electron injecting dye to maximize the cell voltage. Secondly, there must be high diffusion and solubility in the electrolyte medium, for efficient transport of charge carriers, and lastly,

2. Background and literature review

the couple must have high stability and reversibility. Since the discovery of the DSSC about 19 years ago, no redox couple other than I^-/I_3^- has been able to surpass the device performance. Nevertheless, alternative redox couples have been investigated in an attempt to replace the latter due to the mismatch of its potential (-0.4 V vs NHE) with the sensitizer N3 (1.0 V vs NHE), which results in a large driving force of 0.6 V for the restoration of the oxidized dye. Pseudo halogen couples such as $\text{SCN}_2/\text{SCN}^-$, $\text{SeCN}_2/\text{SeCN}^-$ and $\text{SeCN}_3^-/\text{SeCN}^-$ have been evaluated in DSSCs and they all showed promising efficiencies.¹⁰⁹ Wang *et al.* have demonstrated that ionic liquids based on the $\text{SeCN}_3^-/\text{SeCN}^-$ redox couple can achieve an unprecedented 7.5-8.3 % power conversion efficiency under AM 1.5 sunlight with pure ionic liquid electrolytes.¹¹⁰ Even though these mediators are more positive than I^-/I_3^- , no improvement in V_{oc} was observed. Metal complexes such as copper, cobalt, ferrocene and platinum have also been used as alternative redox couples.¹¹¹⁻¹¹³ Although these mediators have the potential to rival the I^-/I_3^- redox couple, for the moment, the performance of these materials is considerably low and more work is still required to make stable devices, especially with ferrocene as the mediator. $\text{Br}^-/\text{Br}_3^-$ has also been successfully used as the mediator in DSSCs and, depending on the sensitizer used, this redox couple can outperform I^-/I_3^- .¹¹⁴ Thus, the choice of dye also plays an important role in achieving high conversion efficiency devices with new redox couples.

Recently, some new, non-corrosive, redox couples have demonstrated good conversion efficiencies with ruthenium based dyes and this has opened up the possibility of using other novel organic dyes in the DSSCs, which have the potential to be more efficient than the commonly used redox couple.¹¹⁵ Wang and colleagues have demonstrated the use of a disulphide/thiolate redox couple combined with a Ru-dye and an exceptional efficiency of 6.4 % was achieved with this alternative redox couple. Further work is underway to improve the conversion efficiency of solar devices using this new redox couple.¹¹⁶ Another redox couple of the same family also shows promising efficiency in DSSCs; a 3.1 % efficiency was achieved using TMTU/TMFDS²⁺ (refer to Figure 2.18) with N3 dye.¹¹⁷ The structure of these new redox couples is shown in Figure 2.18.

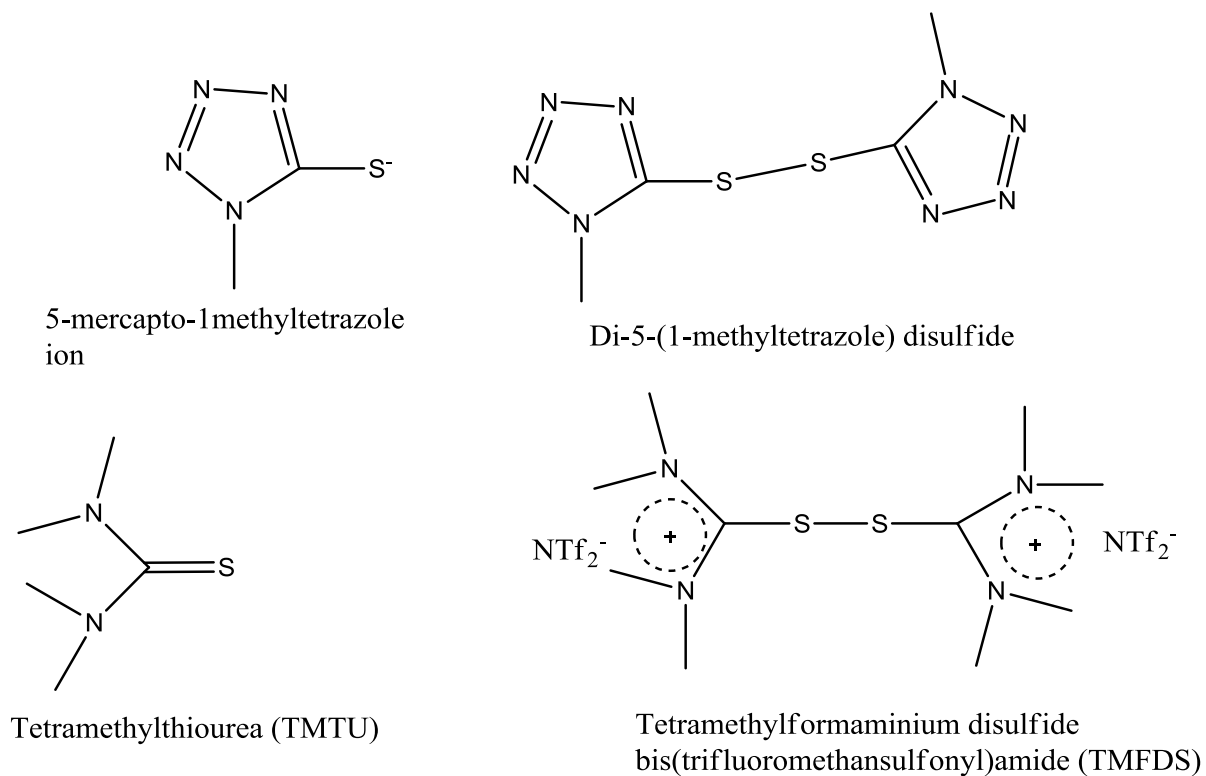


Figure 2.18: New redox couples capable of rivaling I^-/I_3^-

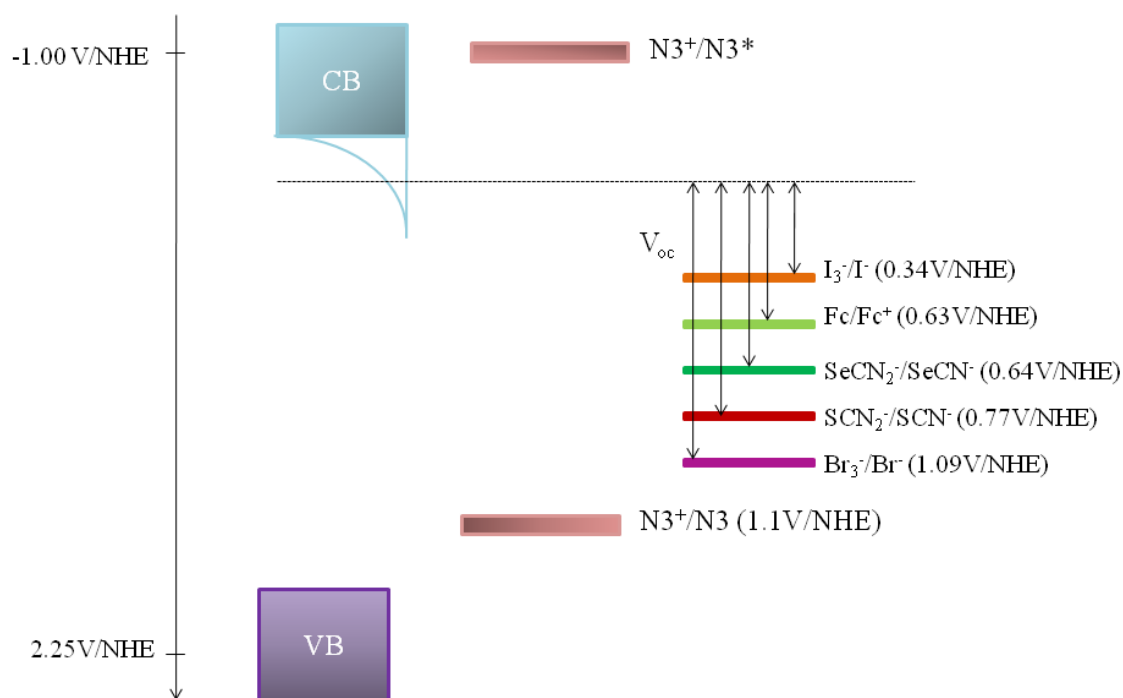


Figure 2.19: Schematic energy diagram of dye/ TiO_2 in contact with different redox couples (Diagram not to scale)

2. Background and literature review

Figure 2.19 illustrates the energy level diagram for TiO₂ electrodes sensitised with N3 dye, in combination with different redox couples. The diagram is not drawn to scale, but nevertheless it gives an indication of why some redox couples performed well, while others show very poor performance. TEMPO, which is a well known redox couple, cannot be used with ruthenium sensitisers due to the mismatch of its redox potential with the redox potential of the dye. A 5.0 % efficiency was obtained with an organic sensitiser (D-149).¹¹⁸

2.4.7 Types of DSSC devices

2.4.7.1 Sandwich and Monolithic dye sensitized solar cells

There are three main types of dye sensitised solar cells. The most common one is the so-called sandwich cell; i.e. the photoanode is made up of TiO₂ film deposited on a substrate and the cathode, on which a catalyst is deposited is the second substrate. In contrast, the monolithic design is made up of a layer of transparent film on which a scattering layer is deposited on top of it, and the counter electrode is finally deposited on top of the spacer. Figure 2.20 illustrates the schematic design of the sandwich cell and a monolithic DSSC.

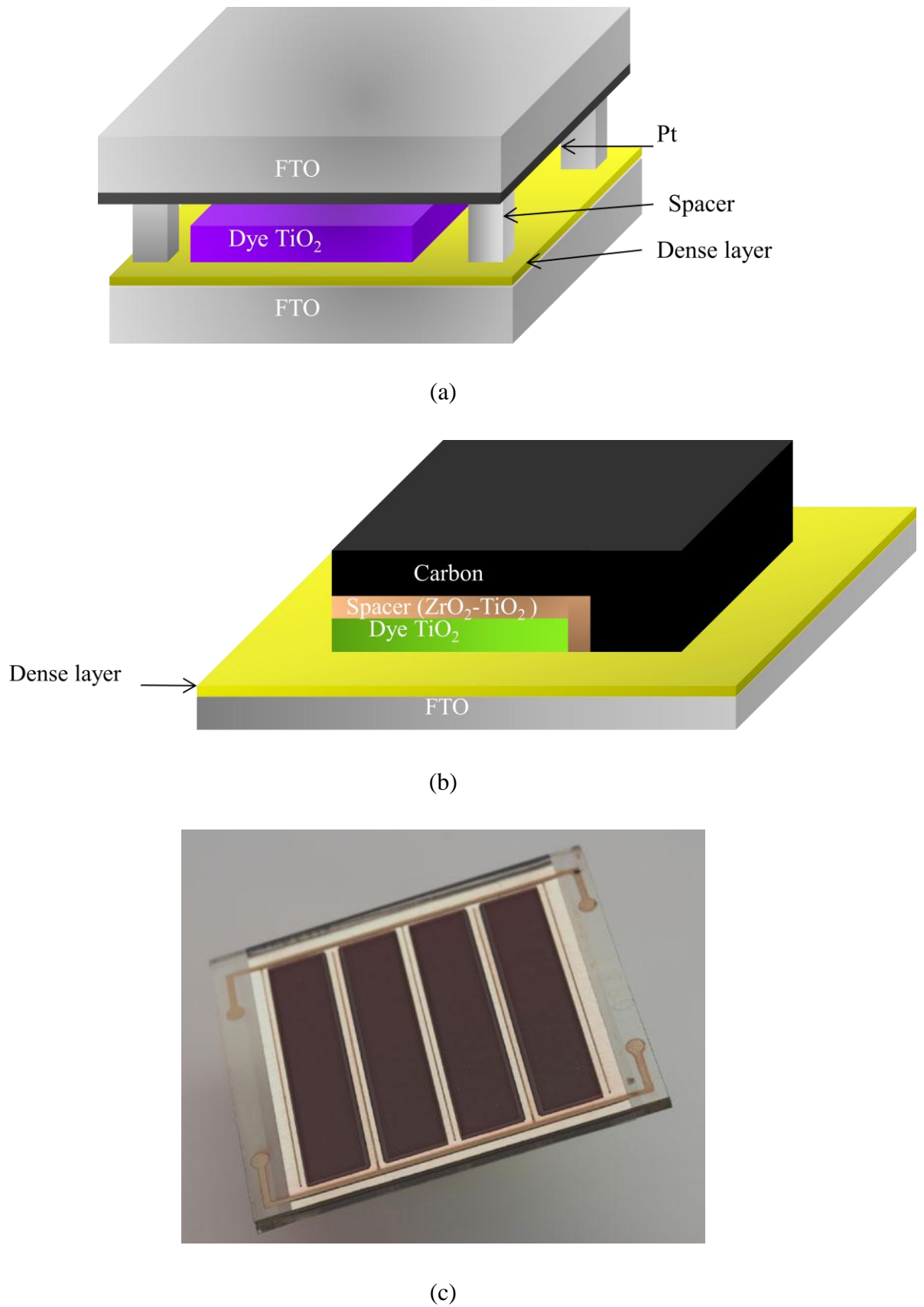


Figure 2.20: (a) Schematic diagram of a sandwich device, (b) a monolithic design of a solar cell and (c) parallel-connected monolithic modules consisting of four cells¹¹⁹

2. Background and literature review

The monolithic design of solar cells has mostly been used for solid state dye sensitised solar cells, where, instead of having a carbon layer, a hole conductor is deposited on top of the spacer layer, and then gold is evaporated on top of the hole conductor to make the connection.¹²⁰

Kay and Grätzel were the first to introduce the monolithic design.¹²¹ They were able to achieve 6.7 % efficiency with a single monolithic cell and 5.7 % with 6 cells connected in series, using a standard acetonitrile-based electrolyte. This has opened the way for both outdoor and indoor applications. Petterson *et al.* developed small modules based on the monolithic design for low power applications in 2003.¹²² They demonstrated that the modules degraded faster at high temperatures and that modules tested without UV-filters are damaged more rapidly. Nevertheless, they obtained reasonable performances and they reported that with further optimization, it might be possible to improve the long term stability of the modules. For example, this can be achieved by replacing the organic solvent with a non volatile electrolyte. Gorlov *et al.* demonstrated the use of ionic liquids in monolithic multi dye sensitised solar cells, giving efficiencies of 3 %. Although this is quite low compared to use of an acetonitrile electrolyte, these results are quite promising and may be further enhanced by optimizing the different parts of the DSSC, such as the sensitiser, the catalyst on the counter electrode, the semiconductor or the ionic liquid electrolyte itself.

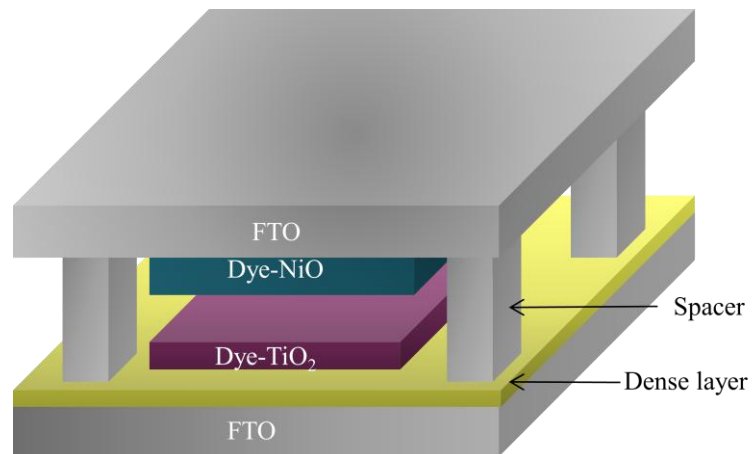
Recently, Han *et al.* constructed a highly efficient W-contact DSSC module with an exceptional 8.2 % efficiency.¹²³ Another important result is the work of Kato and co-workers,¹²⁴ who actually tested their monolithic modules under outdoor conditions for 2.5 years. Despite the low performance, they have been able to prove that DSSCs can have a practical utility.

2.4.7.2 Tandem devices

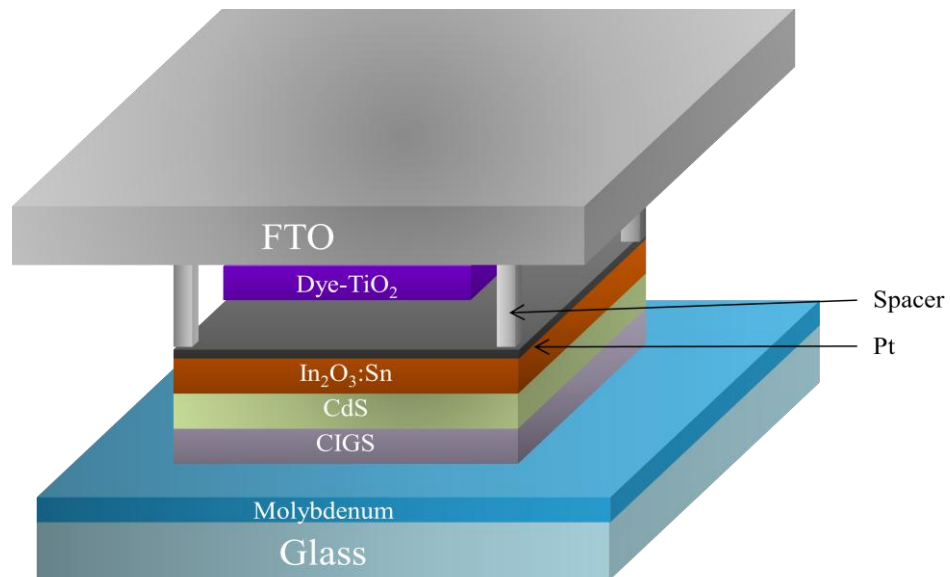
Another type of solar cell design is the tandem device. There are various designs of tandem devices and Figure 2.21 shows two common structures. The first tandem DSSC shown is based on a simple series connection of a dye sensitised photoanode, usually utilising a Ruthenium based dye, with a dye sensitised photocathode, the most common being NiO (usually sensitised with an organic dye).¹²⁵ There is limited research in this field due to the poor performance delivered by such devices, but with optimisation it is possible to improve

the efficiencies.²⁴ The second tandem device is based on coupling DSSCs with a copper-indium-gallium-selenide cell.¹²⁶ These devices are more efficient than tandem devices based on photoanode-photocathode DSSCs and can give 12 % efficiency when using a liquid electrolyte.

Most of the devices described above use molecular liquid electrolytes which have high vapour pressures, therefore having intrinsic problems such as solvent leakage and evaporation, shorting its lifetime. Thus, the use of low volatile materials is of interest.



(a)



(b)

Figure 2.21: The structure of (a) a tandem device based on a photoanode-photocathode design and (b) a tandem device based on a photoanode-CIGS¹²⁷

2.5 Ionic Liquids

Our modern society relies greatly on the chemical industry. From the fabrication of drugs to the production of electricity, the chemical industry plays an important role. With the pressure from leaders of different countries to lower carbon emission, alternative ways to mass produce basic needs should be considered, together with low production costs. To be able to move forward, whilst meeting the demands for cleaner processes, the chemical industry requires the use of green chemistry. Less polluting and non toxic substances are necessary to replace the hazardous and toxic materials in use. One class of materials that meet the requirements are ionic liquids. During the past few years, intensive research in this field is being undertaken for various applications due to their interesting properties such as negligible volatility.

Ionic liquids (ILs) are defined as salts that are entirely composed of ions (cations and anions) with melting points below 100 °C.¹²⁸ These materials are known by numerous other synonyms including: low/ambient/room temperature molten salts, ionic fluids, liquid organic salts and fused salts. Often they contain an organic cation, which is relatively large and asymmetric, with an inorganic anion. By changing the ions, a wide variety of ILs can be obtained (~ 10¹⁸ candidates).¹²⁹ Due to the bulkiness and asymmetric shape of the ions, solidification at room temperature is prevented.¹³⁰

2.5.1 Brief history

In the end of 19th century, the first recognised ionic liquid was made by a chemist performing an AlCl₃-catalysed Friedel-Crafts alkylation. The red oil formed during the process was later identified as a stable salt composed of cation and tetrachloroaluminate anion.¹³¹ Even though this reaction is considered as being the first known room temperature ionic liquid, it is possible that low temperature salts existed far before that time, but the report would have contained very little information on the compound.¹³²

The first ionic liquid deliberately synthesised was ethylammonium nitrate (m.p. 12 °C), made by Walden in 1914.¹³³ He was the first to report the physical and chemical properties of alkylammonium salts and draw conclusions on the association of ions in this new class of materials. Since then, many research groups have revisited this paper and expanded the concept much further. Series of ionic liquids, such as mixtures of 1, 3-dialkylimidazolium or 1-alkylpyridinium halides with trihalogenoaluminates, were developed for use as

electrolytes after this discovery of the low temperature molten salts. But the major drawback of these materials was that they were moisture sensitive, because of the reactivity of the anion. In 1992, Wilkes¹²⁸ reported the synthesis of water stable imidazolium based ionic liquids with anions such as nitrate and sulphate allowing for a wider range of applications.

2.5.2 Application of ionic liquids

The field of ionic liquids has expanded to include a broad range of applications, covering many industries. The use of ionic liquid is now so vast that only a brief summary of certain applications will be given here. Figure 2.22 displays the major fields of application for ionic liquids.

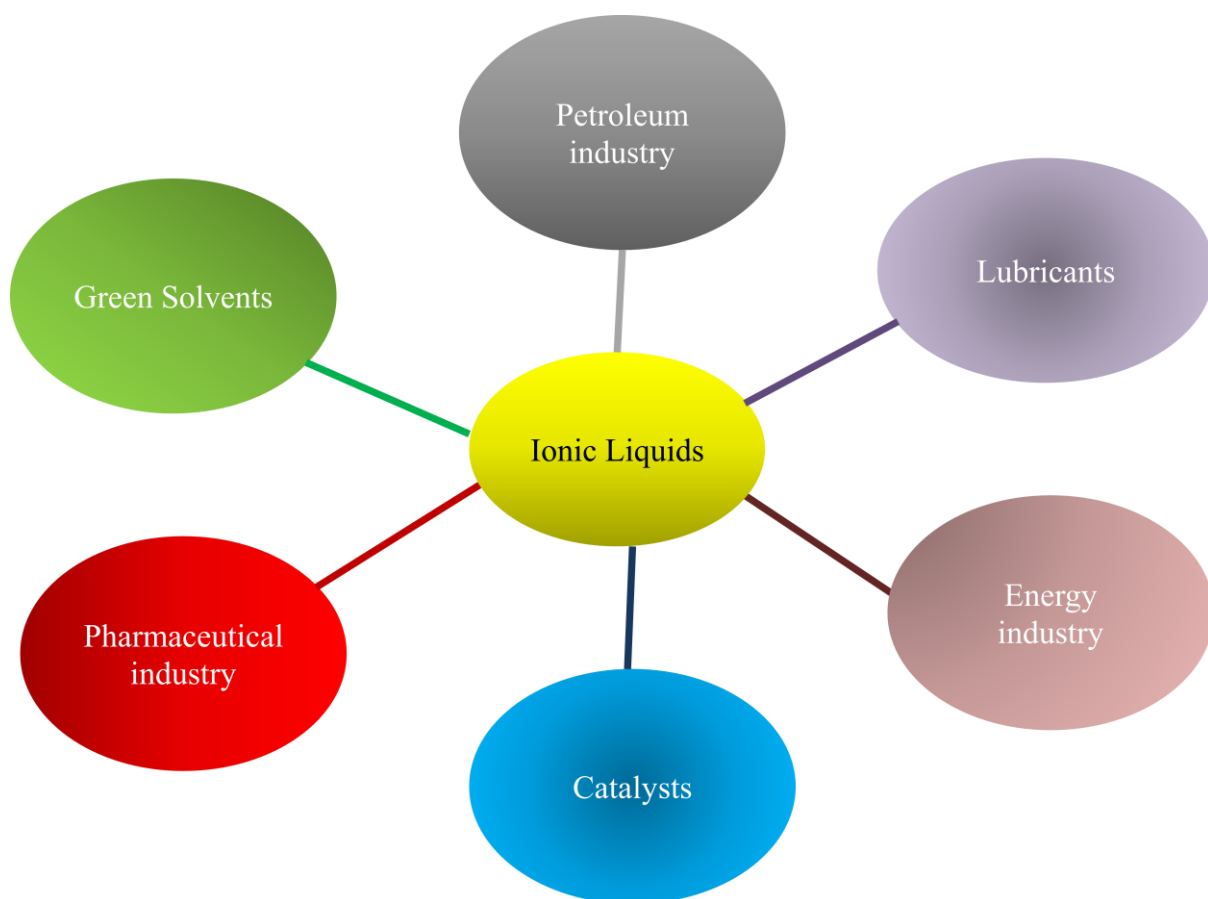


Figure 2.22: Schematic diagram showing the different fields where ionic liquids are routinely used

2. Background and literature review

2.5.2.1 Pharmaceutical ionic liquids

The use of ionic liquids in the pharmaceutical industry is still limited due to problems regarding the purity, toxicity and regulatory approval.¹³⁴ Nevertheless, great efforts are being made by various research groups to incorporate the use of ionic liquids in the biological and pharmaceutical fields. Recently, ionic liquids comprising known active pharmaceutical ingredients (APIs) have been prepared.¹³⁵ The approach used was to first of all to look at the properties of the individual components, and then to combine two carefully chosen pharmaceutically acceptable ingredients, to form a pharmaceutical ionic liquid. For example, benzalkonium chloride, which is an anti-bacterial, is combined with anti-inflammatory sodium ibuprofenate to form a compound having dual functionality.

2.5.2.2 Solvents and catalysts

Ionic liquids have a major role to play in the green chemistry domain and by tuning their physical and chemical properties they have the potential to obey the Ten Commandments set up for industrial application.¹²⁹ ILs are now commonly used as solvents at the laboratory level and are slowly replacing volatile solvents in industrial processes. The advantages of using ILs as solvents, over organic solvents, are that first of all, they are able to dissolve a large variety of compounds that are usually insoluble in organic solvents. Secondly, they can be used in reactions that require high temperatures and high pressures and, last but not least, they can be recycled. Recently, Avellaneda and co-workers reported the use of an ionic liquid for the preparation of high surface area TiO₂ nanoparticles, which is useful in the DSSCs field.¹³⁶ The high homogeneity of the oxide formed is due to the fact that the IL, through its H-bonds, orients the growth of the oxide. Recently, C₄mimOH has been used as both the solvent and as the catalyst in the Konevenagel condensation and in the Michael addition reaction.¹³⁷ A fast, high yield synthesis of Pyrrolo[2,3-*d*]isoxazoles was achieved with the use of an ionic liquid, with no formation of by-products. Ionic liquids having dual functionality were also applied to many other reaction types, such as the Heck reaction,¹³⁸ and esterification reactions,¹³⁹ to name just a few.

2.5.2.3 The energy industry

Ionic liquids find their application as electrolyte materials in the energy industry in a number of contexts.

Fuel cells

Protic ionic liquids (PILs) are now being used as electrolytes in fuel cells. Watanabe and co-workers recently reported the use of a PIL, diethylmethylammonium trifluoromethanesulfonate, as a proton conductor and as an electrolyte for non-humidified polymer membrane fuel cell (PEMFC). They demonstrated that it is possible to operate the device at high temperatures and that they are capable of delivering a high current density.¹²⁷ Another interesting improvement observed in the same field with the use of ionic liquids are their ability to wet the membrane electrode assembly.¹⁴⁰

Batteries

The intrinsically high conductivity, thermal and chemical stability, wide electrochemical window and low volatility displayed by ILs make them ideal as electrolytes for electrochemical devices. Ionic liquids have been demonstrated as being potential candidates for the replacement of molecular solvents in lithium ion batteries.¹⁴¹ Recently, Ruther *et al.* demonstrated stable cycling in lithium batteries with a new ionic liquid based on the boronium cation.¹⁴² These new ionic liquids have an electrochemical window between 4.3 V and 5.8 V, depending on the cations used, which makes them suitable electrolytes for Li/LiFePO₄ devices. The devices were able to deliver a capacity of 145 mA h g⁻¹ with these ILs. Lately, many publications concerning the use of ILs as safe electrolytes for Li-ion batteries have been published, showing the extent of interest in this class of material.^{143, 144}

In addition to this application, ionic liquids have also been used for industrial sewage treatment, in the petrochemical industries for the production of hexenes and octenes, which is one of the most important industrial processes, and are slowly being used in the textile and wood industries.^{129, 145, 146}

2. Background and literature review

Solar cells

As discussed in section 2.4.7, there are different possible solar cell designs. One of the reasons for such interest in developing these devices is to improve the performance of the solar cells. The main drawback is that most of these devices use a volatile electrolyte. One solution to a volatile electrolyte, is to use an ionic liquid based electrolyte, given the ionic liquid generally has negligible vapour pressure.

The most common ionic liquids are based on imidazolium cations. This class of material is used as an electrolyte in many applications and this is still the main area of research. Due to their intrinsically good physical and chemical properties, they have attracted the attention of many researchers. However, other cations are slowly emerging in the energy field, for example phosphonium ionic liquids, where these have been successfully applied in DSSCs with interesting results in Chapter 7.

Even though ionic liquids can solve problems such as leakage and evaporation of electrolyte, one of the main limitations of ionic liquids is the viscosity. They are more viscous than acetonitrile based electrolytes, which causes mass transfer limitations due to the poor diffusion of the redox species, especially triiodide. In the earlier studies, simply replacing the organic solvent with an ionic liquid proved to be very disappointing. In 2003, a 6 % device efficiency under full sun was obtained with an ionic liquid electrolyte containing C₃mimI, with 0.5 M I₂, in a Z907 sensitised solar cell.¹⁴⁷ However, despite the impressive performances obtained, the authors later found out that such high iodide content leads to a reductive quenching of the excited dye molecule, and this is when they thought of adding other ionic liquids with lower viscosities. For example, imidazolium salts containing anions SCN⁻, NTf₂⁻, FSI, B(CN)₄⁻, BF₄⁻ or N(CN)₂⁻ are well known to exhibit high fluidity compared to I⁻. Thus binary mixtures of ionic liquids were investigated by Wang *et al.*¹⁴⁸ The first binary mixture was based on combining C₃mimI with C₂mimN(CN)₂, in a volume ratio of 13:7, with the Z907 sensitiser.¹⁴⁸ They demonstrated that addition of lithium iodide greatly improved the performance of the solar cells from 5.7 % to 6.6 % under AM 1.5 sunlight (100 mW cm⁻²). The high photovoltaic performance was due to the inclusion of Li⁺, which not only accelerated the regeneration of the dye, but also improved the electron injection from the excited state of the dye into the conduction band of the semiconductor. As shown in Chapter 6, small cations are known to have great affinity for the TiO₂ surface and it is understood that Li⁺ can intercalate irreversibly into

the nanoporous structure of the TiO_2 , thus shifting the conduction band edge of the semiconductor and thereby enhancing the electron injection, leading to an increase in current density.^{149, 150} Wachter *et al.* later scrutinized the effect of temperature and physical properties of this binary mixture with varying molar ratios of C_3mimI , which is important for future practical applications of the solar cells.¹⁵¹ They demonstrated that the diffusion of triiodide does not depend solely on the concentration of iodine. They also found that an increase in temperature leads to an increase in photocurrent density, due to an enhancement in the mobility of the triiodide, but further increases in temperature leads to a decrease in photocurrent density due to higher recombination processes. According to the results they obtained from the diffusion measurements and analysis of the photovoltaic response, an optimum ionic liquid electrolyte for DSSCs is 91/9 (molar ratio) to 70/30 (molar ratio) for $\text{C}_2\text{mimN}(\text{CN})_2/\text{C}_3\text{mimI}$ and 0.032 M to 0.089 M for the iodine concentration. Although increasing the temperature seems to be an excellent way of enhancing the device performance by improving the fluidity of the ionic liquid electrolyte, the use of high temperatures can also damage the dye, which consequently lowers the performance and diminishes the lifetime of the device. Thus, consideration of the performance of the device over a range of operating temperatures is required.

Since the accomplishment of high performing devices with binary mixtures of ionic liquids, other ILs containing less reactive anions were also investigated. An ionic liquid electrolyte composed of C_3mimI and C_2mimSCN was studied with the Z907 dye.¹⁵² In this case, the authors added a co-adsorbent (3-phenylpropionic acid) into the dye solution and compared the performance of the device to that without any co-adsorbent. They demonstrated that in the presence of the co-adsorbent, the performance of the solar cell went up from 6.4 % to 7 %, which is much better than the previous binary mixture using the $\text{N}(\text{CN})_2^-$ anion, even though the amount of dye adsorbed is lower, as a result of the adsorption of the co-adsorbent onto the TiO_2 . The presence of the co-adsorbent is known to decrease the recombination processes and thus increase the photocurrent density, which results in an augmentation in device performance. The authors attributed the augmentation of the photocurrent density to better current collection efficiency. At low sun intensity, the device reached an efficiency of 7.7 %. The Hagfeldt group have also used this ionic liquid in monolithic dye sensitised solar cells and the best performance achieved so far is 5.6 % at 250 mW cm^{-2} .¹⁵³

2. Background and literature review

However, although they obtained quite a good performance with the mixture of C₃mimI/C₂mimSCN, the viscosity of the electrolyte was still high, and thus they replaced the C₂mimSCN with a slightly less viscous IL, 1-ethyl-3-methylimidazolium tricyanomethide (C₂mimTCM,) whose viscosity is 18 cP at 22 °C. A 7.4 % efficiency was obtained with the IL mixture now composed of C₂mimI and C₂mimTCM, with the ruthenium sensitiser Z907Na and only 1-methylbenzimidazole as the additive.¹⁵⁴

ILs based on the same family of anions i.e. TCM, N(CN)₂, SCN, B(CN)₄, were also investigated by other groups.¹⁵⁵ Out of this series, B(CN)₄ appeared the most promising. The main problem with these anions is the long term stability of the devices at high temperatures. Kuang *et al.* addressed this using a binary mixture of C₂mimB(CN)₄/C₃mimI (7:13 volume ratio) in combination with a highly stable sensitiser, Z907Na.¹⁵⁶ They demonstrated that the device was able to retain its performance of 7 % even after aging it at 80 °C and under full sunlight at 60° C for 1000 h.

The first ternary ionic liquid mixture was studied by Ito *et al.*¹⁵⁷ The mixture was composed of C₂mimOTf, C₂mimNTf₂ and C₃mimI, in a volume ratio of 1:1:2, with 0.2 M I₂ in conjunction with the organic sensitiser (D149) and a performance of 6.7 % was obtained under full sunlight. Later, Bai and co-workers introduced the same concept, but based on mixing two imidazolium iodide salts (1-ethyl-3-methylimidazolium iodide (C₂mimI) and 1, 3-dimethylimidazolium iodide (C₁mimI)).¹⁵⁸ They demonstrated that the mixed halides have higher ionic conductivity than 1-propyl-3-methylimidazolium iodide (C₃mimI). By combining the mixed halides with a third ionic liquid (C₂mimB(CN)₄), an impressive conversion efficiency of 8.2 % with the Z907Na sensitiser was achieved.

An ionic liquid based on tetrahydrothiophene, usually used as an odorant in natural gas, has also been developed for use in DSSCs.¹⁵⁹ A series of the tetrahydrothiophenium ILs containing different anions, such as I⁻, TCM and N(CN)₂, have been synthesised. The lowest viscosity was obtained with S-ethyl-tetrahydrothiophenium dicyanamide, abbreviated T₂DCA, with a viscosity of 37.3 cP at 25 °C. Even though T₂DCA gives the lowest viscosity, the best performance was obtained with T₂TCM, with an I_{sc} of 12.7 mA cm⁻², a V_{oc} of 714 mV, a fill factor of 0.76 and an overall efficiency of 6.9 %. Another non-imidazolium IL based on the allylpyrrolidinium family also showed promising results in solar cells, yielding a conversion efficiency of 5.6 % at full sun intensity.¹⁶⁰ Consistent with these encouraging results using non-imidazolium ionic liquids as solvent free

electrolytes, we will demonstrated in Chapter 7 that phosphonium-based ionic liquids have the potential to perform as well as imidazolium based ionic liquids with metal free organic sensitisers.

2.6 Ultimate aim

The ultimate aim in the DSSCs research is to be able to combine use of non volatile room temperature ionic liquids, which have good physical and chemical properties, with dye sensitised solar cells fabricated on a flexible substrate. Currently, several products from G24i are in the process of being commercialized. A mobile charger made of DSSCs is being sold at 50 US\$. Backpacks coated with cheap, light and flexible solar cells for recharging electronic devices are going to be put into the market soon. For the moment, the commercialised DSSC products use an organic electrolyte; they have tried to replace the organic solvent with ionic liquids but very poor efficiencies were obtained with smaller modules. In order to improve the efficiency larger surface area modules were fabricated, but the cost of production of such a module was prohibitive. Future application of DSSCs using ionic liquids will require the optimization of the separate components; the replacement of the ruthenium dye with a higher molar extinction coefficient organic sensitiser will improve the overall performance of the device, while the use of alternative counter electrodes, such as PEDOT, will reduce the cost of production of the modules. These are just some examples of the components that need to be adapted in order to successfully incorporate ionic liquids as electrolytes into these devices.

References

1. A. E. Becquerel, *Acad. Sci. Paris*, 1839, **9**, 561.
2. W. Smith, *Nature*, 1873, **7**, 303.
3. W. G. D. Adams, R. E., *Proc. R. Soc. Lond. A* 1877, **25**, 113.
4. J. Nelson, *The Physics of Solar Cells*, Imperial College Press, 2003.
5. R. S. Ohl, ed. B. T. Laboratories, United States Patent, 2402662, 1946.
6. D. M. Chapin, C. S. Fuller and G. L. Pearson, *J. Appl. Phys.*, 1954, **25**, 676-677.
7. J. A. Mazer, *Solar Cells: An Introduction to Crystalline Photovoltaic Technology*, Boston : Kluwer Academic Publishers, 1997.
8. M. A. Green, J. Zhao, A. Wang, P. J. Reece and M. Gal, *Nature*, 2001, **412**, 805-808.
9. A. Shah, P. Torres, R. Tscharnner, N. Wyrsh and H. Keppner, *Science*, 1999, **285**, 692-698.
10. R. Enderlein and N. J. M. Horing, *Fundamentals of Semiconductor Physics and Devices*, World Scientific, 1997.
11. R. Memming, *Semiconductor Electrochemistry*, Weinheim; Cambridge: Wiley-WCH, 2001.
12. S. R. Morrison, *Electrochemistry at Semiconductor and Oxidized Metal electrodes*, Plenum Press, New York, USA, 1980.
13. M. A. Green, *Third Generation Photovoltaics: Advances Solar Energy Conversion*, Springer, New York, 2003.
14. Y. Gong, M. Tapajna, S. Bakalova, Y. Zhang, J. H. Edgar, M. Dudley, M. Hopkins and M. Kuball, *Appl. Phys. Lett.*, 2010, **96**, 223506-223503.
15. T. Markvart, *Solar Electricity*, Wiley, New York, 1994.
16. R. C. Neville, *Solar Energy Conversion: The Solar Cell*, Elviesier, New York, 1995.
17. M. A. Green, K. Emery, Y. Hishikawa and W. Warta, *Prog Photovoltaics: Res. and App.*, 2010, **18**, 346-352.
18. J. M. Woodall and H. J. Hovel, *Solar Cells*, 1990, **29**, 167-172.
19. E. Fanetti, C. Flores, G. Guarini, F. Paletta and D. Passoni, *Solar Cells*, 1981, **3**, 187-194.
20. C. H. Henry, *J. Appl. Phys.*, 1980, **51**, 4494-4500.
21. M. A. Green, K. Emery, Y. Hisikawa and W. Warta, *Prog Photovoltaics: Res. and App.*, 2007, **15**, 425-430.
22. M. A. Green, *Prog Photovoltaics: Res. and App.*, 2001, **9**, 123-135.
23. P. Chiappafreddo and A. Gagliardi, *Transition Studies Review*, 2010, **17**, 346-355.
24. A. Nattestad, A. J. Mozer, M. K. R. Fischer, Y. B. Cheng, A. Mishra, P. Bauerle and U. Bach, *Nat. Mater.*, 2010, **9**, 31-35.
25. E. Barrigon, I. Rey-Stolle, B. Galiana, I. Garcia and C. Algora, in *Electron Devices, 2009. CDE 2009. Spanish Conference on*, 2009, pp. 383-386.
26. J. Szlufcik, S. Sivoththaman, J. F. Nlis, R. P. Mertens and R. Van Overstraeten, *Proc. IEEE*, 1997, **85**, 711-730.
27. G. Conibeer, *Mater. Today*, 2007, **10**, 42-50.
28. M. A. Russak, *Solar Cells*, 1986, **19**, 171-178.

29. A. J. Bard, *Science*, 1980, **207**, 139-144.
30. A. J. Bard and L. R. Faulkner, *Electrochemical Methods: Fundamental and Application*, VHC, New York, USA, 1995.
31. H. Gerischer, *J. Electroanal. Chem.*, 1975, **58**, 263-274.
32. W. Kanzig, *Phys. Rev.*, 1955, **98**, 549.
33. B. O'Regan and M. Grätzel, *Nature*, 1991, **353**, 737-740.
34. Y. Chiba, A. Islam, Y. Watanabe, R. Komiya, N. Koide and L. Han, *Jpn. J. Appl. Phys.*, 2006, **45**, L638-L640.
35. M. K. Nazeeruddin, A. Kay, I. Rodicio, R. Humphrybaker, E. Muller, P. Liska, N. Vlachopoulos and M. Grätzel, *J. Am. Chem. Soc.*, 1993, **115**, 6382-6390.
36. P. K. Sudeep, K. Takechi and P. V. Kamat, *J. Phys. Chem. C*, 2007, **111**, 488-494.
37. A. Burke, L. Schmidt-Mende, S. Ito and M. Grätzel, *Chem. Comm.*, 2007, 234-236.
38. S. A. Sapp, C. M. Elliott, C. Contado, S. Caramori and C. A. Bignozzi, *J. Am. Chem. Soc.*, 2002, **124**, 11215-11222.
39. H. Nusbaumer, S. M. Zakeeruddin, J. E. Moser and M. Grätzel, *Chem. Eur. J.*, 2003, **9**, 3756-3763.
40. D. V. Bavykin, V. N. Parmon, A. A. Lapkin and F. C. Walsh, *J. Mater. Chem.*, 2004, **14**, 3370-3377.
41. D. Bavykin, J. Friedrich and F. Walsh, *Adv. Mater.*, 2006, **18**, 2807-2824.
42. C. Y. Chen, M. Wang, J. Y. Li, N. Pootrakulchote, L. Alibabaei, C. H. Ngoc-Le, J. D. Decoppet, J. H. Tsai, C. Grätzel, C. G. Wu, S. M. Zakeeruddin and M. Grätzel, *ACS Nano*, 2009, **3**, 3103-3109.
43. M. Grätzel, *J. Photochem. Photobiol. A*, 2004, **164**, 3-14.
44. M. K. Nazeeruddin, A. Kay, I. Rodicio, R. Humphry-Baker, E. Mueller, P. Liska, N. Vlachopoulos and M. Grätzel, *J. Am. Chem. Soc.*, 1993, **115**, 6382-6390.
45. B. Burfeindt, T. Hannappel, W. Storck and F. Willig, *J. Phys. Chem.*, 1996, **100**, 16463-16465.
46. S. A. Haque, Y. Tachibana, D. R. Klug and J. R. Durrant, *J. Phys. Chem. B*, 1998, **102**, 1745-1749.
47. A. Hagfeldt and M. Grätzel, *Acc. Chem. Res.*, 2000, **33**, 269-277.
48. http://en.wikipedia.org/wiki/Image:Solar_Spectrum.png, Last accessed 5th October 2010.
49. P. Würfel, *Physics of Solar Cells: From Principles to New Concepts*, Wiley, 2005.
50. M. Toivola, J. Halme, K. Miettunen, K. Aitola and P. D. Lund, *Int. J. Energy Res.*, 2009, **33**, 1145-1160.
51. Y. Jun, J. Kim and M. G. Kang, *Sol. Energy Mater. Sol. Cells*, 2007, **91**, 779-784.
52. K. Miettunen, J. Halme, M. Toivola and P. Lund, *J. Phys. Chem. C*, 2008, **112**, 4011-4017.
53. Z. Liu and M. Misra, *Nanotechnology*, 2010, **21**, 125703.
54. K. Goto, T. Kawashima and N. Tanabe, *Sol. Energy Mater. Sol. Cells*, 2006, **90**, 3251-3260.
55. R. S. Mane, H. M. Pathan, C. D. Lokhande and S. H. Han, *Sol. Energy*, 2006, **80**, 185-190.

2. Background and literature review

56. Q. Zhang, C. S. Dandeneau, S. Candelaria, D. Liu, B. B. Garcia, X. Zhou, Y. H. Jeong and G. Cao, *Chem. Mater.*, 2010, **22**, 2427-2433.
57. E. M. Kaidashev, M. Lorenz, H. von Wenckstern, A. Rahm, H. C. Semmelhack, K. H. Han, G. Benndorf, C. Bundesmann, H. Hochmuth and M. Grundmann, *Appl. Phys. Lett.*, 2003, **82**, 3901-3903.
58. T. Dittrich, E. A. Lebedev and J. Weidmann, *Phys. Status Solidi A*, 1998, **165**, R5-R6.
59. A. Solbrand, K. Keis, S. Södergren, H. Lindström, S. E. Lindquist and A. Hagfeldt, *Sol. Energy Mater. Sol. Cells*, 2000, **60**, 181-193.
60. J. Bingwen, Z. Manhua and S. Tao, *Chin. Sci. Bull.*, 1997, **42**, 1937-1948.
61. K. Keis, E. Magnusson, H. Lindström, S. E. Lindquist and A. Hagfeldt, *Sol. Energy Mater. Sol. Cells*, 2002, **73**, 51-58.
62. A. R. Rao and V. Dutta, *Nanotechnology*, 2008, **19**, 445712.
63. J. B. Baxter and E. S. Aydil, *Appl. Phys. Lett.*, 2005, **86**, 053114-053113.
64. K. Keis, J. Lindgren, S.E. Lindquist and A. Hagfeldt, *Langmuir*, 2000, **16**, 4688-4694.
65. Y. F. Wang, J. W. Li, Y. F. Hou, X. Y. Yu, C. Y. Su and D. B. Kuang, *Chem. Eur. J.*, 2010, **16**, 8620-8625.
66. S. Ito, Y. Makari, T. Kitamura, Y. Wada and S. Yanagida, *J. Mater. Chem.*, 2004, **14**, 385-390.
67. K. Tennakone, G. R. R. A. Kumara, I. R. M. Kottegoda and V. P. S. Perera, *Chem. Commun.*, 1999, 15-16.
68. T.S. Kang, S. H. Moon and K. J. Kim, *J. Electrochem. Soc.*, 2002, **149**, E155-E158.
69. Y. Saito, S. Uchida, T. Kubo and H. Segawa, *Thin Solid Films*, 2010, **518**, 3033-3036.
70. K. S. Ahn, M. S. Kang, J. K. Lee, B. C. Shin and J. W. Lee, *Appl. Phys. Lett.*, 2006, **89**, 013103-013103.
71. H. Pettersson and T. Gruszecki, *Sol. Energy Mater. Sol. Cells*, 2001, **70**, 203-212.
72. K. H. Park, E. M. Jin, H. B. Gu, S. D. Yoon, E. M. Han and J. J. Yun, *Appl. Phys. Lett.*, 2010, **97**, 023302-023303.
73. Y. Ogomi, T. Kato and S. Hayase, *J. Photopolym. Sci. Technol.*, 2006, **19**, 403-408.
74. X. Feng, K. Shankar, M. Paulose and C. A. Grimes, *Angew. Chem. Int. Ed.*, 2009, **48**, 8095-8098.
75. R. H. Tao, J. M. Wu, H. X. Xue, X. M. Song, X. Pan, X. Q. Fang, X. D. Fang and S. Y. Dai, *J. Power Sources*, 2010, **195**, 2989-2995.
76. N. N. Bwana, in *Proc. ISES World Congress 2007 (Vol. I – Vol. V)*, eds. D. Y. Goswami and Y. Zhao, Springer Berlin Heidelberg, 2009, pp. 1073-1076.
77. C. Bae, Y. Yoon, W.-S. Yoon, J. Moon, J. Kim and H. Shin, *ACS Appl. Mater. Interfaces*, 2010, **2**, 1581-1587.
78. S. Chuangchote, T. Sagawa and S. Yoshikawa, *Appl. Phys. Lett.*, 2008, **93**, 033310-033313.
79. D. Kuang, J. R. M. Brillet, P. Chen, M. Takata, S. Uchida, H. Miura, K. Sumioka, S. M. Zakeeruddin and M. Grätzel, *ACS Nano*, 2008, **2**, 1113-1116.

80. M. Adachi, Y. Murata, J. Takao, J. Jiu, M. Sakamoto and F. Wang, *J. Am. Chem. Soc.*, 2004, **126**, 14943-14949.
81. F. D. R. Sauvage, D. Chen, P. Comte, F. Huang, L. P. Heiniger, Y. B. Cheng, R. A. Caruso and M. Grätzel, *ACS Nano*, 2010, **4**, 4420-4425.
82. F. Huang, D. Chen, X. L. Zhang, R. A. Caruso and Y. B. Cheng, *Adv. Funct. Mater.*, 2010, **20**, 1301-1305.
83. B. O'Regan and D. T. Schwartz, *Chem. Mater.*, 1995, **7**, 1349-1354.
84. C. A. N. Fernando, A. Kitagawa, M. Suzuki, K. Takahashi and T. Komura, *Sol. Energy Mater. Sol. Cells*, 1994, **33**, 301-315.
85. S. Nakabayashi, N. Ohta and A. Fujishima, *Phys. Chem. Chem. Phys.*, 1999, **1**, 3993-3997.
86. F. Odobel, L. C. Le Pleux, Y. Pellegrin and E. Blart, *Acc. Chem. Res.*, 2010, **43**, 1063-1071.
87. A. Nattestad, M. Ferguson, R. Kerr, Y. B. Cheng and U. Bach, *Nanotechnology*, 2008, **19**, 295304.
88. S. Sumikura, S. Mori, S. Shimizu, H. Usami and E. Suzuki, *J. Photochem. Photobiol. A*, 2008, **194**, 143-147.
89. J. J. Kim, H. Choi, C. Kim, M. S. Kang, H. S. Kang and J. Ko, *Chem. Mater.*, 2009, **21**, 5719-5726.
90. Z. Jin, H. Masuda, N. Yamanaka, M. Minami, T. Nakamura and Y. Nishikitani, *J. Phys. Chem. C*, 2009, **113**, 2618-2623.
91. C. Y. Chen, J. G. Chen, S. J. Wu, J. Y. Li, C. G. Wu and K. C. Ho, *Angew. Chem. Int. Ed.*, 2008, **47**, 7342-7345.
92. F. Gao, Y. Wang, D. Shi, J. Zhang, M. Wang, X. Jing, R. Humphry-Baker, P. Wang, S. M. Zakeeruddin and M. Grätzel, *J. Am. Chem. Soc.*, 2008, **130**, 10720-10728.
93. M. M. Byranvand, M. H. Bazargana and A. N. Kharat, *Dig. J. Nanomater. and Bios.*, 2010, **5**, 645-650.
94. G. Calogero, F. Bonaccorso, O. M. Marago, P. G. Gucciardi and G. D. Marco, *Dalton Trans.*, 2010, **39**, 2903-2909.
95. G. R. Li, F. Wang, Q. W. Jiang, X. P. Gao and P. W. Shen, *Angew. Chem. Int. Ed.*, 2010, **49**, 3653-3656.
96. Z. Huang, X. Liu, K. Li, D. Li, Y. Luo, H. Li, W. Song, L. Chen and Q. Meng, *Electrochem. Commun.*, 2007, **9**, 596-598.
97. K. C. Huang, Y. C. Wang, R. X. Dong, W. C. Tsai, K. W. Tsai, C. C. Wang, Y. H. Chen, R. Vittal, J. J. Lin and K.C. Ho, *J. Mater. Chem.*, 2010, **20**, 4067-4073.
98. R. A. Sayer, S. L. Hodson and T. S. Fisher, *J. Sol. Energy Eng.*, 2010, **132**, 021007-021004.
99. G. Wang, L. Wang, W. Xing and S. Zhuo, *Mater. Chem. Phys.*, 2010, **123**, 690-694.
100. J. G. Nam, Y. J. Park, B. S. Kim and J. S. Lee, *Scr. Mater.*, 2010, **62**, 148-150.
101. S.Q. Fan, B. Fang, J. H. Kim, B. Jeong, C. Kim, J.S. Yu and J. Ko, *Langmuir*, 2010, **26**, 13644-13649.

2. Background and literature review

102. Q. W. Jiang, G. R. Li, F. Wang and X. P. Gao, *Electrochem. Commun.*, 2010, **12**, 924-927.
103. M. Wang, A. M. Anghel, B. T. Marsan, N. L. Cevey Ha, N. Pootrakulchote, S. M. Zakeeruddin and M. Grätzel, *J. Am. Chem. Soc.*, 2009, **131**, 15976-15977.
104. G. Q. Wang, R. F. Lin, C. N. Zhang, Y. Lin, X. R. Xiao and X. P. Li, *Chin. Chem. Lett.*, 2004, **15**, 1369-1372.
105. Q. W. Jiang, G. R. Li, S. Liu and X. P. Gao, *J. Phys. Chem. C*, 2010, **114**, 13397-13401.
106. J. M. Pringle, V. Armel, M. Forsyth and D. R. MacFarlane, *Aust. J. Chem.*, 2009, **62**, 348-352.
107. S. Ahmad, J. H. Yum, Z. Xianxi, M. Grätzel, H. J. Butt and M. K. Nazeeruddin, *J. Mater. Chem.*, 2010, **20**, 1654-1658.
108. G. Wolfbauer, A. M. Bond, J. C. Eklund and D. R. MacFarlane, *Sol. Energy Mater. Sol. Cells*, 2001, **70**, 85-101.
109. G. Oskam, B. V. Bergeron, G. J. Meyer and P. C. Searson, *J. Phys. Chem. B*, 2001, **105**, 6867-6873.
110. P. Wang, S. M. Zakeeruddin, J. E. Moser, R. Humphry-Baker and M. Grätzel, *J. Am. Chem. Soc.*, 2004, **126**, 7164-7165.
111. H. Nusbaumer, S. M. Zakeeruddin, J. E. Moser and M. Grätzel, *Chem. Eur. J.*, 2003, **9**, 3756-3763.
112. S. A. Sapp, C. M. Elliott, C. Contado, S. Caramori and C. A. Bignozzi, *J. Am. Chem. Soc.*, 2002, **124**, 11215-11222.
113. B. M. Klahr and T. W. Hamann, *J. Phys. Chem. C*, 2009, **113**, 14040-14045.
114. Z. S. Wang, K. Sayama and H. Sugihara, *J. Phys. Chem. B*, 2005, **109**, 22449-22455.
115. T. C. Li, A. M. Spokoyny, C. She, O. K. Farha, C. A. Mirkin, T. J. Marks and J. T. Hupp, *J. Am. Chem. Soc.*, 2010, **132**, 4580-4582.
116. M. Wang, N. Chamberland, L. Breau, J. E. Moser, R. Humphry-Baker, B. Marsan, S. M. Zakeeruddin and M. Grätzel, *Nat. Chem.*, 2010, **2**, 385-389.
117. D. Li, H. Li, Y. Luo, K. Li, Q. Meng, M. Armand and L. Chen, *Adv. Funct. Mater.*, 2010, **20**, 3358-3365.
118. Z. Zhang, P. C. Chen, S. M. Zakeeruddin, J. E. Moser and M. Grätzel, *Mater. Res. Soc. Symp. Proc.*, 2007, **1013**, 1013-Z1006-1002.
119. M. Nedelcu, S. Guldin, M. C. Orilall, J. Lee, S. Huttner, E. J. W. Crossland, S. C. Warren, C. Ducati, P. R. Laity, D. Eder, U. Wiesner, U. Steiner and H. J. Snaith, *J. Mater. Chem.*, 2010, **20**, 1261-1268.
120. U. Bach, D. Lupo, P. Comte, J. E. Moser, F. Weissortel, J. Salbeck, H. Spreitzer and M. Grätzel, *Nature*, 1998, **395**, 583-585.
121. A. Kay and M. Grätzel, *Sol. Energy Mater. Sol. Cells*, 1996, **44**, 99-117.
122. H. Pettersson, T. Gruszecski, L. H. Johansson and P. Johander, *Sol. Energy Mater. Sol. Cells*, 2003, **77**, 405-413.
123. C. C. Han, S. Y. Ho, Y. P. Lin, Y. C. Lai, W. C. Liang and Y. W. Chen-Yang, *Microporous Mesoporous Mater.*, 2010, **131**, 217-223.

124. N. Kato, Y. Takeda, K. Higuchi, A. Takeichi, E. Sudo, H. Tanaka, T. Motohiro, T. Sano and T. Toyoda, *Sol. Energy Mater. Sol. Cells*, 2009, **93**, 893-897.
125. J. He, H. Lindstrom, A. Hagfeldt and S.E. Lindquist, *J. Phys. Chem. B*, 1999, **103**, 8940-8943.
126. S. Wenger, S. Seyrling, A. N. Tiwari and M. Grätzel, *Appl. Phys. Lett.*, 2009, **94**, 173508-173503.
127. S. Y. Lee, T. Yasuda and M. Watanabe, *J. Power Sources*, 2010, **195**, 5909-5914.
128. J. S. Wilkes, J. A. Levisky, R. A. Wilson and C. L. Hussey, *Inorg. Chem.*, 1982, **21**, 1263-1264.
129. N. V. Plechkova and K. R. Seddon, *Chem. Soc. Rev.*, 2008, **37**, 123-150.
130. M. J. Earle and K. R. Seddon, *Pure Appl. Chem.*, 2000, **72**, 1391-1398.
131. S. A. Forsyth, J. M. Pringle and D. R. MacFarlane, *Aust. J. Chem.*, 2004, **57**, 113-119.
132. P. F. Trowbridge and O. C. Diehl, *J. Am. Chem. Soc.*, 1897, **19**, 558-574.
133. P. Walden, *Bull. Acad. Imper. Sci. (St Petersburg)*, 1914, 405-422.
134. J. Stoimenovski, D. MacFarlane, K. Bica and R. Rogers, *Pharm. Res.*, 2010, **27**, 521-526.
135. W. L. Hough, M. Smiglak, H. Rodriguez, R. P. Swatloski, S. K. Spear, D. T. Daly, J. Pernak, J. E. Grisel, R. D. Carliss, M. D. Soutullo, J. J. H. Davis and R. D. Rogers, *New J. Chem.*, 2007, **31**, 1429-1436.
136. R. S. Avellaneda, S. Ivanova, O. Sanz, F. Romero-Sarria, M. A. Centeno and J. A. Odriozola, *Appl. Catal. B: Environ.*, 2009, **93**, 140-148.
137. E. Rajanarendar, S. Raju, A. S. R. Reddy, K. G. Reddy and M. N. Reddy, *Chem. Pharm. Bull.*, 2010, **58**, 833-839.
138. F. Bellina and C. Chiappe, *Molecules*, 2010, **15**, 2211-2245.
139. F. Liu, X. Cui, S. Yu, Z. Li and X. Ge, *J. Appl. Polym. Sci.*, 2009, **114**, 3561-3565.
140. J. C. Padilha, J. Basso, L. G. da Trindade, E. M. A. Martini, M. O. de Souza and R. F. de Souza, *J. Power Sources*, 2010, **195**, 6483-6485.
141. T. Sugimoto, Y. Atsumi, M. Kono, M. Kikuta, E. Ishiko, M. Yamagata and M. Ishikawa, *J. Power Sources*, 2010, **195**, 6153-6156.
142. T. Rütger, T. D. Huynh, J. Huang, A. F. Hollenkamp, E. A. Salter, A. Wierzbicki, K. Mattson, A. Lewis and J. H. Davis, *Chem. Mater.*, 2009, **22**, 1038-1045.
143. H. F. Xiang, B. Yin, H. Wang, H. W. Lin, X. W. Ge, S. Xie and C. H. Chen, *Electrochim. Acta*, 2010, **55**, 5204-5209.
144. B. S. Lalia, N. Yoshimoto, M. Egashira and M. Morita, *J. Power Sources*, 2010, **195**, 7426-7431.
145. S. Zhu, Y. Wu, Q. Chen, Z. Yu, C. Wang, S. Jin, Y. Ding and G. Wu, *Green Chem.*, 2006, **8**, 325-327.
146. S. I. Fletcher, F. B. Sillars, N. E. Hudson and P. J. Hall, *J. Chem. Eng. Data*, 2009, **55**, 778-782.
147. M. Gorlov and L. Kloo, *Dalton Trans.*, 2008, **20**, 2655-2666.
148. P. Wang, S. M. Zakeeruddin, J. E. Moser and M. Grätzel, *J. Phys. Chem. B*, 2003, **107**, 13280-13285.

2. Background and literature review

149. G. Redmond and D. Fitzmaurice, *J. Phys. Chem.*, 1993, **97**, 1426-1430.
150. B. Enright, G. Redmond and D. Fitzmaurice, *J. Phys. Chem.*, 1994, **98**, 6195-6200.
151. P. Wachter, M. Zistler, C. Schreiner, M. Berginc, U. O. Krasovec, D. Gerhard, P. Wasserscheid, A. Hinsch and H. J. Gores, *J. Photochem. Photobiol., A*, 2008, **197**, 25-33.
152. P. Wang, S. M. Zakeeruddin, R. Humphry-Baker and M. Grätzel, *Chem. Mater.*, 2004, **16**, 2694-2696.
153. K. Fredin, M. Gorlov, H. Pettersson, A. Hagfeldt, L. Kloo and G. Boschloo, *J. Phys. Chem. C*, 2007, **111**, 13261-13266.
154. P. Wang, B. Wenger, R. Humphry-Baker, J. E. Moser, J. Teuscher, W. Kantlehner, J. Mezger, E. V. Stoyanov, S. M. Zakeeruddin and M. Grätzel, *J. Am. Chem. Soc.*, 2005, **127**, 6850-6856.
155. Q. Dai, D. B. Menzies, D. R. MacFarlane, S. R. Batten, S. Forsyth, L. Spiccia, Y. B. Cheng and M. Forsyth, *C. R. Chim.*, 2006, **9**, 617-621.
156. D. Kuang, P. Wang, S. Ito, S. M. Zakeeruddin and M. Grätzel, *J. Am. Chem. Soc.*, 2006, **128**, 7732-7733.
157. S. Ito, S. M. Zakeeruddin, R. Humphry-Baker, P. Liska, R. Charvet, P. Comte, M. K. Nazeeruddin, P. Pechy, M. Takata, H. Miura, S. Uchida and M. Grätzel, *Adv. Mater. (Weinheim, Ger.)*, 2006, **18**, 1202-1205.
158. Y. Bai, Y. Cao, J. Zhang, M. Wang, R. Li, P. Wang, S. M. Zakeeruddin and M. Grätzel, *Nat. Mater.*, 2008, **7**, 626-630.
159. C. Xi, Y. Cao, Y. Cheng, M. Wang, X. Jing, S. M. Zakeeruddin, M. Grätzel and P. Wang, *J. Phys. Chem. C*, 2008, **112**, 11063-11067.
160. N. Cai, J. Zhang, D. Zhou, Z. Yi, J. Guo and P. Wang, *J. Phys. Chem. C*, 2009, **113**, 4215-4221.

Chapter 3

Experimental

Chapter overview

The first part of this chapter is dedicated to the description of a variety of analytical techniques used to characterise the identity of compounds prepared in this thesis, as well as the purity of each. Purity is an important factor; presence of impurities can affect the chemical and physical properties of the ionic liquids such as transport properties, thermal behaviour and stability of the compound. Moisture sensitive ionic liquids were handled and stored in a nitrogen filled glove box.

3. Experimental

3.1 Characterisation techniques: Structural analysis

3.1.1 Nuclear magnetic resonance spectroscopy (NMR)

Nuclear magnetic resonance spectroscopy is an important tool used by chemists to determine the molecular structure of compounds and their purity. NMR gives information on the number of hydrogens and carbons present in a molecule and how they are connected. NMR can also be used with other nuclei such as Phosphorus, Nitrogen and Fluorine.

All ionic liquids synthesised in this thesis were analysed using NMR. A Bruker Avance400 (9.4 Tesla magnet) with a 5 mm broadband autotunable probe with Z-gradients and BACS 60 tube autosampler or a Bruker DPX300 (7.05 Tesla magnet) with a 5 mm quad $^1\text{H}/^{13}\text{C}/^{19}\text{F}/^{31}\text{P}$ switchable probe with Z-gradients and a 10 mm tuneable broadband probe or a Bruker AV200 (4.7 Tesla magnet) with 5 mm $^1\text{H}/^{13}\text{C}$ probe with Z-gradients were used. All samples were measured as solutions in d_6 -DMSO, D_2O or CDCl_3 , supplied by Cambridge Isotope Laboratories. Approximately 10 mg of sample was dissolved in the appropriate solvent depending on the solubility of the ionic liquids in these solvents. Each resonance was reported according to the following convention: chemical shift (δ) measured in parts per million (ppm) from the reference signal tetramethylsilane, multiplicity, observed coupling constants (J Hz), number of hydrogen atoms and assignment.

Multiplicities were reported according to their relative splittings, as a singlet (s), doublet (d), doublet of doublets (d.d), triplet (t), triplet of triplets (t.t) quartet (q), broad (b), multiplet (m), equatorial (e), axial (a) or as combinations where necessary. The hydrogen atoms were numbered according to their parent atoms to which they are bonded.

3.1.2 Electrospray ionisation spectrometry (ESI)

Mass spectrometry is an analytical technique that can provide both qualitative (structure) and quantitative (molecular mass or concentration) information on analyte molecules after their conversion to ions. The molecules of interest are first introduced into the ionisation source of the mass spectrometer, where they are ionised to acquire positive or negative charges. The ions then travel through the mass analyser and arrive at different parts of the detector according to their mass/charge (m/z) ratio. After the ions make contact with the

detector, useable signals are generated and recorded by a computer system. The computer displays the signals graphically as a mass spectrum, showing the relative abundance of the signals according to their m/z ratio.¹

Electrospray Mass Spectrometry was carried out on a Micromass Platform II ESI-MS. Samples were run using automatic injections from a Waters Alliance 2690 HPLC system which is coupled to the MS. All samples were run in both positive and negative mode in methanol as the mobile phase with a cone voltage of 25 V or 35 V. Capillary voltage was set to 3.6 kV and the nebulising gas (nitrogen) flow was set to 250 ml min⁻¹. All measurements were carried out by Ms. Sally Duck and Mr. Finlay Shanks at Monash University.

3.1.3 Single crystal x-ray diffraction

Single crystal x-ray diffraction is a non-destructive analytical method to determine the crystal structure of a crystalline substance. This method provides information about the internal lattice of the crystalline solid, the bond angles, bond lengths and the unit cell structure.²⁻³ When a beam of monochromatic x-rays hits the sample, scattered x-ray radiation is produced. These diffracted x-ray beams are detected, processed and counted. A diffraction pattern is obtained, of which the strength and angle of the beams are recorded as the crystal is rotated. As the crystal rotates, the intensity of radiation is measured at every orientation. The data obtained are then refined using the appropriate program and a model of the arrangement of atoms in the crystal is produced.

All crystal structures presented in this thesis were determined by Dr. Pamela Dean at Monash University. A brief description of the instrument used for the determination of crystal structure is given in this section.

Single crystals between 0.2 and 0.5 mm in all dimensions and which were able to extinguish plane polarised light uniformly were selected. These crystals were coated with Paratone N oil (Exxon Chemical Co., TX, U.S.A.) immediately after isolation to prevent decomposition and cooled in a stream of nitrogen vapour on the Diffractometer. The reflection intensity data were measured on a Bruker X8 APEX KAPPA CCD Single Crystal X-ray Diffractometer and a Nonius KAPPA CCD single crystal X-ray Diffractometer using graphite-monochromated MoK α radiation ($\lambda = 0.71073 \text{ \AA}$) produced at 50 kV and 30 mA by the APEX X8 generator.

3. Experimental

Low temperature measurements were performed using a constant stream of N₂ gas with a flow rate of 15 cm³ min⁻¹ maintained by an Oxford Cryostream cooler. Data reduction and unit cell refinement were performed using the programs SAINT and SADABS⁴ with accompanying correction of Lorentz-polarisation effects.

Structures were solved by direct methods using the program SHELXS-97⁵ and refined by full matrix least-squares refinement on F² using SHELXL-97. SHELXL-97⁶ was operated through the X-SEED interface. All non-hydrogen atoms were revealed in the E-map and subsequent difference electron density maps and thus placed and refined anisotropically. All hydrogen atoms were observed in difference syntheses and were either refined isotropically or placed in geometrically idealized positions and constrained to ride on their parent atoms with C-H distances in the range 0.95-1.00 Å and Uiso(H) xUeq(C), where x is 1.5 for methyl and 1.2 for all other C atoms. Specific details of refinement are contained in the relevant CIF files.

Additional available crystallographic software programs used for crystal structure analysis include:

The Cambridge Structural Database (CSD)⁷ was used to publish all new crystal structures of ionic liquids obtained for this thesis and stored in the database.

LAYER⁸ which displays the measured intensity data as simulated precession photographs of all levels of the reciprocal lattice. Systematic absences, and hence space group symmetries, were determined from this program.

Using PLATON,⁹ the analysis of molecular conformations and other structural parameters were performed.

Using POV_RAY,¹⁰ the molecular packing diagrams were created.

The thermal ellipsoid plotting programs ORTEP III¹¹ and POV-RAY¹⁰ were used to produce ball and stick crystal structure illustrations including atoms drawn as ellipsoids at the 50 % probability level.

3.2 Thermal analysis

3.2.1 Differential Scanning Calorimetry (DSC)

The melting point of an ionic liquid and the sharpness of the melting peak can also be used as a measure of purity. Very often a broad melting transition indicates the presence of contaminants. Any impurities present will also decrease the melting point of the ionic liquid. Differential Scanning Calorimetry (DSC) was used to determine the melting point of new ionic liquids, the different phases present in organic ionic plastic crystals (OIPCs) as well as their purity.

Differential Scanning Calorimetry (DSC) is a thermal analytical technique in which the difference in the amount of heat required to increase the temperature of a substance and reference are measured as a function of temperature.¹²⁻¹³ Both the sample and reference are maintained at the same temperature throughout the experiment. There are two types of DSC systems in common use. In power compensation DSC, the temperatures of the sample and reference are controlled independently using separate, identical furnaces. In heat flux DSC, the sample and reference are connected by a low resistance heat flow path (a metal disc). The assembly is enclosed in a single furnace. Figure 3.1 shows the pictures of a heat flux type DSC (TA Instruments Q100).

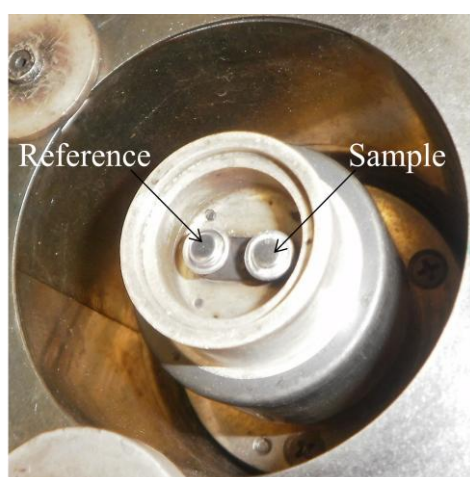


Figure 3.1: Heat flux type DSC. A TA Instruments Q100 differential scanning calorimeter

3. Experimental

All DSC characterization was performed on a heat flux type DSC. A TA Instruments Q100 differential scanning calorimeter was used. All DSC traces presented in this thesis are presented using the convention that endothermic behaviour is up and exothermic behaviour is down.

Scans were carried out at a heating/cooling rate of $10\text{ }^{\circ}\text{C min}^{-1}$ in the range of $-140\text{ }^{\circ}\text{C}$ to $150\text{ }^{\circ}\text{C}$ and in the range of $-100\text{ }^{\circ}\text{C}$ to $80\text{ }^{\circ}\text{C}$ at the same scan rate. Thermal scans below room temperature were calibrated with the cyclohexane solid-solid transition and melting point at $-87.0\text{ }^{\circ}\text{C}$ and $6.5\text{ }^{\circ}\text{C}$ respectively. Thermal scans above room temperature were calibrated with the melting points of indium, tin and zinc ($156.6\text{ }^{\circ}\text{C}$, $231.9\text{ }^{\circ}\text{C}$ and $419.5\text{ }^{\circ}\text{C}$ respectively). All DSC analysis was done in an aluminum pan with a sample weight of approximately 5 mg. Moisture sensitive and hygroscopic compounds were loaded in a nitrogen glove box. Transition temperatures were reported using the peak maximum of the thermal transition.

3.2.2 Thermogravimetry analysis

Thermogravimetric analysis is a thermal analytical technique in which the mass of a substance is measured as a function of temperature, whilst the substance is subjected to a controlled temperature program.¹⁴

Thermogravimetric analysis was conducted using a Perkin Elmer Pyris TGA 1 in a flowing dry nitrogen atmosphere between $25\text{ }^{\circ}\text{C}$ and $800\text{ }^{\circ}\text{C}$ with a heating rate of $10\text{ }^{\circ}\text{C min}^{-1}$ in platinum pans. The instrument was calibrated using four reference materials, Alumel, perkallloy, iron and nickel. The curie reference points were taken and all materials were supplied by Perkin Elmer. Approximately 10 mg of samples were weighed using an internal microbalance. The samples were allowed to equilibrate before taking the measurement. For analysis, the decomposition temperature was determined using the “step tangent” method.

3.2.3 Accelerated Rate Calorimetry (ARC)

Accelerating Rate Calorimetry (ARC) has gained importance in the 1980's for studying the self-heating reactions that cause thermal runaway. The ARC was developed by the Dow Chemical Company and was licensed to Columbia Scientific Industries (now known as Heath Scientific and Company) of Austin, Texas which currently markets the instrument as

CSI-ARCTM. It is widely reported in literature for studying the runaway characteristics of chemical reactions.

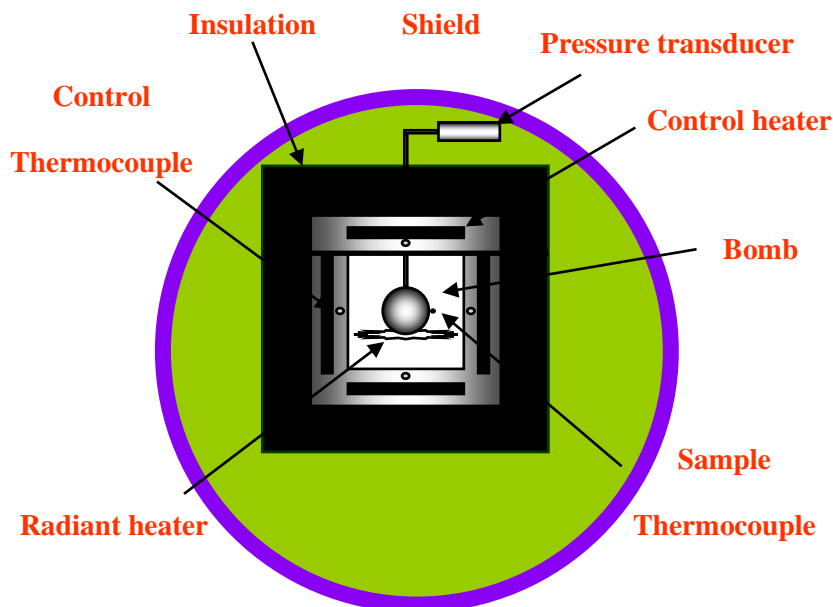


Figure 3.2: Schematic diagram of the accelerated rate calorimetry

Figure 3.2 illustrates the calorimeter part of the ARC. It is a container with its contents maintained at adiabatic conditions with respect to its environment. This is accomplished by constant monitoring of temperature and suitably adjusting the surrounding temperature to minimize the heat gains (or) losses from the container. In order to achieve an adiabatic environment over a temperature range (from ambient to 425 °C), the ARC is equipped with a sophisticated digital controller for the heater system. The calorimeter is divided into three temperature control zones viz., top, middle and bottom with each of them equipped with their own control instrumentation. The sample container or “bomb” is attached to a pressure transducer on the top of the chamber for close monitoring of pressure responses. The radiant heater located at the bottom of the adiabatic chamber is meant for heating the sample container at the start of the experiment.

ARC operates on a ‘Heat-Wait-Search’ principle to identify the initiation and progress of exothermic self heating processes. It follows the thermal process under the adiabatic mode right from the point of onset. An ARC experiment is initiated under the “heat” mode to heat the sample and container temperatures from ambient to 50 °C. It is then kept under the “wait” mode for a minimum of 10 minutes. This is followed by the search mode wherein the rate of temperature rise of the sample container is monitored.

3. Experimental

If the self heat rate is below, say $0.02\text{ }^{\circ}\text{C min}^{-1}$, the calorimeter re-enters heat mode to further enhance the sample temperature by a prefixed increment (usually $5\text{ }^{\circ}\text{C}$). This process of “Heat-Wait-Search” is repeated until the system experiences a self heat rate above the set threshold. When the self accelerating exothermicity is detected, the sample container is maintained under adiabatic conditions as explained earlier. Under these conditions, any increase in sample temperature is attributed totally to the exothermicity of chemical transformation. When the sample temperature exceeds the preset maximum attainable temperature, the ARC run is terminated. The following data plots can be obtained from an ARC experiment.

3.2.3.1 Self heat rate vs. temperature

This plot provides information on the onset temperature of the exothermic activity and qualitative indication of the rate of energy liberation. The adiabatic temperature rise is given by $\Delta T_{\text{ad}} = [T_{\text{f}} - T_{\text{O}}]$. T_{O} and T_{f} are the initial and final temperatures of the exotherm.

3.2.3.2 Temperature vs. time

This provides information on the vigor of the exothermic reaction and also the available time span from the onset of exothermic activity to the end of the reaction.

3.2.3.3 Pressure vs. time/temperature

Information on the rate of pressure and temperature rise will be most useful for estimating the vent area required for the safe operation of a reactor. This information can be further processed employing adiabatic kinetics to generate the following characteristic parameters.

- Time to Maximum Rate (TMR)
- Temperature of No Return (TNR)
- Activation Energy (E_{a})
- Order of Reaction (n)
- Heat of Decomposition (ΔH_{d})

3.2 Physico-chemical properties

3.2.1 Density

Density measurement of ionic liquids was carried out using an Anton Paar DMA 5000 density meter in the temperature range from room temperature to 90 °C. The DMA 5000 measures density by the oscillating tube method. A U-shaped glass tube of known volume and mass is filled with the liquid sample and excited electronically by a Piezo element. The U-tube principle was developed by Dr. Hans Stabingern.¹⁵ The U-tube is kept oscillating continuously at the characteristic frequency, f . Optical pick-ups record the oscillation period, P , as $P = 1/f$. This frequency is inversely proportional to the density, ρ , of the sample contained. The instrument was adjusted with air and water. The density is calculated using the following equation:

$$\rho = \frac{0.0012930}{1 + 0.00367 \times T} \times \frac{P}{1013.25} \quad (\text{Eq 3.1})$$

3.2.2 Viscosity

Viscosity is a very important property of ionic liquids as it determines the transport properties of redox species within the ionic liquid. Ionic liquids have a higher viscosity than conventional solvents. The value of viscosity depends greatly on the chemical structure of the ionic liquid, as well as the presence of impurities such as water, and temperature.

Viscosity is a measure of the resistance of the fluid to being deformed by either shear stress or extensional stress.¹⁶ The instrument used to measure viscosity is an Anton Paar AMVn in the temperature range 20-90 °C. Three cylindrical tubes with different diameters were used as supplied by Anton Paar: 1.8 mm, 3.0 mm and 4.0 mm. For more viscous samples, the 4.0 mm tube was used, whereas for more fluid samples, the 1.8 mm tube was used for measurement. The viscosity of the ionic liquid is determined by observing the rolling time of a solid sphere under the influence of gravity in a cylindrical tube filled with the liquid sample.

3. Experimental

Viscosity can be expressed into two forms: dynamic viscosity (mPa.s) or kinematic viscosity ($\text{mm}^2 \text{s}^{-1}$). Dynamic viscosity is the tangential force per unit area required to move one plate with respect to the other at unit velocity. The two plates are maintained at unit distance.

The dynamic viscosity is given by equation 3.2:

$$\eta = K_1 \alpha \times (\rho_B - \rho_s) \quad (\text{Eq 3.2})$$

Where η is the dynamic viscosity (mPa s), K_1 is the measuring system calibration constant, depending on the inclination angle ($\text{mPa C m}^3 \text{g}^{-1}$), ρ_B is the ball density (g cm^{-3}) (steel ball = 7.85 g cm^{-3})

The constant $K_1(\alpha)$ is given by the equation 3.3:

$$K_1 \alpha = \frac{\eta_C}{\rho_B - \rho_S} \times t_C \quad (\text{Eq 3.3})$$

Where η_C is the dynamic viscosity of the reference sample and ρ_C is the density of the reference sample (g cm^{-3}) and t_C is the average rolling ball time of reference sample for calibration (s).

The kinematic viscosity can then be calculated knowing the dynamic viscosity of the sample and its density.

$$\nu = \frac{\eta}{\rho_s} \quad (\text{Eq 3.4})$$

where ν is the kinematic viscosity ($\text{mm}^2 \text{s}^{-1}$), ρ_s is the density of the sample (g cm^{-3}) and η is the dynamic viscosity of the samples (mPa s)

3.2 Electrochemical methods

3.2.1 Water Content Determination - Coulometric Karl Fischer

Water impurities can affect the physico-chemical properties of ionic liquids. Water contaminants can have both negative and positive effects in electrochemical devices. Thus, quantification of the amount of water present in an ionic liquid is essential in some applications. Coulometric Karl Fischer is a widely used technique to determine the amount of water present in a wide range of products. The fundamental principle of Karl Fischer is based on the Bunsen reaction (Equation 3.5) between iodine and sulphur dioxide in an aqueous medium.¹⁷⁻¹⁸ Karl Fischer discovered that this reaction could be modified for use in the determination of water in a non-aqueous system containing an excess of sulphur dioxide.¹⁹ Figure 3.3 shows pictures of a typical 831KF Coulometer.



Figure 3.3: Coulometric Karl Fischer

There are two different types of coulometric cells: those with a diaphragm and those without. Coulometric determinations were conducted using a generator electrode without a diaphragm (generator current 400 mA, 831KF Coulometer), with Hydranal-Coulomat AG (reagent for coulometric KFT for cells without diaphragm supplied by Reidel-de Haen) as working medium for determination of water standards in this thesis. The cell consists of a generator electrode (platinum mesh) and a measuring electrode (double platinum pin) immersed in the electrolyte. The anode and cathode reaction take place in the same electrolyte. The electrolyte consists of an alcohol (ROH), a base (B), SO_2 and I_2 . A typical

3. Experimental

alcohol that may be used is methanol or diethylene glycol monomethyl ether, and a common base is imidazole.

The Pt anode generates I₂ when current is provided through the electric circuit. The net reaction as shown below is oxidation of SO₂ by I₂. One mole of I₂ is consumed for each mole of H₂O. In other words, 2 moles of electrons are consumed per mole of water.



The end point is detected most commonly by a bipotentiometric method. A second pair of Pt electrodes is immersed in the anode solution. The detector circuit maintains a constant current between the two electrodes during titration. Prior to the equivalence point, the solution contains I⁻ but little I₂. At the equivalence point, excess I₂ appears and an abrupt voltage drop marks the end point. The amount of current needed to generate I₂ in order to reach the end point can then be used to calculate the amount of water in the original sample.

The amount of sample used depends on the anticipated water content and the desired degree of accuracy is summarised in Table 3.1.

Table 3.1: Amount of sample required for detection of water in substance.

Sample water content (ppm)	Coulometric sample size (g)
1	> 50
10	> 5
100	> 0.5
1000	> 0.05
10000	> 0.005

Table 3.1 gives a rough estimate of the amount of sample required to detect the amount of water present in the sample. To get reproducible results, at least 3 concordant measurements are required. This technique requires a lot of sample and also the sample cannot be recovered from the anolyte. In some cases only one measurement was done where the ionic liquids were made in small quantities only.

3.2.2 Ion selective electrode (ISE)

An ion selective electrode can be used to measure the residual amount of halide impurities in the synthesised ionic liquid. An ISE measures the output potential of a specific ion in solution against a reference electrode. The reference electrode is a Ag/Ag⁺ electrode. The potential difference between the reference electrode and the ISE depends on the concentration of the specific ion in solution. Ion selective electrodes were purchased from TPS Ionode (Melbourne, Australia); Ionode S14 for bromide determination was used. A calibration curve was made using 1000 ppm to 10 ppm salt solution in either a mixture of methanol: water or in pure distilled water depending on the solubility of the ionic liquid in the aqueous medium. For the methanol:water calibration curve, tetrabutylammonium bromide was used, and in aqueous media potassium bromide was used.

3.2.3 A.C. Conductivity

Electrochemical impedance spectroscopy (EIS)²⁰⁻²² deals with the theory of interpreting equivalent resistance and capacitance values with respect to interfacial phenomena. Impedance spectroscopy is often used to study the transport properties of materials and measures the conductivity of charged species. The resistance of an ionic solution is given by the following equation:

$$R = \rho \frac{l}{A} \quad (\text{Eq 3.6})$$

where R is the resistance of the ionic solution, ρ is the resistivity of the ionic solution, A is the area bounded between the electrodes and l is the length carrying a uniform current.

The conductivity of the solution, σ , is more commonly used in solution resistance calculations and is given by the following equation:

$$\sigma = \frac{1}{\rho} \quad (\text{Eq 3.7})$$

The ionic conductivity of all samples was evaluated using AC impedance spectroscopy. The measurements were performed with a frequency response analyser, Solartron 1296, driven by custom software Solartron impedance measurement software version 3.2.0. The

3. Experimental

measurements were performed in the frequency range of 0.01 Hz to 1 MHz and a signal voltage 0.1 V in a temperature range from -40 °C to 90 °C at 5 degree intervals. The temperature was controlled using a Eurotherm Model 2204 temperature controller. The Eurotherm was under the Solatron impedance measurement software control.

Two type of cells were used, the barrel cell for the solid materials and the dip cell for liquids.

BARREL CELL (shown in Figure 3.4)

The cell body is made of brass and is 8 cm long. The sample sits on a steel plate contact whilst the second contact is a small steel disk on the end of the spring. The important features of the cell are spring loading, electrical shielding and gas tight seals.

The samples were pressed into pellets using a die of 13 mm in diameter. The thicknesses of the pellets were measured using a digital calliper. The thicknesses of the sample were approximately in the range of 1-2 mm. The pellets were then sandwiched between the two steel electrodes. Samples were handled and the cells sealed in a nitrogen filled glovebox.

The conductivity is calculated by using the following equation

$$\sigma = \frac{t}{RA} \quad \text{(Eq 3.9)}$$

where σ is the conductivity (S cm^{-1}) t is the thickness of the sample (cm), A is the area (cm^2) and R is the resistance (Ω).

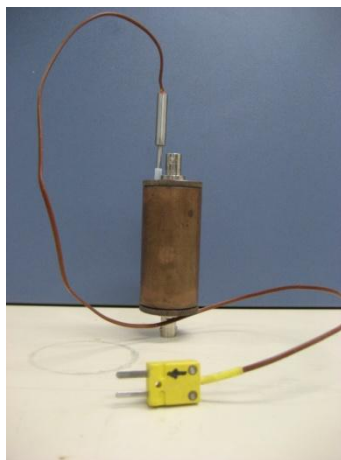


Figure 3.4: Barrel Cell

DIP CELL (shown in Figure 3.5)

A locally designed dip cell was used. The electrode consisted of two platinum wires, 3 mm apart, in a glass tube. The sample vial used an O-ring for proper sealing. A picture of the cell is shown in Figure 3.5. A 240 V cartridge heater and a K type thermocouple, mounted in a brass block were used to heat the samples.

When the sample was loaded, it was necessary to hold a fine piece of wire against the O-ring, thus allowing atmospheric pressure to escape and avoid pressurizing the cell. Once the dip cell was in position, the wire was removed from the cell. Also care was taken in lowering the electrode into the sample vial so as to avoid formation of bubbles.



Figure 3.5: Dip cell

The cell constant of the dip cell was determined at room temperature using an aqueous 0.01 M KCl solution. The measured conductance of the solution was calculated from the real axis touchdown of the Nyquist plot using equation (3.10)

$$\chi_{measured} = \frac{1}{R} \quad (\text{Eq 3.10})$$

where χ is the conductance (S) and R is the resistance (Ω)

The cell constant K was determined using equation 3.11:

3. Experimental

$$K = \frac{\sigma_{KCl}}{\chi_{measured}} \quad (\text{Eq 3.11})$$

where σ_{KCl} is the conductivity of KCl solution at 25 °C (1409 $\mu\text{S cm}^{-1}$).

The specific conductivity (S cm^{-1}) of the sample was thus calculated using equation (3.12):

$$\sigma = \frac{K}{R_{measured}} \quad (\text{Eq 3.12})$$

3.2.4 Basic electrochemistry

3.2.4.1 Experimental set up

The experimental set up was a three electrodes one compartment arrangement connected to the potentiostat. The electrode where the main electrochemical reaction is happening is called the working electrode. To measure the potential difference at the working electrode, a reference electrode is needed. The reference electrode is placed close to the working electrode to minimise the ohmic drop and no current should pass between these two electrodes. The third electrode is the counter electrode, through which current passes. The area of the counter electrode should be sufficiently large to avoid limitation in charge transfer reactions. This set up is used to study redox reactions at the working electrode.

What is a redox reaction?

Redox reactions involve the transfer of electrons from one state to another as shown in the general equation 3.13²³⁻²⁴



A fundamental expression for characterising redox system under equilibrium conditions is the Nernst equation given in equation 3.14²⁵

$$E = E^o - \frac{RT}{nF} \ln \frac{C_{Red}}{C_{Ox}} \quad (\text{Eq 3.14})$$

Where E^0 is the standard reduction potential, R is the gas constant ($8.314 \text{ J K}^{-1} \text{ mol}^{-1}$), T is the temperature in Kelvin, C_{Red} is the concentration of the reducing species, C_{Ox} is the concentration for the oxidised species, n is the number of electron transferred, F is the Faraday constant (96500 C).

3.2.4.2 Electrodes used to study redox reactions

The working electrode is usually made from inert conducting materials such as glassy carbon, gold or platinum. A well defined planar surface can be easily obtained from these materials. These electrodes need to be polished after each reaction to remove any impurities that can be absorbed on the surface. Different diameters of disk electrodes are available. Electrodes of dimension of 1 to 3 mm are often used for electrochemical studies. These electrodes are often called macroelectrodes. A microelectrode has a smaller diameter, usually around $10 \mu\text{m}$ is used.

The reference electrode commonly used in aqueous solvents is the standard saturated calomel electrode, whose potential is 0.24 V vs NHE (normal hydrogen electrode). In organic solvents, Pt wire or silver wire are used as pseudo reference electrodes (meaning that their potential is reproducible but not accurately known on an absolute scale). Alternatively a silver wire in a silver ion solution of known concentration contained in a fritted tube can be used.

The counter electrode is usually composed of either platinum wire or graphite. The counter electrode should be larger than the working electrode.

3.2.4.3 Transport properties of ions

It is important to consider the transport of ions in electrolyte solutions between the working electrode and the counter electrode. The transport of ions to the electrode is governed by three different kinds of transport mechanisms:²⁴

Migration

If charged ions are present in a solution containing two electrodes, when a potential is applied to the electrodes, positive charges will move towards the cathode and negative charges will move to the anode. To suppress this effect, a large excess of inert supporting electrolyte is often added.

3. Experimental

Convection

Convection is due to transport of ions by mechanical movement. This is achieved by vibration, stirring, and heat induced motion. Convective mass transport is used in rotating disk electrodes.

Diffusion

Diffusion is due to a concentration gradient. Diffusion is described by Fick's law

$$J = -D \frac{\delta C}{\delta x} \quad (\text{Eq 3.15})$$

where J is the flux of the ion ($\text{mol cm}^{-2} \text{ s}^{-1}$), $\frac{\delta C}{\delta x}$ is the concentration gradient, D is the diffusion coefficient ($\text{cm}^2 \text{ s}^{-1}$).

Fick's Second Law is the variation of concentration with time and given by the following equation:

$$\frac{\delta C}{\delta t} = -D \frac{\delta^2 C}{\delta x^2} \quad (\text{Eq 3.16})$$

The current response obtained after a change in potential is applied when migration and convection are neglected is often limited by diffusion according to these laws.

3.2.4.4 Cyclic voltammetry

Cyclic voltammetry (CV)²⁶⁻²⁷ is the most universal electrochemical technique, used to elucidate reaction mechanisms or to carry out quantitative analysis. The power of cyclic voltammetry results from its potential to provide important information on the thermodynamics of redox processes, coupled chemical reactions and on the kinetics of electron-transfer reactions. The technique consists of varying the electrode potential of a stationary working electrode in a linear way between two limits: the initial electrode potential E_i and the final electrode potential E_f at a fixed scan rate ($v \text{ mV s}^{-1}$). Figure 3.6 shows the triangular potential waveform applied in the CV technique.

When the potential reaches the E_1 , the scan is reversed and the potential is swept back to E_2 as shown in Figure 3.6. By changing the scan rate, the kinetics and the mass transfer process can be probed.

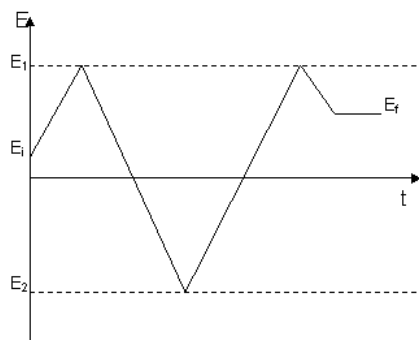


Figure 3.6: Variation of applied potential with time in cyclic voltammetry where E_i is the initial potential, E_1 is the maximum potential, E_2 is the minimum potential and E_f is the final potential

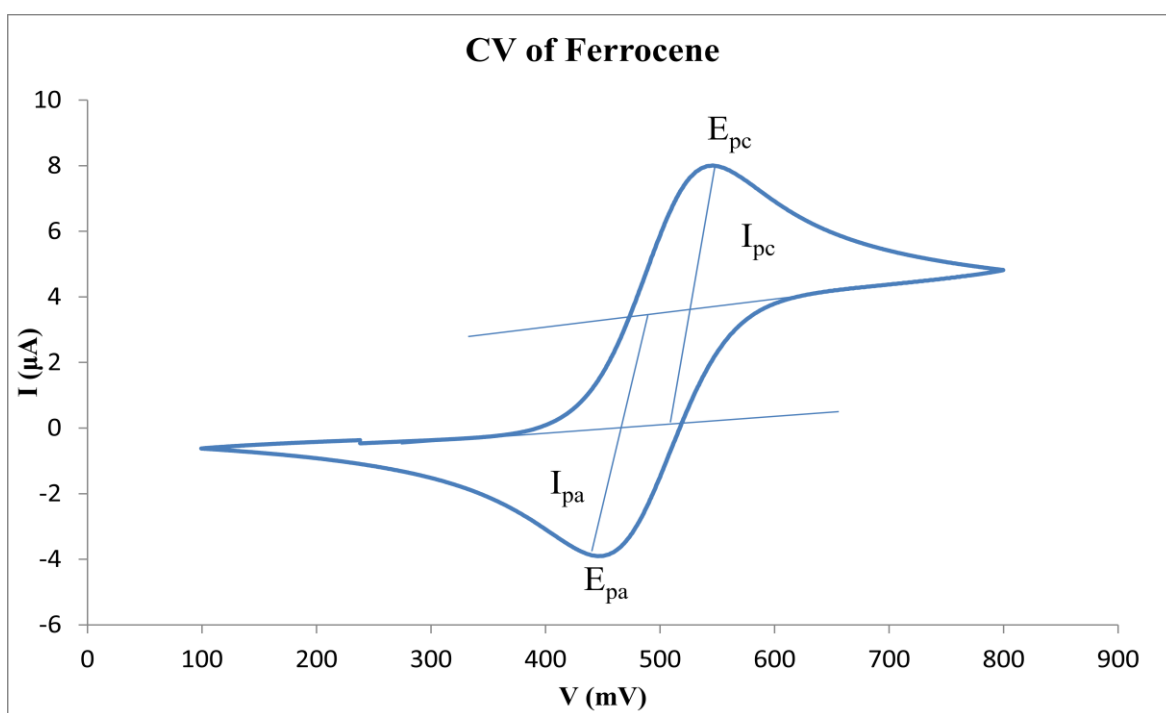
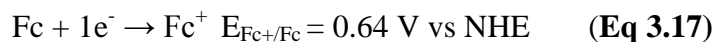


Figure 3.7: CV of 0.5 mM of Ferrocene in acetonitrile at 20 mV s^{-1} on a Pt working electrode (1 mm). E_{pc} is the cathodic peak potential, I_{pc} is the cathodic current, E_{pa} is the anodic peak potential and I_{pa} is the anodic current

3. Experimental

Figure 3.7 illustrates the expected response of a reversible redox couple: in this case ferrocene was used. Initially, only the oxidized form is present.

Ferrocene undergoes a one electron oxidation. It is often used as a standard in electrochemistry.



Cyclic voltammetry at a planar electrode (macroelectrode)

In cyclic voltammetry at planar electrode, for a reversible process the peak current i_p is given by the Randles-Sevcik equation (Eq 3.18). A full description of the derivation of this expression for current is given in Bard and Faulkner.²⁴

$$i_p = 2.69 \times 10^5 n^{3/2} A D^{1/2} C \vartheta^{1/2} \quad (\text{Eq 3.18})$$

where n is the number of electron transferred, A is the active area of the electrode (cm^2), D is the diffusion coefficient of the species ($\text{cm}^2 \text{ s}^{-1}$), C is the concentration of the species in the bulk (mol cm^{-3}) and ϑ is the scan rate (V s^{-1}).

Cyclic voltammetry at microdisk electrodes

Cyclic voltammetry at a macroelectrode is a transient technique, in which the current is a function of time. In steady state techniques, the current is only a function of applied potential. To achieve steady state conditions, a microdisk²⁸⁻³⁰ is usually used. In this case the mass transport is independent of time. Transport of ions at a microelectrode²⁹⁻³¹ is achieved by either radial or edge diffusion to the electrode surface.

The shape of the CV at a microelectrode is shown in Figure 3.8. The magnitude of the current density is much smaller due to the small area of the electrode and a steady state current (or limiting current) is achieved.²⁸

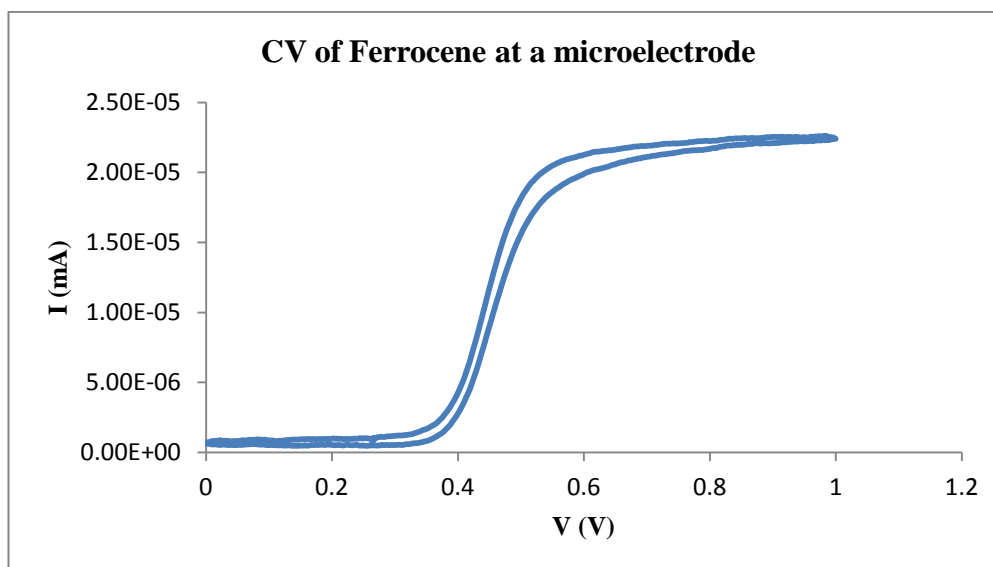


Figure 3.8: CV of 0.5 mM of Ferrocene in acetonitrile at 10 mV s^{-1} at a Pt microelectrode ($10 \text{ }\mu\text{m}$)

The limiting current I_{lim} is given by equation 3.19.³²

$$I_{\text{lim}} = 4nFDcR \quad (\text{Eq 3.19})$$

where n is the number of electron transferred, F is the Faraday constant (96500 C), D is diffusion coefficient ($\text{cm}^2 \text{ s}^{-1}$), C is the bulk concentration (mol cm^{-3}) and r is the dimension of the electrode (cm).

Thin layer cyclic voltammetry

The advantage of thin layer voltammetry³¹ is that the reactant is held between two symmetrical electrodes separated by a very thin film. $25 \text{ }\mu\text{m}$ thick Surlyn was used as the spacer in the present work. Figure 3.9 shows a schematic diagram of a symmetrical cell. The electrolyte is confined in a very small volume. The advantage of using this technique is the ease of obtaining steady state conditions at the electrode.

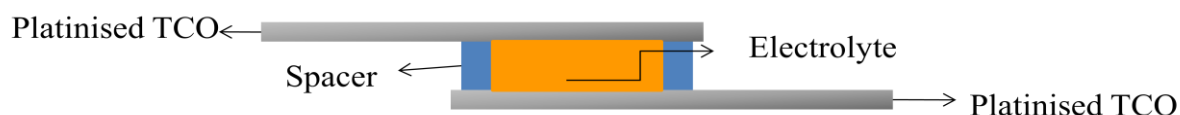


Figure 3.9: Symmetrical cell composed of two platinised TCO glasses

3. Experimental

The steady state current is given by the following equation:³¹

$$I_{ss} = \frac{2nFADC}{l} \text{ (Eq 3.20)}$$

where n is the number of electrons transferred, F is the Faraday constant, A is the cross-section of the enclosed electrolyte, D is the diffusion coefficient, c is the concentration of the redox species and l is the distance between the two electrodes.

3.2.5 Diffusion NMR spectroscopy

Pulsed-field gradient diffusion measurements were carried out on a Bruker 300 MHz Ultrashield with Avance I console utilising a Diff30 diffusion probe and GREAT60 amplifier.³³ Different components of the samples were measured using the ^1H and ^{19}F nuclei for the cation and anion, respectively. For each experiment, the recycle delay was set to $> 5 \times T_1$. For each measurement the gradient pulse (δ) and diffusion time (Δ) were optimised, with gradient strengths (g) up to 1700 G cm^{-1} applied. Due to the conductivity of the samples, the probe was tuned and matched at each temperature with the $\pi/2$ pulse checked and optimised, if required, before any experiments were performed. The sample was filled into 5 mm diameter Schott E NMR tubes to a height of 40 mm in an N_2 atmosphere ($<5 \text{ ppm O}_2$, $<5 \text{ ppm H}_2\text{O}$).

The Stimulated Spin Echo (STE) pulse sequence was used to measure the diffusion coefficients, varying the gradient strength in 16 steps up to the maximum gradient strength. This data is fit to the Stejkal-Tanner equation³⁴ using the non-linear least squares method. The sample was measured in the range of 20-80 °C. The temperature of the probe was calibrated using a 99.9 % ethylene glycol standard in a sealed NMR tube with several measurements taken at 10 K intervals. The temperature difference between the thermocouple and sample was fit to a straight line to obtain accurate correction parameters. As convective flow in the NMR tube can cause erroneously large diffusion coefficients at elevated temperatures, a Δ of 10 ms was used above 50 °C (below this temperature the low diffusion coefficient dictated a Δ of 20 ms). The measurements were performed by Mr. Paul Bayley and Mr. Martin Yoon.

References

1. R. Cody, *Applied Electrospray Mass Spectrometry*, CRC Press, 2010.
2. W. Clegg, *Crystal Structure Determination*, Oxford; New York : Oxford University Press, 1998.
3. W. Massa, *Crystal Structure Determination*, Berlin; New York: Springer, 1944.
4. G. M. Sheldrick, Bruker/Siemens Area Detector Absorption and Other Corrections, 1999.
5. G. M. Sheldrick, C. Kruger and R. Goddard, *Crystallographic Computing 3: Data Collection, Structure Determination, Proteins and Databases*, Oxford University Press, London, 1985.
6. G. M. Sheldrick, *Acta Crystallogr. Section A*, 2008, **64**, 112-122.
7. Cambridge Structural Database system, Last accessed June 28th 2010.
8. L. Barbour, *J. Appl. Crystallogr.*, 1999, **32**, 351-352.
9. A. Spek, *J. Appl. Crystallogr.*, 2003, **36**, 7-13.
10. The Persistence of Vision Raytracer, POV-RAY for Windows, 1991-1999.
11. L. Farrugia, *J. Appl. Crystallogr.*, 1997, **30**, 565.
12. J. A. Dean, *The Analytical Chemistry Handbook*, New York: McGraw-Hill, 1995.
13. P. Patnaik, *Dean's Analytical Chemistry Handbook (2nd Edition)*, McGraw-Hill, 2004.
14. R. C. Mackenzie, *Anal. Proc.*, 1982, **19**, 202-205.
15. O. Kratky, H. Leopold and H. Stabinger, *Device for Density Determination*, United States Patent, 3523446, 1970.
16. D. S. Viswanath, T. K. Ghosh, D. H. L. Prasad, N. V. K. Dutt and K. Y. Rani., *Viscosity of Liquids: Theory, Estimation, Experiment and Data*, Springer Netherlands, 2007.
17. A. S. Meyer and C. M. Boyd, *Anal. Chem.*, 1959, **31**, 215-219.
18. A. Felgner, R. Schlink, P. Kirschenbühler, B. Faas and H. D. Isengard, *Food Chem.*, 2008, **106**, 1379-1384.
19. E. Scholz, *Karl Fischer Titration : Determination of Water*, Berlin; New York: Springer, 1984.
20. M. Martini, T. Matencio, N. Alonso-Vante and M. A. De Paoli, *J. Braz. Chem. Soc.*, 2000, **11**, 50-58.
21. M. E. Orazem and B. Tribollet, *Electrochemical Impedance Spectroscopy*, 2008.
22. E. Barsoukov and J. R. Macdonal, *Impedance Spectroscopy: Theory, Experiment and Application*, Hoboken, N. J : Wiley Interscience, 2005.
23. A. J. Bard, *Science*, 1980, **207**, 139-139.
24. A. J. Bard and L. R. Faulkner, *Electrochemical Methods: Fundamental and Application*, VHC, New York, USA 1995.
25. J. O. M. Bockris, A. K. N. Reddy and M. Gamboa-Aldeco, *Modern Electrochemistry 2A*, Plenum Press, 1970.
26. C. M. A. Brett and A. M. O. Brett, *Electrochemistry: Principles, Methods and Applications*, Oxford Science, 1993.

3. Experimental

27. S. Dong and G. Che, *Electrochim. Acta*, 1992, **37**, 2587-2589.
28. K. Aoki, *Electroanalysis*, 1993, **5**, 627-639.
29. R. M. Penner and C. R. Martin, *Anal. Chem.*, 1987, **59**, 2625-2630.
30. J. Heinze, *Angew. Chem. Int. Ed.*, 1993, **32**, 1268-1288.
31. A. T. Hubbard and F. C. Anson, *Anal. Chem.*, 1968, **40**, 615-617.
32. D. Golub and Y. Oren, *J. Appl. Electrochem.*, 1990, **20**, 877-879.
33. G. Annat, D. R. MacFarlane and M. Forsyth, *J. Phys. Chem. B*, 2007, **111**, 9018-9024.
34. K. I. Momot and P. W. Kuchel, *Concepts in Magnetic Resonance Part A*, 2006, **28A**, 249-269.

Chapter 4

Device fabrication and characterisation

Chapter overview

The first part of this chapter focuses on the description of each component used in the fabrication of dye sensitised solar cells (DSSCs). Transparent conductive oxide glass (TCO), semiconductor (Titanium oxide pastes (TiO_2)), sensitisers, electrolytes and counter electrodes are described, as well as the assembly of the complete device. The second part of the chapter explains the measurement techniques, and their relevant background, used to analyse the system under investigation. The performance of the device was measured using photovoltaic techniques such as white light current-voltage characteristics and the determination of the incident-light-to-current conversion efficiency. Other techniques such as UV-spectroscopy, BET analysis, absorbed photon to current conversion efficiency are also briefly described.

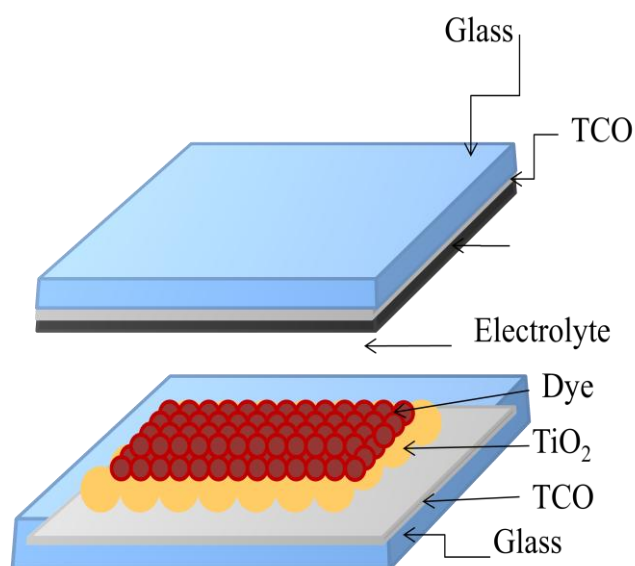


Figure 4.1: Schematic diagram of a dye sensitised solar cell

4. Device fabrication and characterisation

4.1 Materials

This part describes the different materials used in the fabrication of a dye sensitised solar cell. A description of each component is given as well as the advantage of such materials.

4.1.1 TCO coated glass

The substrate acts as a current collector, thus it has to be very conductive. The other important aspect of the substrate is the transparency on the front side so that the dye can absorb light efficiently. Also it has to be able to handle high temperature treatments as well as corrosion from the electrolyte system. Thus, the electrode of the DSSC was prepared using a transparent conductive oxide (TCO) glass. TCO glasses are widely used for silicon solar cells due to their high transparency in the visible light spectral region and high electrical conductivity.¹ Indium-tin oxide (ITO) and fluorine doped tin oxide (FTO) are the two kinds of TCO glass usually used. FTO conducting glass was purchased from Nippon Sheet glass (NSG). Table 4.1 shows the specifications of the TCO used to prepare devices.

Table 4.1: TCO substrate used for the fabrication of dye sensitised solar cells. The nominal resistance, the thickness and the transmission at 550 nm of the TCO glass indicated are from the supplier.

TCO name	Resistance Ω / \square	Transmission at 550 nm (%)	Glass Thickness (mm)
NSG (WE)	13	82	4
NSG (CE)	12	70	3

The sheet resistance of the TCO glass for the working electrode was $13 \Omega / \square$ before sintering. After sintering treatment at $500 \text{ }^\circ\text{C}$, the sheet resistance was increased to $16 \Omega / \square$. Resistivity was measured using a four point probe technique. The probe consists of four equally spaced tips which pass a current through the outer probes and measure the voltage across the two inner probes. A Jandel-RM2 meter was used to measure the resistivity of the TCO glass. The conductive glass was placed underneath the probe and it was lowered until it touched the TCO glass.

Other materials such as metals foils or organic polymers can be also used instead of TCO. The problem with metal substrates is corrosion. In this work, only TCO was considered.

4.1.2 Dense TiO₂ layer

The purpose of the dense layer is to reduce the back electron transfer to the redox electrolyte, i.e. the dark current, and also to provide a good adhesion of the transparent layer to the FTO.

Compact films of TiO₂ were produced by spray pyrolysis using a precursor of titanium diisopropoxide bis(acetylacetonate) (TAA was purchased from Sigma-Aldrich). The TAA was stored in an argon glove box. The TAA was diluted in ethanol in the volume ratio of 1 to 9 prior to use. Under atmospheric conditions, the colour of the precursor solutions changed from yellow to orange.

Although the photovoltaic characteristics of films prepared from old solutions and from fresh solutions did not show any significant difference, the precursor solutions were always freshly prepared before use.

4.1.3 Nanocrystalline TiO₂ layer

TiO₂ is the most famously used semiconductor for DSSC. It has very good chemical stability and it is non-toxic nor expensive. It has a slight n-type doping due to non-stoichiometry² and suitable conduction and valence band energies for use as a photoanode electrode with commonly available sensitiser. Titania electrodes were made in a manner based on the work of Ito *et al.*,³ with a structure shown in section 4.2.

The porous nanocrystalline TiO₂ thin film was prepared by screen printing a TiO₂ paste on the FTO substrate. The screen printing paste was provided by JGC-Catalysts & Chemicals Industries Co. (JGC-CCIC). This contained semiconductor particles nominally 18 nm in diameter as well as a binder and solvent. A 30 nm particle size paste was also used in some work.

4.1.4 Scattering TiO₂ paste

A second screen printing paste was developed following a literature procedure by Thompson *et al.*,⁴ in order to apply a scattering layer. This was based upon an aqueous solution of 400 nm TiO₂ particles, provided once again by JGC-CCIC. The scattering layer is produced by completing a solvent exchange of water for ethanol with commercial 400

4. Device fabrication and characterisation

nm and 18 nm Titania sols (HPW-400C and HPW-18NR). These are mixed together with 10 wt% ethyl cellulose in ethanol and terpineol with a weight ratio of 5:1:35:30.

The ethanol is then removed by rotary evaporation. Ethyl cellulose and terpineol were added in order to give an appropriate porosity during the calcination process. Porosity between 50 to 70 % is desired for the permeation of the electrolytes in the films thus maintaining a good contact between the redox species and the dyes on the TiO₂ surface.

4.1.5 Dyes

The harvesting of the incident light in high performance DSSCs is realised by a ruthenium dye which is chemisorbed onto the surface of the transparent layer. For high energy conversion, the dye should be able to absorb a large part of the solar light and be strongly attached to the surface of the semiconductor. The dye should also be stable in the ground and oxidised states and endure repeated oxidation and regeneration.

Ruthenium complexes are the most successful sensitisers to date. The cost of these dyes is quite high due to the rarity of ruthenium. Alternative dyes are under investigation, such as organic dyes and dyes which can also absorb into the infrared region.

The advantages of organic dyes are that they do not involve scarce elements, they have less impact on the environment, and they can be made quite easily as compared to ruthenium dyes. To date, the efficiency of organic dyes is not as high as the family of ruthenium dyes, but progress is narrowing the gap.

The ruthenium sensitisers *cis*-bis(isothiocyanato)bis(2,2'-bipyridyl-4,4'-dicarboxylato)-ruthenium(II) bis-tetrabutylammonium (N719) and *cis*-di(thiocyanato)-(2,2'-bipyridyl-4,4'-dicarboxylic acid)(4,4'-dinonyl-2,2'-bipyridyl)-ruthenium(II) (Z907) dyes were purchased from DyeSol. These dyes were purified before use. These ruthenium dyes were developed by Nazeeruddin⁵ and Zakeeruddin.⁶ A number of organic dyes such as porphyrin⁷⁻⁸ sensitisers and some new thiophene derivatives were provided by other research groups (full structural and detailed information will be provided in the relevant chapters). The structures of these dyes are given in Chapter 7.

4.1.6 Counter electrodes

The counter electrode of the DSSC usually consists of a FTO glass substrate with a layer of catalyst. During the functioning of a DSSC, a tri-iodide ion is formed by the reaction of the

oxidised ruthenium dye with the iodide ion. The function of the catalyst is to reduce the tri-iodide back to the iodide at the counter electrode. For the reaction to be effective, platinum is usually employed as a counter electrode. Other counter electrodes such as carbon⁹⁻¹⁰ (carbon nanotubes, graphite) and PEDOT¹¹⁻¹³ can also be used. Several techniques¹⁴ can be used for the deposition of Pt on TCO: electrochemical methods, electroplating, sputtering and thermal decomposition. Sputtered platinum electrodes are often very opaque, whereas with thermal deposition the platinised electrode can still be transparent, thus light can enter from both sides which can improve the performance of the device. With electrochemical techniques, the thickness of the catalyst can be varied. Only the thermal decomposition technique was used to prepare the counter electrode in this work.

4.1.7 Cell sealing

An ionomer resin Surlyn (Solaronix) of 25 μm was used as the sealing agent. The sealing material is necessary for keeping the electrolyte solution in between the two electrodes, thus preventing leakage and evaporation of the electrolyte, especially acetonitrile based electrolytes. In the case of solid electrolytes, the sealing material is not necessary. The cell can simply be clamped together. Epoxy resin can also be used as outer sealing materials for long term stability of DSSCs.

4.1.8 Electrolytes

As electrolytes are the main focus of this thesis, their preparation is described in the relevant chapters.

4.1.9 Chemicals and solvents

Hexachloroplatinic acid (H_2PtCl_6), acetonitrile (anhydrous, 99.9 %) valeronitrile (95 %), Hellmanex, lithium iodide (99.9 %), iodine (metal basis 99.99 %), guanidinium thiocyanate, 1-methylbenzimidazole, and tert-butylpyridine (95 %) were purchased from Sigma-Aldrich. Valeronitrile and tert-butylpyridine were purified by distillation and stored in an argon glovebox until use. Chloroform (HPLC grade), isopropanol (reagent grade) and ethanol (reagent grade) were purchased from Merck and used without further purification. All other reagents and solvents were used without further purification.

4.2 Device fabrication

A basic schematic structure of dye sensitised solar cells is shown in Figure 4.2. The device consists of a transparent conducting substrate (F doped Tin oxide), a transparent layer and on top of it, a scattering layer. Prior to the deposition of the dense TiO₂ layer, the FTO glass was cleaned by sonication for 10 minutes in a 5 wt% Hellmanex solution in water, followed by a rinse with distilled water and a further 10 min sonication in ethanol. Glass pieces were then stored in ethanol. Once the glass was removed from the ethanol, it was placed TCO side down, in order to dry. Hellmanex solutions were reused for a long period.

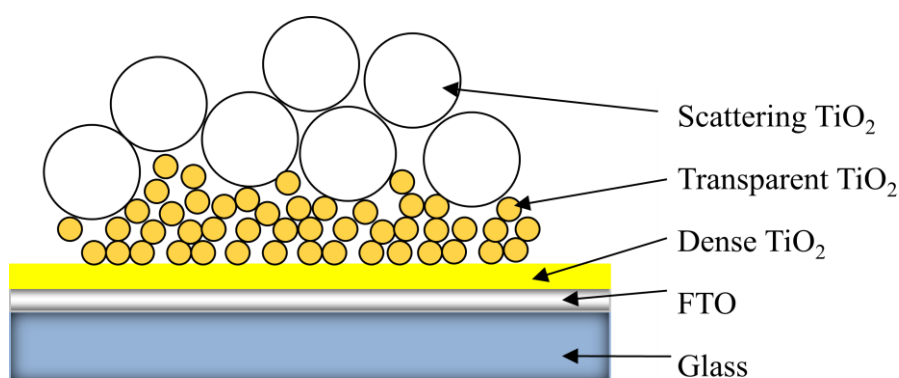


Figure 4.2: Schematic diagram of the photoanode

The dense layer of TiO₂ was deposited by spray pyrolysis of the precursor TAA, following a literature procedure by Kavan¹⁵. The substrates were heated on a temperature controlled hotplate to 450 °C at a ramp of 20 °C min⁻¹. The precursor solution was sprayed from a distance of 10 cm using a chromatographic atomiser (Glass Keller) every 10 seconds for 2 mins in the middle and in each corner of the (100 mm x 100 mm) glass plate.

After spray pyrolysis, the substrates were allowed to thermally equilibrate for 5 mins and then cooled down to room temperature. The substrates were then stored in a closed plastic container. The nature of the dense layer manifests itself by blocking anodic reaction on the bare TiO₂ electrodes. The mesoporous TiO₂ layer was then deposited by using a semi automatic screen printing method on a full sheet of unscored NPG (100 x 100 mm). After the first coating, the TiO₂ layer was allowed to settle for 5 minutes in a closed container and then dried at 125 °C for 15 minutes to remove the solvent, whereupon a second layer may be printed and/or a scattering layer as per requirements. Figure 4.3 and 4.4 show the

4. Device fabrication and characterisation

SEM images of an 18 nm particle TiO_2 film and a 30 nm particle TiO_2 film after full sintering. The films are quite homogenous without any big agglomerates.

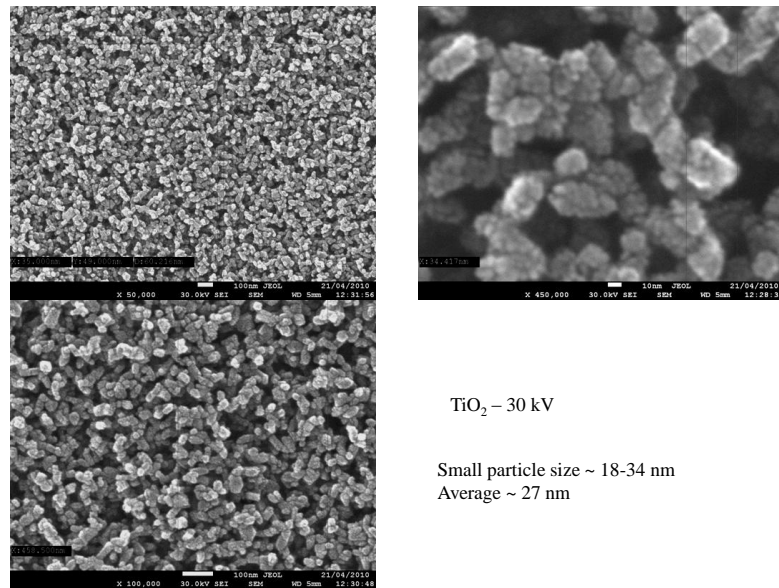


Figure 4.3: SEM images of the transparent layer (TiO_2)

The purpose of the scattering layer is to recapture the light reflected by the transparent layer thus enhancing the light harvesting.

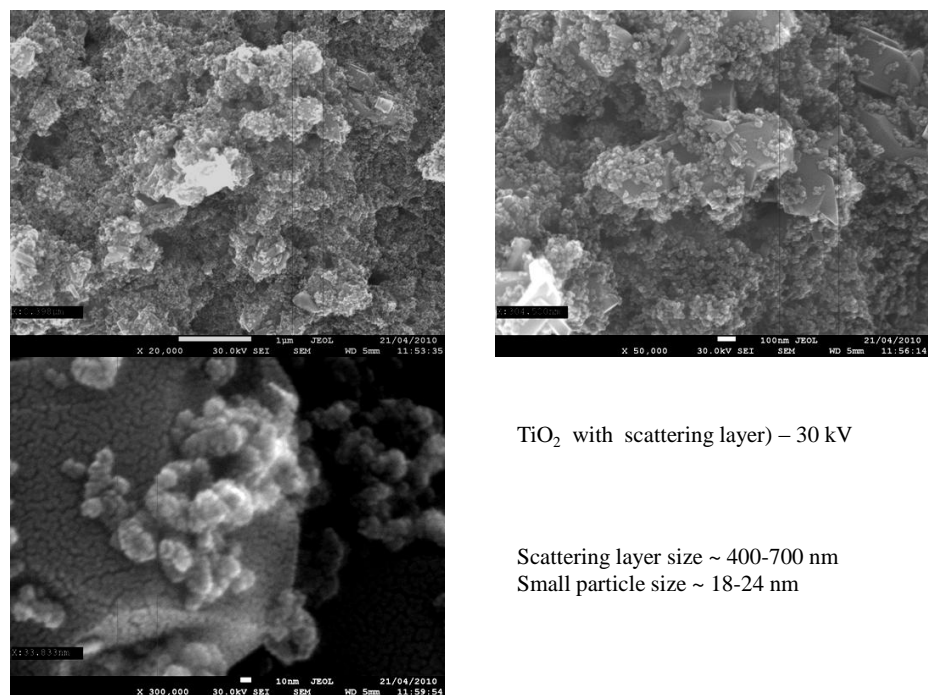


Figure 4.4: SEM images of the scattering layer

4. Device fabrication and characterisation

Once all layers were deposited, the substrates were allowed to settle in a covered container for 15 min. The substrates were then fully sintered according to the following temperature program as shown in Figure 4.5.

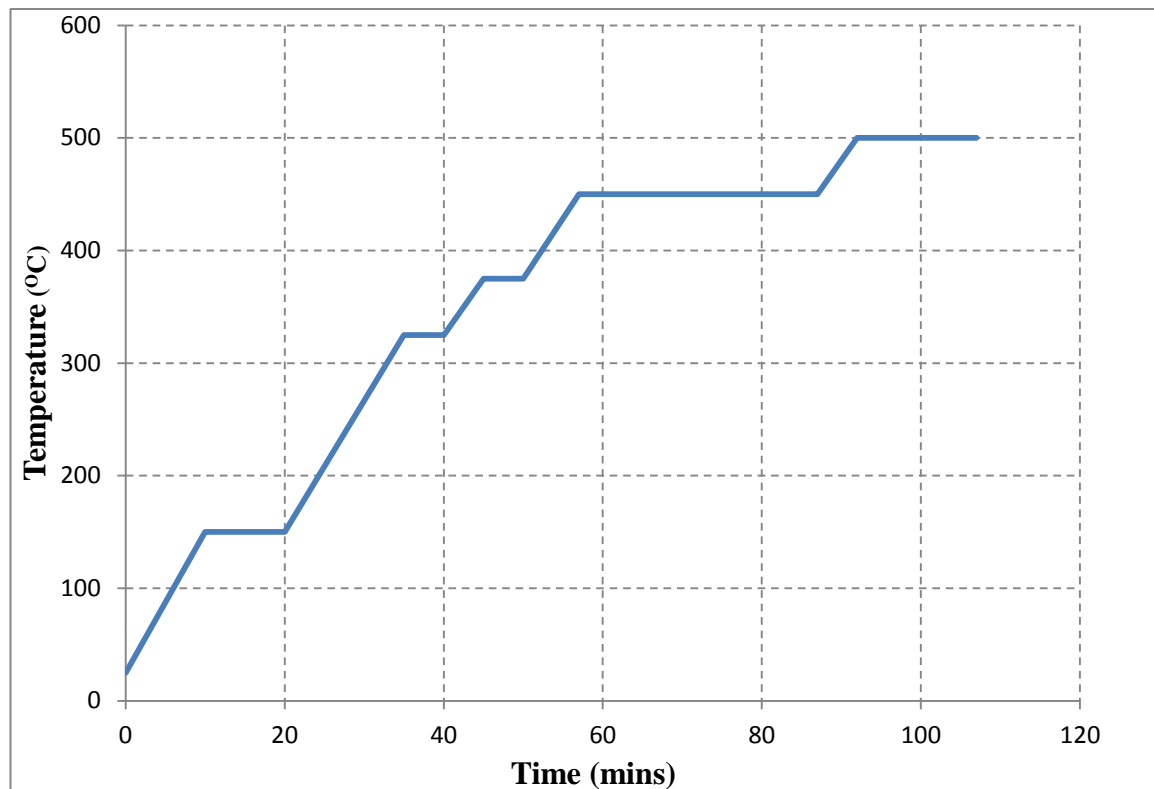


Figure 4.5: Temperature profile for full sintering of substrates

The temperature program consists of heat ramps and isotherms that are chosen to separate the burning of additives present in the pastes. This temperature profile was also used to obtain reproducible grain growth and phase transformation of the TiO_2 . The sintering process was carried out under an oxygen flow. TiO_2 films of various thicknesses were printed using the appropriate mesh.

The Titania films were then subjected to a TiCl_4 post treatment.¹⁶ This treatment was demonstrated by Kay¹⁷ to increase the injection of electrons into the TiO_2 resulting in an increase in current. The downside of this treatment is that it decreases the average pore size and the porosity. Thus the concentration and treatment time needs to be well controlled and optimised. 0.2 M of TiCl_4 in distilled water was made up and kept in the fridge at approximately 4 °C. 20 mM of TiCl_4 solution was produced immediately prior to use to avoid undesired hydrolysis reactions occurring.

The films were immersed in the TiCl_4 solution at 70 °C for 30 min. The films were then washed thoroughly with distilled water and ethanol, and then they were refired at 500 °C for 15 min. If not used directly after preparation, the TiO_2 films were stored in closed plastic container.

Before the dye uptake, the films were once again heat treated at 500 °C for 30 min using a heat gun. The firing leads to a dehydroxylated, highly activated surface for dye adsorption.

Once the electrodes were cooled to 110 °C, the electrodes were placed back to back and dipped into the dye solution at room temperature and in the dark. The dying time for ruthenium based sensitisers is 16 hrs whereas for some organic dyes, only 2 to 4 hrs is required.

Glass used for counter electrodes was scored and broken into 12.5 mm x 16.5 mm sections. Holes of approximately 1 mm diameter were drilled into the counter electrode for filling the cell with electrolyte. A Dremmel drill and a number 835-104-008 burr on setting 5 were used to drill the holes in the counter electrode. The glass was completely immersed in water to prevent the burr breaking during the drilling process. The hole was partially drilled from the non conductive side first and then flipped over to the conductive side and finished. This is done in such way to prevent any “punch through” from occurring; ensuring that in the final device, the area taken up by this hole would not overlap with the active film area. When drilling was complete the glass was cleaned in the same fashion as the working electrodes.

In this work, Pt was applied by thermal decomposition of H_2PtCl_6 . A 10 mM solution of H_2PtCl_6 in ethanol was prepared in a glove box and stored in the dark. A drop of this solution was placed onto the conductive side of the TCO glass electrode and smeared with the end of a Pasteur pipette, and allowed to dry. Then the electrodes were placed on a tile and inserted into a ceramic tube. A round bottom flask was placed at one end of the ceramic tube and a heat gun at the other, as shown in Figure 4.6. The electrodes were fired at 400 °C for 15 min. This results in formation of Pt particles on the surface as shown in the SEM images in Figure 4.7. The properties of the Pt counter electrode directly affect the fill factor of the solar cells.

4. Device fabrication and characterisation

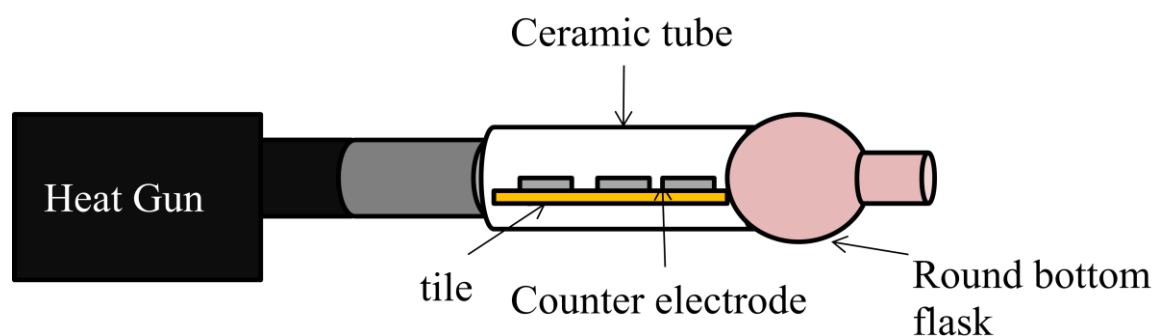


Figure 4.6: Heat gun for platinising counter electrode for dye sensitised solar cells

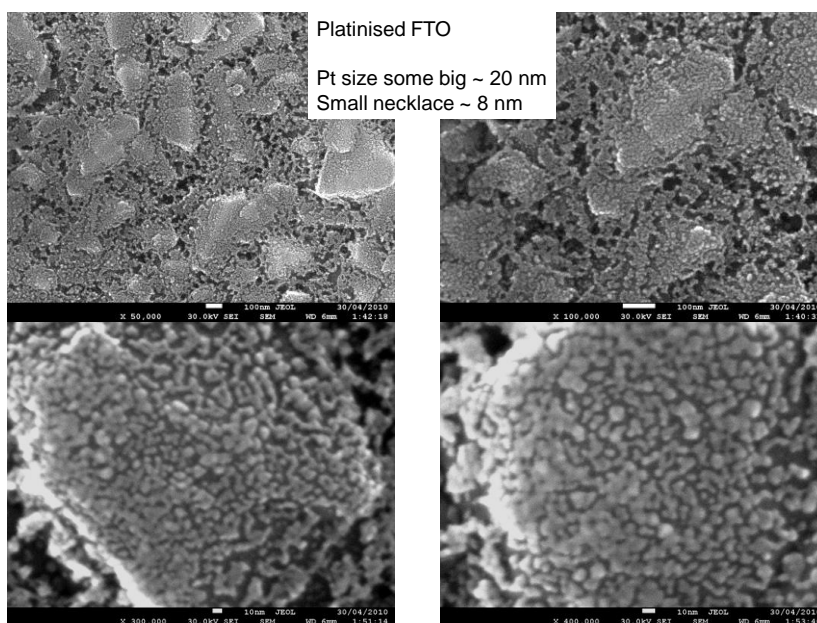


Figure 4.7: SEM images of platinised FTO

Working electrodes, once removed from dye solution, were washed vigorously in the same solvent as the dye solution for a few seconds before being allowed to sit for a minute and then dried. Once dried, electrodes were kept under restricted light until the electrolyte solution has been introduced in order to avoid oxidation and degradation of the dye.

Cells were assembled by pressing the working and counter electrodes together using a 25 μm Surlyn film spacer (purchased from Solaronix) at elevated temperature. This allowed the Surlyn to melt sufficiently to hold the electrodes together at a determined distance. This Surlyn gasket surrounds the dye film and the filling port. The width of the Surlyn is approximately 2 mm. This width allows one to determine if overheating has occurred, where the Surlyn spreads wider than 2 mm. Overheating leads to degradation of the sensitiser, so to this end, a cell press was designed and constructed by SMC Pneumatics

Pty. Ltd., which allowed heating from the counter electrode side and had a copper tip pressed against the working electrode immediately behind the dye film. Heat and pressure were applied for 18 seconds. This was repeated again up to two more times, in case the Surlyn had not created a complete seal.

Once the photoanodes were sandwiched together with the platinised counter electrodes, the cells were then filled with an electrolyte by a vacuum backfilling method. The filling port was then cleaned and sealed using Surlyn and a microscope cover slide or with aluminium. Contacts on cells were made using a sonic soldering iron (using a Cerasolver CS186 at 220 °C, with an oscillation of 60 kHz). Figure 4.8 shows a schematic diagram of an assembled dye sensitised solar cells.

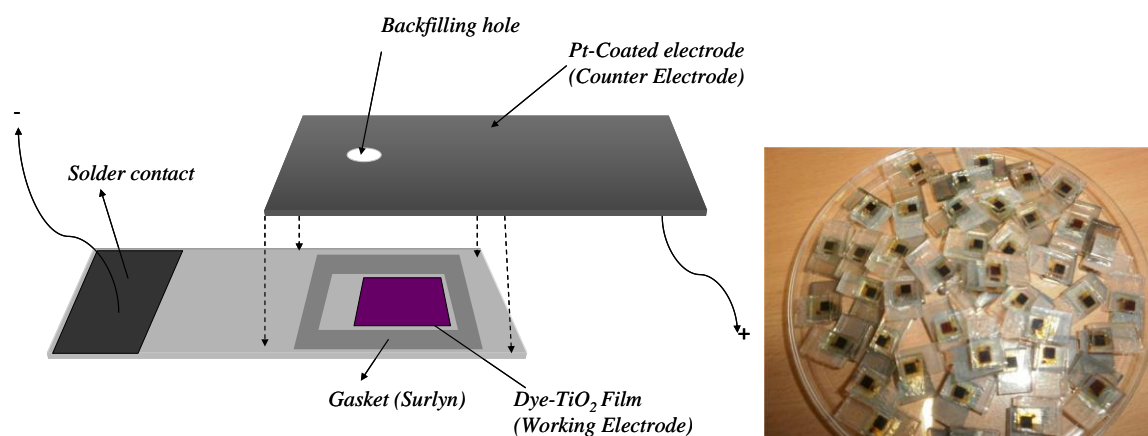


Figure 4.8: Schematic diagram of a dye sensitised solar cells and real devices for testing different dyes and electrolytes

4.3 Characterisation and measurement

4.3.1 Current-Voltage characterisation

Photovoltaic devices were measured using simulated sunlight (AM 1.5, 100 mW cm⁻²) provided by an Oriel solar simulator with an AM 1.5 filter before the Xenon lamp. Current-Voltage characteristics were measured using a computer controlled potentiostat (Keithley 2400, SourceMeter). Cells were biased from high to low, with 10 mV steps and the settling time was varied depending on the electrolytes used. The settling time is the delay between the application of a bias and the current measurement. It was found that this comparatively long settling time was required to avoid measurement artefacts due to mass transport of the redox couples in the electrolyte. The power of the simulated light was

4. Device fabrication and characterisation

calibrated with a reference Silicon photodiode. The light intensity was varied using meshes in front of the Xenon lamp. The set up allowed measurements at 5.8 %, 10 %, 15 %, 38 %, 64 % and 100 % sunlight respectively.

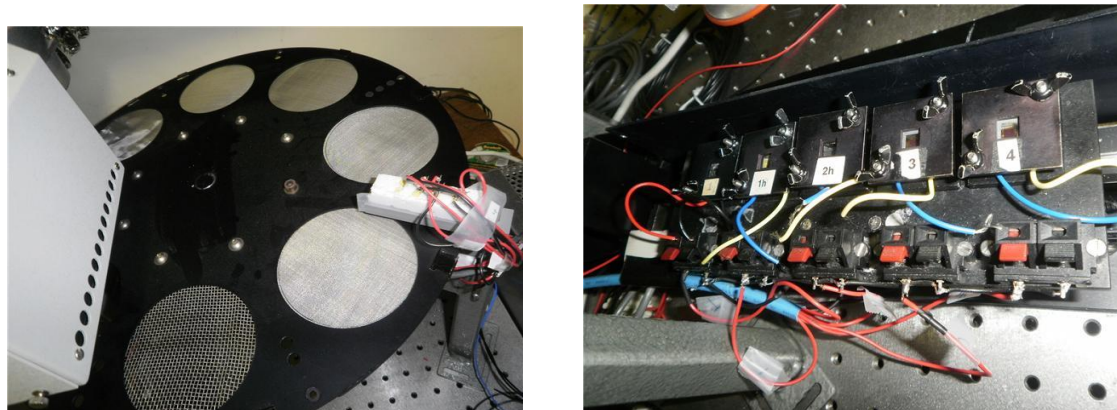


Figure 4.9: Filter wheel used to measure the DSSC at different light intensity (left) and the translation stage used to measure the performance of the device (right)

4.3.2 Incident photon-to-current conversion efficiency (IPCE)

The incident photon-to-current conversion efficiency (IPCE) describes the spectral operation range of a specific solar cell as a function of wavelength. IPCEs were measured with the cell held under short circuit conditions and illuminated by monochromatic light. A Cornerstone 260 monochromator was used in conjunction with an optical fibre, Keithley 2400 SourceMeter and 150 W Oriel Xe lamp.

A silicon diode was used to calibrate the light source prior to testing. Also prior to testing, a 30 second ‘rest’ period was introduced to ensure the dark current dropped to zero once the cell was short circuited. Additionally a 200 ms settling time was used at each frequency step. This was followed by an averaged reading over a 1 second period.

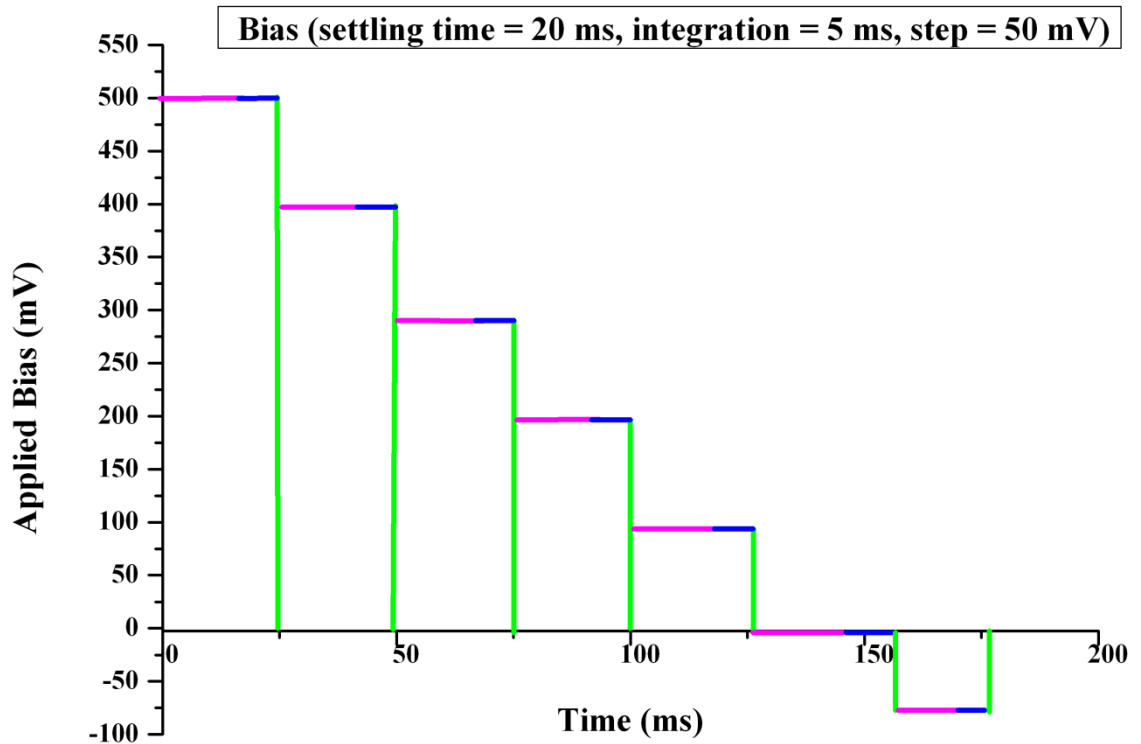


Figure 4.10: Schematic of applied bias as a function of time, showing settling time (red), integration time (blue) and switching (green)

4.3.3 Absorbed photon-to-current conversion efficiency (APCE)

Absorbed photon-to-current conversion efficiency (APCE) is defined as the amount of absorbed photons that generate electrons in the external circuit. The relationship between IPCE and APCE is shown in equation 4.1, where LHE corresponds to the light harvesting efficiency. LHE quantifies absorbance of monochromatic light by a device as a function of absorption.

This gives a more accurate depiction of what is really happening with the photons, since it is possible to separate the photons that have been absorbed and lost, from the photons that have not been absorbed by the dye. This measurement allows for the determination of the charge injection of electrons in the conduction band and gives an idea about recombination reactions occurring in the device.

$$APCE = \frac{IPCE(\lambda)}{LHE} \quad (\text{Eq 4.1})$$

4. Device fabrication and characterisation

4.3.4 UV/Vis spectroscopy

Dye loading was analysed with the aid of a Cary 5000 photospectrometer, measuring the optical absorption of TiO₂ films before and after dyeing (with different organic dyes). Films were characterised optically using an integrating sphere attached to a Cary 5000 UV-Vis-NIR spectrometer. This equipment facilitates the collection of the total transmission, diffusive transmission, total reflection and diffusive reflection. Absorption spectra are measured with a 1 cm optical path quartz cell.

4.3.5 Scanning Electron Microscopy

Scanning Electron Microscopy images were recorded in the Monash Centre for Electron Microscopy. The samples were coated with thin layer of gold and SEM images were obtained using a JEOL 7100F field emission gun scanning electron microscope. Excitation wavelengths used and magnifications are shown on each picture. The SEM images were taken by Dr. Orawan Winther-Jensen.

4.3.6 Profilometer

A semi automatic VeeCo Dektak 150 profilometer was used to measure the thickness of films. The profilometer is a measuring instrument used not only to profile surface topography and waviness, but also the surface roughness in the nanometre range. The Dektak 150 profilometer takes measurement electromechanically by moving the samples beneath a diamond-tipped stylus. The profilometer is able to measure small variation in height from 10 nanometres to 1 millimetre.

4.3.7 BET analysis

Brunauer, Emmett, Teller (BET) analysis was conducted using nitrogen desorption at 77 K on Micrometrics TRiSTAR 3000 equipment, for a series of powders (collected from prepared films). The TiO₂ films used in this research were scratched off from glass plates after full sintering. The data used for the research are shown in Figure 4.11 and were obtained by Dr. Fuzhi Huang.

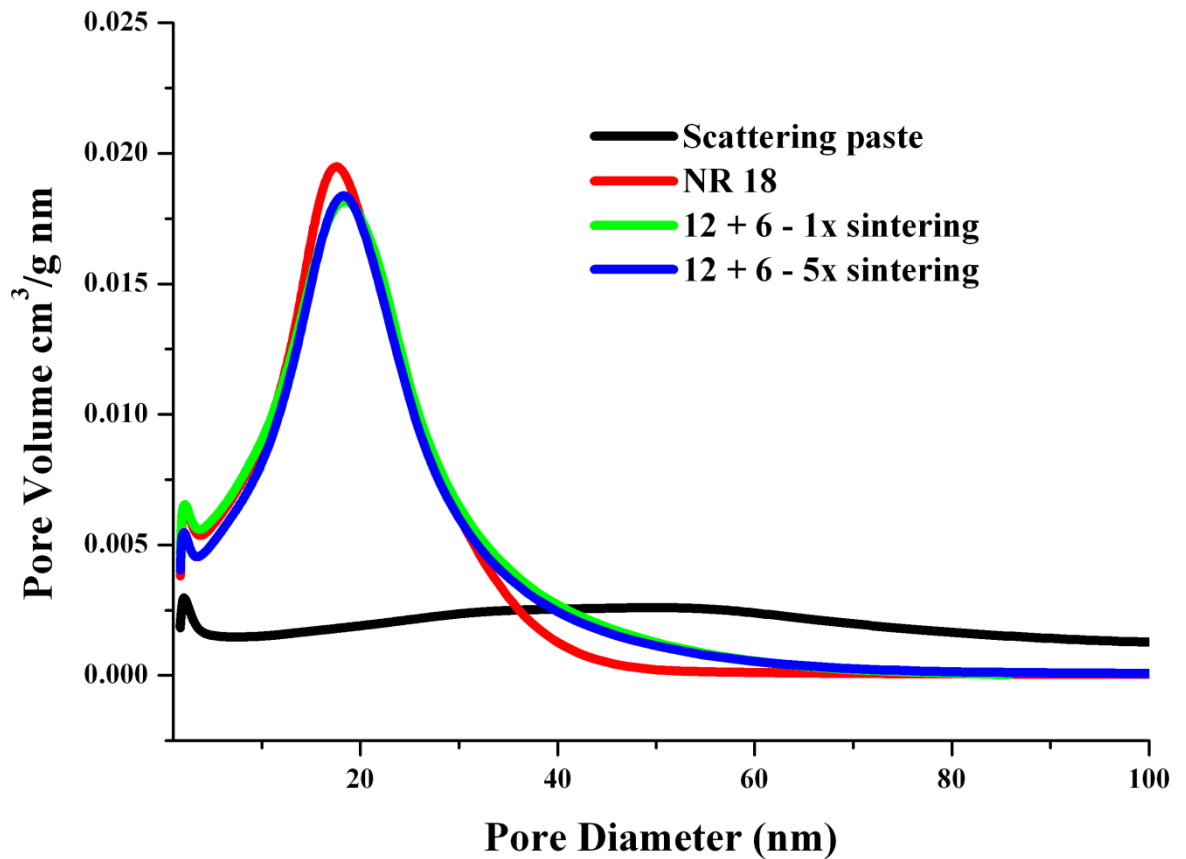


Figure 4.11: Shows the pore distribution of the paste and the scattering layer paste and the effect of sintering

The effect of sintering does not affect the porosity of the films. The porosity of the 18 nm particle based material is about 58 %, the surface area is $86 \text{ m}^2 \text{ g}^{-1}$ and the roughness factor is 138.

These powders were also used for X-Ray Diffraction (XRD) analysis (Phillips powder diffractometer with a 1° divergence slit, 0.2° receiving slit and carbon monochromator) where they were examined under $\text{Cu K}\alpha$ radiation from $25\text{-}60^\circ$ at 0.02° increments.

4.3.8 Error Analysis

In most cases, experiments were carried out multiple times and error bars were calculated. Statistical analyses were used to determine the mean values, as well as the standard deviation. In general, error bars are not included on the graph for clarity, but error results are tabulated.

References

1. N. J. Arfsten, *J. Non-Cryst. Solids*, 1984, **63**, 243-249.
2. E. G. Seebauer, *Charged Semiconductor Defects: Structure, Thermodynamics and Diffusion*, Springer, 2009.
3. S. Ito, T. N. Murakami, P. Comte, P. Liska, C. Grätzel, M. K. Nazeeruddin and M. Grätzel, *Thin Solid Films*, 2008, **516**, 4613-4619.
4. S. J. Thompson, N. W. Duffy, U. Bach and Y. B. Cheng, *J. Phys. Chem. C*, 2010, **114**, 2365-2369.
5. M. K. Nazeeruddin, A. Kay, I. Rodicio, R. Humphry-Baker, E. Mueller, P. Liska, N. Vlachopoulos and M. Grätzel, *J. Am. Chem. Soc.*, 1993, **115**, 6382-6390.
6. S. M. Zakeeruddin, M. K. Nazeeruddin, R. Humphry-Baker, M. Grätzel and V. Shklover, *Inorg. Chem.*, 1998, **37**, 5251-5259.
7. W. M. Campbell, A. K. Burrell, D. L. Officer and K. W. Jolley, *Coord. Chem. Rev.*, 2004, **248**, 1363-1379.
8. W. M. Campbell, K. W. Jolley, P. Wagner, K. Wagner, P. J. Walsh, K. C. Gordon, L. Schmidt-Mende, M. K. Nazeeruddin, Q. Wang, M. Grätzel and D. L. Officer, *J. Phys. Chem. C*, 2007, **111**, 11760-11762.
9. W. J. Lee, E. Ramasamy, D. Y. Lee and J. S. Song, *Sol. Energy Mater.*, 2008, **92**, 814-818.
10. W. W. Ji, X. D. Zhang, Y. Zhao, Z. H. Yang, N. Cai, C. C. Wei, J. Sun and S. Z. Xiong, *Phys. Status Solidi C*, 2010, **7**, 1124-1127.
11. S. Ahmad, J. H. Yum, Z. Xianxi, M. Grätzel, H. J. Butt and M. K. Nazeeruddin, *J. Mater. Chem.*, 2010, **20**, 1654-1658.
12. J. M. Pringle, V. Armel, M. Forsyth and D. R. MacFarlane, *Aust. J. Chem.*, 2009, **62**, 348-352.
13. Y. Saito, W. Kubo, T. Kitamura, Y. Wada and S. Yanagida, *J. Photochem. Photobiol., A*, 2004, **164**, 153-157.
14. B. K. Koo, D. Y. Lee, H. J. Kim, W. J. Lee, J. S. Song and H. J. Kim, *J. Electroceram.*, 2006, **17**, 79-82.
15. L. Kavan and M. Grätzel, *Electrochim. Acta*, 1995, **40**, 643-652.
16. B. C. O'Regan, J. R. Durrant, P. M. Sommeling and N. J. Baker, *J. Phys. Chem. C*, 2007, **111**, 14001-14010.
17. A. Kay and M. Grätzel, *Chem. Mater.*, 2002, **14**, 2930-2935.

Chapter 5

Synthesis of novel phosphonium ionic liquids

Chapter overview

Asymmetric aliphatic short tetraalkyl chain phosphonium ionic liquids comprised of triisobutyl(methyl)phosphonium, diethylmethyl(isobutyl)phosphonium, butyl(triethyl)phosphonium and methyl(triethyl)phosphonium cations combined with different anions such as dicyanamide, bis(trifluoromethanesulfonyl)amide, bis(fluorosulfonyl)amide, thiocyanate, tetrafluoroborate and hexafluorophosphate were synthesised for use in dye sensitised solar cells. The physicochemical properties of this class of material, such as the ionic conductivity, viscosity and thermal behaviour, were compared with the imidazolium or ammonium based ionic liquids and with the two well-known high viscosity phosphonium ionic liquids: tetradecyl(trihexyl)phosphonium bis(trifluoromethanesulfonyl)amide¹⁻² and tetradecyl(trihexyl)phosphonium dicyanamide,³ as well as with the low viscosity phosphonium ionic liquids synthesised by Tsunnashima *et al.*⁴ The viscosity and conductivity of the phosphonium salts were analysed using the Walden rule, to investigate the degree of ion association. The electrochemical window of these new phosphonium ionic liquid were also investigated to determine their suitability for applications other than solar cells.

5. Synthesis of novel phosphonium ionic liquids

5.1 Introduction

Imidazolium based ionic liquids have been extensively studied as potential electrolytes due to their interesting physical and chemical properties, which make them good candidates for many applications such as fuel cells,⁵⁻⁷ batteries,⁸⁻¹¹ super capacitors,¹²⁻¹³ actuators¹⁴⁻¹⁵ and dye sensitised solar cells.¹⁶⁻²³ During the last decade, many publications from academia and industry have discussed the use of this particular class of ionic liquids.²⁴⁻²⁵ In contrast, phosphonium based ionic liquids have been largely ignored for a long time. The main reason for the lack of interest in this class of materials is the high viscosity as well as the hazardous aspect and poor availability of the starting materials: trialkylphosphine, which can be dangerous and may prohibit synthesis even on a laboratory scale. Trialkylphosphines are made by free radical addition of phosphine to olefins. Tetraalkylphosphonium salts are then synthesised from these by nucleophilic addition of the tertiary phosphine with haloalkane.²⁶

Cytec Industries and Nippon Chemical have long histories in manufacturing trialkylphosphine and tetraalkylphosphonium salts,²⁷⁻²⁸ thus making it possible to design a variety of phosphonium ionic liquids. Over the past decade, Cytec Industries have developed a number of high viscosity phosphonium ionic liquids, in combination with different anions such as tosylate, methylsulfate, tetrafluoroborate (BF₄) and bis(trifluoromethanesulfonyl)amide.²⁹ Phosphonium based ionic liquids under the brand name Cyphos are now available and they are manufactured in large scale at Cytec Industries.²⁶

The most commonly studied phosphonium cations are the trihexyl(tetradecyl)phosphonium,³⁰⁻³¹ tetrabutylphosphonium,³²⁻³³ tributyl(ethyl)phosphonium,³⁴ and triisobutyl(methyl) phosphonium,³⁵ combined with various anions such as dicyanamide (N(CN)₂),³⁶ bis(trifluoromethanesulfonyl)amide (NTf₂),^{1, 37} hexafluorophosphate (PF₆)³⁸⁻³⁹ and halides.⁴⁰

5.1.1 Synthetic routes to phosphonium-based ionic liquids

5.1.1.1 Metathesis route

With the growing interest in phosphonium ionic liquids, Bradaric *et al.*²⁶ studied a range of potential ILs for industrial production. They synthesised a variety of phosphonium salts based on anions such as dimethylphosphate, tosylate, tetrafluoroborate and chloride.

Trihexyl(tetradecyl)phosphonium chloride has been the starting material for the synthesis of numerous phosphonium based ionic liquids via anion exchange reactions. The ion exchange reactions can be done in two ways, as shown in equations 5.1 and 5.2.



Where R,R' = alkyl; X = halogen, M = alkali metal and A = anion such as decanoate, carboxylate, tetrafluoroborate and hexafluorophosphate.

5.1.1.2 Halide free route

Phosphonium ionic liquids prepared by the metathesis methods usually contain residual amount of halides, which can have a negative effect on many applications. Seddon *et al.*⁴¹ have demonstrated that halide contaminants can have a negative or positive effect depending on the reaction that is being conducted. For example, chloride ions have a detrimental effect on transition metal catalysed reactions,⁴²⁻⁴³ whereas bromide ions accelerate Heck coupling and have a stabilising effect on palladium.⁴⁴ Halides can also lower the electrochemical window of the ionic liquid, thus limiting its potential use as an electrolyte for lithium batteries.⁴⁵⁻⁴⁶

Anion exchange mechanisms are quite expensive and very wasteful. They also often involved the use of environmentally hazardous organic solvents. Thus a halide free route was developed by Bradaric *et al.*²⁶ to limit the use of hazardous materials and to make it cost effective for industrial applications. The synthesis involved the quaternisation of tertiary phosphine with dialkylsulfates, trialkylphosphates and alkylphosphonates.

5.1.2. Applications of phosphonium based ionic liquids

Phosphonium ionic liquids have been traditionally applied as phase transfer catalysts.⁴⁷⁻⁴⁹ Yadav *et al.*⁵⁰ have studied the alkylation of 2-Naphthol using the trihexyl(tetradecyl)phosphonium cation, with anions such as decanoate, hexafluorophosphate, chloride and bromide. They demonstrated that the use of the phosphonium bromide salts showed more rapid anion exchange with the nucleophile. Shanks *et al.*⁵¹ have also shown that the preparation of esters from 3-amino-4-halobenzoic

5. Synthesis of novel phosphonium ionic liquids

acid via phase transfer catalysis proceeds with better yields using tetraalkylphosphonium halides rather than tetraalkylammonium-based salts.

Phosphonium based ionic liquids have also been successfully used as solvents for strong bases and Grignard reagents.⁵²⁻⁵³ Ramnial *et al.*⁵⁴ have shown that phenylmagnesium bromide in THF was stable for days in trihexyl(tetradecyl)phosphonium chloride. They have demonstrated that phosphonium-based ionic liquids are more suitable for reactions involving strong bases than imidazolium-based ionic liquids. They have also shown that imidazolium based ionic liquids are unsuitable for reactions involving active metals such as sodium or potassium. For instance, imidazolium based ionic liquids react with potassium metal to produce imidazole-2-ylidenes.

Tindale *et al.*⁵⁵ synthesised a new class of highly fluorinated phosphonium ionic liquids designed to form superhydrophobic coatings. Deposition of films of the highly fluorinated phosphonium ionic liquids on silver-coated copper substrate were indeed able to produce water contact angles more than 160 °.

The two well known phosphonium based ionic liquids tetradecyl(trihexyl)phosphonium bis(trifluoromethanesulfonyl)amide and dicyanamide ($P_{66614}NTf_2$ and $P_{66614}N(CN)_2$) have been used as electrolytes in supercapacitors. 5 to 25 wt% of acetonitrile was added to these ILs to lower their viscosity.¹³ Frackowiak *et al.*¹³ were able to design a supercapacitor which can function at 3.4 V with high energy values of 40 W h kg⁻¹ and good cyclability.

While phosphonium ionic liquids have been studied in the fields discussed above and a range of publications detail their use in these applications, one area where phosphonium ionic liquids have been seldom reported is in the dye sensitised solar cells field. The main reason for this is the high viscosity of many of the commercially available phosphonium ionic liquids. However, Cytec Industries are now making asymmetric short alkyl chain phosphonium based salts, thus opening up this family of ionic liquids to an exciting new type of application.

For example, Ramirez *et al.*⁵⁶ have used an asymmetric phosphonium-based ionic liquid as an electrolyte component for dye sensitised solar cells. Isobutyltrihexylphosphonium iodide shows the highest ionic conductivity of the ILs tested and a solar cell efficiency of 5.9 % at 8.9 mW cm⁻² light intensity obtained using a ruthenium based sensitiser with isobutyltrihexylphosphonium iodide in a mixture of propylene carbonate and acetonitrile.

Tsunashima *et al.*⁴ have synthesised a range of triethylalkylphosphonium cations together with anions such as NTf₂⁻, FSI⁻ (bis(fluorosulfonyl)imide) and N(CN)₂⁻, all of which have low viscosities. Addition of a methoxy group to the cation further lowers the room temperature viscosity, to even lower than their ammonium counterparts. Table 5.1 summarises the properties of the phosphonium and corresponding ammonium ILs.⁴

Table 5.1: Physical and thermal properties of phosphonium and ammonium ionic liquids synthesised by Tsunashima *et al.*⁴

Ionic liquid	Viscosity (mPa s at 25 °C)	Decomposition Temperature (°C)
P ₂₂₂₍₂₀₁₎ NTf ₂	44	404
P ₂₂₂₍₁₀₁₎ NTf ₂	35	388
N ₂₂₂₍₂₀₁₎ NTf ₂	85	384
N ₂₂₂₍₁₀₁₎ NTf ₂	69	287

Nippon Chemical is now marketing these low viscous phosphonium ionic liquid such as P₂₂₂₍₁₀₁₎NTf₂, P₂₂₂₍₁₀₁₎FSI (refer to Figure 5.2) and many others.

5.1.3 Transport properties of phosphonium based ionic liquids

The mobility of ions in an ionic liquid is very important for dye sensitised solar cells. The physical properties of ionic liquids, such as the viscosity and conductivity, can greatly affect the device performance. The presence of impurities can also have a great impact on the transport of ions in ILs. The presence of trace amount of halides can increase the viscosity of the ionic liquid whereas the presence of moisture can increase the ionic conductivity of the ILs. Furthermore, water contamination of PF₆⁻ ionic liquids can lead to the formation of HF.

One reason for these effects is the impact of the impurity on the association of the ions in the neat ionic liquids. Ionic liquids are composed of a cation and an anion and thus the concentration of ions is usually very high around 5 M.⁵⁷ Thus, the formation of ion pairs or aggregates is expected to some extent in neat ionic liquids. The formation of ion pairs has been shown to lower the conductivity.⁵⁸⁻⁵⁹ Such conductivity effects are important to discuss as they have an impact on the potential use of the ionic liquids as electrolytes in lithium batteries,^{11, 60-61} fuel cells,^{6, 62} supercapacitors⁶³ and dye sensitised solar cells⁶⁴ where high conductivity of the redox active ions is required for the device to perform

5. Synthesis of novel phosphonium ionic liquids

efficiently. Ion pairs can be identified by conductivity measurements (electrochemical impedance spectroscopy) and NMR techniques (pulse gradient spin echo NMR).

5.1.3.1 Method for assessing the formation of aggregates in an ionic liquid: the Walden plot

The Walden plot⁶⁵⁻⁶⁶ has been widely used in recent years to illustrate the relationship between conductivity and fluidity (inverse of viscosity) of neat ionic liquids.⁵⁸

The product of ionic mobility and solvent viscosity, known as the Walden product,⁶⁷ has been used as a means to gain a perspective on ion-solvent interactions. For infinitely diluted electrolyte solutions, the Walden product is a constant and is expressed by equation 5.3:

$$\Lambda\eta = C \quad (\text{Eq 5.3})$$

$$\text{Log } \Lambda = \text{log } C + \text{log } \eta^{-1} \quad (\text{Eq 5.4})$$

where Λ is the molar conductivity, η is the viscosity and C is a constant.

The molar conductivity of an ionic liquid is defined as the conductivity (σ) of the solution divided by the molar concentration (C) of the charge carriers, and it is given by equation 5.5:

$$\Lambda = \frac{\sigma}{C} = \sigma \frac{M}{\rho} \quad (\text{Eq 5.5})$$

where M is the molecular weight of the ionic liquid, ρ is the density of the ionic liquid and σ is the specific conductivity.

Angell and co-workers^{5, 68-70} have discussed ion dissociation in ionic liquids using the relationship between $\text{log } \Lambda$ and $\text{log } \eta^{-1}$, and compared this behaviour to that of a reference material (which produces the so-called “ideal” line). The ideal behaviour is constructed using data for dilute aqueous KCl solutions, in which the system is completely dissociated and contains equal amount of both ions. The log-log plot thus allows comparison of the behaviour of ionic liquids with respect to their ideal behaviour.

Deviation from the ideal behaviour

Any downward deviation from the ideal line indicates the presence of ion pairing, aggregation or low dissociation of ions according to Angell *et al.*⁶⁹ They have classified the behaviour of ionic liquids, according to the Walden rule, into different categories such as superionic liquids, poor ionic liquids, good ionic liquids and non ionic liquids. All ionic liquids that fall below the reference line by an order of magnitude (one log unit) or more are considered poor ionic liquids, with low conductivity and high vapour pressure. Protic ionic liquids are considered as poor ionic liquids as they fall well below the reference line due to incomplete proton transfer. Nevertheless, protic ionic liquids have been successfully used in fuel cells.⁷¹⁻⁷² Ionic liquids above the line are considered as superionic liquids, while ionic liquids that lie close to the ideal line are classed as good ionic liquids, in which the ions are considered to be completely independent or fully dissociated.

Figure 5.1 shows the classification system of the Walden plot and deviation from the ideal behaviour, as proposed by Angell and co-workers.⁷⁰

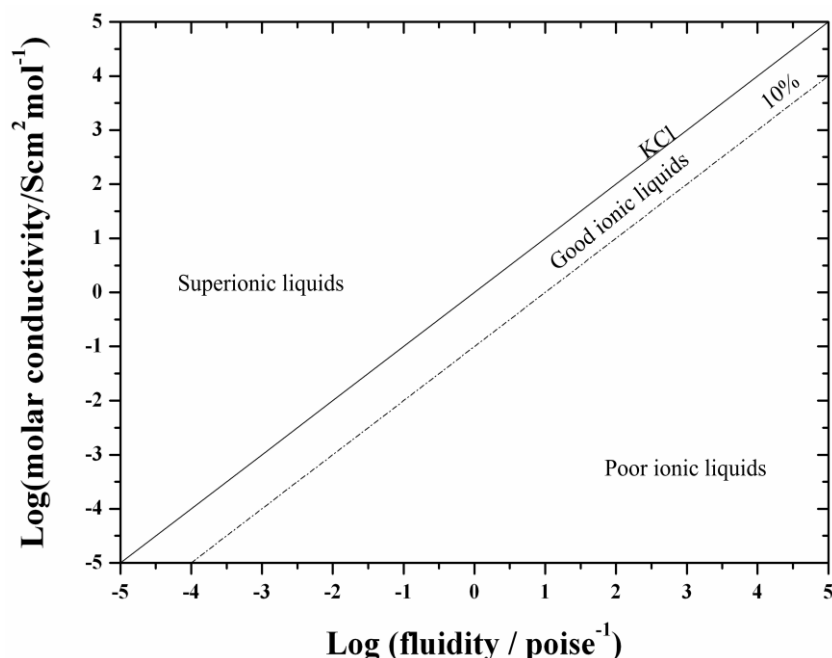


Figure 5.1: Classification of ionic liquids according to Angell *et al.*⁷⁰ The 10 % line indicates the situation where the molar conductivity is only 10 % of that predicted from the viscosity by the Walden rule

5. Synthesis of novel phosphonium ionic liquids

5.1.3.2 Method of assessing ion pairs in ionic liquids: Stokes-Einstein equation and Nernst-Einstein equation

The potential use of ionic liquids as electrolytes depends strongly on the transport properties of the ions i.e. on the rate of ion movement and the way the ions move, either as individual ions or ion pairs or aggregates. In electrochemistry, the transport properties of electrolytes are governed by the diffusion coefficients of the ions and the transference number of the ions. The diffusion coefficient is the measure of the mobility of the ions and the transference number is the fraction of current carried by an ion in the presence of an electric field.

The diffusion coefficient can also be obtained by diffusion NMR analysis. This value is slightly different from the diffusion coefficient obtained from electrochemical methods, which is due to a concentration gradient. In the NMR analysis, the diffusion coefficient is due to self diffusion of the individual ionic species.⁷³

The Stokes-Einstein⁷⁴⁻⁷⁶ equation relates the diffusion of ions in an electrolyte to its viscosity and is given by the following equation

$$D = \frac{k_B T}{X \pi r \eta} \quad (\text{Eq 5.6})$$

where D is the self diffusion coefficient ($\text{m}^2 \text{s}^{-1}$), k_B is the Boltzmann constant (J K^{-1}), T is the temperature (K), r is the hydrodynamic radius (m), η is the viscosity (Pa.s) and X is a constant that varies between 4 and 6.

The Stokes-Einstein equation is usually applied to the diffusion of a molecule in a liquid but it has been shown by Watanabe *et al.* to also relate well to ionic liquid systems.⁷⁷

To connect the diffusivity and conductivity of ions in a liquid, the Nernst-Einstein equation is used. This equation can be obtained by either using Fick's law or by using the Einstein relation and the basic equation of molar conductivity of ions.⁷⁸ The Einstein equation relates the mobility of the species with the diffusion coefficient and it is given by equation 5.7:

$$D = u k_B T \quad (\text{Eq 5.7})$$

where u is the mobility, K is the Boltzmann constant and T is temperature. The total molar conductivity of ions in a 1:1 salt is given by equation 5.8:

$$\Lambda = zeF(u_+ + u_-) \quad (\text{Eq 5.8})$$

where e is the elemental charge, F is the Faraday constant, u_+ and u_- is the mobility of the cation and anion respectively, and z is the valence charge.

By rewriting equation 5.7 and replacing the mobility in equation 5.8, the relation between diffusion and molar conductivity is obtained, which is known as the Nernst-Einstein equation.⁷⁹⁻⁸⁰

$$\Lambda = \frac{zeF}{k_B T} (D_+ + D_-) \quad (\text{Eq 5.9})$$

For a 1:1 salt, equation 5.9 can be rewritten as follows:

$$\Lambda = \frac{N_A e^2}{k_B T} (D_+ + D_-) \quad (\text{Eq 5.10})$$

where N_A is Avogadro's constant, e is the elementary charge, k_B is the Boltzmann constant, T is the absolute temperature (K) and D_+ and D_- are the diffusion coefficient of the cation and anion respectively.

Watanabe *et al.*^{77, 81-83} and MacFarlane *et al.*⁵⁸ have used various plotting methods to obtain a measure of ionicity from a comparison of the molar conductivity calculated by equation 5.10 and molar conductivity measured.

5.1.4 The effect of different cations and anions

The nature of the anions and cations are of primary importance in determining the chemical and physical properties of ionic liquids. For example, small anions with delocalised charges, such as dicyanamide, bis(fluorosulfonyl)amide and tetracyanoborate, are known to increase the conductivity, whereas large anions have the opposite effect. Combinations of cation and anions can either form room temperature ionic liquids or crystalline solids which can have plastic crystals properties in some cases. For example, the BF_4^- anion forms plastic crystals with the C_1mpyr^+ , whereas with C_2mim^+ it forms an ionic liquid. The same is true for anions NTf_2^- , PF_6^- , SCN^- , and $\text{N}(\text{CN})_2^-$.

NTf_2^- is the most widely studied anion as it is known to form thermally and electrochemically stable salts. Due to the high ionic conductivity it imparts, these salts have been used as electrolytes in lithium batteries. Lately, bis(fluorosulfonyl)imide (FSI) is gaining more attention as it forms low viscosity ionic liquids with higher conductivity

5. Synthesis of novel phosphonium ionic liquids

than the NTf₂⁻ salt; for example, C₂mimFSI has a viscosity of 18 mPa s, whereas C₂mimNTf₂ has a viscosity of 33 mPa s.

PF₆⁻ and BF₄⁻ are known to form plastic crystals with some small pyrrolidinium cations. These plastic crystals have been used as solid state electrolytes for lithium batteries.⁸⁴ However, even though these anions are quite interesting and are considered to be “green”, they are known to be highly sensitive to hydrolysis, especially PF₆⁻ which tends to form the highly corrosive HF.

In this chapter, various anions are combined with short and asymmetrical phosphonium cations. Depending on the type of alkyl chain and the anion used, the resultant salts are either solid or liquid at room temperature.

5.1.5 Aims of this chapter

The aim of this work was to synthesise novel phosphonium ionic liquids for use in dye sensitised solar cells. There are limited publications concerning the use of phosphonium ionic liquids in DSSCs, due to the high viscosity of this class of IL compared to aliphatic and aromatic ammonium salts. The phosphonium ionic liquids studied in the literature are quite bulky and their performance in dye sensitised solar cells is often quite poor compared to imidazolium based electrolytes, even when they are used in combination with organic solvents. Short alkyl chain phosphonium salts have been developed recently by Cytec Industries, thus making it possible to synthesise new phosphonium based ionic liquids with interesting properties. Figures 5.2 and 5.3 show the structure of the phosphonium cations and anions investigated in this thesis which were chosen on the fact that when these anions are combined with imidazolium or tetralkylammonium cations, they formed compounds that are liquid at or near room temperature due to a weak ionic interaction. The charge on these anions are known to be highly delocalised over a number of atoms, especially NTf₂⁻. Thus, we were interested in combining the asymmetric phosphonium cations (Figure 5.2) with these weakly interacting anions. Low viscosity phosphonium ionic liquids, purchased from Nippon Chemical, were used for comparisons.

In this chapter, a series of phosphonium salts, in combination with commonly used anions, were prepared and their transport properties and thermal stability were investigated. The transport properties, in term of their position on a Walden plot⁵⁸ were also investigated because ionic conductivity is an important parameter for the potential use of these phosphonium ILs in electrochemical devices. These new phosphonium ILs were then investigated in dye sensitised solar cells using ruthenium and organic based sensitisers, as detailed in Chapter 7. Some of the phosphonium cations formed plastic crystals, depending on the anion used. This is the first time such behaviour has been observed in phosphonium based compounds.

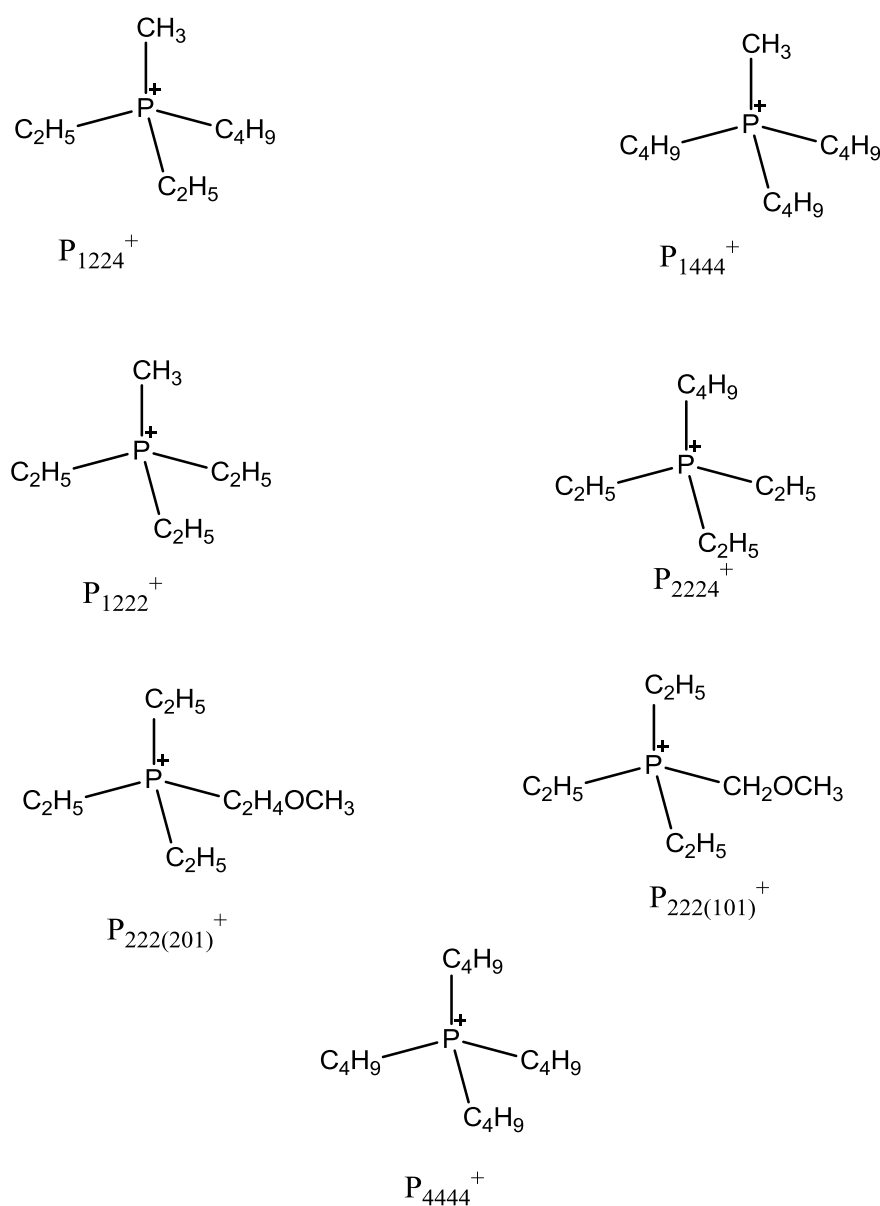


Figure 5.2: The structure of the cations investigated in this study

5. Synthesis of novel phosphonium ionic liquids

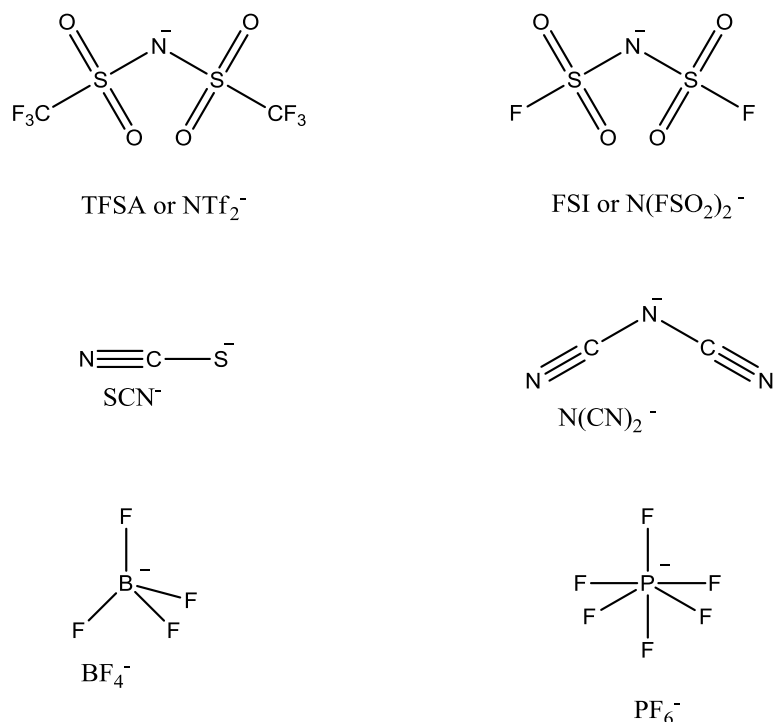


Figure: 5.3: The structure of the anions used in this study

5.2 Experimental

5.2.1 Analysis

Purity analysis such as NMR, ES/MS, and Karl Fischer were used to characterise the series of phosphonium ionic liquids synthesised. Thermal analysis was performed across the temperature range of $-150\text{ }^\circ\text{C}$ to $250\text{ }^\circ\text{C}$, at a scan rate of $10\text{ }^\circ\text{C min}^{-1}$, by differential scanning calorimetry. The thermal decomposition of the phosphonium salts was investigated by thermogravimetric analysis and the electrochemical window was determined by cyclic voltammetry. Full descriptions of these techniques are given in Chapter 3.

5.2.2 Synthesis of phosphonium based ionic liquids

Materials

Sodium tetrafluoroborate (NaBF_4), potassium hexafluorophosphate (KPF_6), sodium dicyanamide ($\text{NaN}(\text{CN})_2$) and potassium thiocyanate were purchased from Aldrich and used as received. Lithium bis(trifluoromethanesulfonyl)amide ($\text{Li}(\text{N}(\text{CF}_3\text{SO}_2)_2$ or $\text{Li}(\text{NTf}_2)$) was purchased from 3M, potassium bis(fluorosulfonyl)imide ($\text{K}(\text{N}(\text{F}_2(\text{SO}_2)_2)$ or KFSl) was purchased from Dai-ichi Kogyo Seikayu (Japan). Diethylmethyltriisobutylphosphonium tosylate, triisobutyl(methyl)phosphonium tosylate, triethyl(methyl)phosphonium tosylate, triethyl(butyl)phosphonium tosylate, trihexyl(tetradecyl)phosphonium bis(trifluoromethanesulfonyl)amide and trihexyl(tetradecyl) phosphonium dicyanamide were purchased from Cytec Industries and used without further purification. Triethyl(methoxymethyl)phosphonium dicyanamide, triethyl(methoxymethyl)phosphonium bis(fluorosulfonyl)amide, triethyl(methoxyethyl)phosphonium bis(fluorosulfonyl)amide, triethyl(methoxymethyl)phosphonium bis(trifluoromethanesulfonyl)amide and triethyl(methoxyethyl)phosphonium bis(trifluoromethanesulfonyl) amide were purchased from Nippon Chemical (Japan). Acetone was distilled using potassium carbonate and used immediately. All glassware was dried overnight in the oven at 120 °C.

*Synthesis***Diethylmethylisobutylphosphonium bis(trifluoromethanesulfonyl)amide ($\text{P}_{1224}\text{NTf}_2$)**

20 g (0.06 mole) of diethylmethylisobutylphosphonium tosylate was dissolved in 100 ml of distilled water. An equimolar amount (18 g, 0.06 mole) of lithium bis(trifluoromethanesulfonyl)amide was then added to the solution. A translucent precipitate was instantly formed. The whole mixture was stirred overnight at room temperature. The solid phase was filtered and washed several times with distilled water. The solid product was then dissolved in dichloromethane and distilled water was added. The two phases were separated and the solvent was removed on a rotary evaporator. The solid product was then dried at 70 °C for 48 hours under vacuum. (Crude yield: 90 %) ^1H NMR (d_6 -DMSO, 400 MHz) δ 1.02 - 1.04 ppm (3H, d, $J=8$ Hz), 1.09 - 1.19 ppm (3H, m), 1.79 - 1.83 ppm (3H, d, $J=13.6$ Hz), 1.96 - 2.08 ppm (1H, m), 2.12 - 2.25 ppm (2H, m).

5. Synthesis of novel phosphonium ionic liquids

ES+ m/z 161.1 ($C_9H_{22}P$)⁺, ES- m/z (NTf_2)⁻

Water content (Karl Fischer): 100 ppm

Diethylmethylisobutylphosphonium bis(fluorosulfonyl)amide (P₁₂₂₄FSI)

The same procedure to that of the synthesis of P₁₂₂₄NTf₂ was used. 10 g (0.03 mole) of diethylmethylisobutylphosphonium tosylate and 7 g (0.03 mole) of KFSI were mixed together in 50 ml of distilled water, forming a clear liquid as a second phase. The two phases were separated and the ionic liquid phase was washed several times with distilled water and then dried in vacuo at 70 °C for several days. ¹H NMR (d₆-DMSO, 400 MHz) δ 1.02 - 1.04 ppm (3H, d, J = 8 Hz), 1.09 - 1.19 ppm (3H, m), 1.79 - 1.83 ppm (3H, d, J = 13.6 Hz), 1.96 - 2.08 ppm (1H, m), 2.12 - 2.25 ppm (2H, m).

ES+ m/z 161.1 ($C_9H_{22}P$)⁺, ES- m/z 180 ($N(SO_2F)_2$)⁻

Water content (Karl Fischer): 120 ppm

Diethylmethylisobutylphosphonium hexafluorophosphate (P₁₂₂₄PF₆)

A similar procedure to that of P₁₂₂₄NTf₂ was used. 20 g (0.06 mole) of diethylmethylisobutylphosphonium tosylate was stirred in distilled water. An equivalent molar amount (11 g, 0.06 mole) of potassium hexafluorophosphate was added to the solution, instantly forming a white precipitate. The precipitate was washed several times with distilled water and dried in vacuo for several days at 100 °C. ¹H NMR (d₆-DMSO, 400 MHz) δ 1.02 - 1.04 ppm (3H, d, J = 8 Hz), 1.09 - 1.19 ppm (3H, m), 1.79 - 1.83 ppm (3H, d, J = 13.6 Hz), 1.96 - 2.08 ppm (1H, m), 2.12 - 2.25 ppm (2H, m).

ES+ m/z 161.1 ($C_9H_{22}P$)⁺, ES- m/z 145 (PF₆)⁻

Diethylmethylisobutylphosphonium tetrafluoroborate (P₁₂₂₄BF₄)

Diethylmethylisobutylphosphonium tosylate (25 g, 0.075 mole) was added to 100 ml of anhydrous acetone in a nitrogen atmosphere. Sodium tetrafluoroborate (9 g, 0.08 mole) was then added and the whole mixture was refluxed overnight at 70 °C. The white precipitate was filtered off and the filtrate was microfiltered (200 nm filter) before the solvent was removed by rotovap. The solid was then washed with dry acetone and recrystallised several time in dichloromethane. ¹H NMR (d₆-DMSO, 400 MHz) δ 1.02 -

1.04 ppm (3H, d, J = 8 Hz), 1.09 - 1.19 ppm (3H, m), 1.79 - 1.83 ppm (3H, d, J = 13.6 Hz), 1.96 - 2.08 ppm (1H, m), 2.12 - 2.25 ppm (2H, m).

ES+ m/z 161.1 ($C_9H_{22}P$)⁺, ES- m/z 89.1 (BF_4)⁻

Diethylmethylisobutylphosphonium thiocyanate (P₁₂₂₄SCN)

The same procedure as P₁₂₂₄BF₄ was used. 10 g (0.03 mole) of diethylmethylisobutylphosphonium tosylate was added to 50 ml of anhydrous acetone and then 3 g (0.03 mole) of potassium thiocyanate was added. The mixture was then stirred at 70 °C for 3 days. The white precipitate was filtered off and the filtrate was microfiltered (200 nm filter) and the solvent removed by rotary evaporator. The solid product was washed with dry acetone and recrystallised several times in dichloromethane. ¹H NMR (d₆-DMSO, 400 MHz) δ 1.02 - 1.04 ppm (3H, d, J = 8 Hz), 1.09 - 1.19 ppm (3H, m), 1.79 - 1.83 ppm (3H, d, J = 13.6 Hz), 1.96 - 2.08 ppm (1H, m), 2.12 - 2.25 ppm (2H, m).

ES+ m/z 161.1 ($C_9H_{22}P$)⁺, ES- m/z 58 (SCN)⁻

Diethylmethylisobutylphosphonium dicyanamide (P₁₂₂₄N(CN)₂)

10 g (0.03 mole) of diethylmethylisobutylphosphonium tosylate was added to 50 ml of anhydrous acetone and 3 g (0.03 mole) of sodium dicyanamide was added and the mixture was stirred at 70 °C overnight. The white precipitate was filtered off, the filtrate was microfiltered and the solvent removed by rotovap. The liquid product was washed with dry acetone. ¹H NMR (d₆-DMSO, 400 MHz) δ 1.02 - 1.04 ppm (3H, d, J = 8 Hz), 1.09 - 1.19 ppm (3H, m), 1.79 - 1.83 ppm (3H, d, J = 13.6 Hz), 1.96 - 2.08 ppm (1H, m), 2.12 - 2.25 ppm (2H, m).

ES+ m/z 161.1 ($C_9H_{22}P$)⁺, ES- m/z 66 (N(CN)₂)⁻

Water content (Karl Fischer): 165 ppm

Triisobutylmethylphosphonium bis(trifluoromethanesulfonyl)amide (P₁₄₄₄NTf₂)

The same procedure as P₁₂₂₄NTf₂ was used. 20 g (0.05 mole) of triisobutylmethylphosphonium tosylate was dissolved in 50 ml of distilled water and 15 g (0.05 mole) LiNTf₂ was added and stirred at room temperature for several hours. The white precipitate was washed several times with distilled water and recrystallised from dichloromethane. The solid product was dried at 100 °C in vacuo for 48 hours. (Crude

5. Synthesis of novel phosphonium ionic liquids

yield 90 %). ^1H NMR (d_6 -DMSO, 400 MHz) δ 0.99 - 1.05 ppm (3H, d, $J = 6.4$ Hz), 1.88 - 1.93 ppm (3H, d, $J = 13.6$ Hz), 2.00 - 2.09 ppm (1H, m, $J = 6.4$ Hz), 2.16 - 2.21 ppm (2H, d, $J = 13.6$ Hz). No trace of tosylate was observed in either the MS or the NMR.

ES+ m/z 217.2 ($\text{C}_{13}\text{H}_{30}\text{P}$)⁺, ES- m/z 280 (NTf_2)⁻.

Triisobutylmethylphosphonium bis(fluorosulfonyl)amide ($\text{P}_{1444}\text{FSI}$)

The same procedure as $\text{P}_{1444}\text{NTf}_2$ was used. 10 g (0.03 mole) of triisobutylmethylphosphonium tosylate was dissolved in 50 ml of distilled water and 6 g (0.03 mole) KFSI was added. The solution was then stirred at room temperature for several hours. The white precipitate was removed by filtration, washed several times with distilled water and recrystallised from dichloromethane. The solid product was dried at 70 °C in vacuo for 48 hours. (Crude yield 86 %). ^1H NMR (d_6 -DMSO, 400 MHz) δ 1.02 - 1.04 ppm (3H, d, $J = 6.8$ Hz), 1.89 - 1.93 ppm (3H, d, $J = 13.6$ Hz), 2.00 - 2.07 ppm (1H, m, $J = 6.4$ Hz), 2.16 - 2.20 ppm (2H, d, $J = 13.6$ Hz).

ES+ m/z 217.2 ($\text{C}_{13}\text{H}_{30}\text{P}$)⁺, ES- m/z 180 ($\text{N}(\text{SO}_2\text{F})_2$)⁻.

Triisobutylmethylphosphonium hexafluorophosphate ($\text{P}_{1444}\text{PF}_6$)

The same procedure as $\text{P}_{1444}\text{NTf}_2$ was used. 30 g (0.08 mole) of triisobutylmethylphosphonium tosylate was dissolved in 50 ml of distilled water, 15 g (0.082 mole) of KPF_6 was added and the solution stirred at room temperature for several hours. The white precipitate was isolated by filtration, washed several times with distilled water and recrystallised from dichloromethane. The solid product was dried at 70 °C in vacuo for 48 hours. ^1H NMR (d_6 -DMSO, 400 MHz) δ 1.03 - 1.05 ppm (3H, d, $J = 6.8$ Hz), 1.89 - 1.93 ppm (3H, d, $J = 13.6$ Hz), 2.00 - 2.06 ppm (1H, m, $J = 6.4$ Hz), 2.16 - 2.21 ppm (2H, d, $J = 13.6$ Hz).

ES+ m/z 217.2 ($\text{C}_{13}\text{H}_{30}\text{P}$)⁺, ES- m/z 145 (PF_6)⁻.

Triisobutylmethylphosphonium thiocyanate (P₁₄₄₄SCN)

The same procedure as P₁₂₂₄SCN was used. 20 g (0.05 mole) of triisobutylmethylphosphonium tosylate was dissolved in 100 ml of dry acetone, 6 g (0.06 mole) of KSCN was added and the solution stirred at 50 °C for 2 days. The white precipitate was filtered off and the filtrate was microfiltered. The solvent was then removed by rotovap. The solid product was then washed several times with dry acetone to remove any impurities. Then it was recrystallised several time from dichloromethane. The solid product was then dried for 2 days at 100 °C under vacuum. ¹H NMR (d₆-DMSO, 400 MHz) δ 1.03 - 1.05 ppm (3H, d, J = 6.8 Hz), 1.89 - 1.93 ppm (3H, d, J = 13.6 Hz), 2.00 - 2.06 ppm (1H, m, J = 6.4 Hz), 2.16 - 2.21 ppm (2H, d, J = 13.6 Hz).

ES+ *m/z* 217.2 (C₁₃H₃₀P)⁺, ES- *m/z* 58 (SCN)⁻.

Triisobutylmethylphosphonium dicyanamide (P₁₄₄₄N(CN)₂)

The same procedure as P₁₄₄₄SCN was used to synthesis P₁₄₄₄N(CN)₂ 30 g (0.08 mole) of triisobutylmethylphosphonium tosylate was dissolved in 100 ml of dry acetone, 8 g (0.09 mole) of Na(N(CN)₂) was added and the solution was stirred at 50 °C for 5 days. The white precipitate was filtered off and the filtrate was microfiltered before removing the solvent. A pale yellow liquid was obtained. The liquid was washed several times with acetone before drying for a week at 100 °C under vacuum. ¹H NMR (d₆-DMSO, 400 MHz) δ 1.03 - 1.05 ppm (3H, d, J = 6.8 Hz), 1.89 - 1.93 ppm (3H, d, J = 13.6 Hz), 2.00 - 2.06 ppm (1H, m, J = 6.4 Hz), 2.16 - 2.21 ppm (2H, d, J = 13.6 Hz).

ES+ *m/z* 217.2 (C₁₃H₃₀P)⁺, ES- *m/z* 66 (N(CN)₂).

Water content (Karl Fischer) 150 ppm.

5. Synthesis of novel phosphonium ionic liquids

Triisobutylmethylphosphonium tetrafluoroborate (P₁₄₄₄BF₄)

The same procedure as P₁₄₄₄NTf₂ was used. 30 g (0.08 mole) of triisobutylphosphonium tosylate was dissolved in 50 ml of distilled water, 9 g (0.083 mole) of NaBF₄ was added and the solution stirred at room temperature for several hours. The white precipitate was isolated by filtration and washed several times with distilled water and recrystallised from dichloromethane. The solid product was dried at 70 °C in vacuo for 48 hours. ¹H NMR (d₆-DMSO, 400 MHz) δ 1.03 - 1.05 ppm (3H, d, J = 6.8 Hz), 1.89 - 1.93 ppm (3H, d, J = 13.6 Hz), 2.00 - 2.06 ppm (1H, m, J = 6.4 Hz), 2.16 - 2.21 ppm (2H, d, J = 13.6 Hz).

ES+ *m/z* 217.2 (C₁₃H₃₀P)⁺, ES- *m/z* 87 (BF₄)⁻

Triethylmethylphosphonium bis(trifluoromethanesulfonyl)amide (P₁₂₂₂NTf₂)

The same procedure as P₁₄₄₄NTf₂ was used. 10 g (0.03 mole) of triethylmethylphosphonium tosylate was dissolved in 50 ml of distilled water, 8 g (0.03 mole) of LiNTf₂ was added and the solution stirred at room temperature for several hours. The white precipitate was then isolated by filtration, washed several times with distilled water and recrystallised from dichloromethane. The solid product was dried at 70 °C in vacuo for 48 hours. ¹H NMR (d₆-DMSO, 400 MHz) δ 1.09 - 1.17 ppm (3H, m), 1.75 - 1.78 ppm (3H, d, J = 14 Hz), 2.14 - 2.23 ppm (2H, m).

ES+ *m/z* 133.1 (C₇H₁₈P)⁺, ES- *m/z* 280 (NTf₂)⁻

Triethylmethylphosphonium bis(fluorosulfonyl)amide (P₁₂₂₂FSI)

The same procedure as P₁₄₄₄NTf₂ was used. 10 g (0.033 mole) of triethylmethylphosphonium tosylate was dissolved in 50 ml of distilled water, 7.2 g (0.033 mole) of KFSI was added and the solution stirred at room temperature for several hours. The white precipitate was isolated by filtration, washed several times with distilled water and recrystallised from dichloromethane. The solid product was dried at 70 °C in vacuo for 48 hours. ¹H NMR (d₆-DMSO, 400 MHz) δ 1.09 - 1.17 ppm (3H, m), 1.75 - 1.78 ppm (3H, d, J = 14 Hz), 2.14 - 2.23 ppm (2H, m).

ES+ *m/z* 133.1 (C₇H₁₈P)⁺, ES- *m/z* 180 (N(SO₂F)₂)⁻

Triethylbutylphosphonium bis(trifluoromethanesulfonyl)amide (P₂₂₂₄NTf₂)

The same procedure as P₁₄₄₄NTf₂ was used. 10 g (0.03 mole) of triethylbutylphosphonium tosylate was dissolved in 50 ml of distilled water, 8 g (0.03 mole) of LiNTf₂ was added and the solution stirred at room temperature for several hours. The white precipitate was isolated by filtration, washed several times with distilled water and recrystallised from dichloromethane. The solid product was dried at 70 °C in vacuo for 48 hours. ¹H NMR (d₆-DMSO, 400 MHz) δ 1.09 -1.11 ppm (3H, m), 0.99 - 1.03, (3H, t), 1.97 - 2.08 ppm (2H, m), 2.17 - 2.26 ppm (2H, m)

ES+ *m/z* 175 (C₁₀H₂₄P)⁺, ES- *m/z* 280 (NTf₂)⁻

Triethylbutylphosphonium bis(trifluoromethanesulfonyl)amide (P₂₂₂₄FSI)

10 g (0.03 mole) of triethylbutylphosphonium tosylate was dissolved in 50 ml of distilled water, 6.5 g (0.03 mole) KFSI was added and the solution was stirred at room temperature for several hours. A colourless liquid formed. This was separated and washed several times with distilled water and then dissolved in dichloromethane to remove any potassium salts present. The liquid was dried at 70 °C in vacuo for 48 hours. ¹H NMR (d₆-DMSO, 400 MHz) δ 1.09 -1.11 ppm (3H, m), 0.99 - 1.03, (3H, t), 1.97 - 2.08 ppm (2H, m), 2.17 - 2.26 ppm (2H, m).

ES+ *m/z* 175 (C₁₀H₂₄P)⁺, ES- *m/z* 180 (N(SO₂F)₂)⁻

5.3 Results and discussions

5.3.1 Thermal properties

Figure 5.4 shows the DSC traces of the new ionic liquids, with P_{1444} as the common cation and variation of the anion. The transition temperature data and the entropy of fusion (ΔS_f) are summarised in Table 5.2 and 5.3. These entropies of fusion are calculated from the melting endotherm area (ΔH_f) using $\Delta S = \frac{\Delta H_f}{T_m}$.

$P_{1444}SCN$, $P_{1444}NTf_2$, $P_{1444}FSI$, $P_{1444}PF_6$ and $P_{1444}BF_4$ are all solid at room temperature, whereas $P_{1444}N(CN)_2$ was the only one that formed a liquid at room temperature. The salts were recrystallised several times from DCM and DSC analysis was performed after each recrystallisation, with the same behaviour observed for each batch. These phosphonium compounds shows similar behaviour to the pyrrolidinium family and tetraalkylammonium family.⁸⁵ All the solid compounds show several phase transitions. This is quite interesting as it is the first time that such behaviour has been observed for salts with phosphonium cations.

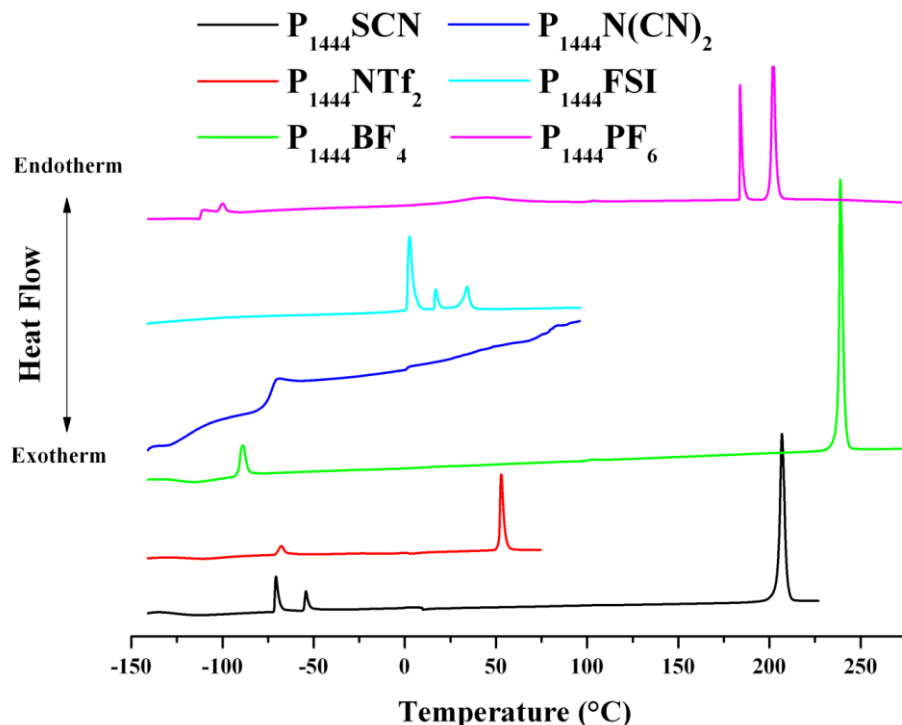


Figure 5.4: DSC traces for the new phosphonium salts, with P_{1444} as the common cation with varying anion. The salts are all solids at room temperature except for the $N(CN)_2$

Figure 5.4 shows the phase behaviour of $P_{1444}PF_6$. There is evidence of four phase transitions over the temperature range studied; the first solid-solid phase transition occurs at $-100\text{ }^\circ\text{C}$, followed by a broad phase transition (III-II) at $25\text{ }^\circ\text{C}$. The phase II \rightarrow I transition displays a sharp peak at $184\text{ }^\circ\text{C}$, before a final melting transition at $202\text{ }^\circ\text{C}$. The entropy of fusion (ΔS_f) of $P_{1444}PF_6$ is $18\text{ J mol}^{-1}\text{ K}^{-1}$, which is within Timmermans' criteria for plastic crystals,⁸⁶ suggesting it may be used as a solid state electrolyte in DSSCs.

$P_{1444}BF_4$ shows evidence of a phase II-I transition at $-89\text{ }^\circ\text{C}$, followed by a very large Phase 1 domain, before melting at $239\text{ }^\circ\text{C}$. Thus this compound exists in phase I over a temperature range of more than $200\text{ }^\circ\text{C}$, which may be very important for device applications.

The entropy of fusion for this compound is quite large, as shown in Table 5.3, it does not fit the Timmermans' criteria and thus cannot be immediately classified as plastic crystals. The solid-solid transition only indicates an increase of disorder in the material, possibly due to the rotational movement of the butyl group on the phosphonium cation.

$P_{1444}FSI$ shows three phase transitions, which are quite close together. The phase III-II transition occurs at $7\text{ }^\circ\text{C}$, with quite a high $\Delta S_{(III-II)}$, followed by the second phase transition (II-I) at $24\text{ }^\circ\text{C}$, before melting at $36\text{ }^\circ\text{C}$. A ΔS_f of $23\text{ J mol}^{-1}\text{ K}^{-1}$, indicates that this compound has a highly disordered molecular orientation in phase I. Because of the narrow plastic range, it is unlikely to be useful as a solid state electrolyte.

$P_{1444}NTf_2$ displays two phase transitions; a solid-solid phase transition at $-68\text{ }^\circ\text{C}$ before the melt at $52\text{ }^\circ\text{C}$. However it has a quite high ΔS_f of $59\text{ J mol}^{-1}\text{ K}^{-1}$. The high ΔS_f is an indication that the first solid-solid transformation may be due to some small disordering event in the material.

$P_{1444}SCN$ exhibits three thermal phase transitions. The first solid-solid phase transition is at $-71\text{ }^\circ\text{C}$, the second transition at $-51\text{ }^\circ\text{C}$ and melting at $207\text{ }^\circ\text{C}$ with a moderately large ΔS_f , this seems to indicate some potential for there to be plastic behaviour in this compound.

$P_{1444}N(CN)_2$ is a room temperature ionic liquid that shows no defined phase transition and no melting point, only a glass transition is observed at $-73\text{ }^\circ\text{C}$.

5. Synthesis of novel phosphonium ionic liquids

Table 5.2: Thermal behaviour of the P₁₄₄₄NTf₂, P₁₄₄₄FSI and P₁₄₄₄PF₆.

Compound	P ₁₄₄₄ NTf ₂		P ₁₄₄₄ FSI		P ₁₄₄₄ PF ₆	
	T / (°C)	ΔS (Jmol ⁻¹ K ⁻¹)	T / (°C)	ΔS (Jmol ⁻¹ K ⁻¹)	T / (°C)	ΔS (Jmol ⁻¹ K ⁻¹)
	± 1	± 5%	± 1	5%	± 1	5%
IV→III					-100	3
III→II			7	46	25	11
II→I	-68	19	24	9	184	8
I→melt	52	59	36	23	202	18

Table 5.3: Thermal behaviour of P₁₄₄₄BF₄, P₁₄₄₄SCN and P₁₄₄₄N(CN)₂.

Compound	P ₁₄₄₄ BF ₄		P ₁₄₄₄ SCN		P ₁₄₄₄ N(CN) ₂
	T / (°C)	ΔS (Jmol ⁻¹ K ⁻¹)	T / (°C)	ΔS (Jmol ⁻¹ K ⁻¹)	T _g / (°C)
	±1	± 5%	±1	± 5%	
					-73
III→II			-71	13	
II→I	-89	32	-51	8	
I→melt	239	45	207	44	

PF₆⁻, BF₄⁻, NTf₂⁻, SCN⁻ and N(CN)₂⁻ are well known anions that have been widely investigated with the pyrrolidinium, imidazolium and tetraalkylammonium cations. When these anions are combined with the C₂mim⁺ cation, they form ionic liquids with low melting points,⁸⁷ whereas when they are combined with C₁mpyr⁺, C₂mpyr⁺ or N₂₂₂₂⁺ cations, they can form plastic crystals.⁸⁵ Thus the choice of cation/anion combination is important in designing new ionic liquids, as it can significantly change the physical properties of the final compound.

P₁₄₄₄PF₆ and P₁₄₄₄FSI show classical plastic crystal behaviour, with ΔS_f ~ 20 J mol⁻¹ K⁻¹. Even though P₁₄₄₄FSI shows solid-solid phase behaviour, it may not be useful as a solid state electrolyte, due to the small temperature range in which it is in phase I (the most conductive phase) and the relatively low melting point. Nevertheless, as its melting point is

< 100 °C, it is considered an ionic liquid and thus it may still be useful as a low volatility electrolyte.

$P_{1444}NTf_2$, $P_{1444}SCN$ and $P_{1444}BF_4$ shows multiple solid-solid phase transitions, followed by a very sharp melt, but they still have a $\Delta S_f \sim 40 - 60 \text{ J mol}^{-1} \text{ K}^{-1}$, and hence these salts do not fit the Timmermans' criterion for molecular plastic crystals. However, it has previously been shown that this criterion may not be applicable to organic ionic plastic crystals. If the plastic crystal contains two different molecular ions and only one of these exhibits rotator motions, then the entropy of melting will be higher, as is observed for a number of other organic ionic plastic crystals.⁸⁸

Figure 5.5 shows the thermal behaviour of P_{1224}^+ in combination with various anions: SCN^- , FSI^- , NTf_2^- , PF_6^- , BF_4^- and $N(CN)_2^-$. $P_{1224}FSI$ and $P_{1224}N(CN)_2$ are room temperature ionic liquids. $P_{1224}PF_6$, $P_{1224}BF_4$ and $P_{1224}SCN$ are solid at 25 °C. These compounds melt at lower temperatures than their P_{1444} analogues. This may be due to the fact that P_{1224}^+ is more asymmetric than P_{1444}^+ ; also P_{1444}^+ is a bulkier cation thus the degree of rotational freedom may be lower compared to P_{1224}^+ in the liquid state. $P_{1224}PF_6$, $P_{1224}SCN$ and $P_{1224}BF_4$ exhibit multiple solid-solid phase transitions below their melting points.

$P_{1224}PF_6$ shows the richest phase behaviour, with at least four different solid phases. The first solid-solid transition, from phase IV to III, occurs at 24 °C. It exists in phase III until it reaches 72 °C. Afterwards it undergoes the phase II to I transition at 122 °C and then melts at 139 °C. The entropy of fusion of this compound is well within Timmermans' criteria ($3 \text{ J K}^{-1} \text{ mol}^{-1}$), suggesting that is sufficiently plastic in phase I to be useful as solid electrolyte in electrochemical devices. $P_{1224}SCN$ shows similar phase behaviour, with a low temperature phase change (III-II) at 15 °C, followed immediately by another solid-solid phase transition (II-I) at 38 °C, and a solid-solid phase I transition, subsequently melting at 175 °C. The wide temperature range between the phase II-I transition and the melt is ideal for the potential application of this material as a solid state electrolyte. The small peak before the melt at 141 °C is too small to be considered as a phase change in the material.

$P_{1224}FSI$ and $P_{1224}N(CN)_2$ are both liquids at room temperature. $P_{1224}FSI$ shows multiple phase transitions at low temperature. The first solid-solid phase transition (II-I) occurs at -68 °C, followed by the melt at -58 °C, and the entropy of fusion for this material is 3 J K^{-1}

5. Synthesis of novel phosphonium ionic liquids

mol^{-1} . As it has such a low entropy of fusion, a quenching of the compound was performed to visually observe crystallisation. Cooling the sample to $-80\text{ }^{\circ}\text{C}$, a white solid formed indicating crystallisation of the material.

$\text{P}_{1224}\text{N}(\text{CN})_2$ shows a typical glass transition at $-106\text{ }^{\circ}\text{C}$.

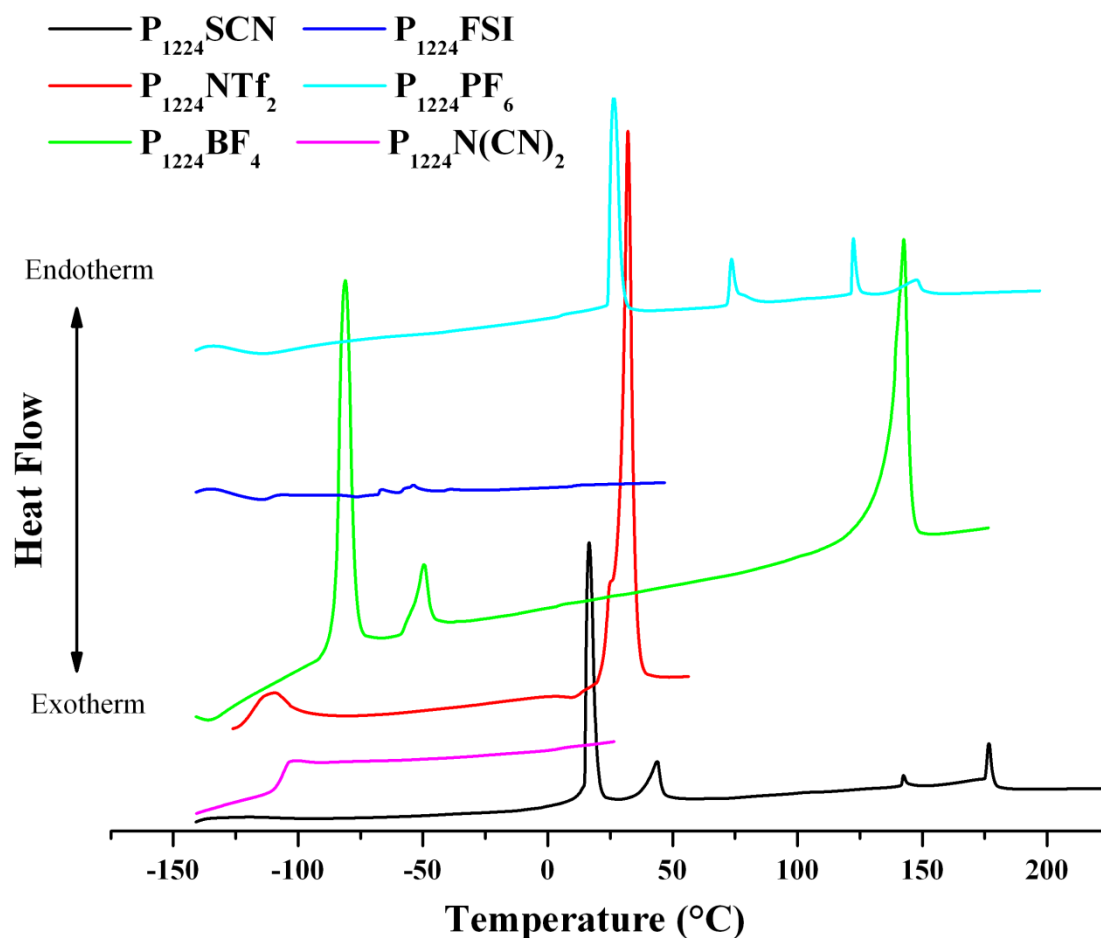


Figure 5.5: DSC traces for the P_{1224} cation with SCN^- , NTf_2^- , BF_4^- , PF_6^- , FSI^- and $\text{N}(\text{CN})_2^-$ anions. The salts are all solids at room temperature except for the FSI^- and $\text{N}(\text{CN})_2^-$ species, which are liquids

The DSC trace of $\text{P}_{1224}\text{BF}_4$ also displays several phase transitions. At $-85\text{ }^{\circ}\text{C}$, phase III transforms to phase II, which is then transformed to phase I at $-55\text{ }^{\circ}\text{C}$. The material then stays in phase I over a relatively wide temperature range, before melting at $136\text{ }^{\circ}\text{C}$.

$P_{1224}BF_4$, $P_{1224}PF_6$ and $P_{1224}SCN$ exhibit all of the classic features of plastic crystal formation, such as multiple solid-solid phase transitions and low entropy of fusion, with PF_6^- and SCN^- exhibiting lower entropy of fusion than the BF_4^- salt.

Tables 5.4 and 5.5 summarises the entropy of fusion and the different phase transitions of the materials with the P_{1224} cation and with the different anions.

Table 5.4: Thermal properties of $P_{1224}SCN$, $P_{1224}BF_4$, $P_{1224}PF_6$ and $P_{1224}FSI$.

Compound	$P_{1224}SCN$		$P_{1224}BF_4$		$P_{1224}PF_6$		$P_{1224}FSI$	
	T	ΔS	T	ΔS	T	ΔS	T	ΔS
Phase transition	(°C)	(Jmol ⁻¹ K ⁻¹)	(°C)	(Jmol ⁻¹ K ⁻¹)	(°C)	(Jmol ⁻¹ K ⁻¹)	(°C)	(Jmol ⁻¹ K ⁻¹)
	± 1	± 5%	± 1	5%	± 1	± 5%	± 1	± 5%
IV→III					24	39		
III→II	15	33	-85	34	72	6		
II→I	38	7	-55	5	122	4	-68	1
I→melt	176	2	136	19	139	3	-58	3

Table 5.5: Thermal properties of $P_{1224}NTf_2$ and $P_{1224}N(CN)_2$.

Phase transition	$P_{1224}NTf_2$		$P_{1224}N(CN)_2$
	T (°C)	ΔS	T (°C)
	± 1	(Jmol ⁻¹ K ⁻¹)	± 1
		± 5%	
T_g (°C)			-106
T_m (°C)	28	50	

PF_6^- , BF_4^- , NTf_2^- and FSI^- are considered to be weakly coordinating anions. Some of these anions can form hydrophobic ionic liquids with the pyrrolidinium cation, which is also the case with the phosphonium cations studied in this thesis. Contrarily, $N(CN)_2^-$ and SCN^- are considered to be strongly coordinating anions and as such they should display similar physical properties, but this is not the case with the P_{1444}^+ and P_{1224}^+ based ionic liquids; the SCN^- species shows multiple phase transitions, whereas the $N(CN)_2^-$ species are liquids at room temperature, with a glass transition at low temperature. This may reflect the ease of packing of the SCN^- anion.

5. Synthesis of novel phosphonium ionic liquids

Figure 5.6 shows a comparison of two different phosphonium cations with the NTf_2^- and FSI^- anions. $\text{P}_{1222}\text{FSI}$ and $\text{P}_{1222}\text{NTf}_2$ show higher melting points than the $\text{P}_{2224}\text{NTf}_2$ and $\text{P}_{2224}\text{FSI}$ salts. Just by varying the length of the alkyl substituent, the physical properties of the phosphonium cations are modified. By also changing the anion, the melting behaviour of the compound also changed, as shown in Figure 5.4. NTf_2^- and FSI^- anions have been widely studied with the imidazolium cation.^{36, 89-92} FSI^- is now well known to form low viscosity ionic liquids with wide electrochemical windows and higher ionic mobility than NTf_2^- when combined with the imidazolium or pyrrolidinium cation; similar behaviour is also observed with the phosphonium cations studied here. Also the molecular weight and the size of the anions are quite different and this will affect the melting behaviour of the ionic liquids.

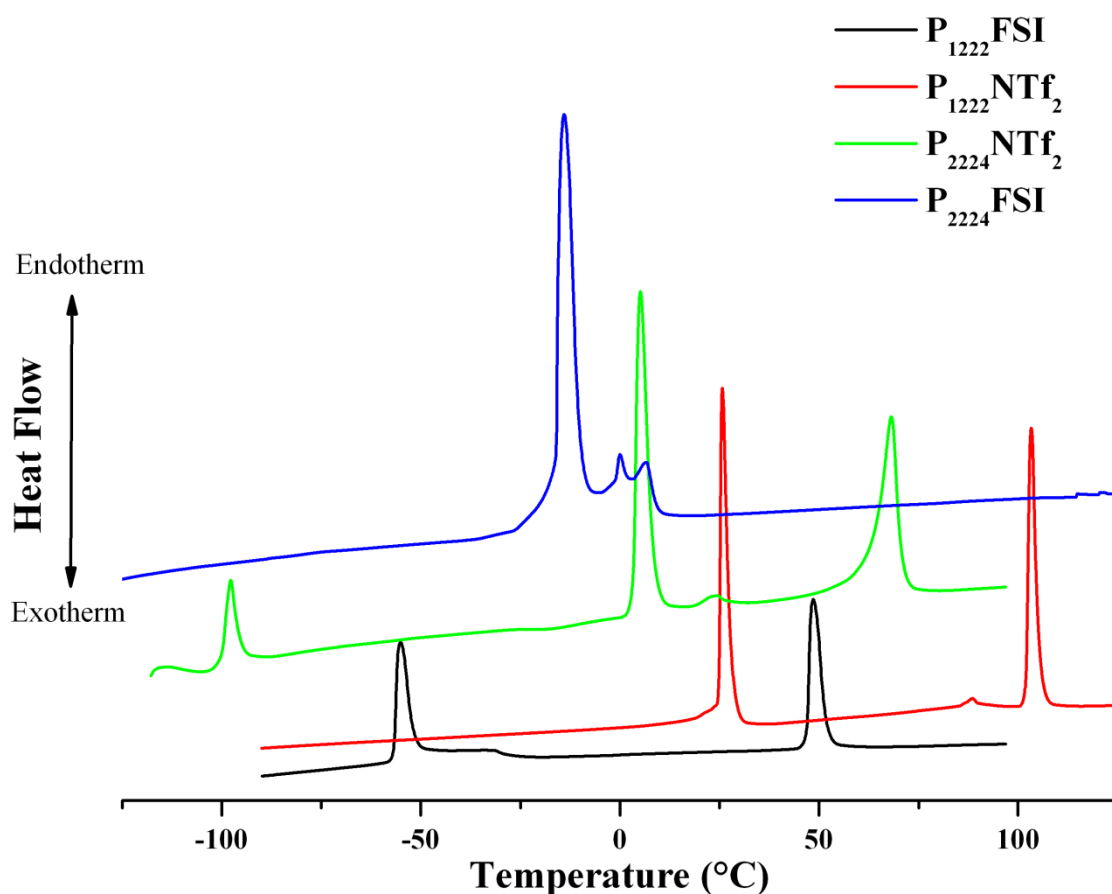


Figure 5.6: DSC traces of P_{1222} and P_{2224} with the NTf_2^- and FSI^- anions

P₁₂₂₂FSI shows evidence of two phase transitions. The first solid-solid transformation occurs at -57 °C, with a large entropy change, followed by the melt at 47 °C. P₁₂₂₂NTf₂ shows similar behaviour as P₁₂₂₂FSI but the phase change occurs at a much higher temperature, with the first solid-solid phase change occurring at 25 °C followed by the melt at 102 °C.⁹³

P₂₂₂₄NTf₂ shows multiple solid-solid phase transitions. There is a solid-solid transition at -100 °C followed by a broad phase transition (II-I) at 3 °C. The material then melts at 63 °C. The entropy of fusion of this material is 25 J K⁻¹ mol⁻¹, which is slightly higher than Timmermans' criteria. This phenomenon has already been observed with the same anion by MacFarlane *et al.*⁹⁴ They suggested that the entropy of melting of ionic plastic crystal phases might be higher than 20 J K⁻¹ mol⁻¹ for ionic materials where only one of the molecular ions participates in the rotations and where both of the ions possess multiple degrees of rotational freedom.

Interestingly, P₂₂₂₄FSI is a liquid at room temperature and it shows similar behaviour to P₁₂₂₄FSI. Multiple phase changes also occur at low temperatures in a narrow temperature window. The first solid-solid thermal transformation happens at -16 °C, consuming most of the total entropy, followed by two consecutive phase changes one at -1 °C and then the melt at 4 °C. The same visual experiment as P₁₂₂₄FSI was performed on P₂₂₂₄FSI. On cooling the sample, a white solid was formed at -80 °C indicating the crystallisation of the material. Table 5.6 summarises the thermal behaviour of the P₂₂₂₄FSI, P₂₂₂₄NTf₂, P₁₂₂₂FSI and P₁₂₂₂NTf₂.

Table 5.6: Thermal properties of P₂₂₂₄FSI, P₂₂₂₄NTf₂, P₁₂₂₂FSI and P₁₂₂₂NTf₂.

Compound	P ₁₂₂₂ NTf ₂		P ₁₂₂₂ FSI		P ₂₂₂₄ FSI		P ₂₂₂₄ NTf ₂	
	T	ΔS	T	ΔS	T	ΔS	T	ΔS
Phase transition	(°C)	(Jmol ⁻¹ K ⁻¹)	(°C)	(Jmol ⁻¹ K ⁻¹)	(°C)	(Jmol ⁻¹ K ⁻¹)	(°C)	(Jmol ⁻¹ K ⁻¹)
	± 1	± 5%	± 1	5%	± 1	± 5%	± 1	± 5%
III→II					-16	46	-100	10
II→I	25	38	-55	27	-1	2	3	25
I→melt	102	26	47	23	3	4	63	20

5. Synthesis of novel phosphonium ionic liquids

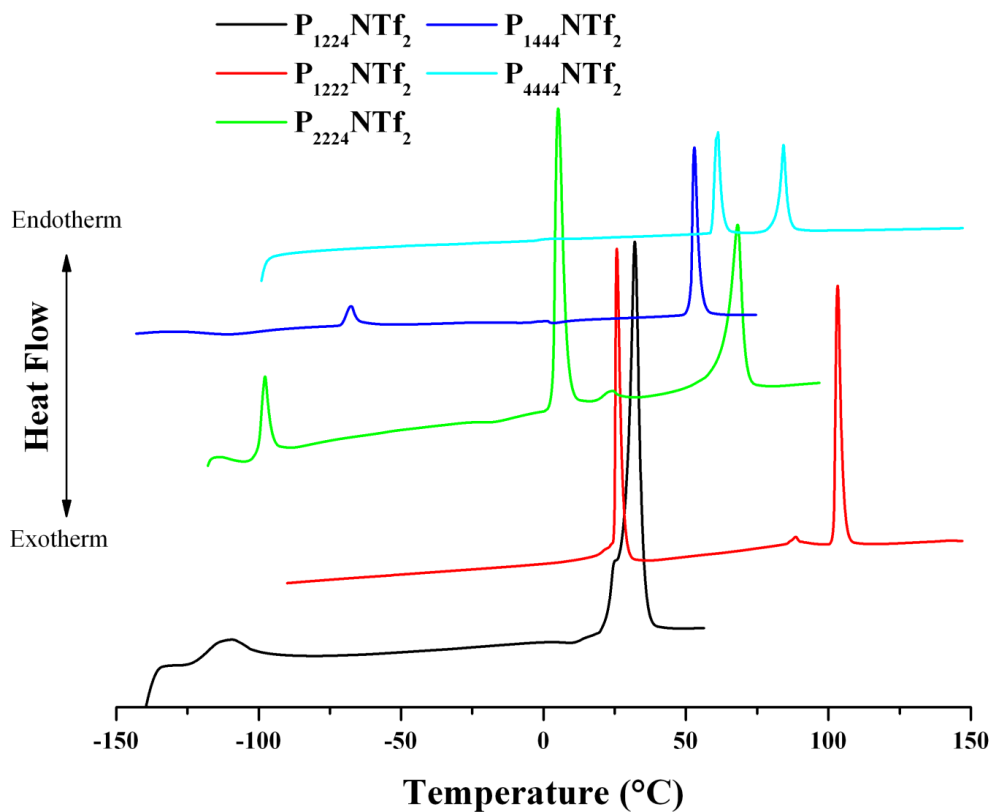


Figure 5.7: The effect on thermal properties of increasing the length of the alkyl chain and the symmetry of the cation, with NTf₂⁻ as the counter ion

The chemical structure of the ionic liquids directly affects its properties, particularly the melting point and thus whether they will form a solid or a liquid at room temperature. As observed in Figure 5.7, changing the size and symmetry of the component ions influences the melting point of the salts, with P₁₂₂₄NTf₂ showing the lowest melting point. In these cases, they were all solids at 25 °C.

Predicting the melting point of ionic liquids is quite challenging as there are many factors that can influence the physical properties. The structure of the cation and the type of anion used can cause changes in the melting point, as observed with the phosphonium family. With small changes in the asymmetry and length of the alkyl chain, a significant change in the phase behaviour is observed. Substituting the anion from the NTf₂⁻ to FSI⁻, a change in the melt is also observed; the FSI⁻ ion forms less viscous ionic liquids (refer to Figure 5.10 for viscosity data) due to the reduced steric hindrance between the cation and the FSI⁻ anion.⁹⁵

Thermogravimetry analysis

Thermal decomposition also depends strongly on the chemical structure of the ionic liquid. The anion has also a strong influence on the stability of the ionic liquids; Figure 5.8 displays the TGA for the FSI and NTf₂ series. The NTf₂ series show better thermal stability than the FSI series, as also observed by others.⁹⁶ P₁₄₄₄FSI and P₁₂₂₂FSI decomposed at about 220 °C while P₁₂₂₄FSI decomposes at around 250 °C. In the NTf₂ series, P₂₂₂₄NTf₂ and P₁₂₂₂NTf₂ display better thermal stability than P₁₄₄₄NTf₂ and P₁₂₂₄NTf₂. The NTf₂ series are stable up to approximately 350 °C.

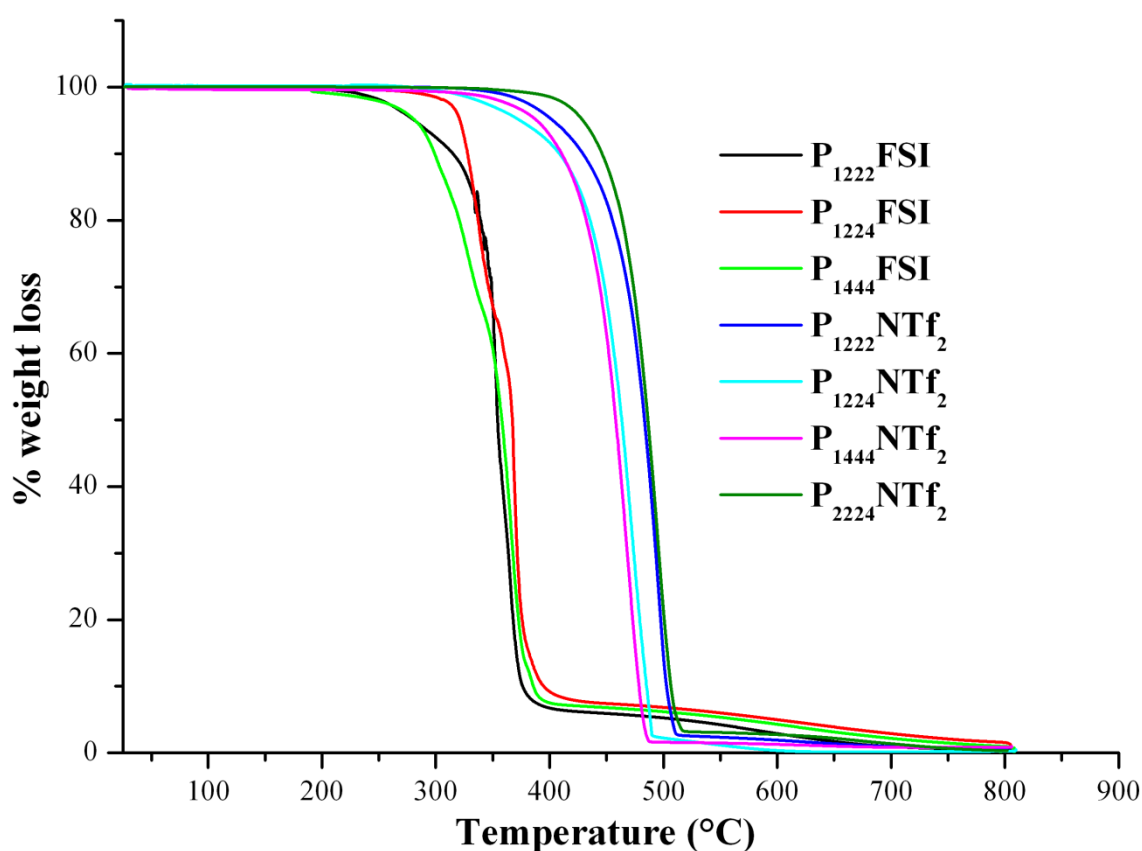


Figure 5.8: Thermogravimetric analysis traces of the NTf₂⁻ and FSI⁻ salts

The P₁₄₄₄⁺ and P₁₂₂₄⁺ cations, in combination with NTf₂⁻, BF₄⁻, PF₆⁻ and SCN⁻, show good thermal stability (Refer to Table 5.7). All of the ionic liquids decompose at about 400 °C; even the N(CN)₂⁻ anion shows better thermal stability with the phosphonium cation than with the imidazolium cation. The observation from the TGA curves suggests that the interactions between the family of cations and anions can give an indication of the thermal

5. Synthesis of novel phosphonium ionic liquids

stability of the molten salts. The synthesised phosphonium ionic liquids are as stable as the phosphonium cations containing the methoxy group. Table 5.7 summarises the thermal decomposition temperatures of the phosphonium ionic liquids.

Table 5.7: Summary of thermal properties of phosphonium ionic liquids.

Decomposition Temperature (°C) (measured at 10 °C min ⁻¹)						
Anion	FSI ⁻	NTf ₂ ⁻	PF ₆ ⁻	BF ₄ ⁻	SCN ⁻	N(CN) ₂ ⁻
Cation						
P₁₄₄₄⁺	220	330	308	310	300	310
P₁₂₂₄⁺	250	300	270	300	295	320
P₁₂₂₂⁺	220	320	-	-	-	-
P₂₂₂₄⁺	250	350	-	-	-	-
P₂₂₂₍₁₀₁₎⁺	290	388*	-	-	-	300
P₂₂₂₍₂₀₁₎⁺	300	404*	-	-	-	-

*Obtained from reference⁴

Accelerated rate calorimetry (ARC) is another technique that can be used to assess the thermal behaviour of ionic liquids,⁹⁷ and it has been used to identify potentially dangerous exothermic behaviour. Figure 5.9 shows the thermal phenomena observed for the following ionic liquids: P₂₂₂₍₂₀₁₎NTf₂, P₁₂₂₄NTf₂, C₂pyrNTf₂ and C₂mimNTf₂. C₂mimNTf₂ showed completely inert behaviour. The enhanced stability of the NTf₂ anion has already been observed.⁹⁷ The ARC results for C₂mimNTf₂ show no exothermic activity and pressure generation at any temperature up to 400 °C. Hence it can be used for high temperature applications. On the other hand, the ionic liquids with the P₁₂₂₄⁺, P₂₂₂₍₂₀₁₎⁺ and C₂mpyr⁺ cations all show exothermic behaviour, with the P₁₂₂₄⁺ and P₂₂₂₍₂₀₁₎⁺ species exhibiting similar behaviour, as shown in Figure 5.9.

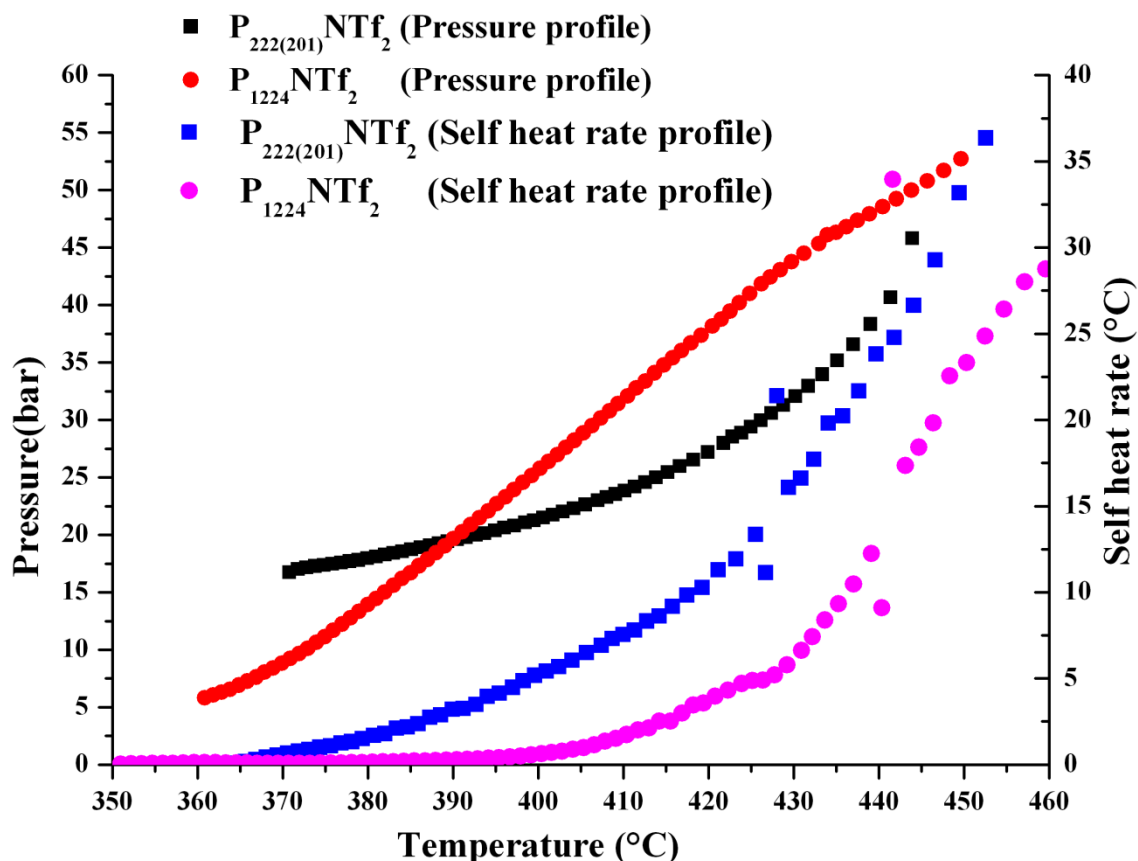


Figure 5.9: Pressure and self heat rate profile for $P_{222(201)}NTf_2$ and $P_{1224}NTf_2$

The ARC results show an onset of exothermic activity at 360 °C and 372 °C for $P_{1224}NTf_2$ and $P_{222(201)}NTf_2$ respectively; at these temperatures the samples continue to release heat and self heat. The maximum self-heat rate of 10 °C min⁻¹ is observed for $P_{1224}NTf_2$ at 432 °C and for $P_{222(201)}NTf_2$ at 422 °C. The time-temperature profile (Appendix, section A.1) for $P_{1224}NTf_2$ indicates that in the event of a runaway scenario, the time available to take safety precautions is much longer (75 min available for temperature to rise from 381 °C to 450 °C) compared to the $P_{222(201)}NTf_2$ sample where only 3 mins will be available for the temperature to rise 400 °C to 443 °C. This shows that $P_{222(201)}NTf_2$ is more vulnerable to a runaway process around this temperature. The pressure temperature profiles are similar for both the samples and the maximum pressure release at 440 °C are observed for $P_{1224}NTf_2$ and $P_{222(201)}NTf_2$ at 38 and 45 bars respectively. However, in the context of DSSC applications, these ionic liquids are quite safe to use because the maximum operating temperature used for this type of device application will be around 100 °C.

5. Synthesis of novel phosphonium ionic liquids

5.3.2 Transport properties

5.3.2.1 Viscosity

One parameter that can limit the performance of electrochemical devices is the viscosity of the electrolyte. Low viscosity is required for electrochemical applications as it influences the ionic conductivity and mass transport of ionic species in the electrolyte. Thus the viscosity and density of the new phosphonium salts were measured to see if they could be useful as electrolytes for electrochemical applications. The viscosity of P₁₂₂₄FSI, P₁₄₄₄N(CN)₂, P₁₂₂₄N(CN)₂, P₂₂₂₍₂₀₁₎NTf₂, P₂₂₂₍₂₀₁₎FSI, P₂₂₂₍₁₀₁₎NTf₂, P₂₂₂₍₁₀₁₎FSI and P₂₂₂₍₁₀₁₎N(CN)₂ were measured from 25 °C to 90 °C. P₁₄₄₄FSI was measured from 40 °C to 90 °C and P₁₂₂₄NTf₂ was measured from 30 °C to 90 °C as these are solids at room temperature. P₁₄₄₄NTf₂ was not measured due to the limitations of the instrument (sample too viscous).

The viscosity of ionic liquids depends strongly on temperature. An increase in temperature usually leads to a decrease in viscosity. An Arrhenius equation is usually used to express the dependence of viscosity on temperature as shown in equation 5.11.⁹⁸

$$\eta = \eta_0 e^{\frac{E_A}{RT}} \text{ (Eq 5.11)}$$

where η is the viscosity of the ionic liquid, η_0 is the viscosity parameter, R is the gas constant and E_A is the activation energy. On plotting the logarithmic of the viscosity versus the inverse of temperature, a straight line is obtained according to this equation.

In the literature, most ionic liquids deviate from the Arrhenius behaviour. When the temperature of the system is dropped, a large increase in viscosity is observed. Thus the Volger-Fulcher-Tammann equation is often used to fit the data as shown in equation 5.12.⁵⁸

$$\eta = \eta_0 e^{\frac{B}{(T-T_0)}} \text{ (Eq 5.12)}$$

where B and T_0 are constants.

Figure 5.10 shows the Arrhenius plot for the phosphonium ionic liquids. The plot shows that the phosphonium ionic liquids deviate from the Arrhenius behaviours. P₁₄₄₄FSI and P₁₄₄₄N(CN)₂ show higher viscosities as the phosphonium cation is quite bulky and the

alkyl length is long compared to the other phosphonium cations studied here. The FSI⁻ and N(CN)₂⁻ series show the lowest viscosity compared to NTf₂⁻ series. P₂₂₂₍₂₀₁₎NTf₂⁻, P₂₂₂₍₂₀₁₎FSI⁻, P₂₂₂₍₁₀₁₎NTf₂⁻, P₂₂₂₍₁₀₁₎FSI⁻ and P₂₂₂₍₁₀₁₎N(CN)₂⁻ show similar viscosity to C₂mimNTf₂⁻ at 25 °C and hence should be of utility in DSSCs. The use of these phosphonium ionic liquids as electrolytes in dye sensitised solar cells, with very promising results, is detailed in Chapter 7. The VTF fitting for these ionic liquids are given in Appendix, section A.2.

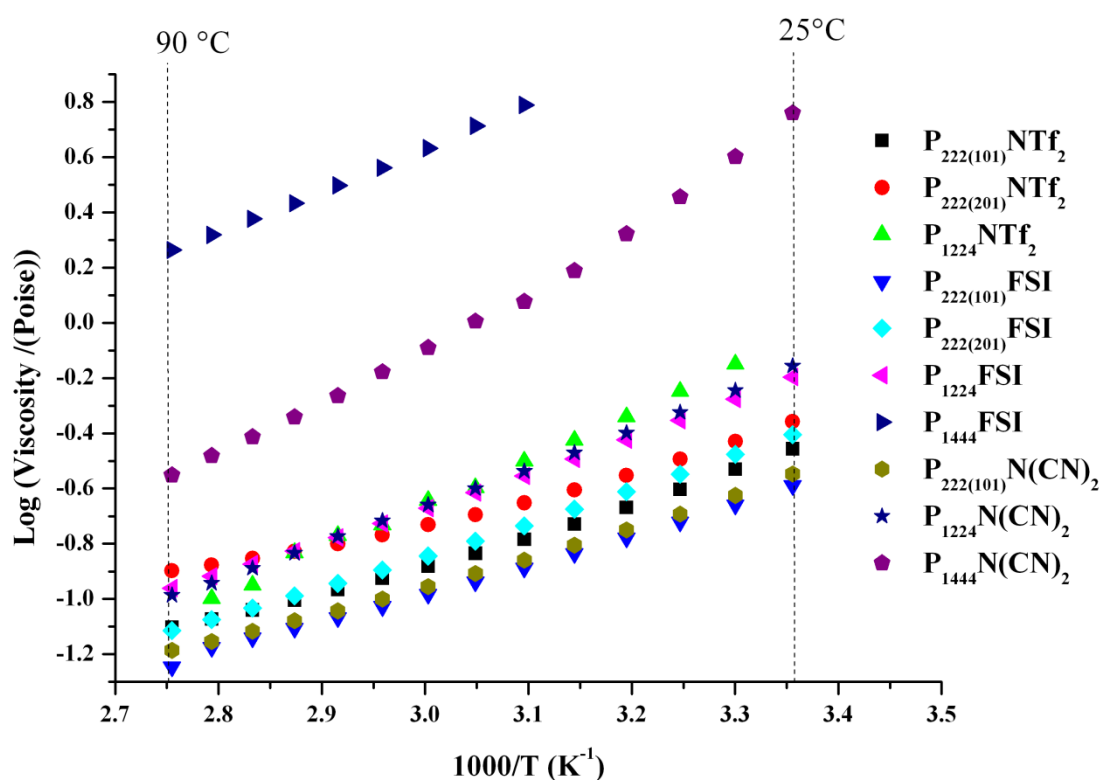


Figure 5.10: The viscosity of phosphonium ionic liquids

The nature of both the anion and the cation greatly affects the viscosity of the ILs. The difference in viscosities is caused by the size, shape and molar mass of the anion, with smaller anions tending to give more viscous ionic liquids.⁹⁹ For the same anion, a change in the symmetry of the cation also affects the viscosity of the ionic liquids, as shown in Figure 5.10. Longer alkyl chain tends to give more viscous ionic liquids, as observed in the P₁₄₄₄⁺ salts. The large viscosity of P₁₄₄₄⁺ is not surprising at all; it is expected since the system as a whole has fewer degrees of motional freedom due to its large size. Table 5.8 summarises the density and viscosity of the phosphonium ionic liquids synthesised in this chapter.

5. Synthesis of novel phosphonium ionic liquids

Table 5.8: Density and viscosity of phosphonium ionic liquids at 25 °C unless stated.

Anion	FSI ⁻		NTf ₂ ⁻		N(CN) ₂ ⁻	
	η (mPa s) (± 0.1)	ρ (gcm ⁻³) (± 0.01)	η (mPa s) (± 0.1)	ρ (gcm ⁻³) (± 0.01)	η (mPa s) (± 0.1)	ρ (gcm ⁻³) (± 0.01)
P₁₄₄₄⁺	61 [#]	1.15 [#]	-	-	576	0.99
P₁₂₂₄⁺	64	1.38	72*	1.40*	69	1.01
P₂₂₂₍₁₀₁₎⁺	27	1.32	36	1.42	34	1.08
P₂₂₂₍₂₀₁₎⁺	39	1.34	45	1.40		

* measured at 30 °C, # measured at 50 °C

5.3.2.2 Ionic conductivity

The ionic conductivity of the pure ionic liquid depends on the mobility of ions, which is influenced by the size of the ion, the formation of any aggregated species, and the viscosity. The conductivity behaviour of the P₁₄₄₄⁺ salts is illustrated in Figure 5.11. P₁₄₄₄NTf₂ shows low conductivity in the lower temperature region, which gradually increases as the temperature increases; at -68 °C, the conductivity is 10⁻¹⁰ S cm⁻¹. Even though there is no phase change in the region between 25 °C and 50 °C, a change in slope is observed. The experiment was repeated and the same behaviour was observed. A further increase in conductivity is observed as the compound melts, at 50 °C, and a conductivity of 10⁻⁴ S cm⁻¹ is achieved. Further increases are also observed as the melt is heated.

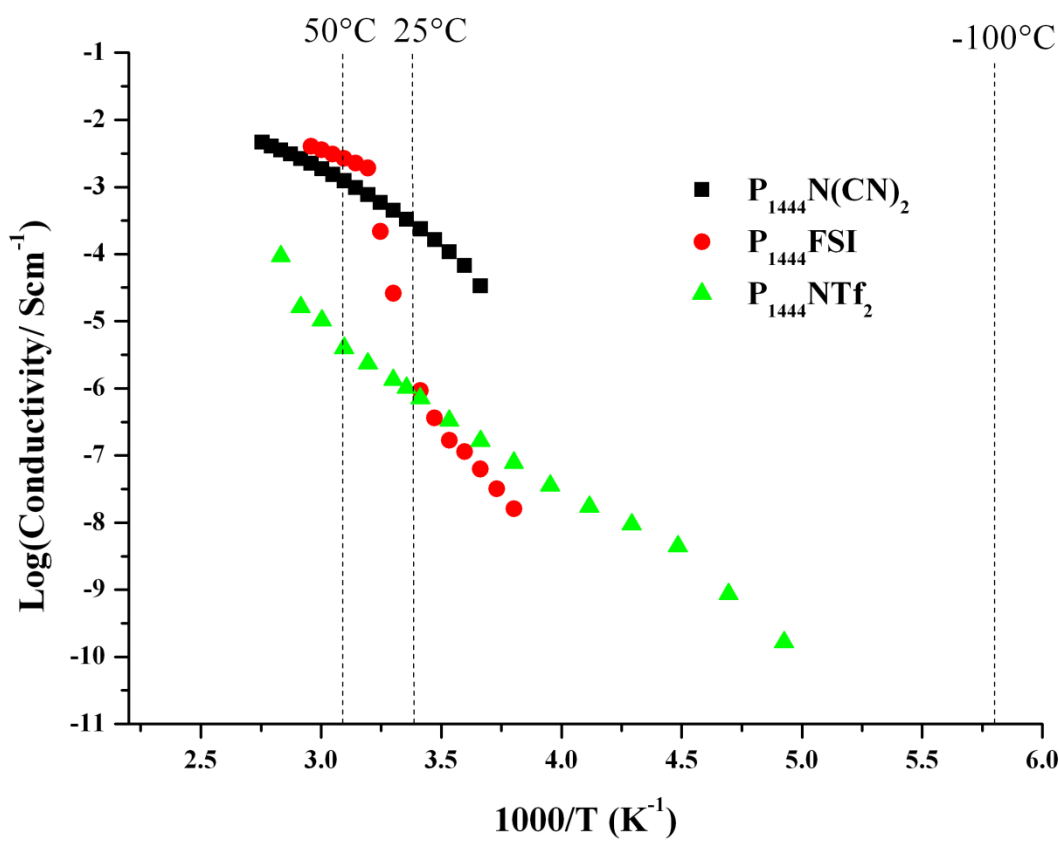


Figure 5.11: Conductivity data for the P₁₄₄₄⁺ cation with different anions

With most plastic crystals, the ionic conductivity is low in the lower temperature region and increases substantially as the temperature is increased in the plastic phases.¹⁰⁰⁻¹⁰⁴ P₁₄₄₄FSI has a strong solid-solid phase transition just below the melting point: hence the conductivity rises steadily from quite a low value to the melt. At the melt (36 °C), the conductivity is 10⁻³ S cm⁻¹ and a steady VTF-like increase in conductivity is observed above the melting point.

The conductivity of P₁₄₄₄N(CN)₂ gradually increases as the temperature increases due to an enhancement in ion mobility resulting from a decrease in viscosity. In the melt region, both P₁₄₄₄FSI and P₁₄₄₄NTf₂ show slightly higher conductivity than P₁₄₄₄N(CN)₂.

5. Synthesis of novel phosphonium ionic liquids

Figure 5.12 shows the effect of changing the anion in combination with the P_{1224}^+ cation. The ionic conductivity of the P_{1224}^+ ionic liquids differ greatly from one another. The most conductive of the ionic liquids synthesised are the $P_{1224}FSI$, $P_{1224}NTf_2$ and $P_{1224}N(CN)_2$ salts; these are all room temperature ionic liquids, except for $P_{1224}NTf_2$ which melts at 30 °C. The conductivity of the $P_{1224}FSI$ and $P_{1224}N(CN)_2$ salts at room temperature are $4.3 \times 10^{-3} S cm^{-1}$, and $3.8 \times 10^{-3} S cm^{-1}$ respectively. At 30 °C, the conductivity of $P_{1224}NTf_2$ is $3.2 \times 10^{-3} S cm^{-1}$. These ionic liquids are quite conductive compared to $P_{66614}N(CN)_2$, which has a conductivity of $5.79 \times 10^{-4} S cm^{-1}$ at 50°C. The conductivities of $P_{1224}FSI$, $P_{1224}NTf_2$ and $P_{1224}N(CN)_2$ are quite similar at temperatures above 30 °C. Below room temperature, the ionic conductivity of $P_{1224}NTf_2$ drops drastically compared to the FSI and $N(CN)_2$ due to a change of phase from liquid to solid state, where the free movement of ions are severely hindered.

The conductivity of $P_{1224}PF_6$, $P_{1224}SCN$ and $P_{1224}BF_4$ increases as a function of temperature and changes in phase. These salts are solid at room temperature. The changes in conductivity can be correlated to the phase transitions observed in the DSC (refer to Figure 5.5 and Table 5.4). For these phosphonium compounds, the conductivity can be divided into several distinct zones, where the increase in conductivity probably corresponds to changes in the orientational disorder of the salt. For the SCN^- salt, there is a steady rise in conductivity from very low values through the region in which the phase III to II and II to I transitions take place, leading to a quite high conductivity in phase I, greater than $2 mS cm^{-1}$. The same behaviour is observed for the $P_{1224}BF_4$ salt. In the case of $P_{1224}PF_6$, from -50 °C to 30 °C a constant increase in conductivity is observed, before a gradual increase from 35 °C to 80 °C. In the low temperature region, $P_{1224}PF_6$ displays better conductivity than $P_{1224}BF_4$, but as the temperature increases (beyond 60 °C) $P_{1224}BF_4$ has higher ionic conductivity.

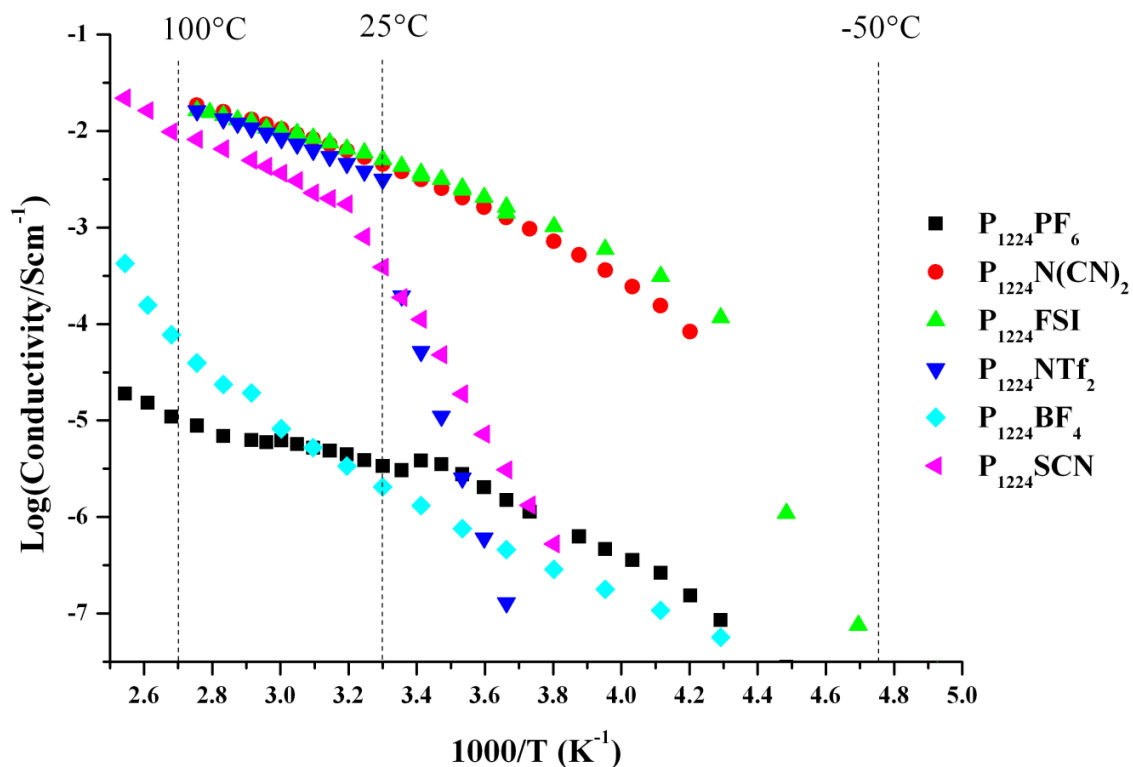


Figure 5.12: Conductivity data for the P_{1224}^+ cation with the PF_6^- , BF_4^- , FSI, NTf_2^- and SCN^- anions

The viscosity of the commercially available phosphonium ionic liquids containing the methoxy group have been compared with the synthesised phosphonium ionic liquids for the FSI, $N(CN)_2$ and NTf_2 series as shown in Figure 5.13, 5.14 and 5.15 respectively. The three sets of data are presented separately for better clarity. $P_{1224}FSI$, $P_{222(101)}FSI$ and $P_{222(201)}FSI$ show similar ionic conductivities and this is the first time that such high conductivities have been achieved with phosphonium ionic liquids.

In Appendix, section A.2, the VTF parameters obtained for these compounds are tabulated. Log conductivity versus T_g/T is also plotted for the ionic liquids that have a glass transition temperature.

5. Synthesis of novel phosphonium ionic liquids

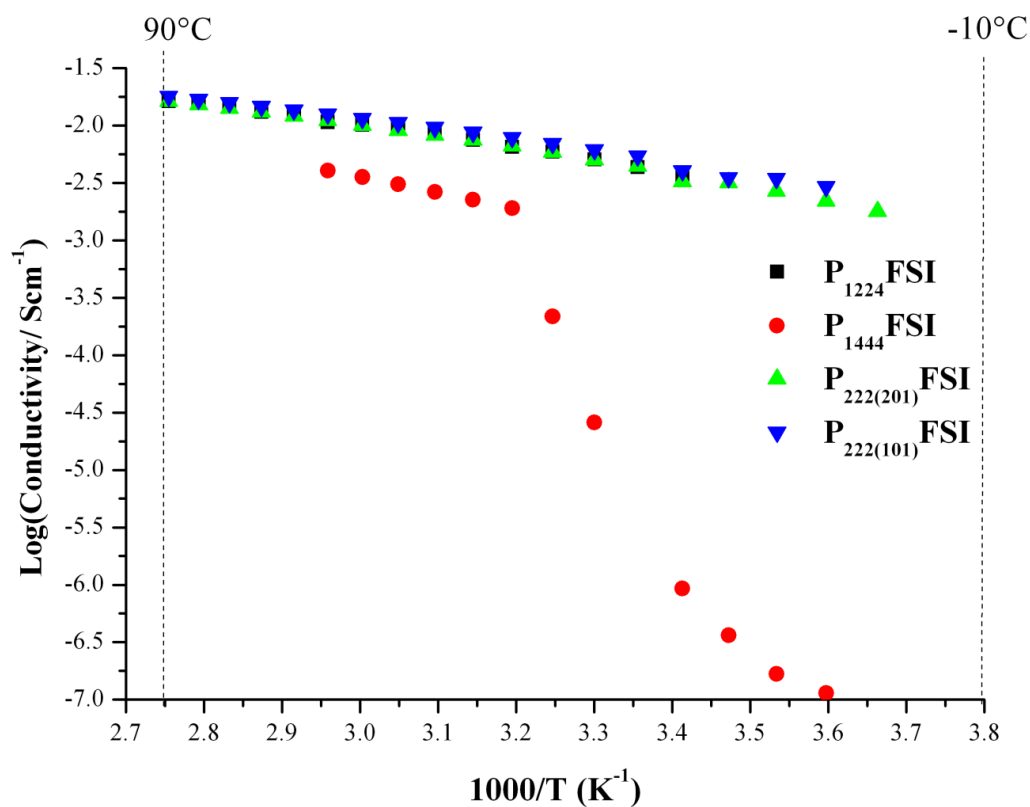


Figure 5.13: Conductivity data for the FSI⁻ series

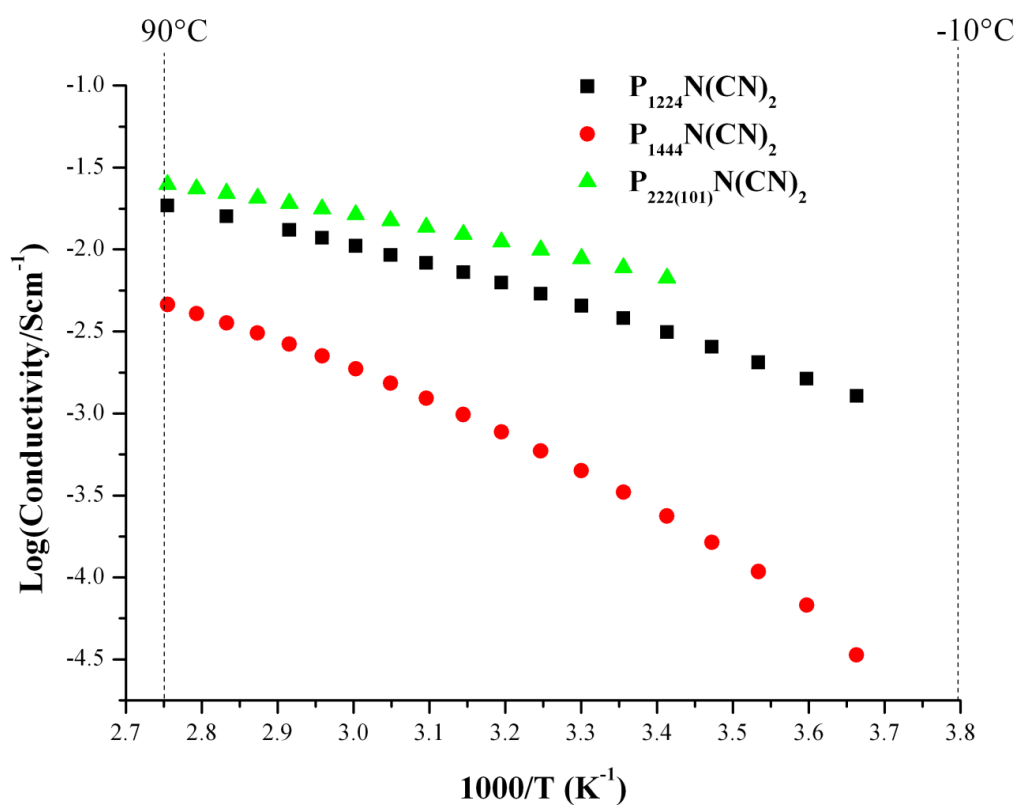


Figure 5.14: Conductivity data for the $\text{N}(\text{CN})_2^-$ series

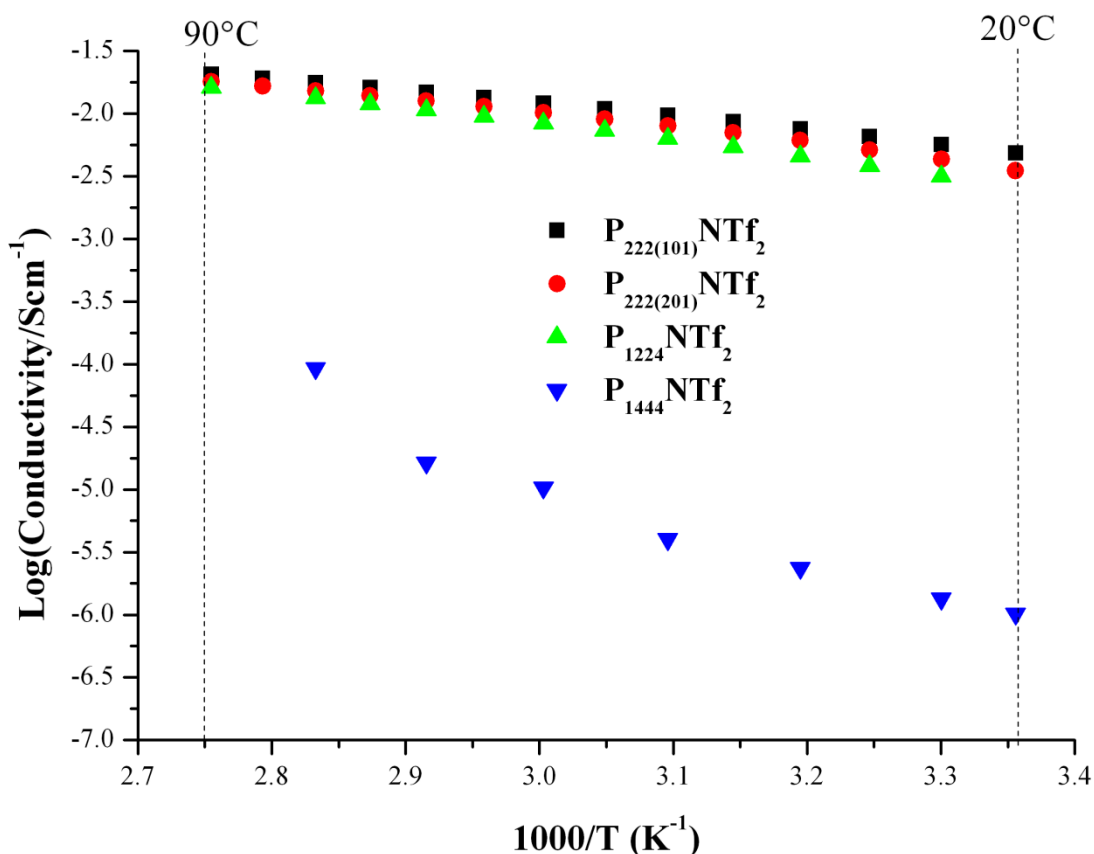


Figure 5.15: Conductivity data for the NTf₂⁻ series

5.3.2.3 The Walden plot

The phosphonium salts that are room temperature ionic liquids can be further analysed using the Walden plot as discussed above. Figure 5.16 shows a Walden plot of the phosphonium salts studied here, over a temperature range of 25 °C to 90 °C. According to Angell *et al.*⁵ all ionic liquids that lie below the 10 % line on the Walden plot are considered as “poor” ionic liquids due to the presence of ion pairs or aggregation.

All phosphonium ionic liquids synthesised in this thesis, as well as those with methoxy groups on the side chain of the cation that were obtained commercially, lie below and close to the ideal KCl line, thus they have low degree of pairing or aggregation type interactions. These ionic liquids are considered to be “good” ionic liquids.

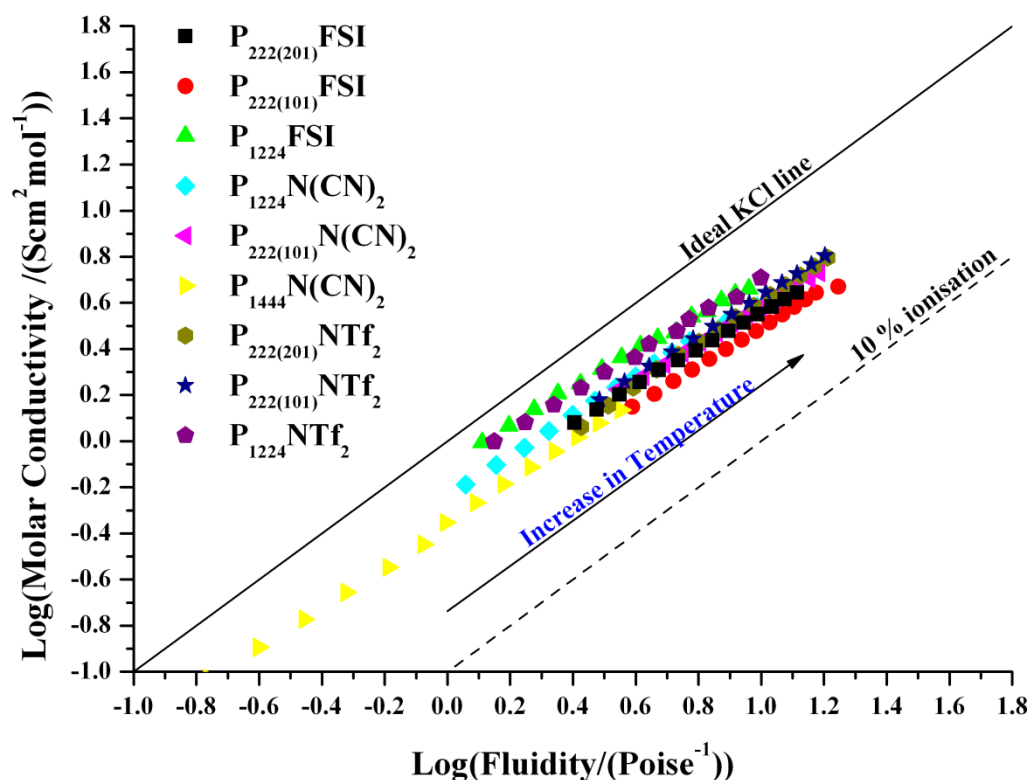
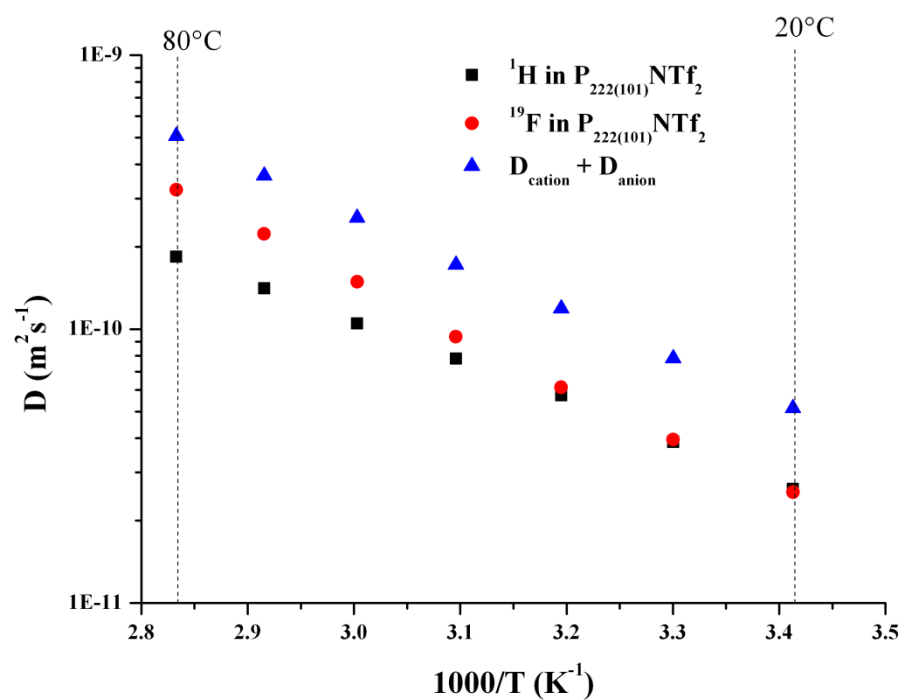


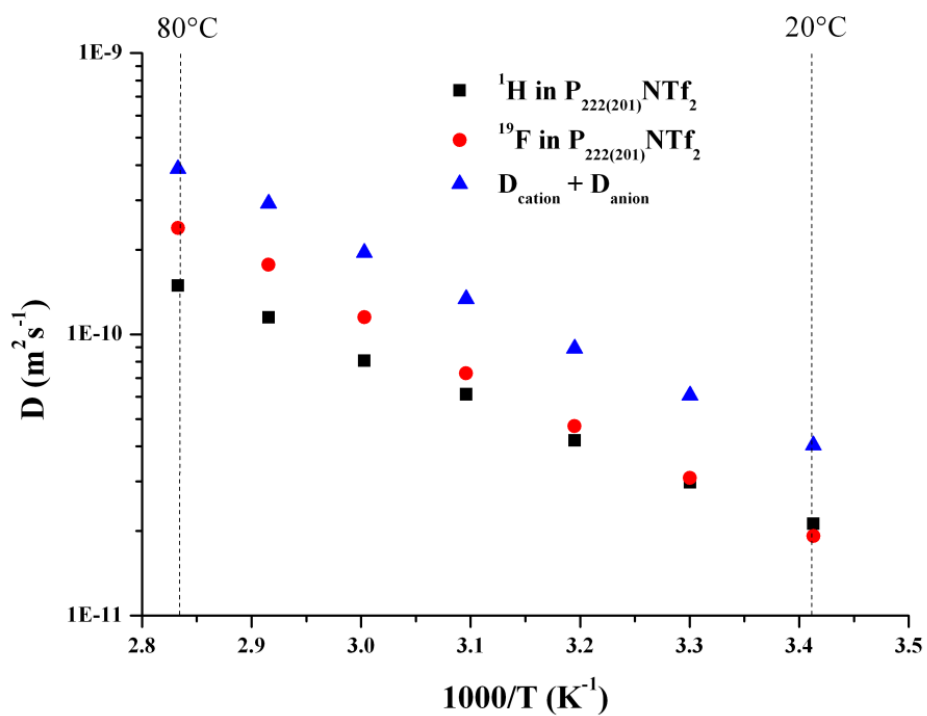
Figure 5.16: The Walden plot of the phosphonium salts

5.3.2.3 Diffusion measurements of neat phosphonium ionic liquids

The diffusion coefficient of two phosphonium ionic liquids, $P_{222(101)}NTf_2$ and $P_{222(201)}NTf_2$, were measured for both the cation and anion (1H and ^{19}F) by pulsed field-gradient stimulated echo NMR. The NMR measurements were carried out by Mr. Paul Bayley and Mr. Hyun Yoon at Monash University. Figure 5.17 (a) and (b) shows the temperature dependent diffusion coefficient of the cation and anion for $P_{222(101)}NTf_2$ and $P_{222(201)}NTf_2$ respectively, over the temperature range of 20 °C to 80 °C. The values obtained for the diffusion coefficient of the cation and anion at different temperatures are summarised in Table 5.9. Figure 5.17 also shows $D_{cation} + D_{anion}$, which is the total diffusion coefficient of the ionic liquids.



(a)



(b)

Figure 5.17: Arrhenius plot of self-diffusion coefficient of the cation and anion for (a) $\text{P}_{222(101)}\text{NTf}_2$, (b) $\text{P}_{222(201)}\text{NTf}_2$

5. Synthesis of novel phosphonium ionic liquids

The Arrhenius plot in Figure 5.17 (a) shows that the $P_{222(101)}^+$ cation and NTf_2^- anion diffuse at nearly the same rate between 20 °C to 40 °C, and at temperatures above this, the anion moves faster. In the case of $P_{222(201)} NTf_2$, the anion moves faster than the cation from 30 °C to 80 °C.

The effective “hydrodynamic radius” can be calculated from this data using a rearrangement of the Stokes-Einstein equation;

$$r = \frac{k_B T}{X \pi \eta D}$$

The constant $X = 6$ is used when the fluid molecules adhere perfectly to the surface of sphere, and $X = 4$ is used for a system where the sphere moves through the liquid medium with no adhesion.¹⁰⁵ It is then of interest to observe how this effective hydrodynamic radius compares to estimates of the ion sizes.

Table 5.9: Diffusion coefficients and calculated effective hydrodynamic radii of the cations and anions for $P_{222(101)}NTf_2$ and $P_{222(201)}NTf_2$.

IL	Cation			Anion		
	T (K)	D (m^2s^{-1})	Radius (\AA)	D (m^2s^{-1})	Radius (\AA)	
		H ($\pm 1\%$)	X = 4 X = 6	F ($\pm 1\%$)	X = 4 X = 6	
$P_{222(101)}NTf_2$						
	293	2.6×10^{-11}	3.3 2.2	2.5×10^{-11}	2.8 1.9	
	303	3.9×10^{-11}	3.1 2.1	3.9×10^{-11}	3.1 2.1	
	313	5.7×10^{-11}	3.1 2.1	6.1×10^{-11}	2.9 1.9	
	323	7.8×10^{-11}	3.2 2.1	9.4×10^{-11}	2.7 1.8	
	333	1.1×10^{-10}	3.2 2.1	1.5×10^{-10}	2.2 1.5	
	343	1.4×10^{-10}	3.1 2.1	2.2×10^{-10}	2.0 1.3	
	353	1.8×10^{-10}	3.1 2.0	3.2×10^{-10}	1.7 1.2	
$P_{222(201)}NTf_2$						
	293	2.1×10^{-11}	3.5 2.3	1.9×10^{-11}	3.8 2.5	
	303	3.0×10^{-11}	3.0 2.0	3.1×10^{-11}	2.9 1.9	
	313	4.2×10^{-11}	2.9 2.0	4.7×10^{-11}	2.6 1.7	
	323	6.1×10^{-11}	2.6 1.7	7.3×10^{-11}	2.2 1.5	
	333	8.1×10^{-11}	2.4 1.6	1.2×10^{-10}	1.7 1.2	
	343	1.2×10^{-10}	2.1 1.4	1.8×10^{-10}	1.3 0.9	
	353	1.5×10^{-10}	1.9 1.2	2.4×10^{-10}	1.2 0.8	

5. Synthesis of novel phosphonium ionic liquids

The hydrodynamic radius of the anion is closer, at the lower temperatures, to the estimated value for this anion, 3.1 Å.¹⁰⁶ This suggests that the $X = 4$ parameter is a better fit in this case. The temperature dependence, which indicates a decreasing effective hydrodynamic radius, is however hard to understand in terms of the simple Stokes-Einstein model.¹⁰⁷ This trend arises as a result of the fact that the diffusivity is rising more rapidly than the fluidity ($=1/\eta$) with temperature. This is not an uncommon observation, which is thought to reflect the fact that the factors that control the viscosity at a molecular level are different from those that control individual, long range ion diffusion and hence that the Stokes-Einstein equation breaks down.

Figure 5.18 shows the cationic transference numbers for $P_{222(101)}NTf_2$ and $P_{222(201)}NTf_2$. The cationic transference numbers ($D_{cation}/(D_{cation} + D_{anion})$) suggest that in both phosphonium ionic liquids as the temperature rises, the anion moves faster than the cation; the cation transference number decreases with increasing temperature.

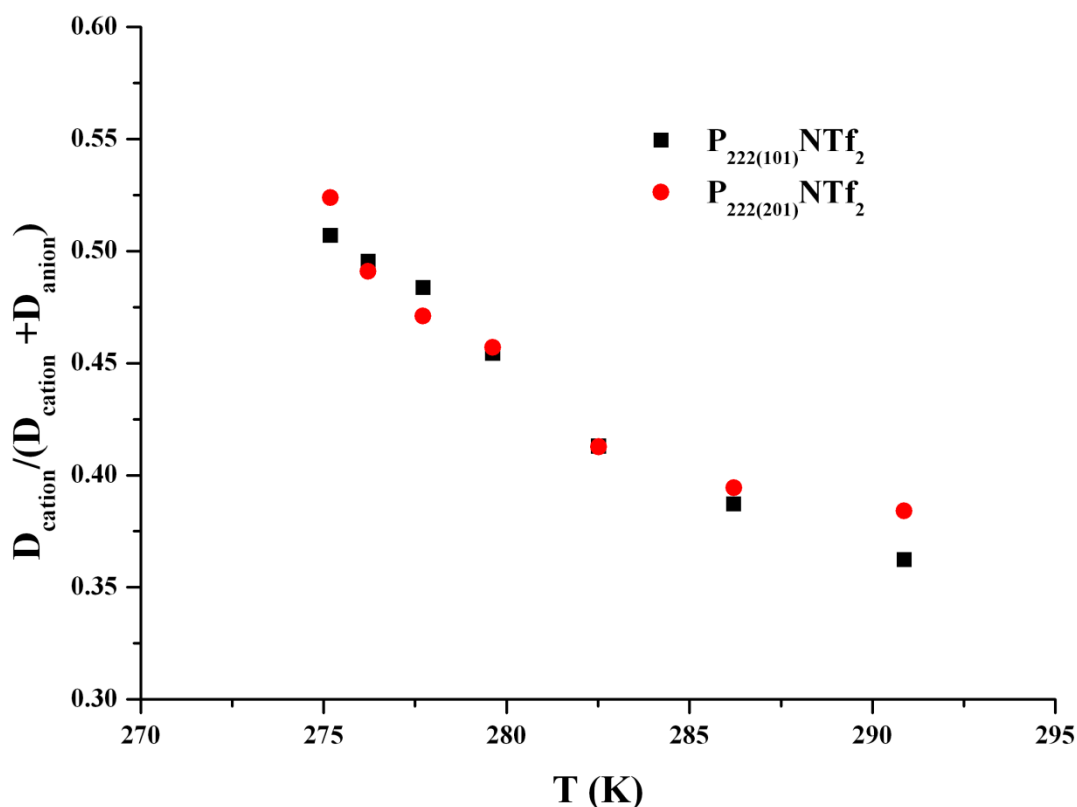


Figure 5.18: Temperature dependence of apparent cation transference number for both $P_{222(101)}NTf_2$ and $P_{222(201)}NTf_2$

For the two phosphonium ionic liquids, the molar conductivity was calculated from the self-diffusion coefficients (Λ_{NMR}), determined by PGSTE-NMR measurements, using the Nernst-Einstein equation. Table 5.10 summarises the different parameters, such as the measured molar conductivity (Λ_{imp}), calculated molar conductivity (Λ_{NMR}), the ratio of ($\Lambda_{\text{imp}}/\Lambda_{\text{NMR}}$), the calculated fraction of ion pairs, ΔW , the vertical distance of the point from the ideal behaviour on the Walden plot and ΔI , the vertical distance of the point from the ideal line on the ionicity plot.

Figure 5.19 illustrates the ionicity plot,¹⁰⁶ i.e. $\text{Log}(\Lambda_{\text{imp}})$ vs. $\text{Log}(\Lambda_{\text{NMR}})$, which displays the data on a scale comparable to the Walden plot. The deviation from the ideal behaviour ($\text{Log}(\Lambda_{\text{imp}}) = \text{Log}(\Lambda_{\text{NMR}})$) suggests that there is some ion aggregations occurring in the ILs, and a similar effect was observed on the Walden plot (Figure 5.17).

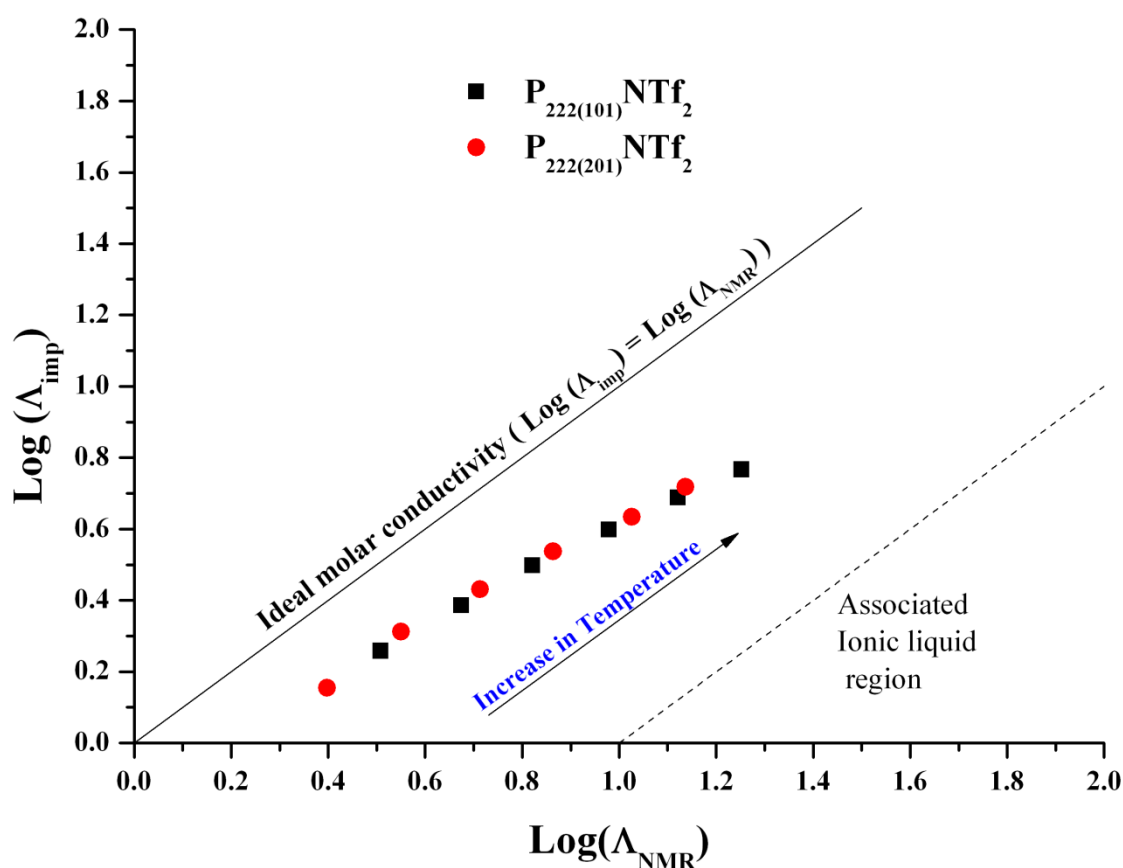


Figure 5.19: Ionicity plot of $\text{P}_{222(101)}\text{NTf}_2$ and $\text{P}_{222(201)}\text{NTf}_2$

5. Synthesis of novel phosphonium ionic liquids

Table 5.10: Molar conductivity values for P₂₂₂₍₁₀₁₎NTf₂ and P₂₂₂₍₂₀₁₎NTf₂ at varying temperatures (K). Λ_{NMR} values calculated using the Nernst-Einstein equation.

IL	Λ_{imp} (S cm ² mol ⁻¹)	Λ_{NMR} (S cm ² mol ⁻¹)	$\frac{\Lambda_{\text{imp}}}{\Lambda_{\text{NMR}}}$	$1 - \left(\frac{\Lambda_{\text{imp}}}{\Lambda_{\text{NMR}}}\right)$	ΔW (± 0.1)	ΔI (± 0.1)
P ₂₂₂₍₁₀₁₎ NTf ₂						
303 K	1.81	3.22	0.56	0.44	0.32	0.25
313 K	2.44	4.72	0.52	0.48	0.34	0.29
323 K	3.15	6.62	0.48	0.52	0.35	0.32
333 K	3.96	9.52	0.42	0.58	0.37	0.38
343 K	4.88	13.2	0.37	0.63	0.39	0.43
353 K	5.85	17.8	0.33	0.67	0.40	0.48
P ₂₂₂₍₂₀₁₎ NTf ₂						
303 K	1.43	2.49	0.57	0.43	0.35	0.24
313 K	2.05	3.55	0.58	0.42	0.36	0.25
323 K	2.69	5.16	0.52	0.48	0.37	0.28
333 K	3.45	7.30	0.47	0.53	0.38	0.33
343 K	4.30	10.6	0.40	0.59	0.39	0.39
353 K	5.23	13.7	0.38	0.62	0.40	0.42

As is often the case in ionic liquids, there is a difference between Λ_{imp} (measured by using a dip cell) and Λ_{NMR} (calculated from the Nernst-Einstein equation) at all temperatures, and especially at higher temperatures, with Λ_{NMR} values being higher than Λ_{imp} . One possible explanation for such a difference is that the IL is to some extent associated such that neutral species, which are unresponsive to the electric field are formed and hence impact on the conductivity measurement.

As proposed by Tokuda *et al.*⁷⁷ the ($\Lambda_{\text{imp}} / \Lambda_{\text{NMR}}$) ratio (Table 5.10) can provide information about the degree of ionic association in the ILs. The ratio of ($\Lambda_{\text{imp}} / \Lambda_{\text{NMR}}$) indicates the

percentage of charged ions that that can diffuse and thus contribute to the ionic conduction. As shown in Table 5.10, as the temperature increases, both ionic liquids appear to become more highly associated, as the ratio of ($\Lambda_{\text{imp}}/\Lambda_{\text{NMR}}$) decreases. The trend is also clearly observed in Figure 5.19: with an increase in ΔI , as ΔI increases as a function of temperature for both ionic liquids. This is also commonly observed by others, but it is not well understood since one would tend to expect the opposite. This may in fact indicate a partial breakdown of the Nernst-Einstein equation in a similar way to that discussed above with respect to the Stokes-Einstein equation.

5.3.3 *Electrochemical window*

The electrochemical stability of ionic liquids is very important for their use in electrochemical devices. The electrochemical window of P₁₄₄₄FSI and P₁₄₄₄NTf₂ were measured at 50 °C and 70 °C, respectively, using a three electrode set up. A Pt wire (1 mm) was used as a pseudo reference electrode and the Ferrocene/Ferrocenium redox couple was used as an internal reference. Figure 5.20 shows the electrochemical window for the NTf₂ series. The CV was performed in an Argon glovebox. All three phosphonium molten salts show similar electrochemical windows. Cyclic voltammetry is quite sensitive to any signs of small impurities; the small shoulder at around -0.3 and +0.8 V is due to the presence of residual water even though the compounds were dried at 100 °C for a week under vacuum.

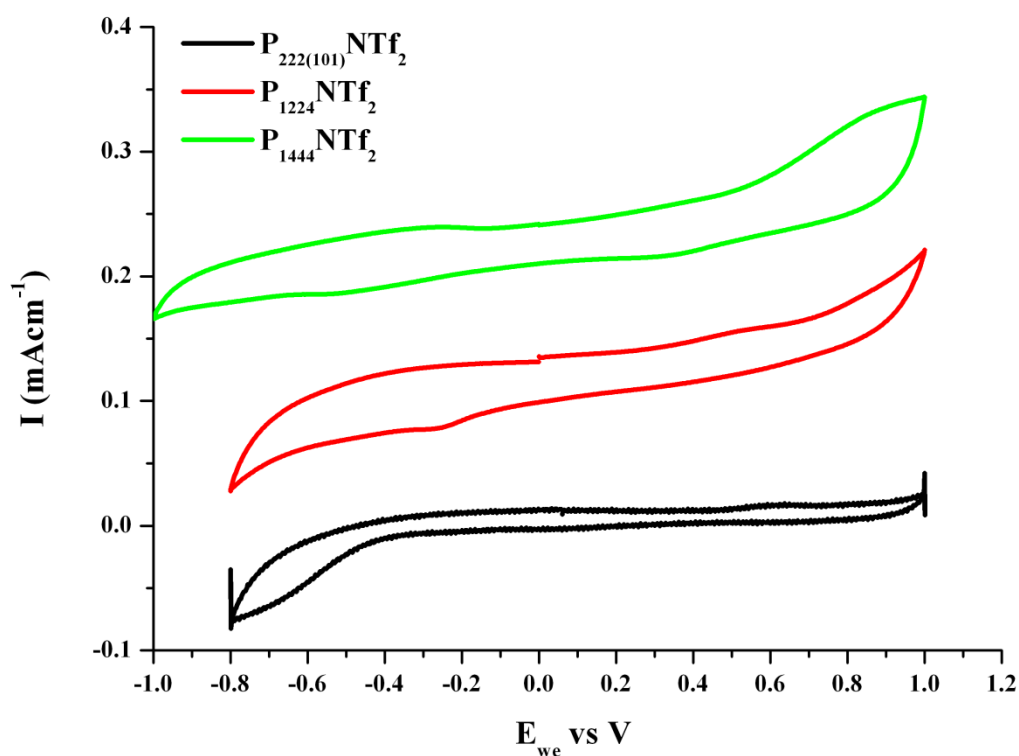


Figure 5.20: The electrochemical stability of the NTf_2^- ionic liquid series

The NTf_2^- anions are known to form ionic liquids with high electrochemical stability.⁸⁹ The methoxy substituted phosphonium ionic liquids in the literature⁴ show wider electrochemical windows than illustrated in this chapter, which may be because Platinum electrodes are more sensitive to any impurities than the glassy carbon electrodes used in the literature. Scanning the phosphonium ionic liquids over a wider potential window shows the presence of several peaks, which may be due to the decomposition of the phosphonium cation in the oxidative region and decomposition of the anion in the reductive region (Refer to Appendix, section A.3). Reduction of the NTf_2^- anion usually starts around 2 V, but presence of residual amounts of lithium salts can lower the reduction potential of this anion.¹⁰⁸ Thus, the ionic liquids were washed in dichloromethane with water several times and dried at 100 °C in vacuo for several days, but no significant improvement in reductive stability was observed.

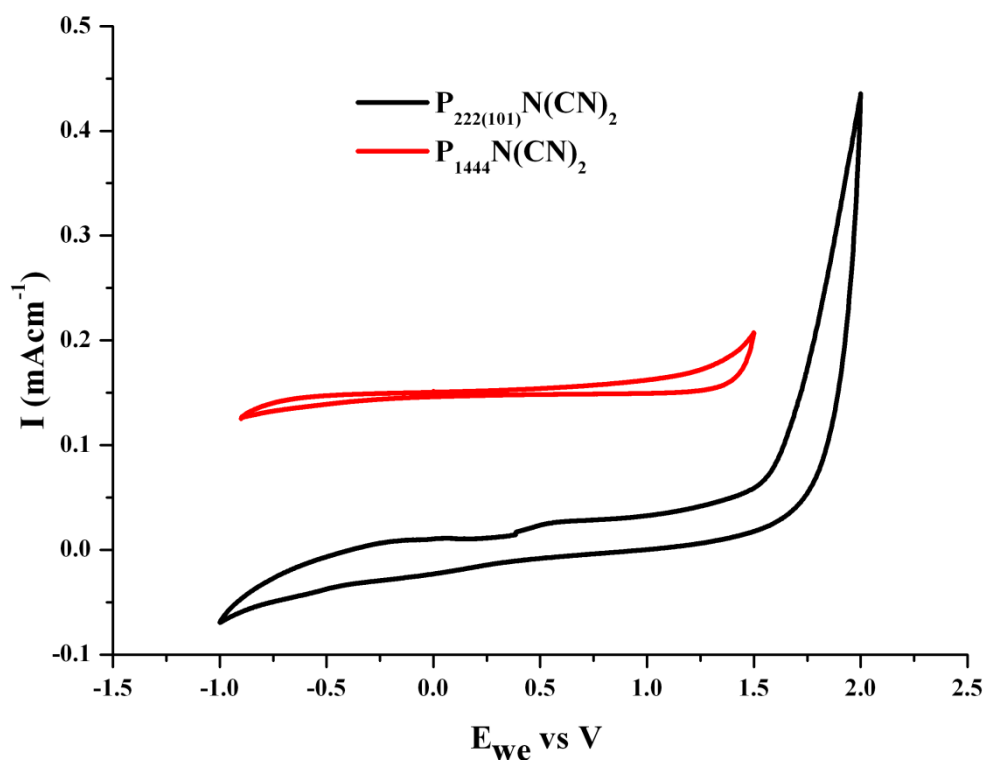


Figure 5.21: The electrochemical window of the N(CN)₂⁻ series

Figures 5.21 and 5.22 show the electrochemical window of the N(CN)₂⁻ and FSI series. Depending on the cations, the potential window varied; in the case of the FSI series, P₁₂₂₄⁺ shows a wider electrochemical window. The methoxy substituted phosphonium ionic liquids and the P₁₄₄₄⁺ salts show similar electrochemical windows. These phosphonium ionic liquids are suitable for use as electrolytes in dye sensitised solar cells as the potential window is sufficient for the device. In a dye sensitised solar cell, beyond 1 V the dye can be easily removed from the surface of the semi-conductor.

5. Synthesis of novel phosphonium ionic liquids

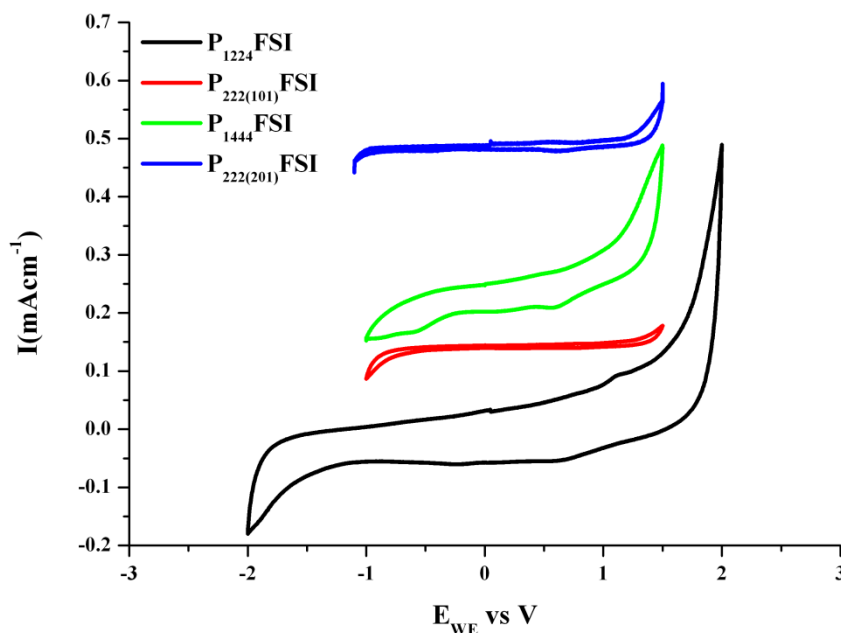


Figure 5.22: The electrochemical window of the FSI series

5.4 Conclusions

Tetraalkyl phosphonium molten salts with anions FSI, NTf₂⁻, PF₆⁻, BF₄⁻, SCN⁻ and N(CN)₂⁻ were synthesised and characterised by TGA, DSC, conductivity and cyclic voltammetry. Some of the phosphonium salts are liquid at room temperature. P₁₄₄₄FSI, P₁₄₄₄PF₆, P₁₂₂₄BF₄, P₁₂₂₄PF₆ and P₁₂₂₄SCN show multiple solid–solid phase transition with a $\Delta S_f \sim 20 \text{ J mol}^{-1} \text{ K}^{-1}$, suggesting that they are plastic crystals that could be used as solid state electrolytes. These “plastic crystals” shows high ion mobility in the different solid–solid phases, as indicated by their conductivity. P₁₄₄₄NTf₂, and P₁₄₄₄BF₄ also show multiple solid–solid phase transitions, but their entropy of fusion are too high to be defined as plastic crystals under Timmermans’ criteria. P₁₂₂₄N(CN)₂ and P₁₂₂₄FSI form ionic liquids and these are quite fluid and have good ionic conductivity compared to the methoxy-substituted phosphonium ionic liquids. All the phosphonium ionic liquids are thermally stable up to around 300 °C, except for the FSI series. The Walden plot for the methoxy-substituted phosphonium ionic liquids and the synthesised phosphonium ionic liquids indicate that these behave as good ionic liquids, without significant ion pairing. Even though the electrochemical window of the salts is quite narrow compared to the imidazolium based ionic liquids, these phosphonium salts may still be used as electrolytes for dye sensitised solar cells.

References.

1. A. L. Revelli, L. M. Sprunger, J. Gibbs, W. E. Acree, G. A. Baker and F. Mutelet, *J. Chem. Eng. Data*, 2009, **54**, 977-985.
2. M. D. Baumann, A. J. Daugulis and P. G. Jessop, *Appl. Microbiol. Biotechnol.*, 2005, **67**, 131-137.
3. D. A. Gerritsma, A. Robertson, J. McNulty and A. Capretta, *Tetrahedron Lett.*, 2004, **45**, 7629-7631.
4. K. Tsunashima and M. Sugiya, *Electrochem. Commun.*, 2007, **9**, 2353-2358.
5. J. P. Belieres, D. Gervasio and C. A. Angell, *Chem. Commun.*, 2006, 4799-4801.
6. M. A. Navarra, S. Panero and B. Scrosati, *Electrochem. Solid-State Lett.*, 2005, **8**, A324-A327.
7. R. F. de Souza, J. C. Padilha, R. S. Gonçalves and J. Dupont, *Electrochem. Commun.*, 2003, **5**, 728-731.
8. M. Diaw, A. Chagnes, B. Carré, P. Willmann and D. Lemordant, *J. Power Sources*, 2005, **146**, 682-684.
9. S. Luo, Z. Zhang and L. Yang, *Chin. Sci. Bull.*, 2008, **53**, 1337-1342.
10. N. Byrne, P. C. Howlett, D. R. MacFarlane and M. Forsyth, *Adv. Mater.*, 2005, **17**, 2497-2501.
11. S. Seki, Y. Kobayashi, H. Miyashiro, Y. Ohno, A. Usami, Y. Mita, N. Kihira, M. Watanabe and N. Terada, *J. Phys. Chem. B*, 2006, **110**, 10228-10230.
12. M. Izmailova, A. Rychagov, K. Den'shchikov, Y. Vol'fkovich, E. Lozinskaya and A. Shaplov, *Russ. J. Electrochem.*, 2009, **45**, 949-950.
13. E. Frackowiak, G. Lota and J. Pernak, *Appl. Phys. Lett.*, 2005, **86**, 164104-164103.
14. J. Wang, C. Xu, M. Taya and Y. Kuga, *Smart Mater. Struct.*, 2007, **16**, S214-S219.
15. B. J. Akle, M. D. Bennett and D. J. Leo, *Sens. Actuators A*, 2006, **126**, 173-181.
16. Y. Bai, Y. Cao, J. Zhang, M. Wang, R. Li, P. Wang, S. M. Zakeeruddin and M. Grätzel, *Nat. Mater.*, 2008, **7**, 626-630.
17. Y. Cao, Y. Bai, Q. Yu, Y. Cheng, S. Liu, D. Shi, F. Gao and P. Wang, *J. Phys. Chem. C*, 2009, **113**, 6290-6297.
18. M. Wang, X. Yin, X. R. Xiao, X. Zhou, Z. Z. Yang, X. P. Li and Y. Lin, *J. Photochem. Photobiol. A*, 2008, **194**, 20-26.
19. P. Wang, C. Klein, R. Humphry-Baker, S. M. Zakeeruddin and M. Grätzel, *Appl. Phys. Lett.*, 2005, **86**, 123508-123503.
20. P. Wang, S. M. Zakeeruddin, I. Exnar and M. Grätzel, *Chem. Commun.*, 2002, 2972-2973.
21. P. Wang, S. M. Zakeeruddin, J. E. Moser, R. Humphry-Baker and M. Grätzel, *J. Am. Chem. Soc.*, 2004, **126**, 7164-7165.
22. P. Wang, S. M. Zakeeruddin, P. Comte, R. Charvet, R. Humphry-Baker and M. Grätzel, *J. Phys. Chem. B*, 2003, **107**, 14336-14341.
23. P. Wang, S. M. Zakeeruddin, M. Grätzel, W. Kantelehner, J. Mezger, E. V. Stoyanov and O. Scherr, *Appl. Phys. A: Mater. Sci. Process.*, 2004, **79**, 73-77.
24. N. V. Plechkova and K. R. Seddon, *Chem. Soc. Rev.*, 2008, **37**, 123-150.

5. Synthesis of novel phosphonium ionic liquids

25. K. R. Seddon, *Nat. Mater.*, 2003, **2**, 363-365.
26. C. J. Bradaric, A. Downard, C. Kennedy, A. J. Robertson and Y. Zhou, *Green Chem.*, 2003, **5**, 143-152.
27. R. E. Del Sesto, C. Corley, A. Robertson and J. S. Wilkes, *J. Organomet. Chem.*, 2005, **690**, 2536-2542.
28. H. Imoto, S. Hayakawa, N. Morita and T. Saito, *Inorg. Chem.*, 1990, **29**, 2007-2014.
29. R. Byrne, S. Coleman, S. Gallagher and D. Diamond, *Phys. Chem. Chem. Phys.*, 2010, **12**, 1895-1904.
30. J. McNulty, J. J. Nair, S. Cheekoori, V. Larichev, A. Capretta and A. J. Robertson, *Chem. Eur. J.*, 2006, **12**, 9314-9322.
31. P. G. Rickert, M. R. Antonio, M. A. Firestone, K. A. Kubatko, T. Szreder, J. F. Wishart and M. L. Dietz, *J. Phys. Chem. B*, 2007, **111**, 4685-4692.
32. J. Kagimoto, K. Fukumoto and H. Ohno, *Chem. Commun.*, 2006, 2254-2256.
33. G. Zhou, X. Liu, S. Zhang, G. Yu and H. He, *J. Phys. Chem. B*, 2007, **111**, 7078-7084.
34. F. S. Oliveira, M. G. Freire, M. J. Pratas, J. R. M. Pauly, J. L. Daridon, I. M. Marrucho and J. O. A. P. Coutinho, *J. Chem. Eng. Data*, 2009, **55**, 662-665.
35. J. L. Anthony, J. L. Anderson, E. J. Maginn and J. F. Brennecke, *J. Phys. Chem. B*, 2005, **109**, 6366-6374.
36. J. N. Canongia Lopes and A. A. H. Pádua, *J. Phys. Chem. B*, 2006, **110**, 19586-19592.
37. J. M. Pringle, D. R. MacFarlane and M. Forsyth, *Synth. Met.*, 2005, **155**, 684-689.
38. N. D. Khupse and A. Kumar, *J. Phys. Chem. B*, 2009, **114**, 376-381.
39. M. J. Earle, J. M. S. S. Esperanca, M. A. Gilea, J. N. Canongia Lopes, L. P. N. Rebelo, J. W. Magee, K. R. Seddon and J. A. Widegren, *Nature*, 2006, **439**, 831-834.
40. M. C. Tseng, H. C. Kan and Y. H. Chu, *Tetrahedron Lett.*, 2007, **48**, 9085-9089.
41. K. R. Seddon, A. Stark and M. J. Torres, *Pure Appl. Chem*, 2000, **72**, 2275-2287.
42. H. Cao, L. McNamee and H. Alper, *J. Org. Chem.*, 2008, **73**, 3530-3534.
43. E. Janus and W. Stefaniak, *Catal. Lett.*, 2008, **124**, 105-110.
44. S. T. Handy and M. Okello, *Tetrahedron Lett.*, 2003, **44**, 8395-8397.
45. T. Rütger, T. D. Huynh, J. Huang, A. F. Hollenkamp, E. A. Salter, A. Wierzbicki, K. Mattson, A. Lewis and J. H. Davis, *Chem. Mater.*, 2009, **22**, 1038-1045.
46. M. Ishikawa, T. Sugimoto, M. Kikuta, E. Ishiko and M. Kono, *J. Power Sources*, 2006, **162**, 658-662.
47. C. M. Starks, *J. Am. Chem. Soc.*, 1971, **93**, 195-199.
48. C. M. Starks, in *Phase-Transfer Catalysis*, American Chemical Society, Washington, DC, 1987, pp. 1-7.
49. C. Emnet, K. M. Weber, J. A. Vidal, C. S. Consorti, A. M. Stuart and J. A. Gladysz, *Adv. Synth. Catal.*, 2006, **348**, 1625-1634.
50. G. D. Yadav and S. P. Tekale, *Org. Process Res. Dev.*, 2010, **14**, 722-727.
51. T. E. Shanks and R. J. Maleski, US, 2006/0135807 A1.

52. T. Ramnial, S. A. Taylor, M. L. Bender, B. Gorodetsky, P. T. K. Lee, D. A. Dickie, B. M. McCollum, C. C. Pye, C. J. Walsby and J. A. C. Clyburne, *J. Org. Chem.*, 2008, **73**, 801-812.
53. J. Marták and Š. Schlosser, *Chem. Pap.*, 2006, **60**, 395-398.
54. T. Ramnial, D. D. Ino and J. A. C. Clyburne, *Chem. Commun.*, 2005, 325-327.
55. J. J. Tindale and P. J. Ragogna, *Chem. Commun.*, 2009, 1831-1833.
56. R. E. Ramirez and E. M. Sanchez, *Sol. Energy Mater. Sol. Cells*, 2006, **90**, 2384-2390.
57. R. Katoh, M. Hara and S. Tsuzuki, *J. Phys. Chem. B*, 2008, **112**, 15426-15430.
58. D. R. MacFarlane, M. Forsyth, E. I. Izgorodina, A. P. Abbott, G. Annat and K. Fraser, *Phys. Chem. Chem. Phys.*, 2009, **11**, 4962-4967.
59. K. J. Fraser, E. I. Izgorodina, M. Forsyth, J. L. Scott and D. R. MacFarlane, *Chem. Commun.*, 2007, 3817-3819.
60. S. Seki, R. Kawano and M. Watanabe, *Kagaku to Kogyo (Tokyo, Japan)*, 2006, **59**, 760-763.
61. A. Guerfi, M. Dontigny, Y. Kobayashi, A. Vijnh and K. Zaghbi, *J. Solid State Electrochem.*, 2009, **13**, 1003-1014.
62. R. Hagiwara, T. Nohira, K. Matsumoto and Y. Tamba, *Electrochem. Solid-State Lett.*, 2005, **8**, A231-A233.
63. A. Balducci, U. Bardi, S. Caporali, M. Mastragostino and F. Soavi, *Electrochem. Commun.*, 2004, **6**, 566-570.
64. S. M. Zakeeruddin and M. Grätzel, *Adv. Funct. Mater.*, 2009, **19**, 2187-2202.
65. L. Iberl, *J. Electroanal. Chem.*, 1988, **248**, 15-21.
66. U. Tormin and F. Beck, *Electrochim. Acta*, 1995, **40**, 1955-1962.
67. P. Walden, *Z. Physik. Chem.*, 1906, **55**, 207.
68. C. A. Angell, *J. Am. Ceram. Soc.*, 1968, **51**, 117-124.
69. J. P. Belieres and C. A. Angell, *J. Phys. Chem. B*, 2007, **111**, 4926-4937.
70. M. Yoshizawa, W. Xu and C. A. Angell, *J. Am. Chem. Soc.*, 2003, **125**, 15411-15419.
71. B. Lin, S. Cheng, L. Qiu, F. Yan, S. Shang and J. Lu, *Chem. Mater.*, 2010, **22**, 1807-1813.
72. S. Y. Lee, T. Yasuda and M. Watanabe, *J. Power Sources*, 2010, **195**, 5909-5914.
73. A. Noda, K. Hayamizu and M. Watanabe, *J. Phys. Chem. B*, 2001, **105**, 4603-4610.
74. A. L. Kholodenko and J. F. Douglas, *Phys. Rev. E: Stat. Nonlinear Soft Matter Phys.*, 1995, **51**, 1081.
75. H. A. Kooijman, *Ind. Eng. Chem. Res.*, 2002, **41**, 3326-3328.
76. J. T. Edward, *J. Chem. Educ.*, 1970, **47**, 261.
77. H. Tokuda, K. Hayamizu, K. Ishii, M. A. B. H. Susan and M. Watanabe, *J. Phys. Chem. B*, 2004, **108**, 16593-16600.
78. A. J. Bard and L. R. Faulkner, *Electrochemical Methods: Fundamental and Application*, VHC, New York, USA 1995.
79. G. E. Murch, *Philos. Mag. A*, 1982, **45**, 685 - 692.
80. C. A. Angell and J. W. Tomlinson, *Discuss. Faraday Soc.*, 1961, **32**, 237-249.

5. Synthesis of novel phosphonium ionic liquids

81. H. Shobukawa, H. Tokuda, S. I. Tabata and M. Watanabe, *Electrochim. Acta*, 2004, **50**, 305-309.
82. H. Tokuda, K. Hayamizu, K. Ishii, M. A. B. H. Susan and M. Watanabe, *J. Phys. Chem. B*, 2005, **109**, 6103-6110.
83. H. Tokuda, K. Ishii, M. A. B. H. Susan, S. Tsuzuki, K. Hayamizu and M. Watanabe, *J. Phys. Chem. B*, 2006, **110**, 2833-2839.
84. D. R. MacFarlane and M. Forsyth, *Adv. Mater.*, 2001, **13**, 957-966.
85. J. M. Pringle, P. C. Howlett, D. R. MacFarlane and M. Forsyth, *J. Mater. Chem.*, 2010, **20**, 2056-2062.
86. J. Timmermans, *J. Phys. Chem. Solids*, 1961, **18**, 1-8.
87. D. R. MacFarlane, S. A. Forsyth, J. Golding and G. B. Deacon, *Green Chem.*, 2002, **4**, 444-448.
88. D. R. MacFarlane, P. Meakin, N. Amini and M. Forsyth, *J. Phys. Condens. Matter*, 2001, **13**, 8257.
89. A. I. Bhatt, A. S. Best, J. Huang and A. F. Hollenkamp, *J. Electrochem. Soc.*, 2010, **157**, A66-A74.
90. J. N. Canongia Lopes, K. Shimizu, A. A. H. Pádua, Y. Umebayashi, S. Fukuda, K. Fujii and S. I. Ishiguro, *J. Phys. Chem. B*, 2008, **112**, 9449-9455.
91. J. N. Canongia Lopes, K. Shimizu, A. A. H. Pádua, Y. Umebayashi, S. Fukuda, K. Fujii and S. I. Ishiguro, *J. Phys. Chem. B*, 2008, **112**, 1465-1472.
92. S. F. Lux, M. Schmuck, S. Jeong, S. Passerini, M. Winter and A. Balducci, *Int. J. Energy Res.*, 2010, **34**, 97-106.
93. J. Saint, A. S. Best, A. F. Hollenkamp, J. Kerr, J. H. Shin and M. M. Doeff, *J. Electrochem. Soc.*, 2008, **155**, A172-A180.
94. D. R. MacFarlane, P. Meakin, J. Sun, N. Amini and M. Forsyth, *J. Phys. Chem. B*, 1999, **103**, 4164-4170.
95. S. F. Lux, M. Schmuck, G. B. Appetecchi, S. Passerini, M. Winter and A. Balducci, *J. Power Sources*, 2009, **192**, 606-611.
96. Q. Zhou, W. A. Henderson, G. B. Appetecchi, M. Montanino and S. Passerini, *J. Phys. Chem. B*, 2008, **112**, 13577-13580.
97. R. Vijayaraghavan, M. Surianarayanan, V. Armel, D. R. MacFarlane and V. P. Sridhar, *Chem. Commun.*, 2009, 6297-6299.
98. C. Schreiner, S. Zugmann, R. Hartl and H. J. Gores, *J. Chem. Eng. Data*, 2010, **55**, 1784-1788.
99. J. D. Holbrey, R. D. Rogers, R. A. Mantz, P. C. Trulove, V. A. Cocalia, A. E. Visser, J. L. Anderson, J. L. Anthony, J. F. Brennecke, E. J. Maginn and T. Welton, *Physicochemical Properties*, Wiley-VCH Verlag GmbH & Co. KGaA, 2008.
100. J. Adebahr, M. Grimsley, N. M. Rocher, D. R. MacFarlane and M. Forsyth, *Solid State Ionics*, 2008, **178**, 1798-1803.
101. J. Adebahr, F. C. Grozema, S. W. de Leeuw, D. R. MacFarlane and M. Forsyth, *Solid State Ionics*, 2006, **177**, 2845-2850.
102. E. I. Cooper and C. A. Angell, *Solid State Ionics*, 1986, **18-19**, 570-576.

103. J. Huang, A. Hill, M. Forsyth, D. MacFarlane and A. Hollenkamp, *Solid State Ionics*, 2006, **177**, 2569-2573.
104. D. R. MacFarlane, J. Huang and M. Forsyth, *Nature*, 1999, **402**, 792-794.
105. R. Brookes, A. Davies, G. Ketwaroo and P. A. Madden, *J. Phys. Chem. B*, 2005, **109**, 6485-6490.
106. K. Fraser, "Physical properties of phosphonium based ionic liquids", PhD thesis, Monash University, Melbourne, 2008, p. 287.
107. I. Avramov, *J. Non-Cryst. Solids*, 2009, **355**, 745-747.
108. N. Hirai, T. Yokogawa and T. Tanaka, *Jpn. J. Appl. Phys.*, 2006, **45**, 2295-2297.

Chapter 6

Effect of the ionic liquid on the flatband potential of an n-type semiconductor (Titania)

Chapter overview

This chapter is about determining the flatband potential of Titania in contact with different types of ionic liquids. The influence on the flatband potential of changes in the anion and cation of the ionic liquid was investigated, as well as the effect of the purity of the ionic liquids. Any trace of impurities will potentially modify the flat band potential of the TiO₂. Heinzl and co-workers¹ have shown that the addition of water to an organic solvent drastically changed the flatband potential of the semiconductor due to the specific adsorption of H⁺ ions on the surface of the TiO₂ electrode. In this thesis, the same study was undertaken in an organic solvent, as well as in ionic liquids, to observe whether any change occurred upon addition of water or additives such as lithium iodide,²⁻⁴ tert-butylpyridine⁵⁻⁶ and N-methylbenzimidazole,⁷⁻⁹ which are known to shift the conduction band of the semiconductor.

In an attempt to increase the performance of dye sensitised solar cells, which is mostly limited by recombination processes,¹⁰ many strategies have been employed to overcome this intrinsic limitation. Many are aimed at protecting the surface of the exposed TiO₂ surface.¹¹ The approaches used to protect the TiO₂ surface is by molecular engineering of the dye, to include for example long alkyl chains,¹²⁻¹³ or by treating the surface with an organic acid.¹⁴⁻¹⁵ These will also have an effect on the flatband potential of the TiO₂. Therefore the effect of treating the TiO₂ film with either a base or an acid was investigated in this work.

6. Effect of ionic liquid on the flatband potential of an n-type semiconductor

6.1 Introduction

6.1.1 General Overview

There is considerable interest in developing different types of semiconductor electrodes for more efficient conversion of light energy into a useable form of energy, such as chemical or electrical energy. Titanium dioxide is the preferable choice of semiconductor, as it has a wide band gap, is stable and also inexpensive. This material has been extensively studied in many fields since the discovery of water photolysis (where H_2O converts into H_2 and O_2 on TiO_2) by Fujishima and co-workers in 1972.¹⁶ This report was published during a period of an oil crisis, where the price of fuel rose sharply. This has led to an increased interest in understanding the semiconductor-electrolyte junction and it remains an active area of research.

To have an idea about the full potential of the TiO_2 electrode, a better understanding of the factors that affect the band energy in non aqueous media is essential. Thus, it is critical to determine the key parameters that influence the flatband potential at the semiconductor-electrolyte interface (as discussed in Chapter 2, section 2.4.2). The study of the semiconductor-electrolyte junction is important, as it permits the determination of not only the position of the flatband potential of the junction, but also other fundamental parameters such as the total number of charge carriers (donor density or acceptor density), the position of the conduction band edge and valence band edge at the interface, and lifetime of the minority carriers. Knowing these parameters, one can predict and interpret the mechanism of charge transfer taking place at the junction of the semiconductor and the liquid, and therefore select the right type of semiconductor for a chosen application. These considerations are essential to optimising the properties of this junction, especially in the field of solar energy conversion.

Methods to determine flatband potential

Several methods exist in determining the above parameters: dark current and photocurrent measurements as a function of potential difference,¹⁷ electromodulated infrared spectroscopy,¹⁸ electro-optical methods,¹⁹ spectroscopy measurements²⁰ and the most commonly used one is capacitance measurement.²¹⁻²² The latter two are described here in more detail.

6. Effect of ionic liquid on the flatband potential of an n-type semiconductor

Spectroscopic Determination of the Flatband potential

This method works on the basis that as the potential applied to a semi-conductor electrode is made more negative, the Fermi level reaches the flatband potential. According to Fitzmaurice and co-workers, the first change in UV-spectra as a function of the applied potential is related to the flatband potential at the semiconductor-electrolyte junction.²⁰ With further increases in applied potential, electrons begin to populate the conduction band. These electrons are then able to induce intraband transitions, where the material becomes more absorbing throughout the visible spectrum, with transitions especially observed in the near infrared regions. This method usually chooses an arbitrary wavelength in the red colour region, examining absorption vs. potential to detect the flat band potential, before a fit to the experimental data is used to determine the final flatband potential value.

Capacitance Method

The capacitance method is based on the validity of the Mott-Schottky plot. The Mott-Schottky method involves the measurement of the differential capacitance, C , of the semiconductor as a function of applied voltage. A plot of C^{-2} versus applied potential yields a straight line with the intercept at $C^{-2} = 0$ equal to the flatband potential, V_{fb} , and from the slope of the plot, the carrier density can be determined, assuming that the dielectric constant and the area of the semiconductor are known. The Mott-Schottky equation (Eq 5.1) is obtained by solving Poisson's equation.²³⁻²⁴

$$\frac{1}{C^2} = \frac{2}{\epsilon\epsilon_0 A^2 e N_D} \left(V - V_{fb} - \frac{k_B T}{e} \right) \quad (\text{Eq 5.1})$$

where C is the interfacial capacitance, A is the area, N_D is the effective donor density, ϵ is the dielectric constant of the semiconductor, ϵ_0 is the permittivity of free space, V is the applied potential, e is the electronic charge, T is the absolute temperature, V_{fb} is the flatband potential and k_B is the Boltzmann constant.

Capacitance-voltage measurements have previously been used to determine the flatband potential of semiconductors.²¹⁻²² It has also been shown that the Mott-Schottky plots often exhibit frequency dependence and this effect has been fully studied;²⁵⁻²⁷ when the Mott-Schottky plots have different slopes for different frequencies, but converges to a common intercept, giving valid values for the flatband potential.

6. Effect of ionic liquid on the flatband potential of an n-type semiconductor

As stated earlier, a plot of C^{-2} vs. applied potential commonly yields straight lines and the capacitance measured is usually taken to be that of the semiconductor, assuming that the Helmholtz capacitance on the electrolyte side is so large that it is negligible according to the following equation:²⁸

$$\frac{1}{C_{Obs}} = \frac{1}{C_H} + \frac{1}{C_{SC}} \quad (\text{Eq 5.2})$$

In a paper by Albery *et al.*,²⁸ no assumption was made concerning the Helmholtz capacitance and they were able to solve the full Poisson-Boltzmann equation under these circumstances. Thus they were able to propose a method to fit the experimental data obtained from capacitance measurements without making assumptions about the size of the Helmholtz capacitance. The following equations were used to fit the experimental data:

$$\frac{C_0}{C_{Obs}} = \frac{C_0}{C_H} + 2(P_{DC} - 1) \quad (\text{Eq 5.3})$$

$$y = \frac{C_H C_{Obs}}{1 + C_H C_{Obs}} \quad (\text{Eq 5.4})$$

$$P_? = 1 - \frac{1}{2} \frac{C_0}{C_H} \quad (\text{Eq 5.5})$$

$$\Delta P = P_{DC} - P_? \quad (\text{Eq 5.6})$$

where C_0 is the capacitance of the semiconductor at the flat band potential, C_{Obs} is the observed capacitance, P_{DC} is a dimensionless potential, and C_H is the Helmholtz capacitance.

$$\Delta P = (F RT) (E_{DC} - E_?) \quad (\text{Eq 5.7})$$

where F is the Faraday constant, R is the gas constant and T is the temperature (K), E_{DC} is the applied potential and $E_?$ is the pseudo flatband potential. A full description of the derivation of these equations is given in reference 28.

The experimental curve is plotted as $\ln(1 - C_{Obs}^2)$ vs. $\ln(\Delta P)$ (ΔP is calculated from equation 5.7). The curve is then fitted by plotting $\ln(y^2)$ (y obtained from equation 5.4) vs. $\ln(\Delta P)$. The flatband potential value is obtained where the curve crosses the line at $\ln(y^2) = 0$. The typical error in flatband potential was found to be approximately $\pm 10\%$.

6. Effect of ionic liquid on the flatband potential of an n-type semiconductor

Using the above fitting method, Albery and co-workers were able to find a good agreement with literature flatband potentials. Thus, this fitting method was used here to determine the exact flatband potential of the semiconductor-ionic liquid junction without the need to assume a negligible contribution from the Helmholtz layer.

6.2 Aim of this work

The aim of this work is to measure the flatband potential of the n-type semiconductor, TiO₂, when it is in contact with various ionic liquids in order to gain better insight into what is happening at the junction of the semiconductor-ionic liquid electrolyte system. A great deal of work has been previously reported for the TiO₂-H₂O junction,²⁹⁻³⁰ as well as TiO₂-organic solvent junctions,³¹⁻³² but there is limited information available on the TiO₂-ionic liquid system.³³ In this work, the influence of additives and impurities was also investigated at the TiO₂-ionic liquid junction. The flatband potential value was obtained by the capacitance measurement using the Mott-Schottky plot, as well as the UV spectroscopic measurement in some cases. This measurement will allow a better understanding of why some ionic liquids performed better than others in dye sensitised solar cells. The flatband potential was also measured when the TiO₂ electrodes were treated with acids and bases.

6.3 Experimental

6.3.1 Electrochemical measurement of the flatband potential

For electrochemical measurements, the working electrodes used in all experiments consisted of a 2.2 µm thick layer of TiO₂ particles, with an average diameter of 18 nm, deposited onto a conductive fluorine-doped SnO₂ (FTO) glass. The TiO₂ paste was purchased from JCG-CCIC (TiO₂ paste PST-18NR). Before printing the Titania layer, the FTO glass was cleaned in 5 wt% Hellmanex solution in distilled water, sonicated for 15 mins. The electrodes were then washed with distilled water and further sonicated in ethanol. The thin TiO₂ layer was screen-printed using a semi-automatic screen-printer. The working electrodes were sintered at 500 °C for 30 mins prior to use. The measurement was carried out in a conventional three-electrode set up in a single compartment. The working electrode consisted of TiO₂ film on FTO glass, the counter electrode was a platinum sheet and the reference electrode used was a non-aqueous saturated calomel electrode (1 M LiCl in acetonitrile) purchased from Radiometer Analytical. The Mott-Schottky measurement

6. Effect of ionic liquid on the flatband potential of an n-type semiconductor

was carried out in 5 ml of ionic liquid with a 20 mV amplitude signal at a fixed frequency of 100 Hz starting from an anodic potential (0.5 V vs SCE (1 M LiCl)) towards the cathodic potential (-0.8 V vs SCE (1 M LiCl)) with an increment of 100 mV in an Argon-filled glove box as well as outside the glove box. The electrochemical measurements were performed using a Variable Multiple Potentiostat (EC-Lab). The measurement was repeated several times with fresh electrodes.

6.3.2 Materials and Ionic liquids

For this study, several types of ionic liquids were used. 1-ethyl-3-methylimidazolium tetracyanoborate ($C_2mimB(CN)_4$), 1-ethyl-3-methylimidazolium tetrafluoroborate (C_2mimBF_4), triethylsulfonium bis(trifluoromethanesulfonyl)amide ($S_{222}NTf_2$), 1-butyl-3-methylimidazolium tetrafluoroborate (C_4mimBF_4) and 1-(2-methoxyethyl)-1-methylpiperidinium bis(trifluoromethanesulfonyl)amide ($MOEMPIPNTf_2$) were purchased from Merck and used without any further purification. 1-ethyl-3-methylimidazolium thiocyanate ($C_2mimSCN$), 1-ethyl-3-methylimidazolium tetrafluoroborate (C_2mimBF_4) and 1-ethyl-3-methylimidazolium dicyanamide ($C_2mimN(CN)_2$) were purchased from Iolitec and used without any further purification. Lithium iodide (LiI), lithium perchlorate ($LiClO_4$), tetrabutylammonium perchlorate (TBAP or $N_{4444}ClO_4$) (recrystallised several times in a mixture of ethanol and water and dried for 2 days at 150 °C in vacuo), tert-butylpyridine (TBP), tetraethylammonium iodide, triethylamine, diisooctylphosphinic acid, propionic acid and N-methylbenzimidazole (NMB) were purchased from Sigma-Aldrich. Triethyl(methoxymethyl)phosphonium bis(trifluoromethanesulfonyl)amide ($P_{222(101)}NTf_2$) and triethyl(methoxyethyl)phosphonium bis(trifluoromethanesulfonyl)amide ($P_{222(201)}NTf_2$) were purchased from Nippon Chemical.

Anhydrous acetonitrile was purchased from Sigma-Aldrich. 1-ethyl-3-methylimidazolium bis(trifluoromethanesulfonyl)amide ($C_2mimNTf_2$), 1-ethyl-3-methylimidazolium diethylphosphate ($C_2mimDEP$) and N,N-propyl-methylpyrrolidinium bis(trifluoromethanesulfonyl)amide ($C_3mpyrNTf_2$) were synthesised according to literature method.³⁴ The structures of the ions used are summarised in the Glossary for reference.

6.3.3 FTIR

ATR-FTIR measurements were performed on the treated films, to see whether the base or acid was present at the surface of the TiO_2 , using a Varian FTIR spectrometer. The data reported here was obtained using a germanium prism. Spectra were derived from 256 scans at a resolution of 2 cm^{-1} . An untreated TiO_2 film was used as a reference. The spectra are shown in Appendix, section A.4.2.

6.3.4 UV spectroscopy

A UV spectrometer was also used to measure the flatband potential of TiO_2 in an aqueous medium. A three-electrode single compartment cell was used, the counter electrode being a platinum wire, the reference electrode a saturated calomel electrode and the TiO_2 on FTO glass formed the working electrode. The applied potential was controlled using a potentiostat. For each determination of V_{fb} , a new working electrode was used. This method was only used in aqueous medium for comparison with the literature³¹⁻³² and also for the Mott-Schottky measurements at different pHs in aqueous solution. Figure 6.1 displays the schematic diagram of the three electrode set up for the UV-spectroscopy measurements.

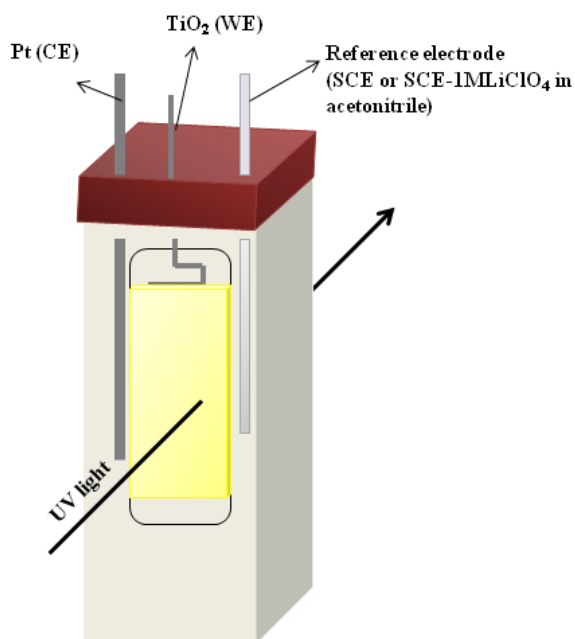


Figure 6.1: 3-electrode set up for measuring the flatband potential using UV-spectroscopy

6. Effect of ionic liquid on the flatband potential of an n-type semiconductor

6.4 Results and discussion

6.4.1 Determination of the flatband potential of TiO_2 in aqueous media using UV-spectroscopy and Mott-Schottky measurements

Aqueous electrolyte solutions were prepared from distilled water using LiClO_4 and potassium dihydrogen phosphate (KH_2PO_4). The pH of the aqueous solution was adjusted using HClO_4 or NaOH . Figure 6.2 shows the absorbance spectra for a TiO_2 electrode, biased at a potential of -100 mV to -1200 mV. The electrolyte was 0.2 M KH_2PO_4 , adjusted to pH 12 by addition of NaOH . As observed in Figure 6.2, the absorption at shorter wavelength (300 - 350 nm) corresponds to the fundamental absorption edge of the TiO_2 . As the TiO_2 electrode is biased at more negative potentials (-1100 mV), a decrease in adsorption is observed in the short wavelength region (370 nm). This is due to the accumulation of electrons (majority carriers) at the semiconductor-electrolyte junction. The accumulation of electrons in the conduction band results in an increase in the band gap energy, thus shifting the adsorption edge; this shift in adsorption is often called the Burstein-Moss shift.²⁰ At higher wavelengths ($\lambda > 400$ nm) an enhancement in absorption is observed. This can be due to intraband transitions,²⁰ due to electrons occupying the conduction band of the TiO_2 , or localised electrons in the bulk or surface defects. Surface defects can give rise to electron traps. Under UV irradiation, the electrons and holes produced diffuse to the surface, thus reacting with the species present at the interface. TiO_2 is well known to contain Ti^{3+} , which can act as an electron trap for photogenerated electrons.³⁵ In aqueous media, such a mechanism occurs where the electrons are trapped at the surface defect sites (Ti^{3+}). This mechanism has been demonstrated in other papers, based on the identification of hydroxylated reaction intermediates.³⁶⁻⁴¹ Experimental evidence for surface defects has also been reported by EPR measurements, which are used to detect hydroxide radicals.⁴²⁻⁴³

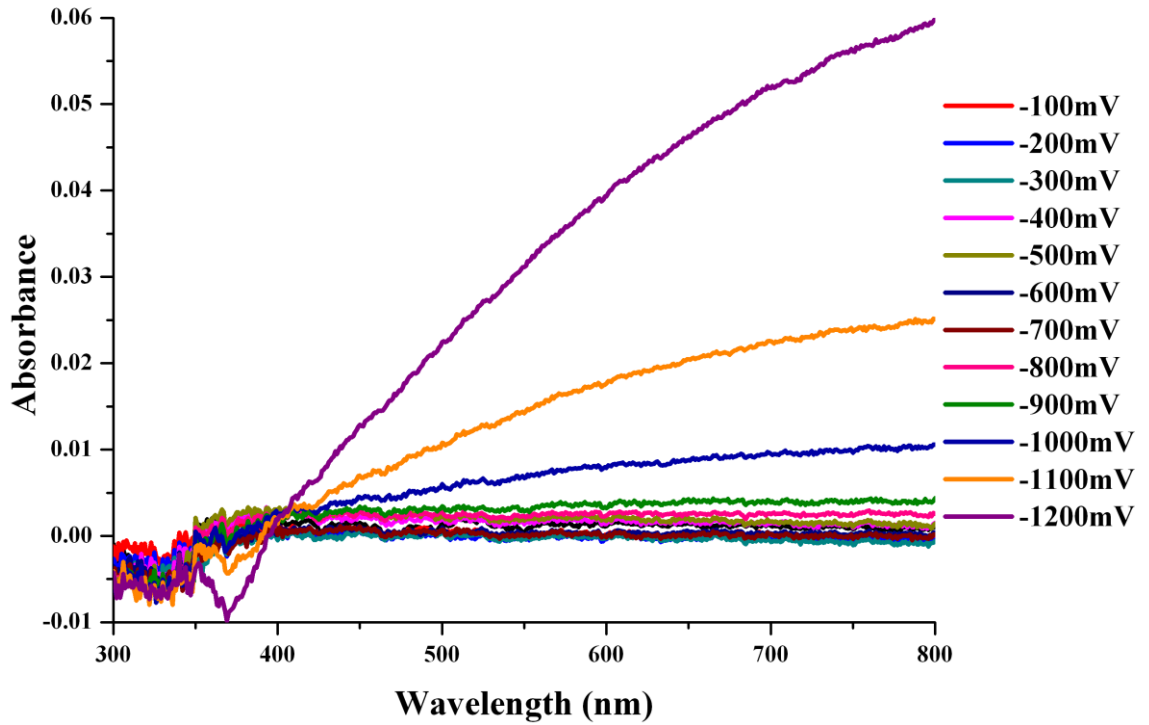


Figure 6.2: Absorbance of TiO₂ in a phosphate buffer (pH 12) under various applied potentials

Figure 6.3 shows the absorbance measured at 780 nm as a function of applied bias for an aqueous solution of 0.2 M KH₂PO₄ adjusted to pH 12. The flatband pseudo-potential is obtained by fitting the data with two straight lines in the region of -0.2 V to -0.8 V and -0.8 V to -1.2 V and the point of intersection of the two straight lines gives the final potential. In this case, the flatband pseudo-potential obtained is -0.832 ± 0.058 V vs. SCE at pH 12. The experiment was repeated in another electrolyte solution containing 0.2 M LiClO₄. Figure 6.4 shows the absorbance spectra of 0.2 M LiClO₄ adjusted to pH 2 by addition of HClO₄ and pH 12 by adding NaOH. By changing the pH of the solution, a shift in flatband pseudo-potential is observed. The flatband pseudo-potential measured in 0.2 M LiClO₄ is -0.221 ± 0.066 V vs. SCE in pH 2 and -0.821 ± 0.063 V vs. SCE in pH 12. The value obtained in this thesis is close to the one obtained by Nogami and co-workers.⁴⁴ Similar behaviour of the pH dependence of the flatband potential has been reported by Grätzel and co-workers.²⁰ They report that semiconductors have a Nernstian behaviour at the interface due to the interaction of the oxides of the semiconductor with protons in the electrolyte; an acid – base equilibrium is thus established at the interface.⁴⁵

6. Effect of ionic liquid on the flatband potential of an n-type semiconductor

A change in pH produces a change in the potential difference within the Helmholtz layer of $2.3RT/F$ or 59 mV/pH. The slope obtained in this thesis (not shown) is 55 mV/pH.

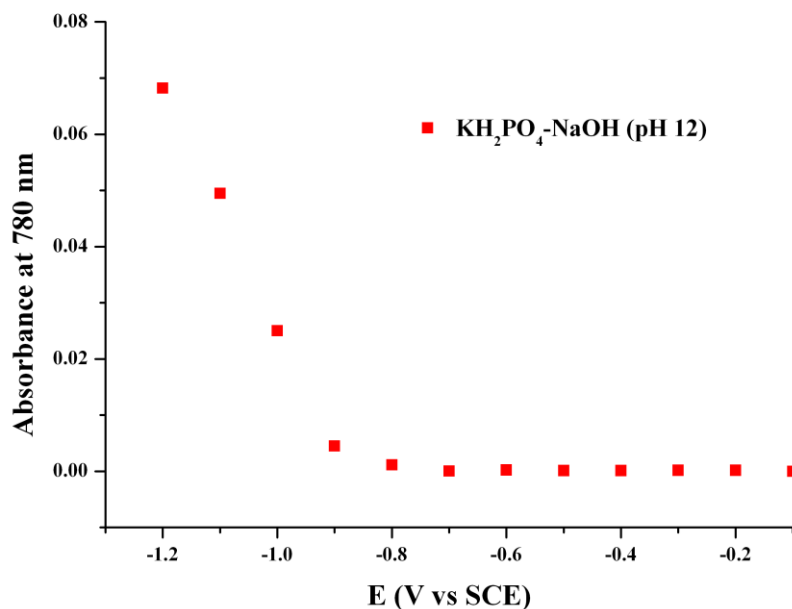


Figure 6.3: Absorbance of TiO_2 film as function of applied potential at 780 nm

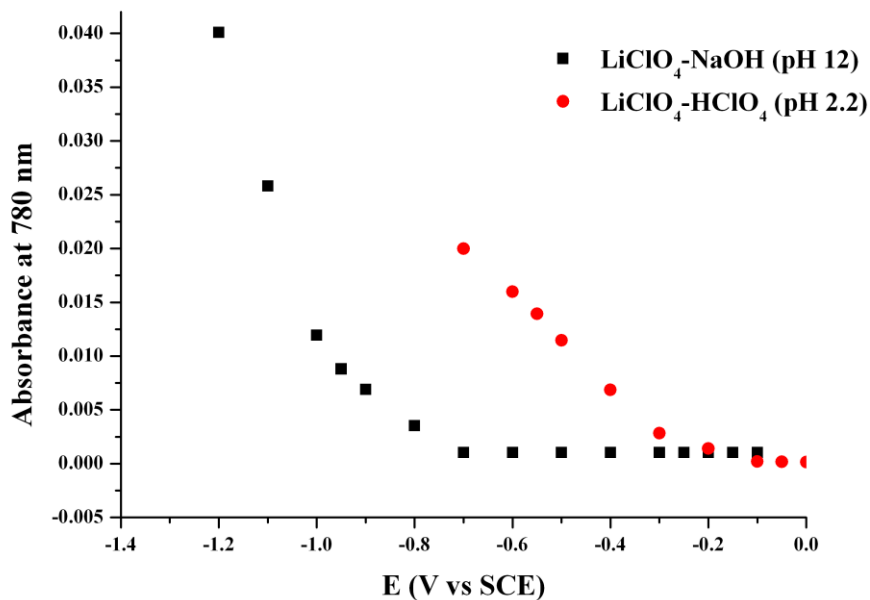


Figure 6.4: Absorbance of TiO_2 electrode at different pH in 0.2 M LiClO_4 solution at 780 nm

6. Effect of ionic liquid on the flatband potential of an n-type semiconductor

The same measurements were repeated using capacitance measurements (Figure 6.5) and were found to be the same within experimental error; the flatband pseudo-potentials measured were -0.241 ± 0.018 V vs. SCE and -0.831 ± 0.062 V vs. SCE at pH 2 and pH 12 respectively, with a slope of 59 mV/pH.

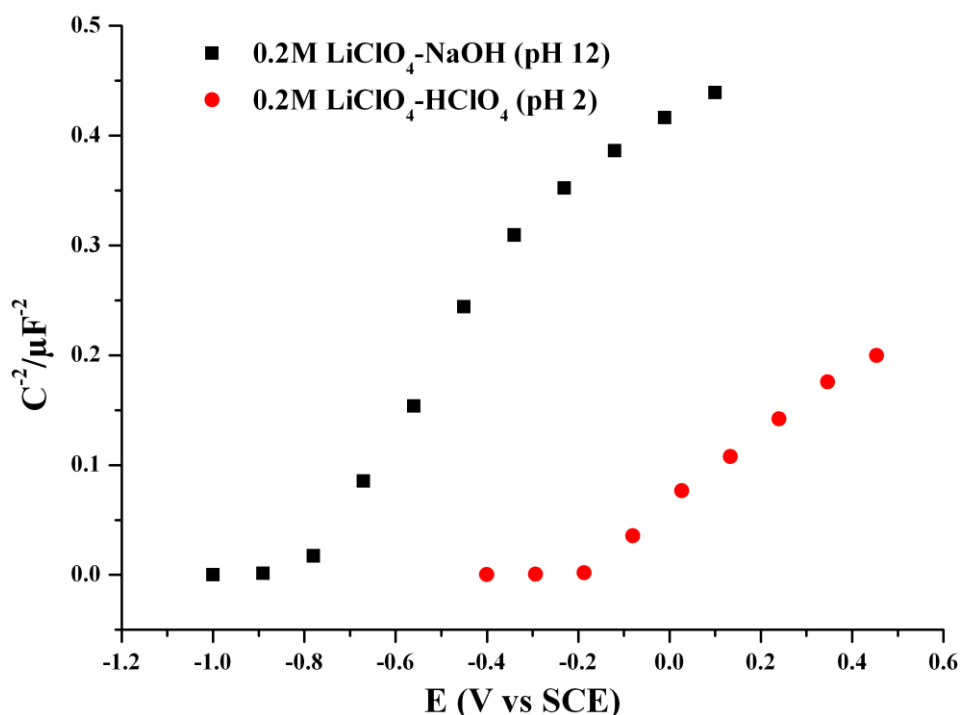


Figure 6.5: Mott-Schottky plots of TiO_2 in 0.2 M LiClO_4 at pH 2 and pH 12 in the dark

From the above observations, it can be concluded that the Mott-Schottky and UV spectroscopy measurements can both be used to determine the flatband pseudo-potential of TiO_2 in aqueous media. In both methods, the experiment was repeated several times with freshly prepared electrolytes and electrodes. In some cases, non linearity was observed, which might be due to surface defects of the TiO_2 . After the measurement, visual observation showed that the electrode appeared to have been burnt, with the electrolyte turning yellow. Thus, these measurements were not included in calculation of the flatband pseudo-potential.

6. Effect of ionic liquid on the flatband potential of an n-type semiconductor

The Mott-Schottky plot was then fitted using the equations described in section 6.1.1. Reasonable agreement is found for the basic solution, and a lower V_{fb} is found at pH 2, as shown in Table 6.1.

Table 6.1: Summary of the data obtained from the Mott-Schottky plot and the fitted potential using the method described in section 6.1.1.

	Flatband pseudo-potential V vs. SCE	Flatband potential* V vs. SCE ($\pm 10\%$)
pH 2	-0.241 ± 0.018	-0.198
pH 12	-0.831 ± 0.062	-0.780

*Flatband potential obtained by fitting the experimental data using equation 5.2 to 5.7.

6.4.2 Determination of E_{fb} in non aqueous media using the Mott Schottky method

6.4.2.1 Neat ionic liquids

The electrochemistry of semiconductors has mainly been investigated in aqueous and organic solvents. In the studies, the influence of an acid and base was demonstrated and, depending on the type of organic solvents, some behave similar to water. In this section, the behaviour of the flatband potential in ionic liquids was investigated. A wide range of ionic liquids was studied to observe whether, by changing either the cation or anion, a shift in flatband potential occurred.

Figures 6.6 and 6.7 show the results of the capacitance measurements, presented in the format of the Mott-Schottky plot, on TiO_2 films, showing the effect of the anion and cation on the flatband pseudo-potential of the semiconductor. The positive slope of the C^{-2} vs. E plots indicates the n-type semiconductivity of the film. Table 6.2 summarises the flatband potentials obtained by fitting the Mott-Schottky equation to the data over the linear region of the measurements, and in some cases, using the method described in reference 28 as a comparison.²⁸ In some cases, the very negative value of the flat band potential meant that the measurements were terminated before V_{fb} was reached, to avoid damaging the electrode or decomposition of the IL. In these cases, the V_{fb} is a short extrapolation of the data.

6. Effect of ionic liquid on the flatband potential of an n-type semiconductor

The UV-spectroscopy measurement was also used to determine the position of the flatband potentials in the cases of C_2mimBF_4 , $C_2mimNTf_2$ and $C_2mimSCN$; the data is also summarised in Table 6.2. (The absorbance plot and fitting are given in Appendix, section A.4). Reasonable agreement between the two methods was obtained, with the results being within two standard deviations of each other in most cases, except in the case of the BF_4^- salt, where there was a slightly larger discrepancy.

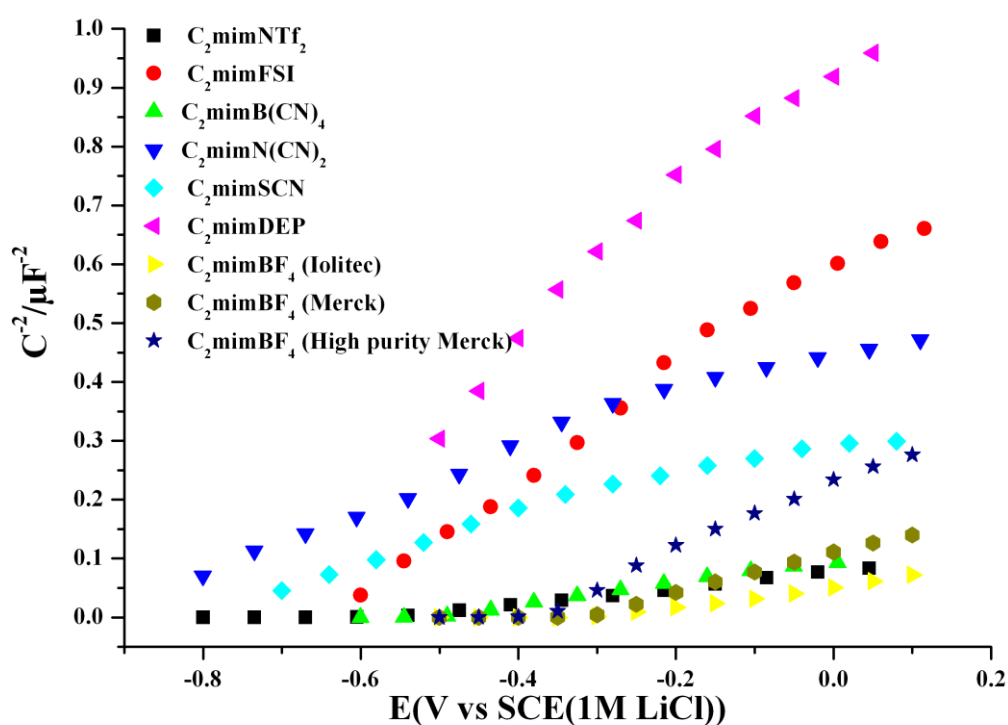


Figure 6.6: Mott-Schottky plot showing the effect of various anions with the 1-ethyl-3-methylimidazolium cation

6. Effect of ionic liquid on the flatband potential of an n-type semiconductor

Table 6.2: Flatband potential in different ionic liquids (and from different supplier in the cases noted); (mean and standard deviation of 6 films) and the flatband potential obtained from fitting the experimental data using the method described in section 6.1.1.

Ionic liquids	Flatband pseudo-potential	Flatband potential	Supplier
	V vs. SCE (1 M LiCl)	V vs. SCE (1 M LiCl) (± 10 %)	
C ₂ mimNTf ₂	-0.579 ± 0.021	-0.539	Synthesised
	-0.550 ± 0.035 [#]		
C ₂ mimB(CN) ₄	-0.573 ± 0.081	-0.518	Merck (High purity)
C ₂ mimFSI	-0.587 ± 0.012	-0.545	Daichi Kyoto (High purity)
C ₂ mimSCN	-0.856 ± 0.012	-0.700	Iolitec
	-0.900 ± 0.025 [#]		
C ₂ mimBF ₄	-0.378 ± 0.052	-0.250	Merck
C ₂ mimBF ₄	-0.437 ± 0.007	-0.351	Merck (High purity for electronic purpose)
	-0.500 ± 0.012 [#]		
C ₂ mimBF ₄	-0.278 ± 0.033	-0.250	Iolitec
C ₂ mim N(CN) ₂	-0.909 ± 0.009	-0.800	Iolitec
C ₃ mpyrNTf ₂	-0.443 ± 0.048	-0.380	Synthesised
C ₃ mpyrFSI	-0.505 ± 0.007	-0.410	Daichi Kyoto
S ₂₂₂ NTf ₂	-0.511 ± 0.056	-0.400	Merck
MOEMPIP NTf ₂	-0.627 ± 0.030	-0.500	Merck
C ₄ mimBF ₄	-0.602 ± 0.036	-0.545	Merck
C ₂ mimDEP	-0.724 ± 0.029	-0.650	Synthesised
P ₂₂₂₍₁₀₁₎ NTf ₂	-0.402 ± 0.018	-0.400	Nippon Chemical
P ₂₂₂₍₂₀₁₎ NTf ₂	-0.404 ± 0.016	-0.350	Nippon Chemical

#: Flatband potential value obtained from UV-spectroscopy method.

6. Effect of ionic liquid on the flatband potential of an n-type semiconductor

Depending on the type of anion and purity of the ionic liquid, a shift in V_{fb} occurred. A decrease in slope is also observed for NTf_2^- , $\text{N}(\text{CN})_2^-$, SCN^- , $\text{B}(\text{CN})_4^-$ and BF_4^- ; this is likely a reflection of the dependence of the capacitance measurements determined in this way (i.e. at a single fixed frequency) on the conductivity of the IL. The SCN^- , $\text{N}(\text{CN})_2^-$, FSI and DEP^- ILs exhibit a bending character in the positive potential region between -0.2 V to 0.1 V; this may also be due to the influence of the conductivity. As observed in Figure 6.6 and Table 6.2, $\text{C}_2\text{mimNTf}_2$, C_2mimFSI and $\text{C}_2\text{mimB}(\text{CN})_4$ have similar flatband potentials; -0.576 ± 0.021 V vs. SCE (1 M LiCl), -0.587 ± 0.012 V vs. SCE (1 M LiCl) and -0.573 ± 0.081 V vs. SCE (1 M LiCl) respectively. These anions are usually considered to be “neutral” in the Lewis acid/base sense, i.e. that they are very weakly basic. Compared to the flatband potential measured in an aqueous medium at pH 7, which is -0.453 ± 0.011 V vs. SCE, one can say that the ionic liquids are behaving in a similar way to H_2O , but with a slight shift in the basic direction, probably as a result of the charge on the anion.

C_2mimBF_4 purchased from two different chemical companies showed different flatband potentials. The one purchased from Iolitec (> 98 % pure) gives a flatband potential of -0.278 ± 0.033 V vs. SCE (1 M LiCl) and the one from Merck gives a flatband potential of -0.378 ± 0.052 V vs. SCE (1 M LiCl) for the synthesis grade and -0.437 ± 0.007 V vs. SCE (1 M LiCl) for the high purity grade (used for electronic purposes). One possible explanation for such behaviour is the presence of impurities. Small amounts of water in C_2mimBF_4 are known to form decomposition products such as hydrofluoric acid. There is a possibility that the C_2mimBF_4 from Iolitec contains more acid, thus shifting the conduction band positively as a result of adsorption of protons onto the surface of the TiO_2 , as already demonstrated in acidic aqueous medium (-0.241 V vs. SCE at pH 2).

C_2mimSCN , $\text{C}_2\text{mimN}(\text{CN})_2$ and C_2mimDEP have flatband pseudo-potentials of -0.856 ± 0.012 V vs. SCE (1 M LiCl), -0.909 ± 0.009 V vs. SCE (1 M LiCl) and -0.724 ± 0.029 V vs. SCE (1 M LiCl) respectively. The flatband potential of these ionic liquids are quite comparable to those obtained in aqueous media at pH 12 (-0.831 V vs. SCE). These ionic liquids are considered to be somewhat “basic” in the Lewis and Brønsted senses due to their electron donating ability and, as would be expected in this case, are shifting the conduction band of the TiO_2 to more negative potentials, presumably by charge donation to the TiO_2 surface layer.

6. Effect of ionic liquid on the flatband potential of an n-type semiconductor

The above results show that the flatband potential of TiO₂ semiconductor depends greatly on the purity of the ionic liquid as well as on the choice of anion. This shift in V_{fb} is due to a change of the state of charge of the surface of the film.

The experimental Mott-Schottky data was also fitted using the equations discussed in section 6.1.1, and the data is tabulated in Table 6.2. A good agreement between the flatband pseudo-potential and flatband potential can be found for the following ionic liquids; C₂mimNTf₂, C₂mimB(CN)₄, C₂mimFSI, C₃mpyrNTf₂, C₂mimBF₄ (Iolitec), P₂₂₂₍₁₀₁₎NTf₂, P₂₂₂₍₂₀₁₎NTf₂, C₄mimBF₄ and C₂mimDEP, whereas C₂mimSCN, C₂mimBF₄ (Merck), S₂₂₂NTf₂, C₂mpyrFSI, C₂mimN(CN)₂ and MOEMPIPNTf₂ all show a large difference between the flatband pseudo-potential value and the flatband potential.

The Albery flatband potential is uniformly less negative than the flatband pseudo-potential values. This is expected as a result of the removal of the effect of the Helmholtz layer capacitance and potential drop from the measurement. The shift is typically between 50 - 100 mV, with some being as great as 150 mV. The variation in the Helmholtz layer effect is presumably due to the differences in the double structure and composition.

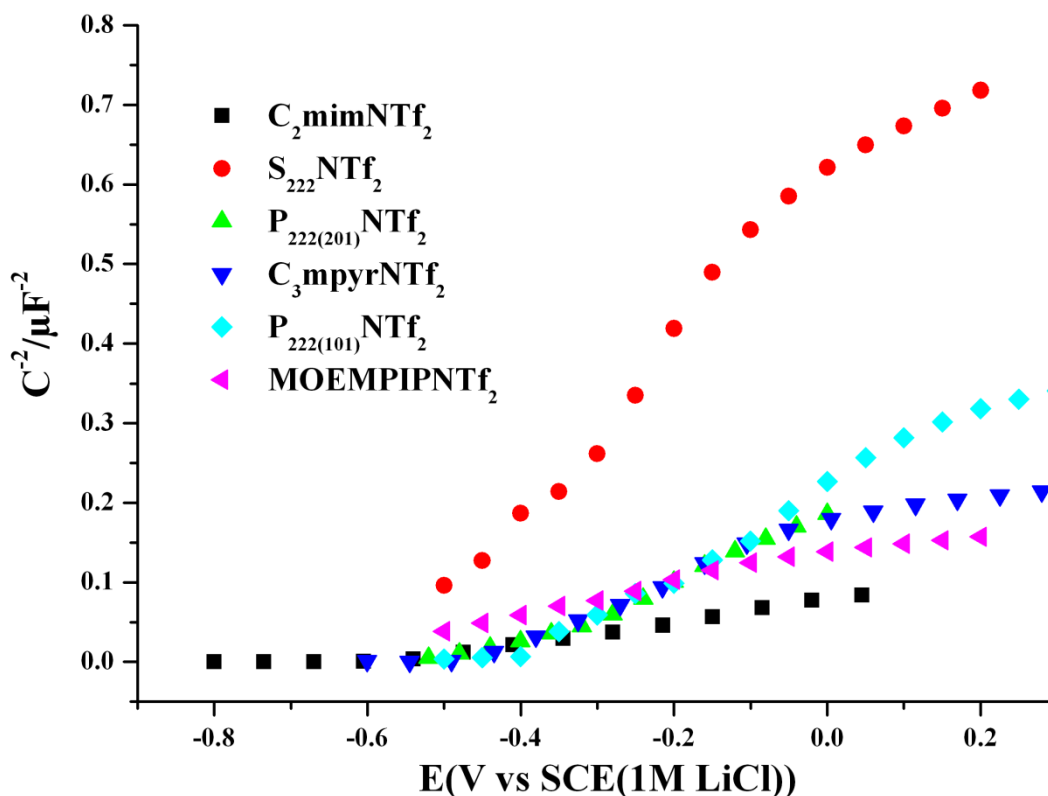


Figure 6.7: Mott-Schottky plot showing the effect of different cations

Figure 6.7 shows the effect of substitution of cations, with a fixed anion, on the measurement of the V_{fb} . There is a much less substantial change in V_{fb} with different cations compared to the effect of changing the anion; the effect of the cation variations fall in the range of - 400 mV to - 600 mV. Anions clearly have a greater effect on the position of V_{fb} than the cations, due to their electron donating abilities.

Figure 6.8 shows the capacitance-potential behaviour of both undyed and dyed TiO_2 films. The dye used for this study is a dithienothiophene derivative dye, THD3 (structure is shown in Chapter 7, Figure 7.3). The dyed films show a curvature in the potential region 0 V to -0.15 V and a linear region between -0.20 V to -0.45 V. The curvature may be due to the presence of a monolayer of dye attached to the surface of the TiO_2 electrodes modifying the surface state of the semiconductor.

6. Effect of ionic liquid on the flatband potential of an n-type semiconductor

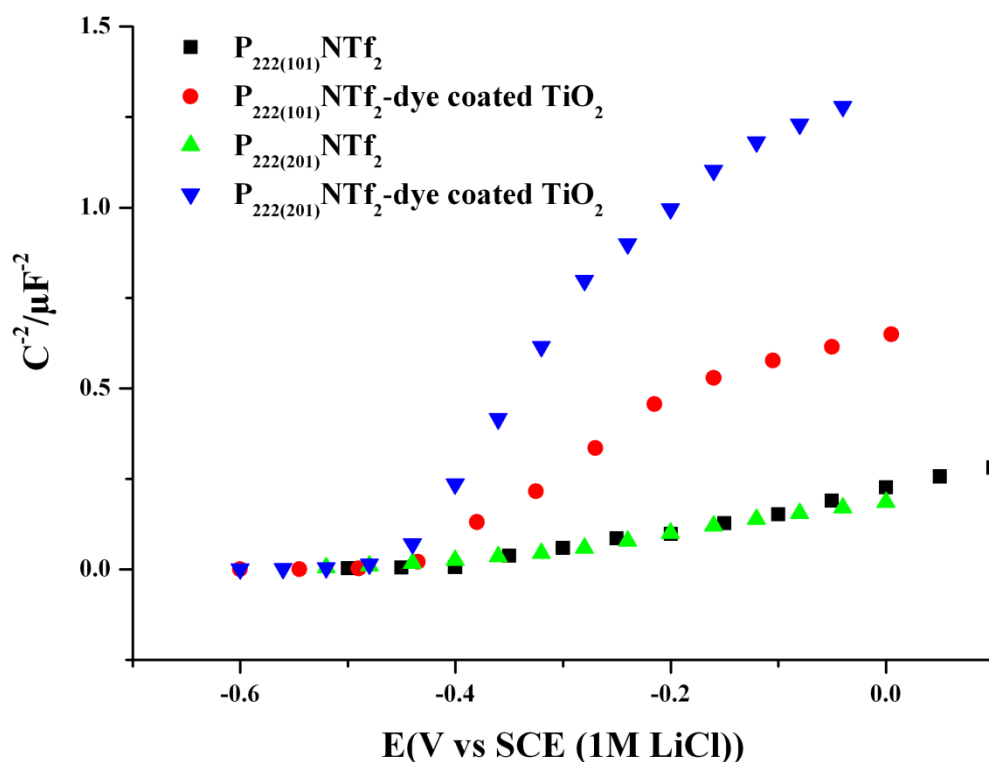


Figure 6.8: Capacitance-voltage plot of dyed and undyed TiO₂ films

Comparison of the flatband pseudo-potentials of the dyed and undyed TiO₂ films in different ionic liquids is presented in Table 6.3. A negative shift of 50 to 70 mV in flatband pseudo-potential is observed in the P₂₂₂₍₁₀₁₎NTf₂ and P₂₂₂₍₂₀₁₎NTf₂ respectively due to the presence of the dye. Zaban *et al.* have shown that when the ruthenium based dyes are adsorbed onto an oxide surface, they became pH-dependent, due to an electrostatic effect between the dye and the oxide surface.⁴⁶ As explained earlier, the presence of adsorbed species on the surface of the TiO₂ can cause a drop in the potential of the double layer, thus shifting the V_{fb} more negatively. Table 6.3 summarises the data obtained from Figure 6.8 and the fitting obtained from equation described in section 6.1.1 (Equation 5.2 to 5.7). Quite good agreement is obtained between the two methods in this case.

Table 6.3: Difference in flatband potentials on dyed and undyed TiO₂ films.

Ionic liquids	Flatband pseudo-potential V vs. SCE (1 M LiCl)	Flatband potential V vs. SCE (1 M LiCl) (± 10 %)
P ₂₂₂₍₁₀₁₎ NTf ₂	-0.402 ± 0.018	-0.402
P ₂₂₂₍₂₀₁₎ NTf ₂	-0.404 ± 0.016	-0.350
P ₂₂₂₍₁₀₁₎ NTf ₂ -Dye coated TiO ₂	-0.450 ± 0.023	-0.435
P ₂₂₂₍₂₀₁₎ NTf ₂ -Dye coated TiO ₂	-0.475 ± 0.006	-0.440

To conclude, changing the anion has a greater effect on the position of the TiO₂ conduction band edge than changes in the cation, as demonstrated by basic anions such as SCN⁻, DEP⁻ and N(CN)₂⁻. These can easily access the surface of the semiconductor, thus negatively charging the double layer and moving the conduction band edge upwards. Cations such as S₂₂₂⁺, P₂₂₂₍₁₀₁₎⁺, MEMPIP⁺ and C₃mpyr⁺ do not have a pronounced effect on the position of the flatband potential. This may be due to the lack of accessibility of these ions to the surface of the TiO₂. When the TiO₂ is coated with a monolayer of dye, the V_{fb} is shifted more negatively.

6.4.2.2 Effect on V_{fb} of the addition of water to C₂mimNTf₂

A measurement in acetonitrile was performed in order to observe the baseline effect on V_{fb} when water is added to an electrolyte. The V_{fb} for a TiO₂ electrode in anhydrous acetonitrile containing 0.1 M TBAP and added water was determined by Mott-Schottky capacitance measurement. The same measurement was also performed in neat ionic liquid (C₂mimNTf₂) (Figure 6.9 and Table 6.4). The interesting feature in Figure 6.9 is the shift of V_{fb} to more positive potential after addition of water to the MeCN, whereas in the ionic liquid system, only a small shift in V_{fb} is observed. As demonstrated in Figure 6.9, the Mott-Schottky measurement in anhydrous MeCN leads to more positive V_{fb} values when compared to literature. The difference might be due to the frequency used to record the V_{fb}, difference in the TiO₂ electrodes (surface state defects or doping level), the presence of residual amount water in the anhydrous MeCN (purchased from Sigma Aldrich), which was used without further purification, or even in the supporting electrolyte (TBAP). Even though the supporting electrolyte was dried for several days at 50 °C in vacuo, trace

6. Effect of ionic liquid on the flatband potential of an n-type semiconductor

amounts of water might still be present. Karl Fischer analysis of the anhydrous MeCN shows the presence of 200 ppm of water.

Nonetheless, the objective of the present experiment was to observe the effect of the addition of water to an ionic liquid as compared to a standard electrolyte. The influence of water on the V_{fb} is shown in Figure 6.9; in both systems the shift to less negative values is presumably related to solvation effects. It has already been demonstrated that protons can be adsorbed at the TiO_2 electrode and are a determining factor on the position of the V_{fb} , hence the dissociation of water to release protons may also contribute to this effect.

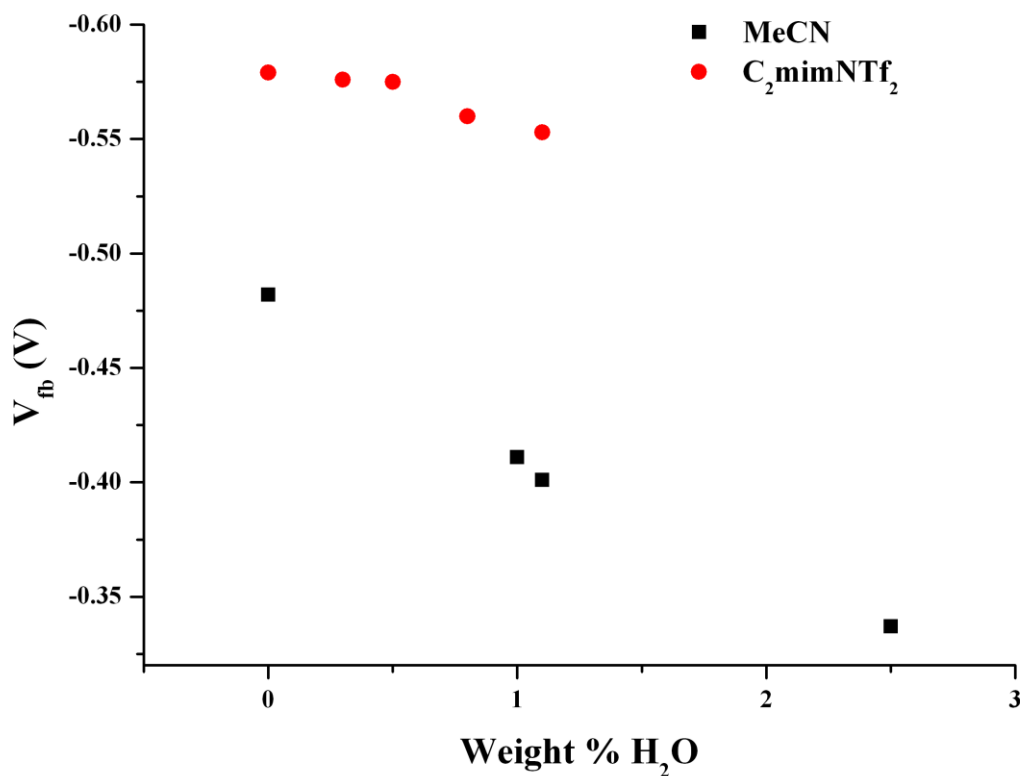


Figure 6.9: Variation of V_{fb} with water in MeCN and C₂mimNTf₂

Table 6.4 displays the data obtained from the capacitance measurements (Figure 6.9) and the fitted data obtained by equations described by Albery and co-workers.²⁸ There is approximately a 50 mV to 100 mV difference between the flatband pseudo-potential and the flatband potential obtained from a fit to the experimental curve using the equation

6. Effect of ionic liquid on the flatband potential of an n-type semiconductor

described in section 6.1.1 (Equation 5.2 to 5.7). As already stated previously, the difference might be related to the double layer structure and composition.

Table 6.4: Flatband potential of TiO₂ electrodes in non-aqueous solvent and with added water.

	Water content (μL)	% (Weight)	Flatband pseudo-potential V vs. SCE (1 M LiCl)	Flatband potential V vs. SCE (1 M LiCl) (± 10 %)	
0.1 M TBAP in anhydrous acetonitrile (200 ppm water)	0	0	-0.482 ± 0.052	-0.401	
	40	1	-0.411 ± 0.011	-0.375	
	70	1.7	-0.401 ± 0.008	-0.325	
	100	2.5	-0.337 ± 0.012	-0.250	
	0	0	-0.579 ± 0.021	-0.540	
	C₂mimNTf₂ (5 ml)	20	0.3	-0.576 ± 0.032	-0.540
		40	0.5	-0.575 ± 0.031	-0.540
60		0.8	-0.560 ± 0.021	-0.525	
80		1.1	-0.553 ± 0.055	-0.501	
100		1.3	-0.537 ± 0.043	-0.501	

One would expect that the addition of water to an ionic liquid would have a similar effect on the flatband potential as it does for the acetonitrile system. However, a smaller shift in V_{fb} is observed in the case of ionic liquids; this may be due to the fact that the ionic liquid is protecting the surface of the TiO₂ and keeping the water away from the surface. The water molecules might also be shielded in the ionic liquids.

6.4.2.3 Addition of bases and acids to ionic liquids

Addition of HNTf₂ to “neutral” ionic liquids C₂mimNTf₂ and C₂mimB(CN)₄

A small amount of a very strong acid was added to C₂mimNTf₂ and C₂mimB(CN)₄, producing a pronounced effect on the V_{fb} of the TiO₂ electrode. Addition of as little as 1 mg (0.6 mM of HNTf₂) produced a positive shift in ΔV_{fb} of 0.311V; with larger addition of acid leading to a greater shift. Repetition of a similar experiment with C₂mimB(CN)₄ yielded similar behaviour. The results of these experiments are summarised in Table 6.5,

6. Effect of ionic liquid on the flatband potential of an n-type semiconductor

and the flatband potential values obtained from fitting the curve are also displayed. Reasonable agreement between the two methods is obtained.

The presence of protons is changing the pH of these otherwise quite “neutral” electrolytes, thus affecting the position of the conduction band edge. Thus, the presence of any acid impurities in ionic liquids will affect the V_{fb} ; hence care must be taken in purifying the ionic liquids before use.

Table 6.5: Addition of HNTf₂ to C₂mimNTf₂ and C₂mimB(CN)₄.

	Mass of HNTf ₂ (mg)	% (weight)	Flatband pseudo- potential V vs. SCE (1 M LiCl)	Flatband potential V vs. SCE (1 M LiCl) (± 10 %)
	0	0	-0.579±0.021	-0.539
C ₂ mimNTf ₂	1	0.01	-0.288±0.011	-0.201
	2	0.03	-0.188±0.033	-0.111
	5	0.07	+0.0068±0.0002	+0.0045
C ₂ mimB(CN) ₄	0	0	-0.573±0.081	-0.518
	2	0.04	-0.144±0.043	-0.101

Smaller ions, such as H⁺ or Ag⁺, can easily intercalate into the nanoporous network of the TiO₂, thus modifying the position of the conduction band edge in a similar way as Li⁺, which will then affect the photovoltage.

Addition of N-methylbenzimidazole (NMB) to ionic liquids C₂mimNTf₂ and C₂mimB(CN)₄

A well known base usually used in dye sensitised solar cells was added to the ionic liquid to investigate its effect. As expected, addition of only 0.2 M NMB drastically changed the V_{fb} , as shown in Table 6.6. The V_{fb} is shifted negatively by ~ 300 mV. Further addition of NMB resulted in only a slightly larger shift in V_{fb} . Adsorption of NMB onto the surface of TiO₂ would increase the V_{fb} ; the partial charge of the nitrogen atom in the NMB allows the base to be adsorbed easily onto the Lewis acid sites of the TiO₂ surface, thus negatively shifting the conduction band edge of the TiO₂.

Similar effects are observed in C₃mpyrNTf₂, where addition of 0.5 M NMB gave a negative shift in the V_{fb} . The flatband potential is shifted negatively by ~ 200 mV.

6. Effect of ionic liquid on the flatband potential of an n-type semiconductor

Table 6.6 shows the flatband pseudo-potential and flatband potential of the two ionic liquids with NMB. Comparable results are obtained in both cases; the difference is only around 50 mV to 80 mV.

Table 6.6: Addition of NMB to C₂mimBF₄.

	Concentration of NMB	Flatband pseudo-potential V vs. SCE (1 M LiCl)	Flatband potential V vs. SCE (1 M LiCl) (± 10 %)
	0	-0.278 ± 0.033	-0.250
C₂mimBF₄	0.2 M	-0.575 ± 0.028	-0.501
(Iolitec)	0.5 M	-0.581 ± 0.008	-0.520
C₃mpyrNTf₂	0	-0.443 ± 0.048	-0.380
	0.5 M	-0.658 ± 0.027	-0.585

In summary, the presence of an acid contaminant from ionic liquids purchased from suppliers can modify the V_{fb} of the semiconductor, as demonstrated by adding acid impurities to C₂mimNTf₂ and C₂mimB(CN)₄. Adding a base to the acid contaminated C₂mimBF₄ shifts the conduction band upward (negatively), perhaps due to the formation of a complex of the NMB with the acid,⁴⁷ suppressing its presence at the surface of the TiO₂; NMB is known to have a high donor ability and thus a stronger affinity with the TiO₂ surface.

6.4.2.4 Addition of lithium iodide and then tert-butylpyridine to C₃mpyrNTf₂

Lithium iodide (LiI), guanidinium thiocyanate (GSCN), 4-tert-butylpyridine (TBP) and N-methylbenzimidazole (NMB) are known to affect the position of the conduction band edge of the TiO₂. It has been demonstrated that the Li⁺ ion can intercalate easily into the Lewis base sites of the TiO₂ surface, shifting the energy of the TiO₂ conduction band in the positive direction.⁴⁸⁻⁵² This positive shift allows a better injection of the electron into the conduction band of the TiO₂, thereby increases the electron injection efficiency, which leads to higher photocurrent in the dye sensitised solar cells. Table 6.7 shows the effect of addition of 0.1 M lithium iodide to C₃mpyrNTf₂, followed by the addition of 0.5 M TBP. When 0.1 M lithium iodide was added to the C₃mpyrNTf₂, the conduction band was shifted downward to more positive potentials, as expected.

6. Effect of ionic liquid on the flatband potential of an n-type semiconductor

On the other hand, higher open circuit voltages are usually achieved by addition of additives such as NMB⁵³⁻⁵⁵ and TBP.^{5, 56} When 0.5 M TBP was introduced into the ionic liquid containing 0.1 M LiI, the V_{fb} of the nanostructured TiO₂ was shifted more negative by ~ 300 mV. The negative shift of the TiO₂ Fermi level by adsorption of the additive is attributed to the affinity of the additive with the surface of the TiO₂ due to the presence of the lone pair of electrons on the nitrogen atom. Fitting the Mott-Schottky plots with a theoretical curve obtained from the equations described in the paper of Albery,²⁸ gives similar potential values, indicating that the Helmholtz layer only affects the V_{fb} to a small extent in this case.

Table 6.7: Effect of Li⁺ and TBP in an ionic liquid on V_{fb} .

	Concentration of LiI	Concentration of TBP	Flatband pseudo- potential V vs. SCE (1 M LiCl)	Flatband potential V vs. SCE (1 M LiCl) (± 10 %)
C₃mpyrNTf₂	0 M	0 M	-0.443 ± 0.048	-0.380
	0.1 M	0 M	-0.221 ± 0.007	-0.200
	0.1 M	0.5 M	-0.569 ± 0.031	-0.520

6.4.2.5 Base and Acid treatment of the TiO₂ film

Several strategies that involve the surface treatment of the TiO₂ surface have been used to improve the open circuit voltage.⁵⁷⁻⁵⁸ A method involving the deposition of metal oxides such as Al₂O₃,⁵⁹ MgO⁶⁰ and Nb₂O₅,⁶¹ to name a few, have been employed to increase the photovoltage by slowing down the recombination reaction. However, the deposition of a coating on TiO₂ can be difficult and irreproducible if the same conditions are not used. Thus another alternative to core-shell structures, the treatment of the TiO₂ with either acid or base prior to cell assembly, has been investigated.⁶²⁻⁶³ It is believed that treating the TiO₂ with a carboxylic acid or phosphinic acid causes these molecules to coordinate to the Ti species at the TiO₂ surface, leaving the hydrophobic end as a buffer between the TiO₂ and the electrolyte.⁶⁴ A higher photovoltage is thus observed due to the shielding of the electrons in the TiO₂ from oxidized species in the electrolyte, i.e. decreasing the back reactions.

6. *Effect of ionic liquid on the flatband potential of an n-type semiconductor*

Table 6.9 summarises the effect of treating the TiO₂ electrode for 4 hours in an acid or base bath. It also gives the potential values obtained from the extrapolation of the straight line to $C^{-2} = 0$, yielding the flatband pseudo-potential by neglecting the effect of the double layer, and by fitting the curve with equations 5.2 to 5.7 without the assumption that the double layer is negligible. The use of the two methods yields comparable results and thus both methods can be used to determine the position of the V_{fb} . A slight negative shift in potential is observed for the acid treatment and a significant shift is observed for the base treatment. FTIR measurements, which are not presented here, confirmed the presence of the acid and base on the surface of the TiO₂.

Table 6.9: Effect of acid and base treatment on the TiO₂ electrodes.

	Acid and base	Flatband pseudo-potential V vs. SCE (1 M LiCl)	Flatband potential V vs. SCE (1 M LiCl) (± 10 %)
	No treatment	-0.443 ± 0.048	-0.380
	Diisooctylphosphinic acid	-0.501 ± 0.021	-0.440
C₃mpyrNTf₂	Propionic acid	-0.499 ± 0.018	-0.440
	Triethylamine	-0.559 ± 0.017	-0.480
	4-tert-butylpyridine	-0.861 ± 0.015	-0.765

6.5 *Conclusions*

It is important to characterise the position of the conduction band edge in the semiconductor electrodes and to understand the effect of impurities and additives on the position of the flat band potential, V_{fb} . Here, the Mott-Schottky plots have been used to determine the flatband potential values and when compared to UV-spectroscopy measurements quite a good agreement between the two methods were obtained. The Mott-Schottky plots were also fitted with a method described by Albery and colleagues, where no assumption concerning the double layer capacitance was made, and reasonable agreement was obtained in some cases.

Such parameters are essential for designing the photoanode electrodes for dye sensitised solar cells as these flatband positions established the maximum photovoltage attainable in the electrolyte junction of the device. Small cations show high affinities for the TiO_2 surface and thus have a strong influence on the conduction band of the TiO_2 electrode. The sign of the charge or dipole orientation of an adsorbent will determine the direction of the movement of the conduction band edge of the semiconductor. For example, a negatively charged surface (with TBP or NMB) will induced a potential drop across the Helmholtz layer, causing the conduction band edge to shift towards more negative potentials, leading to a higher photovoltage. In contrast, the presence of small cations, such as Li^+ or H^+ , will shift the flatband potential downward to more positive potentials. Several strategies are available to protect the surface; treating the surface with either an acid or a base can lead to an increase in V_{oc} , as demonstrated in section 6.4.2.5. The presence of residual amounts of water has a more drastic effect on the position of the flatband potential in an organic solvent than in ionic liquids.

“Basic ionic liquids”, such as $C_2mimSCN$ and $C_2mimN(CN)_2$, shift the flatband potential to more negative potentials compared to “neutral ionic liquids”, such as $C_2mimNTf_2$ and $C_2mimB(CN)_4$. These “basic ionic liquids” behave similarly to TBP in the DSSC; in most cases higher V_{oc} and lower photocurrent densities are obtained, as will be demonstrated in Chapter 7 and 8.

References

1. A. B. Heinzl, D. M. Teschner and R. Schumacher, *Ber. Bunsenges. Phys. Chem.*, 1981, **85**, 1117-1119.
2. *J. Photochem. Photobiol. A*, 2004, **164**, 23-27.
3. M. A. Reddy, M. S. Kishore, V. Pralong, V. Caignaert, U. V. Varadaraju and B. Raveau, *Electrochem. Commun.*, 2006, **8**, 1299-1303.
4. D. Kuang, C. Klein, H. J. Snaith, J. E. Moser, R. Humphry-Baker, P. Comte, S. M. Zakeeruddin and M. Grätzel, *Nano Letters*, 2006, **6**, 769-773.
5. G. Boschloo, L. Hagman and A. Hagfeldt, *J. Phys. Chem. B*, 2006, **110**, 13144-13150.
6. G. Boschloo, H. Lindström, E. Magnusson, A. Holmberg and A. Hagfeldt, *J. Photochem. Photobiol. A*, 2002, **148**, 11-15.
7. A. Fischer, H. Pettersson, A. Hagfeldt, G. Boschloo, L. Kloo and M. Gorlov, *Sol. Energy Mater. Sol. Cells*, 2007, **91**, 1062-1065.
8. C. Zhang, Z. Huo, Y. Huang, S. Dai, M. Wang, Y. Tang and Y. Sui, *J. Photochem. Photobiol. A*, 2010, **213**, 87-92.
9. H. Kusama and H. Arakawa, *J. Photochem. Photobiol. A*, 2004, **162**, 441-448.
10. B. A. Gregg, F. Pichot, S. Ferrere and C. L. Fields, *J. Phys. Chem. B*, 2001, **105**, 1422-1429.
11. Y. Kim, C. H. Yoon, K. J. Kim and Y. Lee, *AVS*, 2007, pp. 1219-1225.
12. J. E. Kroeze, N. Hirata, S. Koops, M. K. Nazeeruddin, L. Schmidt-Mende, M. Grätzel and J. R. Durrant, *J. Am. Chem. Soc.*, 2006, **128**, 16376-16383.
13. D. Kim, M. S. Kang, K. Song, S. O. Kang and J. Ko, *Tetrahedron*, 2008, **64**, 10417-10424.
14. S. Hao, J. Wu, L. Fan, Y. Huang, J. Lin and Y. Wei, *Sol. Energy*, 2004, **76**, 745-750.
15. A. Allegrucci, N. A. Lewcenko, A. J. Mozer, L. Dennany, P. Wagner, D. L. Officer, K. Sunahara, S. Mori and L. Spiccia, *Energy Environ. Sci.*, 2009, **2**, 1069-1073.
16. A. Fujishima and K. Honda, *Nature*, 1972, **238**, 37-38.
17. N. Jaffrezic-Renault, H. Perrot and C. Nguyen van Huong, *Electrochim. Acta*, 1989, **34**, 1739-1743.
18. B. H. Erne, F. Ozanam and J. N. Chazalviel, *J. Phys. Chem. B*, 2000, **104**, 11591-11593.
19. P. Lemasson, J. P. Dalbera and J. Gautron, *J. Appl. Phys.*, 1981, **52**, 6296-6300.
20. G. Rothenberger, D. Fitzmaurice and M. Grätzel, *J. Phys. Chem.*, 1992, **96**, 5983-5986.
21. C. Zeyer and H. R. Grüniger, *Electrochim. Acta*, 1992, **37**, 2791-2793.
22. A. Zimmer, N. Stein, L. Johann, H. Terryn and C. Boulanger, *Surf. Interface Anal.*, 2008, **40**, 593-596.
23. A. Natarajan, G. Oskam and P. C. Searson, *J. Phys. Chem. B*, 1998, **102**, 7793-7799.
24. M. Tomkiewicz, *J. Electrochem. Soc.*, 1979, **126**, 1505-1510.

6. Effect of ionic liquid on the flatband potential of an n-type semiconductor

25. A. J. Nozik, *Annu. Rev. Phys. Chem.*, 1978, **29**, 189-222.
26. A. J. Bard, *Science*, 1980, **207**, 139-144.
27. N. S. Lewis, *Annu. Rev. Mater. Sci.*, 1984, **14**, 95-117.
28. W. J. Albery, G. J. O'Shea and A. L. Smith, *J. Chem. Soc., Faraday Trans.*, 1996, **92**, 4083-4085.
29. R. Schumacher, *J. Electroanal. Chem.*, 1983, **159**, 41-48.
30. K. Kobayashi, M. Takata, S. Okamoto, a. Y. Aikawa and M. Sukigara, *Chem. Phys. Lett.*, 1983, **96**, 366-370.
31. G. Redmond and D. Fitzmaurice, *J. Phys. Chem.*, 1993, **97**, 1426-1430.
32. B. Enright, G. Redmond and D. Fitzmaurice, *J. Phys. Chem.*, 1994, **98**, 6195-6200.
33. R. Thapar and K. Rajeshwar, *Electrochim. Acta*, 1983, **28**, 195-198.
34. P. Bonhote, A. P. Dias, N. Papageorgiou, K. Kalyanasundaram and M. Grätzel, *Inorg. Chem.*, 1996, **35**, 1168-1178.
35. M. I. Litter, *Appl. Catal. B: Environ.*, 1999, **23**, 89-114.
36. G. Lu, A. Linsebigler and J. T. Yates, *J. Phys. Chem.*, 1995, **99**, 7626-7631.
37. H. Mest'ánková, G. Mailhot, J. Jirkovský, J. Krýsa and M. Bolte, *Appl. Catal. B: Environ.*, 2005, **57**, 257-265.
38. V. Augugliaro, V. Loddo, L. Palmisano and M. Schiavello, *J. Catal.*, 1995, **153**, 32-40.
39. M. A. Fox and M. T. Dulay, *Chem. Rev.*, 1993, **93**, 341-357.
40. F. N. Castellano, J. M. Stipkala, L. A. Friedman and G. J. Meyer, *Chem. Mater.*, 1994, **6**, 2123-2129.
41. J. Schwitzgebel, J. G. Ekerdt, H. Gerischer and A. Heller, *J. Phys. Chem.*, 1995, **99**, 5633-5638.
42. R. F. Howe and M. Grätzel, *J. Phys. Chem.*, 1985, **89**, 4495-4499.
43. R. F. Howe and M. Grätzel, *J. Phys. Chem.*, 1987, **91**, 3906-3909.
44. G. Nogami, Y. Ogawa and Y. Nishiyama, *J. Electrochem. Soc.*, 1988, **135**, 3008-3015.
45. C. Mathieu, A. Etcheberry, M. Herlem, F. Iranzo-Marín, J. Liang and J. L. Sculfort, *Electrochim. Acta*, 1993, **38**, 781-786.
46. A. Zaban, S. Ferrere, J. Sprague and B. A. Gregg, *J. Phys. Chem. B*, 1997, **101**, 55-57.
47. C. H. Roeder and A. R. Day, *J. Org. Chem.*, 1941, **06**, 25-35.
48. B. Bakhmatyuk, I. Grygorchak, A. Pidluzhna and E. Ripetskii, *Inorg. Mater.*, 2007, **43**, 537-540.
49. T. P. Chou, Q. Zhang, B. Russo, G. E. Fryxell and G. Cao, *J. Phys. Chem. C*, 2007, **111**, 6296-6302.
50. M. Manickam, P. Singh, T. Issa and S. Thurgate, *J. Appl. Electrochem.*, 2006, **36**, 599-602.
51. N. Kopidakis, K. D. Benkstein, J. van de Lagemaat and A. J. Frank, *J. Phys. Chem. B*, 2003, **107**, 11307-11315.
52. M. Grätzel, in *Stud. Surf. Sci. Catal.*, eds. V. K. Prashant and M. Dan, Elsevier, 1997, pp. 353-375.

6. Effect of ionic liquid on the flatband potential of an n-type semiconductor

53. H. L. Lu, Y. H. Lee, S. T. Huang, C. Su and T. C. K. Yang, *Sol. Energy Mater. Sol. Cells*, DOI: **10.1016/j.solmat.2010.02.018**.
54. X. Sheng, Y. Zhao, J. Zhai, L. Jiang and D. Zhu, *Appl. Phys. A: Mater. Sci. Process.*, 2007, **87**, 715-719.
55. N. Mohmeyer, D. Kuang, P. Wang, H. W. Schmidt, S. M. Zakeeruddin and M. Grätzel, *J. Mater. Chem.*, 2006, **16**, 2978-2983.
56. M. K. Nazeeruddin, A. Kay, I. Rodicio, R. Humphry-Baker, E. Mueller, P. Liska, N. Vlachopoulos and M. Grätzel, *J. Am. Chem. Soc.*, 1993, **115**, 6382-6390.
57. H. Park, D. J. Yang, H. G. Kim, S. J. Cho, S. C. Yang, H. Lee and W. Y. Choi, *J. Electroceram.*, 2009, **23**, 146-149.
58. R. Jose, V. Thavasi and S. Ramakrishna, *J. Am. Ceram. Soc.*, 2009, **92**, 289-301.
59. J. Kim, S. Lee, J. Noh, H. Jung and K. Hong, *J. Electroceram.*, 2009, **23**, 422-425.
60. A. Kay and M. Grätzel, *Chem. Mater.*, 2002, **14**, 2930-2935.
61. F. Lenzenmann, J. Krueger, S. Burnside, K. Brooks, M. Grätzel, D. Gal, S. Rühle and D. Cahen, *J. Phys. Chem. B*, 2001, **105**, 6347-6352.
62. S. Ito, T. Saitou, H. Imahori, H. Uehara and N. Hasegawa, *Energy Environ. Sci.*, 2010, **3**, 905-909.
63. K. H. Park, E. M. Jin, H. B. Gu, S. E. Shim and C. K. Hong, *Mater. Lett.*, 2009, **63**, 2208-2211.
64. N. R. Neale, N. Kopidakis, J. van de Lagemaat, M. Grätzel and A. J. Frank, *J. Phys. Chem. B*, 2005, **109**, 23183-23189.

Chapter 7

Ionic liquids in dithienothiophene based organic dye sensitised solar cells

Chapter overview

This chapter discusses the use of new phosphonium ionic liquids as electrolytes for metal-free organic dye sensitised solar cells. The new metal-free dyes were synthesised by Dr. Tae-Hyuk Kwon from the University of Melbourne. A section of the chapter will be dedicated to their electrochemical and spectroscopic characterisation. The effect of film thickness, dyeing time, solvent and addition of co-absorbent have also been investigated in an attempt to further improve the performance of the devices. Intensity modulated photovoltage and photocurrent (IMVS/IMPS) techniques were used in an attempt to understand the behaviour of the ionic liquids with organic sensitisers. High energy conversion efficiencies were obtained for the first time with the new phosphonium ionic liquids with THD3 sensitisers showing the best performance.

7.1 Introduction

Dye sensitised solar cells have been widely investigated as potential candidates for renewable energy systems as a result of their attractive features, such as the use of inexpensive materials and facile device fabrication. As explained previously in Chapter 2, these devices are composed of a wide band gap TiO_2 semiconductor deposited onto a TCO substrate. The sensitizer most often consists of metal-complex dye, and the DSSC also contains a redox couple (I_3^-/I^- or Ferrocene/ Ferrocenium or $\text{Br}_3^-/\text{Br}^-$ or TMTU/TMFDS²⁺, as discussed in Chapter 2, Figure 2.18) in an organic solvent, an ionic liquid, a polymer gel or a plastic crystal. For the DSSCs to perform efficiently, the sensitizers should satisfy three main conditions.¹ The first criterion requires that the HOMO level of the dye is positive enough, compared to the standard redox potential of the redox couple in the electrolyte, to regenerate the dye effectively.² The second condition is that the LUMO level of the dye should be sufficiently negative, compared to the conduction band edge of the semiconductor, that the injection of the electron in the semiconductor is uniform.³ Finally, good light adsorption within the visible spectrum is necessary.⁴ In designing sensitizers, these conditions should all be satisfied, in addition to good stability under long periods of light exposure.

7.1.1 Sensitizers for DSSCs

7.1.1.1 Ruthenium based sensitizers

Ruthenium based complexes such as N3 or N719,⁵⁻⁶ black dye⁷ and Z907^{6, 8} (Figure 7.1) have been extensively investigated as dyes for DSSCs and a substantial solar energy conversion efficiency of 11.1 % was recently obtained with the black dye.⁹ These dyes attach to the surface of the TiO_2 layer via a functional group, which can either be a carboxylic acid group or phosphinic acid.¹⁰ Most ruthenium based sensitizers that exhibit good performance contain a carboxylic moiety. A large variety of ruthenium based sensitizers have previously been studied in order to improve the photovoltaic performance and stability of DSSCs.¹¹⁻¹⁷ Although Z907 gives very stable devices under continuous light exposure, the molar extinction coefficient of this sensitizer is lower than the standard N719 dye, thereby reducing the light harvesting efficiency. Thus, an alternative ruthenium sensitizer (K19) has been developed which is not only very stable, but also has a high molar extinction coefficient (Figure 7.1).¹⁶ The enhanced absorption observed is due to the extended conjugated system of the ligand.

7. Ionic liquids in dithienothiophene based organic dye sensitised solar cells

Chen *et al.* have developed a ruthenium sensitiser with a carbazole antenna, which gave an energy conversion efficiency of 9.6 % with an acetonitrile based electrolyte under AM 1.5. They successfully demonstrated that under harsh conditions, the dye was quite stable and maintained its performance over a long period of time.¹⁴ Ruthenium sensitisers are currently the most popular and heavily investigated type of dye. However, even though they meet the necessary requirement for high device performance, the major drawbacks concerning these dyes are the high cost and the rarity of the ruthenium metal used. The synthesis and purification of these ruthenium-based dyes also requires a long procedure to obtain a pure compound, and further improvements of the purification technique are still required. Thus, there is significant interest in the development of metal-free organic dyes that do not require tedious synthesis procedures and extensive purification steps.

7. Ionic liquids in dithienothiophene based organic dye sensitised solar cells

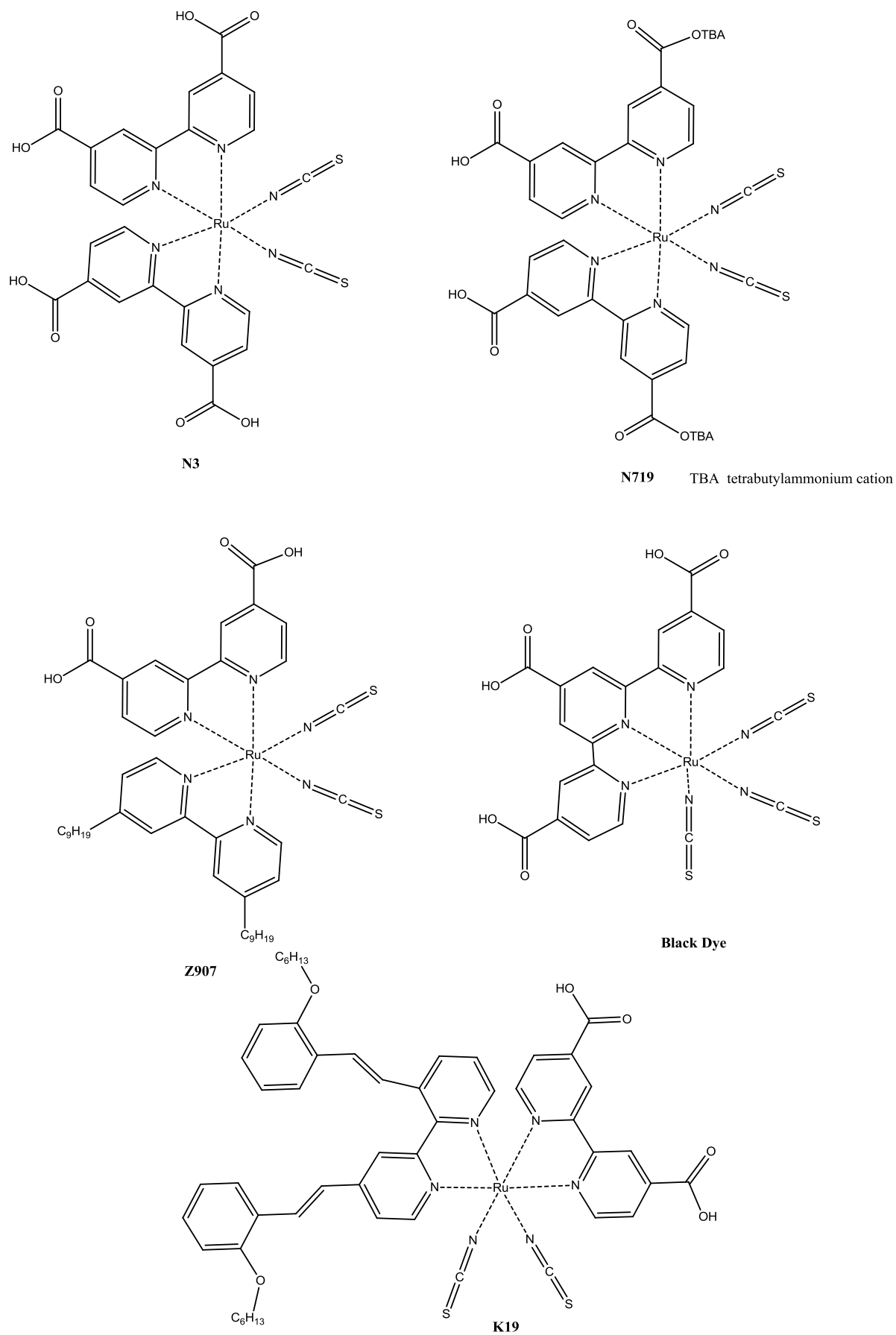


Figure 7.1: Examples of Ruthenium based sensitizers for DSSCs

7. Ionic liquids in dithienothiophene based organic dye sensitised solar cells

7.1.1.2 Metal free Organic sensitisers

Organic dyes have many advantages over the ruthenium based sensitisers. Firstly, they have higher molar extinction coefficients due to an intermolecular π - π^* transition.¹⁸ Thus, they are suitable for thin TiO₂ films, which are required for solid state devices when mass transport and insufficient pore filling limits the performance of the solar cells. Secondly, they have various structures and can be easily modified by molecular engineering, i.e. introduction of electron-withdrawing or electron-donating substituents to further improve their optimal absorption spectra.¹⁹ These dyes are less expensive than ruthenium based sensitisers, as they do not contain rare and noble metals, therefore it is possible to produce them in very large quantities. Also, the preparation and purification of organic dyes is easier than Ru-complexes. Many organic dyes have been synthesised and used in dye sensitised solar cells; Figure 7.2 shows examples of organic dyes reported in the literature.

Great progress has been made in developing high performing devices using metal free organic sensitisers during the past few years. A variety of coumarin,²⁰⁻²³ indoline,²⁴⁻²⁷ hemicyanines,²⁸⁻³² cyanines,³³⁻³⁴ merocyanines³⁵⁻³⁷ and triphenylamine³⁸⁻⁴¹ based organic sensitisers have been recently developed and all of these sensitisers are quite efficient in solar cells. For example, an efficiency of 5.1 % was achieved with hemicyanines on an acid treated TiO₂ substrate.³² A further improvement of the power conversion efficiency ($\eta = 6.3$ %) was obtained by introducing a hydroxyl group on the hemicyanine dye.⁴² Cyanine dyes are well known sensitisers in photography, and these dyes show good performance under moderate light intensity ($\eta = 7.62$ %).⁴³ Amongst all these sensitisers, the most efficient metal-free organic dye to date was obtained using an indoline dye, with an efficiency of 9.52 %.²⁷ However, additional improvements of the organic sensitisers are still required to increase the performance, if DSSCs are to be used for commercial purposes. One method of improving the organic dyes is by extending their absorption range in the near infrared region, thus increasing the number of photons absorbed, which can result in higher photocurrent densities. Nevertheless, organic dyes have shown very promising results so far, and have the potential to be very competitive.

7. Ionic liquids in dithienothiophene based organic dye sensitised solar cells

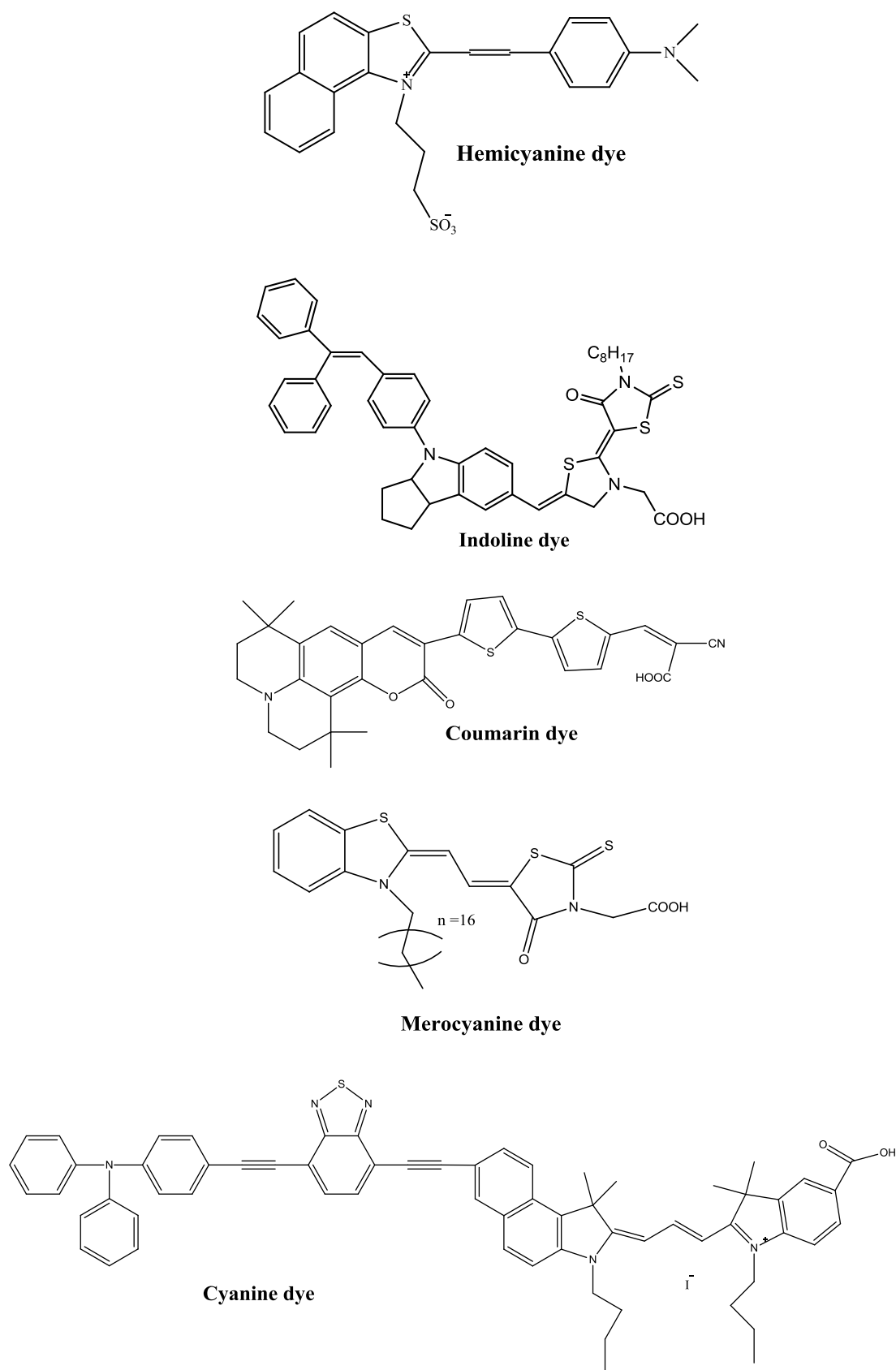


Figure 7.2: Examples of high performing organic dyes^{20, 27, 32, 35}

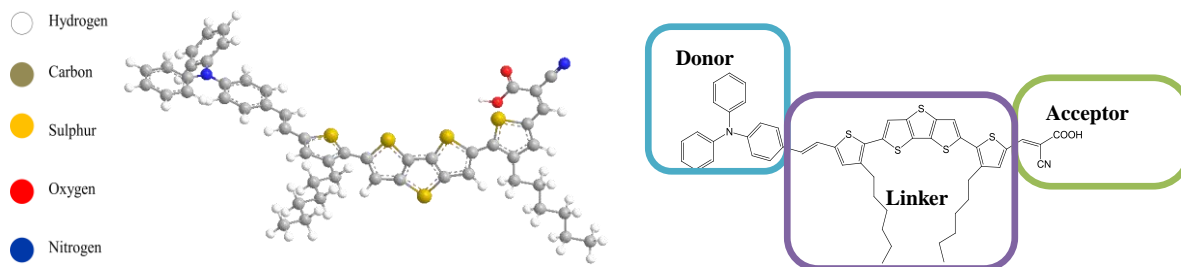
7.1.2 Aim

The aim of this study was to replace the organic solvents commonly used with organic dyes with a room temperature ionic liquid, in this case phosphonium based ionic liquids were used, and to characterise and compare the different dyes. The properties of the dyes in solution, as well as directly adsorbed onto the TiO₂ surface, were analysed using a range of techniques. DFT calculations and Raman spectroscopy were performed by Dr. Tae-Hyuk Kwon in order to calculate the HOMO and LUMO levels of the dyes, to see whether they fit the basic criteria, described in section 7.1.1, for a good organic sensitiser. The performance of the dyes in ionic liquid electrolytes has been compared to their performance with acetonitrile based electrolytes, and the dependence of the performance of the solar cells on the film thickness, solvent and dye used is discussed. High solar-to-current conversion efficiencies were obtained using the phosphonium based electrolytes with THD3 dye (see structure in Figure 7.3 (c)). This work demonstrates that phosphonium ionic liquids can be used as electrolytes and, in some cases, can out-perform imidazolium based electrolytes in DSSCs. This is the first time that such high solar-to-current energy conversion efficiencies have been obtained with phosphonium based ionic liquids.

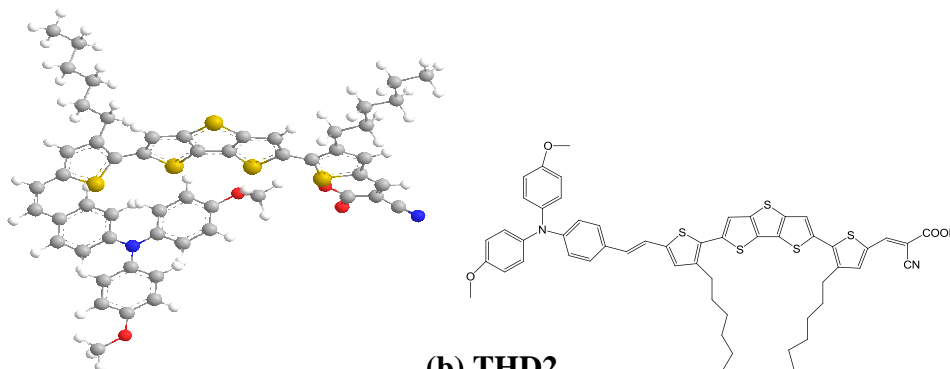
7.2 Experimental

In order to understand the properties and performance of the new dyes for use in DSSC, a comparison was made of the dye in solution, directly attached to the surface of the TiO₂ and in the solar cell device itself. Several methods were used to examine properties such as the energy levels and redox potentials of the new dyes. Figure 7.3 shows the structure and acronyms for these new dithienothiophene-based organic dyes. THD1 and THD8 are structurally similar, except that there is no conjugated linker in THD8. THD2 and THD9 are also similar, except that in the case of THD9 the triphenylamine is directly connected to the thiophene. The main studies were on THD1 and THD3 dyes, are these performed best in the solar cells.

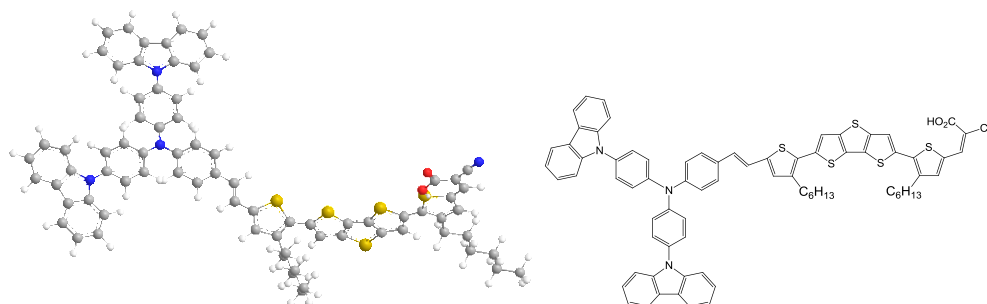
7. Ionic liquids in dithienothiophene based organic dye sensitised solar cells



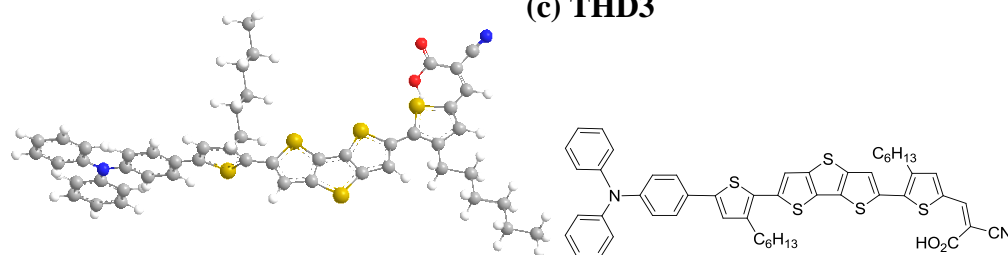
(a) THD1



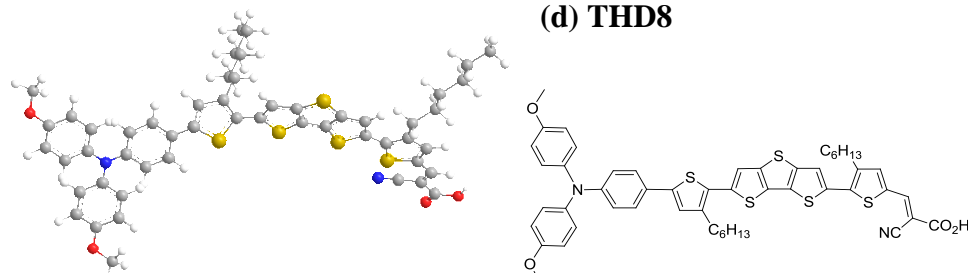
(b) THD2



(c) THD3



(d) THD8



(e) THD9

Figure 7.3: New organic dyes synthesised by Dr. Tae Hyuk Kwon; (a) THD1, (b) THD2, (c) THD3, (d) THD8, (e) THD9

7.2.1 UV-Vis

UV-Vis was used to compare the dyes in solution and adsorbed on the TiO₂. Several solvents were used for comparison; chloroform, ethanol, dichloromethane, chlorobenzene, acetonitrile. In the case of the dye directly attached onto TiO₂, a thin film of 2 µm was used. The film was prepared by screen printing and dimensions of 7 mm x 7 mm were used. These films were very transparent and UV-Vis measurements were made using an integrating sphere. The integrating sphere was used to ensure that all the light was collected.

Dye adsorption was measured over time in a simple set-up, as shown in Figure 7.4. 1 - 2 µm TiO₂ transparent films were prepared by doctor blading on a microscope slide. The films were sintered using a heat gun at 500 °C for 30 mins and used immediately after cooling to 80 °C. The amount of dye molecules attached to the surface was then measured. This measurement was done in different solvents; chloroform, chlorobenzene, dichloromethane, dichloroethane and a 1:1 mixture of chloroform and ethanol.

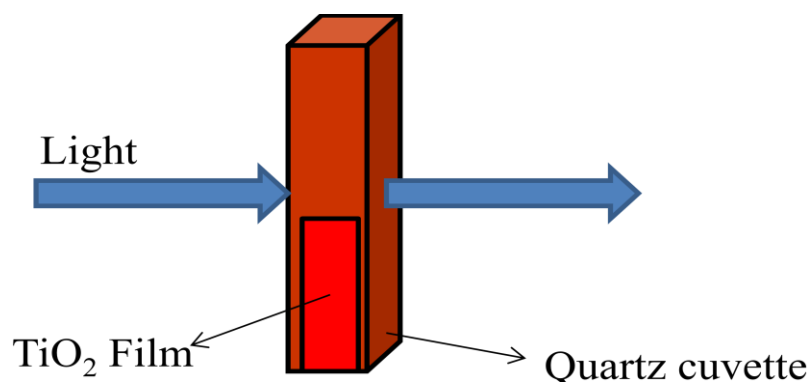


Figure 7.4: Dye uptake equipment

The Beer Lambert equation can be used to calculate the molar extinction coefficient of the sensitisers, as well as the amount of dye that is adsorbed onto the TiO₂;

$$A = \epsilon l C \quad (\text{Eq 7.1})$$

where A is the absorbance, ϵ is the molar extinction coefficient (M cm^{-1}), l is the path length of the cuvette (1 cm) and C is the concentration of the dye.

7. Ionic liquids in dithienothiophene based organic dye sensitised solar cells

7.2.2 Cyclic voltammetry

Cyclic voltammetry of the dye was performed in solution and on the TiO₂ surface, in dry dichloromethane, to determine the HOMO level. 0.1 M tetrabutylammonium hexafluorophosphate was used as the supporting electrolyte, and the experiment was performed in an argon-filled glove box. A three electrode set-up was used, consisting of either platinum or the dyed TiO₂ as the working electrode, a platinum wire as the counter electrode and a non-aqueous calomel electrode (1 M LiCl in acetonitrile, purchased from Radiometer analytical) as the reference electrode. Ferrocene/Ferrocenium was used as the internal reference to calibrate the system.

7.2.3 Preparation of the dye sensitised solar cells

A brief description of the preparation of the solar cells is given here (see Chapter 4 for a full description). 0.2 mM of the organic dye was dissolved in a mixture of solvents e.g. chloroform:ethanol or dichloromethane:ethanol. A screen-printed TiO₂ film of desired thickness, and area of 0.16 cm², was put in a heat gun for 30 min at 500 °C. Once the electrodes were cooled down to ~80 °C, they were immersed in the dye solution overnight. Platinised TCO glass was used as the counter electrode. The two electrodes were sealed using a 25 µm Surlyn and the electrolyte was injected into a pre-drilled hole on the counter electrode and the hole covered with a cover slide. The ionic liquid electrolytes were back filled at 80 °C where all the electrolytes were homogenous.

7.2.4 Evaluation of DSSC performance

The solar cells were tested using simulated sunlight (AM 1.5, 1000 W m⁻²) provided by an Oriel solar simulator with an AM 1.5 filter. Current-voltage characteristics were measured using a Keithley 2400 SourceMeter. Cells were biased from high to low potential, with 10 mV steps and 400 ms settling time for ionic liquid electrolytes and 40 ms for the standard electrolyte. Incident photo-to-charge carrier conversion efficiency (IPCE) measurements were conducted with the cell held under short circuit conditions and illuminated by monochromatic light. A Cornerstone 260 monochromator was used in conjunction with an optical fibre, Keithley 2400 SourceMeter and 150 W Oriel Xe lamp. A full description is given in Chapter 4.

7.3 Results and discussion

7.3.1 UV spectroscopy

Figure 7.5 shows the UV-Vis spectra of the novel organic dyes, THD1, THD2, THD3, THD8 and THD9, measured in dichloromethane solution. The absorption spectrum in the visible range displays two prominent absorption peaks, attributed to the π - π^* /charge transfer (CT) transitions, for all the sensitisers. THD1 displays a strong visible band at 423 nm ($\epsilon = 30000 \text{ M}^{-1} \text{ cm}^{-1}$). THD2, which contains a methoxy group, show a slightly red shifted absorption maxima compared to THD1 (490 nm, $\epsilon = 34500 \text{ M}^{-1} \text{ cm}^{-1}$). THD3, which contains a carbazole moiety, exhibits similar spectral properties to THD2 (absorption maxima at 497 nm, $\epsilon = 30200 \text{ M}^{-1} \text{ cm}^{-1}$). The slight red-shift in the position of the lower energy peak for THD3 is attributed to an increased donor capacity, which slightly raises the level of the HOMO level. Such red-shifting in the absorption spectra implies a more effective utilisation of the solar light. THD8 displays similar spectral behaviour to THD1, with a maximum adsorption at 477 nm ($\epsilon = 34000 \text{ M}^{-1} \text{ cm}^{-1}$). THD9 exhibits similar spectral behaviour to THD2 (500 nm, $\epsilon = 29986 \text{ M}^{-1} \text{ cm}^{-1}$). The molar extinction coefficients of these new organic dyes are larger than those of ruthenium sensitisers; N3 has a molar extinction coefficient of $13000 \text{ M}^{-1} \text{ cm}^{-1}$.³ As a result of their high molar extinction coefficients, these dyes should have good light harvesting ability and therefore thinner films can be used without any loss in performance of the devices. This may be a useful feature with an ionic liquid electrolyte, given the lower diffusivities in these materials.

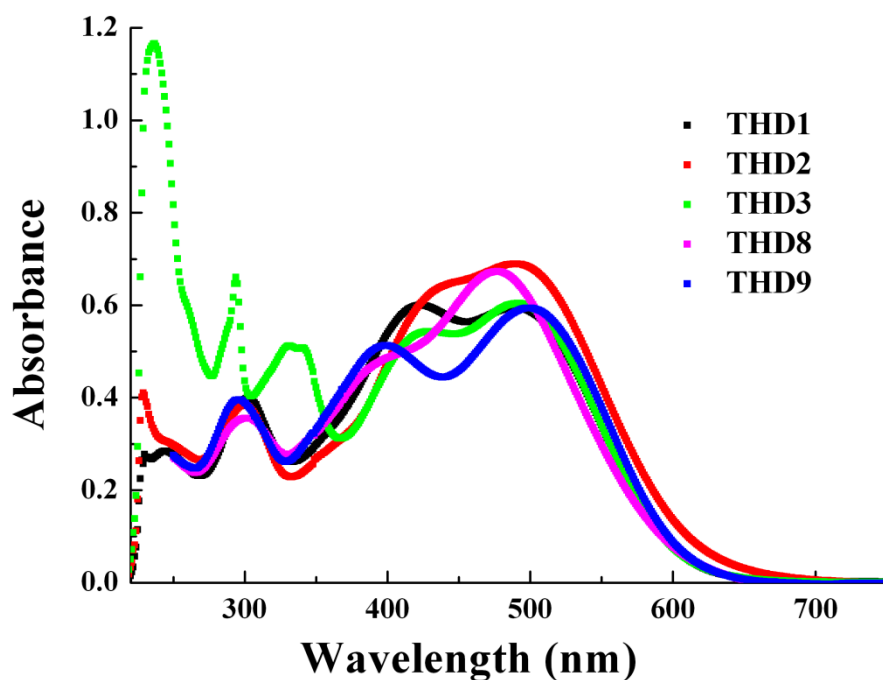


Figure 7.5: UV-absorption of dyes; THD1, THD2, THD3, THD8 and THD9 in dichloromethane

Absorption of sensitisers on TiO₂

Figure 7.6 displays the absorption spectra of the sensitisers, THD1, THD2, THD3, THD8 and THD9 adsorbed onto a transparent TiO₂ film, in EtOH-CH₂Cl₂ (50:50 by vol). When the THD1, THD2, THD3, THD8 and THD9 dyes are attached to the semiconductor, a blue shift of 21 nm, 57 nm, 51 nm, 31 nm and 49 nm respectively, is observed in comparison to the dyes in solution, due to a strong interaction between the dye and the TiO₂ surface. Nazeeruddin *et al.*⁵ reported that a blue shift was also observed with black dye as the pH of the solution increased. They concluded that the blue shift was due to the deprotonation of the carboxylic acid when attached to the TiO₂.⁵ Hara *et al.*⁴⁴ also saw similar effects with coumarin dyes and they attributed this blue shift to the formation of the H-aggregation. (H stands for hypsochromic, i.e. blue shift). The blue shift observed in this case might be due to the formation of H-aggregation of the dyes. Dyes are known to self-associate either in solution or at a solid-liquid interface, due to the strong intermolecular van der Waals-like attractive forces between the molecules, thus giving rise to either J-aggregation (J stand for Jelly, named after the author,⁴⁵ i.e. bathochromic shift (red shift)).⁴⁶

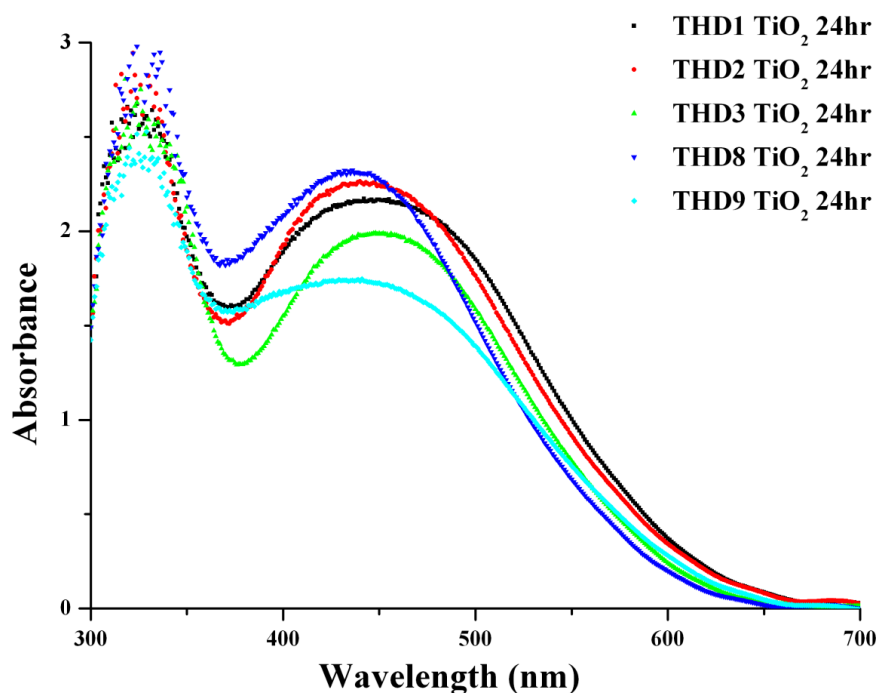


Figure 7.6: Absorption spectra of the dyes on TiO₂

7.3.2 Determination of the redox potential of organic sensitisers

To understand the likelihood of electron transfer from the excited state of the dye molecule into the conduction band of the TiO₂ and the regeneration of the dye, the oxidation and reduction potentials of THD1, THD2, THD3, THD8 and THD9, in DCM solution and on a TiO₂ surface, were measured using cyclic voltammetry.

The standard redox potentials of the sensitisers obtained from electrochemical analysis are summarised in Table 7.1. The oxidation potential of the dyes (D⁺/D) was obtained from the first oxidation potential E_{ox} vs. NHE measured using cyclic voltammetry. The excited state potential of the dye, E (D⁺/D*), was calculated using the equation:²¹

$$E (D^+/D^*) = E (D^+/D) - E_{0-0} \quad (\text{Eq 7.2})$$

where E (D⁺/D) is the ground state oxidation potential of the sensitiser and E₀₋₀ is the zero-zero transition value, obtained from the intersection of the lowest energy absorption peak from the UV spectra and the highest energy emission peak from the photoemission spectra, as shown in Figure 7.7 for THD8.

7. Ionic liquids in dithienothiophene based organic dye sensitised solar cells

Figure 7.8 shows the typical cyclic voltammograms of the THD1, THD2, THD3, THD8 and THD9 dyes adsorbed onto the surface of the TiO₂, recorded using 0.1 M tetrabutylammonium hexafluorophosphate in dry dichloromethane. The dyes show evidence of two reversible one electron transfer oxidation waves, at half potentials of 0.83 and 1.05 V vs. NHE for THD2, 0.96 and 1.29 V vs. NHE for THD3, 0.95 and 1.18 V vs. NHE for THD9, 1.03 and 1.38 V vs. NHE for THD8 and finally 0.97 and 1.31 V vs. NHE for THD1. The first oxidation potential is attributed to the removal of an electron from the triphenylamine unit (NPh₃) and the second quasi reversible one electron oxidation wave at a higher potential may be from the oxidation of the thiophene group. The first redox potential is 60 mV more positive for the THD2 dye on the TiO₂ than in solution, 50 mV more positive for THD3, 20 mV for THD9 and 30 mV for THD8. This increase may be due to the interaction of the dye with the surface of the semiconductor. In either case, the dyes show good electrochemical reversibility.

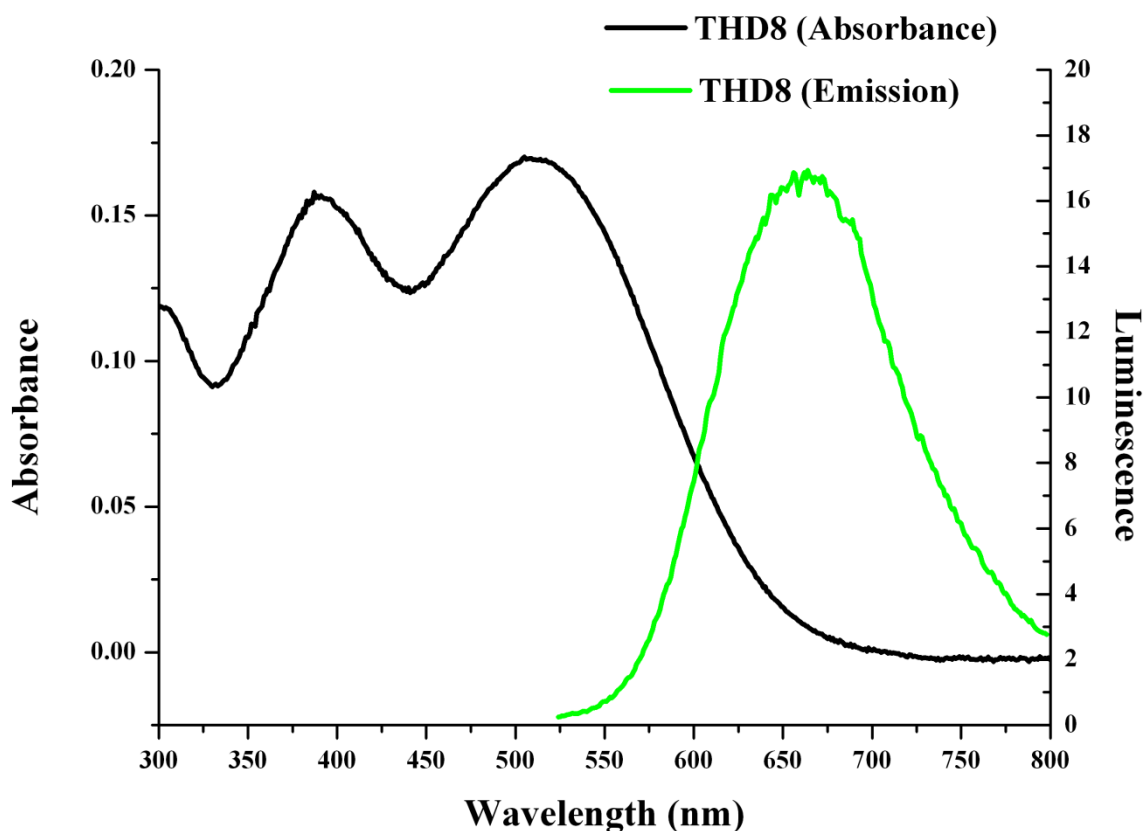


Figure 7.7: Adsorption and Emission spectra of THD8

Table 7.1 summarises the data obtained from the absorption and emission spectra of the sensitisers, as well as the redox potentials obtained by cyclic voltammetry in dichloromethane. The amount of dye adsorbed (Γ) on a 2 μm film of dimension 7 mm x 7 mm is also shown in the table. The amount of dye absorbed on the TiO_2 is quite similar in all cases.

Table 7.1: Experimental data of dyes.

Dye	λ_{max} (nm) (± 1 nm)	ϵ ($\text{M}^{-1}\text{Cm}^{-1}$) (± 0.01 %)	λ_{max} (on TiO_2) (± 1 nm)	Γ $\text{molcm}^{-2}\mu\text{m}^{-1}$ (± 0.01 %)	E_{ox} (V vs. NHE) (± 0.01)	E_{0-0} (± 0.01)	$E_{\text{ox}}-E_{0-0}$ (V vs. NHE) (± 0.01)
THD1	423	30000	402	2.23×10^{-15}	0.98	2.27	-1.29
THD2	490	34500	433	2.15×10^{-15}	0.77	2.10	-1.33
THD3	497	30200	446	2.25×10^{-15}	0.91	2.11	-1.20
THD8	477	34000	446	2.16×10^{-15}	1.06	2.11	-1.05
THD9	500	29986	451	2.14×10^{-15}	0.93	2.00	-1.07

All of the dyes reported in Table 7.1 show more negatively excited state potentials than the potential of N719 (-0.98 V/NHE)⁴⁷ and the TiO_2 conduction band edge. Thus, these dyes have a sufficient driving force to inject electrons into the conduction band of the TiO_2 . They can also be used with other types of semiconductors (e.g. ZnO) which have more negative conduction bands than that of TiO_2 . Nevertheless, to date TiO_2 shows the best performance in DSSCs.

One other important key component in a DSSC is the redox couple. When designing a sensitiser, it is essential to see whether the sensitiser will be regenerated efficiently by the redox couple in the electrolyte. For this to occur the oxidation potential of the dyes should be more positive than the redox potential of the mediator (I/I_3^-) ($E = 0.35$ V/NHE).⁴⁷ As illustrated in Table 7.1, all of the dyes have more positive oxidation potential than the redox couple, thus there is adequate driving force for the dye regeneration reaction to compete efficiently with the recombination reaction of the dye radical and the injected electron.⁴⁸ The introduction of a carbazole unit or methoxy group on the triphenylamine moiety slightly reduces the oxidation potential of the sensitisers, and where there is no conjugated linker between the thiophene unit and the triphenylamine, an increase in

7. Ionic liquids in dithienothiophene based organic dye sensitised solar cells

oxidation potential is observed. Thus by modifying the donor unit, the energy level can be modified.

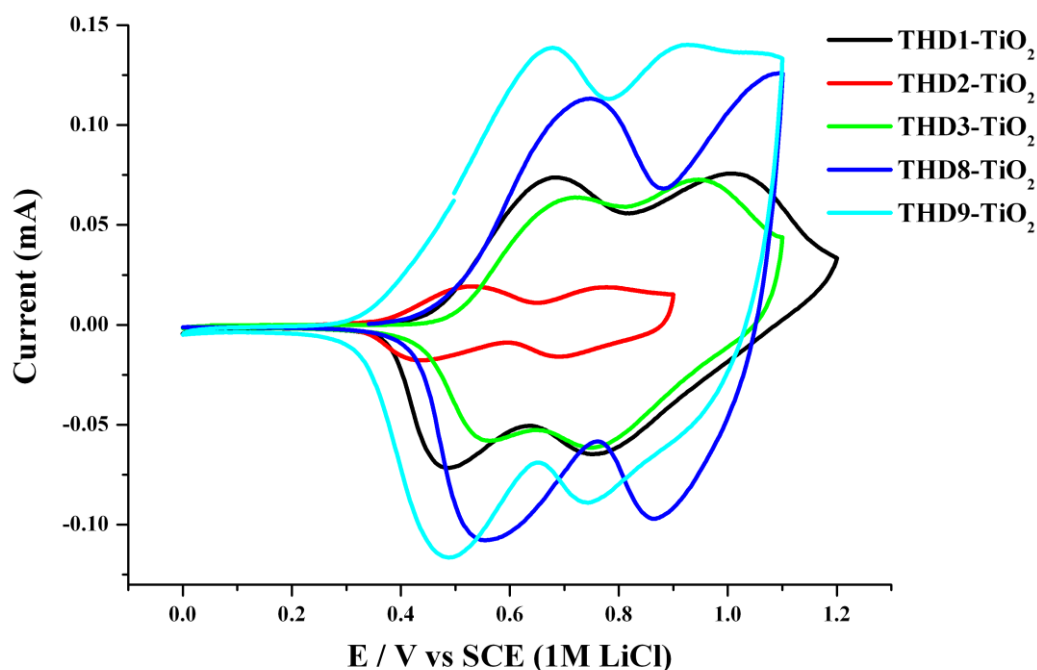


Figure 7.8: Cyclic voltammetry of dye-loaded TiO₂ films, using 0.1 M tetrabutylammonium hexafluorophosphate in DCM, with a non aqueous calomel reference electrode. The scan rate was 5 mV s⁻¹

7.3.3 Electrolytes

An electrolyte is a system containing ions that acts as a medium between the photoanode and cathode, and it can exist in a molten salt, solid or solution form. Electrolytes used in solar cells are generally based on organic solvents containing a redox mediator. For long term function, organic solvents are not suitable, as they easily evaporate and are quite air and moisture sensitive. The most commonly used mediator is triiodide/iodide (I₃⁻/I⁻). As explained in Chapter 2, the iodide ions are used to regenerate the oxidized dye, which in the process is converted back into the triiodide ions. The triiodide ions are reduced to the iodide at the counter electrode, which is catalysed by platinum. The choice of electrolyte for solar cell applications is crucial as it affects the overall performance of the device.

7.3.3.1 Ionic liquid electrolytes

The objective of this study was to replace the organic solvents with ionic liquid electrolytes. They have one major drawback, in that they are quite often viscous, which reduces the mobility of the mediator in the system. In order to overcome this problem, higher concentrations of the iodide and iodine are necessary. Addition of high concentrations of iodine leads to the formation of polyiodides, such as triiodide. The triiodide can interact with other iodine molecules to give larger polyiodides, which are known to have good electrical conductivities. The conductivity mechanism then becomes a relay mechanism, in which the charge carrier transfer is achieved without any mass transfer.⁴⁹

The ionic liquid electrolytes were prepared by combining dialkylimidazolium iodide, iodine and other additives, such as lithium iodide, 4-*tert*-butylpyridine and N-methylbenzimidazole, in the phosphonium ionic liquids. Compositions are listed in Table 7.2. All of the different electrolyte combinations, with the new phosphonium ionic liquids (synthesised in Chapter 6), were applied to dye sensitised solar cells using the new organic dyes, as well as with ruthenium dyes, in order to study their impact on the device performance. A standard acetonitrile-based electrolyte was used as a control.

During the preparation of the ionic liquid electrolytes, in some cases, crystals of iodide and triiodide salts of the ionic liquid were formed, which were analysed by X-ray crystallography (Appendix, section A.5). The final liquidus point of each electrolyte was determined visually; these are also listed in Table 7.2. Electrolytes were always warmed above the liquidus temperature before samples were taken for diffusion coefficient and conductivity measurements.

The standard molecular liquid electrolyte for the dithienothiophene organic sensitisers was composed of 0.6 M C₃dmimI, 0.03 M of GuanidiniumSCN, 0.05 M of I₂, 0.03 M LiI and 0.5 M TBP.

The diffusion coefficient of the redox species in the ionic liquid systems was measured as described in Chapter 3, section 3.2.4.4 using a three-electrode set up, with a Pt microelectrode working electrode, a Pt wire counter electrode and a Ag or Pt wire reference electrode. Data is summarised in Table 7.2.

Table 7.2: The composition of the prepared ionic liquid and acetonitrile-valeronitrile based electrolytes, as well as the diffusion coefficient of the triiodide ion.

Electrolyte IL	Composition (molar ratio)						D (I ₃ ⁻) C m ² s ⁻¹
	IL	C ₂ mimI	C ₁ mimI	I ₂	LiI	NMB [#]	
P ₂₂₂₍₂₀₁₎ NTf ₂	14	12	12	1.67	1	4	2.5 x 10 ⁻⁷
P ₂₂₂₍₂₀₁₎ FSI	14	12	12	1.67	1	4	4.0 x 10 ⁻⁷
P ₂₂₂₍₁₀₁₎ NTf ₂ [#]	14	12	12	1.67	1	4	4.1 x 10 ⁻⁷
P ₂₂₂₍₁₀₁₎ FSI [#]	14	12	12	1.67	1	4	5.2 x 10 ⁻⁷
P ₂₂₂₍₁₀₁₎ N(CN) ₂ [#]	14	12	12	1.67	1	4	5.3 x 10 ⁻⁷
P ₁₂₂₄ NTf ₂ [#]	14	12	12	1.67	1	4	2.2 x 10 ⁻⁷
P ₁₂₂₄ FSI	14	12	12	1.67	1	4	2.5 x 10 ⁻⁷
P ₁₄₄₄ N(CN) ₂	14	12	12	1.67	1	4	1.8 x 10 ⁻⁷
P ₁₄₄₄ NTf ₂ *	12	12	12	1.67	1	4	1.2 x 10 ⁻⁷
P ₁₄₄₄ FSI*	12	12	12	1.67	1	4	1.5 x 10 ⁻⁷
C ₂ mimNTf ₂	16	12	12	1.67	1	4	4.7 x 10 ⁻⁷
C ₂ mimFSI	16	12	12	1.67	1	4	5.8 x 10 ⁻⁷
C ₃ mpyrNTf ₂	16	12	12	1.67	1	4	4.4 x 10 ⁻⁷
		C₄mimI	GSCN[@]	I₂	LiI	TBP[*]	
Standard (N719)		0.6M	0.1M	0.03M	-	0.5M	4.7 x 10 ⁻⁶
		C₃dmimI	GSCN[@]	I₂	LiI	TBP[*]	
Standard (THDn)		0.6M	0.03M	0.05M	0.03M	0.5M	4.3 x 10 ⁻⁶

* measured at 40 °C, [@] Guanidinium thiocyanate, # indicates that at the temperature of measurement the sample was partly crystalline. The electrolytes were homogenous at 70 °C.

7. Ionic liquids in dithienothiophene based organic dye sensitised solar cells

Viscosity and density of electrolytes as function of temperature

The viscosity and density of P₂₂₂₍₁₀₁₎NTf₂, P₂₂₂₍₂₀₁₎NTf₂, P₂₂₂₍₂₀₁₎FSI, P₂₂₂₍₁₀₁₎FSI, P₂₂₂₍₁₀₁₎N(CN)₂, P₁₂₂₄NTf₂, P₁₂₂₄N(CN)₂, P₁₂₂₄FSI and P₁₄₄₄N(CN)₂ electrolytes, which contain C₂mimI, C₁mimI, LiI, I₂ and N-methylbenzimidazole, was measured as function of temperature. The density and viscosity of a binary ionic liquid mixture, containing C₄mimI as the iodide source (with LiI, I₂ and N-methylbenzimidazole) was also measured. The electrolytes were dried under vacuum overnight at 50 °C and their viscosities were measured from 25 °C to 90 °C, except for P₂₂₂₍₁₀₁₎NTf₂, where the density and viscosity was measured from 30 °C to 90 °C due to the formation of P₂₂₂₍₁₀₁₎I (crystallised out see Appendix for crystal structure) at room temperature.

The electrolytes have higher viscosity and density compared to the neat ionic liquids, which is expected as the electrolyte contains other components that can potentially increase the density of the electrolyte, such as iodine atoms. The density and viscosity behaviour of the electrolytes as a function of temperature are shown in Figure 7.9 and Figure 7.10 respectively. Of all the electrolytes studied, P₁₄₄₄N(CN)₂ shows the lowest density, even though it contains the same molar concentration of the different additives. Even neat P₁₄₄₄N(CN)₂ show lowest density, possibly due to steric hindrance from the butyl groups. As the temperature increases, a decrease in density is observed for all ionic liquid electrolytes, which is due to the lower ion packing density.⁵⁰ In order to have a better understanding of the density behaviour versus temperature of the ionic liquids electrolytes, the molar volume of the electrolyte is calculated using the following equation:

$$V_m = \frac{\sum_{i=1}^n x_i M_i}{\rho_{mixture}} \quad (\text{Eq 7.3})$$

where V_m is the molar volume, x_i is the mole ratio and M_i is the molecular weight.⁵¹

7. Ionic liquids in dithienothiophene based organic dye sensitised solar cells

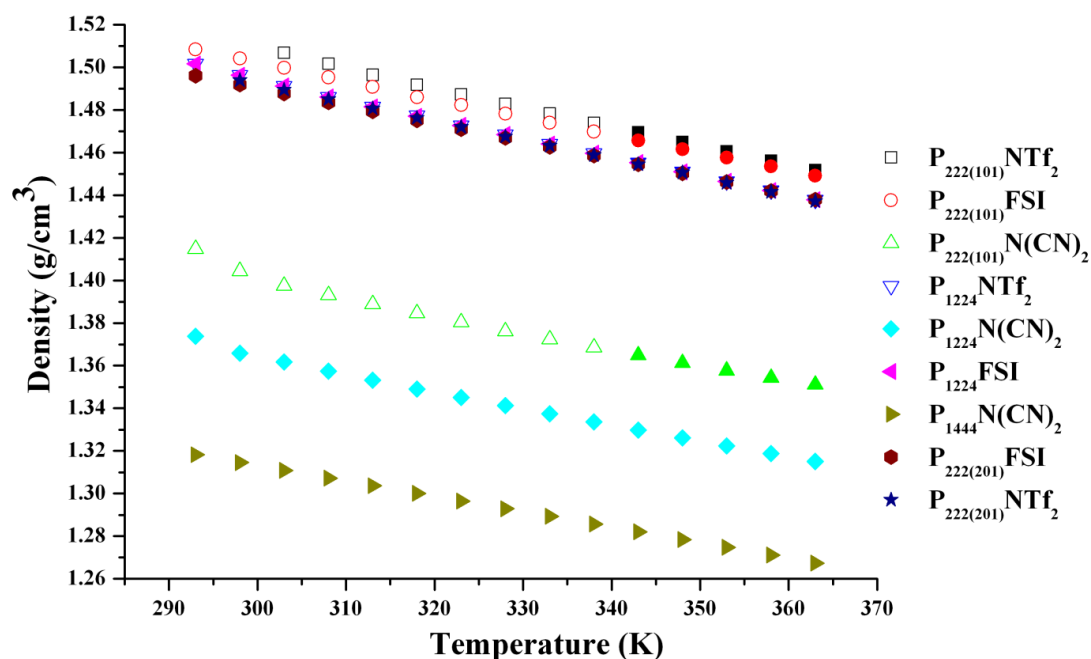


Figure 7.9: Density as function of temperature of ternary mixtures, Empty symbols indicate that at the temperature of measurement the sample was partly crystalline. All electrolytes were homogenous at 70 °C

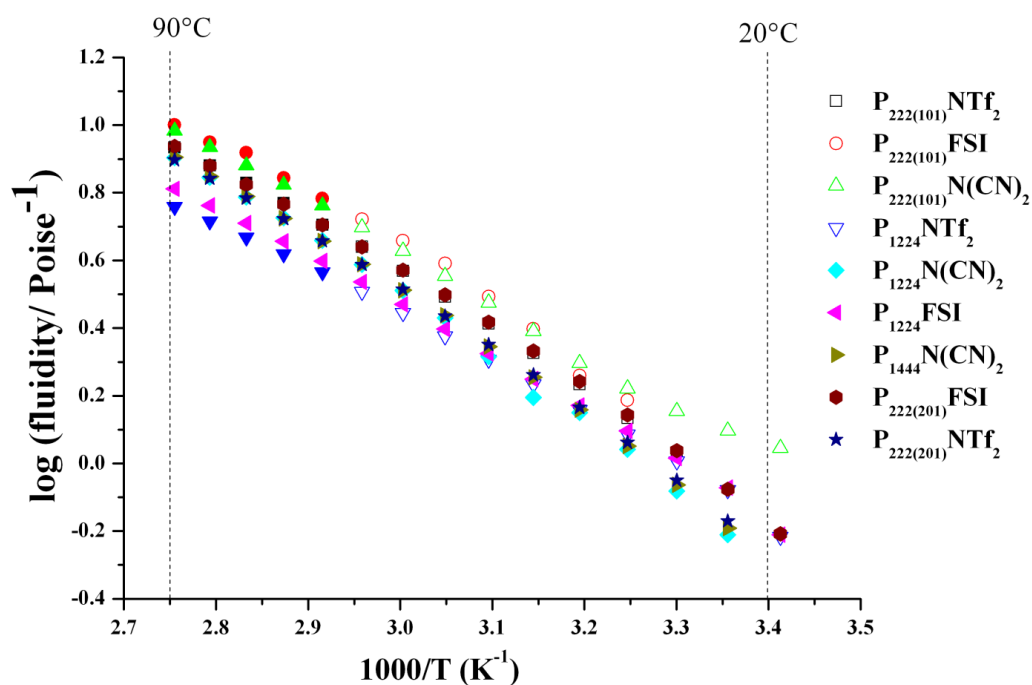


Figure 7.10: Logarithmic plot of fluidity as function of the inverse of temperature, Empty symbols indicate that at the temperature of measurement the sample was partly crystalline. The electrolytes were homogenous at 70 °C

Table 7.3 summarises the density, molar volume, molar concentration, molar conductivity and viscosity of the electrolytes at room temperature.

Figure 7.10 shows the effect of temperature on the fluidity of the ionic liquid electrolytes and similar Arrhenius-like trends are observed for the different systems with some downward (VTF-like) curvature appearing at the lower temperatures as discussed in Chapter 6.

Ionic conductivity of the electrolytes

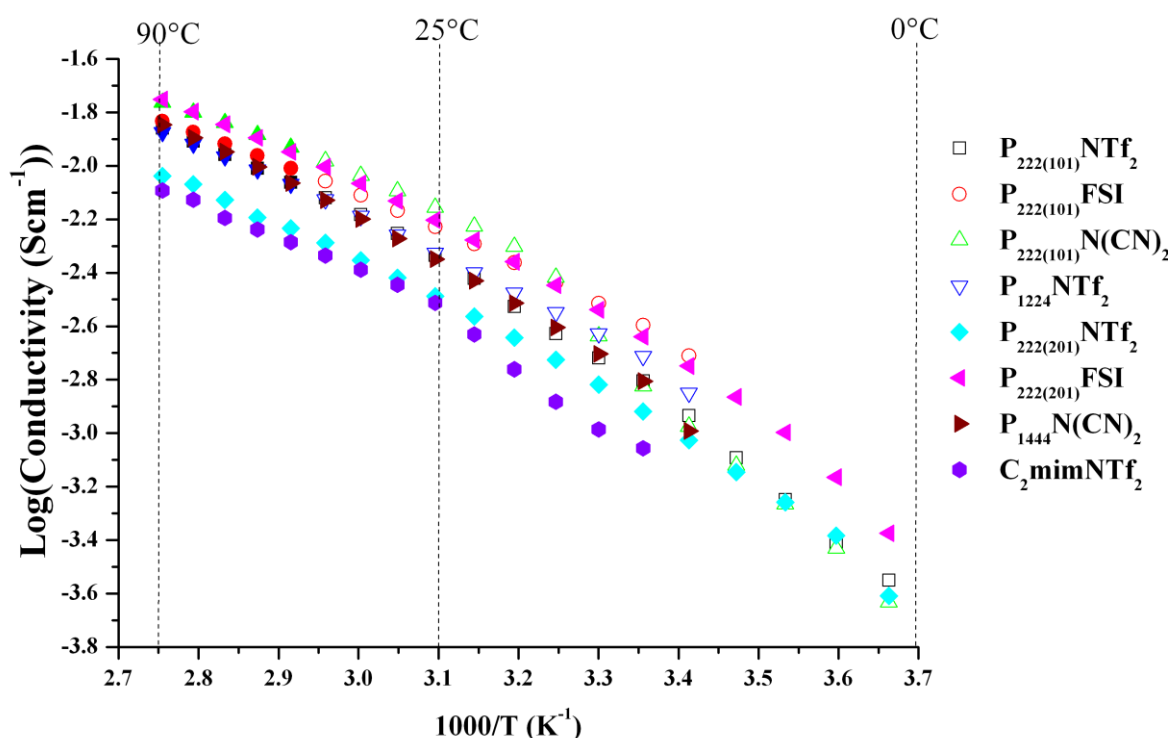


Figure 7.11: The ionic conductivity of the electrolytes as function of inverse of temperature, Empty symbols indicate that at the temperature of measurement the sample was partly crystalline. The electrolytes were homogenous at 70 °C

The phosphonium based ionic liquids electrolytes show good ionic conductivity despite the fact that their viscosities are quite high as shown in Figure 7.11. Figure 7.12 presents a Walden plot of this data; all of the phosphonium ionic liquid electrolytes lie between the ideal line and the 10 % ionisation line. Thus, they are considered to be good ionic liquids, and there is a low degree of association between all the species present in the electrolytes.

7. Ionic liquids in dithienothiophene based organic dye sensitised solar cells

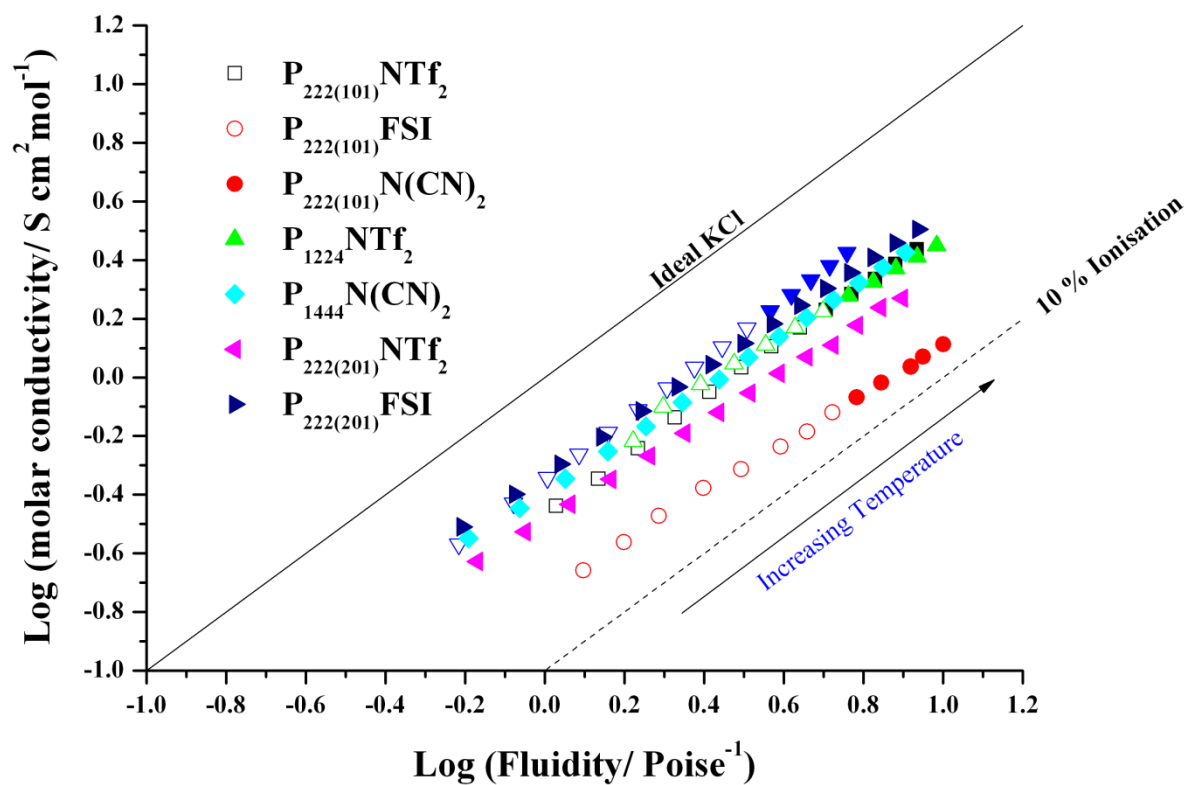


Figure 7.12: Walden plots of molar conductivity versus fluidity of phosphonium based ionic liquid electrolytes. The straight line is the “ideal” Walden line for 1 M KCl. Empty symbols indicate that at the temperature of measurement the sample was partly crystalline. The electrolytes were homogenous at 70 °C

Table 7.3: The physical properties of the electrolytes at 30 °C.

Electrolytes	ρ (gcm^{-3}) (± 0.01)	V_m ($\text{cm}^3 \text{mol}^{-1}$)	σ (mS cm^{-1}) (± 1)	Λ (molar conductivity) ($\text{S cm}^2 \text{mol}^{-1}$)	η (Poise) (± 0.1)
P₂₂₂₍₂₀₁₎NTf₂	1.49	192	1.51	0.289	1.12
P₂₂₂₍₂₀₁₎FSI	1.49	174	2.89	0.497	1.19
P₂₂₂₍₁₀₁₎NTf₂	1.51	190	1.91	0.357	0.94
P₂₂₂₍₁₀₁₎FSI	1.50	170	1.41	0.236	0.82
P₂₂₂₍₁₀₁₎N(CN)₂	1.40	158	2.31	0.364	0.81
P₁₂₂₄NTf₂	1.49	191	2.36	0.444	0.99
P₁₄₄₄N(CN)₂	1.31	181	1.98	0.447	1.15

Effect of temperature

Figure 7.13 displays the effect of temperature on the apparent diffusion coefficients of triiodide. The diffusion coefficient of I_3^- increased as the temperature rises. This increase in the mobility of the redox species is related to the increase in the limiting current and a drop in the viscosity of the system with temperature. The transport of triiodide is also governed by the Grotthuss bond exchange mechanism, thereby further increasing the mobility of the triiodide, despite the fact that the electrolyte system is quite viscous.⁵²

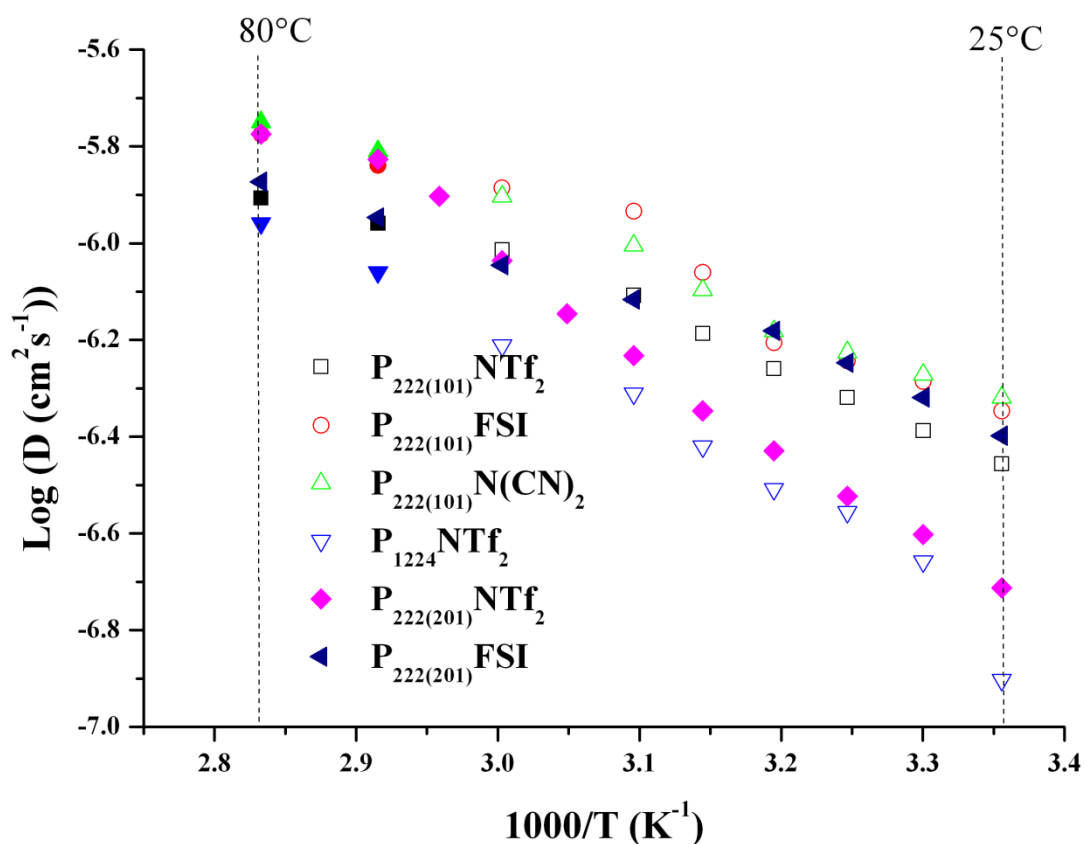


Figure 7.13: The triiodide diffusion coefficient versus temperature. Empty symbols indicate that at the temperature of measurement the sample was partly crystalline. The electrolytes were homogenous at 70 °C

7.3.4 Current-Voltage measurements

7.3.4.1 Effect of solvents on the sensitization of electrodes using THD1 dye

It is possible that dyes dissolved in different solvents will show different behaviour as a result of interactions between the sensitizer and the solvent. For this reason, an appropriate solvent for the dyeing of the semiconductor is required to accomplish high solar-to-current conversion efficiencies. To select the appropriate solvent for the new organic sensitizers discussed above, the THD1 dye was dissolved in a variety of solvents, and then applied to the TiO₂ films, and the properties of the resultant DSSC measured. Figures 7.14 and 7.15 show the IPCE spectra and the IV characteristics of THD1-based dye sensitised solar cells prepared using different dye baths. Table 7.4 summarises the photovoltaic data obtained from the IV curves and the IPCE spectra. The IPCE data shows different behaviour

depending on the solvents used for the sensitisation of TiO₂ photoanode, and correspondingly, a large difference in the conversion efficiency of the THD1-based DSSCs is observed.

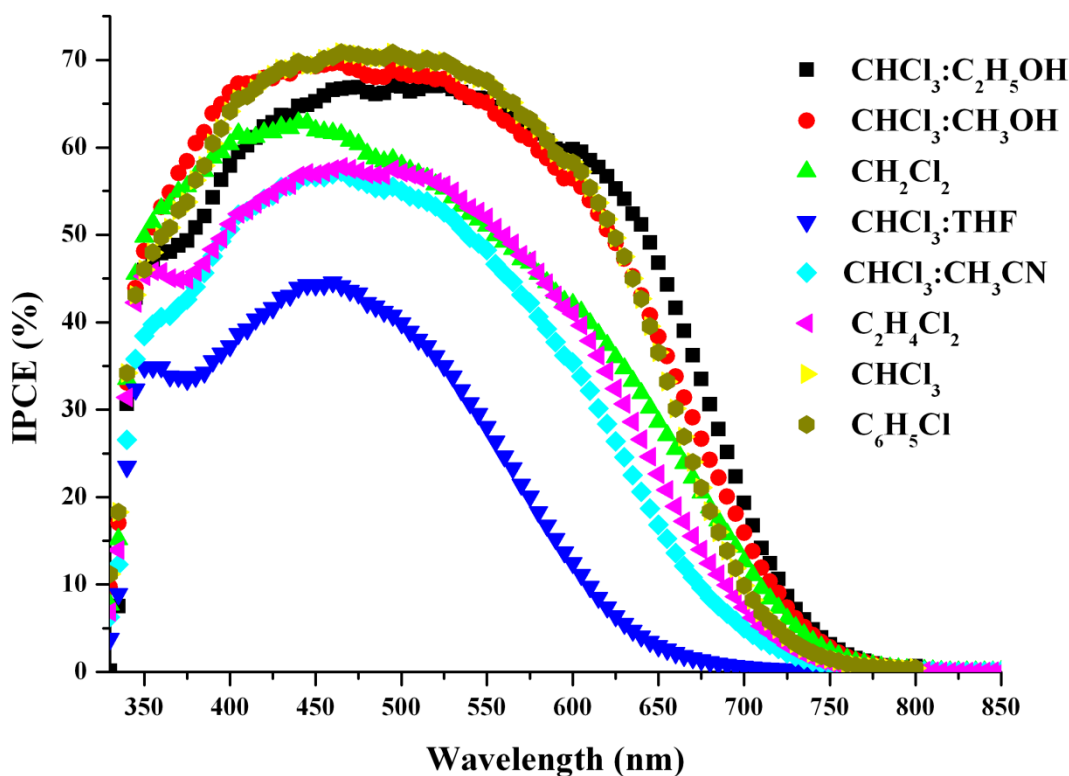


Figure 7.14: IPCE of THD1 prepared using different dye solvents

The worst cell performance was obtained using a dye mixture of THF and chloroform ($\eta = 2.6\%$), and the best power conversion efficiency was obtained using a mixture of chloroform and ethanol ($\eta = 7.3\%$). A broad spectrum (330–650 nm) with IPCE values more than 65% was obtained from the mixture of chloroform and ethanol, whereas a narrow IPCE spectrum with 45% at 460 nm was produced using the mixture of THF and chloroform. The IPCE shows a narrow spectrum in the case of the mixture of THF and chloroform, and this correlates well with the IV characteristics, which show that the photocurrent is quite low compared to the other solvents. Using a mixture of acetonitrile and chloroform, or neat dichloromethane or neat dichloroethane, each display similar IPCE behaviour, with a small shift to lower wavelength and therefore decrease the amount of photons adsorbed in the region between 650 nm and 500 nm, giving rise to a loss in photocurrent. The maximum IPCE is achieved at 440 nm for dichloromethane (63%) and at 465 nm for either dichloroethane or mixture of acetonitrile and chloroform: 58% and 57

7. Ionic liquids in dithienothiophene based organic dye sensitised solar cells

% respectively. Even though the IPCE is similar for the DSSCs made using the dye solutions of neat chloroform, neat chlorobenzene, chloroform:MeOH and chloroform:EtOH, one can see a small red shift for the chloroform:EtOH; more light is harvested in this region, thus increasing the device performance.

Figure 7.15 shows the current-voltage characteristics of the dye sensitised solar cells using THD1 sensitiser applied using different solvents, under standard AM 1.5 solar light conditions. At full sunlight, THD1 from a mixture of chloroform and ethanol gives an I_{sc} of 14.7 mA cm^{-2} , a V_{oc} of 698 mV, a ff of 0.70 and an $\eta = 7.1 \%$. They all have similar fill factors, except for the one containing dichloromethane, where the fill factor is only 0.63. There are many factors that can affect the fill factor. One main factor is due to the series and shunt resistance, having a great impact in the power output. As shown in Figure 7.15, the IV curve of the THD1 device sensitised in dichloromethane shows high series resistance and a low shunt resistance, compared to those prepared using other dyeing solvents. This can arise due to a defect in the cell, a bad contact or high sheet resistance of the counter electrode. The mixture of THF and chloroform also shows low V_{oc} , which may be due to an increase in series resistance or higher interfacial charge recombination reactions.

The difference in device efficiency is mainly due to the low photocurrent compared to the device prepared using the mixture of chloroform and ethanol as the dye solution. This may be related to the amount of dye adsorbed on the surface of the TiO_2 , or dye aggregation and this is discussed further in the next section.

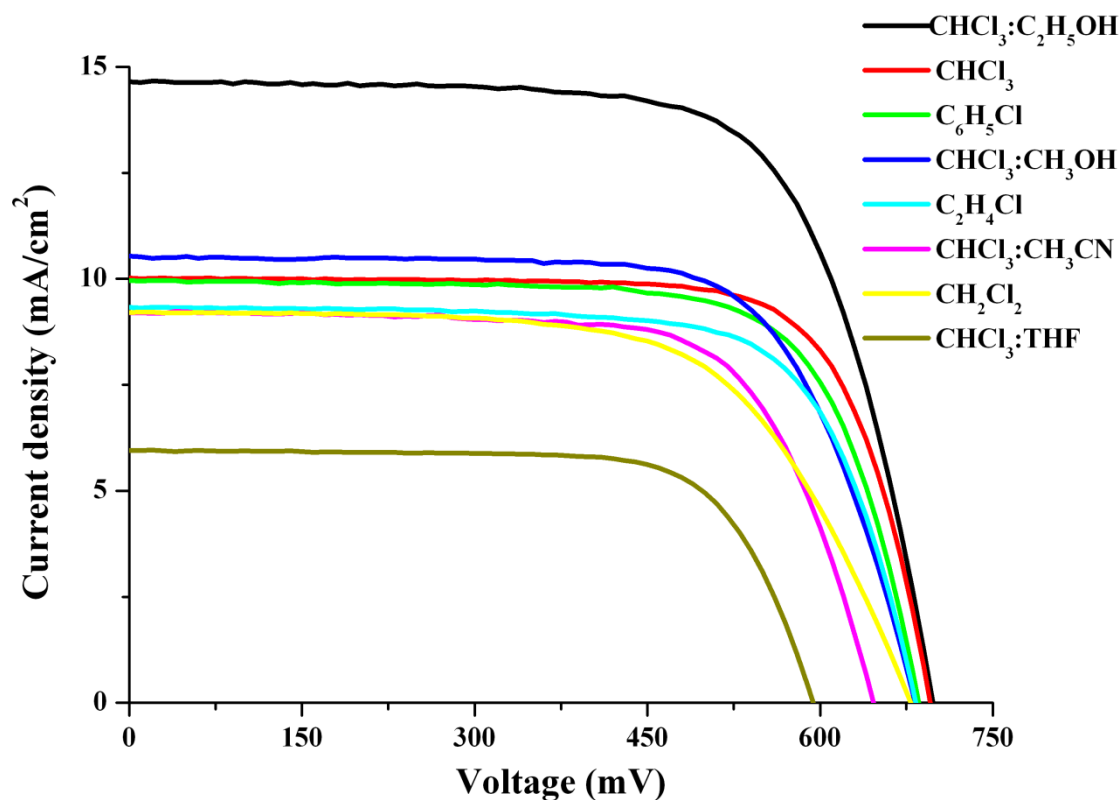


Figure 7.15: IV curves of DSSCs using the THD1 dye applied from different solvents

Table 7.4: IV parameters of DSSCs based on THD1, sensitised using different solvents.

Solvent	V_{oc} (mV)	I_{sc} (mA cm ⁻²)	ff	H (%)	IPCE (%) (λ_{max} nm)	Γ molecules cm ⁻² μ m ⁻¹
CHCl ₃ :THF	594 (\pm 1)	6.0 (\pm 0.2)	0.72 (\pm 0.01)	2.6 (\pm 0.1)	45 (440)	0.13 x 10 ¹⁴
CHCl ₃ : CH ₃ CN	646 (\pm 1)	9.2 (\pm 0.2)	0.70 (\pm 0.02)	4.2 (\pm 0.1)	57 (465)	2.9 x 10 ¹⁵
CH ₂ Cl ₂	679 (\pm 5)	9.2 (\pm 0.6)	0.63 (\pm 0.02)	4.0 (\pm 0.1)	63 (440)	2.2 x 10 ¹⁵
C ₂ H ₄ Cl ₂	683 (\pm 2)	9.3 (\pm 0.5)	0.72 (\pm 0.01)	4.6 (\pm 0.2)	59 (465)	3.5 x 10 ¹⁵
C ₆ H ₅ Cl	686 (\pm 2)	10.0 (\pm 0.1)	0.72 (\pm 0.01)	4.9 (\pm 0.3)	70 (465)	1.7 x 10 ¹⁵
CHCl ₃ : CH ₃ OH	683 (\pm 2)	10.5 (\pm 0.2)	0.70 (\pm 0.01)	5.1 (\pm 0.2)	69 (450)	3.1 x 10 ¹⁵
CHCl ₃	696 (\pm 3)	10.0 (\pm 0.2)	0.75 (\pm 0.01)	5.2 (\pm 0.2)	70 (455)	1.8 x 10 ¹⁵
CHCl₃: C₂H₅OH	698 (\pm 1)	14.7 (\pm 0.2)	0.70 (\pm 0.01)	7.1 (\pm 0.1)	68 (445)	3.2 x 10 ¹⁵

Irradiation light AM 1.5 simulated solar light (100 mW cm⁻¹) at room temperature: working area is 0.16 cm²; standard electrolyte (Table 7.2). The concentration of the dye is 0.2 mM in the various solvents.

7. Ionic liquids in dithienothiophene based organic dye sensitised solar cells

UV spectroscopy measurements to study the behaviour of THD1 dye in different solvents

To understand the change in performance of the DSSCs prepared using different dye solutions, the amount of dye adsorbed and the adsorption spectra of THD1 in solution and on the surface of TiO₂ was measured, and is shown in Figures 7.16 and 7.17. The amount of dye adsorbed was estimated by desorbing the dye into a basic solution and measuring the absorption of the resultant solution.

In dichloromethane, dichloroethane and chloroform, THD1 displays similar absorption spectra (Figure 7.16), but a slight blue shift is observed in chlorobenzene. A significant hypsochromic shift (blue shift) occurred in the chloroform/ethanol, methanol/chloroform, acetonitrile/chloroform and tetrahydrofuran/chloroform mixtures, which may be due to the increase in polarity of the solvent. Another possibility is that the dye is capable of forming hydrogen bonding with the ethanol or methanol solvent, or the fact that the dye is capable of self-dimerisation through the carboxylic groups. Further, dye containing a conjugated linker can be quite sensitive to the presence of moisture and oxygen, which can cause degradation of the dye over time. Yang *et al.*⁵³ have also observed a blue shift depending on the solvent used, and they attributed the effect to the strong interaction of the dye molecule with the polar solvent, thus weakening the O-H bond of the carboxylic acid, and as a consequence, reducing the electron-withdrawing ability of the carboxylic group. For a device to have high conversion efficiency, absorption in the red is preferable, which is not the case for the THD1 sensitiser in some solvents.

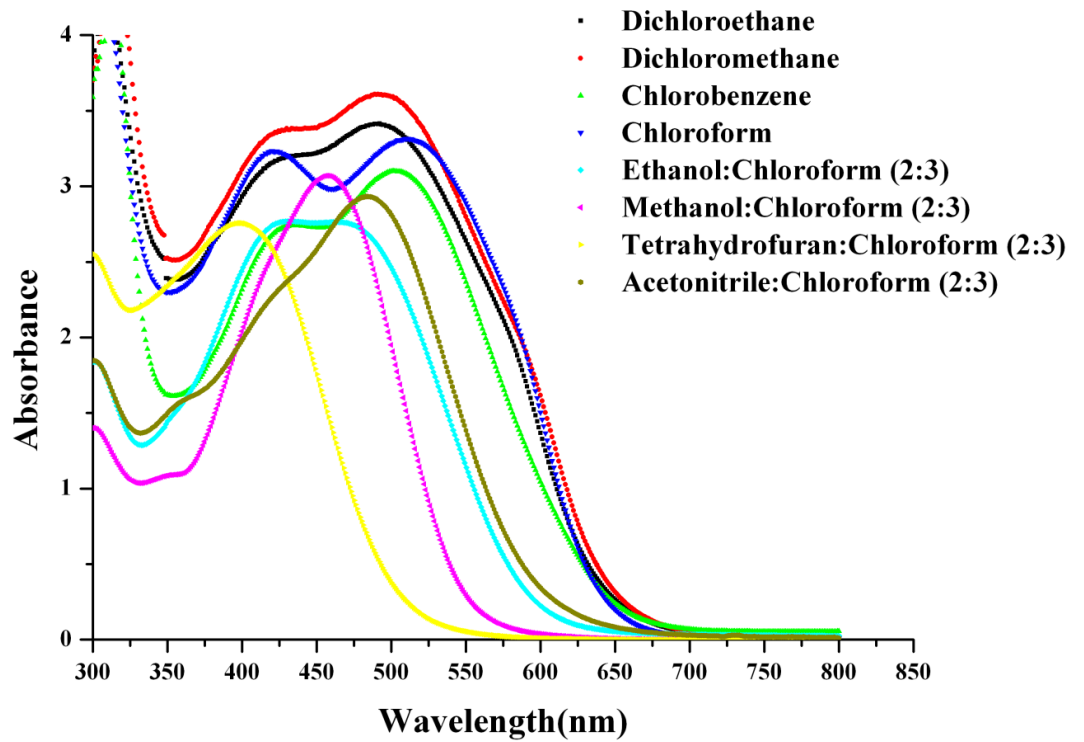


Figure 7.16: Absorption spectra of THD1 in different solvents

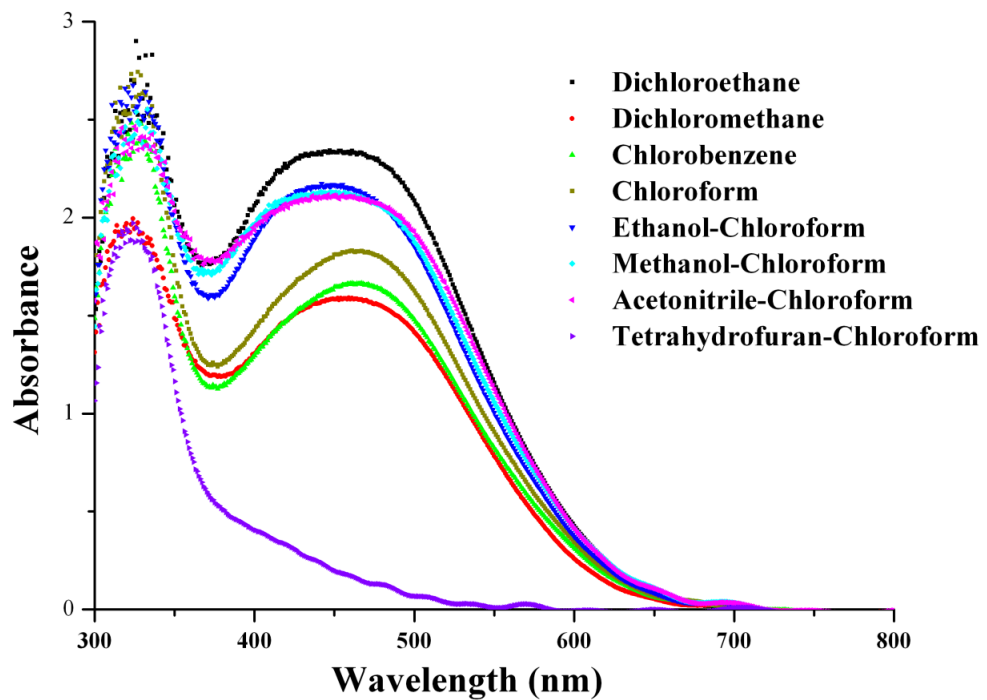


Figure 7.17: Absorption spectra of THD1 adsorbed onto TiO₂ from different solutions

7. Ionic liquids in dithienothiophene based organic dye sensitised solar cells

The amount of dye adsorbed on the TiO₂ is summarised in Table 7.4. From the results, we can conclude that the decrease in photocurrent of the THD1 based solar cells made using the various solvents can be related to the amount of dye adsorbed on the TiO₂. A decrease in the amount of dye adsorbed leads to a decrease in photocurrent, as shown in the case of THF:chloroform, where there is the least amount of dye adsorbed and the photocurrent generated from the device is the lowest, at 5.9 mA cm⁻². In this solvent mixture, the dye is not able to bind properly to the surface of the TiO₂. Visual inspection of the film also showed that the film did not look as well dyed as the others, which show a greater intensity in colour.

Films from the mixture of chloroform and ethanol show a broader absorption compared to the others, which can lead to an increase in the IPCE spectrum as observed in Figure 7.14. In the case of dichloroethane, chloroform and chlorobenzene solvents, no such behaviour is observed. Even though they give DSSCs with similar IPCEs for the devices using chloroform:ethanol, with similar amounts of dye adsorbed, the device performance is quite poor. Thus the amount of dye adsorbed is not the only factor that can influence the photocurrent; charge injection and charge collection are also important in determining the overall performance of the DSSCs. The presence of unattached dyes on the surface can also lead to a decrease in the performance of the devices.

The effect of dye solvent on the performance of the DSSC is quite complex. There are several factors, other than the amount of dye adsorbed on the surface of the semiconductor, that can affect the performance of the solar cells. For instance, the binding mode of the dye onto the surface of the TiO₂, which is connected to the injection process, can differ between the various solvent systems. The way in which the dyes are attached or aligned onto the surface of the TiO₂, also play an important role in the device efficiency. Wang and co-workers⁵⁴ have shown that there are three ways that coumarin dyes can be fixed onto the TiO₂ surface. The carboxylic acid group can coordinate to the titanium via a unidentate mode, chelating mode or bridging mode.⁵⁵ Further characterisation is underway to verify the binding mode of the dyes reported here in the different solvents, and thus to get a better understanding of the performance of the dye in relation to the solvents used.

From the current observations, one can suggest that the mixture of chloroform and ethanol is the best co-solvent for the sensitisation of the Titania with the THD1 dye, as it gives the best device performance. Nevertheless, one should keep in mind that for other organic dyes

this mixture might not work. For instance, porphyrin dyes will not be as efficient in this mixture due to presence of residual acid in chloroform. Thus, the choice of solvent depends strongly on the sensitisers. Furthermore, optimisation of the dye solution is being undertaken to try to achieve further improvements.

7.3.4.2 The effect of chenodeoxycholic acid and film thickness using standard electrolyte

In this section, the effect of adding different amounts of co-adsorbent and changing the film thicknesses were investigated. According to previous studies, an improvement in the performance of the solar cells, via an increase in both photocurrent and open circuit voltage, was observed with addition of chenodeoxycholic acid (DCA) in the dye solution.⁵⁶ The addition of co-adsorbent is known to suppress the dark current and also prevent dye aggregation.

Figure 7.18 displays the photocurrent density-photovoltage of the best performing devices using standard acetonitrile-valeronitrile electrolytes (see Table 7.2 for the composition). Table 7.5 summarises the photovoltaic data for the solar cells based on THD1, THD2 and THD3 dyes, with and without co-adsorbent, different thicknesses of Titania film, with and without scattering layer, under full sunlight. As observed from Table 7.5, THD2 shows low conversion efficiency ($\eta = 5.5\%$) without any co-adsorbent, with a film thickness of 6 microns. Addition of 10 mM chenodeoxycholic acid results in an increase in both V_{oc} and I_{sc} for all three dyes (highlighted in red). A decrease in the UV-Vis adsorption spectra of the THD1, THD2 and THD3 is observed in presence of co-adsorbent (see Figure 7.18). Even though there is a decrease in the amount of dye adsorbed on the TiO_2 , the I_{sc} is still higher, as shown in Table 7.5. The main reason for such behaviour is a decrease in dye aggregation, and thus more efficient electron injection into the conduction band of the TiO_2 . Organic dyes are known to easily aggregate; from observation of the dye solution, when the TiO_2 is immersed in the dye bath, some of the dyes precipitate into the solution, whereas in the presence of chenodeoxycholic acid (DCA), no such behaviour was observed. The increase in V_{oc} is attributed to the shift in the conduction band edge of the TiO_2 , as demonstrated in Chapter 5, where treating the surface with an acid showed an upward movement of the band edge towards more negative potentials.

7. Ionic liquids in dithienothiophene based organic dye sensitised solar cells

Chenodeoxycholic acid might also be present at the surface of the Titania, forming a protecting layer, thus reducing the recombination reaction between the injected electrons and the triiodide. There is no direct evidence for such behaviour, but Wang *et al.* have studied the effect of chenodeoxycholic acid with a coumarin dye and they have used FTIR measurements to demonstrate that the chenodeoxycholic acid is present on the surface of the TiO₂.²⁰

Table 7.5: Data extracted from IV curves.

Dyes	Film – thickness (μm)	Concentration of co-adsorbent (mM)	V _{oc} (mV)	I _{sc} (mA cm ⁻²)	ff	η (%)
TH-D1	6	0	700	11.0	0.73	5.61
TH-D1	6+6 (sl)	10	686	11.3	0.77	5.94
TH-D1	12+6 (sl)	10	710	14.4	0.70	7.17
TH-D2	6	0	695	11.4	0.69	5.46
TH-D2	6+6 (sl)	10	705	12.1	0.72	6.16
TH-D2	12+6 (sl)	10	704	13.0	0.71	6.48
TH-D3	6	0	720	13.0	0.69	6.37
TH-D3	6+6 (sl)	0	716	12.7	0.71	6.49
TH-D3	6+6 (sl)	2	718	13.4	0.73	7.02
TH-D3	6+6 (sl)	10	729	13.2	0.73	7.01

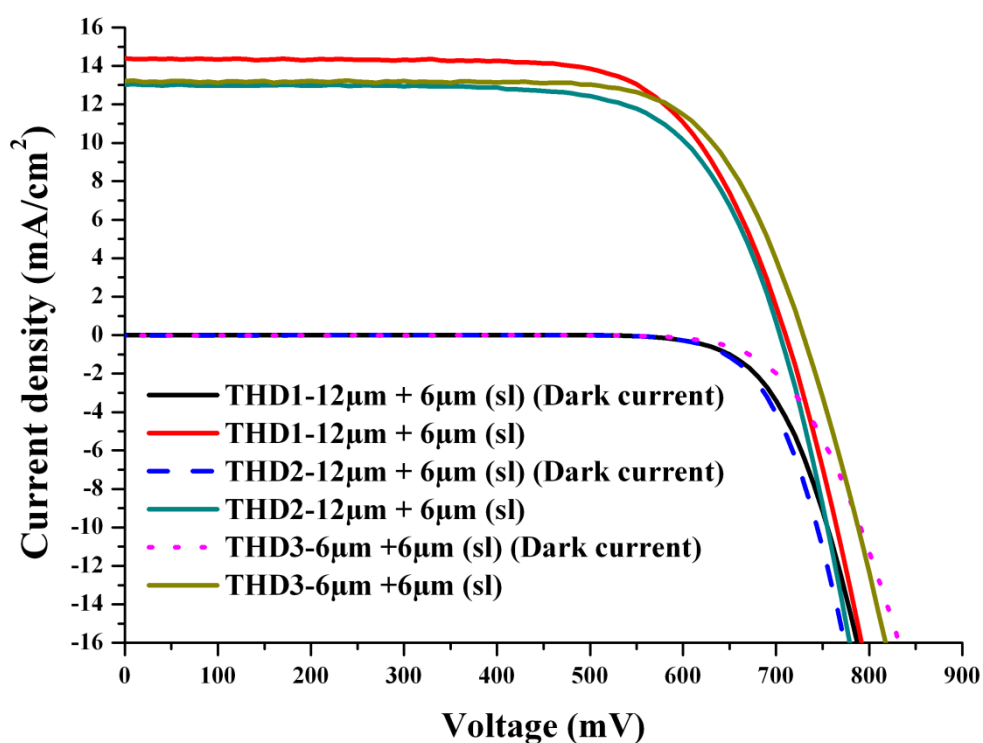


Figure 7.18: IV curves of THD1, THD2 and THD3 DSSCs using a 12 μm transparent film and a 6 μm scattering layer (sl) for THD1 and THD2 and a 6 μm transparent film with a 6 μm scattering layer for THD3

Figure 7.19 displays the IPCE, as a function of wavelength, for the best performing devices using the three sensitiser THD1, THD2 and THD3. Figure 7.19 also compares the IPCE of THD3 with and without the addition of 10 mM chenodeoxycholic acid. THD1 and THD2 show similar IPCE spectra, with the maximum IPCE of 67 % occurring at a wavelength of 500 nm for both dyes. THD1 and THD2 are more red shifted compared to THD3, thus they are able to absorb more photons in this region, generating higher current densities. The maximum IPCE is obtained with the THD3 sensitiser. The maximum IPCE for THD3 in the presence of chenodeoxycholic acid is at 450 nm and is 74 %; without any co-adsorbent. The maximum IPCE is reached at a wavelength of 455 nm and is 72 %. According to the literature, the characteristic value for unity electron injection is 85 % and the 15 % loss is mainly due to the loss of light by reflection and absorption of the TCO glass.²⁰ The IPCE values obtained for the three dyes is lower than 85 %, meaning that electron injection, light harvesting and electron-collecting efficiency are not in unity.²⁰ Additional improvements are therefore required to optimise these dyes.

Optimisation of the electrolytes can lead to an enhancement in the device performance, while additional absorption in the infrared region can augment the photocurrent density.

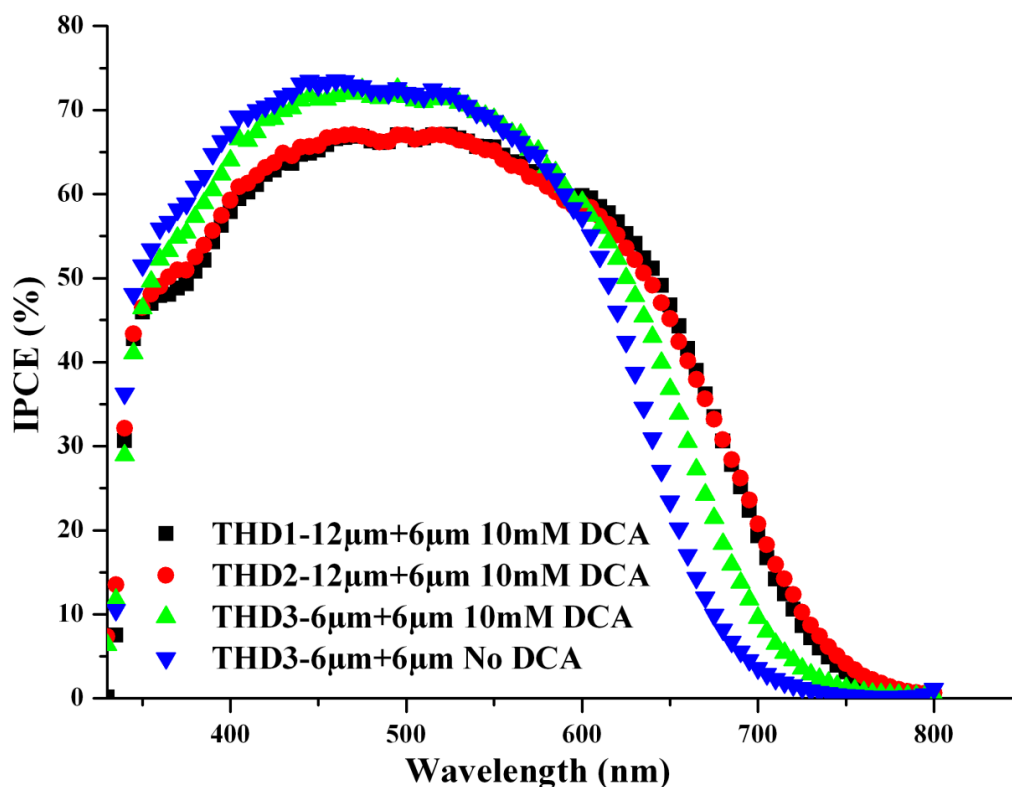


Figure 7.19: IPCE of THD1, THD2, THD3, with and without any co-adsorbent

Figure 7.20 shows the UV-Vis absorption spectra of THD3, THD2 and THD1, on the TiO_2 surface, with and without DCA. The dye adsorption is decreased upon addition of 10 mM chenodeoxycholic acid. The drop in dye adsorption shows that there is competition between the co-adsorbent and the dye molecules for adsorption onto the TiO_2 surface. The amount of dye attached to the surface of the TiO_2 is 2.2×10^{15} molecules $\text{cm}^{-1} \mu\text{m}^{-1}$ without co-adsorbent, and with co-adsorbent is 1.8×10^{15} molecules $\text{cm}^{-1} \mu\text{m}^{-1}$.

For the THD3 sensitiser, there is almost no difference between the maximum absorption wavelength on the TiO_2 in the presence and absence of chenodeoxycholic acid, even though a decrease in absorption is observed in the UV-Vis absorption spectra of THD3 on the TiO_2 film (Figure 7.20). Similar behaviour was observed by Jiang and co-workers,⁵⁷ where they also observed no shift in the maximum spectra of their triphenylamine

sensitiser in the presence of a co-adsorbent, where they attributed this behaviour to several possibilities, with one of them being that the “agglomerates” formed might be different to the well known H or J aggregates, and thus not detectable in the absorption spectra.

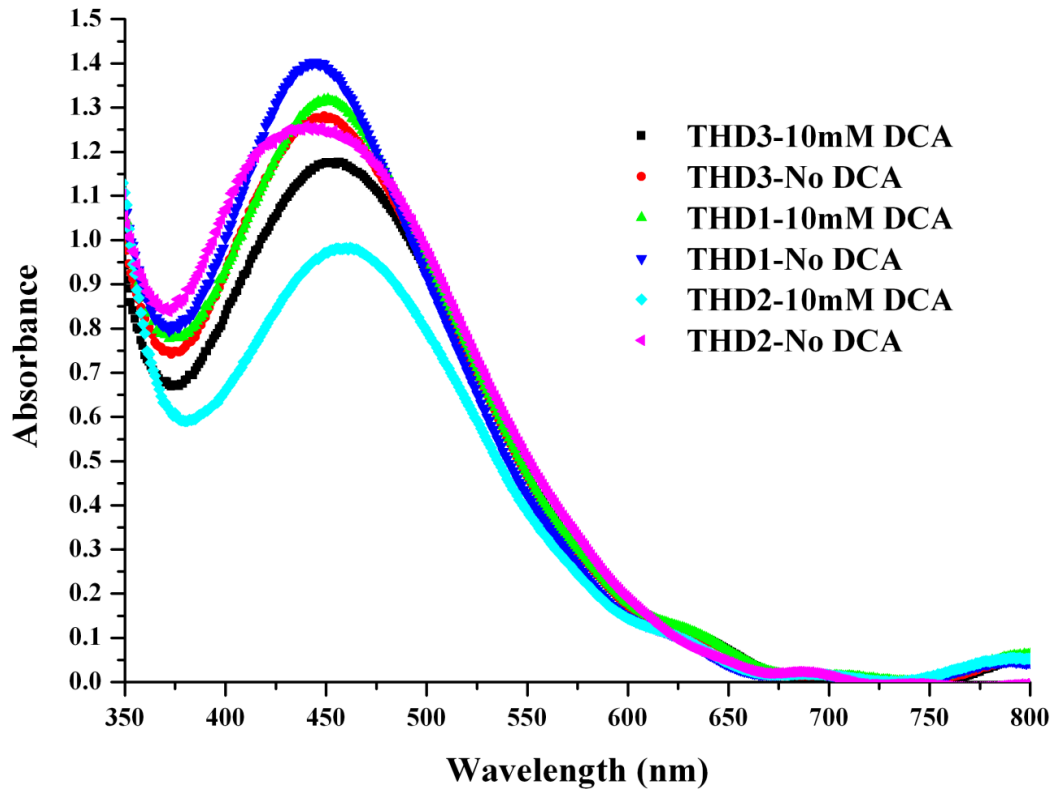


Figure 7.20: Absorption spectra of THD3 in the presence of a co-adsorbent

To summarise, THD1 shows the best performance compared to THD2 and THD3 in standard acetonitrile-valeronitrile based electrolytes. The addition of chenodeoxycholic acid gives an increase in V_{oc} and I_{sc} , thus increasing the conversion efficiency of the devices. The presence of a scattering layer without any chenodeoxycholic acid gives a slight improvement in the performance of the dye. The increase in V_{oc} in the presence of DCA is probably due to the negative shift in the electrochemical potential of the TiO_2 . Also, the presence of the acid protects the surface from oxidised species present in the electrolyte, thus decreasing the recombination reactions.

7. Ionic liquids in dithienothiophene based organic dye sensitised solar cells

7.3.4.3 Photovoltaic performance of DSSCs utilising phosphonium ionic liquids

The main limiting factor in the use of ionic liquids in DSSCs is the slow diffusion of the redox species in the ionic liquid, which limits their potential use, due to generation of low current densities, leading to a lower overall efficiency. In order to resolve this problem, a thin semiconductor film is required to reach high conversion efficiencies. In order to compensate for the low adsorption of dye for such thin films, a higher molecular extinction coefficient dye is necessary, hence the interest in using thiophene derivative organic dyes with the phosphonium ionic liquids. Phosphonium ionic liquids were investigated as they are known to be more thermally stable than the aliphatic ammonium based ionic liquids. Even though the phosphonium ionic liquids synthesised have slightly higher viscosity than the imidazolium based ionic liquids, they have good ionic conductivity and the viscosity can be tuned by adding additives such as lithium iodide (LiI), 1-methylbenzimidazole (NMB) or nanoparticles. THD1, THD2 and THD3 dyes, which have a molar extinction coefficient of more than $30,000 \text{ M}^{-1} \text{ cm}^{-1}$, were studied for the first time with the newly synthesised phosphonium ionic liquids. The effect of the thickness of the nanocrystalline Titania films on the photovoltaic performance of the molten salts was studied. Changing the particle size of the transparent layer was also investigated, to see whether any improvement could be obtained due to better permeation of the electrolyte into the nanoporous network of the photoanode. Ruthenium dye based DSSCs were also investigated, for comparison with the performance of the new organic dyes with the phosphonium ionic liquids.

7.3.4.3.1 Phosphonium ionic liquid electrolytes with Z907 and N719

In this section, we demonstrate the use of some new phosphonium ionic liquids as described in Chapter 6, with iodine, N-methylbenzimidazole, lithium iodide, 1-ethyl-3-imidazolium iodide and 1,1-dimethylimidazolium iodide, as the ionic liquids or soft solid electrolytes in the dye sensitised solar cells. A standard acetonitrile (ACN) based electrolyte was used as a control for comparison with the ionic liquid electrolytes. Two ruthenium based sensitisers were investigated; Z907 and N719. Z907 sensitisers are known to perform well with ionic liquid electrolytes in the presence of a co-adsorbent. These sensitisers were used as a reference and compared to the organic sensitisers.

Figures 7.21 and 7.22 illustrate the photocurrent density - voltage curves of the DSSCs using Z907 and N719 dyes and a variety of phosphonium ionic liquid electrolytes, compared to a standard ACN electrolyte. The efficiency of the Z907 and N719 devices with the standard electrolyte is 6.8 % and 8.1 % respectively. This is somewhat lower compared to the best literature value, probably due to the difference in the technique used to deposit the film, the use of different paste and the substrate itself.⁹ The best performance was obtained using the mixture containing $P_{222(101)}NTf_2/C_2mimI/C_1mimI/LiI/I_2/NMB$ (molar ratio 14:12:12:1:1.67:4) with the Z907 dye, giving an I_{sc} of 10.6 mA cm^{-2} , a V_{oc} of 672 mV, a fill factor of 0.75 and an efficiency 5.3 % with the Z907 dye. The $P_{222(101)}N(CN)_2/C_2mimI/C_1mimI/LiI/I_2/NMB$ (molar ratio 14:12:12:1:1.67:4) electrolyte gave the best performance for the N719 dye, giving an I_{sc} of 9.4 mA cm^{-2} , a V_{oc} of 734 mV, a fill factor of 0.77 and an efficiency of 5.5 %.

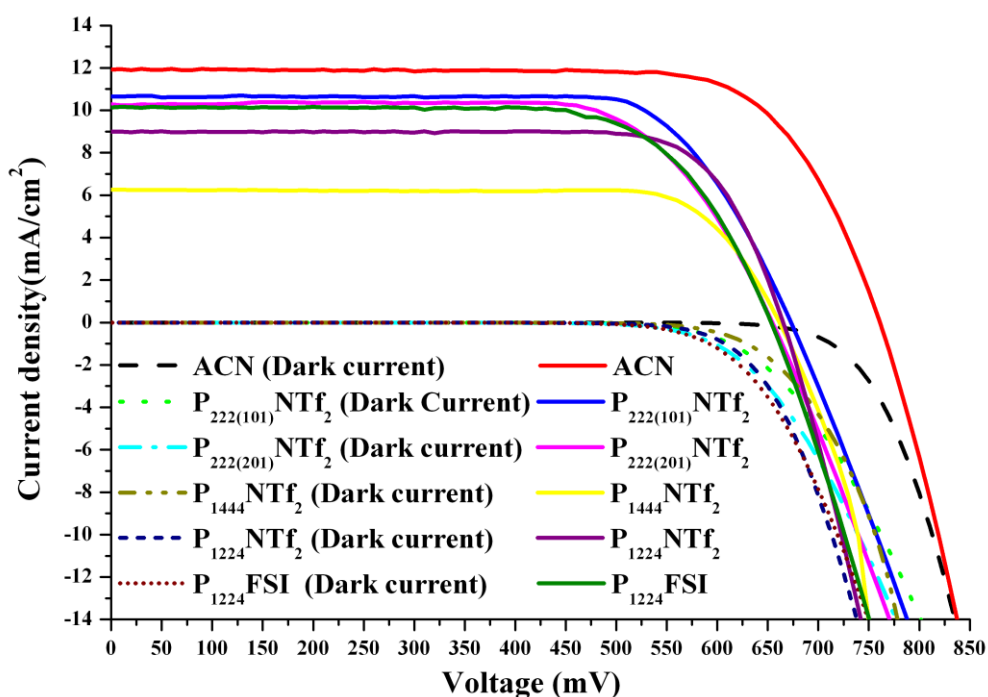


Figure 7.21: IV curves of Z907-based DSSCs using various phosphonium ionic liquid electrolytes, and a control experiment using a standard molecular liquid electrolyte

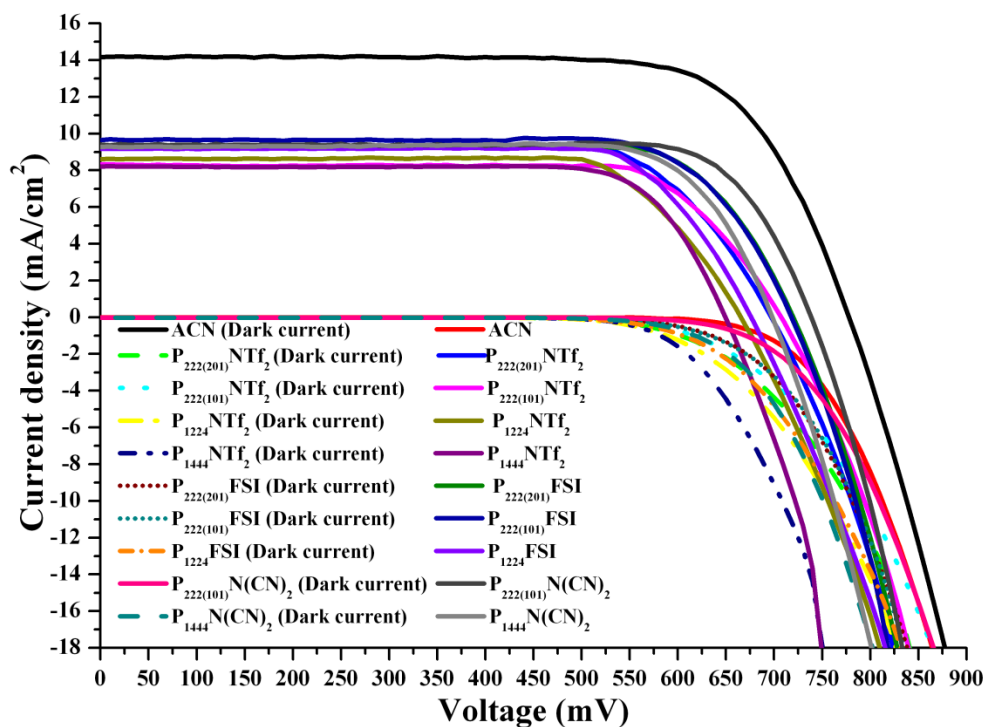


Figure 7.22: I-V characteristic of DSSCs N719, with a variety of phosphonium ionic liquid electrolytes and a control experiment using the standard acetonitrile based electrolyte (composition given in Table 7.2)

The results obtained from the ionic liquid electrolytes and the ACN electrolytes are presented in Table 7.6. For the series of ionic liquid electrolytes investigated with the Z907 dye, the $P_{222(101)}NTf_2$ electrolyte showed the best efficiency as it has better ionic conductivity and better diffusion of the triiodide ion, thus resulting in a higher photocurrent density. $P_{1444}NTf_2$ shows poor performance compared to the other phosphonium ionic liquids systems with the same phosphonium cation. $P_{1444}NTf_2$ is a solid at room temperature (see Chapter 5), with a solid-solid phase transition at $-68\text{ }^\circ\text{C}$ and a melt at $52\text{ }^\circ\text{C}$. However, addition of I_2 , LiI, NMB and the iodide salts to the $P_{1444}NTf_2$ gives a soft solid electrolyte that is completely liquid at $60\text{ }^\circ\text{C}$. Thus all the devices were back-filled at $60\text{ }^\circ\text{C}$ to make sure that the ionic liquids permeated well through the layers of the dyed TiO_2 films. Visual observation after filling the device with the soft solid electrolyte showed solidification of the electrolyte. For the $P_{1444}NTf_2$ electrolyte system, a longer settling time was necessary ($\sim 1\text{ s}$) during measurement of the IV curves for the system to equilibrate due to mass transport limitations. A loss in photocurrent density (6.3 mA cm^{-2}) occurred, which limits the performance of the device compared to the other ionic liquid electrolyte systems, which give a higher photocurrent density ($\sim 10\text{ mA cm}^{-2}$). If we compare the best

7. Ionic liquids in dithienothiophene based organic dye sensitised solar cells

performing device in the ionic liquid systems ($P_{222(101)}NTf_2$) with the ACN standard electrolyte and the Z907 dye, the major loss is in the photovoltage, where a drop of around 90 mV is observed. The decreased in V_{oc} can be partially rationalized in terms of the Nernstian shift in the redox potential of the I_3^-/I^- couple that leads to a reduced built-in potential of the solar cell.⁵⁸ The redox potential of a couple is given by the following Nernst equation:

$$E_{Redox} = E^o - \frac{RT}{2F} \ln \frac{[I_3^-]}{[I^-]^3} \quad (\text{Eq 7.4})$$

where E_{redox} is the redox potential of the I_3^-/I^- couple, E^o is the standard potential, R is the gas constant ($8.314 \text{ J K}^{-1} \text{ mol}^{-1}$), T is the absolute temperature (298 K), F is the Faraday constant (96500 C), $[I_3^-]$ is the concentration of the triiodide and $[I^-]$ is the concentration of the iodide.⁵⁸

The difference in potential $\Delta E = (E_{Redox}^{IL} - E_{Redox}^{ACN})$ calculated from equation 7.4 is 40 mV.

Another possibility for the loss in V_{oc} is the movement of the flatband potential as shown in equation 7.5, where V_{oc} depends not only of the redox potential, but also on the position of the flatband potential, when in direct contact with the electrolyte. A shift in the dark current is also observed when $[I_3^-]$ is increased, because of a higher charge recombination rate and thus causing a loss in V_{oc} .

The photovoltage of a dye sensitised solar cell is given by the following equation:

$$V_{oc} = |V_{fb} - V_{red}| \quad (\text{Eq 7.5})$$

where V_{red} is the standard reduction potential of a redox couple, V_{oc} is the open circuit photovoltage and V_{fb} is the flatband potential of the TiO_2 .

Figure 7.22 depicts the photovoltaic characteristics of N719 devices with a variety of phosphonium ionic liquids. The best performance is obtained with $P_{222(101)}N(CN)_2$ based electrolyte systems, with the device achieving a power conversion efficiency of 5.5 %. Similar performances were obtained with $P_{1224}NTf_2$ and $P_{1444}NTf_2$. The poor performance in these ionic liquids may be due to the formation of $P_{1224}I$ crystals in the $P_{1224}NTf_2$, which solidify the electrolyte over time, and $P_{1444}NTf_2$ is a solid at room temperature. Nevertheless, the performance of the devices is comparable to those we obtained using an

7. Ionic liquids in dithienothiophene based organic dye sensitised solar cells

imidazolium based electrolyte (Chapter 8) with a ruthenium dye. This is the first time that such high performances have been obtained with phosphonium based ionic liquids.

Table 7.6: Data obtained from DSSCs with Z907 and N719 dye, with a variety of phosphonium ionic liquid electrolytes and a control experiment using the standard acetonitrile based electrolyte (Figure 7.21 and Figure 7.22).

Dye	Electrolyte	V_{oc} (mV)	I_{sc} (mA/cm ²)	ff	η (%)
Z907	ACN*	761 ± 2	11.9 ± 0.1	0.75 ± 0.01	6.8 ± 0.1
	P₂₂₂₍₁₀₁₎NTf₂	673 ± 3	10.6 ± 0.1	0.75 ± 0.01	5.3 ± 0.2
	P ₂₂₂₍₂₀₁₎ NTf ₂	655 ± 2	10.2 ± 0.3	0.72 ± 0.03	4.8 ± 0.2
	P ₁₄₄₄ NTf ₂	662 ± 4	6.3 ± 0.2	0.78 ± 0.01	3.3 ± 0.2
	P ₁₂₂₄ NTf ₂	657 ± 2	9.2 ± 0.1	0.76 ± 0.01	4.6 ± 0.1
	P ₁₂₂₄ FSI	653 ± 3	10.1 ± 0.1	0.74 ± 0.02	4.9 ± 0.1
N719	ACN*	778 ± 3	14.2 ± 0.1	0.74 ± 0.02	8.1 ± 0.2
	P ₂₂₂₍₂₀₁₎ NTf ₂	697 ± 8	9.3 ± 0.2	0.75 ± 0.01	4.8 ± 0.2
	P ₂₂₂₍₁₀₁₎ NTf ₂	708 ± 1	8.3 ± 0.1	0.77 ± 0.02	4.5 ± 0.2
	P ₁₄₄₄ NTf ₂	649 ± 4	8.2 ± 0.3	0.77 ± 0.01	4.1 ± 0.3
	P ₁₂₂₄ NTf ₂	665 ± 2	8.3 ± 0.5	0.74 ± 0.04	4.4 ± 0.2
	P ₂₂₂₍₂₀₁₎ FSI	720 ± 1	9.3 ± 0.4	0.78 ± 0.01	5.2 ± 0.4
	P ₂₂₂₍₁₀₁₎ FSI	718 ± 1	9.7 ± 0.1	0.77 ± 0.01	5.3 ± 0.2
	P ₁₂₂₄ FSI	676 ± 3	9.2 ± 0.3	0.78 ± 0.01	4.8 ± 0.1
	P₂₂₂₍₁₀₁₎N(CN)₂	734 ± 5	9.4 ± 0.2	0.77 ± 0.01	5.5 ± 0.2
P ₁₄₄₄ N(CN) ₂	698 ± 2	9.3 ± 0.1	0.77 ± 0.01	5.0 ± 0.1	

*standard electrolyte for ruthenium chromophore.

Figure 7.23 shows the IPCE spectra of N719 in selected ionic liquid electrolytes. The incident-photon-to-current conversion efficiency spectrum reveals that the maximum efficiency is 54 % at 535 nm for P₂₂₂₍₂₀₁₎NTf₂, with an I_{sc} calculated from the IPCE of 7.62 mA cm⁻², much lower than the I_{sc} from the IV curves. The IPCE for P₁₂₂₄NTf₂ is 62.8 % and I_{sc} obtained from the integration of the IPCE is 10.3 mA cm⁻². The IPCE of P₂₂₂₍₂₀₁₎FSI is 61.7 %, with a calculated I_{sc} of 9.80 mA cm⁻², which correlates well with the I_{sc} obtained from the IV plot. The IPCE of P₂₂₂₍₁₀₁₎FSI is 56.5 %, with a calculated I_{sc} of 8.53 mA cm⁻², and P₂₂₂₍₁₀₁₎N(CN)₂ is 56 % with a calculated I_{sc} of 8.43 mA cm⁻².

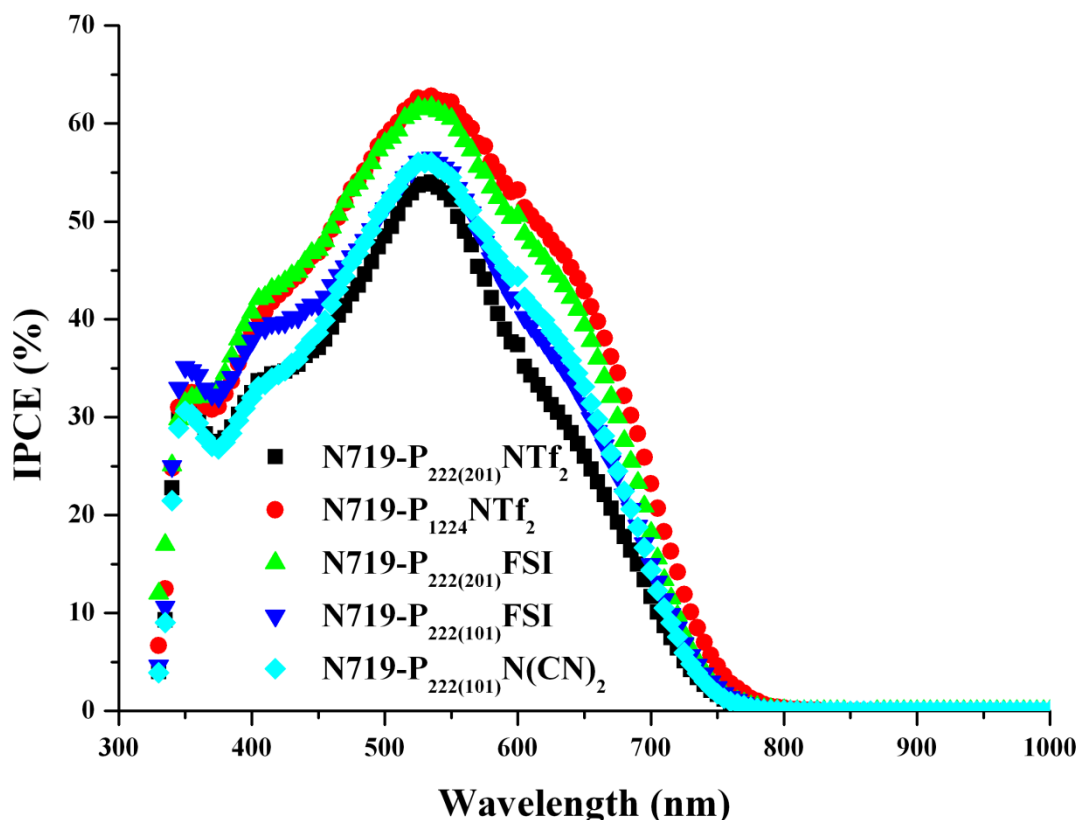


Figure 7.23: The IPCE of solar cells with various ionic liquids and N719 dye

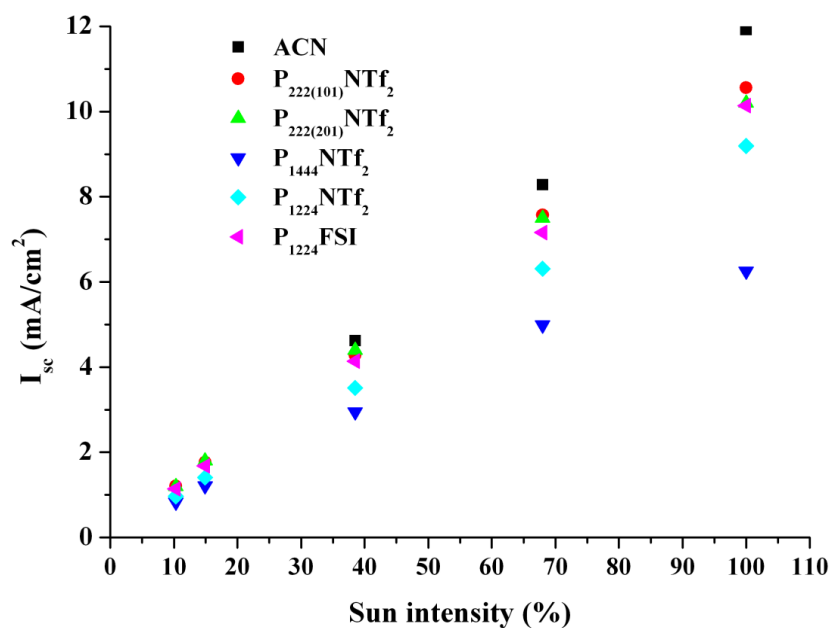
Variation of light intensity

The effect of varying the light intensity on the overall conversion efficiency of the DSSCs containing the ionic liquid electrolytes was studied. The aim of this investigation is to determine the light intensity at which the device efficiency will be at its maximum. Photoelectrochemical measurements were performed at different percentages of sun intensity, from 10 % to 100 % sun, under AM 1.5 solar spectrum with both ruthenium sensitisers. At only 15 % simulated light intensity, the solar cells containing $P_{222(201)}NTf_2$, $P_{222(101)}NTf_2$, $P_{1224}NTf_2$, $P_{1444}NTf_2$ and $P_{1224}FSI$ electrolyte mixtures gave an overall conversion efficiency of 5.6 %, 6.0 % , 4.6 % 3.8 % and 5.2 % respectively, with the Z907 dye.

7. Ionic liquids in dithienothiophene based organic dye sensitised solar cells

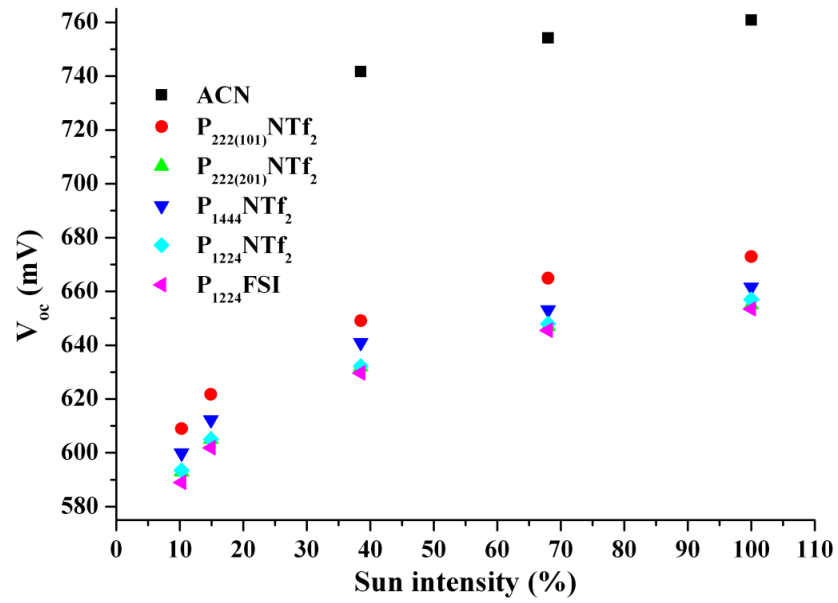
Figure 7.24 (a) shows the effect of light intensity on the photocurrent density of the ionic liquid/Z907 DSSCs. At 100 % sun, the saturation current has not yet been reached; higher sun intensities were required for such behaviour to occur, but this is beyond the limitations of the equipment. However, a gradual upward shift in photocurrent is observed in the series as the light intensity goes up. The DSSC with $P_{1444}NTf_2$ starts to show a saturation of the photocurrent density at 100 % sun intensity, due to mass transport limitations caused by the high viscosity of the electrolyte system.

Generally, an improvement in I_{sc} and V_{oc} is usually observed upon an increase in light intensity. There is no linear increase in V_{oc} and fill factor, as the light intensity increases as shown in Figure 7.24 (b) and (c). In contrast, the I_{sc} shows a linear increase over all sun intensity ranges for all of the ionic liquids except for $P_{1444}NTf_2$, which starts to reach its limiting value at 100 % sun as shown in Figure 7.24 (a).

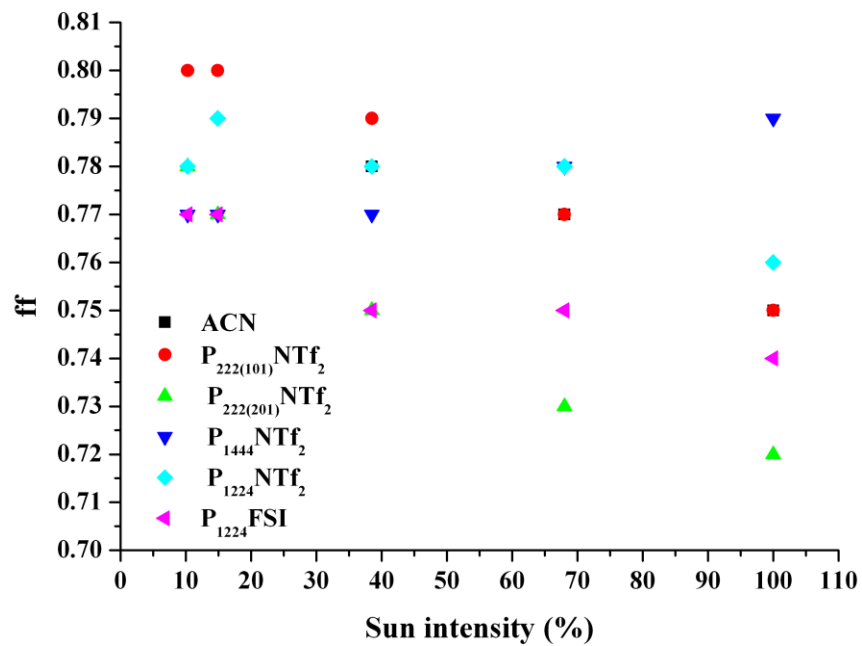


(a)

7. Ionic liquids in dithienothiophene based organic dye sensitised solar cells

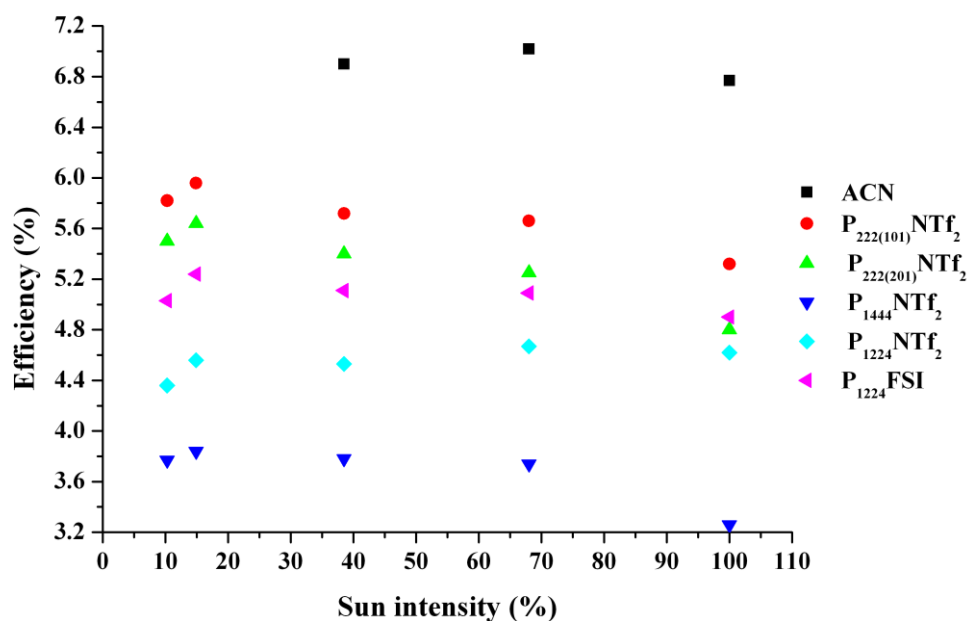


(b)



(c)

7. Ionic liquids in dithienothiophene based organic dye sensitised solar cells



(d)

Figure 7.24: Variation of (a) photocurrent density, (b) photovoltage, (c) fill factor and (d) efficiency, obtained from IV measurements, as a function of light intensity, with the Z907 dye

As the sun intensity increases, the photocurrent density also rises steadily. Figure 7.24 (b) shows the variation of photovoltage with light intensity; no great effect is observed, with the V_{oc} depending mostly on the electrolyte system. Figure 7.24 (c) shows the variation of fill factor as a function of sun intensity, where a small variation is observed in all electrolyte systems. Figure 7.26 (d) shows the variation of efficiency as a function of relative light intensity. The maximum efficiency is reached in most cases at ~15 % sun intensity, and then there is a slight drop in performance as the sun intensity rises; this seems to be due to changes in fill factor as photocurrent increases. This is the first time that such high efficiencies are obtained with phosphonium ionic liquid electrolytes using a ruthenium based sensitiser. Further improvements may yet be obtained by acid treatment, or by improving the composition of the electrolyte.

Figure 7.25 illustrates the photovoltaic characteristics of the solar cells using a lower viscous electrolyte system, made using 10 μl of water, tetraglyme or valeronitrile in 1ml of $\text{P}_{1444}\text{N}(\text{CN})_2$, to see whether any gain in device performance can be obtained. A slight decrease in photocurrent density for all three devices containing the electrolyte with additional solvent is observed. On the other hand, a significant increase in V_{oc} of 150 mV is observed using the electrolyte containing tetraglyme and valeronitrile, and an increase of 99 mV with the addition of water. At low sun intensities a high fill factor is also obtained.

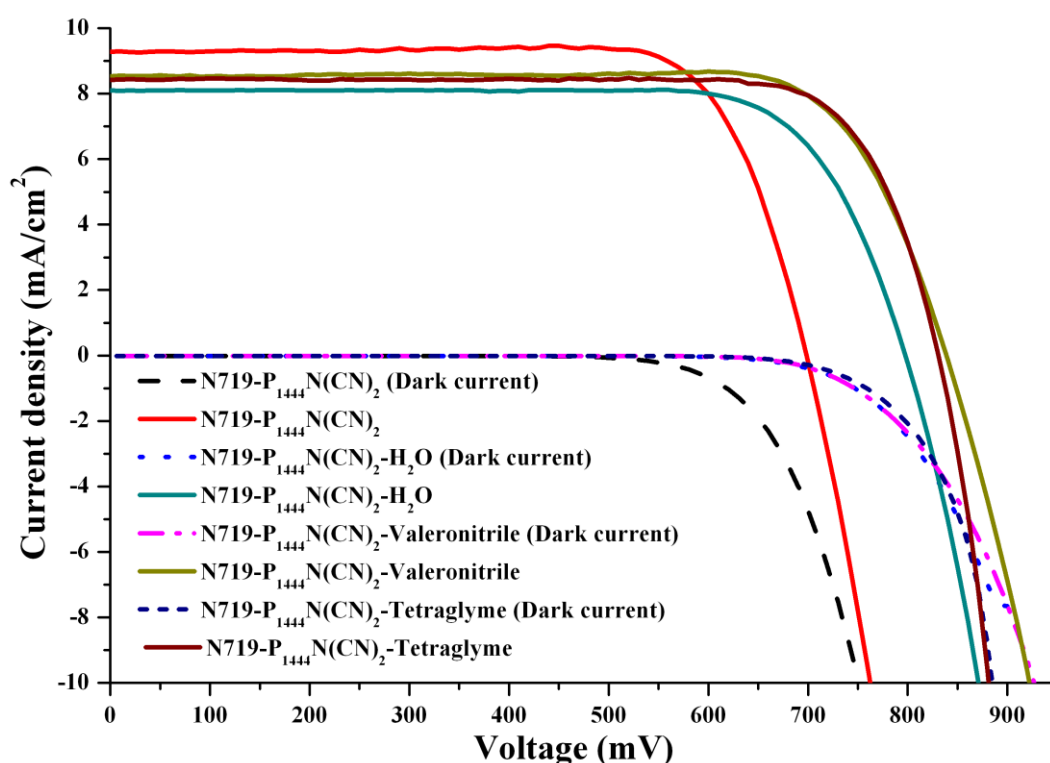


Figure 7.25: The effect of additives in $\text{P}_{1444}\text{N}(\text{CN})_2$ electrolytes with N719 dye

The effect of adding solvent to ionic liquid electrolytes has been studied by Papageorgiou *et al.*⁵⁹ where they reported an increase in photocurrent density, on addition of 5 wt% acetonitrile to an ionic liquid electrolyte, due to a decrease in the viscosity of the ionic liquid. In contrast, Lui *et al.*⁶⁰ and Mikoshiba *et al.*⁶¹ reported that on water addition, the photocurrent density decreased due to dissolution of the dye from the TiO_2 surface. The same effect is observed in the systems studied here (Figure 7.25); on adding water, a drop in I_{sc} is observed.

7. Ionic liquids in dithienothiophene based organic dye sensitised solar cells

It is possible that this is a result of dye desorption even though this could not be visually observed. Nazeeruddin *et al.*⁵ also observed a decrease in photocurrent due to poor injection efficiency of the dye upon addition of water. Cyclic voltammetry of the electrolyte containing water showed lower catalytic activity for the reduction of I_3^- to I^- at a Pt electrode, and therefore it is possible that the regeneration of I^- is limiting the performance of the device. Figure 7.26 displays the voltammogram of the $P_{1444}N(CN)_2$ based ionic liquid electrolyte, with the addition of tetraglyme and valeronitrile, using a symmetrical cell.

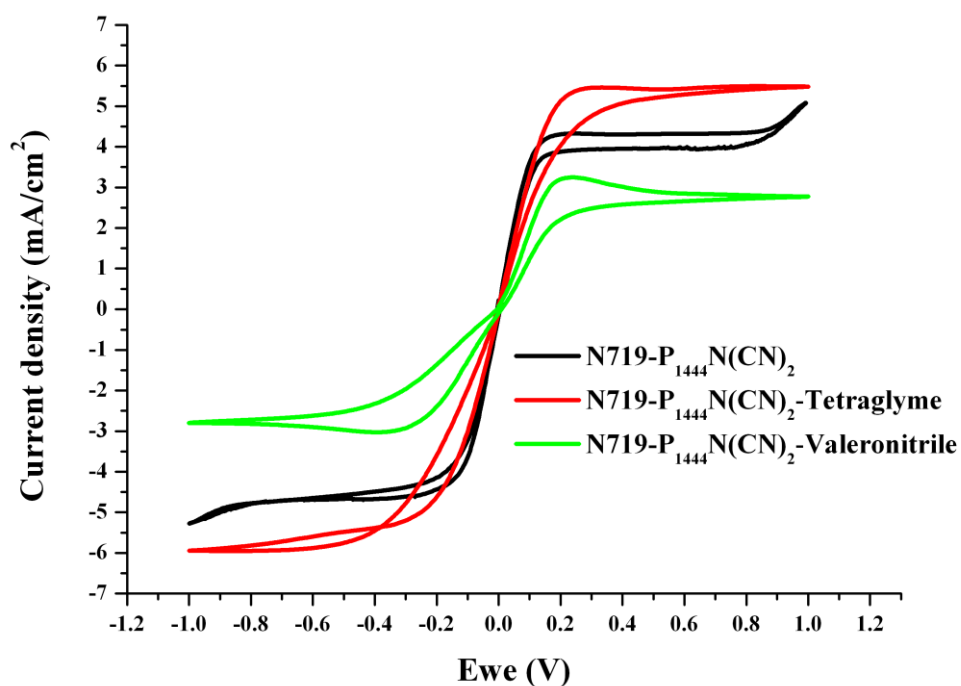


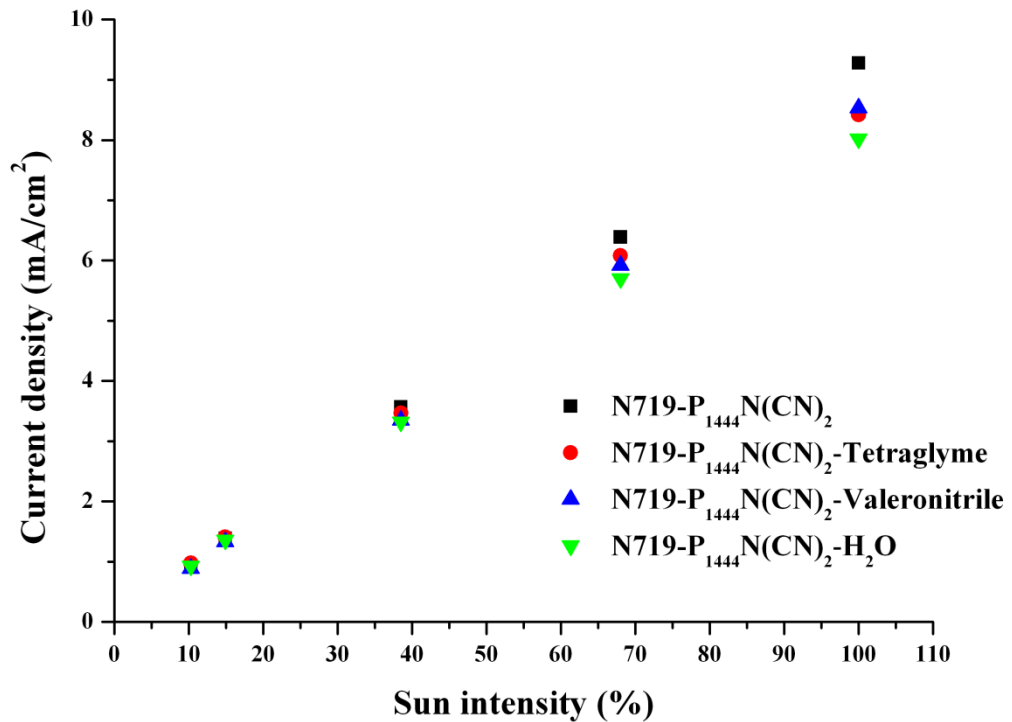
Figure 7.26: Characteristic cyclic voltammograms for the symmetrical cells, with a separation of 25 μm and surface area 0.33 cm^2 , filled with different ionic liquid electrolytes, at a scan rate of 5 mV s^{-1}

The diffusion coefficients obtained from these CVs, of I_3^- in $P_{1444}N(CN)_2$, $P_{1444}N(CN)_2$ -tetraglyme and $P_{1444}N(CN)_2$ -valeronitrile are $1.5 \times 10^{-7} \text{ cm}^2 \text{ s}^{-1}$, $1.9 \times 10^{-7} \text{ cm}^2 \text{ s}^{-1}$ and $1.0 \times 10^{-7} \text{ cm}^2 \text{ s}^{-1}$ respectively. A decrease in the transport properties of I_3^- in the ionic liquid containing valeronitrile is observed, which corresponds to the changes in current density of the solar cells (Figure 7.24).

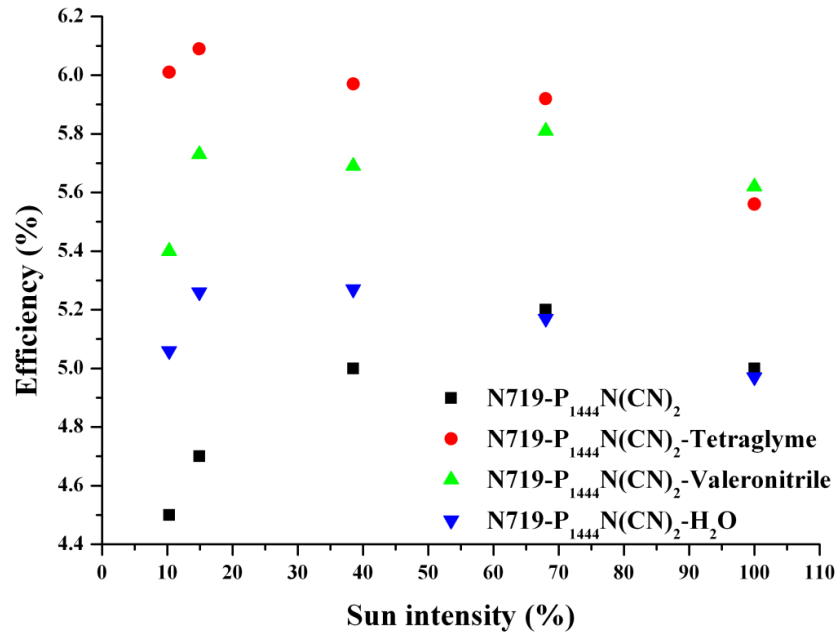
7. Ionic liquids in dithienothiophene based organic dye sensitised solar cells

On the other hand, an increase in diffusion coefficient is observed for the tetraglyme mixture, which does not seem to correlate with the IV curves. It is possible, as discussed further below, that the main effect of adding the diluent in this IL, is causing a shift in the flat band potential, hence explaining the increasing in V_{oc} , at the expense of some charge injection efficiency.

Figure 7.27 displays the effect of light intensity on fill factor, V_{oc} and power conversion efficiency of devices with neat ionic liquid electrolytes and addition of solvents in the ionic liquid electrolyte. They performed well at low light intensities, and the highest efficiency is achieved at 15 % sun intensity.



(a)



(d)

Figure 7.27: Effect of light intensity on I_{sc} , ff , V_{oc} and η for devices with neat ionic liquid electrolytes, with the addition of solvents in the ionic liquid electrolyte, using the N719 dye

One interesting feature of these devices is the high fill factor, which is related to the high V_{oc} obtained in the presence of additives. As demonstrated by De Vos,⁶² V_{oc} influences the ff as shown in equation 7.6 and 7.7 where v_{oc} is the dimensionless open circuit voltage ($v_{oc} = \frac{qV_{oc}}{k_B T}$).

$$FF = \frac{1 - \frac{\ln v_{oc}}{v_{oc}}}{1 - e^{-v_{oc}}} \frac{1 - \frac{1}{v_{oc}}}{v_{oc}} \text{ for } v_{oc} > 4.17 V \quad (\text{Eq 7.6})$$

$$FF = \frac{1}{4} + \frac{v_{oc}}{16} + \frac{v_{oc}^2}{256} - \frac{v_{oc}^3}{1024} \text{ for } v_{oc} < 4.17 V \quad (\text{Eq 7.7})$$

7. Ionic liquids in dithienothiophene based organic dye sensitised solar cells

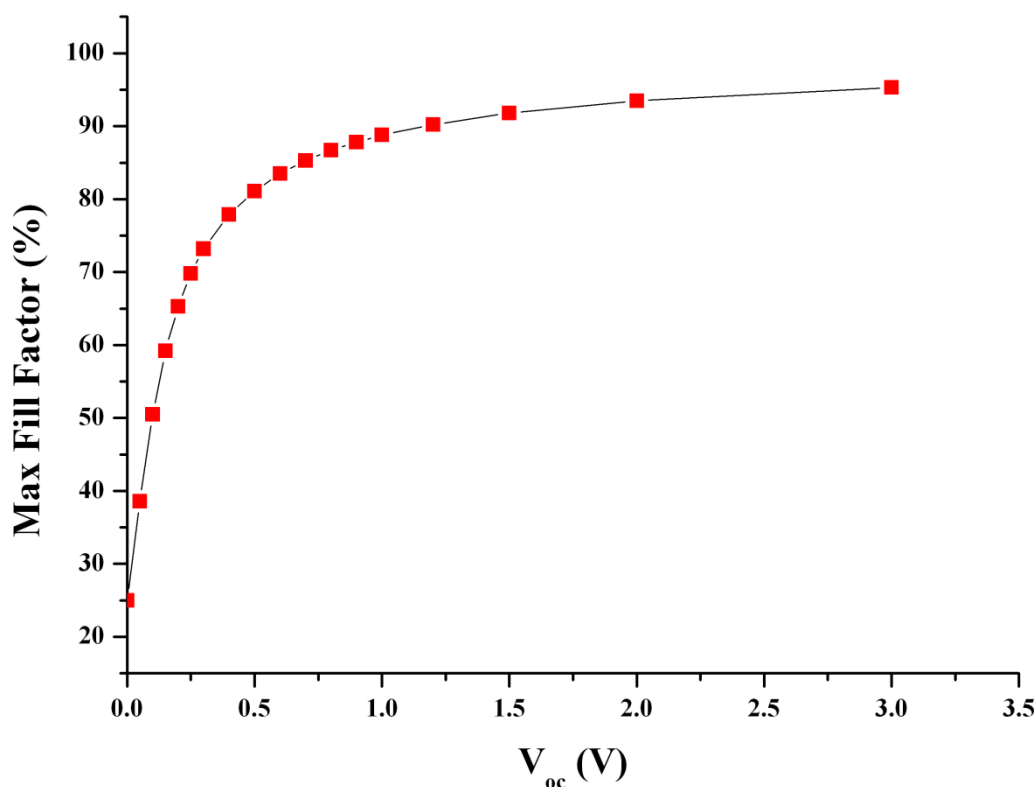


Figure 7.28: Approximation for the function FF (V_{oc})

The De Vos equation 7.6 above fits well with the fill factor and V_{oc} for the devices containing the additional solvent (Figure 7.27 (b) and (c)). Thus the high fill factor is not necessarily due to mass transport limitations in the case of the ionic liquid containing tetraglyme, where the diffusion of I_3^- is much better than in the neat ionic liquid. Figure 7.28 demonstrates the theoretical fill factor as a function of V_{oc} . The V_{oc} can be raised by movement of the conduction band edge, as demonstrated in Chapter 5, by the presence of the additives. As observed in Figure 7.27 (b), such behaviour did not occur in the DSSCs studied here. Therefore, the high V_{oc} might be due to a drop in the recombination rate of the back reaction, as evident by the increase in the onset potential in the dark current curve. The presence of additives might also form a protecting layer on the surface of TiO_2 , thus blocking the reaction of the I_3^- with the electrons in the conduction band, as demonstrated by Liu and co-workers.⁶⁰ The short circuit current density in all the electrolyte systems are similar in the region of low light intensity, and differs slightly at 68 % and 100 % sun intensity.

7. Ionic liquids in dithienothiophene based organic dye sensitised solar cells

In summary, we have demonstrated that the efficiency of the DSSCs can be improved by adding solvents to the ionic liquid electrolytes. The high performance is mainly due to an increase in V_{oc} rather than the photocurrent density. Addition of valeronitrile actually elevates the viscosity of the electrolyte system, as demonstrated by the low diffusion of the I_3^- .

7.3.4.3.2 The $P_{222(201)}NTf_2$ electrolyte with the THD3 sensitiser in DSSCs

Preliminary studies on use of the new phosphonium ionic liquids with the THD3 sensitiser in dye sensitised solar cells were performed. The effect of varying the film thickness was investigated, as well as the addition of chenodeoxycholic acid, and the performance of the device at elevated temperatures was examined. For this study, the electrolyte containing the following components: $P_{222(201)}NTf_2/C_2mimI/C_1mimI/LiI/I_2/NMB$ (molar ratio 14:12:12:1:1.67:4) was used.

Effect of film thickness on the device performance of THD3-dyed solar cells

Figure 7.29 depicts the photocurrent-voltage curves of DSSCs based on the electrolyte $P_{222(201)}NTf_2/C_2mimI/C_1mimI/LiI/I_2/NMB$, with various film thicknesses, at 15 % sun intensity. In order to compare the effect of film thickness, all of the other parameters of the measurement were kept constant. It is noted that the photocurrent density increases from 4 mA cm^{-2} to 6 mA cm^{-2} with an increase in film thickness from $0.8 \text{ }\mu\text{m}$ to $2 \text{ }\mu\text{m}$, and a drop in photocurrent density to 5 mA cm^{-2} is observed with a $6 \text{ }\mu\text{m}$ thick film. The drop in photocurrent with a $6 \text{ }\mu\text{m}$ film may be due to mass transport limitations or poor permeation of the electrolyte through the TiO_2 network. The diffusion coefficient of triiodide measured in $P_{222(101)}NTf_2$ and $C_2mimNTf_2$ is $2.5 \times 10^{-7} \text{ cm}^2 \text{ s}^{-1}$ and $4.8 \times 10^{-7} \text{ cm}^2 \text{ s}^{-1}$ respectively. Thus, the transport properties of the redox species in the TiO_2 network will have a huge impact on the photocurrent generated from the device. The photocurrent also depends on the amount of dye adsorbed on the TiO_2 film, but the main effect is the viscosity of the electrolyte system.

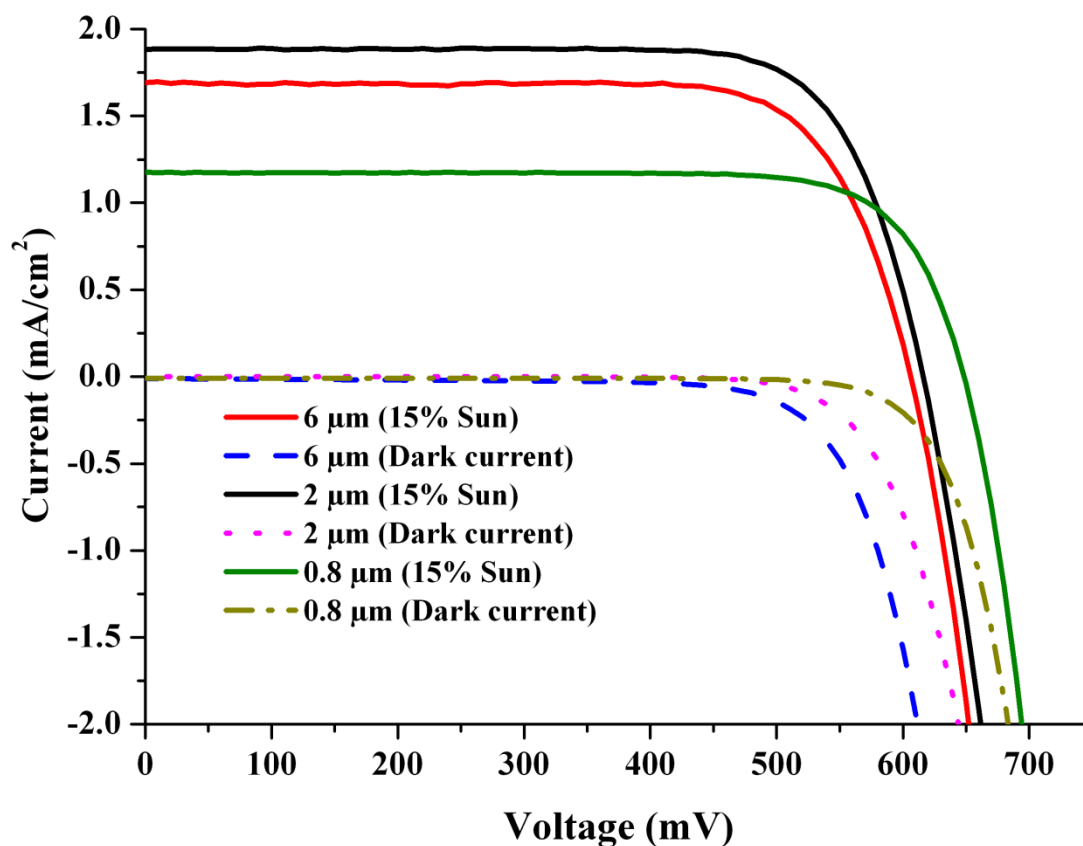


Figure 7.29: IV curves demonstrating the effect of changing film thickness using THD3 as the sensitizer

On the other hand, the V_{oc} decreases as the film thickness was increased over the same range, from 648 mV to 606 mV. A drop in fill factor is also observed, from 0.77 to 0.76 as the film thickness increases. The performance of the devices show similar trends in the photocurrent density, where an increase is observed from 4 % to 6 %, and then drops down to 5 % with a thicker film. The optimal performance with the 2 μm film is mainly due to the augmentation of the I_{sc} . The increasing photocurrent density up to 2 μm is attributed to an increase in the amount of dye adsorbed on the TiO_2 surface with the increased film thickness. Beyond this thickness, even though more dye will be present, photocurrent decreases due to increased recombination, mass transport limitations, especially at the innermost layer. In contrast to photocurrent density, there is a drop in V_{oc} with increased surface area, due to increases in the charge recombination reaction, as shown in Figure 7.31, where a shift in the onset potential of the dark current to lower potential is observed

7. Ionic liquids in dithienothiophene based organic dye sensitised solar cells

as the film thickness increases.⁶³⁻⁶⁴ Thus, it can be concluded that a 2 μm transparent film is required for this device to perform most efficiently. Since the organic dye has a high molar extinction coefficient, the use of a thin film is preferable. Figure 7.30 summarises the basic parameters (I_{sc} , V_{oc} , ff and efficiency) of the DSSCs as a function of film thickness.

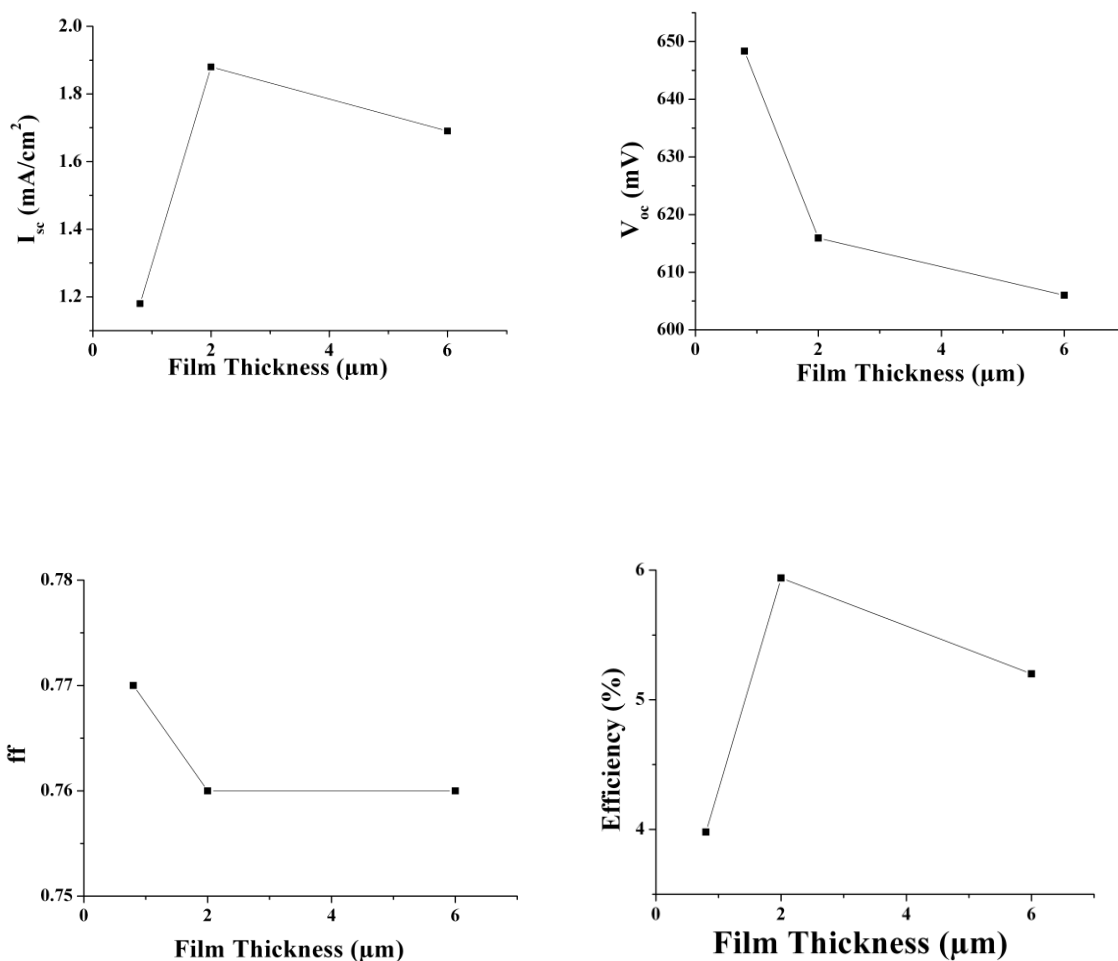


Figure 7.30: The effect of film thickness used in THD3-dye sensitised solar cells with $\text{P}_{222(201)}\text{NTf}_2$ electrolyte

The effect of temperature on dye sensitised solar cells using THD3 as the sensitiser

Here, we looked at the effect of increasing the temperature to 55 $^{\circ}\text{C}$, for DSSCs with the phosphonium ionic liquid and the organic dye, to see whether any benefit could be obtained from increasing the temperature.

Figure 7.31 displays the I-V characteristics of a DSSC at room temperature and at 55 $^{\circ}\text{C}$, under 1 sun illumination, with $\text{P}_{222(201)}\text{NTf}_2$ based electrolytes. At elevated temperatures, an

7. Ionic liquids in dithienothiophene based organic dye sensitised solar cells

increase in photocurrent density and efficiency are observed, which might be due to an increase in mobility of the triiodide ions in the electrolyte. The diffusion coefficient of I_3^- is $7.15 \times 10^{-7} \text{ cm}^2 \text{ s}^{-1}$ at 55°C . On the other hand, a decrease in fill factor and V_{oc} is commonly observed at high temperature. According to Nazeeruddin *et al.*, the decrease in V_{oc} with temperature is due to an increase in the charge recombination reaction at the photoanode and an increase in the dark current in the cell.⁵ Usami *et al.* have also demonstrated the temperature dependence of the V_{oc} ;⁶⁵ as the temperature increases the band gap of the semiconductor decreases, probably due to a shift in the conduction band edge. The V_{oc} is given by the following equation:⁶⁵

$$V_{oc} = E_{Redox} - E_C - \frac{\gamma k_B T}{e} \ln\left(\frac{N_e}{n}\right) \quad (\text{Eq 7.8})$$

where E_{Redox} is the redox potential of I_3^-/I , E_C is the potential of the conduction band of the semiconductor, k_B is the Boltzmann constant, T is the temperature, e is the elementary charge, N_e is the effective density of states, n is the density of states, γ is a characteristic constant of the TiO_2 tailing states.

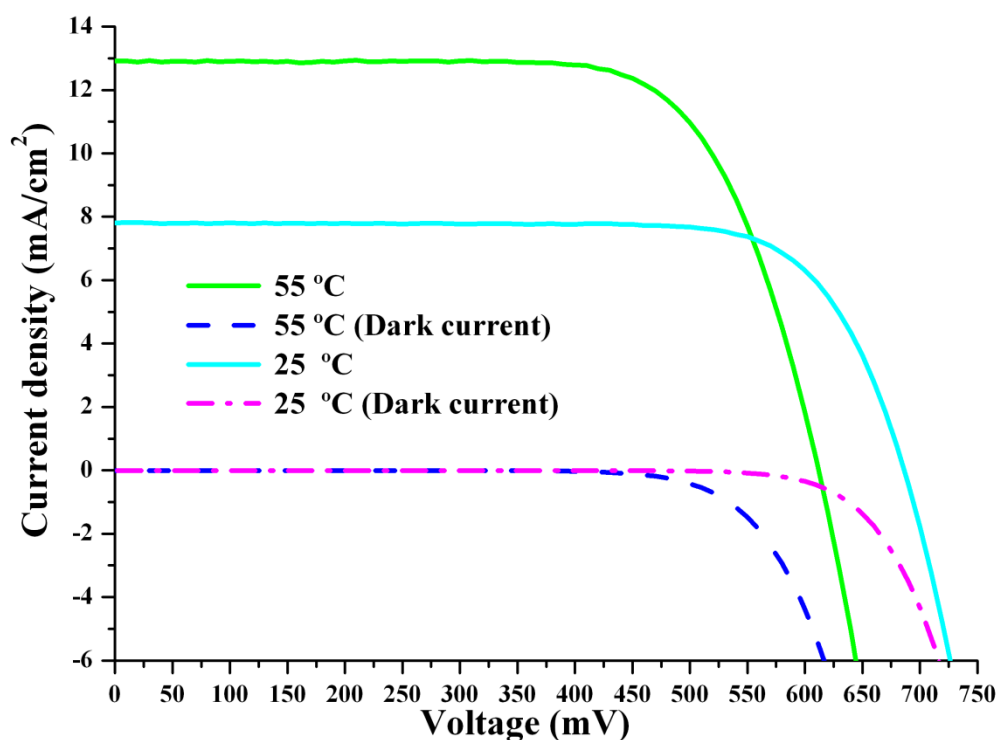


Figure 7.31: The effect of temperature on device performance with THD3 as sensitizer using $P_{222(201)}NTf_2$ based electrolytes with a $2 \mu\text{m}$ film at 25°C and at 55°C

Table 7.8: Summary of the photovoltaic data obtained from Figure 7.31.

Temperature	25 °C	55 °C
V_{oc} (mV)	686 (\pm 5)	612 (\pm 3)
I_{sc} (mA cm ⁻²)	7.8 (\pm 0.5)	12.9 (\pm 0.8)
ff	0.76 (\pm 0.01)	0.70 (\pm 0.02)
η (%)	4.1 (\pm 0.5)	5.6 (\pm 0.3)

The same experiment was carried out using a more viscous phosphonium ionic liquid electrolytes based on P₁₄₄₄N(CN)₂. At room temperature, the performance of the devices with THD3-dye shows very poor performance, as shown in Table 7.9. On increasing the temperature from room temperature to 50 °C, a significant increase in the photocurrent density is observed; the I_{sc} increased from 5.5 mA cm⁻² to 10.5 mA cm⁻², whereas the V_{oc} dropped by 26 mV. The overall performance of the device increased from 2.8 % to 4.9 % under full light intensity, as a result of the increase in current density. A further increase in temperature leads to a moderate rise in I_{sc} , but at temperatures > 65 °C a drop in I_{sc} is observed, as the dominant factor is due to the rise in the recombination processes. Further investigation should be undertaken to fully understand the impact of temperature on device performance; long term testing is required to observe the influence of temperature on the solar cells and to see whether any degradation of the dye occurs over long periods.

Table 7.9: Photovoltaic data of THD3-DSSCs in combination with P₁₄₄₄N(CN)₂ electrolyte.

Temperature	25 °C	50 °C	60 °C	65 °C	70 °C
V_{oc} (mV)	646 (\pm 8)	620 (\pm 5)	600 (\pm 2)	588 (\pm 3)	552 (\pm 5)
I_{sc} (mA cm ⁻²)	5.5 (\pm 0.8)	10.5 (\pm 0.5)	11.4 (\pm 0.4)	11.5 (\pm 0.5)	11.2 (\pm 0.2)
ff	0.78 (\pm 0.01)	0.75 (\pm 0.02)	0.70 (\pm 0.01)	0.69 (\pm 0.01)	0.69 (\pm 0.01)
η (%)	2.8 (\pm 0.6)	4.9 (\pm 0.2)	4.8 (\pm 0.1)	4.7 (\pm 0.2)	4.3 (\pm 0.1)

7. Ionic liquids in dithienothiophene based organic dye sensitised solar cells

Effect of chenodeoxycholic acid on THD3 dye

The behaviour of the DSSCs with ionic liquids upon use of chenodeoxycholic acid (DCA) coabsorbent is similar to that of the standard acetonitrile based electrolyte DSSCs; an increase in both I_{sc} and V_{oc} is observed. The V_{oc} increases from 686 mV to 693 mV in the presence of the co-adsorbent. An even more significant increase in photocurrent is observed, with an increase from 7.8 mA cm^{-2} to 9.6 mA cm^{-2} . The performance of the device depends greatly on I_{sc} , thus an increase in device efficiency is also observed with co-adsorbent (Figure 7.32). The increase in photocurrent is probably due to a decrease in dye aggregation, thus lowering the recombination rate. As explained in Chapter 6, on treating the film with an acid, a more negative flatband potential of the TiO_2 was observed with an ionic liquid electrolyte.

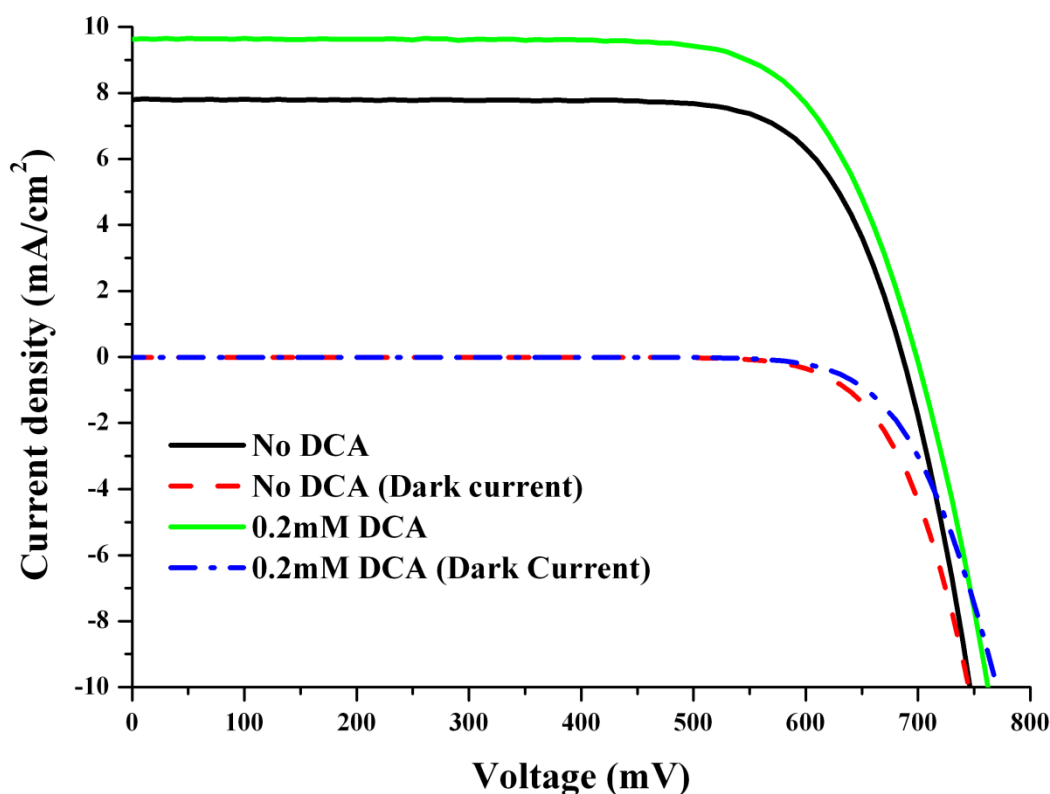


Figure 7.32: The effect of co-adsorbent on the performance of the DSSCs using THD3 as sensitizer

7. Ionic liquids in dithienothiophene based organic dye sensitised solar cells

7.3.4.3.3 Different phosphonium ionic liquid electrolytes in DSSCs with various organic sensitisers

The effect of changing the alkyl chain on the phosphonium cation and varying the anions were investigated with the following sensitisers: THD1, THD2, THD3, THD8 and THD9. The device performance was evaluated using different ionic liquids at varying light intensities. An increase in the thickness of the scattering layer, while keeping the transparent layer constant, was also investigated to see whether more light could be harvested with a thicker scattering layer film. In this study, a 2 μm transparent film thickness was used throughout the study unless otherwise stated. 10 mM co-adsorbent was added to all dye baths. The effect of changing the particle size of the transparent layer was also investigated. In some cases, the cells were tested at elevated temperatures, depending on the viscosity of the electrolytes.

Use of different size of TiO_2 particles in $\text{P}_{222(101)}\text{NTf}_2$ electrolyte with THDn ($n=1-3$) sensitisers

The most commonly used and efficient TiO_2 film is composed of interconnected networks of 20 nm particles. This type of particle size is known to give a large surface area, which is suitable for efficient dye adsorption, good light adsorption and charge formation.^{3, 66-67} There are benefits and drawback in the use of smaller or larger nanoparticles. As stated by Chou and co-workers,⁶⁸ the benefit of using 20 nm particles is the availability of a larger active surface area and a greater number of connections between the TiO_2 nanoparticles permitting the adsorption of a larger amount of dye, which will boost the photocurrent delivered by the device. In the case of bigger particles, a larger contact between TiO_2 nanoparticles is obtained, and thus the dye can easily access the surface of the TiO_2 and organise itself better onto the surface.⁶⁸ The use of larger particles also allows for better mobility of the triiodide in the TiO_2 network. However, using a film with larger particles also gives rise to a small surface area, and thus the amount of dye adsorbed on the surface is reduced, which can greatly affect the performance of the device.⁶⁹⁻⁷⁰ The disadvantage of using smaller particles is the increase in grain boundary effects, which can produce higher electron trapping.⁷⁰⁻⁷¹

7. Ionic liquids in dithienothiophene based organic dye sensitised solar cells

Figure 7.33 describes the IV characteristics of THD1, THD2 and THD3 using two different Titania particles sizes, 20 nm and 30 nm, with an electrolyte composing of $P_{222(101)}NTf_2/C_2mimI/C_1mimI/LiI/I_2/NMB$ (molar ratio 14:12:12:1:1.67:4). This electrolyte was chosen because it has good ionic conductivity and is relatively fluid, thus allowing good mobility of the triiodide through the porous structure of the TiO_2 film. The large particle size gives higher current density with all dyes, and an increase in the overall conversion efficiency is observed in all cases. The THD2 sensitiser gave the highest I_{sc} , at 12 mA cm^{-2} at full sun intensity.

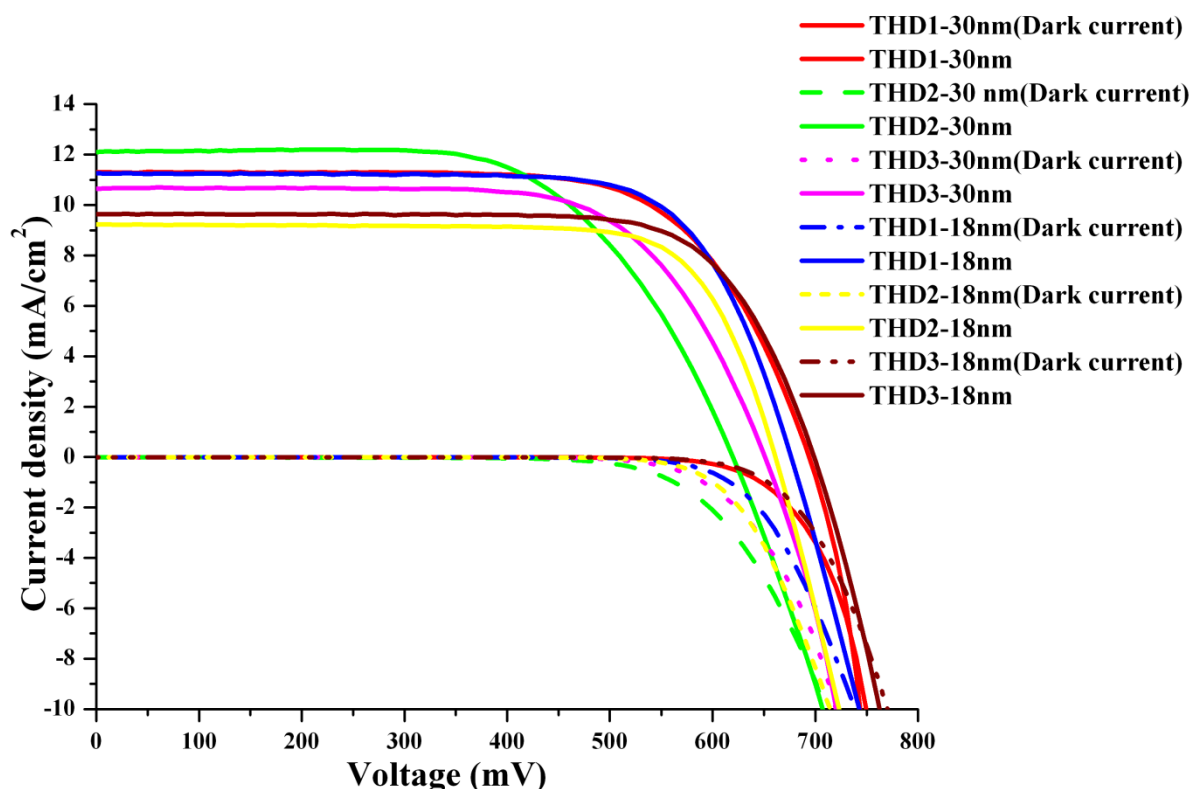


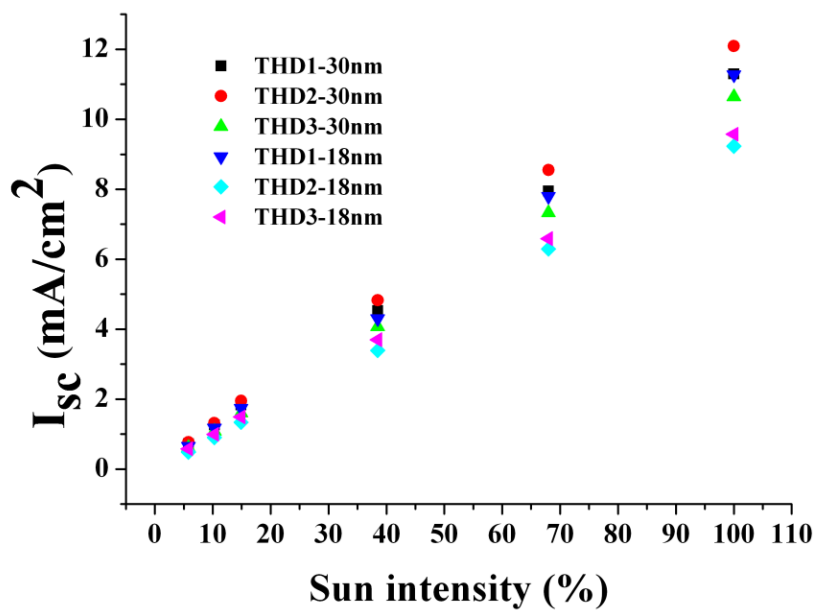
Figure 7.33: The performance of DSSCs with THD1, THD2 and THD3 sensitizers using different size particles, with a $P_{222(101)}NTf_2$ electrolyte

7. Ionic liquids in dithienothiophene based organic dye sensitised solar cells

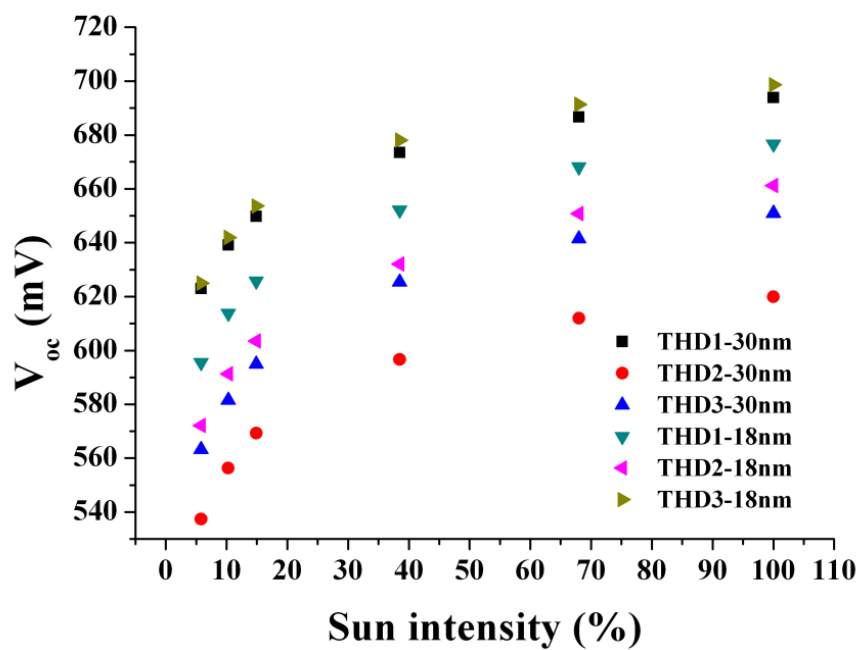
Figure 7.34 (a) illustrates the variation of I_{sc} as a function of light intensity for the devices with different particle sizes. As the light intensity increases, a gradual increase in photocurrent can be observed, and at 100 % sun saturation, I_{sc} has not yet occurred. The effect of light intensity is more obvious on V_{oc} , and a change in V_{oc} among the dyes is also observed. Figure 7.34 (b) shows the variation of the V_{oc} as the sun intensity is increased. Initially there is a sharp increase in V_{oc} , and it rises more gradually above 40 % sun. Figure 7.34 (c) displays the effect of light intensity on the fill factor of the device. Figure 7.34 (d) shows the device efficiency as a function of light intensity. A similar trend in efficiency is observed with either the smaller or larger particles, reaching a maximum performance at 15 % sun.

This trend is also observed with the different dyes, with THD1 showing the best performance ($\eta = 6.1\%$ at 15 % sun with a film consisting of nanostructured particles of 18 nm) over the range of sun intensities. Note that this high efficiency was obtained with the phosphonium ionic liquids without any addition of organic solvents. At 1 sun, the device performance for the THD1, THD2 and THD3 sensitisers, with the 18 nm particles sized TiO_2 film, are 5.5 %, 4.6 % and 4.9 % respectively.

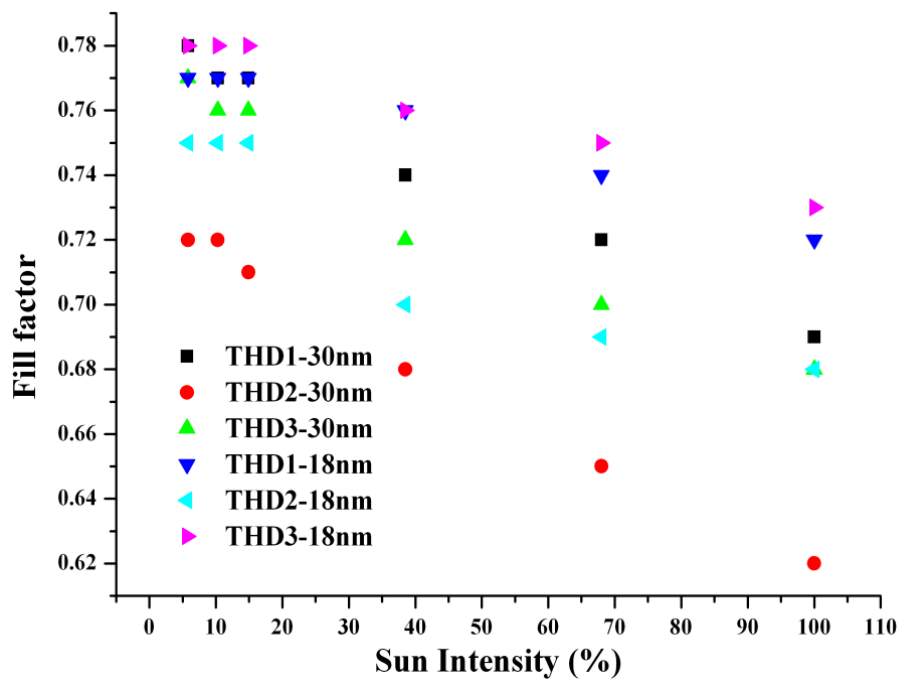
7. Ionic liquids in dithienothiophene based organic dye sensitised solar cells



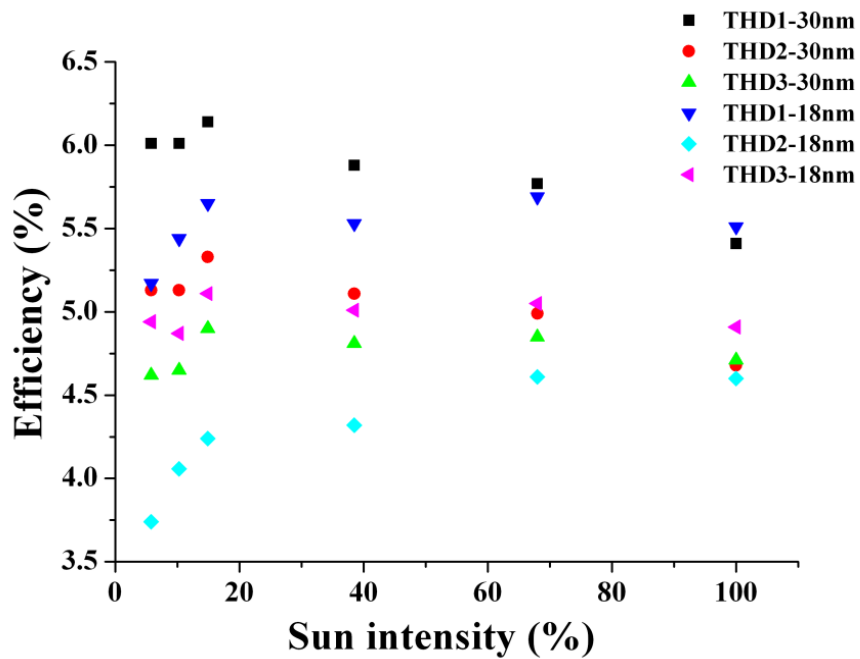
(a)



(b)



(c)



(d)

Figure 7.34: The variation of (a) current density, (b) photovoltage, (c) fill factor and (d) efficiency as function of light intensity for the DSSCs with different particle sizes and a $P_{222(101)}NTf_2$ electrolyte

7. Ionic liquids in dithienothiophene based organic dye sensitised solar cells

In summary, the use of smaller particles sizes gives better overall conversion efficiencies, except at low light intensity, even though the current density is much lower in some cases. In the case of larger particles, a low V_{oc} is obtained compared to smaller particles.

7.3.4.3.4 Effect of scattering layer on the performance of DSSCs with organic sensitisers

The effect of increasing the thickness of the scattering layer was also investigated, with the THD3 sensitiser, in ionic liquids with slightly different viscosities. This was to determine if an improvement in photocurrent could be observed with thicker scattering layers, and also see whether the viscosity of the electrolyte plays an important role in the device performance.

The two electrolytes used were $P_{222(101)}NTf_2/C_2mimI/C_1mimI/LiI/I_2/NMB$ and $P_{222(101)}FSI/C_2mimI/C_1mimI/LiI/I_2/NMB$ (molar ratio 14:12:12:1:1.67:4 for both). The only difference between the phosphonium ionic liquids is the anion; the FSI anion normally imparts more fluidity to the ionic liquid than the NTf_2 . A 2 μm transparent high surface area Titania film and an additional scattering layer of TiO_2 paste of 400 nm particle size, varied from 2 μm to 8 μm thick, were used for the study.

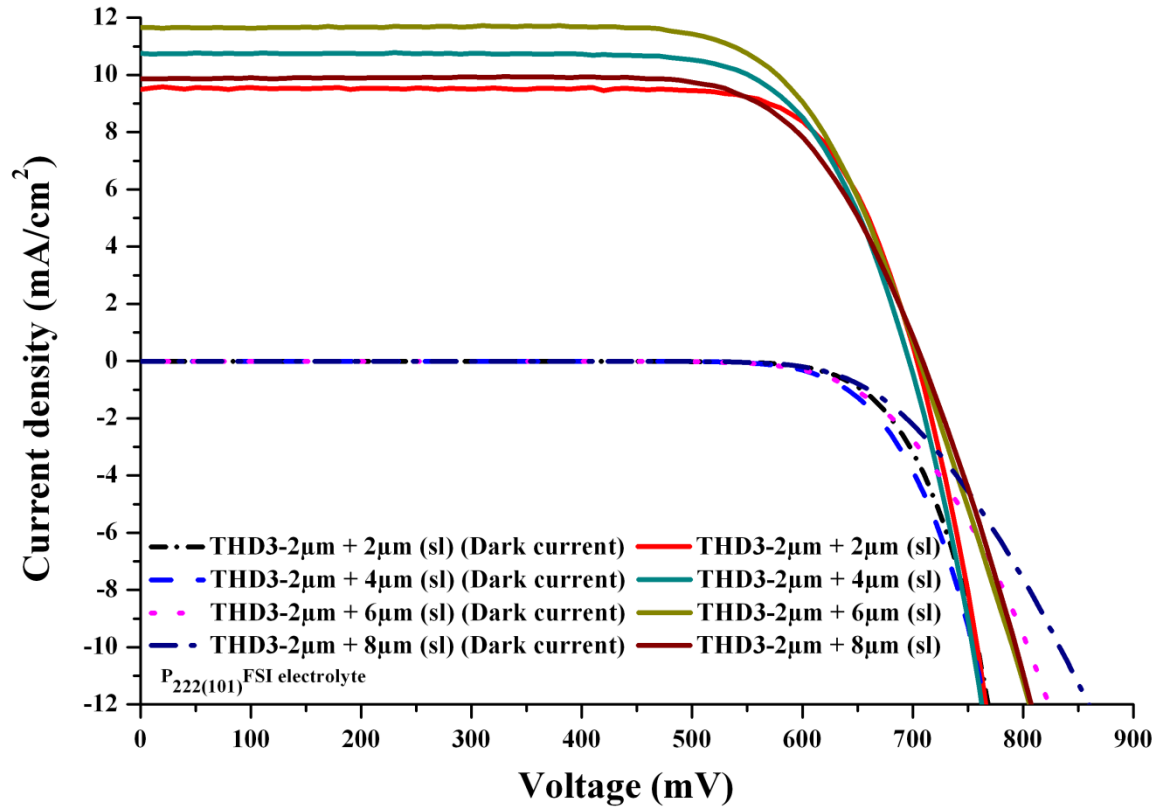


Figure 7.35: The effect of increasing the scattering layer thickness on device performance using THD3 sensitiser and a P₂₂₂₍₁₀₁₎FSI electrolyte

Figure 7.35 shows the photovoltaic characteristics of THD3-dye sensitised solar cells using P₂₂₂₍₁₀₁₎FSI as an electrolyte with different thicknesses of scattering layer. The DSSC performance depends significantly on the scattering layer thickness; the photocurrent goes up gradually, as we increase the scattering layer thickness from 2 μm to 6 μm, but decreases after this point, with any further thickness increase. One possible reason for such a drop in I_{sc} is the fact that the dye uptake is lower. The amount of dye adsorbed on the TiO₂ dropped from 1.4×10^{16} dye molecules cm⁻² μm⁻¹ to 0.9×10^{16} dye molecules cm⁻² μm⁻¹. However, if this was the reason for the lower current, then it would be expected that the devices with the P₂₂₂₍₁₀₁₎NTf₂ electrolyte would exhibit similar behaviour, but this is not the case. Instead, the best performance with the P₂₂₂₍₁₀₁₎NTf₂ electrolyte was obtained with the 8 μm thick scattering layer. Another hypothesis is that the master plate was damaged, in a way not visible to the eye, or that the applied blocking layer before printing the films was too thick, thus increasing the resistivity of the films.

7. Ionic liquids in dithienothiophene based organic dye sensitised solar cells

With a 2 μm and 4 μm scattering film thicknesses, the V_{oc} remains the same, while the use of a thicker scattering layer gives an increased in V_{oc} .

Figure 7.36 depicts the IV characteristics of the THD3-dye sensitised solar cells with the $P_{222(101)}NTf_2$ ionic liquid electrolyte and different scattering layer thicknesses. A sudden increase in the photocurrent is observed going from a 2 μm to 4 μm thick scattering layer, followed by a more gradual increase in I_{sc} upon increasing the thickness to 8 μm . Thus, increasing the scattering layer greatly enhances the light harvesting capability. In this particular electrolyte, the best performance is obtained with the thicker scattering film.

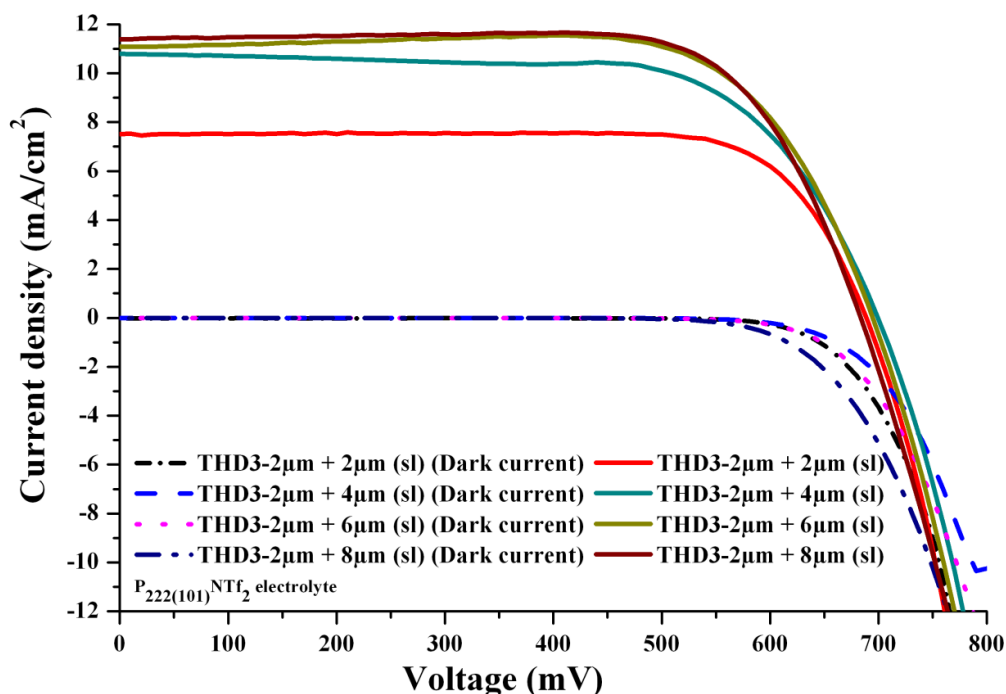


Figure 7.36: The IV curves of the DSSCs with the THD3 dye and the $P_{222(101)}NTf_2$ electrolyte, with different thicknesses of scattering layer

Table 7.10 summarises the parameters obtained from the two IV curves. An efficiency of 6 % is obtained using the $P_{222(101)}FSI$ electrolyte with a scattering film thickness of 6 - 8 μm , whereas with $P_{222(101)}NTf_2$, the devices performed better with a 6 μm film.

Table 7.10: Data obtained from Figure 7.35 and Figure 7.36 (THD3 sensitiser).

Electrolyte	Film thickness	2 μm + 2 μm (sl)	2 μm + 4 μm (sl)	2 μm + 6 μm (sl)	2 μm + 8 μm (sl)
$\text{P}_{222(101)}\text{FSI}$	V_{oc} (mV)	703 (± 2)	697 (± 3)	706 (± 2)	708 (± 3)
/C ₂ mimI	I_{sc} (mA cm ⁻²)	9.5 (± 0.5)	10.8 (± 0.2)	11.7 (± 0.3)	9.9 (± 0.2)
/C ₁ mimI/LiI	<i>ff</i>	0.77 (± 0.01)	0.74 (± 0.01)	0.73 (± 0.02)	0.73 (± 0.02)
/I ₂ /NMB	η (%)	5.1 (± 0.1)	5.5 (± 0.2)	6.0 (± 0.2)	5.1 (± 0.1)
$\text{P}_{222(101)}\text{NTf}_2$	V_{oc} (mV)	689 (± 3)	700 (± 1)	695 (± 2)	684 (± 1)
/C ₂ mimI	I_{sc} (mA cm ⁻²)	7.5 (± 0.5)	11 (± 0.2)	11.1 (± 0.1)	11.4 (± 0.1)
/C ₁ mimI/LiI	<i>ff</i>	0.76 (± 0.01)	0.68 (± 0.02)	0.73 (± 0.01)	0.74 (± 0.01)
/I ₂ /NMB	η (%)	4.0 (± 0.2)	5.1 (± 0.2)	5.6 (± 0.1)	5.7 (± 0.1)

7.3.4.3.5 The effect of different ionic liquid anions and cations on device performance

In section 7.3.3, the properties of the electrolytes used were evaluated in term of conductivity, viscosity and density, as defined by the Walden plot, and the diffusivity of the redox couples. Here, the influence of the physical properties of the electrolytes was further investigated in terms of the photovoltaic performance of the dye sensitised solar cells with the THD3, THD1 and THD8 sensitisers. THD2 and THD9 were also investigated but the performance of the devices with these dyes was poor compared to the THD3, THD1 and THD8 devices. The poor performance can be related to the HOMO and LUMO level of these two dyes. The regeneration of the dye by the iodide may also not be very efficient, thus lowering the performance of the dyes. Therefore the studies were mainly focussed on THD3, THD1 and THD8.

Figure 7.37, 7.39 and 7.40 present the IV characteristics, under full sunlight and in the dark, of the devices with THD3, THD8 and THD1 respectively. Detailed cell parameters are listed in Table 7.11 for THD8, and Table 7.12 for THD1. The best performance was obtained with $\text{P}_{222(101)}\text{FSI}$ and the THD3 sensitiser. The photocurrent density, open circuit voltage and fill factor are 11.7 mA cm⁻², 706 mV, 0.72 respectively, yielding an overall efficiency of 5.92 %. $\text{P}_{222(101)}\text{FSI}$, $\text{P}_{222(201)}\text{FSI}$, $\text{P}_{222(101)}\text{N}(\text{CN})_2$, $\text{P}_{222(101)}\text{NTf}_2$ and $\text{P}_{222(201)}\text{NTf}_2$ give comparable photocurrent densities, which is probably related to the comparable transport properties of the redox couple in the electrolyte systems. The change in overall performance is mainly due to the difference in the V_{oc} and fill factor with the

7. Ionic liquids in dithienothiophene based organic dye sensitised solar cells

above electrolytes. Under lower sun intensity, the power conversions are even higher, up to 6.1 %, partly because of a higher fill factor.

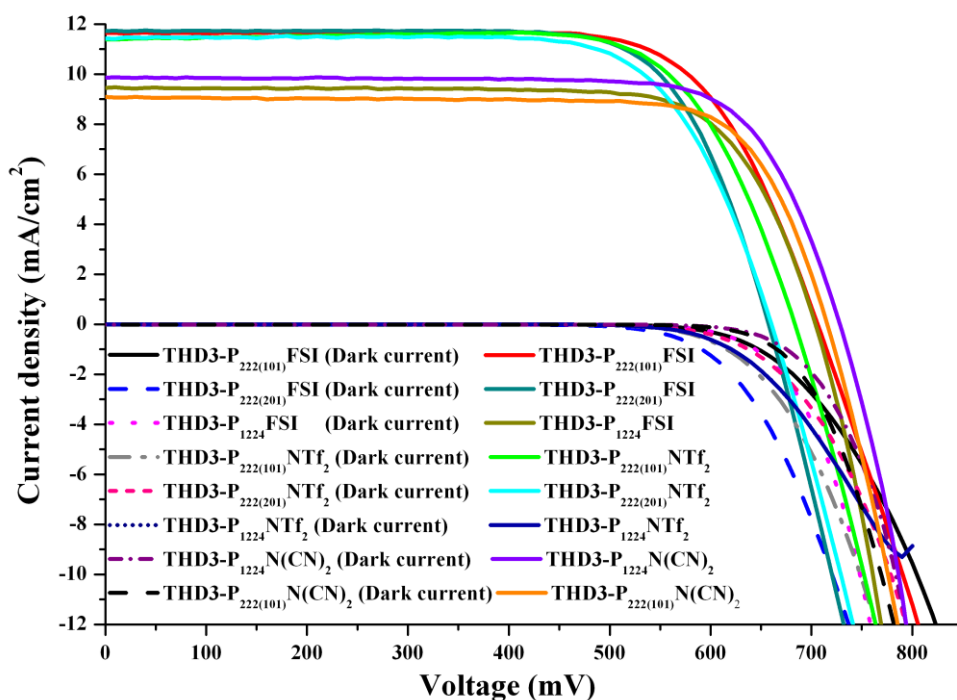
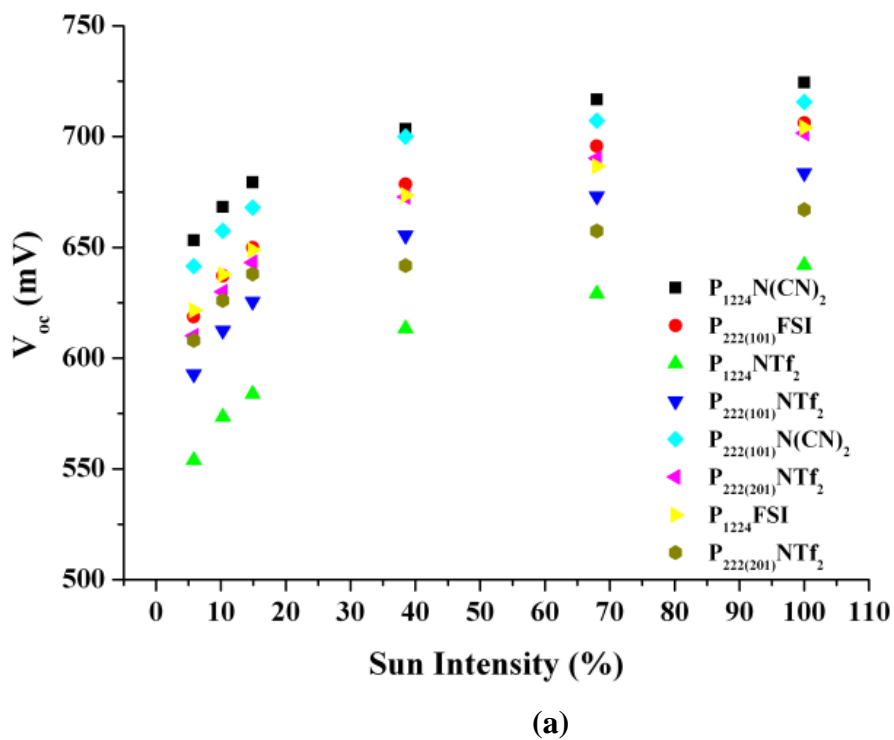
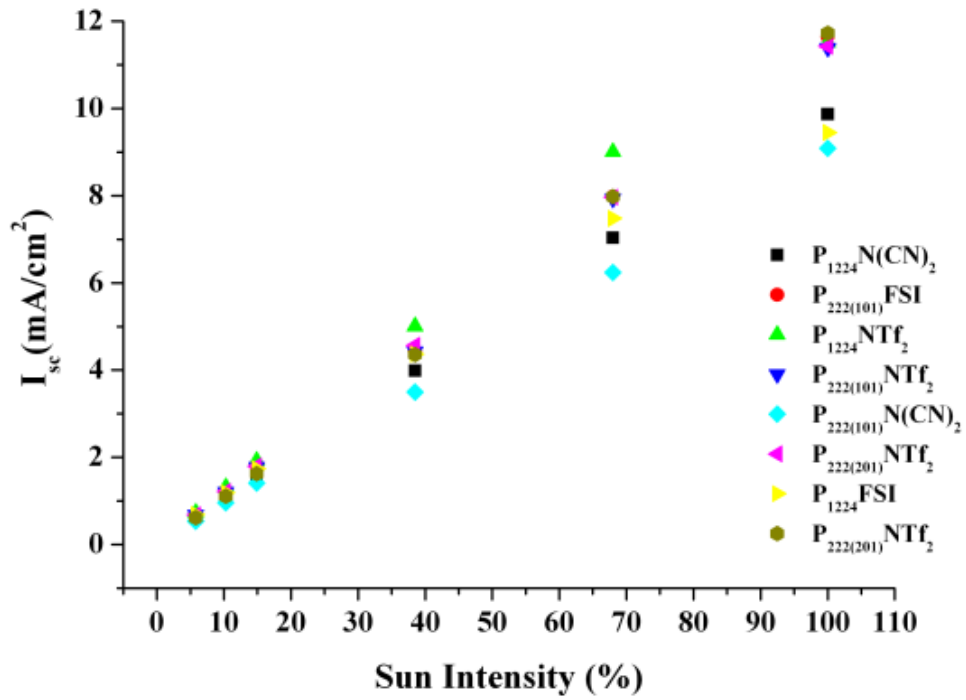
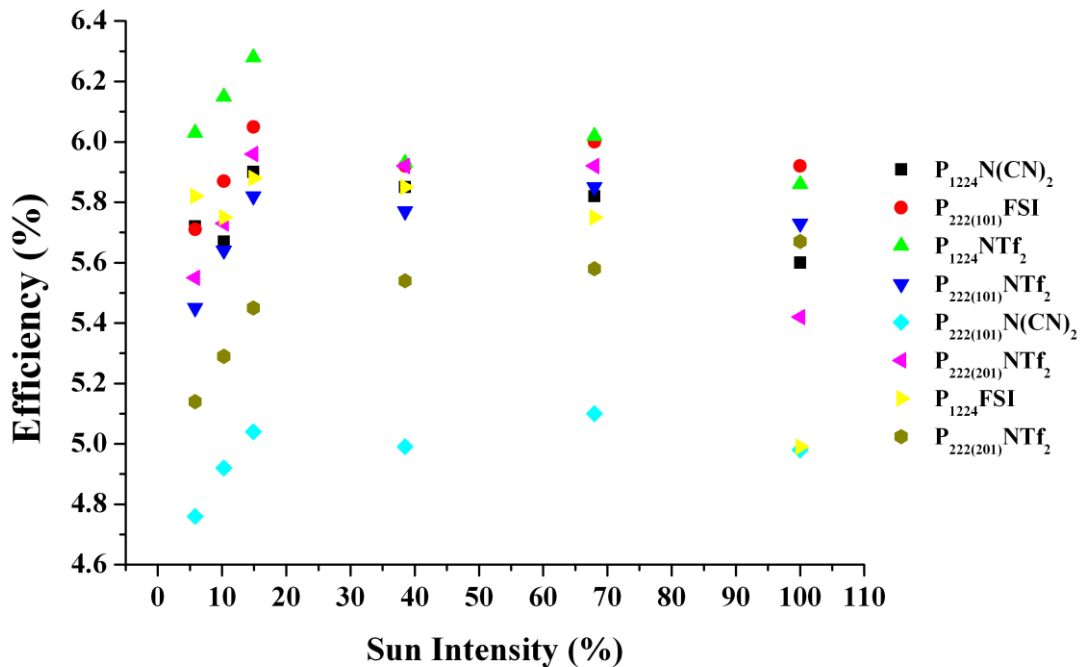


Figure 7.37: The effect of different electrolyte systems on the THD3 devices





(b)



(c)

Figure 7.38: Variation of (a) V_{oc} , (b) I_{sc} and (c) efficiency as a function of light intensity

7. Ionic liquids in dithienothiophene based organic dye sensitised solar cells

Figure 7.39 illustrates the photovoltaic characteristic of THD8 sensitised devices with a range of phosphonium ionic liquid electrolytes. As shown in Table 7.11, some of the ionic liquids give better performances than others. For example, as described earlier in section 7.3.5 3.1, P₁₄₄₄NTf₂ forms a soft solid electrolyte, and therefore the poor achievement of the device is mainly due to a very low photocurrent density; 7.9 mA cm⁻².

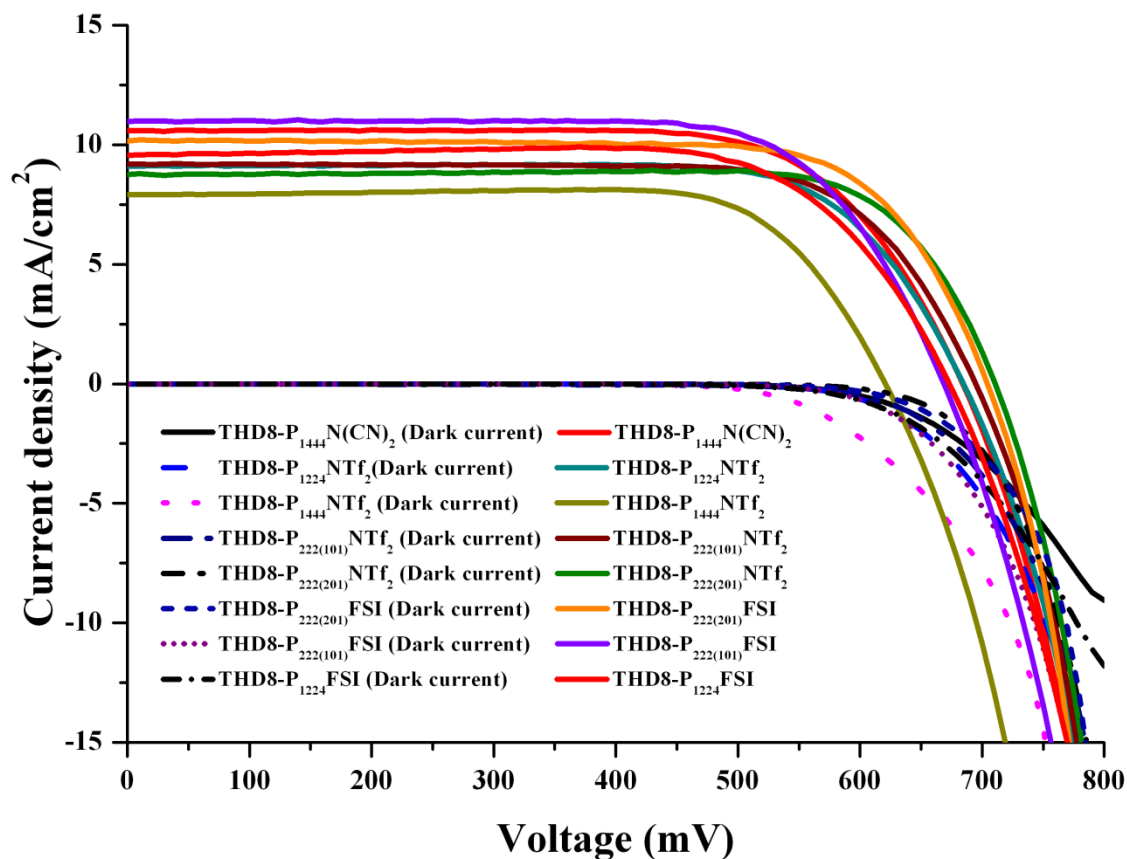


Figure 7.39: The effect of different electrolytes in THD8 sensitised devices

Table 7.11: Photovoltaic parameters extracted from Figure 7.39.

Dye	Electrolyte	V_{oc} (mV)	I_{sc} (mA cm ⁻²)	ff	η (%)
THD8	P ₁₄₄₄ N(CN) ₂	684 ± 9	10.6 ± 0.4	0.71 ± 0.01	5.1 ± 0.2
	P ₁₂₂₄ NTf ₂	685 ± 3	9.1 ± 0.1	0.73 ± 0.02	4.6 ± 0.1
	P ₁₄₄₄ NTf ₂	621 ± 4	7.9 ± 0.5	0.75 ± 0.01	3.7 ± 0.3
	P ₂₂₂₍₁₀₁₎ NTf ₂	694 ± 2	9.2 ± 0.2	0.73 ± 0.02	4.7 ± 0.4
	P ₂₂₂₍₂₀₁₎ NTf ₂	710 ± 2	8.8 ± 0.2	0.77 ± 0.01	4.8 ± 0.5
	P ₂₂₂₍₂₀₁₎ FSI	704 ± 1	10.2 ± 0.3	0.74 ± 0.01	5.3 ± 0.1
	P ₂₂₂₍₁₀₁₎ FSI	669 ± 2	11 ± 0.1	0.72 ± 0.02	5.3 ± 0.2
	P ₁₂₂₄ FSI	673 ± 3	9.6 ± 0.2	0.72 ± 0.01	4.6 ± 0.3

Figure 7.40 displays the photovoltaic characteristic of THD1-dye sensitised solar cells with a selection of phosphonium ionic liquid electrolytes. The best achievement of the device is attained with the P₂₂₂₍₁₀₁₎FSI electrolyte, followed closely by P₂₂₂₍₂₀₁₎FSI. The photovoltaic parameters of the devices with the different electrolytes under full sunlight are given in Table 7.12. They all show comparable V_{oc} , except for P₂₂₂₍₁₀₁₎N(CN)₂ and P₁₂₂₄N(CN)₂, which is likely to be a result of movement of the conduction band edge of the TiO₂ to more negative potentials, attributed to the N(CN)₂ anion having more “basic” properties than the FSI and NTf₂ anions (Chapter 6). The movement of the flatband potential will not only influence the V_{oc} , but also the charge injection and electron collection efficiency of the device and, as a consequence, will have a negative effect on the photocurrent density. Thus, even though the mobility of the redox couple is to some extent better than in the other ionic liquid electrolyte, the photocurrent density delivered by the device is lower compared to the best performing device in P₂₂₂₍₁₀₁₎FSI. It is important to note that the presence of additives such as LiI and NMB also control the position of the flatband potential, and therefore it is important to choose the electrolyte compositions accordingly to the nature of the ionic liquid used. However, in this study, for the sake of comparison, the composition of the electrolyte systems was kept constant and these devices all show comparable performance.

7. Ionic liquids in dithienothiophene based organic dye sensitised solar cells

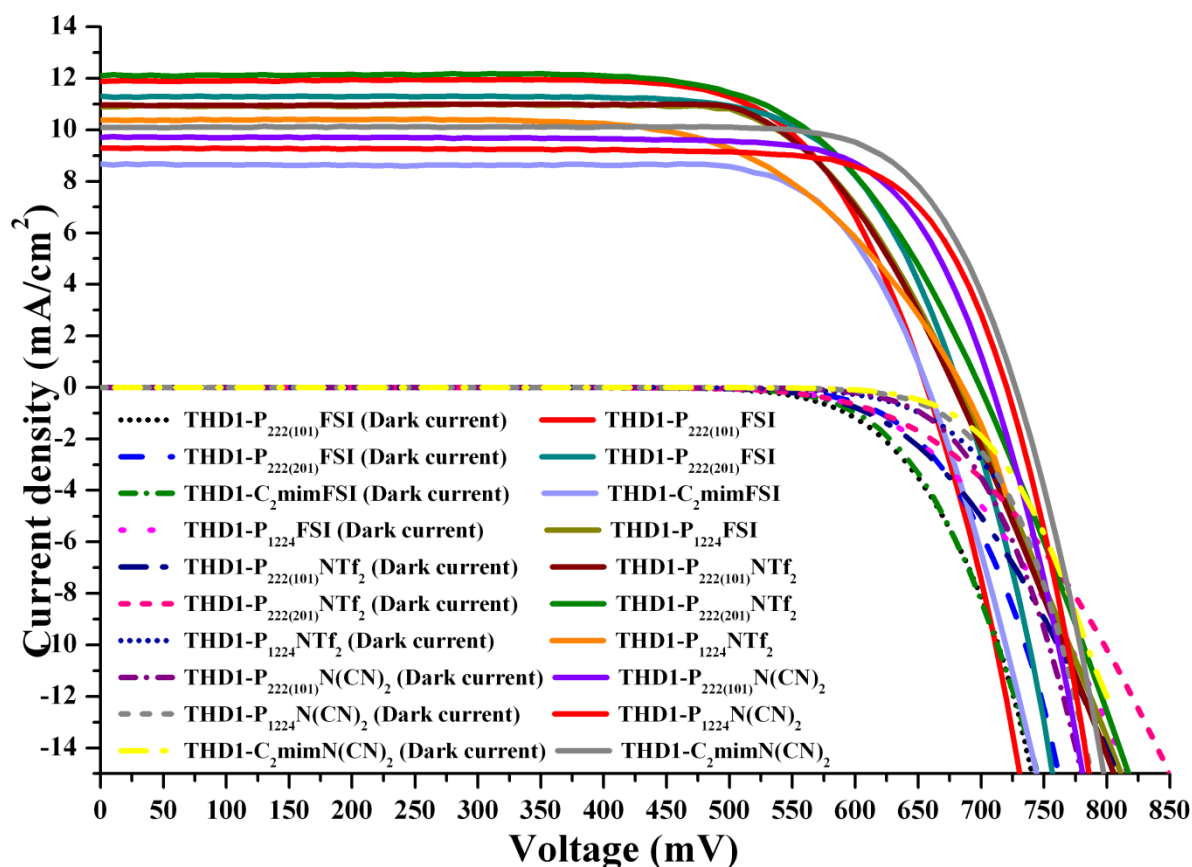


Figure 7.40: The effect of different electrolyte systems on THD1 sensitised devices

As observed in Table 7.12, the imidazolium based electrolytes show similar performance as the phosphonium based electrolytes. It is the first time that such good performance is obtained with a phosphonium ionic liquid combined with an organic sensitiser. The electron lifetime and transit time of the phosphonium based electrolytes are given in Appendix, section A.6.

Table 7.12: Summarised data extracted from Figure 7.40

Dye	Electrolyte	V_{oc} (mV)	I_{sc} (mA cm ⁻²)	ff	η (%)
THD1	P ₂₂₂₍₁₀₁₎ FSI	657 ± 2	11.9 ± 0.2	0.72 ± 0.02	5.7 ± 0.3
	P ₂₂₂₍₂₀₁₎ FSI	683 ± 1	11.3 ± 0.3	0.73 ± 0.01	5.6 ± 0.2
	P ₁₂₂₄ FSI	658 ± 3	10.4 ± 0.2	0.77 ± 0.01	5.2 ± 0.1
	C ₂ mimFSI	658 ± 5	8.5 ± 0.1	0.77 ± 0.01	4.4 ± 0.2
	P ₂₂₂₍₁₀₁₎ NTf ₂	679 ± 3	11.0 ± 0.1	0.74 ± 0.01	5.5 ± 0.1
	P ₂₂₂₍₂₀₁₎ NTf ₂	650 ± 8	12.1 ± 0.3	0.68 ± 0.05	5.3 ± 0.2
	P ₁₂₂₄ NTf ₂	685 ± 2	10.4 ± 0.1	0.66 ± 0.04	4.6 ± 0.3
	P ₂₂₂₍₁₀₁₎ N(CN) ₂	710 ± 8	9.7 ± 0.5	0.75 ± 0.02	5.3 ± 0.1
	P ₁₂₂₄ N(CN) ₂	720 ± 2	9.3 ± 0.2	0.76 ± 0.01	5.2 ± 0.1
C ₂ mimN(CN) ₂	730 ± 2	10.1 ± 0.3	0.77 ± 0.01	5.7 ± 0.2	

To summarise, these observations with phosphonium ILs and organic dyes, it appears that the optimum combination in this work is the use of 18 nm particles size TiO₂ paste which gives better overall devices performance, which is turn relates to a better fill factor. We also demonstrate that the used of a scattering layer on top of the transparent layer gives better current densities, which might be related to more efficient light capturing. All the different phosphonium based electrolytes display good performance with all the three dyes (THD1, THD3 and THD8) with P₂₂₂₍₁₀₁₎FSI giving the best performance.

7.4 Conclusions

We have demonstrated that phosphonium ionic liquids can perform as well as imidazolium based ionic liquids, depending on the sensitisers used. Even though the phosphonium ionic liquids exhibit higher viscosity, they still show good behaviour with thinner TiO₂ films. The use of a thin transparent TiO₂ film with additional layers of 6 μm or 8 μm scattering layer definitely improves the device performance. The use of thin films is favourable as diffusion of the redox species is not hindered to the same extent as that of thicker TiO₂ films, and the high molecular extinction coefficient of the organic sensitisers studied means that no real loss in current density is observed with the thicker films. Addition of co-adsorbents has also demonstrated a beneficial effect on the overall power conversion efficiency. Insertion of the co-adsorbent into empty sites of the TiO₂, which the dye cannot access, provides additional protection of the surface, and thus decreases the back electron transfer from the conduction band of the TiO₂ to the triiodide in the electrolyte. When the temperature of the device is increased, an increase photocurrent density occurred and at the same time a drop in V_{oc} was observed, leading to an increase in the overall efficiency of the device. However, higher temperatures lead to a decrease in both I_{sc} and V_{oc}, probably due to higher rate of recombination processes.

References

1. S. Kim, J. K. Lee, S. O. Kang, J. Ko, J. H. Yum, S. Fantacci, F. De Angelis, D. Di Censo, M. K. Nazeeruddin and M. Grätzel, *J. Am. Chem. Soc.*, 2006, **128**, 16701-16707.
2. P. Qin, X. Yang, R. Chen, L. Sun, T. Marinado, T. Edvinsson, G. Boschloo and A. Hagfeldt, *J. Phys. Chem. C*, 2007, **111**, 1853-1860.
3. M. Grätzel, *J. Photochem. Photobiol. C: Photochem. Rev.*, 2003, **4**, 145-153.
4. C. A. Bignozzi, R. Argazzi and C. J. Kleverlaan, *Chem. Soc. Rev.*, 2000, **29**, 87-96.
5. M. K. Nazeeruddin, A. Kay, I. Rodicio, R. Humphry-Baker, E. Mueller, P. Liska, N. Vlachopoulos and M. Grätzel, *J. Am. Chem. Soc.*, 1993, **115**, 6382-6390.
6. S. M. Zakeeruddin and M. Grätzel, *Adv. Funct. Mater.*, 2009, **19**, 2187-2202.
7. M. K. Nazeeruddin, P. Pechy, T. Renouard, S. M. Zakeeruddin, R. Humphry-Baker, P. Comte, P. Liska, L. Cevey, E. Costa, V. Shklover, L. Spiccia, G. B. Deacon, C. A. Bignozzi and M. Grätzel, *J. Am. Chem. Soc.*, 2001, **123**, 1613-1624.
8. P. Wang, C. Klein, R. Humphry-Baker, S. M. Zakeeruddin and M. Grätzel, *Appl. Phys. Lett.*, 2005, **86**, 123508-123503.
9. Y. Chiba, A. Islam, Y. Watanabe, R. Komiya, N. Koide and L. Han, *Jpn. J. Appl. Phys.*, 2006, **45**, L638-L640.
10. C. Houarner-Rassin, F. Chaignon, C. She, D. Stockwell, E. Blart, P. Buvat, T. Lian and F. Odobel, *J. Photochem. Photobiol. A: Chem.*, 2007, **192**, 56-65.
11. M. Grätzel, *Inorg. Chem.*, 2005, **44**, 6841-6851.
12. C. Y. Chen, S. J. Wu, C. G. Wu, J. G. Chen and K. C. Ho, *Angew. Chem. Int. Ed.*, 2006, **45**, 5822-5825.
13. K. J. Jiang, N. Masaki, J. B. Xia, S. Noda and S. Yanagida, *Chem. Comm.*, 2006, 2460-2462.
14. C. Y. Chen, N. Pootrakulchote, S. J. Wu, M. Wang, J. Y. Li, J. H. Tsai, C. G. Wu, S. M. Zakeeruddin and M. Grätzel, *J. Phys. Chem. C*, 2009, **113**, 20752-20757.
15. J. J. Kim, H. Choi, C. Kim, M. S. Kang, H. S. Kang and J. Ko, *Chem. Mater.* 2009, **21**, 5719-5726.
16. P. Wang, C. Klein, R. Humphry-Baker, S. M. Zakeeruddin and M. Grätzel, *J. Am. Chem. Soc.*, 2004, **127**, 808-809.
17. S. R. Jang, C. Lee, H. Choi, J. J. Ko, J. Lee, R. Vittal and K. J. Kim, *Chem. Mater.*, 2006, **18**, 5604-5608.
18. Z. Ning, Q. Zhang, W. Wu, H. Pei, B. Liu and H. Tian, *J. Org. Chem.*, 2008, **73**, 3791-3797.
19. W. Zeng, Y. Cao, Y. Bai, Y. Wang, Y. Shi, M. Zhang, F. Wang, C. Pan and P. Wang, *Chem. Mater.*, 2010, **22**, 1915-1925.
20. Z. S. Wang, Y. Cui, Y. Dan-Oh, C. Kasada, A. Shinpo and K. Hara, *J. Phys. Chem. C*, 2007, **111**, 7224-7230.
21. K. Hara, Z. S. Wang, T. Sato, A. Furube, R. Katoh, H. Sugihara, Y. Dan-Oh, C. Kasada, A. Shinpo and S. Suga, *J. Phys. Chem. B*, 2005, **109**, 15476-15482.
22. X. Zhang, J. J. Zhang and Y. Y. Xia, *J. Photochem. Photobiol. A: Chem.*, 2008, **194**, 167-172.
23. K. Hara, K. Sayama, H. Arakawa, Y. Ohga, A. Shinpo and S. Suga, *Chem. Comm.*, 2001, 569-570.
24. T. Horiuchi, H. Miura, K. Sumioka and S. Uchida, *J. Am. Chem. Soc.*, 2004, **126**, 12218-12219.
25. L. Huang, L. Jiang and M. Wei, *Electrochem. Commun.*, 2010, **12**, 319-322.

7. Ionic liquids in dithienothiophene based organic dye sensitised solar cells

26. W. H. Howie, F. Claeysens, H. Miura and L. M. Peter, *J. Am. Chem. Soc.*, 2008, **130**, 1367-1375.
27. S. Ito, H. Miura, S. Uchida, M. Takata, K. Sumioka, P. Liska, P. Comte, P. Pechy and M. Grätzel, *Chem. Comm.*, 2008, 5194-5196.
28. Z. S. Wang, F. Y. Li, C. H. Huang, L. Wang, M. Wei, L. P. Jin and N. Q. Li, *J. Phys. Chem. B*, 2000, **104**, 9676-9682.
29. Y. S. Chen, C. Li, Z. H. Zeng, W. B. Wang, X. S. Wang and B. W. Zhang, *J. Mater. Chem.*, 2005, **15**, 1654-1661.
30. E. Stathatos, P. Lianos, A. Laschewsky, O. Ouari and P. Van Cleuvenbergen, *Chem. Mater.*, 2001, **13**, 3888-3892.
31. Z. S. Wang, F. Y. Li and C. H. Huang, *Chem. Comm.*, 2000, 2063-2064.
32. Z. S. Wang, F. Y. Li and C. H. Huang, *J. Phys. Chem. B*, 2001, **105**, 9210-9217.
33. W. J. Wu, W. H. Zhan, J. L. Hua and H. Tian, *Res. Chem. Intermed.*, 2008, **34**, 241-248.
34. A. Wulf, K. Fumino, R. Ludwig and P. F. Taday, *ChemPhysChem*, 2010, **11**, 349-353.
35. A. Imanishi, H. Suzuki, N. Ohashi, H. Kondoh, T. Ohta and Y. Nakato, *J. Phys. Chem. C*, 2009, **113**, 17254-17261.
36. V. Shirinian and A. Shimkin, *Merocyanines: Synthesis and Application*, 2008, pp. 75-105.
37. A. Burke, S. Ito, H. Snaith, U. Bach, J. Kwiakowski and M. Grätzel, *Nano Lett.*, 2008, **8**, 977-981.
38. W. Xu, B. Peng, J. Chen, M. Liang and F. Cai, *J. Phys. Chem. C*, 2008, **112**, 874-880.
39. M. Liang, W. Xu, F. Cai, P. Chen, B. Peng, J. Chen and Z. Li, *J. Phys. Chem. C*, 2007, **111**, 4465-4472.
40. T. Marinado, K. Nonomura, J. Nissfolk, M. K. Karlsson, D. P. Hagberg, L. Sun, S. Mori and A. Hagfeldt, *Langmuir*, 2009, **26**, 2592-2598.
41. P. Shen, Y. Liu, X. Huang, B. Zhao, N. Xiang, J. Fei, L. Liu, X. Wang, H. Huang and S. Tan, *Dyes Pigm.*, 2009, **83**, 187-197.
42. Q. H. Yao, L. Shan, F. Y. Li, D. D. Yin and C. H. Huang, *New J. Chem.*, 2003, **27**, 1277-1283.
43. X. Ma, J. Hua, W. Wu, Y. Jin, F. Meng, W. Zhan and H. Tian, *Tetrahedron*, 2008, **64**, 345-350.
44. K. Hara, T. Horiguchi, T. Kinoshita, K. Sayama and H. Arakawa, *Sol. Energy Mater. Sol. Cells*, 2001, **70**, 151-161.
45. E. E. Jelley, *Nature*, 1936, **138**, 1009-1010.
46. A. Eisfeld and J. S. Briggs, *Chem. Phys.*, 2006, **324**, 376-384.
47. F. Lenzmann, J. Krueger, S. Burnside, K. Brooks, M. Grätzel, D. Gal, S. Ruhle and D. Cahen, *J. Phys. Chem. B*, 2001, **105**, 6347-6352.
48. M. Grätzel, *Nature*, 2001, **414**, 338-344.
49. H. Stegemann, A. Rohde, A. Reiche, A. Schnittke and H. Füllbier, *Electrochim. Acta*, 1992, **37**, 379-383.
50. M. H. Ghatee, M. Zare, F. Moosavi and A. R. Zolghadr, *J. Chem. Eng. Data*, 2010, **55**, 3084-3088.
51. I. Mills, T. Cvitas, K. Homann, N. Kallay and K. Kuchitsu, *International Union of Pure and Applied Chemistry : Quantities, Units and Symbols in Physical Chemistry*, Oxford: Blackwell Science, 1993.
52. Y. Bai, Y. Cao, J. Zhang, M. Wang, R. Li, P. Wang, S. M. Zakeeruddin and M. Grätzel, *Nature Materials*, 2008, **7**, 626-630.

53. H. Y. Yang, Y. S. Yen, Y. C. Hsu, H. H. Chou and J. T. Lin, *Org. Lett.*, 2009, **12**, 16-19.
54. Z. S. Wang, K. Hara, Y. Dan-Oh, C. Kasada, A. Shinpo, S. Suga, H. Arakawa and H. Sugihara, *J. Phys. Chem. B*, 2005, **109**, 3907-3914.
55. C. Klein, M. K. Nazeeruddin, D. Di Censo, P. Liska and M. Grätzel, *Inorgan. Chem.*, 2004, **43**, 4216-4226.
56. J. H. Yum, S. J. Moon, R. Humphry-Baker, P. Walter, T. Geiger, F. Nüesch, M. Grätzel and M. D. K. Nazeeruddin, *Nanotechnology*, 2008, 424005.
57. X. Jiang, T. Marinado, E. Gabrielsson, D. P. Hagberg, L. Sun and A. Hagfeldt, *J. Phys. Chem. C*, 2010, **114**, 2799-2805.
58. A. J. Bard and L. R. Faulkner, *Electrochemical Methods: Fundamental and Application*, VHC, New York, USA 1995.
59. N. Papageorgiou, Y. Athanassov, M. Armand, P. Bonhote, H. Pettersson, A. Azam and M. Grätzel, *J. Electrochem. Soc.*, 1996, **143**, 3099-3108.
60. Y. Liu, A. Hagfeldt, X. R. Xiao and S. E. Lindquist, *Sol. Energy Mater. Sol. Cells*, 1998, **55**, 267-281.
61. S. Mikoshiba, S. Murai, H. Sumino, T. Kado, D. Kosugi and S. Hayase, *Curr. Appl. Phys.*, 2005, **5**, 152-158.
62. V. Alexis De, *Solar Cells*, 1983, **8**, 283-296.
63. M. Grätzel, *J. Photochem. Photobiol. A: Chem.*, 2004, **164**, 3-14.
64. S. Ito, S. M. Zakeeruddin, R. Humphry-Baker, P. Liska, R. Charvet, P. Comte, M. K. Nazeeruddin, P. Pechy, M. Takata, H. Miura, S. Uchida and M. Grätzel, *Adv. Mater.*, 2006, **18**, 1202-1205.
65. A. Usami, S. Seki, Y. Mita, H. Kobayashi, H. Miyashiro and N. Terada, *Sol. Energy Mater. Sol. Cells*, 2009, **93**, 840-842.
66. A. Hagfeldt and M. Grätzel, *Chem. Rev.*, 1995, **95**, 49-68.
67. C. J. Barbé, F. Arendse, P. Comte, M. Jirousek, F. Lenzmann, V. Shklover and M. Grätzel, *J. Am. Chem. Soc.*, 1997, **80**, 3157-3171.
68. T. P. Chou, Q. Zhang, B. Russo, G. E. Fryxell and G. Cao, *J. Phys. Chem. C*, 2007, **111**, 6296-6302.
69. M. Grätzel, *J. Photochem. Photobiol. C: Photochem. Rev.*, 2003, **4**, 145-153.
70. F. Gracia, J. P. Holgado and A. R. González-Elipe, *Langmuir*, 2004, **20**, 1688-1697.
71. M. Grätzel, *J. Photochem. Photobiol. A: Chem.*, 2004, **168**, 235-235.

Chapter 8

Ionic liquids for porphyrin dye sensitised solar cells

Chapter overview

In this chapter we describe the use of a variety of ionic liquid electrolytes with porphyrin sensitisers and compare these to the standard ruthenium based sensitisers. During the past few years, imidazolium ionic liquids have been tested with different ruthenium based dyes and, more recently, with many organic sensitisers, giving good efficiencies. In this chapter, the use of imidazolium ionic liquids with porphyrin dyes is described, as well as other non-imidazolium based ionic liquids.

8.1 Introduction

8.1.1 Porphyrin chromophores for dye sensitised solar cells

Porphyrin sensitisers have attracted the attention of many researchers due to their major role as light harvesting pigments in the photosynthesis process.¹ The first application of porphyrin sensitisers in photoelectrochemical cells was demonstrated by Kalyanasundaram *et al.*² They used a (tetrakis(4-carboxyphenyl)porphyrinato) Zinc, abbreviated ZnTPPC, to sensitise the TiO₂ and showed that dye adsorption was quite efficient and the colour was intense after only 1 hr. Although quite low IPCEs were obtained in that first study, it nevertheless triggered the interest of many researchers in designing new organic dyes with the porphyrin structures for use in DSSCs. In 2005, Campbell *et al.* reported a conversion efficiency of 5.2 %, with an I_{sc} of 13.5 mA cm⁻², a V_{oc} of 566 mV and an IPCE >70 %, in a standard acetonitrile based electrolyte with a porphyrin dye abbreviated as Zn-3 (see Figure 8.1).³ Further improvements have since been obtained by careful design of the zinc porphyrin sensitiser.⁴ By introducing a malonic acid anchoring group, and different aryl groups as the electron donor, they have been able to further increase the device performance. The efficiency went up to 7.1 % with a methyl substituent on the aryl groups; the dye named GD2. The main interesting features of porphyrin sensitisers, apart from the fact that they can be used to mimic nature, are that the Soret and Q-band have large molar extinction coefficients. The Soret band has an extinction coefficient of 10⁵ M⁻¹ cm⁻¹ in the region of 400-500 nm, and the Q-band has an extinction coefficient of 10⁴ M⁻¹ cm⁻¹ in the range of 600-800 nm, which are much higher than for ruthenium complexes.

Since the development of high performing devices based on porphyrin sensitisers, numerous publications on porphyrin sensitisers in DSSCs have appeared.⁵⁻⁷ For instance, Xiang *et al.* developed a porphyrin sensitiser containing a thiophene bridge, which gave a conversion efficiency of 6.5 %.⁸ Recently, Lu *et al.* reported a 6.7 % efficiency with a push-pull zinc porphyrin chromophore (YD12).⁵ The same dye was further enhanced to 11 % by applying a scattering layer on top of the transparent TiO₂ layer, with standard molecular liquid electrolytes.⁹ This is the first time that such a high performance has been obtained with an organic sensitiser.

8.2 Aim

The aim of this work was to study the use of ionic liquids based on imidazolium, ammonium and phosphonium cations with porphyrin sensitisers. The porphyrin sensitisers (P159, P135, GD2, GD3 and EM41) were obtained from Professor David Officer's group at the University of Wollongong.

In comparing the efficiencies of devices discussed here, it is important to note that the best performance obtained with ruthenium sensitisers in our lab is 9 % using molecular liquid based electrolytes, compared to 12 % in Grätzel's lab at EPFL, and 5.5 % with ionic liquids based electrolyte compared to 8.2 % in EPFL. The difference in efficiency might be related to factors such as the TiO₂ paste, the method used to deposit the TiO₂ film, the solvent used for the dye, the dye itself (with different batches of dye, different efficiency was obtained) or any number of mundane factors. Therefore the performance of the porphyrin sensitisers will be compared to the best performing device obtained with Ruthenium sensitisers fabricated in our lab.

8. Ionic liquids for porphyrin dye sensitised solar cells

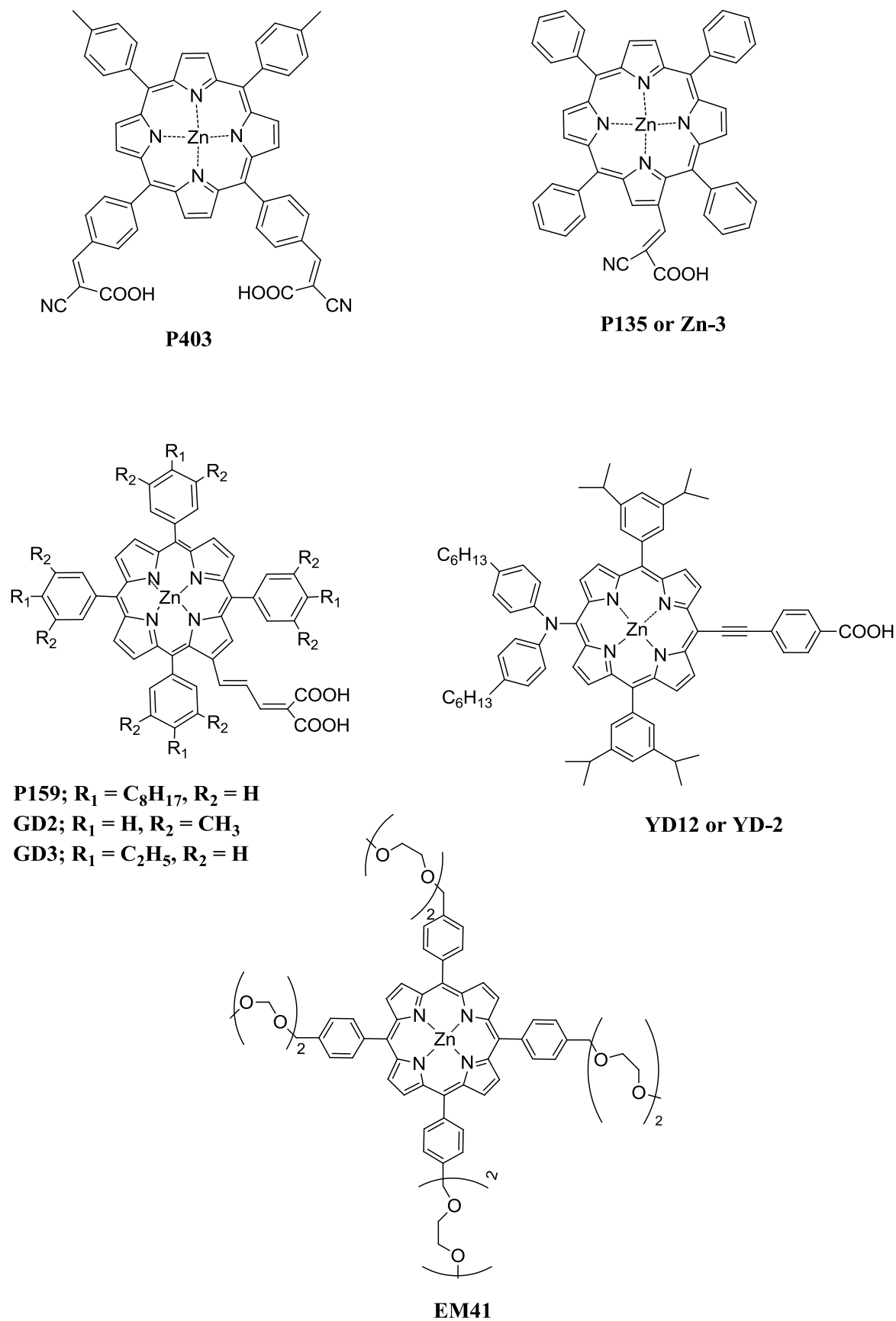


Figure 8.1: The structure of some porphyrin dyes

8.3 Experimental

A description of the methods used to analyse the ionic liquids has already been provided in Chapter 3 and the synthesis of the $P_{1224}NTf_2$ is described in Chapter 6. Full descriptions of the equipment and cell assembly are given in Chapters 3 and 4.

8.3.1 Transient adsorption spectroscopy

Transient absorption spectroscopy was performed using the ns pulses of a Lab 170 – MOPO as the pump laser and CW Xe lamp modulated by bandpass / cutoff filters as the probe. 100 k points were recorded with full 500 MHz bandwidth, 512 averages per measurements and further mathematical averages using the custom-built labview filter. The repetition rate was 10 Hz except in one measurement, where 1 Hz was used – no difference in the recombination rate was observed. All samples were sealed with a microscope cover glass and illuminated from the FTO side unless otherwise noted as backside illumination.

8.3.2 Ionic liquids

Below is a list of the different ionic liquids studied in porphyrin dye sensitised solar cells. Some ionic liquids were purchased from commercial suppliers and other ionic liquids were synthesised.

1-ethyl-3-methylimidazolium tetracyanoborate ($C_2mimB(CN)_4$), 1-ethyl-3-methylimidazolium thiocyanate ($C_2mimSCN$) and 1-butyl-3-methylimidazolium iodide (C_4mimI) were purchased from Merck, used as received and handled in a nitrogen filled glove box. Triethyl(2-methoxyethyl)phosphonium bis(trifluoromethanesulfonyl)amide ($P_{222(201)}NTf_2$) and triethyl(methoxymethyl) phosphonium bis(trifluoromethanesulfonyl) amide ($P_{222(101)}NTf_2$) were obtained from Nippon Chemical. These were also handled only in the glove box. Diethyl-isobutylmethylphosphonium bis(trifluoromethanesulfonyl) amide ($P_{1224}NTf_2$), 1-ethyl-3-methylimidazolium iodide (C_2mimI), 1,3- dimethylimidazolium iodide (C_1mimI), 1-propyl-3-methylimidazolium iodide (C_3mimI), 1-ethyl-3-methylimidazolium bis(trifluoromethanesulfonyl)amide ($C_2mimNTf_2$), 1-ethyl-3-methylimidazolium dicyanamide ($C_2mimN(CN)_2$) and hexyl(triethyl)ammonium bis(trifluoromethanesulfonyl) amide ($N_{2226}NTf_2$) were synthesised by the literature method.¹⁰

8. Ionic liquids for porphyrin dye sensitised solar cells

1-ethyl-3-methylimidazolium iodide (C₂mimI)

¹H NMR (d₆-DMSO, 300 MHz) δ 1.2 - 1.6 ppm (t, 3H), 4.2 - 4.3 ppm (q, 2H), 7.4 - 7.5 ppm (m, 2H), 4.8 ppm (s 3H), 8.7 ppm (s 1H).

MS (ESI): ES+ *m/z* 110.8 (C₆H₁₁N₂⁺), ES- *m/z*, 126.9 (I).

1,3-dimethylimidazolium iodide (C₁mimI)

¹H NMR (d₆-DMSO, 300 MHz) δ 3.7 ppm (s, 3H), 4.3 ppm (s, 3H), 7.4 - 7.5 ppm (m, 2H), 8.7 ppm (s, 1H).

MS (ESI): ES+ *m/z* 97.08 (C₅H₉N₂⁺), ES- *m/z*, 126.9 (I).

1-propyl-3-methylimidazolium iodide (C₃mimI)

¹H NMR (d₆-DMSO, 300 MHz) δ 0.8 - 0.9 ppm (t, 3H), 4.1 - 4.2 ppm (t, 2H), 3.8 - 3.9 ppm (s, 3H), 7.7 - 7.8 ppm (m, 2H), 9.1 ppm (s, 1H).

MS (ESI): ES+ *m/z* 125.1 (C₇H₁₃N₂⁺), ES- *m/z*, 126.9 (I).

1-ethyl-3-methylimidazolium bis(trifluoromethanesulfonyl)amide (C₂mimNTf₂)

¹H NMR (d₆-DMSO, 300 MHz) δ 1.3 - 1.4 ppm (t, 3H), 4.1 - 4.2 ppm (q, 2H), 7.7 - 7.8 ppm (m, 2H), 3.8 ppm (s 3H), 9.1 ppm (s 1H).

MS (ESI): ES+ *m/z* 110.7 (C₆H₁₁N₂⁺), ES- *m/z*, 280 (NTf₂⁻).

Water content (Karl Fischer): 160 ppm.

1-ethyl-3-methylimidazolium dicyanamide (C₂mimN(CN)₂)

¹H NMR (d₆-DMSO, 300 MHz) δ 1.3 - 1.4 ppm (t, 3H), 4.1 - 4.2 ppm (q, 2H), 7.7 - 7.8 ppm (m, 2H), 3.8 ppm (s 3H), 9.1 ppm (s 1H).

MS (ESI): ES+ *m/z* 110.7 (C₆H₁₁N₂⁺), ES- *m/z*, 66 (N(CN)₂⁻).

Water content (Karl Fischer): 260 ppm.

Hexyl(triethyl)ammonium bis(trifluoro-methanesulfonyl) amide (N₂₂₂₆NTf₂)

¹H NMR (d₆-DMSO, 300 MHz) δ 0.8 - 0.9 ppm (t, 3H), 1.1 - 1.2 ppm (t, 3H), 1.3 - 1.4 ppm (m, 2H), 1.6 - 1.7 ppm (m, 2H), 3.1 - 3.2 ppm (m, 2H), 3.3 - 3.4 ppm (m, 2H).

MS (ESI): ES+ *m/z* 186 (C₁₂H₂₈N₂⁺), ES- *m/z*, 280 (NTf₂⁻).

Water content (Karl Fischer): 190 ppm.

8.3.3 Preparation of electrolytes

Preparation of standard electrolyte for porphyrin sensitisers

The standard acetonitrile-valeronitrile based electrolyte was composed of an acetonitrile:valeronitrile mixture (75:25 vol %), iodine (0.03 M), 4-*tert*-butylpyridine (TBP) (0.5 M), 1-butyl-3-methylimidazolium iodide (0.6 M) and lithium iodide (0.1 M). The effect of an additive other than TBP was also investigated in the acetonitrile based electrolyte. N-methylbenzimidazole (NMB) was used as an additive in the ionic liquid systems because of its low vapour pressure compared to TBP, which is beneficial for long term stability.

Preparation of binary and ternary ionic liquid electrolytes

According to the literature, binary mixtures, as well as more complex multi-component eutectic mixtures, work well with ruthenium-based DSSCs.¹¹ Thus, these ionic liquids were studied for the first time with porphyrin DSSCs. The general composition of the ionic liquid electrolytes was C₁mimI/C₂mimI/IL/LiI/I₂/NMB (12: 12: 16: 1: 1.67: 4 by mol) with different types of IL as the third component. The following ILs were used in this study: C₂mimB(CN)₄, P₁₂₂₄NTf₂, P₂₂₂₍₁₀₁₎NTf₂, P₂₂₂₍₂₀₁₎NTf₂, N₁₁₂₃NTf₂, N₂₂₂₆NTf₂, C₂mimNTf₂, C₂mimN(CN)₂, C₂mimBF₄ and C₂mimSCN, each chosen because of their stability and fluidity.

The binary ionic liquid electrolyte was composed of 35 vol % imidazolium or pyrrolidinium based ionic liquids, 65 vol % C₃mimI, 0.1 M of lithium iodide, 0.5 M *tert*-butylpyridine and 0.2 M iodine.

The electrolytes were injected through a pre-drilled hole in the counter electrode by vacuum backfilling, while the DSSC was sitting on a hot plate, and then the holes were sealed with a 25 µm Surlyn sheet and a microscope coverslip.

Preparation of dye solution

Five porphyrin dyes were investigated in this study. 0.2 M dye was dissolved in dry ethanol. As a comparison, N719 was used; 0.5 M N719 was dissolved in a mixture of *tert*-butanol: acetonitrile.

8.4 Results and discussion

8.4.1 Physical and chemical properties of ionic liquids

Density, viscosity and electrical conductivity of the neat ionic liquids

For comparison, the physical properties of the imidazolium and phosphonium ILs, as measured in this work, are summarized in Table 8.1. C₂mimN(CN)₂ had the highest conductivity and N₁₁₂₃NTf₂ the lowest. The introduction of the ether side chain significantly decreased the viscosity of the phosphonium ionic liquids and thus P₂₂₂₍₂₀₁₎NTf₂ was of comparable viscosity to the well known C₂mimNTf₂.¹² However, the ‘‘cyano’’ (i.e. the SCN, N(CN)₂, C(CN)₃¹³ and B(CN)₄) ILs of the C₂mim cation retained the lowest viscosity.

Table 8.1: The physical properties of the pure ionic liquids at 25 °C.

Pure ionic liquids	Density (g cm ⁻³) ± 0.01	Viscosity (mPa s) ± 0.1	Conductivity (mS cm ⁻¹) ±1
C ₂ mimB(CN) ₄	1.04	21	16.1
C ₂ mimBF ₄	1.28	38	17.5
C ₂ mimNTf ₂	1.51	33	10.3
C ₂ mimN(CN) ₂	1.09	19	20.2
C ₂ mimSCN	1.11	21	22.2
N ₁₁₂₃ NTf ₂	1.41	101	2.30
N ₂₂₂₆ NTf ₂ ¹⁴	1.27	167	0.67
P ₁₂₂₄ NTf ₂	1.40	71	2.60
P ₂₂₂₍₂₀₁₎ NTf ₂	1.39	44	4.40
P ₂₂₂₍₁₀₁₎ NTf ₂	1.42	35	3.58

The ionic conductivity of the ionic liquid electrolytes

Figure 8.2 displays the plots of ionic conductivity of the electrolytes as a function of temperature. Of the electrolytes studied, the imidazolium series showed the best ionic conductivity and the N₂₂₂₆NTf₂ electrolyte exhibits the lowest. This is probably due to the high viscosity of the neat ionic liquid, as shown in Table 8.1. C₂mimNTf₂ displays the lowest ionic conductivity in the family of C₂mim based electrolytes. Within the phosphonium series, the electrolytes all show similar ionic conductivity.

In all cases, as the temperature increases, the ionic conductivity of the electrolyte system also increases, as a result of a decrease in the viscosity of the system, which produces a higher degree of freedom for the ionic species.

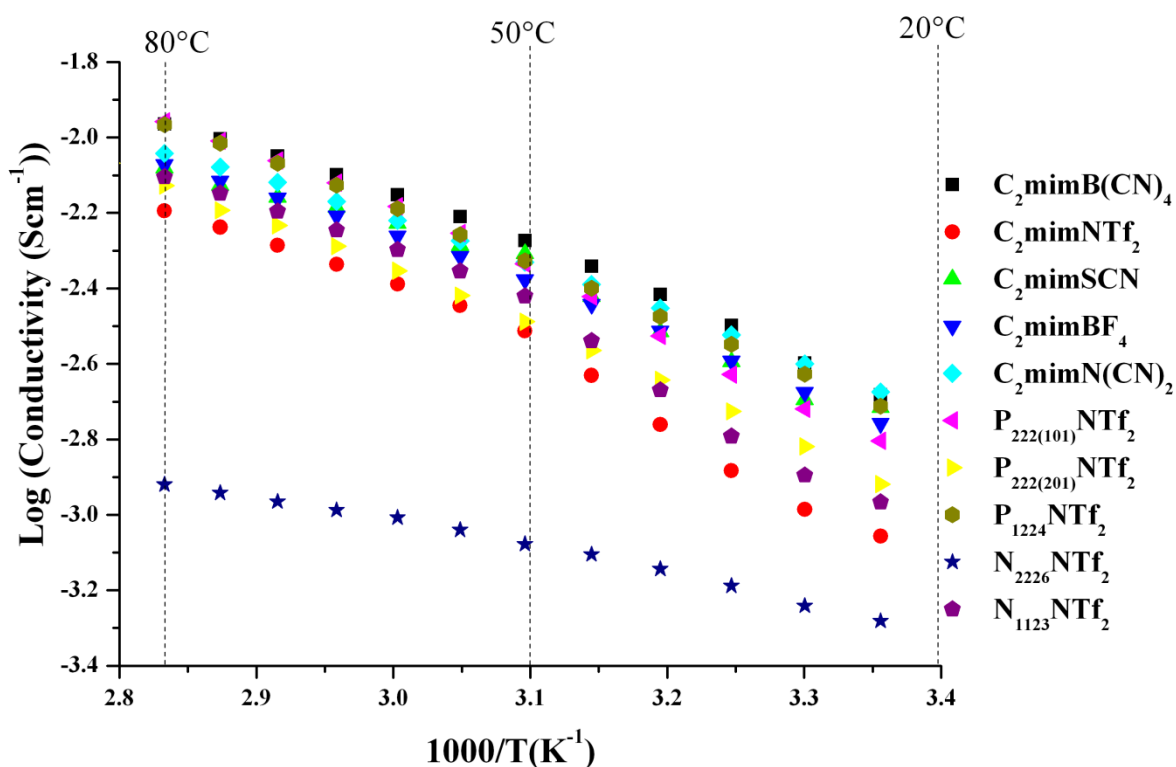


Figure 8.2: Ionic conductivity of ionic liquid based electrolytes as function of inverse of temperature

Diffusion coefficients of triiodide in different ionic liquid electrolyte systems

Several methods are available to measure the diffusion coefficient of iodide and triiodide, such as cyclic voltammetry and chronoamperometry, using a three electrode set up with a microelectrode as working electrode, or electrochemical impedance spectroscopy and polarisation measurements using a two electrode set up, usually composed of two pieces of platinised FTO glass. In this section, cyclic voltammetry on a symmetrical cell was used. Some ionic liquid electrolytes were also analysed using the former method for comparison.

8. Ionic liquids for porphyrin dye sensitised solar cells

The diffusion coefficient of the redox mediators gives an indication of the mobility of the electroactive species, to determine if this can be correlated to the performance of the dye sensitised solar cells.

Figure 8.3 shows the cyclic voltammetry of a variety of electrolyte systems using symmetrical cells, and Table 8.2 summarises the data. The imidazolium series shows quite similar behaviour, except for the C_2mimBF_4 system that shows lower current density, which might be related to the viscosity of the ionic liquid.

Within the phosphonium family, $P_{222(101)}NTf_2$ shows the highest current density and $P_{1224}NTf_2$ the lowest, which also might be related to the viscosity of the ionic liquids; $P_{1224}NTf_2$ is a solid at 25 °C and melts at 30 °C (see Chapter 5, Figure 5.5).

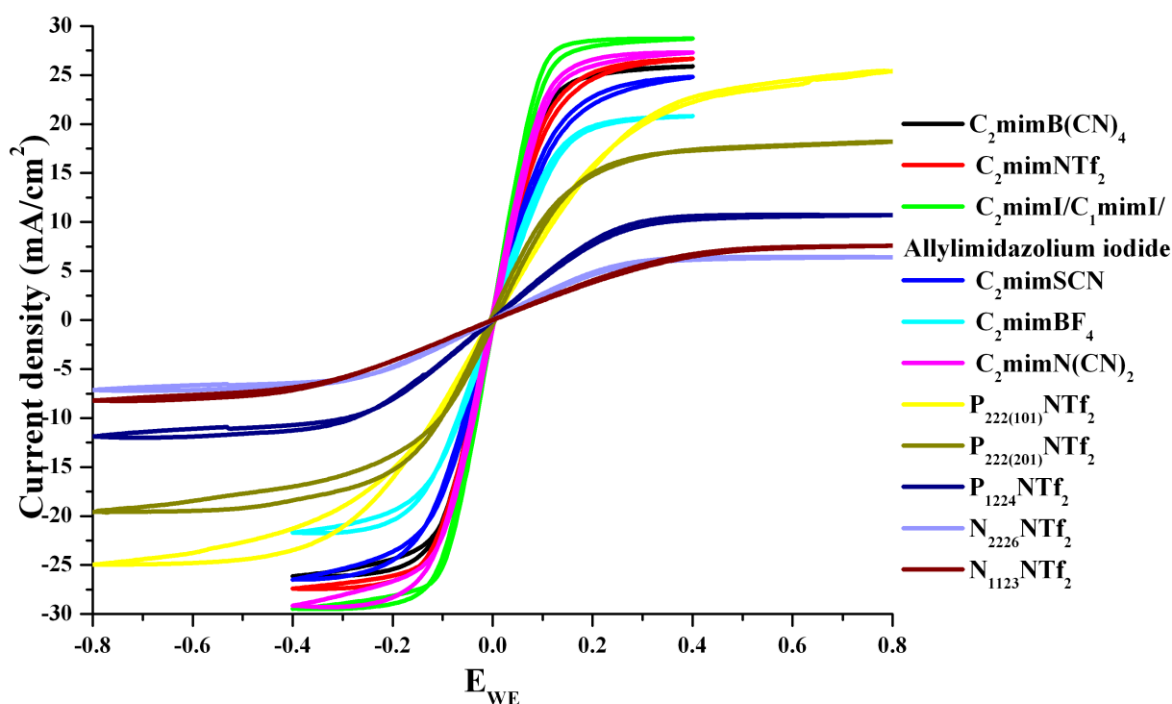


Figure 8.3: CV of the different ionic liquids containing I^- (2.5 M) and I_3^- (0.125 M) at room temperature using a symmetrical cell at a scan rate of 5 mV s^{-1}

The diffusion coefficients of I_3^- were determined using the following equation:

$$J_{Lim} = \frac{2nFC_{I_3^-}D_{I_3^-}}{l} \quad (\text{Eq 8.1})$$

where J_{lim} is the limiting current density (mA cm^{-2}), n is the number of electrons transferred ($n = 2$) F is the Faraday constant (96500 C), C is the concentration of the I_3^- (mol cm^{-3}) and D is the diffusion coefficient of I_3^- ($\text{cm}^2 \text{ s}^{-1}$).¹⁵

Table 8.2: The diffusion coefficients of I^- and I_3^- , determined using two different methods.

Electrolyte	Symmetrical cell ($\pm 8 \%$)		Microelectrode ($\pm 5 \%$)	
	$D(I^-) \text{ cm}^2 \text{ s}^{-1}$	$D(I_3^-) \text{ cm}^2 \text{ s}^{-1}$	$D(I^-) \text{ cm}^2 \text{ s}^{-1}$	$D(I_3^-) \text{ cm}^2 \text{ s}^{-1}$
Acetonitrile- valeronitrile	5.4×10^{-6}	4.8×10^{-6}	5.9×10^{-6}	4.7×10^{-6}
$C_2\text{mimB}(\text{CN})_4$	2.9×10^{-7}	5.2×10^{-7}	3.1×10^{-7}	4.7×10^{-7}
$C_2\text{mimNTf}_2$	2.8×10^{-7}	5.1×10^{-7}	2.9×10^{-7}	4.7×10^{-7}
$C_2\text{mimI}/C_1\text{mimI}/$ allylimidazolium iodide	3.5×10^{-7}	5.6×10^{-7}	-	-
$C_2\text{mimSCN}$	2.1×10^{-7}	5.1×10^{-7}	2.6×10^{-7}	4.9×10^{-7}
$C_2\text{mimBF}_4$	2.0×10^{-7}	5.2×10^{-7}	2.3×10^{-7}	4.6×10^{-7}
$C_2\text{mimN}(\text{CN})_2$	2.4×10^{-7}	5.4×10^{-7}	2.6×10^{-7}	4.9×10^{-7}
$P_{222(101)}\text{NTf}_2$	1.5×10^{-7}	4.5×10^{-7}	2.1×10^{-7}	4.1×10^{-7}
$P_{222(201)}\text{NTf}_2$	1.9×10^{-7}	2.8×10^{-7}	2.0×10^{-7}	2.5×10^{-7}
$P_{1224}\text{NTf}_2$	1.8×10^{-7}	2.5×10^{-7}	1.9×10^{-7}	2.2×10^{-7}
$N_{2226}\text{NTf}_2$	1.5×10^{-7}	1.7×10^{-7}	1.7×10^{-7}	1.8×10^{-7}
$N_{1123}\text{NTf}_2$	1.7×10^{-7}	1.9×10^{-7}	1.6×10^{-7}	1.5×10^{-7}

The diffusion coefficient of I_3^- using the two different experiment set ups are quite comparable within error. The mobility of I_3^- is 10 times faster in acetonitrile than in the ionic liquids, which is expected as a result of the viscosity and solvation properties of the ionic liquids. Nevertheless, the transport property of I_3^- is quite high in the ionic liquid systems, which might be due to the high content of iodine in the electrolyte, or according to Wachter *et al.*,¹⁶ the high diffusion of I_3^- can be related to the high ionic strength of the ionic liquids which facilitates the transport of I_2 .

8. Ionic liquids for porphyrin dye sensitised solar cells

As previously reported,¹⁶⁻¹⁸ the transport mechanism of I_3^- is achieved by the Grotthuss exchange mechanism, which occurs as a result of the high concentration of the iodine, which gives rise to formation of polyiodides, thus enabling the rapid exchange of bonding electrons and therefore increasing the apparent movement of the triiodide species.

To further support this hypothesis, the Stokes-Einstein equation is used to calculate the diffusion coefficient of the triiodide.

$$D = \frac{k_B T}{6\pi\eta r} \quad (\text{Eq 8.2})$$

where D is the diffusion coefficient, k_B is the Boltzman constant ($1.3807 \times 10^{-23} \text{ J K}^{-1}$), T is the temperature (K), r is the hydrodynamic radius for triiodide ($\sim 2.1 \text{ \AA}$) and η is the viscosity of the electrolyte.

Using this equation, the diffusion coefficient of the triiodide in $P_{222(101)}\text{NTf}_2$ is only expected to be $1.2 \times 10^{-7} \text{ cm}^2 \text{ s}^{-1}$ which is lower than the measured diffusion coefficient by a factor of about 4 times. Another example is $P_{222(201)}\text{NTf}_2$ whose diffusion coefficient is $0.7 \times 10^{-7} \text{ cm}^2 \text{ s}^{-1}$; also a factor of about 4. This confirms that there is a mechanism operative that is not taken into consideration by the Stokes-Equation.

8.4.2 Photovoltaic characterisation

The performance of six porphyrin sensitisers was investigated using standard molecular liquid electrolyte, and this is used to compare the performance of the devices with ionic liquids. For each dye, four devices were fabricated and constructed on the same day.

8.4.2.1 Different porphyrin sensitisers

Figure 8.4 shows the performance of P159, GD3, GD2, P135, EM41 and P403 under full light intensity, and Table 8.3 summarises the photovoltaic parameters. The structure of the porphyrin sensitisers are shown in Figure 8.1.

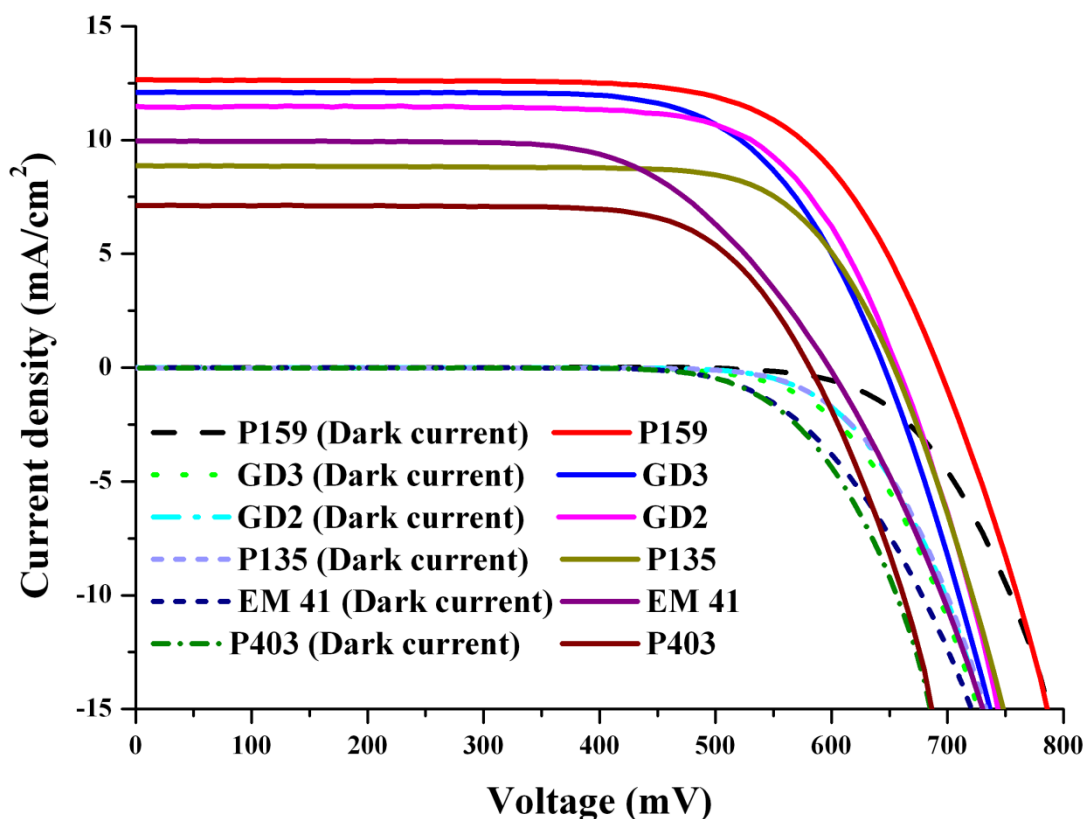


Figure 8.4: IV curves for different porphyrin sensitizer DSSCs using a standard acetonitrile-valeronitrile based electrolyte, under full sunlight (AM 1.5) or in the dark

The results obtained from the IV curves of the DSSC based on P403 are 7.12 mA cm^{-2} , 582 mV and 0.72 for I_{sc} , V_{oc} and fill factor respectively. These give an overall performance of 2.96% . The low V_{oc} may be due to an increase in the back reaction process, as observed by the dark current which is shifted to lower potential. The structure of the P403 sensitizer can also have an effect on the performance of the devices. As shown in Figure 8.1, P403 contains two binding groups attached to the benzene ring, a carboxylic acid and a nitrile group. It is possible that the dyes are loosely attached to the surface of the TiO_2 , or that they aggregate, leading to a lower current density. If the dye is not properly attached to the semiconductor, this will lower the charge injection efficiency, which will have an effect on the current density delivered.¹⁹

8. Ionic liquids for porphyrin dye sensitised solar cells

DSSCs based on EM 41 generates an I_{sc} of 10 mA cm^{-2} , a V_{oc} of 598 mV and a fill factor of 0.64, yielding an overall conversion efficiency of 3.81 %. Even though the sensitiser has a good dye coverage, $6.5 \times 10^{15} \text{ molecules cm}^{-1} \mu\text{m}^{-1}$ which is similar to the best performing dye P159, the performance is poor. This is mainly due to the low V_{oc} , which may be due to a high recombination rate between the TiO_2 and the electrolyte, arising from a different structure/shape of the adsorbed dye molecule. A low performance is also observed with P135. The I_{sc} , V_{oc} and ff generated by the device containing P135 are 8.9 mA cm^{-2} , 654 mV and 0.74 respectively, resulting in an overall performance of 4.3 %. The main limitation of P135 is the low current density, which is due to dissolution of the dye when the molecular liquid electrolyte is injected into the device. Visual observation of the device shows that the electrolyte turned green within 5 mins. The dissolution of the dye may be due to poor binding between the dye and the semiconductor. GD2, GD3 and P159 show quite good performance compared to the P403, EM41 and P135. P159 gives the best device performance, with an I_{sc} of 12.7 mA cm^{-2} , a V_{oc} of 692 mV and a fill factor of 0.69, yielding an overall performance of 6.0 % under 1 sun. The high performance may be due to the presence of the long alkyl chains on the peripheral benzene ring, providing a shielding effect from the back electron transfer from the TiO_2 , as indicated by the dark current.

Table 8.3: Photovoltaic parameters for the DSSCs with the porphyrin dyes.

Dyes	V_{oc} (mV)	I_{sc} (mA/cm ²)	ff	η (%)
P159	693 (± 2)	12.7 (± 0.2)	0.69(± 0.01)	6.0 (± 0.1)
GD3	645 (± 3)	12.1 (± 0.1)	0.69(± 0.02)	5.4 (± 0.2)
GD2	657 (± 2)	11.5 (± 0.2)	0.71(± 0.01)	5.4 (± 0.1)
P135	654 (± 3)	8.9 (± 0.1)	0.74(± 0.01)	4.3 (± 0.1)
EM41	598 (± 2)	10.0 (± 0.1)	0.64(± 0.02)	3.8 (± 0.2)
P403	582 (± 5)	7.1 (± 0.2)	0.72(± 0.01)	3.0 (± 0.1)

8.4.2.2 The effect of adding chenodeoxycholic acid and increasing the concentration of 4-tert-butylpyridine in GD2-based DSSCs

To study the effect of chenodeoxycholic acid and the concentration of TBP, a $12 \mu\text{m}$ transparent TiO_2 film, on top of which an additional scattering layer was screen printed, was used. The films were dyed for two hours. The electrolyte use for the investigation of

the effect of chenodeoxycholic acid was composed of 0.1 M LiI, 0.05 M I₂, 0.6 M C₃mimI and 0.5 M TBP in the standard acetonitrile-valeronitrile mixture.

Addition of different concentrations of chenodeoxycholic acid (DCA)

The effect of chenodeoxycholic acid (DCA) was investigated with the GD2 porphyrin sensitiser. 0.02 mM, 0.2 mM and 2 mM of DCA was dissolved in a 0.2 mM GD2 dye solution (UV-Vis spectrum is shown in Appendix, section A.7). As already discussed in Chapter 7, a co-adsorbent is used to reduce dye aggregation and thereby increase the photovoltaic performance of the device. Figure 8.5 compares the IV characteristics of devices, made using the GD2 sensitiser, with various dye/DCA ratios. The corresponding photovoltaic data is summarised in Table 8.4.

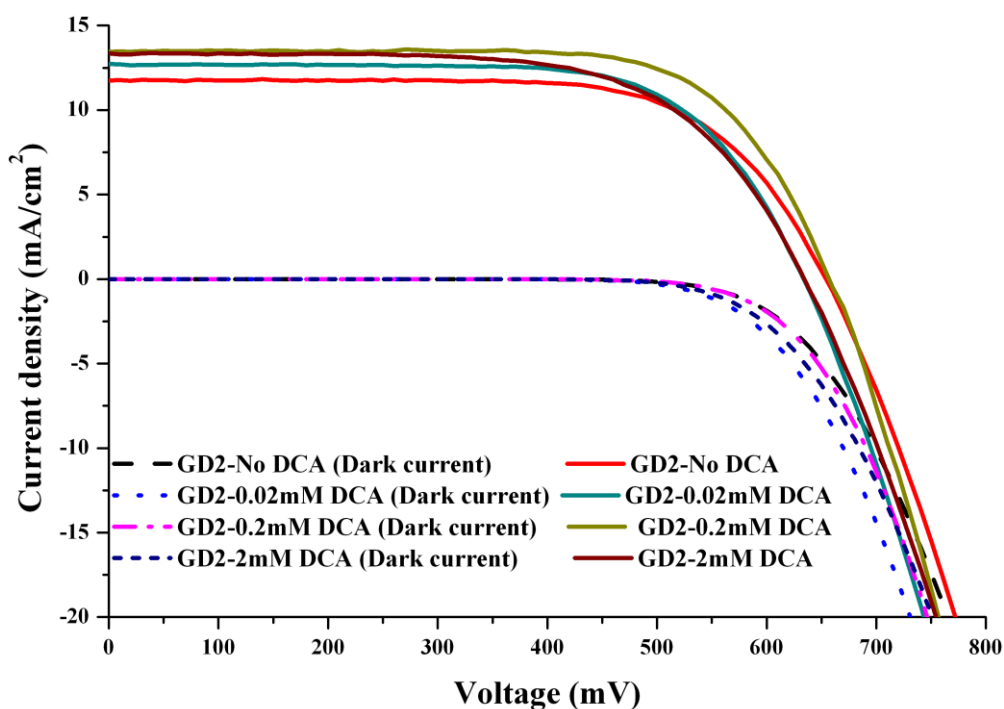


Figure 8.5: IV curves of GD2-dye sensitised solar cells using standard acetonitrile-valeronitrile based electrolyte, and the effect of increasing the concentration of chenodeoxycholic acid, under AM 1.5 sunlight

Table 8.4: Photovoltaic parameters of GD2 sensitised solar cells with varying concentrations of DCA at full sunlight (AM 1.5) and active area of 0.16 cm².

Dye:DCA	V _{oc} (mV)	I _{sc} (mA cm ⁻²)	ff	η (%)
0.2 mM: 0	654 (± 2)	11.8 (± 0.2)	0.68 (± 0.01)	5.3 (±0.05)
0.2 mM: 0.02 mM	635 (± 1)	12.4 (± 0.1)	0.71 (± 0.02)	5.6 (± 0.04)
0.2 mM: 0.2 mM	657 (± 2)	13.5 (± 0.3)	0.70 (± 0.01)	6.2 (± 0.02)
0.2 mM: 2 mM	634 (± 3)	13.4 (± 0.1)	0.64 (± 0.01)	5.4 (± 0.02)

The results indicate that the presence of DCA, together with the dye at an optimum ratio, adsorbed on the surface of TiO₂, helps to prevent the formation of dye aggregates and thereby yields an increase in both V_{oc} and I_{sc} in some cases, thus an improvement in efficiency is observed. The best cell performance is obtained in the presence of equivalent amounts of dye and co-adsorbent, yielding an I_{sc}, V_{oc}, ff and η of 13.5 mA cm⁻², 657 mV, 0.70 and 6.2 % respectively. UV spectroscopy of the dye adsorbed on the surface of TiO₂, with different DCA ratios, was also measured and showed that the DCA occupies not only the available space on the TiO₂ surface, but also there is direct competition between the dye and the DCA to go onto the surface of the TiO₂; there is a decrease in dye absorption as the concentration of DCA increases. The cell with no DCA shows a lower I_{sc} value (11.8 mA cm⁻²), and therefore a lower device performance, than those with the co-adsorbent. With the highest concentration of DCA, a drop in device performance is observed, with the cell reaching only 5.4 %, which is comparable to the device without DCA. This drop in device performance is mainly due to a decreased fill factor, as well as lower V_{oc}. The low fill factor is due to the high photoshunt (in other words, shunt resistance) that may be due to presence of impurities or crystal damage in the TiO₂.²⁰

The influence of 4-tert-butylpyridine on the performance of the DSSCs

The open circuit voltage is one of the parameters that can influence the overall conversion efficiency of the device. This is the potential between the Fermi level of the TiO₂ under illumination and the potential of the redox couple in the electrolyte. There are two main processes that can influence the V_{oc}; the back reaction process between the TiO₂ and the redox couple in the electrolyte, and a band edge shift of the TiO₂. It is well known that one way to suppress the back reaction is to use a pyridine derivative.

Huang *et al.* demonstrated that treating the film with pyridine derivatives, such as poly(2-vinylpyridine) and 2-vinylpyridine, can significantly increase the V_{oc} , and the overall performance of the device.²¹ Thus, the effect of TBP was investigated with GD2 dye.

In this study, a series of molecular liquid-based electrolytes with different amounts of TBP were investigated. Table 8.5 shows the effects of increasing the concentration of TBP in the standard electrolyte on the performance of the GD2-sensitised solar cells under 100 % sun intensity. Figure 8.6 shows the current voltage characteristics of the devices.

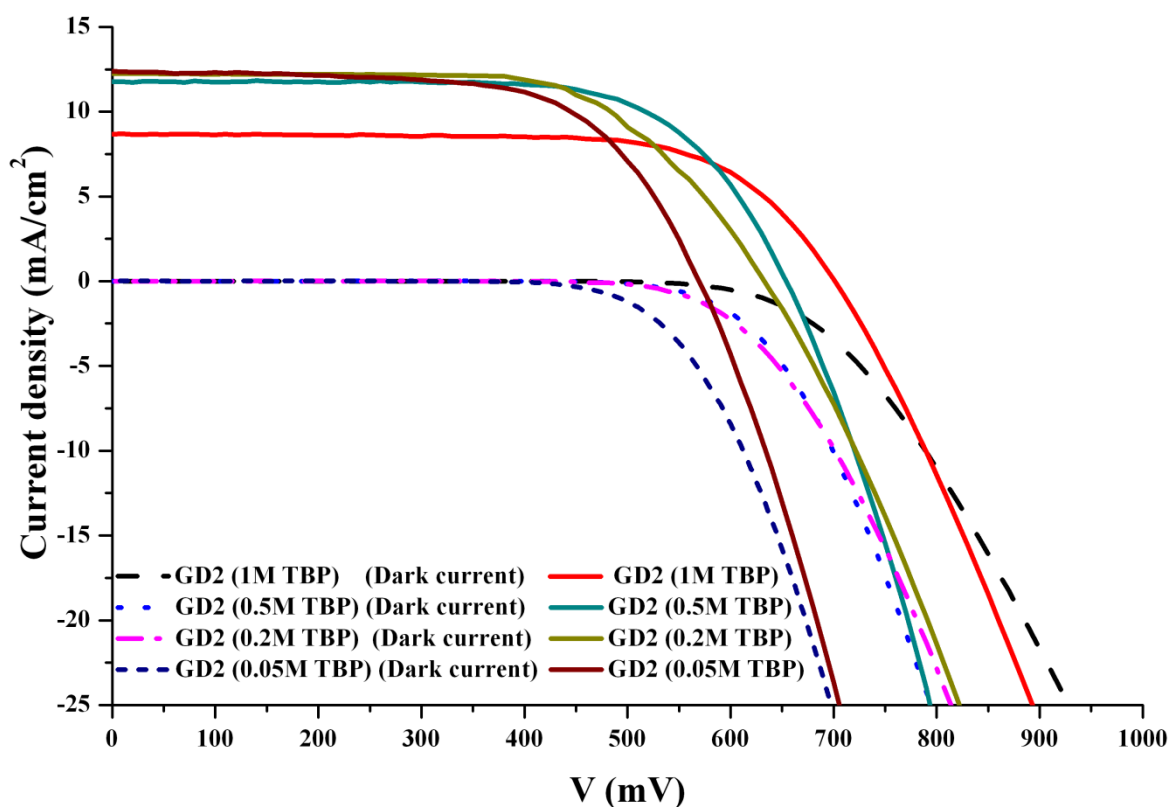


Figure 8.6: IV curves of GD2-DSSCs and the effect of increasing the concentration of TBP in the molecular liquid-based electrolyte system

8. Ionic liquids for porphyrin dye sensitised solar cells

When the concentration of TBP is gradually increased, a clear enhancement in V_{oc} from 569 to 701 mV is observed, whereas the tendency for I_{sc} is the opposite; varying from 12.4 to 8.7 mA cm⁻² at 100 % sun intensity. As demonstrated in Chapter 6, addition of a base results in a shift in the conduction band of the TiO₂ to more negative potentials, which may affect electron injection and collection efficiency, reducing the current density. With high concentrations of TBP, dissolution of the sensitiser was visually observed.

TBP is known to have a good affinity with the TiO₂ surface; it is possible that at high concentrations, the TBP is displacing the dye from the surface, resulting in a decreased amount of dye and therefore a drop in current density. A slight rise in fill factor is also noted. The increase in V_{oc} and fill factor is probably because the TBP forms a blocking layer on the surface of the TiO₂, reducing the dark current reaction at the semiconductor-electrolyte junction. As the I₃⁻ is relatively small, there is a possibility that the ion can go through the dye layer. Another possibility is that there is some surface of the TiO₂ not completely covered with the dye, which is exposed to the electrolyte at low concentrations of TBP, leading to a decrease in V_{oc} and fill factor.²² The addition of TBP is intended to reduce the rate of reduction of the triiodide, as is observed in the dark current curves in Figure 8.6. Even though the V_{oc} and ff are much better at 1 M TBP, the reduction in current density is quite substantial, and this has more effect on the overall performance of the device. Table 8.5 summarises the photovoltaic parameters extracted from Figure 8.6.

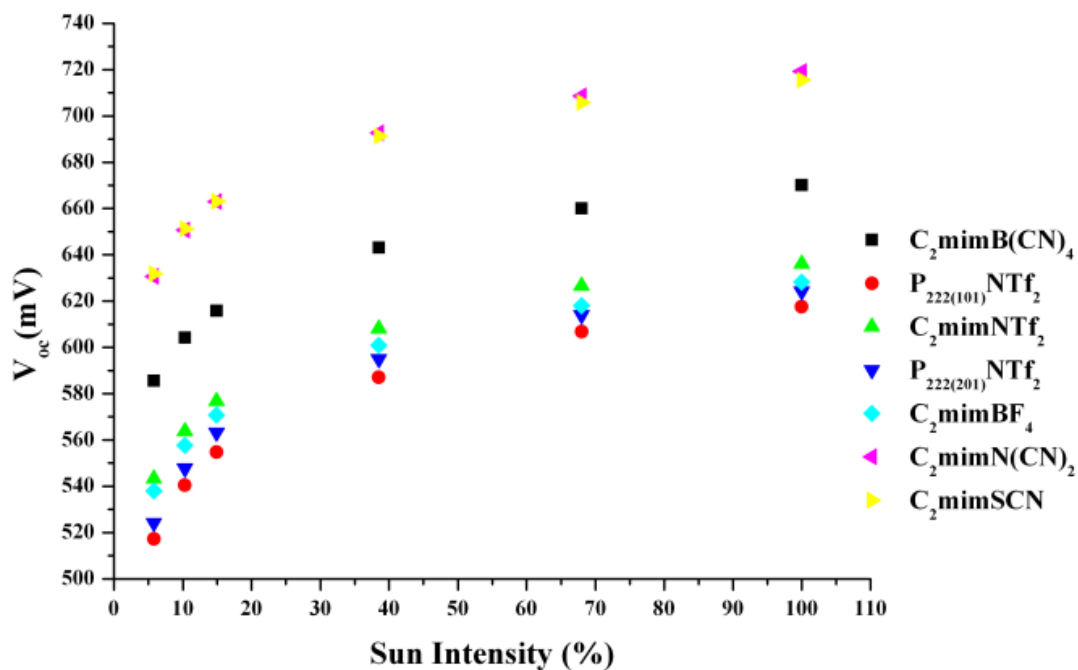
Table 8.5: IV data on the effect of increasing the concentration of TBP.

Concentration of TBP	V_{oc} (mV)	I_{sc} (mA cm ⁻²)	ff	η (%)
0.05 M	569 (\pm 3)	12.4 (\pm 0.5)	0.64 (\pm 0.03)	4.5 (\pm 0.2)
0.2 M	632 (\pm 2)	12.3 (\pm 0.1)	0.65 (\pm 0.02)	5.0 (\pm 0.1)
0.5 M	654 (\pm 3)	11.8 (\pm 0.2)	0.68 (\pm 0.01)	5.3 (\pm 0.3)
1 M	701 (\pm 2)	8.7 (\pm 0.1)	0.69 (\pm 0.02)	4.2 (\pm 0.3)

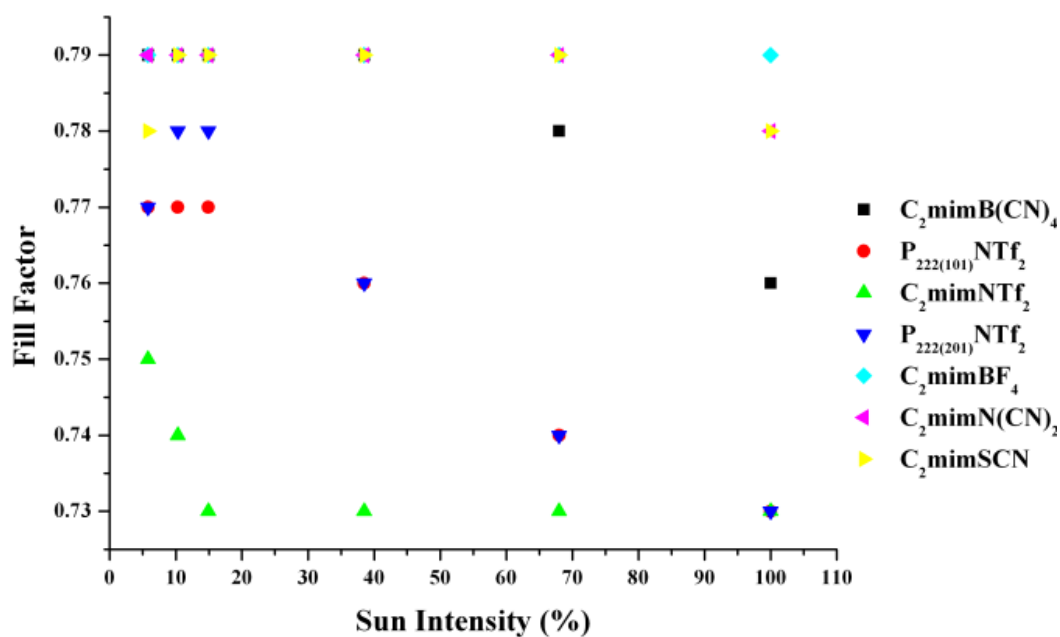
8.4.2.3 Ionic liquids electrolytes with Porphyrin sensitisers

8.4.2.3.1 Binary ionic liquids with the P159 sensitiser

Figure 8.7 illustrates the performance of DSSCs utilising binary mixtures of ILs with the P159 sensitiser, as a function of light intensity.

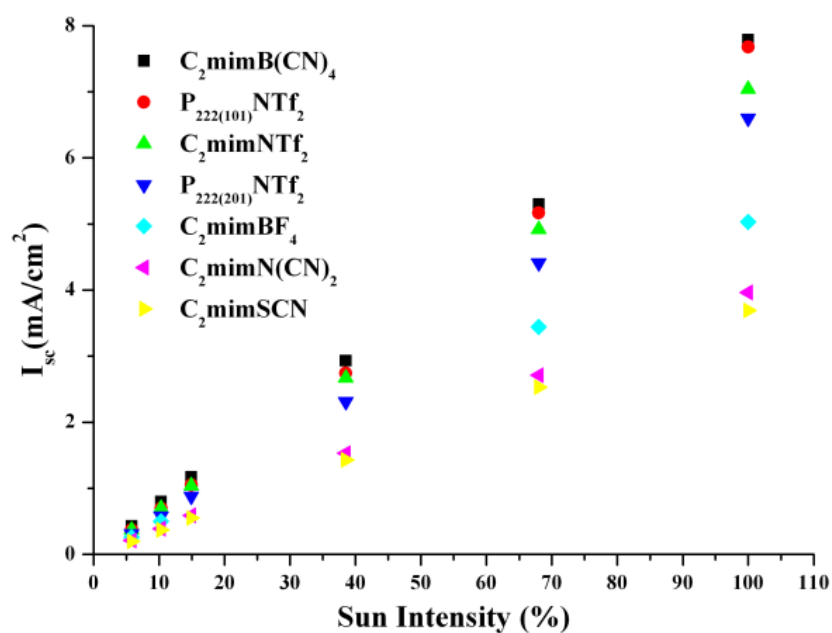


(a)

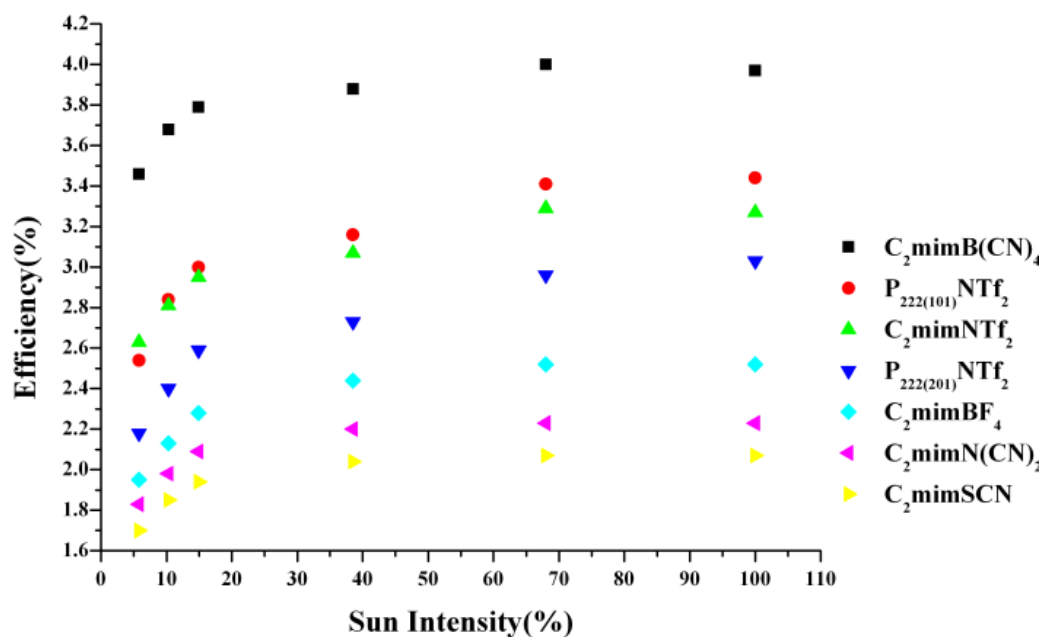


(b)

8. Ionic liquids for porphyrin dye sensitised solar cells



(c)



(d)

Figure 8.7: (a) V_{oc} , (b) fill factor, (c) I_{sc} and (d) efficiency as a function of sun intensity of P159-dye sensitised solar cells with binary ionic liquid mixtures

In the series of binary mixtures investigated with P159, C₂mimBF₄, C₂mimSCN and C₂mimN(CN)₂ show the worst performance in the solar devices; similar to those obtained with GD2 sensitisers. The short circuit current density, the V_{oc} and the fill factor with C₂mimBF₄ electrolyte is 5.0 mA cm⁻², 628 mV and 0.79 respectively, yielding an efficiency of 2.5 % as shown in Figure 8.7 at 100 % sun intensity. In the case of C₂mimSCN, the I_{sc} is 3.7 mA cm⁻², V_{oc} is 715 mV, the fill factor is 0.78 and the η is 2.1 %. C₂mimN(CN)₂ also has similar photovoltaic characteristics as C₂mimSCN with an I_{sc} of 3.9 mA cm⁻², a V_{oc} of 719 mV, a fill factor of 0.78 and an overall performance of 2.2 %.

C₂mimN(CN)₂ and C₂mimSCN show lower current densities and higher open circuit voltages, which might be due to the negative shift in the conduction band edge of the semiconductor when it is in contact with a more basic ionic liquid, as discussed in Chapter 6. This shift in conduction band has a negative effect on the photocurrent current density, due to the inefficient charge injection and collection efficiency.

APCE (absorbed photon-to-current-conversion efficiency) measures the number of electrons collected in the external circuit per number of absorbed photons. The APCE was measured using the ionic liquid electrolyte (C₂mimSCN) and using the standard porphyrin liquid electrolyte. In the case of the molecular liquid electrolyte, the APCE value was 70 %, and in the case of the C₂mimSCN the APCE was only 40 %. This suggests that the low performance of the device with the IL is due to inefficient charge injection and charge collection. Another possibility is the interaction of these ionic liquids with the porphyrin sensitisers; discoloration of the dyed films (turning from green to dark red in appearance) was observed when C₂mimN(CN)₂ and C₂mimSCN were used. Free base porphyrin sensitisers (i.e. without the metal centre) are usually dark red. However, UV spectroscopy on the discoloured films showed that the zinc was still retained in the core structure of the P159 and therefore further surface analysis of the discoloured film is required to understand this colour change.

The best conversion efficiency was achieved with C₂mimB(CN)₄ electrolytes. This electrolyte gives an I_{sc} of 7.8 mA cm⁻², a V_{oc} of 670 mV, a fill factor of 0.76 and an efficiency of 4 %. In the NTf₂ series, P₂₂₂₍₁₀₁₎ yield slightly better conversion efficiency than C₂mimNTf₂ and P₂₂₂₍₂₀₁₎NTf₂.

8. Ionic liquids for porphyrin dye sensitised solar cells

Table 8.6 summarises the photovoltaic parameters of the devices using different binary ionic liquids with P159-sensitised solar cells.

Table 8.6: Summary of IV parameters obtained from Figure 8.7.

IL	V_{oc} (mV)	I_{sc} (mA cm ⁻²)	ff	η (%)
C ₂ mimB(CN) ₄	670 (± 7)	7.8 (± 0.2)	0.76 (± 0.01)	4.0 (± 0.1)
P ₂₂₂₍₁₀₁₎ Ntf ₂	618 (± 8)	7.7 (± 0.1)	0.73 (± 0.02)	3.4 (± 0.2)
C ₂ mimNtf ₂	636 (± 5)	7.0 (± 0.1)	0.73 (± 0.01)	3.3 (± 0.1)
P ₂₂₂₍₂₀₁₎ Ntf ₂	624 (± 3)	6.6 (± 0.2)	0.73 (± 0.02)	3.0 (± 0.1)
C ₂ mimBF ₄	628 (± 4)	5.0 (± 0.2)	0.79 (± 0.01)	2.5 (± 0.2)
C ₂ mimN(CN) ₂	719 (± 5)	4.0 (± 0.1)	0.78 (± 0.01)	2.2 (± 0.2)
C ₂ mimSCN	716 (± 5)	3.7 (± 0.2)	0.78 (± 0.01)	2.1 (± 0.1)

8.4.2.3.2 Ternary ionic liquids mixtures with porphyrin sensitisers GD2, GD3 and P159

We demonstrated in the above section that the use of binary mixtures shows only moderate performance with the porphyrin dyes. Here we investigate the use of ternary ionic liquid mixtures, which have been shown to work very well in Ruthenium-based dye sensitised solar cells. Figure 8.8 displays the IV characteristics of DSSCs using GD2, GD3 and P159, in this case using the C₁mimI/C₂mimI/C₂mimB(CN)₄/LiI/I₂/NMB electrolyte. The best performance was obtained with P159. At 1 sun illumination, the V_{oc} , I_{sc} , and the ff are 637 mV, 10.5 mA cm⁻² and 0.71 respectively, yielding an efficiency of 4.7 %.

After light soaking for an hour, the performance of the device slightly increased, yielding an efficiency of 4.9 % with an increase in I_{sc} to 11.9 mA cm⁻².

Similar open circuit voltages were observed for all dyes as expected, as they have similar electronic configuration, but a much higher short circuit current density was observed for P159. The poorer performance of GD2 and GD3 could be due to the interaction of I₃⁻ with the porphyrin increasing the recombination of I₃⁻ with the TiO₂, as previously demonstrated by Mozer *et al.*²³ In contrast to GD2 and GD3, P159 has long hydrophobic alkyl chains on the peripheral benzene rings, providing a barrier layer for back electron transfer from the TiO₂, as proposed for amphiphilic ruthenium sensitisers.²⁴

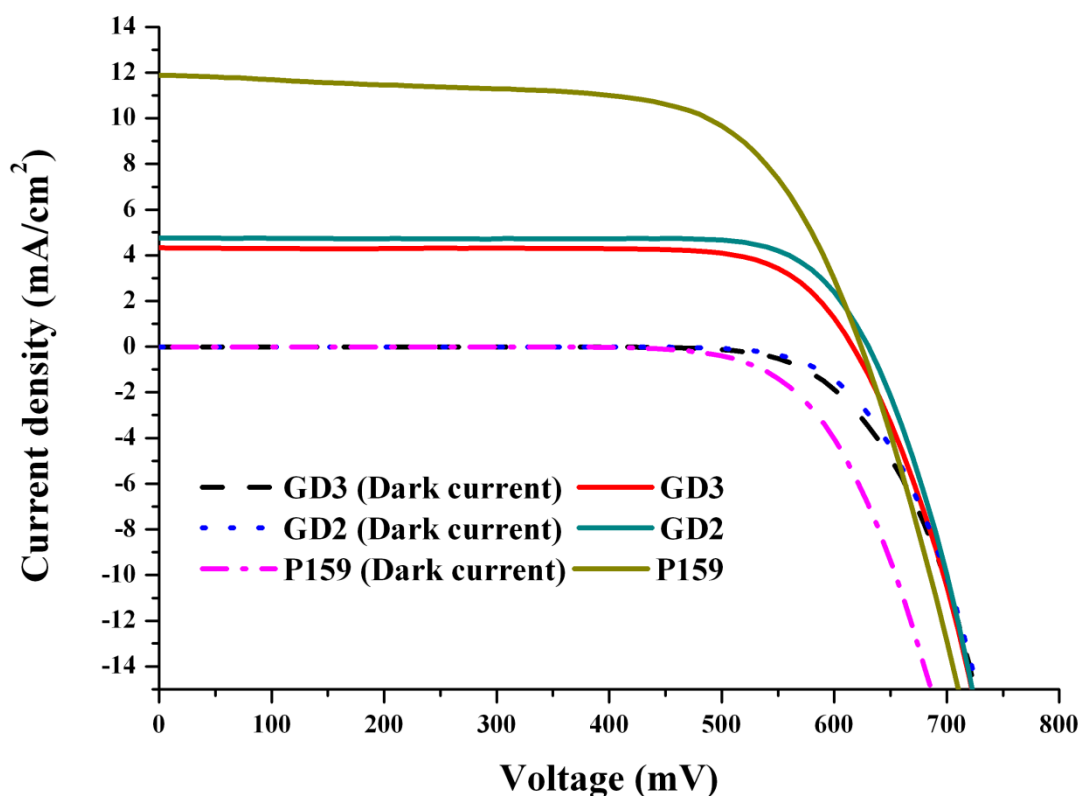
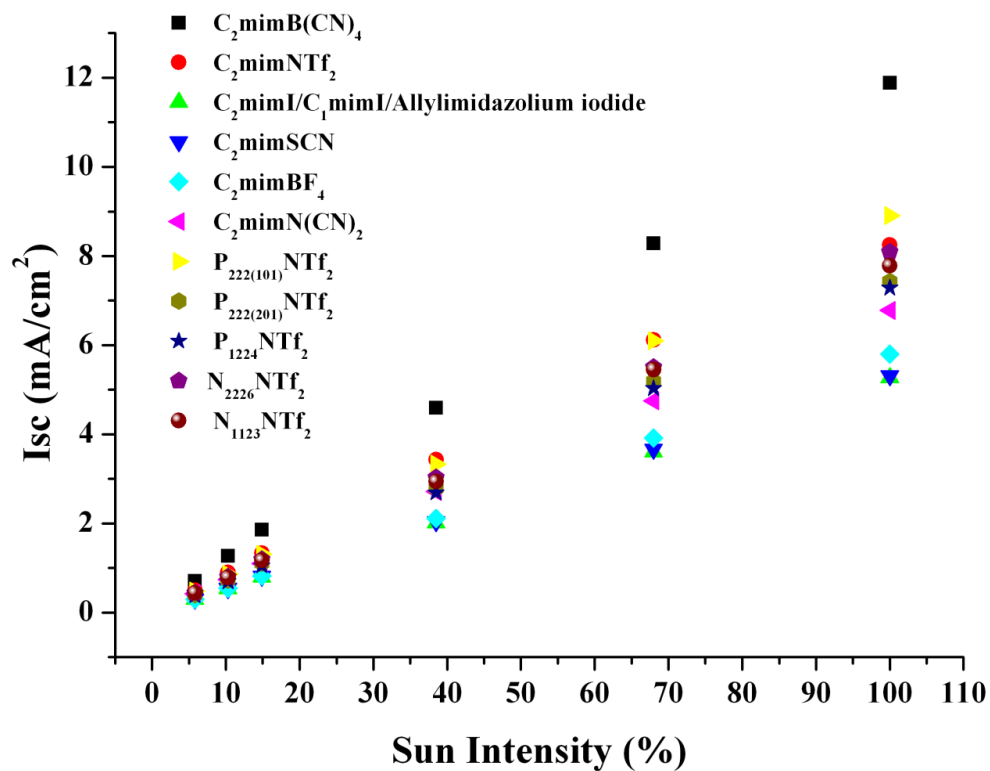


Figure 8.8: IV curves of DSSCs with different porphyrin dyes GD2, GD3 and P159 using an ionic liquid electrolyte ($C_2mimI/C_1mimI/C_2mimB(CN)_4/LiI/I_2/NMB$) under simulated sunlight AM 1.5

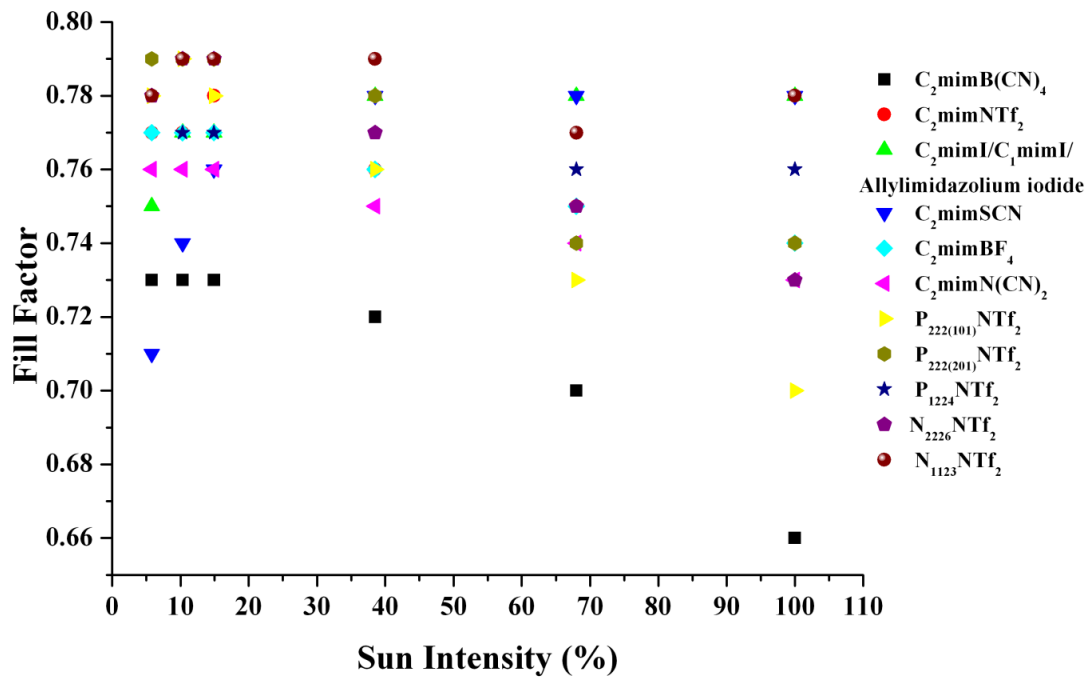
Different Ternary electrolytes with P159 DSSCs

Figure 8.9 shows the different parameters of the solar cells, as a function of light intensity, with various ionic liquid electrolytes and P159 as the sensitiser. The light intensity was varied from 5 % to 100 % sun intensity under AM 1.5. As shown in Figure 8.9 (a), the short circuit current density, I_{sc} , went up linearly with incident light intensity up to 100 % sun, with all of the different electrolyte systems. This indicates that the I_{sc} is not limited by diffusion of triiodide or iodide ions in the TiO_2 network. This trend of increase in I_{sc} with light intensity is related to the mobility of electrons in the TiO_2 , which can be explained by the trapping and detrapping model proposed by Durrant *et al.*²⁵ They reported that when the light intensity is increased, the deep traps are filled with the injected electrons, and thus do not hinder the transport of electrons at high sun intensity. As a result, when the light intensity is increased, the detrapping of electrons from shallow traps is much quicker, giving rise to higher electron diffusions in the TiO_2 and hence higher I_{sc} .

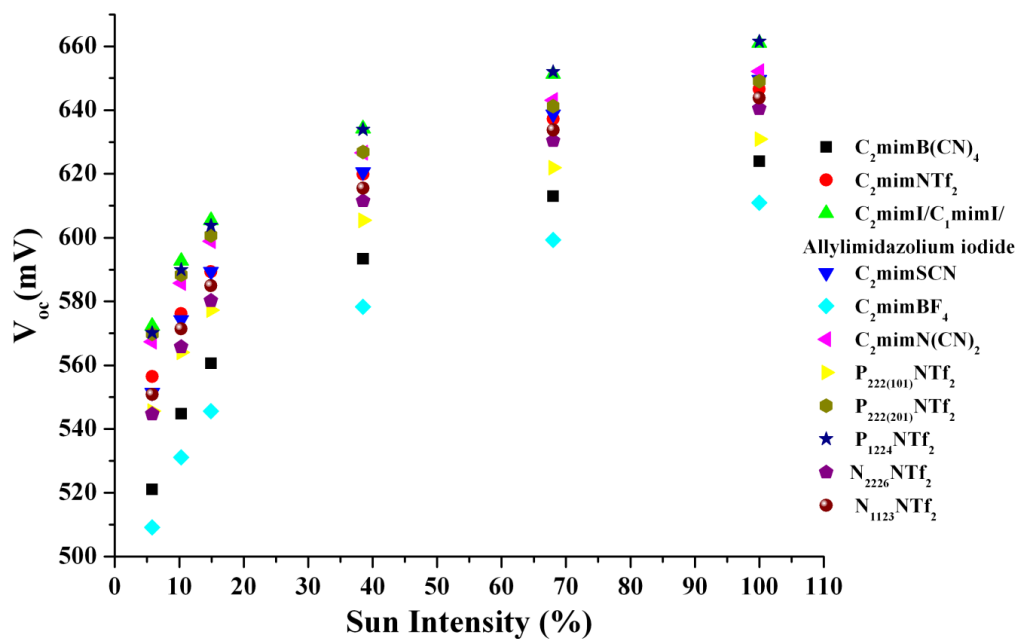
8. Ionic liquids for porphyrin dye sensitised solar cells



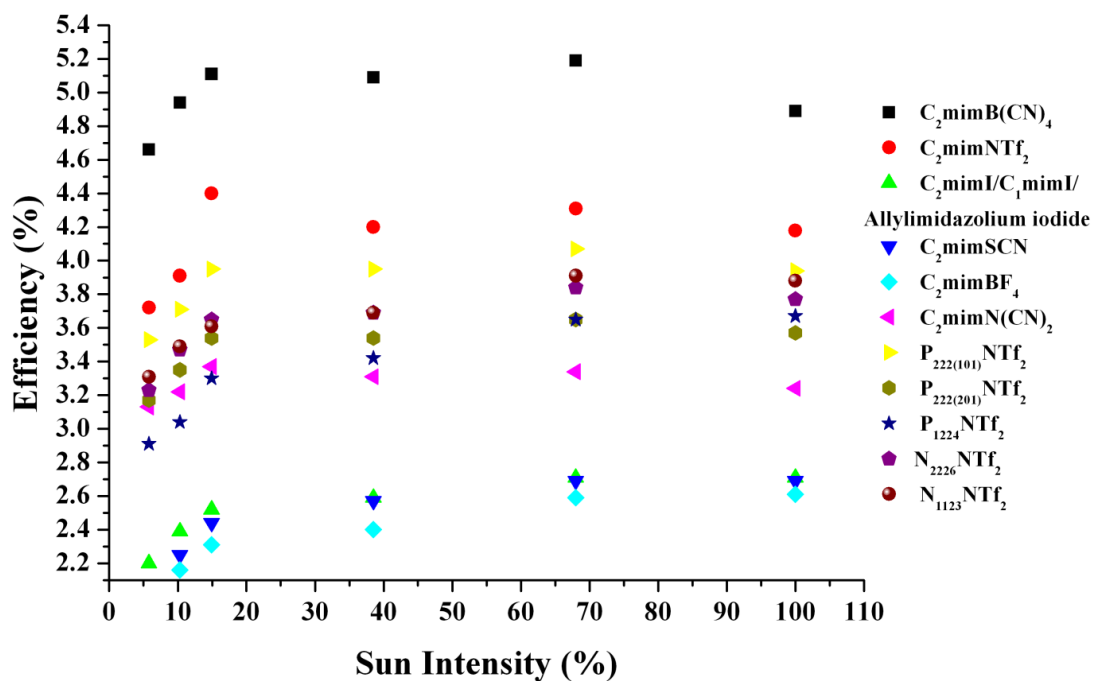
(a)



(b)



(c)



(d)

Figure 8.9: (a) I_{sc} , (b) fill factor, (c) V_{oc} and (d) efficiency as a function of light intensity for various ionic liquid electrolytes with the P159 sensitizer

8. Ionic liquids for porphyrin dye sensitised solar cells

Figure 8.9 (b) shows the dependence of fill factor with light intensity. In all cases, the fill factor of the DSSCs remain relatively constant, except with $C_2mimB(CN)_4$ and $P_{222(101)}NTf_2$. The decrease in fill factor with increasing light intensity may be due to the ohmic losses in the device.

Figure 8.9 (c) displays the dependence of open circuit voltage as a function of light intensity. In all cases the V_{oc} of the devices increased linearly until 15 % sun intensity and reached a plateau between 38 % and 100 % sun intensity. C_2mimBF_4 shows the lowest V_{oc} over all intensity ranges. As demonstrated in Chapter 6, this could be due to the shift in the conduction band edge of the TiO_2 in contact with the electrolyte. C_2mimBF_4 is known to hydrolyse quite easily resulting in the formation of HF, which will shift the conduction band edge upwards to a more positive potential and hence lower the V_{oc} .

Figure 8.9 (d) shows the effect of light intensity on the performance of the devices. In all electrolyte systems, the best performance is achieved at low sun intensity. The best performance is obtained with the ionic liquid electrolyte containing $C_2mimB(CN)_4$ at 68 % sun, yielding a performance of 5.2 %. The worst performance is obtained with C_2mimBF_4 , followed closely by $C_2mimSCN$.

Table 8.7 summarises the influence of different ionic liquids in the mixture with the P159, compared to the data for the $C_2mimB(CN)_4$ cell described previously. Even though $C_2mimSCN$ and $C_2mimN(CN)_2$ show similar viscosity and ionic conductivity as $C_2mimB(CN)_4$ (refer to Table 8.1), they show relatively poor performance in the DSSCs. Fredin *et al.* reported that $C_2mimSCN$ gave the best efficiency in monolithic Ru-based DSSCs due to the formation of pseudo halides such as I_2SCN^- , which may lower the concentration of triiodide.²⁶ This is not observed in our case. One possible explanation is that the thiocyanate might interact with the porphyrin dye. As shown in Table 8.7, the performance of the DSSCs is not highly correlated with the physical properties of the ionic liquids. $C_2mimSCN$ and $C_2mimN(CN)_2$ are highly hygroscopic and distinctly basic compared to $C_2mimB(CN)_4$, hence there might be some interaction with the dye in these cases. The best of the IL cells ($C_2mimB(CN)_4$) compares quite favourably with the standard acetonitrile electrolyte (Table 8.7, bottom), the IL only lowering the efficiency by about 1 % as a result of the higher viscosity of these systems.

The decrease in device performance is mainly a result of the lower I_{sc} , which is due to the slow diffusion of the triiodide. Higher concentrations of the iodide source and iodine are needed to avoid the mass transport limitation of the I_{sc} , but higher concentrations of iodine also increases the dark current, resulting in a lower V_{oc} and lower efficiency.

In the lower half of Table 8.7 are the results for the DSSCs, sensitised with P159, for a number of other ionic liquids containing quaternary ammonium and phosphonium cations. Phosphonium ionic liquids are usually based on relatively large cations and therefore they tend to have high viscosities. As demonstrated in Chapter 7 and here, the use of phosphonium ionic liquids based on small cations show quite good performance. These phosphonium ionic liquids are used as they are generally thought to be more stable than the corresponding imidazolium-based ionic liquids. An efficiency of 3.9 % was achieved at 1 sun using $P_{222(101)}NTf_2$. The other variants are slightly lower in efficiency, but with further optimisation of the electrolyte, it should be possible to further enhance the performance of the device. $C_2mimNTf_2$ remains the highest efficiency member of this NTf_2 anion family when used with P159.

Table 8.7: The photovoltaic characteristics of DSSCs sensitised with porphyrin P159 using different ILs in the electrolyte C₁mimI/C₂mimI/IL/LiI/I₂/NMB, after light soaking for 30 mins.

IL	V _{oc} (mV)	I _{sc} (mA cm ⁻²)	ff	η (%)
C ₂ mimB(CN) ₄	624 (± 5)	11.9 (± 0.2)	0.66 (± 0.02)	4.9 (± 0.1)
C ₂ mimNTf ₂	647 (± 2)	8.3 (± 0.6)	0.78 (± 0.01)	4.2 (± 0.1)
C ₁ mimI/C ₂ mimI/ Allylimidazolium iodide	661 (± 5)	5.3 (± 0.8)	0.78 (± 0.01)	2.7 (± 0.3)
C ₂ mimSCN	649 (± 4)	5.3 (± 0.4)	0.78 (± 0.01)	2.7 (± 0.2)
C ₂ mimBF ₄	613 (± 3)	5.8 (± 0.1)	0.74 (± 0.01)	2.6 (± 0.1)
C ₂ mimN(CN) ₂	652 (± 10)	6.9 (± 0.3)	0.73 (± 0.04)	3.2 (± 0.2)
P ₂₂₂₍₁₀₁₎ NTf ₂	631 (± 4)	8.9 (± 0.3)	0.70 (± 0.03)	3.9 (± 0.2)
P ₂₂₂₍₂₀₁₎ NTf ₂	649 (± 5)	7.4 (± 0.5)	0.74 (± 0.02)	3.6 (± 0.1)
P ₁₂₂₄ NTf ₂	664 (± 6)	7.0 (± 0.3)	0.76 (± 0.01)	3.5 (± 0.1)
N ₂₂₂₆ NTf ₂	636 (± 7)	7.9 (± 0.2)	0.75 (± 0.03)	3.8 (± 0.1)
N ₁₁₂₃ NTf ₂	644 (± 4)	7.8 (± 0.1)	0.78 (± 0.01)	3.9 (± 0.1)
Standard acetonitrile-valeronitrile electrolyte				
Standard (Porphyrin)	698 (±7)	12.3 (± 0.1)	0.69 (± 0.05)	6.0 (± 0.1)

8.4.2.3.3 Transient light absorption spectroscopy of DSSCs with the P159 dye

To further understand the difference between the electrolyte systems with P159, transient light absorption spectroscopy was performed. For this study, two ionic liquids were used, the best performing electrolyte C₂mimB(CN)₄, and the worst performing electrolyte C₂mimSCN. This measurements were performed in collaboration with Dr. Attila Mozer at the University of Wollongong.

The first experiment focused on measuring the dye⁺ reduction rates using the P159 dye. For this experiment, the C₂mimI/C₁mimI/C₂mimB(CN)₄/LiI/I₂/NMB electrolyte was used. The aim of the experiment was to determine whether the pore filling with the electrolyte was complete or incomplete.

Virtually no change was observed by varying the TiO₂ film thicknesses from 1.9 μm (S1), 4.9 μm (S2), 7.6 μm (S3), 9.4 μm (S4) to 15.9 μm (S5) as shown in Figure 8.10. The different signal magnitude is quite possibly related to the different absorbance at the pump wavelength of 605 nm with increasing thickness, but the decays were similar. One would expect slower or incomplete regeneration in thicker samples if the electrolyte did not permeate all the way to the FTO interface (that is where the majority of the dyes are excited in thicker films).

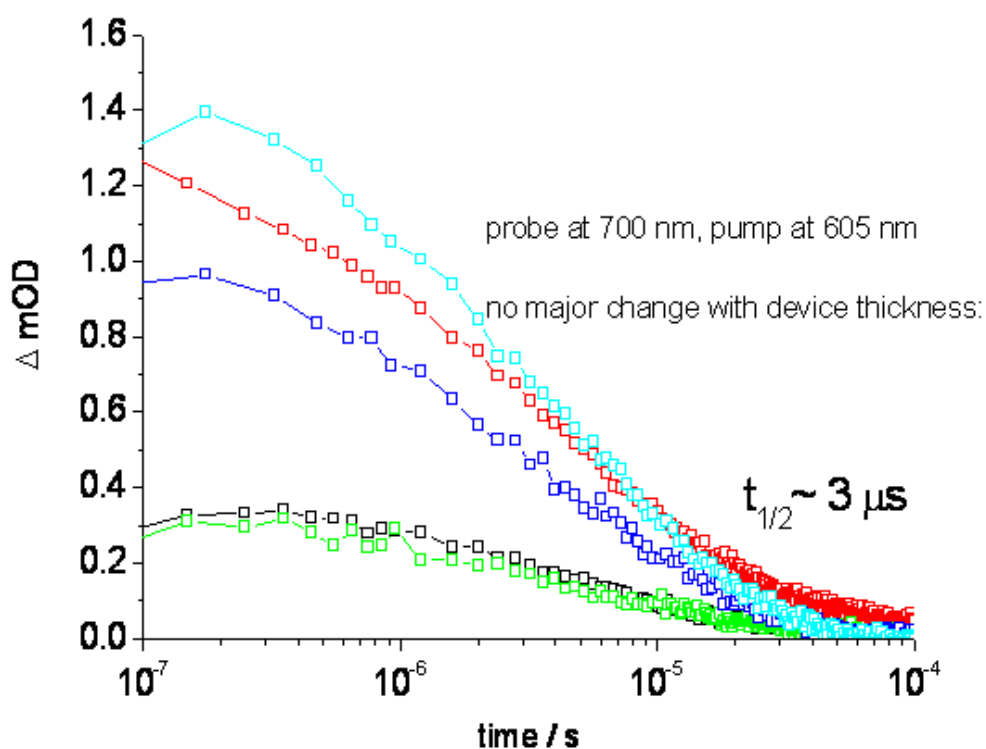


Figure 8.10: Transient absorption decay of P159 sensitizers with C₂mimI/C₁mimI/C₂mimB(CN)₄/LiI/I₂/NMB electrolyte with different film thicknesses, S1 (□), S2 (□), S3 (□), S4 (□), S5 (□)

8. Ionic liquids for porphyrin dye sensitised solar cells

We checked the pump light intensity dependence and back and front illumination, and again no major difference was observed, as shown in Figure 8.11.

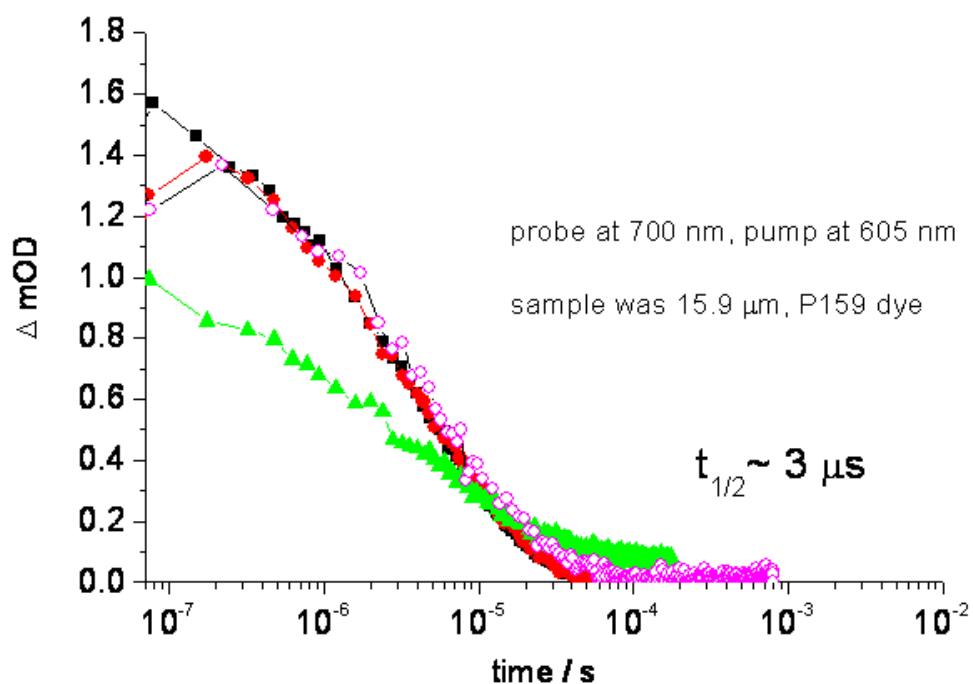


Figure 8.11: Transient absorption decay of P159 sensitizers with the $C_2mimI/C_1mimI/C_2mimB(CN)_4/LiI/I_2/NMB$ electrolyte with front and back illumination, S5- $C_2mimB(CN)_4$ -low light intensity (\blacktriangle), S5- $C_2mimB(CN)_4$ -back illumination (\square), S5- $C_2mimB(CN)_4$ -full light intensity (\bullet), S5- $C_2mimB(CN)_4$ -front illumination (\blacksquare)

Dye⁺ regeneration yield can be estimated at the time indicated by the dashed line in Fig. 8.12; the dye⁺ recombination with TiO₂ electrons (Figure 8.12 (black)) is negligible when the reduction of dye⁺ by I⁻ is complete (Figure 8.12 (red)).

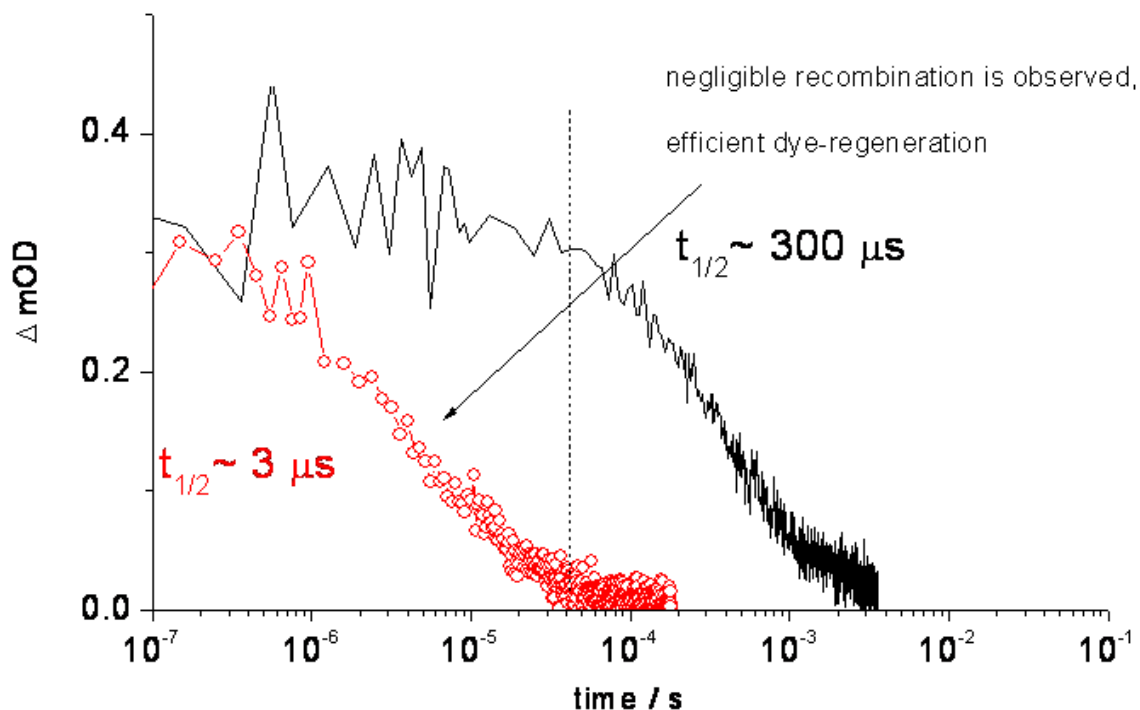


Figure 8.12: Transient absorption decay of P159 sensitizers, S3-C₂mimB(CN)₄-LiClO₄ (—), S3-C₂mimB(CN)₄ (○)

The dye⁺ signal was checked at 1 Hz and 10 Hz repetition rate, and no difference was observed, which confirms that dye⁺ + e⁻ (TiO₂) recombination is completed within 0.1 s (no build-up of e⁻ between pulses).

The same experiment was repeated with a C₂mimSCN based electrolyte and similar trends were observed.

8. Ionic liquids for porphyrin dye sensitised solar cells

With some level of confidence, it can therefore be concluded that the dye⁺ regeneration / dye⁺ + e⁻ (TiO₂) recombination is not the reason behind the differences in using the various ionic liquids. The possible reasons for that may be due to:

- (i) The recombination process (e⁻(TiO₂) + I₃⁻) i.e. the injection efficiency of the dyes into the CB of the TiO₂. The dye* excited state lifetime depends to some extent on the electrolyte. For example, it is shorter in the presence of LiI/I₂/acetonitrile, TBP electrolyte. If the injection is not too fast, the shortening of the excited state lifetime would influence the injection yield.
- (ii) As already stated, the shift in conduction band edge in the presence of the various electrolytes might influence the overall performance of the devices.

Further studies such as SLIM-PCV and electron density measurements on thin films would clearly indicate whether the conduction band is shifted in various electrolytes, and also whether the recombination rate is different in different electrolyte systems. The measurements described here were performed on thick films and were not conclusive. Thus the experiments in the future on thin films could produce a better understanding of the effect of the different electrolytes on porphyrin dye sensitised solar cells.

8.5 Conclusions

In summary, porphyrin dye sensitised solar cells containing electrolytes based on mixtures of ionic liquids were fabricated. The influence of different anions and cations were investigated. The highest efficiency was recorded for cells containing the C₂mimB(CN)₄ ionic liquid in a ternary mixture, with a power conversion efficiency of 5.2 % at 68 % light intensity with the P159 dye. The relatively high efficiency and promising results for the phosphonium and ammonium ionic liquids indicates the possible practical use of these electrolytes with the porphyrin dyes. In the porphyrin dye series, P159 behaves the best, probably due to the presence of the long hydrophobic alkyl chains that protect the surface of the TiO₂ from the electrolytes.

References

1. S. L. Wu, H. P. Lu, H. T. Yu, S. H. Chuang, C. L. Chiu, C. W. Lee, E. W. G. Diau and C. Y. Yeh, *Energy Environ. Sci.*, 2010, **3**, 949-955.
2. K. Kalyanasundaram, N. Vlachopoulos, V. Krishnan, A. Monnier and M. Grätzel, *J. Phys. Chem.*, 1987, **91**, 2342-2347.
3. Q. Wang, W. M. Campbell, E. E. Bonfantani, K. W. Jolley, D. L. Officer, P. J. Walsh, K. Gordon, R. Humphry-Baker, M. K. Nazeeruddin and M. Grätzel, *J. Phys. Chem. B*, 2005, **109**, 15397-15409.
4. W. M. Campbell, K. W. Jolley, P. Wagner, K. Wagner, P. J. Walsh, K. C. Gordon, L. Schmidt-Mende, M. K. Nazeeruddin, Q. Wang, M. Grätzel and D. L. Officer, *J. Phys. Chem. C*, 2007, **111**, 11760-11762.
5. H. P. Lu, C. L. Mai, C. Y. Tsia, S. J. Hsu, C. P. Hsieh, C. L. Chiu, C. Y. Yeh and E. W. G. Diau, *Phys. Chem. Chem. Phys.*, 2009, **11**, 10270-10274.
6. M. Tanaka, S. Hayashi, S. Eu, T. Umeyama, Y. Matano and H. Imahori, *Chem. Commun.*, 2007, 2069-2071.
7. A. Kira, Y. Matsubara, H. Iijima, T. Umeyama, Y. Matano, S. Ito, M. Niemi, N. V. Tkachenko, H. Lemmetyinen and H. Imahori, *J. Phys. Chem. C*, 2010, **114**, 11293-11304.
8. N. Xiang, X. Huang, X. Feng, Y. Liu, B. Zhao, L. Deng, P. Shen, J. Fei and S. Tan, *Dyes Pigm.*, DOI: 10.1016/j.dyepig.2010.05.003.
9. T. Bessho, S. Zakeeruddin, C. Y. Yeh, E. G. Diau and M. Grätzel, *Angew. Chem. Int. Ed.*, 2010, **49**, 6646-6649.
10. P. Bonhote, A. P. Dias, N. Papageorgiou, K. Kalyanasundaram and M. Grätzel, *Inorg. Chem.*, 1996, **35**, 1168-1178.
11. Y. Bai, Y. Cao, J. Zhang, M. Wang, R. Li, P. Wang, S. M. Zakeeruddin and M. Grätzel, *Nat. Mater.*, 2008, **7**, 626-630.
12. K. Tsunashima and M. Sugiya, *Electrochem. Commun.*, 2007, **9**, 2353-2358.
13. S. A. Forsyth, S. R. Batten, Q. Dai and D. R. MacFarlane, *Aust. J. Chem.*, 2004, **57**, 121-124.
14. J. Sun, M. Forsyth and D. R. MacFarlane, *J. Phys. Chem. B*, 1998, **102**, 8858-8864.
15. A. J. Bard and L. R. Faulkner, *Electrochemical Methods: Fundamental and Application*, VHC, New York, USA 1995.
16. P. Wachter, M. Zistler, C. Schreiner, M. Fleischmann, D. Gerhard, P. Wasserscheid, J. Barthel and H. J. Gores, *J. Chem. Eng. Data*, 2008, **54**, 491-497.
17. P. Wachter, M. Zistler, C. Schreiner, M. Berginc, U. O. Krasovec, D. Gerhard, P. Wasserscheid, A. Hinsch and H. J. Gores, *J. Photochem. Photobiol. A*, 2008, **197**, 25-33.
18. P. Wachter, C. Schreiner, M. Zistler, D. Gerhard, P. Wasserscheid and H. J. Gores, *Microchim. Acta*, 2008, **160**, 125-133.
19. W. M. Campbell, A. K. Burrell, D. L. Officer and K. W. Jolley, *Coord. Chem. Rev.*, 2004, **248**, 1363-1379.
20. E. L. Meyer and E. Ernest van Dyk, in *Photovoltaic Specialists Conference, 2005. Conference Record of the Thirty-first IEEE*, 2005, pp. 1331-1334.

8. Ionic liquids for porphyrin dye sensitised solar cells

21. S. Y. Huang, G. Schlichthorl, A. J. Nozik, M. Grätzel and A. J. Frank, *J. Phys. Chem. B*, 1997, **101**, 2576-2582.
22. M. K. Nazeeruddin, A. Kay, I. Rodicio, R. Humphry-Baker, E. Mueller, P. Liska, N. Vlachopoulos and M. Grätzel, *J. Am. Chem. Soc.*, 1993, **115**, 6382-6390.
23. A. J. Mozer, P. Wagner, D. L. Officer, G. G. Wallace, W. M. Campbell, M. Miyashita, K. Sunahara and S. Mori, *Chem. Commun.*, 2008, 4741-4743.
24. P. Wang, S. M. Zakeeruddin, J. E. Moser and M. Grätzel, *J. Phys. Chem. B*, 2003, **107**, 13280-13285.
25. J. Nelson, S. A. Haque, D. R. Klug and J. R. Durrant, *Phys. Rev. B: Condens. Matter*, 2001, **63**, 205321.
26. K. Fredin, M. Gorlov, H. Pettersson, A. Hagfeldt, L. Kloo and G. Boschloo, *J. Phys. Chem. C*, 2007, **111**, 13261-13266.

Chapter 9

Solid state materials in dye sensitised solar cells

Chapter overview

Here we described the use of a new class of material, known as organic ionic plastic crystals (OIPCs), as solid state electrolytes for dye sensitised solar cells using ruthenium based sensitisers. This is the first time that such materials have been used in DSSCs, despite the fact that they have been heavily studied as electrolytes for fuel cells and lithium batteries. Another class of material with similar properties to OIPCs are molecular plastic crystals; succinonitrile is one such example of this class of material and this was studied with both zinc porphyrin dyes (Chapter 6) and with the novel metal free organic sensitisers described in Chapter 7. Succinonitrile has previously been used as a solid state electrolyte in ruthenium based dye sensitised solar cells, yielding an efficiency of more than 6.5 % under moderate light intensity.¹ Thus, we were interested in investigating use of this molecular plastic material with zinc porphyrin and dithienothiophene-based sensitisers. The performance of the solar cells were evaluated under different light intensities, and the addition of silica nanoparticles, which are known to increase the performance of the devices, was also studied. Interesting performance was achieved using these solid state electrolytes, with either ruthenium based sensitisers or organic sensitisers, indicating that organic ionic plastic crystals have the potential to be used as solid state electrolytes in solar cells.

9.1 Introduction

9.1.1 Organic ionic plastic crystals

Organic ionic plastic crystals are a new class of material closely related to the family of aprotic ionic liquids.² They are typically based on the same family of cations and anions as ionic liquids. One of the main criteria to identify a molecular plastic crystals is the entropy of fusion, ΔS_f which should be less than $20 \text{ J mol}^{-1} \text{ K}^{-1}$, which is known as the Timmermans' criteria,³ and this criteria can often (but not always) also be applied to organic ionic plastic crystals.

Another typical behaviour of organic ionic plastic crystals is a solid-solid phase transition below the melting point and waxiness or plasticity, in the highest temperature solid phase.⁴ The plastic properties often derive from the fact that one or more species within the crystal lattice can undergo some kind of rotational motion. The existence of rotational motions in the crystalline phase, below the melting point, raises the entropy of the solid state closer to the liquid, thus producing a small entropy of fusion compared to fully ordered crystals.⁵

Organic ionic plastic crystals have all the physical properties of molecular plastic crystals, but also have an extended range of thermal stability, and are generally chemically inert as they are a solid state version of their ionic analogues. Because the thermodynamic state of the plastic crystal phase is close to that of the liquid state, these materials often exhibit solid-state diffusion of one or both ions and high ionic conductivity can be observed.⁶ Hence, they can be used as solid state electrolytes, thus solving the problem of electrolyte leakage from DSSCs. The imidazolium cation is not likely to form plastic crystals, as it has a tendency to melt rather than forming a stable rotator phase, which is one of the origins of plastic crystal behaviour.

Figure 9.1 shows some examples of known organic ionic plastic crystals. Many salts of the pyrrolidinium cation are plastic crystals. Shorter alkyl chains on the pyrrolidinium ring are likely to produce plastic crystal phases due to minimal steric hindrance to rotation.⁷ The pyrrolidinium series are the most studied OIPCs in the literature as a result of their high ionic conductivity in the neat state. Upon doping, the ionic conductivity is further improved, thus it is possible to modify the properties of the materials by adding "impurities" such as lithium salts or nanoparticles.

One of the most studied OIPCs in the group is N-ethyl-N-methyl pyrrolidinium bis(trifluoromethanesulfonyl)amide ($C_2\text{mpyrNTf}_2$). For example, Howlett and co-workers have demonstrated the high stability of the $C_2\text{mpyrNTf}_2$ in lithium batteries over a range of applied potentials and currents.⁸⁻⁹ No decomposition product of the electrolyte was detected, even under harsh conditions.

Other pyrrolidinium OIPCs studied are the BF_4^- and PF_6^- series; these materials also exhibit good ionic conductivity and a range of solid-solid phase transitions before melting, but with a shorter alkyl chain, these materials decompose before melting. The high melting point of these materials limits their potential use as solid state electrolytes for solar cells. Nevertheless, by adding different components, it is still possible to lower the melting point.

Tetraethylammonium dicyanamide displays the whole spectrum of behaviours associated with plastic crystal and rotator phases.¹⁰ As stated by Pringle *et al.*, this OIPC exhibits highly conductive plastic crystal phase domains and the lowest entropy of fusion, thus making it very attractive as a potential solid state electrolyte.⁶

Some recently discovered materials that show multiple solid-solid phase transitions are the trialkylsulfonium series¹¹ and the tetraalkylphosphonium series; in Chapter 5 we demonstrated that some asymmetric phosphonium ionic liquids exhibit a range of solid-solid phase changes over a large temperature range.

Plastic crystals have previously been studied in fuel cells and lithium batteries, and they performed quite well in these applications, hence the interest in this work in applying OIPCs to dye sensitised solar cells.

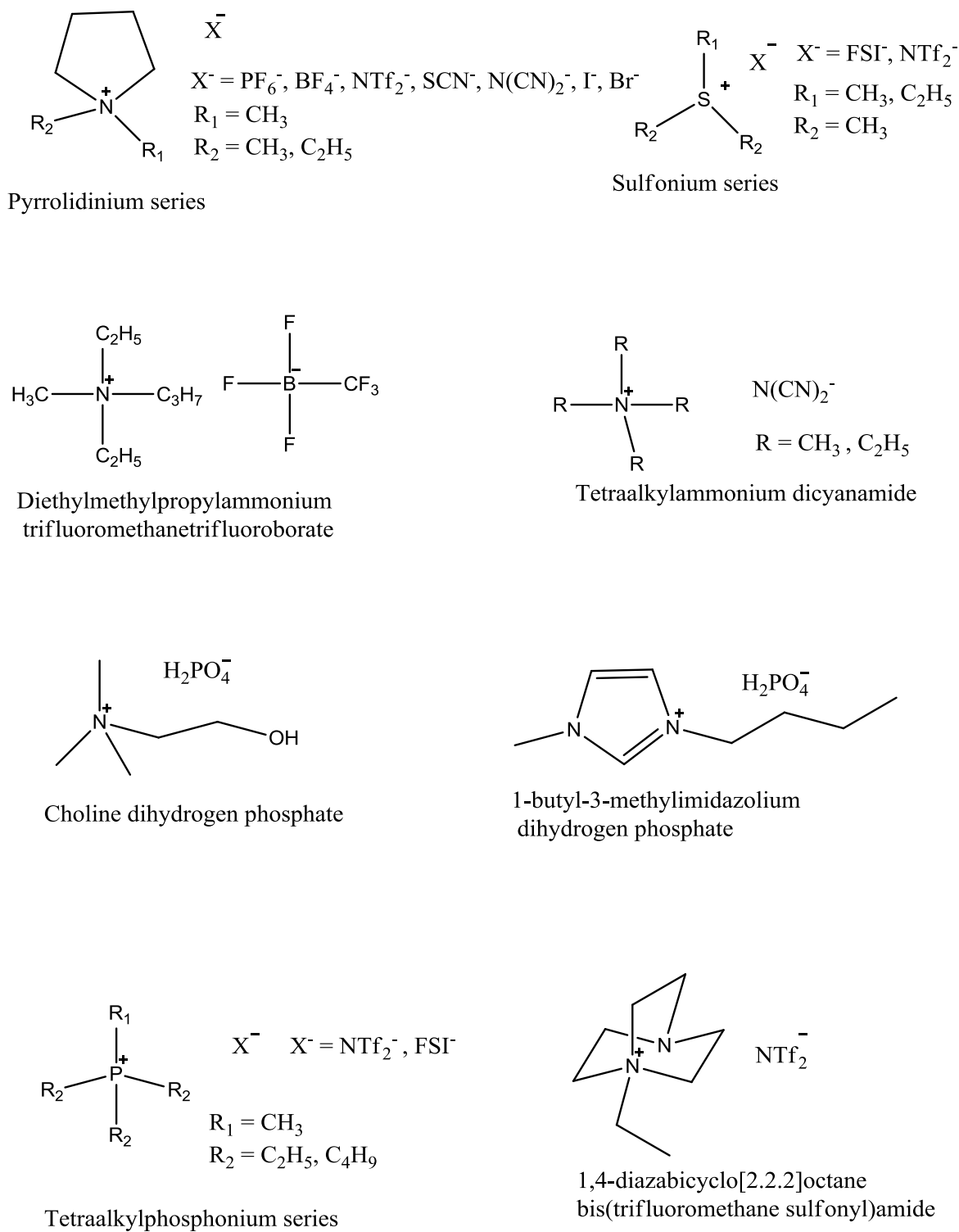


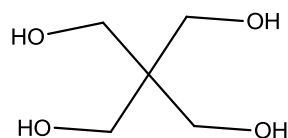
Figure 9.1: Examples of organic ionic plastic crystals

9.2 Types of solid state electrolyte already studied in DSSCs

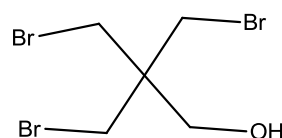
In the previous chapters, we discussed the use of ionic liquids as electrolytes for dye sensitised solar cells using zinc porphyrin dyes and thiophene derivative sensitisers. We have demonstrated that these dyes show quite interesting performance with phosphonium and imidazolium-based ionic liquids. Here we report the use of different solid materials as solid state electrolytes. A brief summary of the solid state materials previously studied as electrolytes for DSSCs is given in the following sections.

9.2.1 Molecular plastic crystals

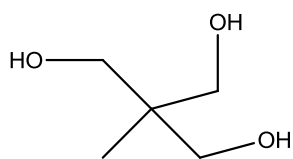
Molecular plastic crystals have the same properties as organic ionic plastic crystals, but they are composed of neutral molecules. These materials were identified many decades ago and were classified by Timmermans, in his 1961 review of plastic crystals.³ Figure 9.2 shows some examples of plastic crystals studied in the literature.



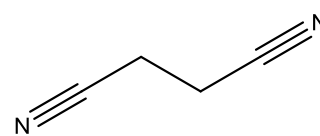
Pentaerythritol
(2,2-Bis(hydroxymethyl)-1,3-propanediol)



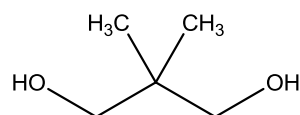
Pentaerythritol tribromide
(3-bromo-2,2-bis(bromomethyl)propanol)



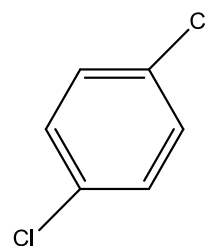
Pentaglycerine
(1,1,1-trishydroxy(methylethane))



Succinonitrile
(Butanedinitrile)



Neopentyl glycol
(2,2-dimethyl-1,3-propanediol)



1,4-Dichlorobenzene

Figure 9.2: Examples of molecular plastic crystals

Of the molecular plastic crystals shown in Figure 9.2, succinonitrile is the most studied for batteries and solar cells due to its ability to dissolve a number of salts, its low melting point and interesting properties upon doping, as demonstrated by Long and co-workers.¹² The addition of lithium salts greatly increases the ionic conductivity of this material, making it a good candidate for a solid state electrolyte for electrochemical devices.¹² Due to its neutrality, it acts as a good matrix for any type of salts and succinonitrile is still under investigation in various fields.¹³⁻¹⁴ Pentaglycerine has also been studied as a potential electrolyte for batteries due to its good ionic conductivity and an increase in ionic conductivity upon doping.¹⁵ Unfortunately, pentaglycerine decomposes before melting, which limits its use. The main application of pentaerythritol is in the paint and varnish industry, where it is used to produce resins, lubricant and explosives. Pentaerythritol also exhibits plastic behaviour. However, the high melting point and the difficulty in mixing this material with iodide salts and 1-methylbenzimidazole restrict its use as a solid state electrolyte for DSSCs. Derivatives of pentaerythritol are known to have a lower melting point and in some cases they exhibit multiple solid-solid phase transitions.¹⁶

9.2.2 Inorganic P-type semiconductors

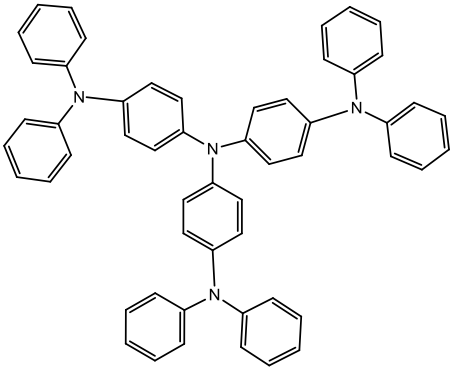
The first solid state DSSCs was fabricated by Tennakone *et al.* in 1988.¹⁷ They used an inorganic p-type semiconductor (P-CuSCN) with an n-type SnO₂ sensitised with Rhodamine B dye. However, at that time only a poor efficiency was obtained. A recent improvement in device performance using a modified method to prepare CuSCN was obtained by Premalal *et al.*¹⁸ They successfully increased the device energy conversion efficiency from 2.4 % to 3.4 %. Other inorganic p-type semiconductors, such as CuI and CuBr, were also investigated and an efficiency of more than 2 % was measured for a solid state DSSC based on CuI.¹⁹ At that time, this was the highest recorded efficiency for a solid state DSSC. Later, Meng and co-workers further improved the performance of the device to 3.8 % by using a molten salt capped CuI.²⁰ However, the problem with such inorganic p-type semiconductors is that they are not stable for a long period of time. Many attempts to improve the stability of the cells with this class of material have been reported by various research groups.²¹⁻²² For example, Taguchi and co-workers,²¹ as well as Kumara and co-workers,²² coated the TiO₂ layer with MgO, and have shown that the device was improved in both performance and stability.

However, although they improved the deposition method without causing any damage to the dye, and were able to regenerate the dye efficiently, the performance of such devices were still quite low compared to those using liquid electrolytes. Given the poor performance of the devices using inorganic p-type semiconductors as solid state electrolytes, other alternatives need to be looked at, for example, organic hole conducting materials or polymers.

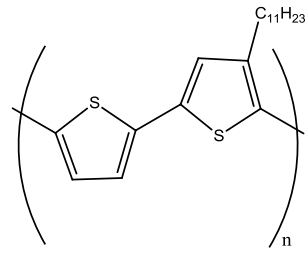
9.2.3 Organic p-type semiconductors

The other type of hole transporting material (HTM) available is the organic p-type semiconductors. These materials are widely available and they are easy to fabricate. The most common and highly performing hole conducting molecule so far is spiro-OMeTAD. The first use of spiro-OMeTAD was in 1998,²³ where an efficiency of 0.74 % was achieved, which was further improved to 5.1 % in 2009.²⁴ One major challenge to overcome with this type of material is the filling of the pores of the semiconductor, and to make sure that there is good contact between the HTM and the dye coated TiO₂ film. A further issue that needs to be addressed is the use of solvents, for example, chlorobenzene or acetonitrile. Solvents are required to dissolve and deposit the HTMs onto the dye coated TiO₂ film. There is a possibility that some of the solvents infiltrate into the pores of the TiO₂, which can lead to inefficient filling of the HTM into the TiO₂ network. HTMs are known to have high melting temperatures, but recently Fredin and co-workers²⁵⁻²⁶ developed a new method where the hole conductor is melted onto the dye-coated TiO₂. This method requires HTMs with a lower melting point, as higher temperatures (> 125 °C) are known to degrade the dye, thus leading to poor conversion efficiency of the solid state device.²⁵ Electrochemically deposited PEDOT as the hole conductor have also been used as the HTM in dye sensitised solar cells using a ruthenium dye, giving an I_{sc} of 2.3 mA cm⁻² and an efficiency of 0.53 %.²⁷ Polyaniline is the most studied conducting polymer and is used in many applications; for instance as membranes or as the anode in fuel cells,²⁸ as counter electrodes and as the hole conducting material in DSSCs.²⁹⁻³⁰ Using this material as the solid state electrolyte, the best conversion efficiency ever achieved was 1.2 %.³⁰ Figure 9.3 shows the structures of some well known HTMs utilised in solid state dye sensitised solar cells (SSDSSCs).

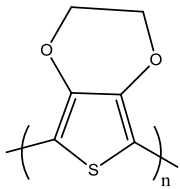
9. Solid state materials in dye sensitised solar cells



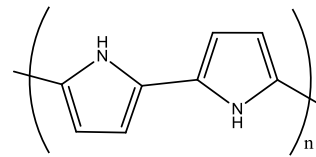
4,4',4''-tris(N,N-diphenyl-amino)-triphenylamine



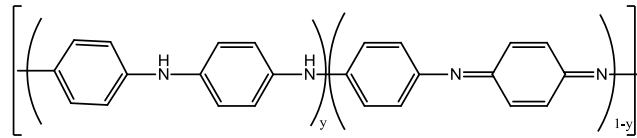
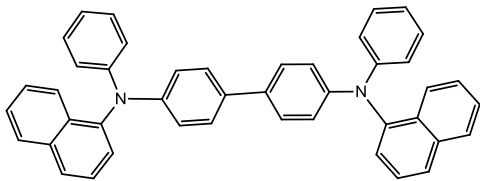
poly(4-undecyl-2,2'-bithiophene)



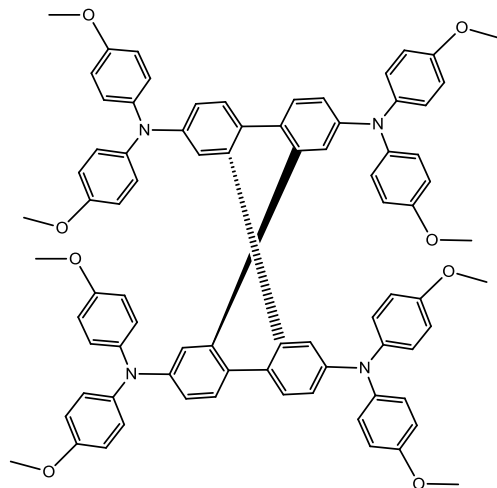
poly(3,4-ethylenedioxythiophene)



polypyrrole



Polyaniline



Spiro-OMeTAD

Figure 9.3: Hole conducting materials used in SSDSSCs

9.2.4 Solid polymer electrolytes and polymer gel electrolytes

Another interesting class of solid state materials are polymers. Polymer electrolytes have been heavily used in lithium batteries,³¹ supercapacitors,³² actuators³³ and more recently, in DSSCs.³⁴ They can also be used in lithium ion batteries,³⁵ giving an increase in the ionic conductivity of the electrolyte when LiNTf_2 is present and as an enhancement for electrochemical stability. DSSCs combined with the polymer electrolytes have shown much progress to date. Li and co-workers have shown that by varying the amounts of poly(vinylpyridine-co-acrylonitrile) added to an electrolyte containing ethylene carbonate, propylene carbonate, KI and I_2 , to form a polymer electrolyte for DSSCs, an improvement in efficiency from 6.2 % to 6.7 % was achieved.³⁶ In 2007, Lan *et al.* reported the use of a mixture of poly(ethylene glycol) and poly (acrylic acid), which was used as a matrix to prepare the polymer gel electrolyte.³⁷ As mentioned above, polymer electrolytes are prepared by adding the polymer to a liquid based electrolyte and stirring it until it forms a gel. However, there is a possibility that some of the liquid electrolyte is still trapped in the gel network, and during the operation of the solar cells, slow evaporation of the volatile components occurs, thus reducing the stability of the device. By building the hybrid matrix, Lan and co-workers wanted to address this problem and at the same time improve the power conversion efficiency. They were able to demonstrate a conversion efficiency of 6.3 % and assumed that the large amount of liquid electrolyte absorbed to form the gel electrolyte was not going to affect the long term stability of the device.³⁷ Recently, an iodine-free solid state electrolyte for DSSCs reaching a performance of 5.8 % was demonstrated by Lee *et al.*³⁸ They reported that the addition of a small amount of iodine had a rather negative effect on the photovoltaic performance of the device.

One concern that is often raised with solid electrolytes is the low ionic conductivity. However, Cha *et al.* recently reported that poor ionic conductivity in polymer based electrolytes is not the only factor that limits the performance of the DSSCs; other factors such as electron recombination may also be the cause of poor performance of the devices.³⁹ They demonstrated that the solid electrolytes with higher ionic conductivity actually did not give the best performance, indicating that ionic conductivity might not be the only factor determining the performance of the device.

Quasi solid state electrolytes based on mixing an ionic liquid with a polymer have also proved quite efficient.⁴⁰ Fan and colleagues demonstrated that a DSSC with an optimised polymer gel electrolyte, composed of polyvinylpyrrolidone at 35 wt% and C₄mimI of 0.9 M, gives an efficiency of 5.41 % under 1 sun.⁴⁰ They also reported that the DSSCs fabricated with the gel electrolytes showed better long term stability than the liquid electrolytes. Figure 9.4 shows some of the polymers used in DSSCs as quasi solid state electrolytes. Even though polymer electrolytes are quite interesting and showed high conversion efficiency, they still contain a volatile component, which can limit the long term stability of the device. Nevertheless, they have the potential to replace the acetonitrile based electrolytes.

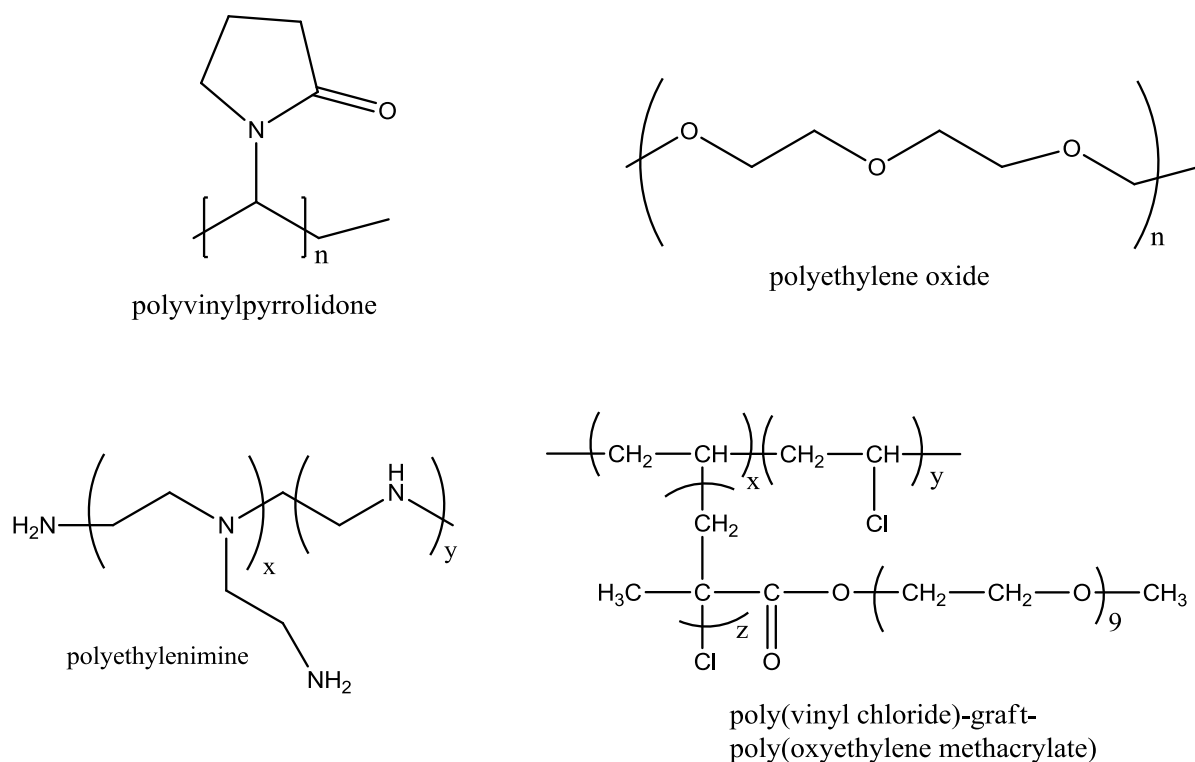


Figure 9.4: Polymers used as solid state electrolytes in DSSC

9.3 Experimental

Thermal analysis, conductivity measurement and EIS experimental procedures have previously been discussed in Chapters 3 and 5.

9.3.1 Synthesis of organic ionic plastic crystals

The organic plastic crystals were synthesised according to the literature procedure.⁴¹ Briefly, N-methylpyrrolidine, iodomethane, bromoethane and 1-bromopropane were purchased from Aldrich. N-methylpyrrolidine was distilled over KOH before use. The tetrafluoroborate, hexafluorophosphate, dicyanamide and thiocyanate salts were prepared by a two-step process. The first step is the formation of the halides salts, followed by the metathesis with silver tetrafluoroborate, potassium hexafluorophosphate, silver dicyanamide or silver thiocyanate.

N,N-dimethylpyrrolidinium tetrafluoroborate (C₁mpyrBF₄)

¹H NMR δ (d₆-DMSO, 300 MHz) ppm 2.0 - 2.2 (m, 2H), 3.1 (s, 3H), 3.4 - 3.5 (m, 2H). MS (ESI): ES+ *m/z* 100.1 (C₆H₁₄ N⁺), ES- *m/z*, 86.7 (BF₄⁻).

N-ethyl-N-methylpyrrolidinium tetrafluoroborate (C₂mpyrBF₄)

¹H NMR δ (d₆-DMSO, 300 MHz) ppm 2.0 - 2.2 (m, 2H), 3.0 (s, 3H), 3.2 - 3.3 (m, 2H), 3.4-3.5 (m, 2H).

MS (ESI): ES+ *m/z* 114.1 (C₇H₁₇ N⁺), ES- *m/z*, 86.7 (BF₄⁻).

N,N-dimethylpyrrolidinium dicyanamide (C₁mpyrN(CN)₂)

¹H NMR δ (d₆-DMSO, 300 MHz) ppm 2.0 - 2.2 (m, 2H), 3.1 (s, 3H), 3.4 - 3.5 (m, 2H). MS (ESI): ES+ *m/z* 100.1 (C₆H₁₄ N⁺), ES- *m/z*, 66 (N(CN)₂⁻).

N,N,N,N-tetraethylammonium dicyanamide (N₂₂₂₂N(CN)₂)

¹H NMR δ (d₆-DMSO, 300 MHz) ppm 1.4 - 1.5 (m, 3H), 3.3 - 3.5. (q, 2H).

MS (ESI): ES+ *m/z* 130 (C₆H₁₄ N⁺), ES- *m/z*, 86.7 (BF₄⁻).

N-ethyl-N-methylpyrrolidinium bis(trifluoromethanesulfonyl)amide (C₂mpyrNTf₂)

¹H NMR δ (d₆-DMSO, 300 MHz) ppm 1.2 - 1.3 (m, 3H), 2.0 - 2.1. (m, 2H)., 2.9 (s, 3H), 3.2 - 3.5 (m, 2H).

MS (ESI): ES+ *m/z* 113.9 (C₇H₁₆ N⁺), ES- *m/z*, 280 (NTf₂⁻).

9.4 Results and discussion

9.4.1 Molecular plastic crystals: Succinonitrile

Succinonitrile is a well known molecular plastic crystal that exhibits a distinct solid-solid phase transition from -38 °C and melts at 58 °C, as shown in Figure 9.5. According to Wulff and co-workers, phase II is an ordered phase with a monoclinic structure and phase I is highly disordered and exists in a body-centred cubic structure.⁴²⁻⁴³ The disorder is due to the onset of rotation about the principal axis passing through the C-C bond.^{42, 44} Succinonitrile as a solid state electrolyte in dye sensitised solar cells was investigated by Wang *et al.*¹ A power conversion efficiency of ~5 % was achieved at full sun in a ruthenium based dye sensitised solar cell.¹

Dai *et al.* have shown high mobility of the iodide-triiodide redox couple in this molecular plastic crystal.⁴⁵ They investigated the thermal behaviour of the plastic material with different iodide salts and varying compositions to investigate if any change in the solid-solid phase transition occurred and found that, depending on the symmetry of the cations of the iodide salts used, changes in the transition temperature occurred in some cases. They also observed quite complex behaviour of this plastic material upon addition of the iodide salts and iodine. Nevertheless, high diffusivity of the I_3^- and I^- was observed in the plastic crystal, hence our interest in investigating this molecular plastic crystal as a solid state electrolyte with organic sensitisers, as described previously in Chapter 7 and 8. For porphyrin sensitisers, spiro-OMeTAD is the only solid state material that has been investigated so far, and an efficiency of 3.7 % was achieved at full sun intensity.⁴⁶⁻⁴⁷

In the quest to improve the mobility of I_3^- and I^- in heavily viscous, gel polymer or solid electrolytes, several strategies have been employed, such as adding an ionic liquid, a small amount of solvent or nanoparticles, which improve, to a certain extent, the transport properties of the redox species, and therefore give an enhancement in device performance.⁴⁸⁻⁴⁹ Hence, the effect of adding nanoparticles to neat succinonitrile and the plastic electrolyte mixtures was investigated to see whether any improvement in the mobility of the redox species took place.

9.4.1.1 Thermal analysis

Addition of nanoparticles to neat succinonitrile

Figure 9.5 exhibits a typical thermal trace for neat succinonitrile and shows the effect of doping the material with different amounts of silica nanoparticles. The neat succinonitrile shows a solid-solid phase transition at $-39\text{ }^{\circ}\text{C}$ and a melt at $57\text{ }^{\circ}\text{C}$, with an entropy of fusion of $9.4\text{ J mol}^{-1}\text{ K}^{-1}$ (Table 9.1), and the solid-solid phase change (II to I) is moderately affected by the addition of SiO_2 . There is no linear trend in the change in onset temperature of the solid-solid transition with increasing SiO_2 content. With a 2 wt% of SiO_2 , the entropy of fusion of the solid-solid phase transition is $26\text{ J mol}^{-1}\text{ K}^{-1}$ compared to $23\text{ J mol}^{-1}\text{ K}^{-1}$ for the pure material. With a further increase in the content of SiO_2 to 5 wt%, the entropy of fusion of the II to I phase transition is $23\text{ J mol}^{-1}\text{ K}^{-1}$, which is closer to that of the neat succinonitrile. The material with 10 wt% of SiO_2 shows a broader solid-solid transition and melt. With the higher content of filler, the melt peak is tilted and the onset temperature is shifted to lower temperatures, while retaining a similar entropy of fusion to the neat succinonitrile. Visual observation during the preparation of the sample with high silica content showed difficulty in stirring the mixture, even at temperatures $> 100\text{ }^{\circ}\text{C}$, as the sample was quite viscous.

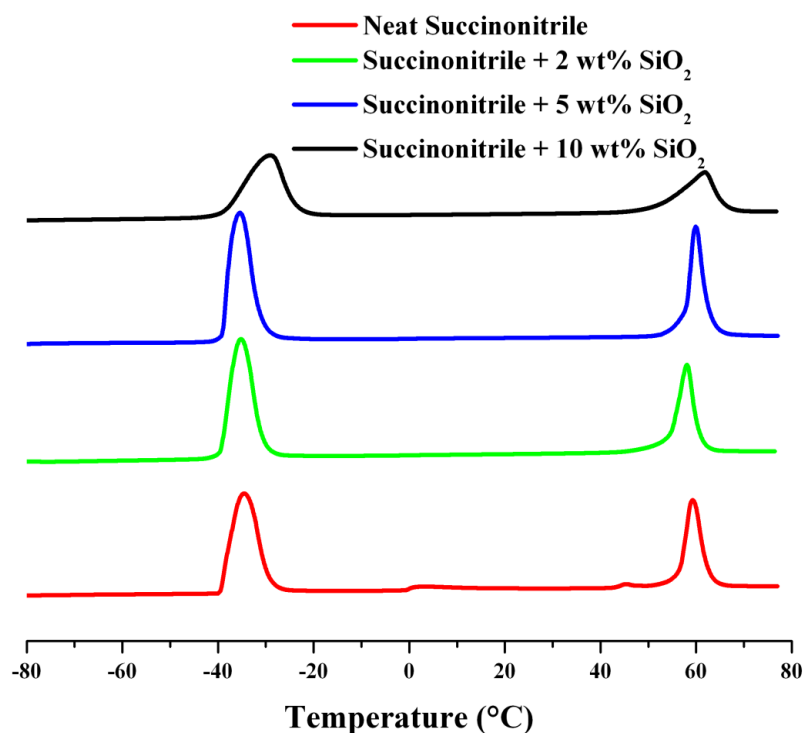


Figure 9.5: DSC traces of neat succinonitrile and with added SiO_2 nanoparticles (7

nm)

Table 9.1: Thermal parameters obtained from Figure 9.5.

Compound	II-I		I-melt	
	Onset T_{s-s} ($^{\circ}\text{C}$)	ΔS ($\text{Jmol}^{-1}\text{K}^{-1}$)	Onset T_m ($^{\circ}\text{C}$)	ΔS ($\text{Jmol}^{-1}\text{K}^{-1}$)
	± 2	± 0.01	± 2	± 0.01
Succinonitrile	-35	23	57	9.5
Succinonitrile+2wt% SiO_2	-37	26	57	11
Succinonitrile+5wt% SiO_2	-35	23	57	10
Succinonitrile+10wt% SiO_2	-32	21	53	9.7

In general, it can be concluded that there is no significant change in the thermal behaviour of succinonitrile upon the addition of SiO_2 , thus the material maintains its crystallinity. Further studies are required to investigate the morphology of the mixed compounds to have a full idea of what might be occurring (for example, the influence on the ionic conductivity, the grain boundary) when fillers are added to the neat succinonitrile.

Addition of additives to neat succinonitrile

Figure 9.6 displays the thermal behaviour of succinonitrile in presence of additives such as C_4mpyrI (0.4 M), LiI (0.1 M), I_2 (0.1 M) and NMB (0.2 M).

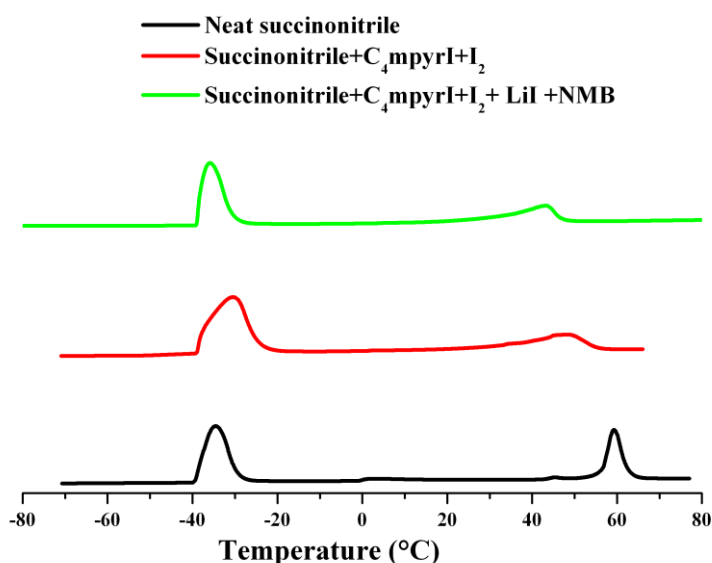


Figure 9.6: DSC traces of neat succinonitrile and with C_4mpyrI , LiI , I_2 , NMB and SiO_2

As demonstrated by the thermal trace, the solid-solid phase transformation temperature is not affected by addition of C₄mpyrI, I₂, LiI and NMB. In contrast, a decrease in the onset temperature of the melt is observed, as well as a broadening of the peak. The entropy of fusion of the mixed compound is slightly smaller than for the neat succinonitrile. For example, in the presence of only iodine and C₄mpyrI, the entropy of fusion of the solid-solid phase transition is 21 J mol⁻¹ K⁻¹, whereas for the neat succinonitrile this is 23 J mol⁻¹ K⁻¹. However, this change is sufficiently small, that one can say that the physical properties of the succinonitrile remained relatively unchanged in presence of “impurities”.

Table 9.2: Thermal data obtained from Figure 9.6.

Compound	II-I		I-melt	
	Onset T _{s-s} (°C)	ΔS (Jmol ⁻¹ K ⁻¹)	Onset T _m (°C)	ΔS (Jmol ⁻¹ K ⁻¹)
	± 2	± 0.01	± 2	± 0.01
Succinonitrile	-35	23	57	9.5
Succinonitrile + C ₄ mpyrI	-39	21	40	5.1
+ I ₂				
Succinonitrile + C ₄ mpyrI	-39	21	37	5.0
+ I ₂ + LiI + NMB				

9.4.1.2 Ionic Conductivity

Figure 9.7 shows the ionic conductivity of neat succinonitrile and in presence of additives and SiO₂, over the temperature range of -65 °C and 65 °C. In the neat system, the ionic conductivity of the succinonitrile is quite low, whereas on addition of C₄mpyrI and I₂, a significant increase in ionic conductivity is observed. One should keep in mind that in theory, neat succinonitrile should not have a measurable ionic conductivity, as it is a neutral species.¹⁵ The measured conductivity might be due to the presence of residual impurities that are difficult to remove by purification alone. Nevertheless, the conductivity goes up from 7.9 x 10⁻⁶ S cm⁻¹ to approximately 3.3 x 10⁻³ S cm⁻¹ at room temperature in the presence of C₄mpyrI and I₂, which is the result of an increase in the concentration of ions such as I⁻ and I₃⁻. These ions are quite mobile and thus will contribute to the overall conductivity of the systems. The ionic conductivity in the presence of the additional components is 2 x 10⁻³ S cm⁻¹ at room temperature. SiO₂ does not seem to significantly augment the ionic conductivity (4.2 x 10⁻³ S cm⁻¹ at room temperature).

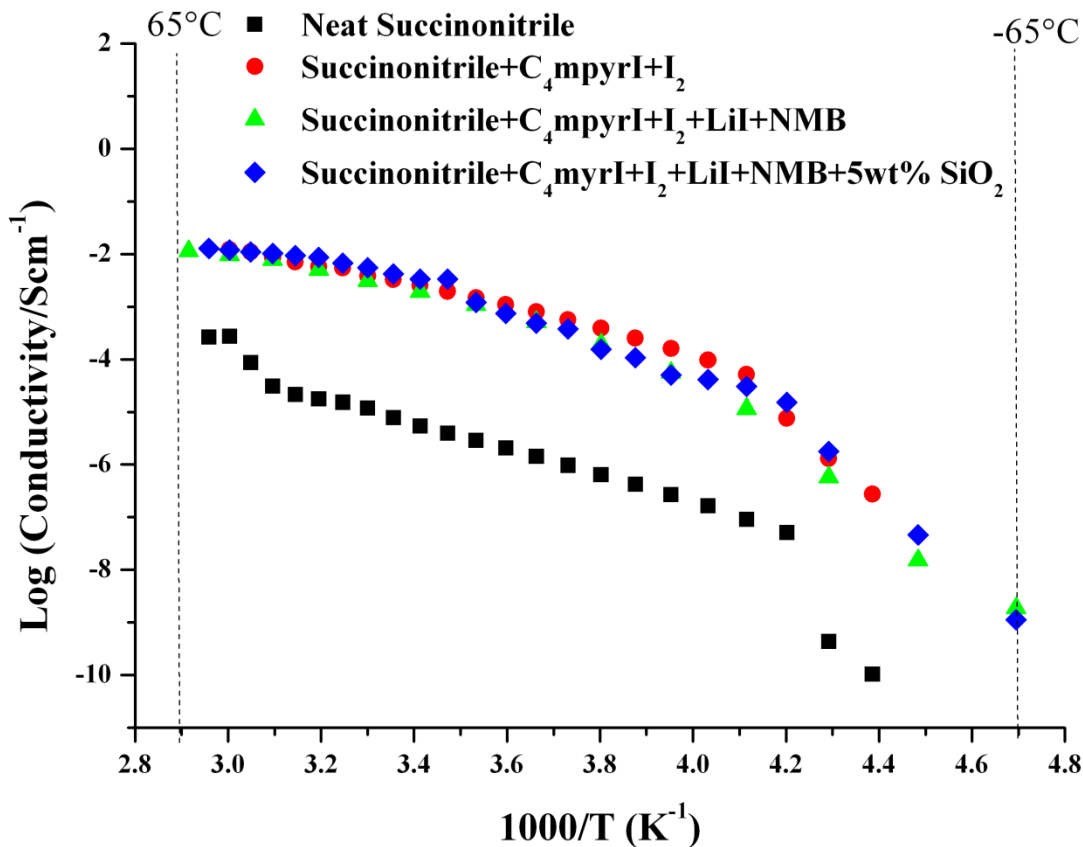


Figure 9.7: Logarithmic plot of ionic conductivity versus the inverse of temperature for succinonitrile containing additives such as C₄mpyr, LiI, I₂ NMB and SiO₂

9.4.1.3 Electrochemical measurements

Diffusion coefficient of iodide and triiodide

In order to study the diffusion coefficient of iodide and triiodide in succinonitrile, three different plastic crystal based electrolyte systems were prepared. Electrolyte S1 was composed of 0.5 M C₄mpyrI and 0.1 M iodine in pure succinonitrile, which is the same composition as reported by Wang *et al.*¹ Electrolyte S2 was made up of 0.4 M C₄mpyrI, 0.1 M lithium iodide, 0.1 M iodine and 0.2 M N-methylbenzimidazole dissolved in neat succinonitrile. Electrolyte S3 was the same as electrolyte S2, but with 5 wt% of SiO₂ nanoparticles used (7 nm). The electrolyte S4 is the same as electrolyte S2, but with 10 wt% SiO₂. The electrolytes were mixed at 70 °C to make sure that all additives were properly dissolved. At room temperature, the electrolytes S1, S2 and S3 were all waxy solids. As a comparison, the diffusion in an ionic liquid containing 0.5 M C₄mimI and 0.1 M I₂ in C₂mimNTf₂ was measured. Table 9.3 displays the diffusion coefficients of I⁻ and I₃⁻ in the solid electrolyte compared to an ionic liquid electrolyte.

Table 9.3: The diffusion coefficient (D) of I₃⁻ and I⁻ in the solid electrolytes and in an ionic liquid electrolyte.

Electrolytes	D (I ₃ ⁻ /cm ² s ⁻¹) (± 8 %)	D (I ⁻ /cm ² s ⁻¹) (± 8%)
S1	2.2 x 10 ⁻⁶	3.7 x 10 ⁻⁶
S2	2.5 x 10 ⁻⁶	3.8 x 10 ⁻⁶
S3	2.4 x 10 ⁻⁶	3.6 x 10 ⁻⁶
S4	2.0 x 10 ⁻⁶	2.9 x 10 ⁻⁶
C ₂ mimNTf ₂	4.7 x 10 ⁻⁷	3.1 x 10 ⁻⁷

Surprisingly, the diffusion coefficient of iodide and tri-iodide, summarised in Table 9.3, are much higher than in the ionic liquid based electrolyte. In fact, the diffusion of the redox species in the ionic liquid is 10 times slower than in the solid plastic crystal electrolyte. Every *et al.*⁵⁰ has shown that mobility of ions can be much higher in the solid state than in the liquid state, due to the presence of defects in the long range ordered crystalline lattice. Another possible reason for the higher diffusivity of the redox species is the formation of polyiodides, which can facilitate the diffusion of the iodide via a Grotthuss type mechanism.⁵¹ No significant change in the mobility of the redox species on addition of lithium iodide and N-methylbenzimidazole was observed, while addition of 5 wt% of silica gave a slight decrease in mobility of the triiodide. Addition of 10 wt% SiO₂ to the plastic crystal electrolyte containing lithium iodide and N-methylbenzimidazole further decreased the mobility of the triiodide, to 2.0 x 10⁻⁶ cm² s⁻¹. This may be the result of a blocking effect at the grain boundary, due to the presence of SiO₂, thus hindering the movement of the redox species.⁵

EIS measurements were also used to understand the behaviour of the electrolyte at the counter electrode. Li *et al.*⁵² have previously studied the effect of nanoparticles in a mixture of ethylcarbonate and propylene carbonate, and an increase in the diffusivity of tri-iodide and a decrease in the charge resistance at the Pt/electrolyte interface was observed. However, such a trend was not observed in this case; the charge transfer resistance at the Pt/electrolyte interface was measured using a symmetrical cells and all three solid electrolyte mixtures showed similar charge transfer resistance, as shown in Figure 9.8.

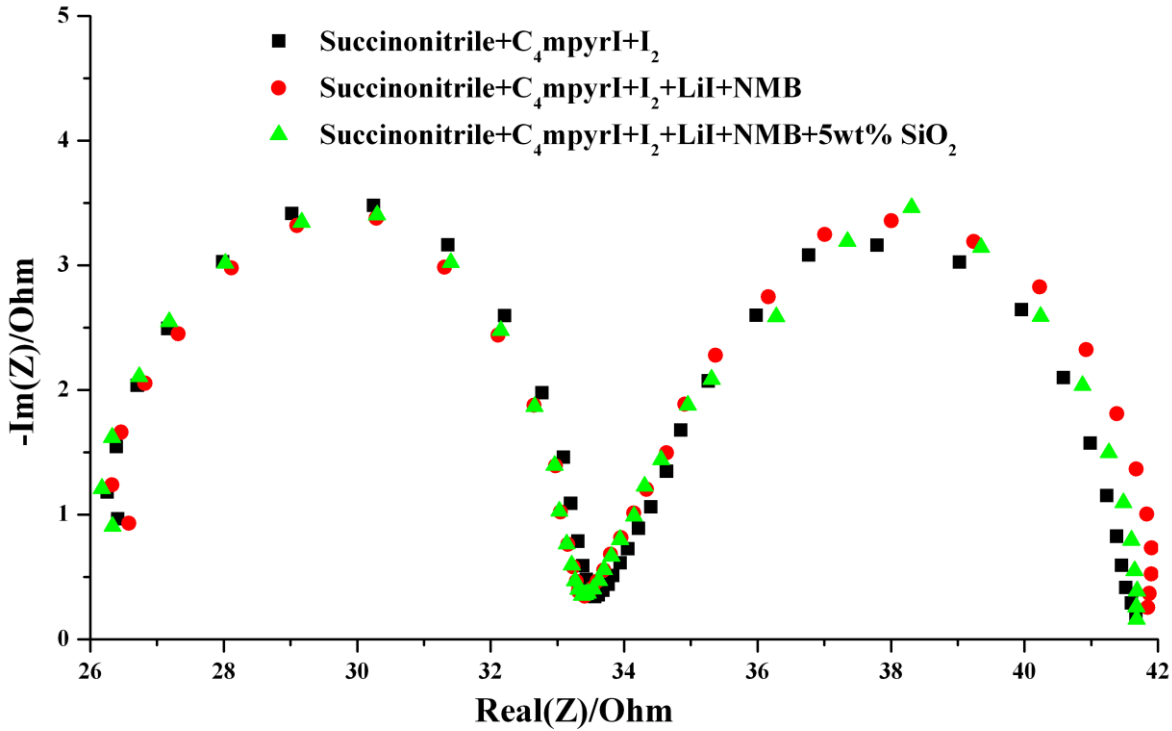


Figure 9.8: The EIS spectra of the solid electrolytes

9.4.1.4 Photovoltaic measurements

Ruthenium based DSSCs in different electrolytes

Electrolytes S1, S2, S3 and S4 were investigated in ruthenium based (N719) DSSCs. Electrolyte S4 was composed of 0.4 M C₄mpyrI, 0.1 M Lithium iodide, 0.1 M iodine, 0.2 M N-methylbenzimidazole and 10 wt% of SiO₂ dissolved in neat succinonitrile. This experiment was done as a basis for comparison, where porphyrin sensitisers were used instead.

Figure 9.9 shows the IV characteristics of the DSSCs, utilising the different electrolytes, at 100 % sun intensity and room temperature. The I_{sc} , V_{oc} , ff and η are presented in Table 9.4.

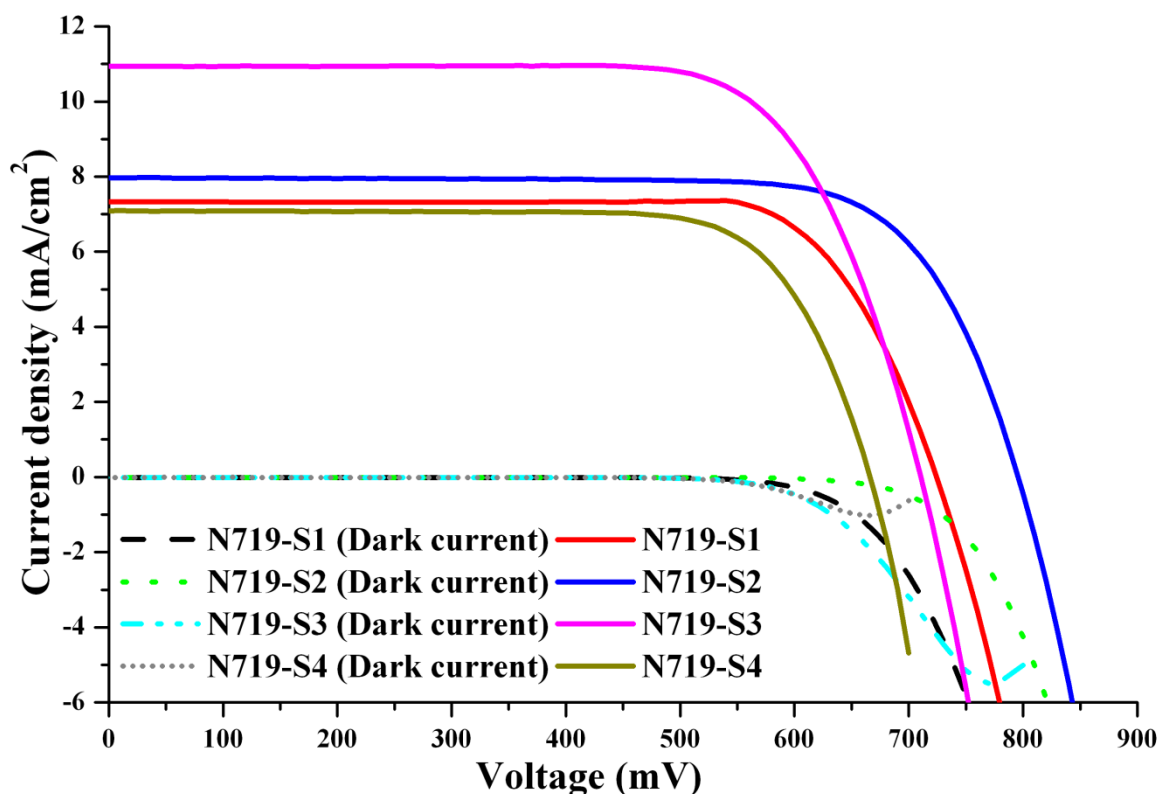


Figure 9.9: IV curves for DSSCs based on electrolytes S1, S2, S3 and S4

The solar cell with electrolyte S1 gives an I_{sc} of 7.3 mA cm^{-2} , a V_{oc} of 724 mV and a ff of 0.77. The efficiency of the device is only 4.1 %, which is lower than previously reported by Wang and co-workers. This is probably due to differences such as the film, the dye and the paste. Electrolyte S1 was used as a control to compare the performance of this electrolyte with the porphyrin-DSSCs.

The device containing the electrolyte S2 gives an I_{sc} of 8 mA cm^{-2} , a V_{oc} of 796 mV, a ff of 0.75 and an overall efficiency of 5 %. On adding 5 wt% of SiO_2 to the electrolyte (S3), an enhancement in the I_{sc} is observed (11 mA cm^{-2}), giving a device performance of 5.5 %. The increase in efficiency is mainly due to an increase in current, which may be related to better electron injection and charge collection efficiency. The slight drop in V_{oc} may be due to the increased in dark current reaction, as shown by the dark current curve in Figure 9.9. Further addition of SiO_2 (S4) leads to a decrease in both V_{oc} and I_{sc} . This drop in I_{sc} might be related to the poor diffusion ($2.0 \times 10^{-6} \text{ cm}^2 \text{ s}^{-1}$) of the redox species in the electrolyte, thus affecting the performance of the device.

Table 9.4: The photovoltaic parameters of DSSCs with different solid state electrolytes at room temperature.

Electrolyte	V_{oc} (mV)	I_{sc} (mA cm⁻²)	ff	η (%)
S1	724 (± 6)	7.3 (± 0.5)	0.77 (± 0.02)	4.1 (± 0.5)
S2	796 (± 2)	8.0 (± 0.1)	0.75 (± 0.02)	5.0 (± 0.1)
S3	716 (± 5)	11 (± 0.2)	0.72 (± 0.01)	5.5 (± 0.1)
S4	666 (± 7)	7.1 (± 0.4)	0.75 (± 0.01)	4.0 (± 0.5)
Standard acetonitrile-valeronitrile base electrolyte (composition outlined in Chapter 7, section 7.3.4.1)				
Standard (N719)	769 (± 10)	14.7 (± 0.4)	0.73 (± 0.02)	8.4 (± 0.3)

Porphyrin based DSSCs with solid state electrolytes

Figure 9.10 shows the IV characteristics of DSSCs utilising the P159 porphyrin dye, with S1, S2 and S3 electrolytes, at 100 % sun intensity. Only these electrolytes were investigated because with the S4 electrolyte, poor performance was obtained with the Ru-DSSCs. The device with S3 shows the best overall performance. An increase in current is observed, compared to the electrolyte systems S2 and S1, which is due to the presence of lithium iodide. Addition of 5 wt% of SiO₂ (S3) gives an increase of 100 mV in the open circuit voltage. One possible explanation for this is that the SiO₂ is acting as a blocking layer on the Titania surface, suppressing the dark current, and increasing the open circuit voltage. Interestingly, the effect of changing the electrolyte on the device parameters is different for the P159 and N719 devices, although S3 gives the best performance for both. Table 9.5 sums up the photovoltaic parameters of the P159-DSSCs with the different electrolytes.

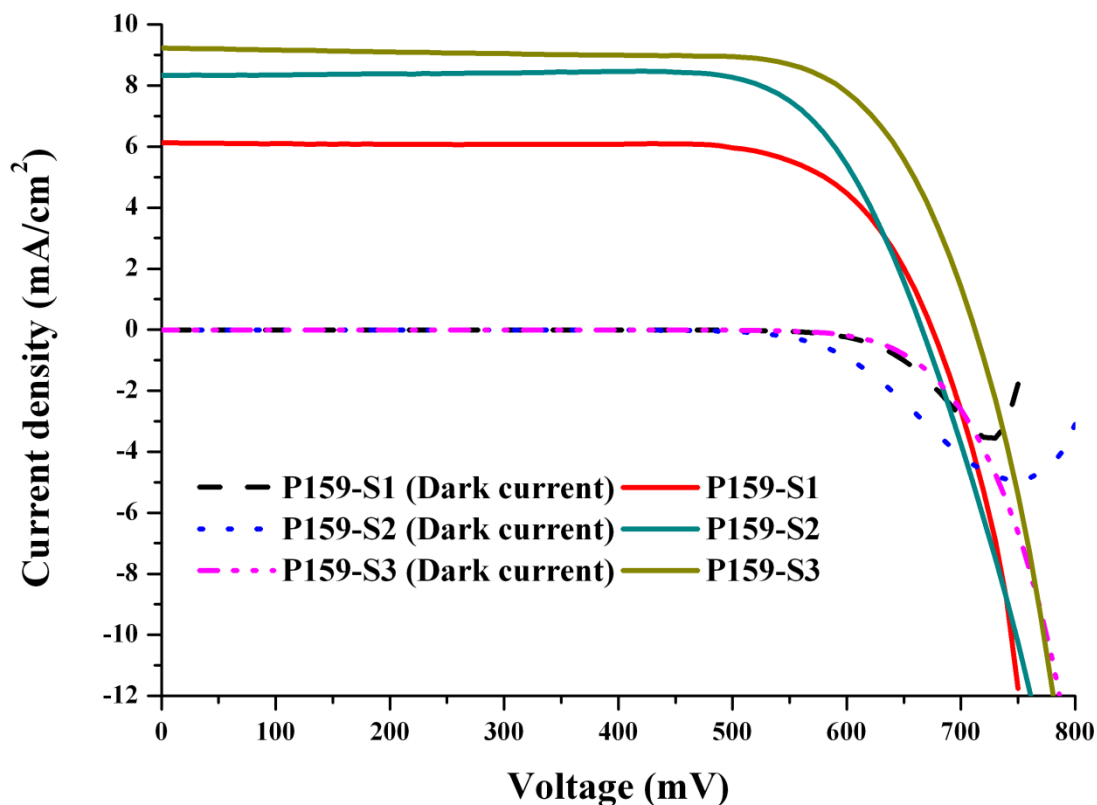


Figure 9.10: IV characteristics of P159-DSSCs based on electrolytes S1, S2 and S3 at 25 °C

Table 9.5: Photovoltaic parameters of P159-DSSCs with S1, S2 and S3.

Electrolyte	V_{oc} (mV)	I_{sc} (mA cm ⁻²)	ff	η (%)
S1	674 (± 2)	6.1 (± 0.4)	0.74 (± 0.01)	3.1 (± 0.1)
S2	665 (± 4)	8.4 (± 0.2)	0.75 (± 0.02)	4.2 (± 0.2)
S3	712 (± 2)	9.2 (± 0.1)	0.73 (± 0.02)	4.8 (± 0.2)
Standard acetonitrile-valeronitrile (composition outlined in Chapter 8, section 8.3.3)				
Standard (Porphyrin)	698 (± 7)	12.3 (± 0.1)	0.69 (± 0.05)	6.0 (± 0.1)

Figure 9.11 and Table 9.6 shows the performance of the P159 devices, at different light intensities, with the S3 electrolyte. At low sun intensities, the device performs better (5.3 % at 15 % sun), with a drop in the efficiency of the device to 4.8 % at full sun intensity. This may be due to mass transport limitations or inefficient charge screening of electron transport in the TiO₂ film. Nevertheless, this is the first time such high performances have been obtained with porphyrin sensitisers and a solid electrolyte.

Table 9.6: IV parameters, at different light intensity, for the P159-DSSC with S3.

Sun intensity (%)	V _{oc} (mV)	I _{sc} (mA cm ⁻²)	ff	η (%)
5	632 (± 3)	0.6 (± 0.2)	0.78 (± 0.01)	5.0 (± 0.2)
10	649 (± 2)	1.1 (± 0.1)	0.78 (± 0.01)	5.1 (± 0.3)
15	660 (± 2)	1.5 (± 0.2)	0.77 (± 0.01)	5.3 (± 0.2)
38	687 (± 3)	3.8 (± 0.3)	0.77 (± 0.01)	5.2 (± 0.1)
68	702 (± 2)	6.6 (± 0.2)	0.74 (± 0.03)	5.1 (± 0.1)
100	712 (± 2)	9.2 (± 0.1)	0.73 (± 0.02)	4.8 (± 0.2)

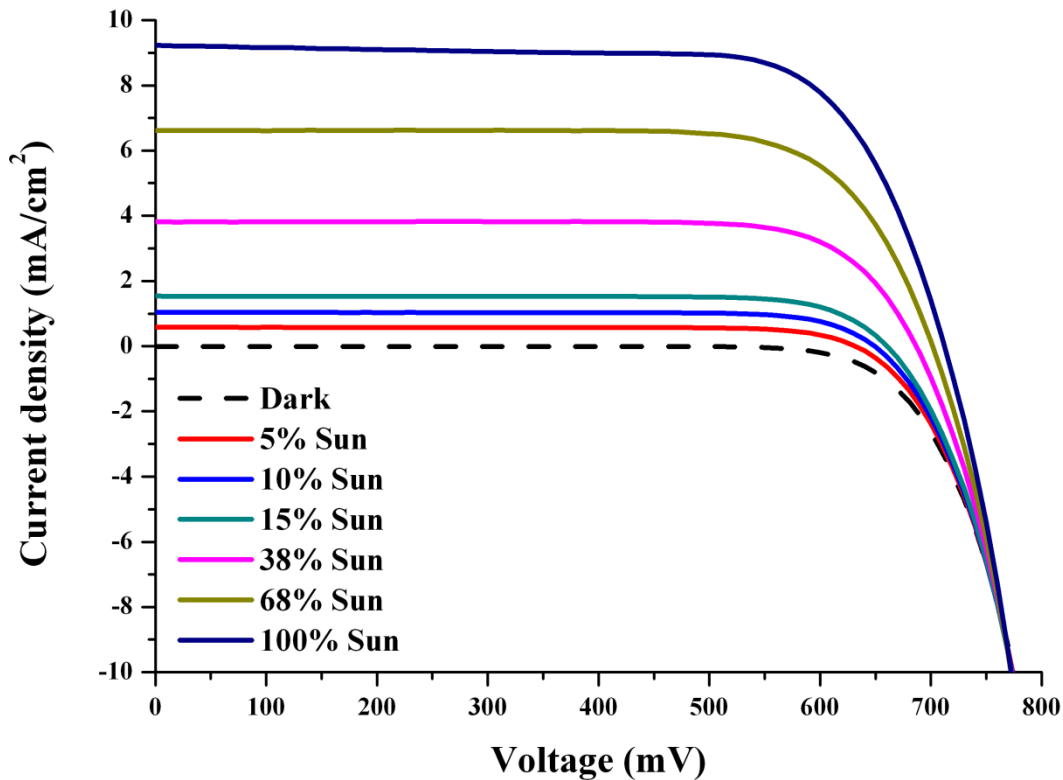


Figure 9.11: The effect of light intensity on P159-DSSCs with S3 electrolyte

9.4.2 Organic ionic plastic crystals

The different types of OIPCs used for the study are C₁mpyrN(CN)₂, C₁mpyrSCN, C₁mpyrBF₄, C₁mpyrPF₆, C₂mpyrBF₄, N₂₂₂₂N(CN)₂, C₁mpyrI and C₂mpyrNTf₂ (Some DSC traces can be found in Appendix, section A.8). As already explained in section 9.1.1, OIPCs are another class of material that has been studied as a potential solid state electrolyte for lithium batteries.⁵³ These materials are of great interest, as they exhibit high ionic conductivity as well as good plastic mechanical properties.⁵³ Thus, we were interested in investigating these materials as solid state electrolytes for dye sensitised solar cells.

9.4.2.1 Thermal analysis

The DSC trace of the sample of neat C₂mpyrNTf₂ is shown in Figure 9.12. The neat material goes through three solid-solid phase transitions before melting at 91 °C, which is consistent with previous literature reports.⁵⁴ The first solid-solid phase transition occurs at -85 °C, followed by a broad phase transition (III-II) at 16 °C. Another transition occurs at 46 °C, before the sharp melting peak at 91 °C. On addition of 2 mol% lithium iodide, no significant change in the solid-solid phase transitions is observed, except for a slight broadening of the melt. Further addition of lithium iodide gives rise to an additional peak at 23 °C. According to Forsyth and co-workers, they attribute the additional peak to the metastable solid state behaviour of the plastic crystals (C₁mpyrNTf₂ with high content of LiNTf₂),⁵⁵ and they suggested that it may represent a eutectic transition. We can assume that the same conclusion can be applied to this system, as the only difference in their case was the use of LiNTf₂, whereas we added LiI to the neat C₂mpyrNTf₂.

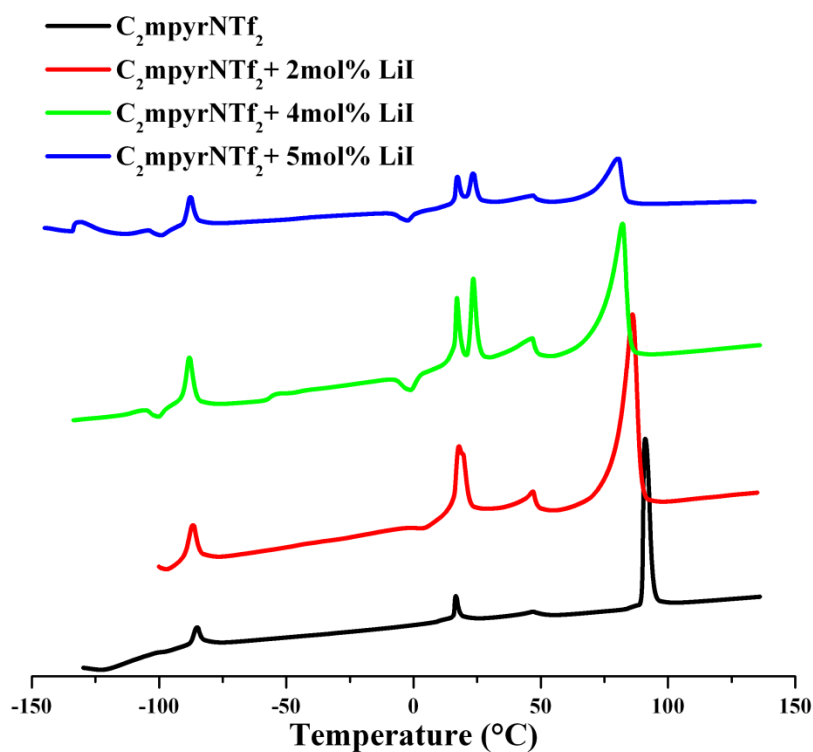


Figure 9.12: DSC traces of pure $C_2\text{mpyrNTf}_2$ and with different concentrations of LiI

Figure 9.13 displays the thermal traces of neat $C_2\text{mpyrNTf}_2$ and the material doped with 2 mol% of lithium iodide and 10 wt% SiO_2 . A broader melt transition is observed in the presence of the additives and the onset temperatures are shifted to a lower temperature. The entropy of fusion in the presence of SiO_2 is not significantly affected, but on addition of SiO_2 , the phase transition peak (IV to III) becomes slightly smaller.

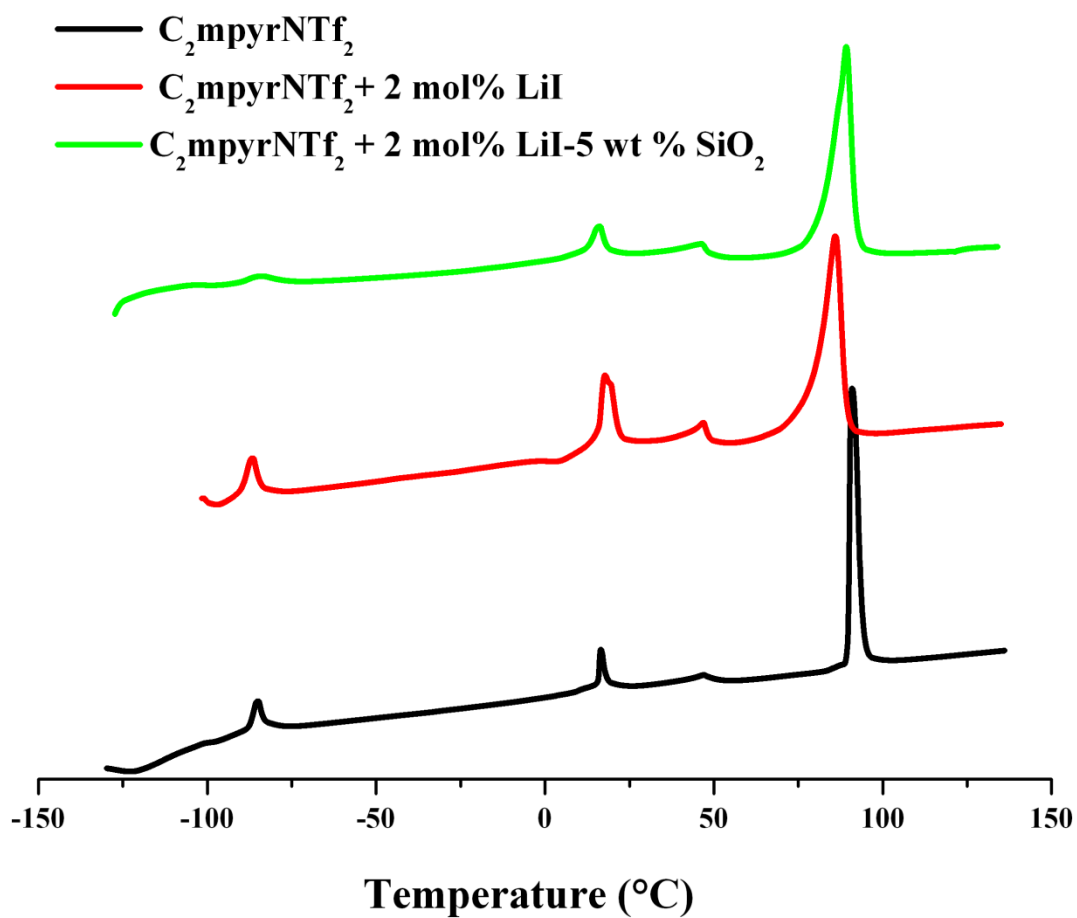


Figure 9.13: DSC trace of $C_2\text{mpyrNTf}_2$ in presence of LiI and SiO_2

Table 9.7 summarises the onset temperatures of the different solid-solid phase transitions and the melting transition, as well as the entropy of fusion for neat $C_2\text{mpyr}$ and in the presence of additives (from both Figure 9.12 and 9.13).

Table 9.7: Phase transition temperatures and entropies of pure C₂mpyrNTf₂ and C₂mpyrNTf₂ doped with LiI or LiI and SiO₂.

Compound	T _{IV-III}	T _{III-II}	T _{II-I}	T _m	ΔS _f J mol ⁻¹ K ⁻¹
C ₂ mpyrNTf ₂	-85	15	48	91	24
C ₂ mpyrNTf ₂	-86	15	47	86	22
+2 mol% LiI					
C ₂ mpyrNTf ₂	-87	17,23	47	82	10
+4 mol% LiI					
C ₂ mpyrNTf ₂	-88	17,23*	47	81	9
+ 5 mol% LiI					
C ₂ mpyrNTf ₂	-83	17	47	88	22
+2 mol% LiI					
+ 5wt% SiO₂					

Figure 9.14 displays the thermal analysis of tetraethylammonium dicyanamide (N₂₂₂₂N(CN)₂). The DSC trace of the pure material shows a lower temperature phase (II), a solid-solid phase transformation at 21 °C, with an entropy change of 40 J mol⁻¹ K⁻¹, and the material stays in this plastic phase until melting at 60 °C, with an entropy of fusion of 6 J mol⁻¹ K⁻¹. On addition of 2 mol% LiI, a shift in the onset temperature is observed for the solid-solid phase transition, to a lower temperature of 16 °C, and a slight decrease is observed in the melt transition temperature, to 58 °C, with an entropy of fusion of 5.8 J mol⁻¹ K⁻¹.

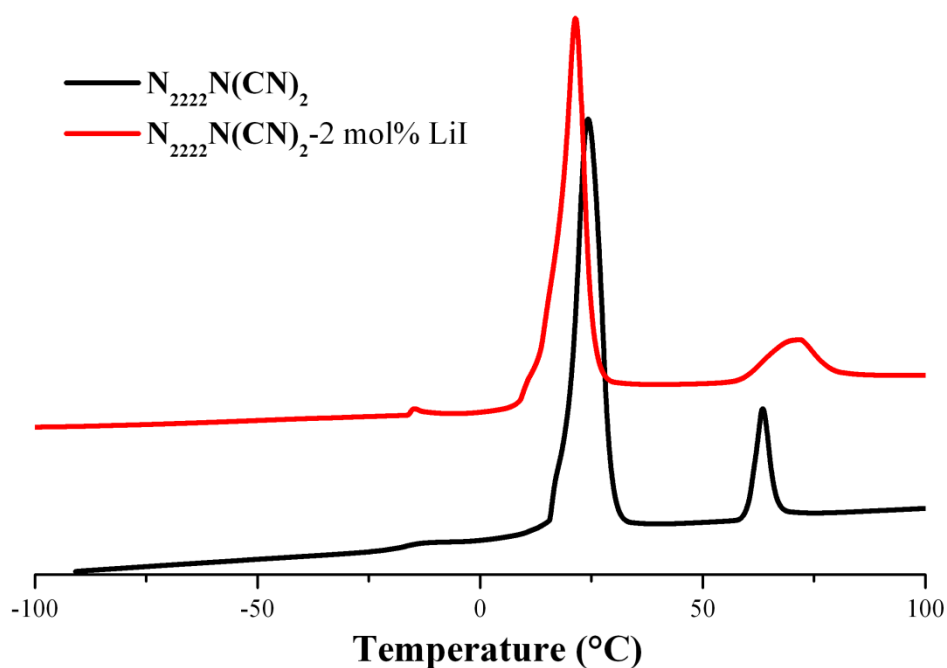


Figure 9.14: DSC traces for $N_{222}N(CN)_2$ neat and with 2 mol% LiI

9.4.2.2 Conductivity

Ionic conductivity of $C_2mpyrNTf_2$ doped and with filler

Figure 9.15 displays the temperature dependent ionic conductivity of neat $C_2mpyrNTf_2$ and $C_2mpyrNTf_2$ doped with LiI, or LiI with SiO_2 . The neat compound is moderately conductive, and this increases with respect to temperature. Addition of 5 mol% LiI into the neat matrix results in an increase in conductivity, which might be related to an augmentation of the number of charge carriers or higher mobility of the charged ions. Addition of nanoparticles to the doped plastic crystal results in a small drop in conductivity, but the conductivity of this material is still significantly greater than that of the pure salt.

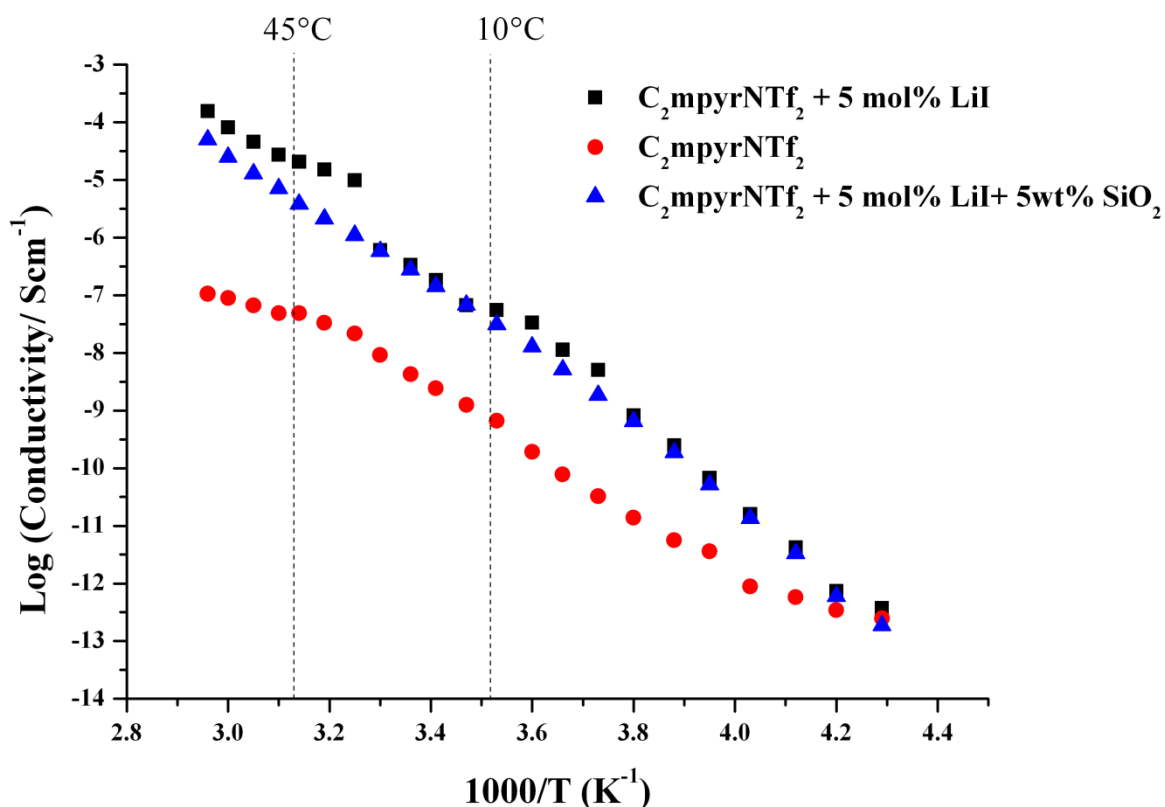


Figure 9.15: Logarithmic plot of ionic conductivity as a function of inverse temperature for neat C₂mpyrNTf₂, and doped C₂mpyrNTf₂ with 5 mol% LiI and 5 wt% SiO₂

Ionic conductivity of N₂₂₂₂N(CN)₂ neat and doped with LiI

The ionic conductivity for pure N₂₂₂₂N(CN)₂, N₂₂₂₂N(CN)₂ + 2 mol% LiI and the solid electrolyte composed of N₂₂₂₂N(CN)₂/C₂mimI/LiI/I₂ in the molar ratio 100:12:1:2 respectively, are displayed in Figure 9.16. As with most plastic crystals, the ionic conductivity is low in the lower temperature region, and steadily increases as the temperature rises. Doping the neat material with 2 mol% LiI results in an increase in conductivity. Further augmentation of the ionic conductivity is also observed in the presence of other additives (C₂mimI and I₂).

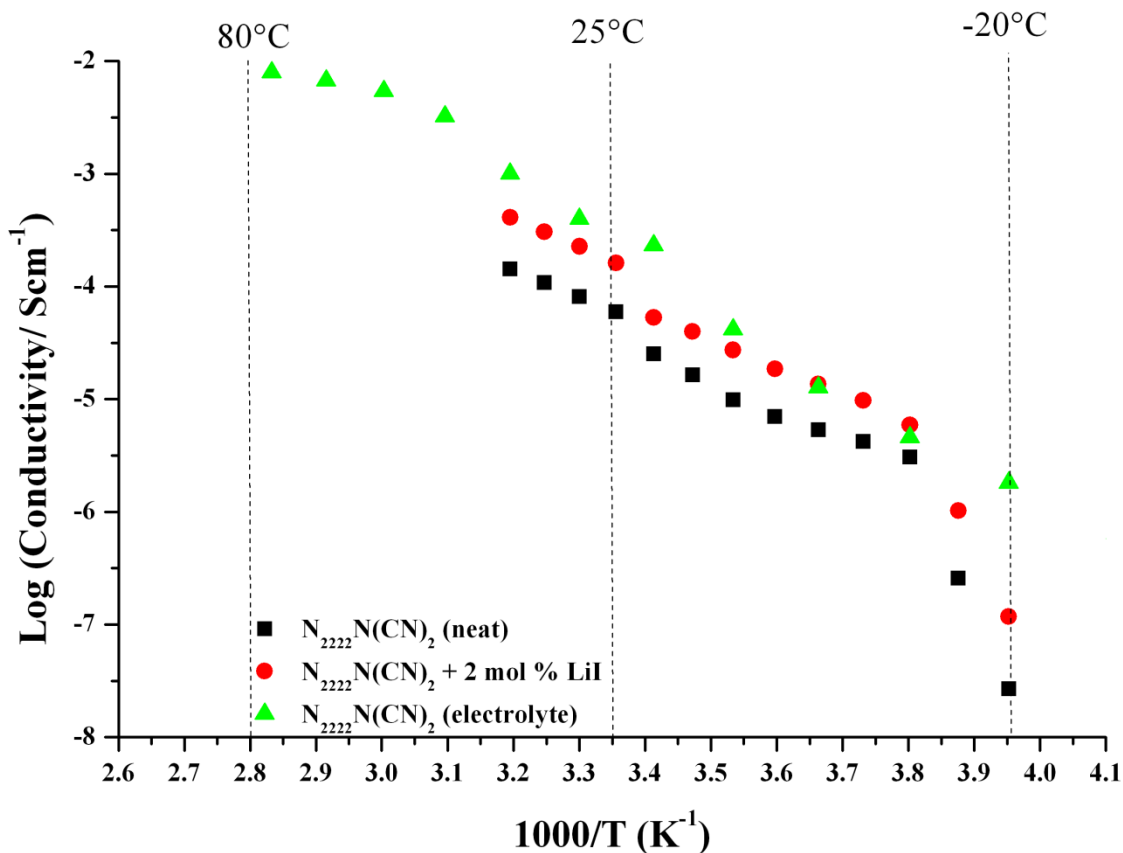


Figure 9.16: Ionic conductivity as a function of the inverse of temperature for neat $N_{2222}N(CN)_2$, $N_{2222}N(CN)_2 + 2 \text{ mol}\% \text{ LiI}$, and the $N_{2222}N(CN)_2$ -based electrolyte with $C_2\text{mimI}$ and I_2

Figure 9.17 demonstrates the variation of ionic conductivity of a number of other plastic crystal electrolytes, as a function of the inverse of temperature. $C_2\text{mimI}$, LiI , I_2 and NMB were added in all cases to make up the solid electrolyte, except for $N_{2222}N(CN)_2$ where no NMB was added due to the formation of two phases. In the higher temperature region, $C_1\text{mpyrN(CN)}_2$ displays highest conductivity compared to the other plastic electrolytes.

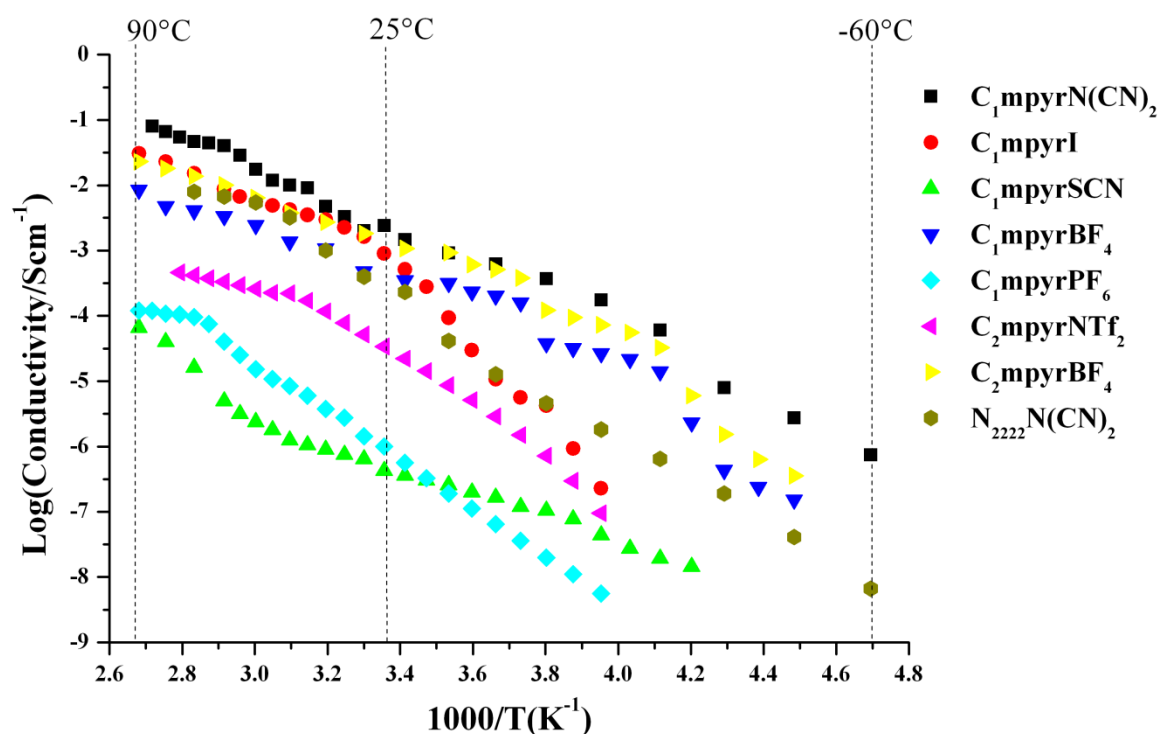


Figure 9.17: Ionic conductivity as a function of the inverse temperature for different solid state electrolytes. The molar ratio of the components $C_2mimI:Li:I_2:NMB$ are **8:1:1:2** respectively

9.4.2.3 Electrochemical analysis

Diffusion coefficients of I^- and I_3^- and charge transfer resistance in the solid electrolyte

The cell kinetics were studied on a system containing the OIPC, with the other additives commonly present in a DSSC electrolyte, and these were compared with the kinetics of a molecular organic solvent system. The diffusion coefficient of I^- and I_3^- cannot be measured at room temperature using either a microelectrode or a symmetrical cell, due to the solidification of the electrolyte, which results in a bad contact with the electrodes. Thus, the diffusion was measured at high temperatures (80 °C), to provide information about the mobility of the I_3^- and I^- in the plastic electrolyte. Table 9.8 summarises the transport properties of I^- and I_3^- in the plastic electrolytes and in an organic solvent electrolyte.

Table 9.8: Diffusion coefficient (D) of redox species measured at 80 °C.

Electrolyte	D I ₃ ⁻ (cm ² s ⁻¹) (± 8%)	D I ⁻ (cm ² s ⁻¹) (± 8%)
Standard*	4.7 x 10 ⁻⁶	5.9 x 10 ⁻⁶
Acetonitrile-valeronitrile		
C₁mpyrN(CN)₂	6.2 x 10 ⁻⁷	4.2 x 10 ⁻⁷
N₂₂₂₂N(CN)₂	5.4 x 10 ⁻⁷	3.3 x 10 ⁻⁷
C₂mpyrBF₄	4.4 x 10 ⁻⁷	1.1 x 10 ⁻⁷
C₂mpyrNTf₂	3.2 x 10 ⁻⁷	3.9 x 10 ⁻⁷
C₁mpyrI	2.8 x 10 ⁻⁷	2.5 x 10 ⁻⁷
C₁mpyrSCN	2.1 x 10 ⁻⁷	2.1 x 10 ⁻⁷
C₁mpyrPF₆	1.5 x 10 ⁻⁷	7.4 x 10 ⁻⁸
C₁mpyrBF₄	9.9 x 10 ⁻⁸	6.2 x 10 ⁻⁸

*measured at room temperature.

The diffusion coefficient of I₃⁻ at 80 °C is 10 times slower in the plastic crystal systems than in the organic solvent. This poor mobility is consistent with the lower conductivities, and is associated which hinders the movement of the I₃⁻ through the solid matrix. In all the solid electrolyte systems, the diffusion coefficient of I₃⁻ is higher than I⁻. As with the conductivity comparisons, C₁mpyrN(CN)₂ shows the highest diffusivities.

Charge resistance of electrolytes

The fitting parameters of the EIS spectra of the different plastic electrolytes were obtained by fitting the spectra with an appropriate equivalent circuit (Appendix, section A.9). R_s is the series resistance, related to the resistance of the electrolyte and the sheet resistance of the FTO glass. R_{ct} is the charge transfer resistance of the electrochemical reaction between the two Pt-electrolyte interfaces, and C is the capacitance. As summarised in Table 9.9, the R_s values of C₁mpyrI, C₁mpyrBF₄ and C₁mpyrSCN based electrolytes are much higher than for C₂mpyrNTf₂, C₁mpyrN(CN)₂, C₂mpyrBF₄, C₁mpyrPF₆ and N₂₂₂₂N(CN)₂. The charge transfer resistance is particularly high for C₁mpyrBF₄, and this may affect the performance of the device due to the high energy loss that can occur.

Table 9.9: Fitting parameters from the EIS spectrum.

Electrolyte	R_s (Ω)	R_{ct} (Ω)	C (μ F)
C_2 mpyrNTf ₂	25.4	6.1	2.1
C_2 mpyrBF ₄	23.9	16.7	2.6
C_1 mpyrBF ₄	37.8	1321	0.6
C_1 mpyrPF ₆	22.2	6.8	1.9
C_1 mpyrN(CN) ₂	25.7	1.9	2.0
C_1 mpyrSCN	32.8	7.6	2.6
C_1 mpyrI	32.2	5.1	2.2
N_{2222} N(CN) ₂	27.8	1.5	2.9

9.4.2.4 Photovoltaic performance of OIPC electrolyte using ruthenium dye.

Ruthenium dye

Figure 9.18 shows the IV curves of the DSSCs, assembled using the different solid state electrolytes, under full sun intensity.

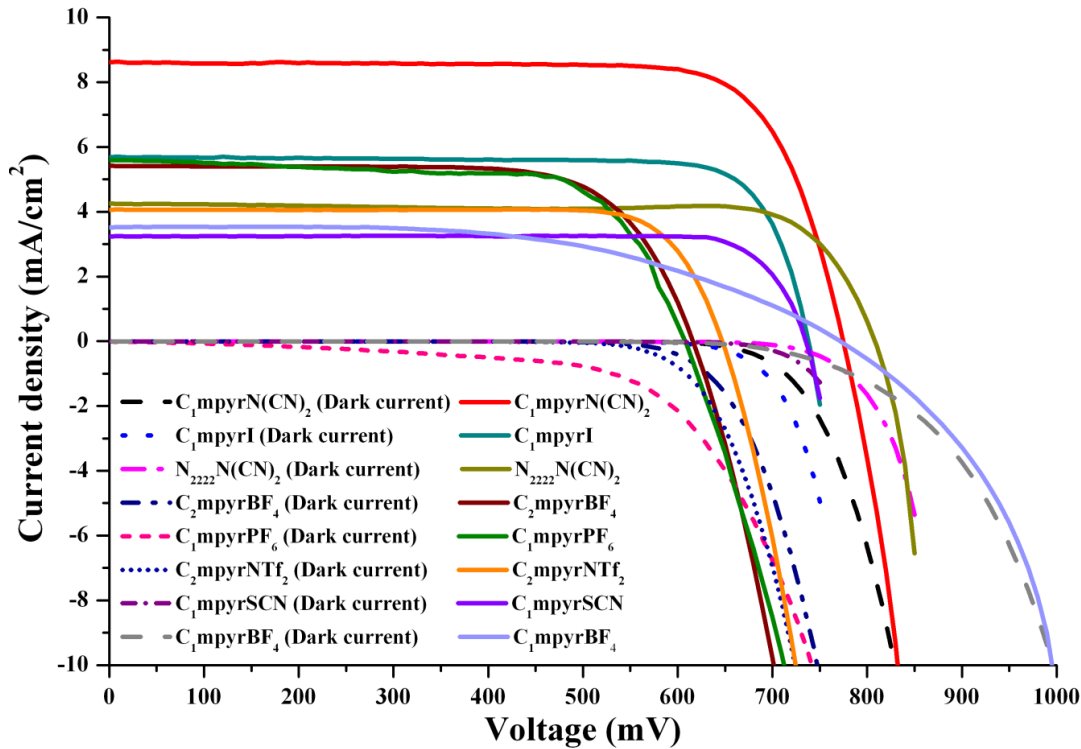


Figure 9.18: IV curves for DSSCs with ruthenium sensitiser (N719) and plastic crystal electrolytes

The performance of the DSSCs varied depending on the type of solid state electrolyte used. The DSSC containing the C₁mpyrN(CN)₂ electrolyte gives a better performance than with the other plastic crystal electrolytes. The I_{sc}, V_{oc} and *ff* are 8.1 mA cm⁻², 775 mV and 0.77 respectively, with an overall performance of 5.1 % under full sun intensity. At 68 % sun intensity, the performance of the device is 5.3 %. As shown in Figure 9.18, C₁mpyrI, N₂₂₂₂N(CN)₂ and C₂mpyrBF₄ also exhibit quite good ionic conductivity, but the performance of the devices is quite poor. In the case of C₁mpyrI, the main limitation is due to the low short circuit current density compared to C₁mpyr N(CN)₂, related to the poor diffusion of the redox species, as shown in Table 9.8. Correspondingly, C₁mpyrPF₆, C₂mpyrNTf₂ and C₁mpyrSCN display lower ionic conductivities and the efficiency of the device is also quite low with these solid state electrolytes.

Table 9.9: Photovoltaic parameters of the DSSCs with different plastic crystal electrolytes.

Electrolytes	V _{oc} (mV)	I _{sc} (mA cm ⁻²)	<i>ff</i>	η (%)
C ₁ mpyrN(CN) ₂	775 (± 5)	8.6 (± 0.2)	0.77 (± 0.02)	5.1 (± 0.2)
C ₁ mpyrI	738 (± 3)	5.7 (± 0.5)	0.78 (± 0.01)	3.4 (± 0.5)
N ₂₂₂₂ N(CN) ₂	808 (± 5)	4.1 (± 0.7)	0.79 (± 0.01)	2.8 (± 0.4)
C ₂ mpyrBF ₄	616 (± 7)	5.4 (± 0.5)	0.72 (± 0.01)	2.4 (± 0.5)
C ₁ mpyrPF ₆	608 (± 7)	5.6 (± 0.2)	0.70 (± 0.02)	2.3 (± 0.4)
C ₂ mpyrNTf ₂	650 (± 5)	4.1 (± 0.6)	0.79 (± 0.01)	2.1 (± 0.2)
C ₁ mpyrSCN	736 (± 5)	3.2 (± 0.5)	0.79 (± 0.01)	2.0 (± 0.5)
C ₁ mpyrBF ₄	771 (± 2)	3.5 (± 0.2)	0.54 (± 0.05)	1.5 (± 0.2)

9.5 Conclusions

In this chapter, we have demonstrated the use of solid electrolytes in both porphyrin-based and ruthenium-based dye sensitised solar cells. Relatively good performance was achieved with porphyrin-DSSCs containing the molecular plastic crystal electrolyte in the presence of silica. This good performance might be related to the presence of the nanoparticles, which may act as a blocking layer on the surface of the TiO₂ resulting in an increase in V_{oc} .

We have also reported the first use of an organic ionic plastic crystal as a solid state electrolyte in ruthenium-based DSSCs. The best performance was obtained with C₁mpyrN(CN)₂, which is related to the high ionic conductivity of the materials. This results in better diffusivity of the electroactive species, and a higher short circuit current density.

References

1. P. Wang, Q. Dai, S. M. Zakeeruddin, M. Forsyth, D. R. MacFarlane and M. Grätzel, *J. Am. Chem. Soc.*, 2004, **126**, 13590-13591.
2. D. R. MacFarlane, P. Meakin, J. Sun, N. Amini and M. Forsyth, *J. Phys. Chem. B*, 1999, **103**, 4164-4170.
3. J. Timmermans, *J. Phys. Chem. Solids*, 1961, **18**, 1-8.
4. D. R. MacFarlane, S. A. Forsyth, J. Golding and G. B. Deacon, *Green Chem.*, 2002, **4**, 444-448.
5. Y. Shekibi, S. J. Pas, N. M. Rocher, B. R. Clare, A. J. Hill, D. R. MacFarlane and M. Forsyth, *J. Mater. Chem.*, 2009, **19**, 1635-1642.
6. J. M. Pringle, P. C. Howlett, D. R. MacFarlane and M. Forsyth, *J. Mater. Chem.*, 2010, **20**, 2056-2062.
7. J. M. Pringle, J. Adebahr, D. R. MacFarlane and M. Forsyth, *Phys. Chem. Chem. Phys.*, 2010, **12**, 7234-7240.
8. P. C. Howlett, Y. Shekibi, D. R. MacFarlane and M. Forsyth, *Adv. Eng. Mater.*, 2009, **11**, 1044-1048.
9. Y. Shekibi, A. Gray-Weale, D. R. MacFarlane, A. J. Hill and M. Forsyth, *J. Phys. Chem. C*, 2007, **111**, 11463-11468.
10. J. Adebahr, F. C. Grozema, S. W. deLeeuw, D. R. MacFarlane and M. Forsyth, *Solid State Ionics*, 2006, **177**, 2845-2850.
11. H. B. Han, J. Nie, K. Liu, W. K. Li, W. F. Feng, M. Armand, H. Matsumoto and Z. B. Zhou, *Electrochim. Acta*, 2010, **55**, 1221-1226.
12. S. Long, D. R. MacFarlane and M. Forsyth, *Solid State Ionics*, 2003, **161**, 105-112.
13. T. H. Kuo, C. Y. Hsu, K. M. Lee and K. C. Ho, *Sol. Energy Mater. Sol. Cells*, 2009, **93**, 1755-1760.
14. R. N. Rai and R. S. B. Reddi, *Thermochim. Acta*, 2009, **496**, 13-17.
15. S. Long, P. C. Howlett, D. R. MacFarlane and M. Forsyth, *Solid State Ionics*, 2006, **177**, 647-652.
16. S. F. Marrian, *Chem. Rev.*, 1948, **43**, 149-202.
17. G. R. R. A. Kumara, K. Tennakone, V. P. S. Perera, A. Konno, S. Kaneko and M. Okuya, *J. Phys. D: Appl. Phys.*, 2001, 868.
18. E. V. A. Premalal, G. R. R. A. Kumara, R. M. G. Rajapakse, M. Shimomura, K. Murakami and A. Konno, *Chem. Commun.*, 2010, **46**, 3360-3362.
19. G. R. A. Kumara, S. Kaneko, M. Okuya and K. Tennakone, *Langmuir*, 2002, **18**, 10493-10495.
20. Q. B. Meng, K. Takahashi, X. T. Zhang, I. Sutanto, T. N. Rao, O. Sato, A. Fujishima, H. Watanabe, T. Nakamori and M. Uragami, *Langmuir*, 2003, **19**, 3572-3574.
21. T. Taguchi, X. T. Zhang, I. Sutanto, K. I. Tokuhira, T. N. Rao, H. Watanabe, T. Nakamori, M. Uragami and A. Fujishima, *Chem. Commun.*, 2003, 2480-2481.
22. G. R. A. Kumara, M. Okuya, K. Murakami, S. Kaneko, V. V. Jayaweera and K. Tennakone, *J. Photochem. Photobiol. A*, 2004, **164**, 183-185.

23. U. Bach, D. Lupo, P. Comte, J. E. Moser, F. Weissortel, J. Salbeck, H. Spreitzer and M. Grätzel, *Nature*, 1998, **395**, 583-585.
24. H. J. Snaith, A. J. Moule, C. Klein, K. Meerholz, R. H. Friend and M. Grätzel, *Nano Lett.*, 2007, **7**, 3372-3376.
25. K. Fredin, K. F. Anderson, N. W. Duffy, G. J. Wilson, C. J. Fell, D. P. Hagberg, L. Sun, U. Bach and S.-E. Lindquist, *J. Phys. Chem. C*, 2009, **113**, 18902-18906.
26. K. Fredin, E. M. J. Johansson, T. Blom, M. Hedlund, S. Plogmaker, H. Siegbahn, K. Leifer and H. Rensmo, *Synth. Met.*, 2009, **159**, 166-170.
27. Y. Saito, N. Fukuri, R. Senadeera, T. Kitamura, Y. Wada and S. Yanagida, *Electrochem. Commun.*, 2004, **6**, 71-74.
28. X. Li, D. Chen, D. Xu, C. Zhao, Z. Wang, H. Lu and H. Na, *J. Membr. Sci.*, 2006, **275**, 134-140.
29. S. Ameen, M. S. Akhtar, Y. S. Kim, O. B. Yang and H. S. Shin, *J. Phys. Chem. C*, 2010, **114**, 4760-4764.
30. S. Tan, J. Zhai, M. Wan, Q. Meng, Y. Li, L. Jiang and D. Zhu, *J. Phys. Chem. B*, 2004, **108**, 18693-18697.
31. F. Wu, T. Feng, C. Wu, Y. Bai, L. Ye and J. Chen, *J. Phys. D: Appl. Phys.*, 2010, **43**, 035501.
32. J. Trigueiro, R. Borges, R. Lavall, H. Calado and G. Silva, *Nano Res.*, 2009, **2**, 733-739.
33. H. J. Cho, Y. M. Song, I. Chung, K. S. Ryu, and N. J. Jo, *Smart Mater. Struct.*, 2009, **18**, 024006.
34. J. W. Kim and Y. C. Bae, *J. Appl. Polym. Sci.*, 2010, **117**, 3582-3587.
35. Y. H. Liao, M. M. Rao, W. S. Li, L. T. Yang, B. K. Zhu, R. Xu and C. H. Fu, *J. Membr. Sci.*, 2010, **352**, 95-99.
36. M. Li, S. Feng, S. Fang, X. Xiao, X. Li, X. Zhou and Y. Lin, *Electrochim. Acta*, 2007, **52**, 4858-4863.
37. Z. Lan, J. Wu, S. Hao, J. Lin, M. Huang and Y. Huang, *Energy Environ. Sci.*, 2009, **2**, 524-528.
38. C. P. Lee, P. Y. Chen, R. Vittal and K. C. Ho, *J. Mater. Chem.*, 2010, **20**, 2356-2361.
39. S. Y. Cha, Y. G. Lee, M. S. Kang and Y. S. Kang, *J. Photochem. Photobiol. A*, 2010, **211**, 193-196.
40. L. Fan, S. Kang, J. Wu, S. Hao, Z. Lan and J. Lin, *Energy Sources Part A*, 2010, **32**, 1559 - 1568.
41. J. Golding, N. Hamid, D. R. MacFarlane, M. Forsyth, C. Forsyth, C. Collins and J. Huang, *Chem. Mater.*, 2001, **13**, 558-564.
42. C. A. Wulff and E. F. Westrum, *J. Phys. Chem.*, 1963, **67**, 2376-2381.
43. O. I. Fengler and A. Ruoff, *Spectrochim. Acta, Part A*, 2001, **57**, 105-117.
44. T. Bischofberger and E. Courtens, *Phys. Rev. Lett.*, 1974, **32**, 163.
45. Q. Dai, D. R. MacFarlane, P. C. Howlett and M. Forsyth, *Angew. Chem.*, 2005, **117**, 317-320.

46. W. M. Campbell, A. K. Burrell, D. L. Officer and K. W. Jolley, *Coord. Chem. Rev.*, 2004, **248**, 1363-1379.
47. W. M. Campbell, K. W. Jolley, P. Wagner, K. Wagner, P. J. Walsh, K. C. Gordon, L. Schmidt-Mende, M. K. Nazeeruddin, Q. Wang, M. Grätzel and D. L. Officer, *J. Phys. Chem. C*, 2007, **111**, 11760-11762.
48. M. Berginc, M. Hocevar, U. Opara Krasovec, A. Hirsch, R. Sastrawan and M. Topic, *Thin Solid Films*, 2008, **516**, 4645-4650.
49. T. Katakabe, R. Kawano and M. Watanabe, *Electrochem. Solid-State Lett.*, 2007, **10**, F23-F25.
50. H. A. Every, A. G. Bishop, D. R. MacFarlane, G. Oradd and M. Forsyth, *J. Mater. Chem.*, 2001, **11**, 3031-3036.
51. Q. Dai, D. R. MacFarlane and M. Forsyth, *Solid State Ionics*, 2006, **177**, 395-401.
52. B. Li, P. Cheng and C. S. Deng, *Chin. J. Chem. Phys.*, 2007, **20**, 816.
53. J. Adebahr, N. Ciccossillo, Y. Shekibi, D. R. MacFarlane, A. J. Hill and M. Forsyth, *Solid State Ionics*, 2006, **177**, 827-831.
54. D. R. MacFarlane, P. Meakin, N. Amini and M. Forsyth, *J. Phys. Condens. Matter*, 2001, **13**, 8257.
55. M. Forsyth, J. Huang and D. R. MacFarlane, *J. Mater. Chem.*, 2000, **10**, 2259-2265.

Chapter 10

Conclusions and Future work

10.1 Conclusions

The aims of this thesis were to:

- Synthesis and characterise a range of new phosphonium ILs for DSSCs.
- Study the effect of ILs on the flatband potential of an n-type semiconductor.
- Develop and test phosphonium based IL electrolytes with dithienothiophene organic sensitisers.
- Test imidazolium and phosphonium based electrolytes with porphyrin dyes.
- Investigate the performance of DSSCs with solid state electrolytes.

10.2 Synthesis of novel phosphonium ionic liquids

In Chapter 6, the synthesis and physical properties of new ionic liquids based on the phosphonium family were studied. The chemical and physical properties, such as thermal behaviour, viscosity, density and ionic conductivity of the phosphonium ionic liquids were measured. The P_{1224}^+ cation combined with BF_4^- , PF_6^- , or SCN^- anions forming salts that show multiple solid-solid phase transitions with a $\Delta S_f \sim 20 \text{ J mol}^{-1} \text{ K}^{-1}$. These phosphonium based salts can potentially be used as solid state electrolytes for dye sensitised solar cells.

The low viscous phosphonium ionic liquids, such as those composed of $P_{222(201)}^+$, $P_{222(101)}^+$ and P_{1224}^+ cations combined with FSI^- or NTf_2^- or $N(CN)_2^-$ anions, are considered to be good ionic liquids according to the Walden plot, without significant ion pairing.

The phosphonium series synthesised in this chapter show relatively good thermal stability, except those based on the FSI^- anion and this is mainly related to the ease in breaking the S-F bond relative to the C-F bond. Nevertheless, these ionic liquids can be used as electrolytes in DSSCs as the operation of these devices will never exceed 300 °C and the electrochemical window is sufficient for the proper functioning of the solar cells.

10.3 The effect of the ionic liquid on the flatband potential of n-type semiconductors

The aim of this work was to study the position of the flatband potential of the TiO₂ when it is in contact with an ionic liquid. This investigation was performed in an attempt to understand how the flatband potential of the TiO₂ is modified according to the neutrality, basicity or acidity of the ionic liquids. A range of ionic liquids were used for the study - some were purchased from different commercial suppliers and some were synthesised.

It was interesting to observe that C₂mimBF₄ purchased from different suppliers gives different flatband potentials; there is nearly a 100 mV difference from ILs purchased from Iolitec and Merck. This difference is mainly related to the purity of the ionic liquids. Further, C₂mimBF₄ is considered to be a ‘neutral’ ionic liquid, but when in contact with the TiO₂ electrode, it shifts the conduction band of the TiO₂ to more positive potentials, showing an acidic behaviour. The BF₄⁻ anion is known to hydrolyse easily when in contact with water, to form HBF₄, thus potentially acidifying the ionic liquid.

Addition of a lithium salt to C₃mpyrNTf₂ gives a positive shift in the flatband potential due to the insertion of the Li ion into the TiO₂ network. Contrary to this behaviour, addition of a base, such as TBP, moves the conduction band to more negative potential, which usually results in higher V_{oc} due to the protecting behaviour of the base. Ionic liquids containing SCN⁻ or N(CN)₂⁻ anions have the same effect on the flatband potential of the TiO₂ as TBP. Consistent with this observation, these ILs are known to have basic behaviour. Solar devices containing these ionic liquids usually give higher V_{oc} and lower I_{sc}.

While these initial investigations have provided some interesting insight into the influence of the ionic liquid on the flat band potential, further research is still required to fully understand the behaviour of the TiO₂-ionic liquid interface.

10.4 Phosphonium based ionic liquids with dithienothiophene organic sensitisers

In Chapter 7, the use of phosphonium ionic liquids as electrolytes in dye sensitised solar cells using either organic sensitisers (THD1, THD2, THD3, THD8) or ruthenium based sensitisers (N719 and Z907) were investigated. All of the phosphonium salts show relatively good performance in the solar cell devices with either type of sensitiser. The addition of chenodeoxycholic acid in the organic dye solutions (with THD1, THD2 or THD3) resulted in an increase in device performance, which is mostly related to an increase in the short circuit current density. This higher I_{sc} is probably due to a reduction in dye aggregation. In some cases, better V_{oc} was also obtained, which might be due to the chenodeoxycholic acid present on the surface of the TiO_2 , acting as a barrier and protecting the surface from being directly in contact with the electrolyte. The viscosity, ionic conductivity and diffusivity of the redox species also play an important role in determining the overall performance of the device. Consequently, the low viscous phosphonium ionic liquids, such as $P_{222(101)}NTf_2$, $P_{222(201)}NTf_2$, $P_{222(101)}FSI$, $P_{222(201)}FSI$, $P_{222(101)}N(CN)_2$, $P_{1224}FSI$, $P_{1224}NTf_2$, $P_{1444}N(CN)_2$, gives relatively good device performance.

The addition of 10 μ L tetraglyme, water and valeronitrile to $P_{1444}N(CN)_2$ was also investigated with Ru-based DSSCs. These additives gave an improvement in the device efficiency, which is mainly the result of a higher V_{oc} and fill factor. This is the first time that such high device performance have been obtained with phosphonium ionic liquid electrolytes. Further investigations will focus on determining the limiting factors of the performance and also the long term stability of the devices.

10.5 Ionic materials for porphyrin dye sensitised solar cells

In Chapter 8, the use of imidazolium, phosphonium and ammonium ionic liquids was investigated with three porphyrin dyes (GD2, GD3 and P159). Out of these three dyes, P159 surpassed the performance of the two other dyes using either an ionic liquid or molecular liquid electrolyte. The main reason for such behaviour is probably the presence of the long alkyl chain present on the periphery of the benzene ring, which acts as a barrier between the TiO_2 surface and the electrolyte.

10. Conclusions and Future work

The treatment of the TiO₂ film with a phosphinic acid (diisooctylphosphinic acid) gave an improvement in both V_{oc} and I_{sc} when a molecular liquid electrolyte was used. The best improvement was obtained with the electrolyte that did not contain any additives (LiI or TBP). Unfortunately, no improvement was observed with the acid treatment when ionic liquid electrolytes were used; rather a drop in performance was observed. This shows that the solvent behaviour of the ionic liquid is completely different to the organic solvents. The other factor that should be taken into consideration is the viscosity of the ionic liquid electrolytes, which will limit the performance of the devices.

Discoloration of the porphyrin-based DSSCs was observed when the ionic liquids C₂mimSCN and C₂mimN(CN)₂ were used. This is possibly a result of interaction of the anion with the porphyrin sensitizers, but further surface analysis of the dyed TiO₂ film is required to confirm this hypothesis.

Ternary mixtures containing C₂mimB(CN)₄, C₂mimI, C₁mimI, LiI, I₂ and NMB gave the best performance with P159-DSSCs. This good performance is related to the high short circuit current density afforded by this ionic liquid electrolyte.

10.6 Solid state electrolytes in dye sensitised solar cells

In Chapter 9, the use of molecular plastic crystals and organic ionic plastic crystals as solid state electrolytes in DSSCs was investigated. The thermal properties and the ionic conductivity of the neat materials and the electrolytes were measured. The addition of SiO₂ to the succinonitrile electrolyte gives an improvement in the device performance with the P159-DSSCs. This was also the first time that organic ionic plastic crystals have been used as solid electrolytes in DSSCs. The best performance was obtained with C₁mpyrN(CN)₂ with a ruthenium based dye, and this high performance is related to high short circuit current density in this device.

10.7 Future work

Understanding the behaviour of the TiO₂-ionic liquid junction is important in designing high performing devices. Mott-Schottky capacitance measurements were used in this work to determine the flatband potential of the TiO₂ when in contact with the ionic liquids. Good correlation between this method and analysis by UV-spectroscopy has been obtained in aqueous media, thus UV-spectroscopy measurements should also be undertaken to determine the flatband potential of the TiO₂ in ionic liquids, and compare to the Mott-Schottky measurements.

In order to have a complete understanding of the factors underpinning the good performance of the phosphonium ionic liquids, measurement of the electron lifetime and the rate of recombination reaction with the new organic dyes is essential in order to understand why these dyes performed better than porphyrin dye sensitisers. APCE measurements with the phosphonium ionic liquids is required to provide information about the charge collection and charge injection efficiency, and therefore which other factors are limiting the device performance. Further investigations into the use of phosphonium ionic liquids, and optimisation of the electrolyte with THD9 dye, should be undertaken to see whether any further device improvement can be achieved. Long term testing is also required to study the stability of the devices with the phosphonium ionic liquid electrolytes.

Alternative redox couples and other organic dyes with different linkers should also be investigated and optimised, using both acetonitrile and ionic liquid-based media.

The effect of increasing the concentration of I₂ in the organic plastic crystals would be worth studying to see if a further improvement in device performance can be achieved. There are also a number of different analytical techniques that could be incorporated into future research into the use of these materials in DSSCs. For example, alternative electrochemical methods are required to measure the diffusion of the redox species at room temperature, and surface analysis of the organic plastic crystals is necessary to understand the behaviour of these materials in solar cells. Measurement of electron lifetime, using either EIS or IMVS/IMPS, is required to provide information about the limiting factors determining the efficiency of the devices, and also whether heating the devices affects the overall performance.

Appendix

A.1 Time-Temperature profile

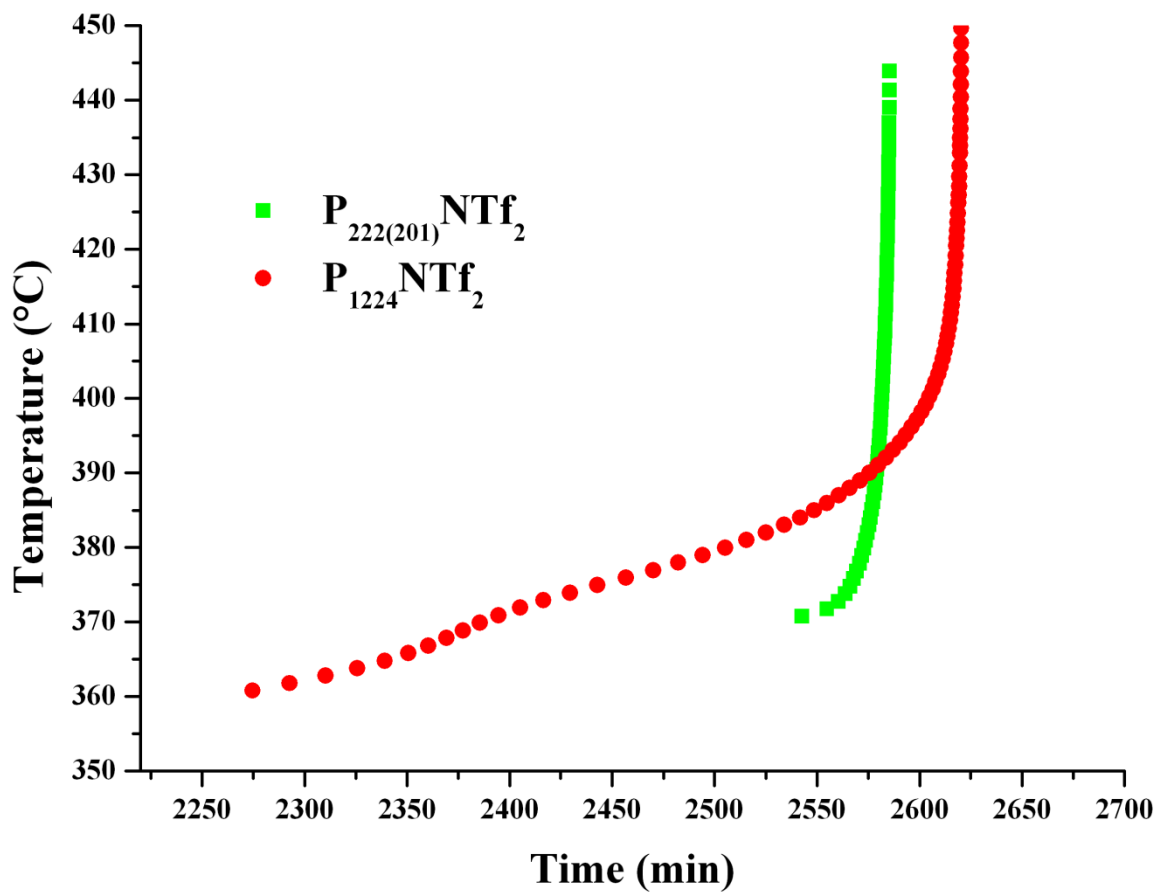


Figure A.1: Temperature-Time profile of $P_{222(201)}NTf_2$ and $P_{1224}NTf_2$

A.2 VTF behaviour of ionic liquids

A.2.1 Viscosity

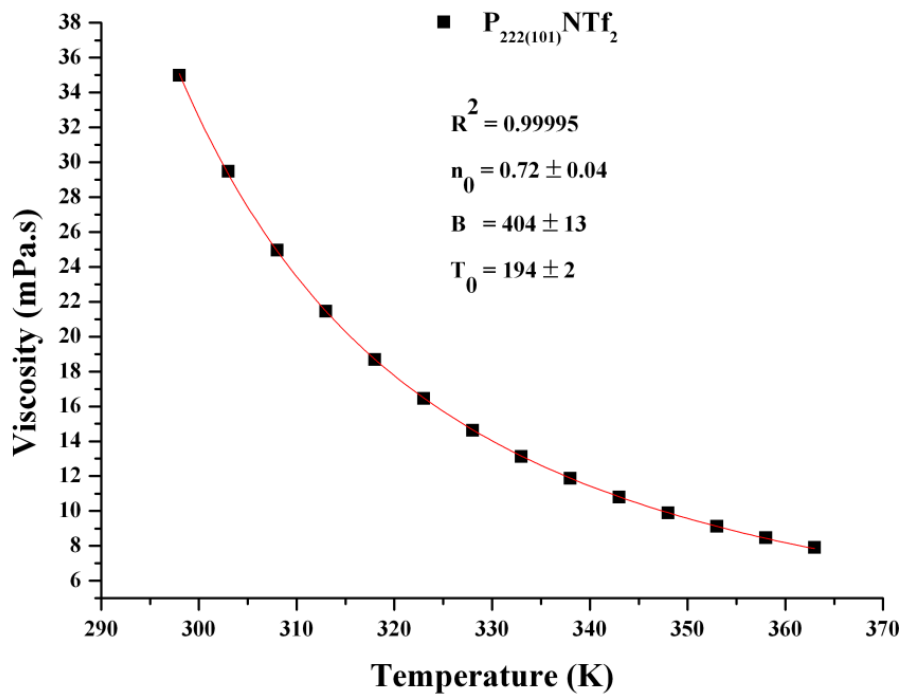


Figure A.2: VTF model of viscosity behaviour of $P_{222(101)}NTf_2$

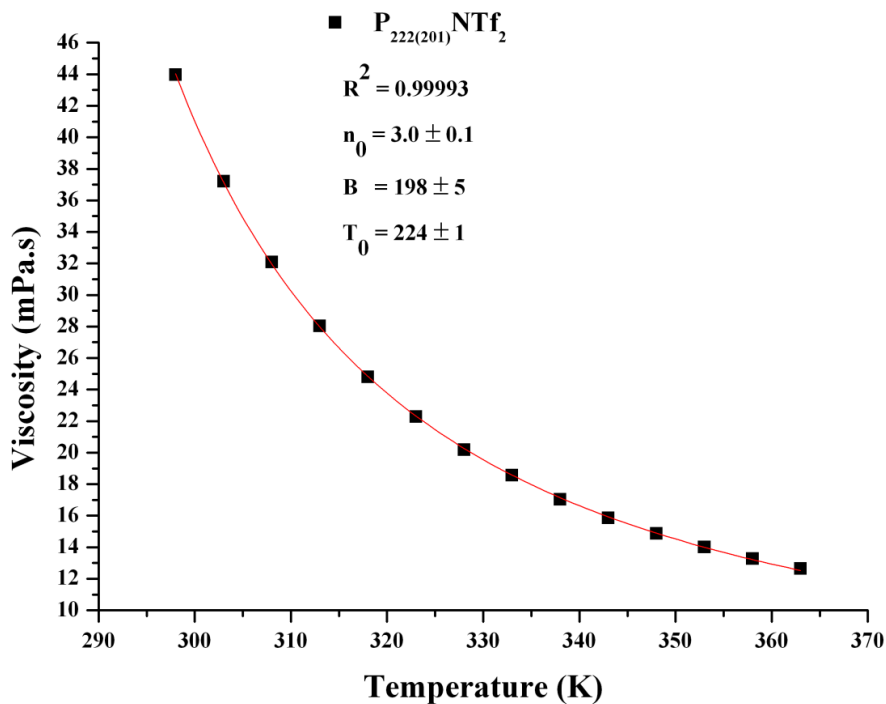
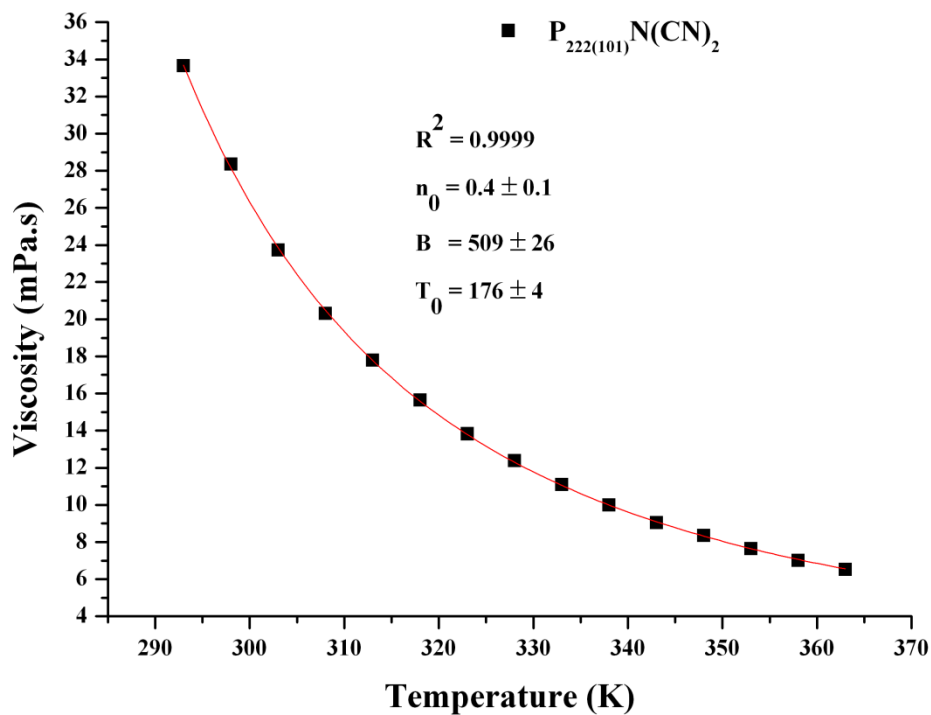
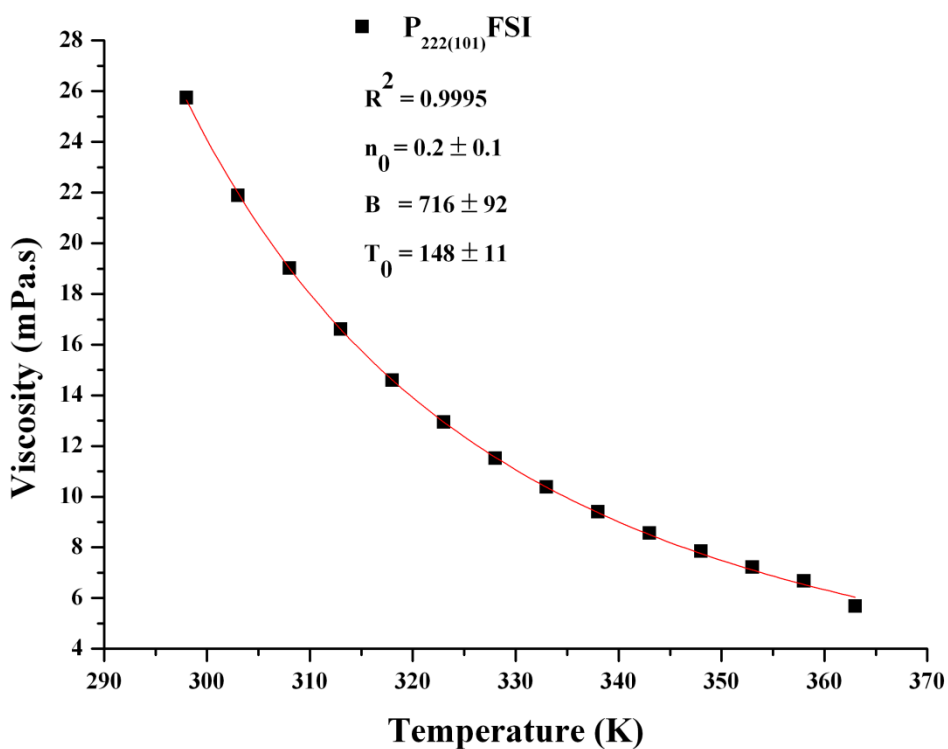


Figure A.3: VTF model of viscosity behaviour of $P_{222(201)}NTf_2$

Figure A.4: VTF model of viscosity behaviour of $P_{222(101)}N(CN)_2$ Figure A.5: VTF model of viscosity behaviour of $P_{222(101)}FSI$

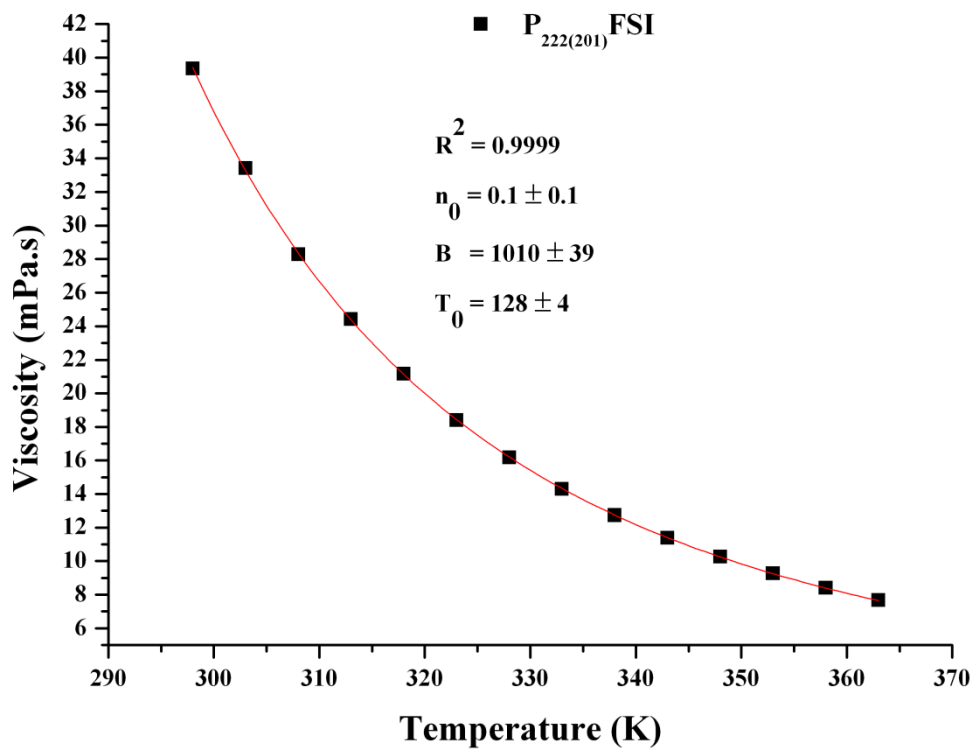


Figure A.6: VTF model of viscosity behaviour of P₂₂₂₍₂₀₁₎FSI

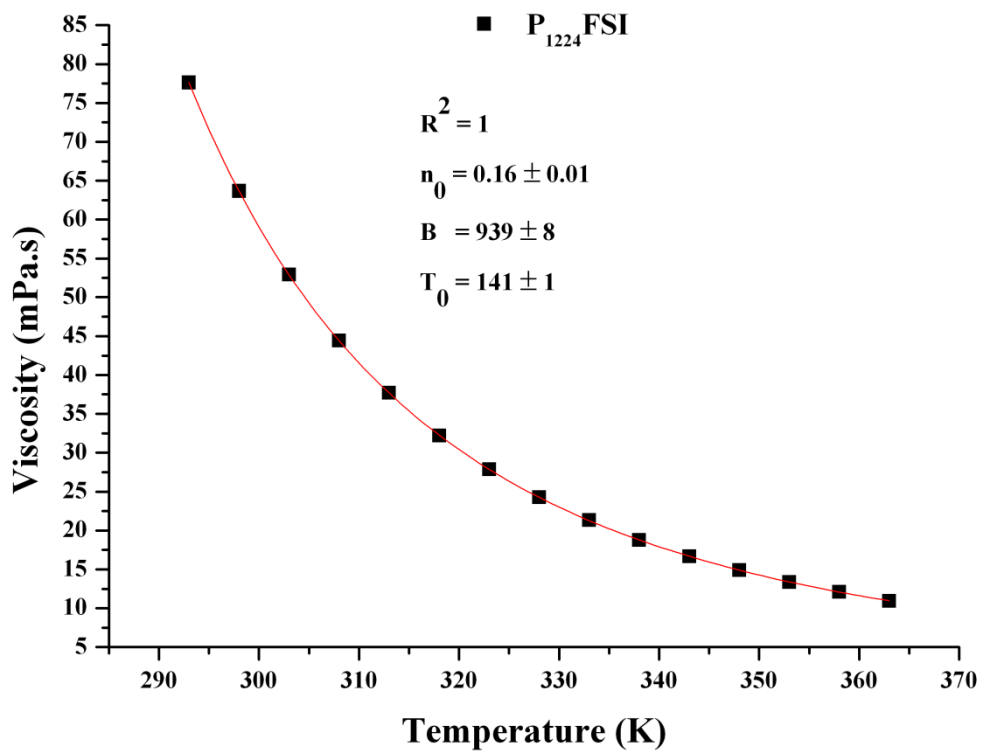
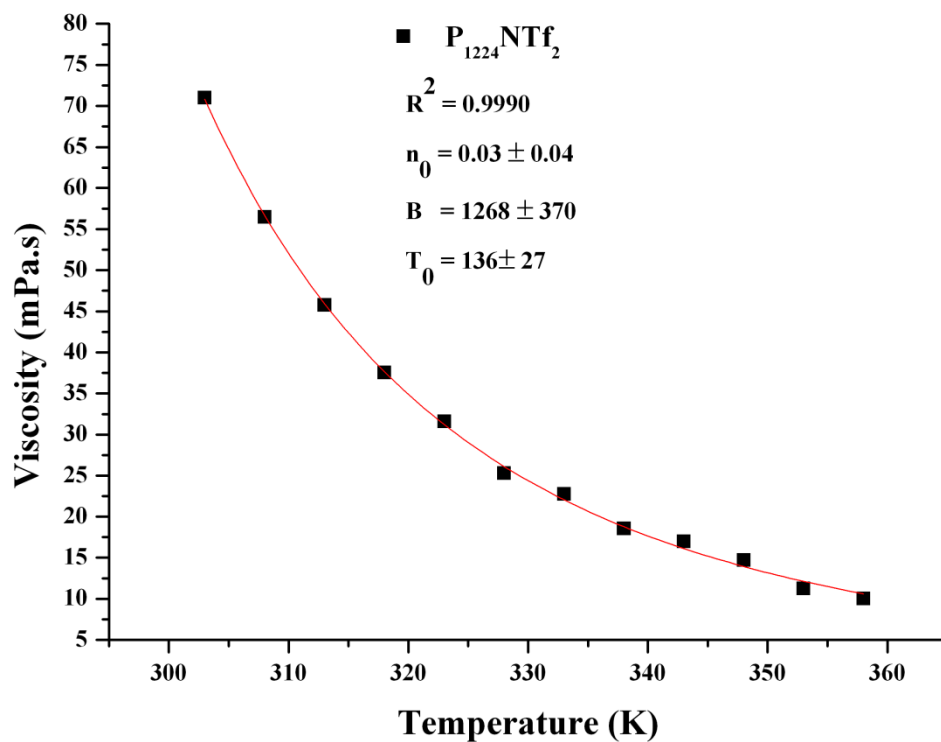
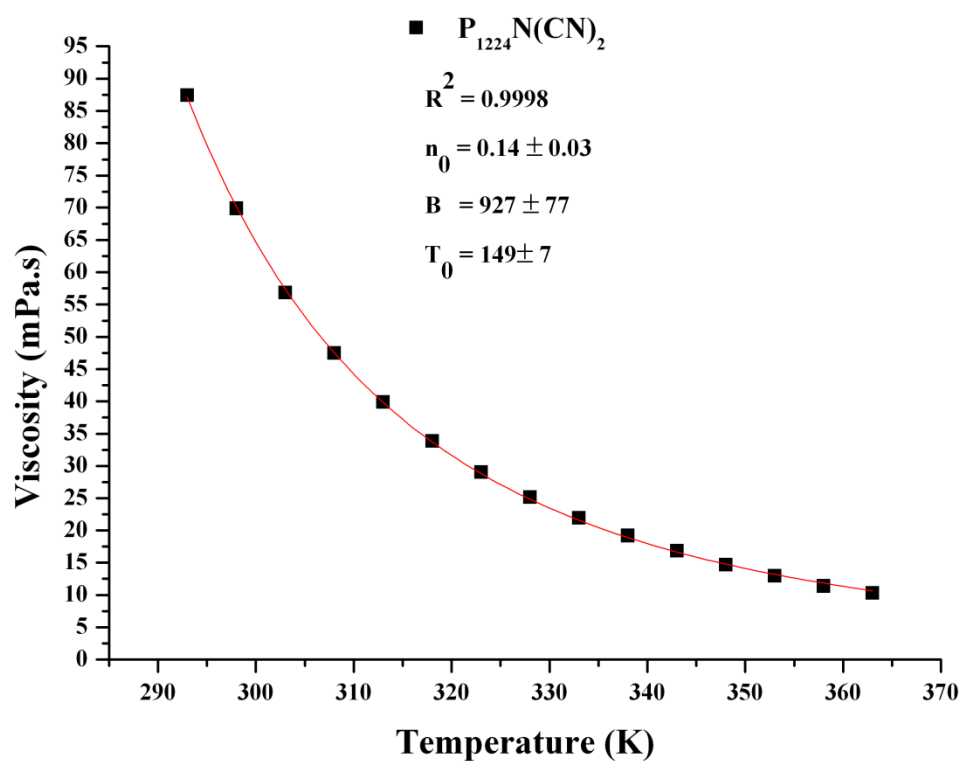


Figure A.7: VTF model of viscosity behaviour of P₁₂₂₄FSI

Figure A.8: VTF model of viscosity behaviour of $P_{1224}NTf_2$ Figure A.9: VTF model of viscosity behaviour of $P_{1224}N(CN)_2$

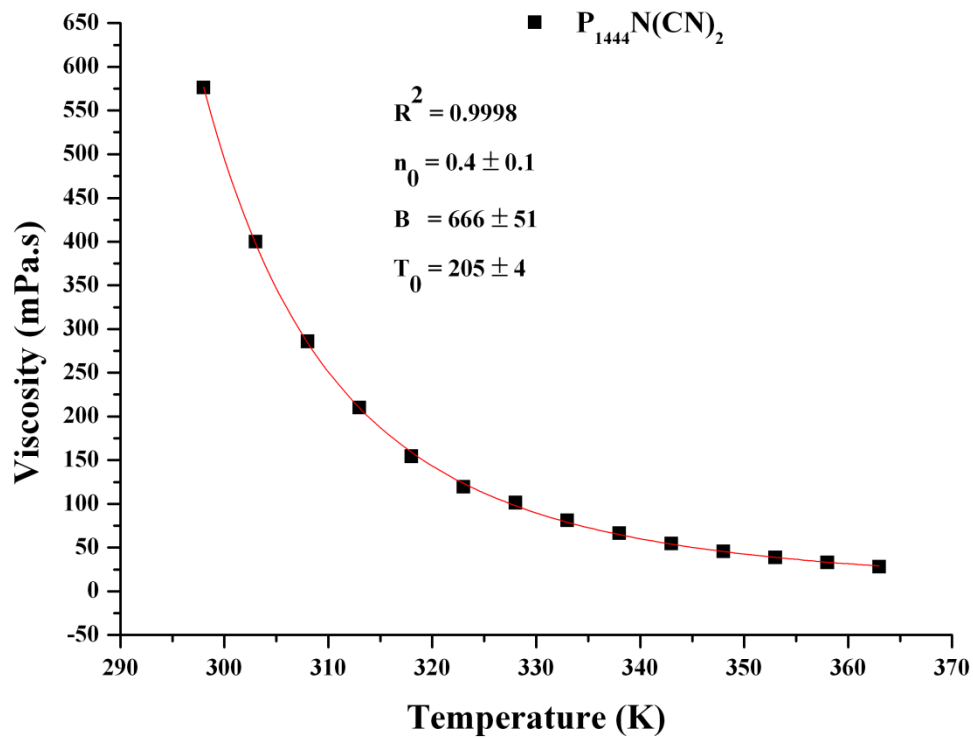


Figure A.10: VTF model of viscosity behaviour of $P_{1444}N(CN)_2$

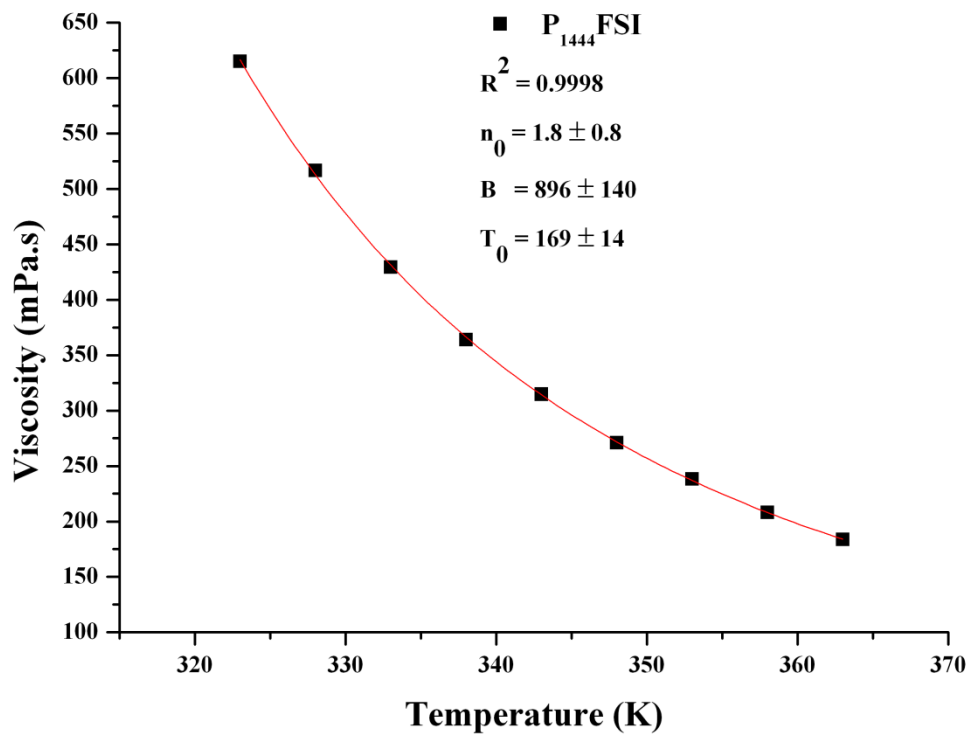
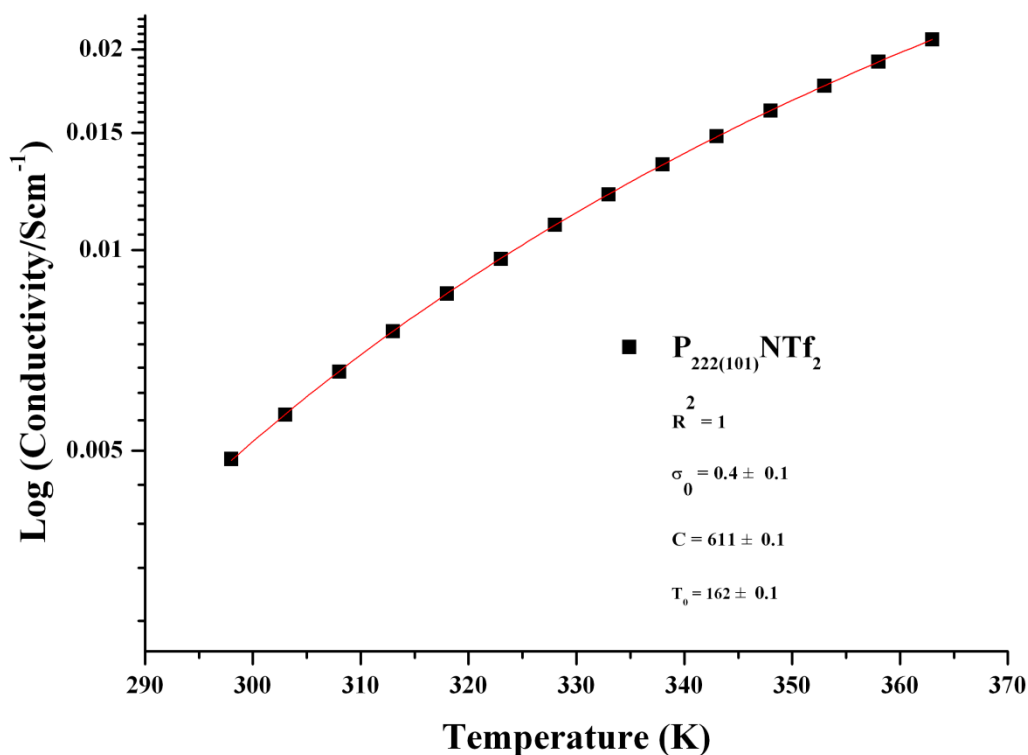


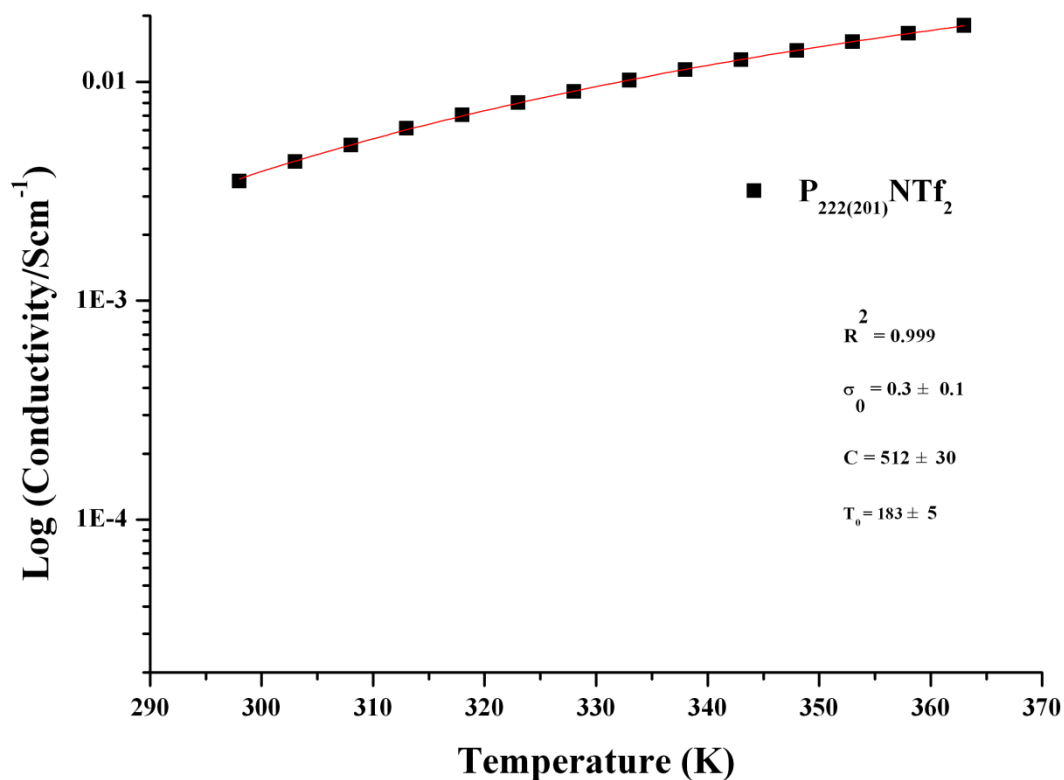
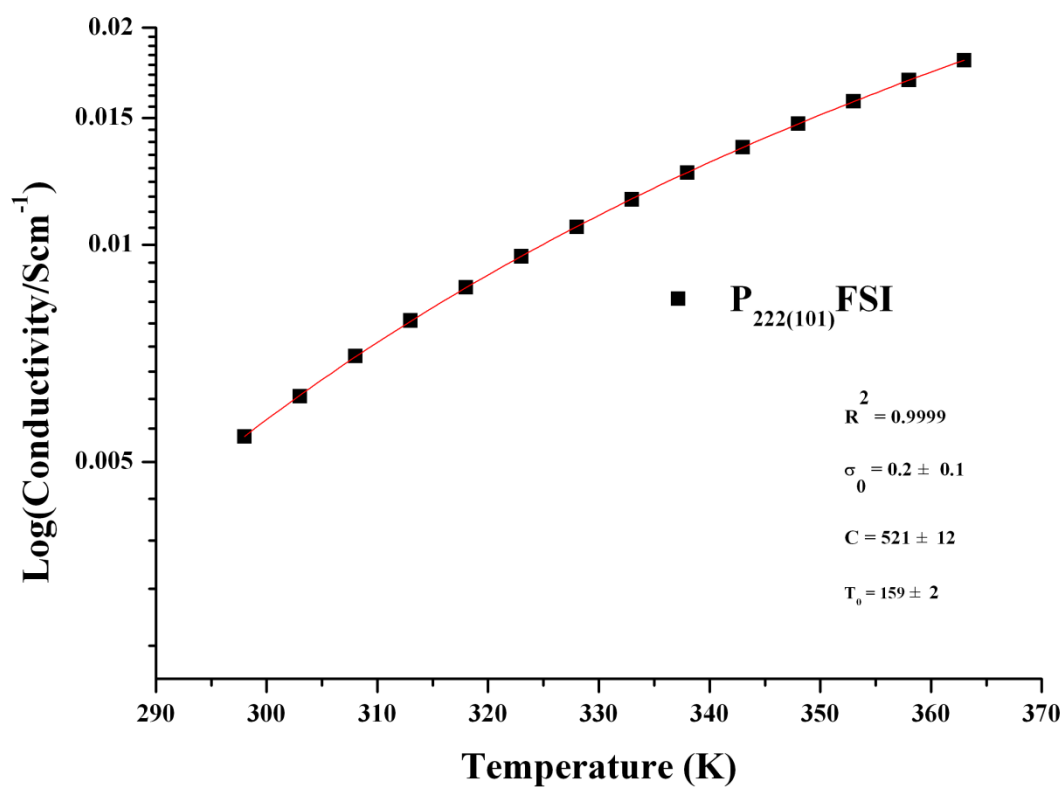
Figure A.11: VTF model of viscosity behaviour of $P_{1444}FSI$

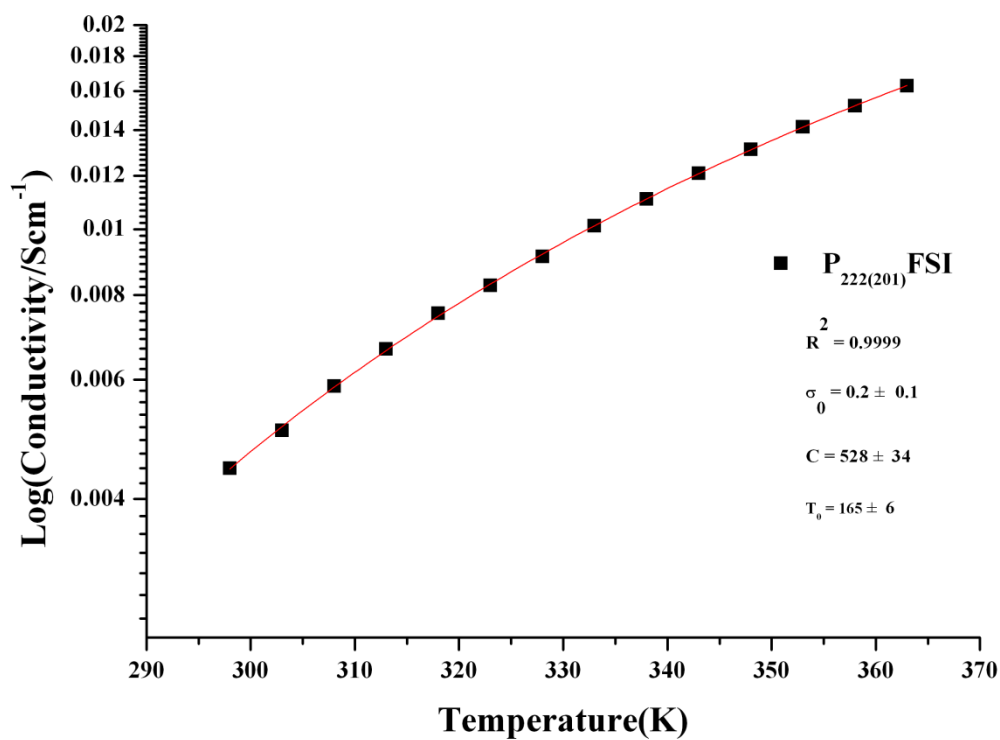
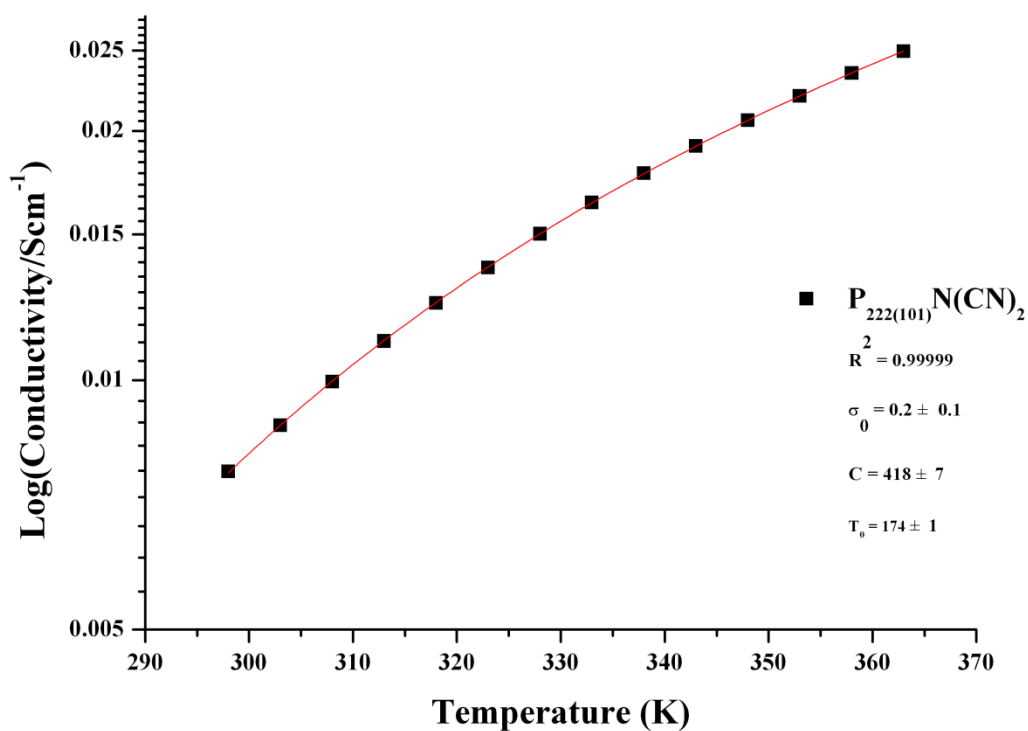
A.2.2 Ionic conductivity

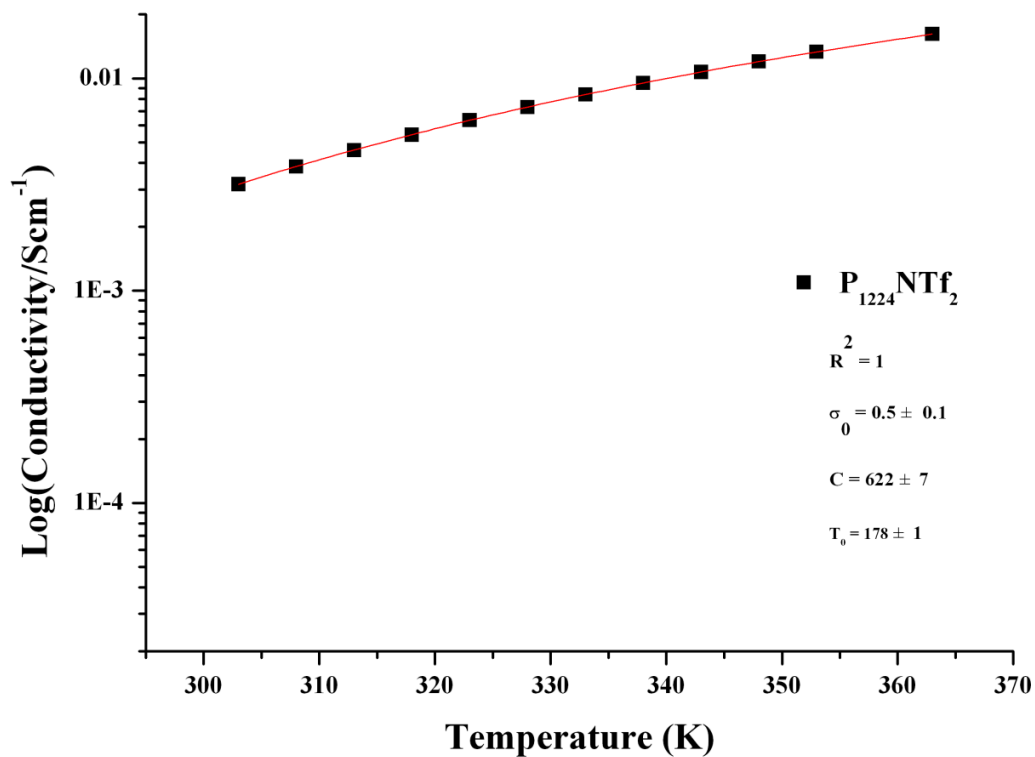
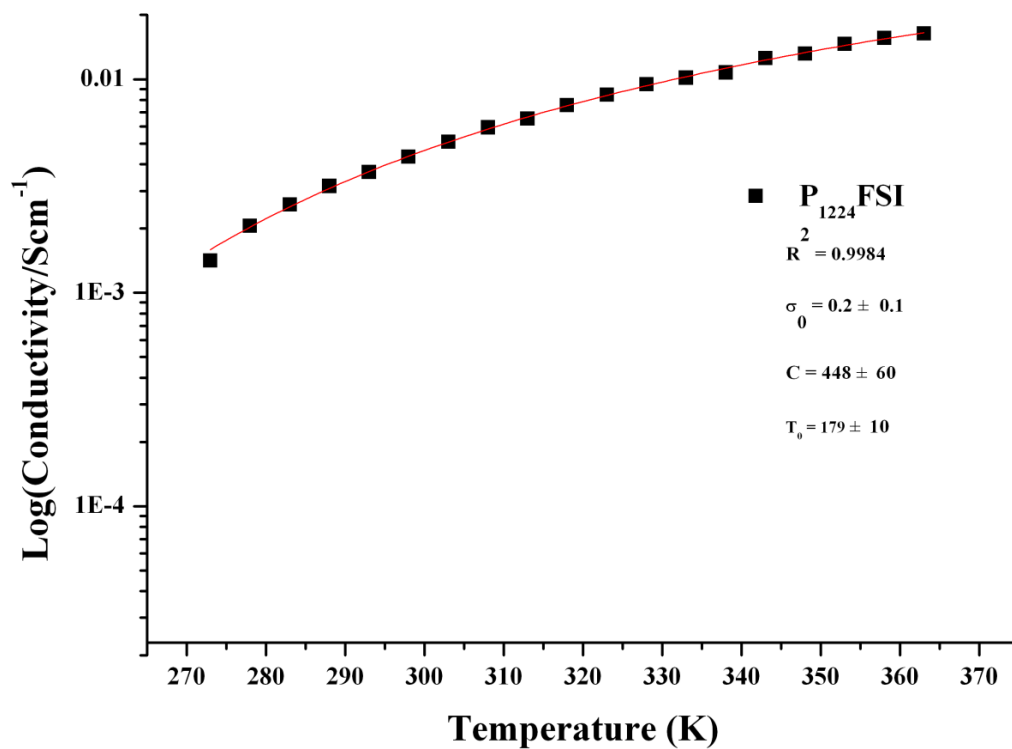
Table A.1: VTF equation parameters for Ionic conductivity data where σ_0 (S cm⁻¹), C (K) and T₀ (K) are constants.

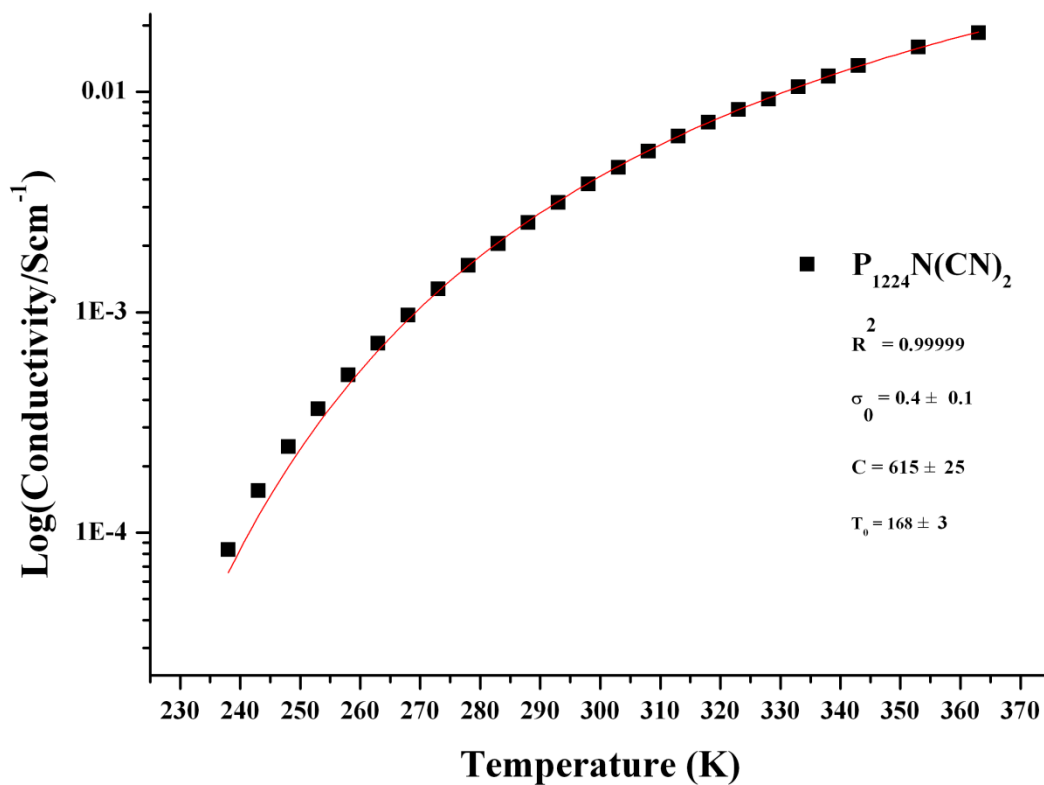
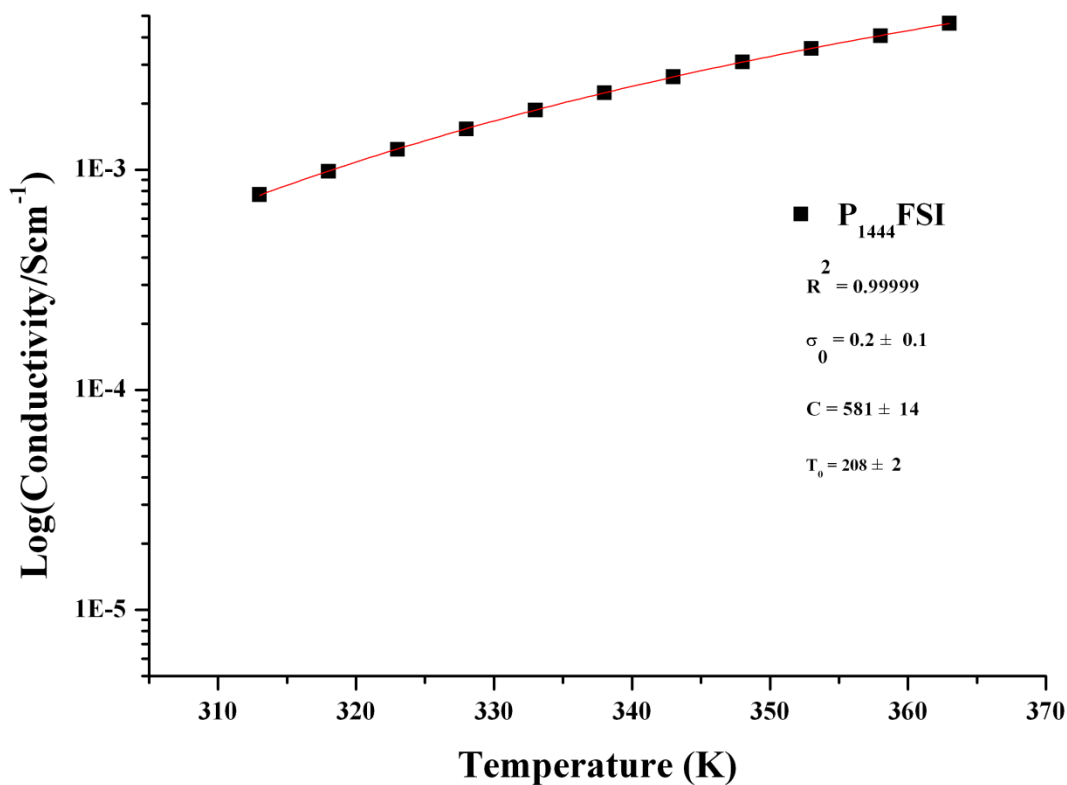
IL	σ_0	$\sigma = \sigma_0 \exp(-C/(T-T_0))$			$\Delta T_g - T_0$
		C (K)	T ₀ (K)	T _g (K)	
P ₂₂₂₍₁₀₁₎ NTf ₂	0.4 ± 0.1	611 ± 0.1	162 ± 0.1	N/A	
P ₂₂₂₍₂₀₁₎ NTf ₂	0.3 ± 0.1	512 ± 30	183 ± 5	N/A	
P ₂₂₂₍₁₀₁₎ FSI	0.2 ± 0.1	521 ± 12	159 ± 2	N/A	
P ₂₂₂₍₂₀₁₎ FSI	0.2 ± 0.1	528 ± 34	168 ± 6	N/A	
P ₂₂₂₍₁₀₁₎ N(CN) ₂	0.2 ± 0.1	418 ± 7	174 ± 1	N/A	
P ₁₂₂₄ NTf ₂	0.5 ± 0.1	622 ± 7	178 ± 1	N/A	
P ₁₂₂₄ FSI	0.2 ± 0.1	448 ± 60	179 ± 10	N/A	
P ₁₂₂₄ N(CN) ₂	0.4 ± 0.1	615 ± 25	168 ± 3	167	-1
P ₁₄₄₄ FSI	0.2 ± 0.1	581 ± 14	208 ± 2	N/A	
P ₁₄₄₄ N(CN) ₂	0.2 ± 0.1	635 ± 21	202 ± 2	200	-2

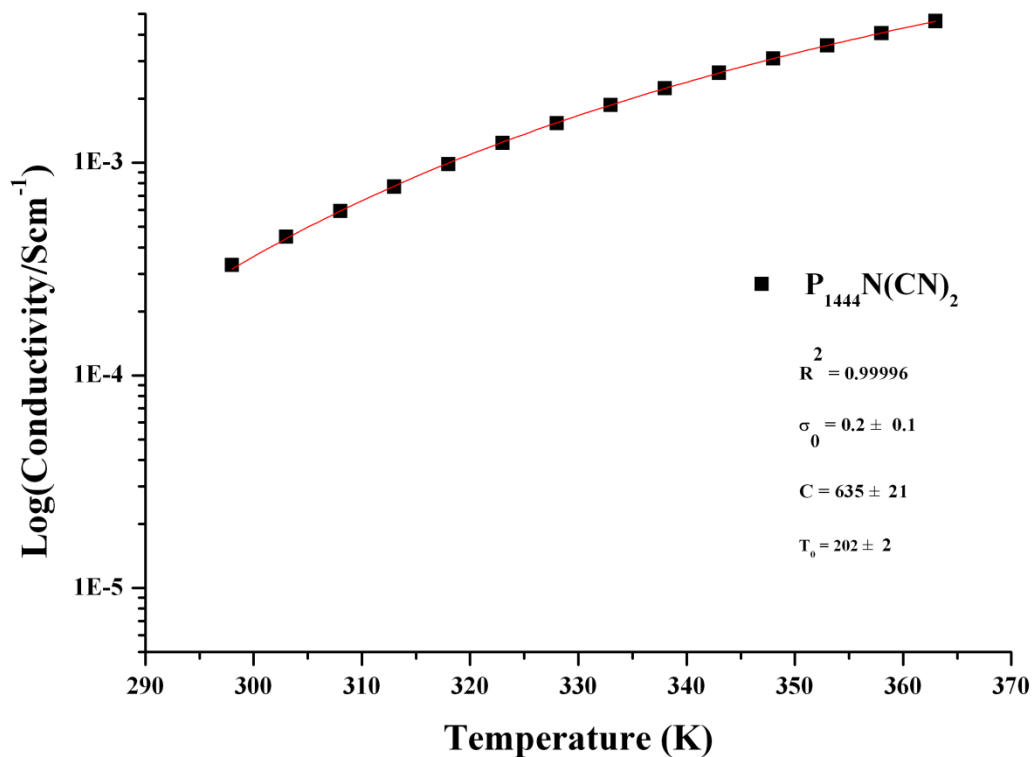
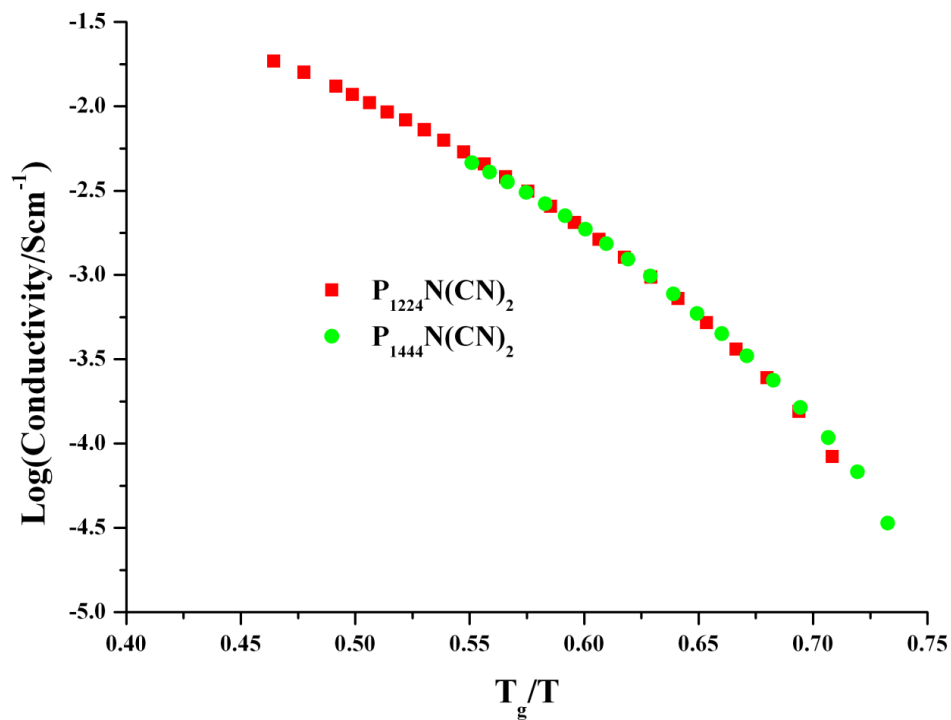
**Figure A.12: VTF model of ionic conductivity behaviour of P₂₂₂₍₁₀₁₎NTf₂**

Figure A.13: VTF model of ionic conductivity behaviour of $P_{222(201)}NTf_2$ Figure A.14: VTF model of ionic conductivity behaviour of $P_{222(101)}FSI$

Figure A.15: VTF model of ionic conductivity behaviour of $P_{222(201)}FSI$ Figure A.16: VTF model of ionic conductivity behaviour of $P_{222(101)}N(CN)_2$

Figure A.17: VTF model of ionic conductivity behaviour of $P_{1224}NTf_2$ Figure A.18: VTF model of ionic conductivity behaviour of $P_{1224}FSI$

Figure A.19: VTF model of ionic conductivity behaviour of $P_{1224}N(CN)_2$ Figure A.20: VTF model of ionic conductivity behaviour of $P_{1444}FSI$

Figure A.21: VTF model of ionic conductivity behaviour of $P_{1444}N(CN)_2$ Figure A.22: Arrhenius plot of ionic conductivity-temperature of $P_{1224}N(CN)_2$ and $P_{1444}N(CN)_2$

A.3 Cyclic voltammetry of NTf_2^- anion

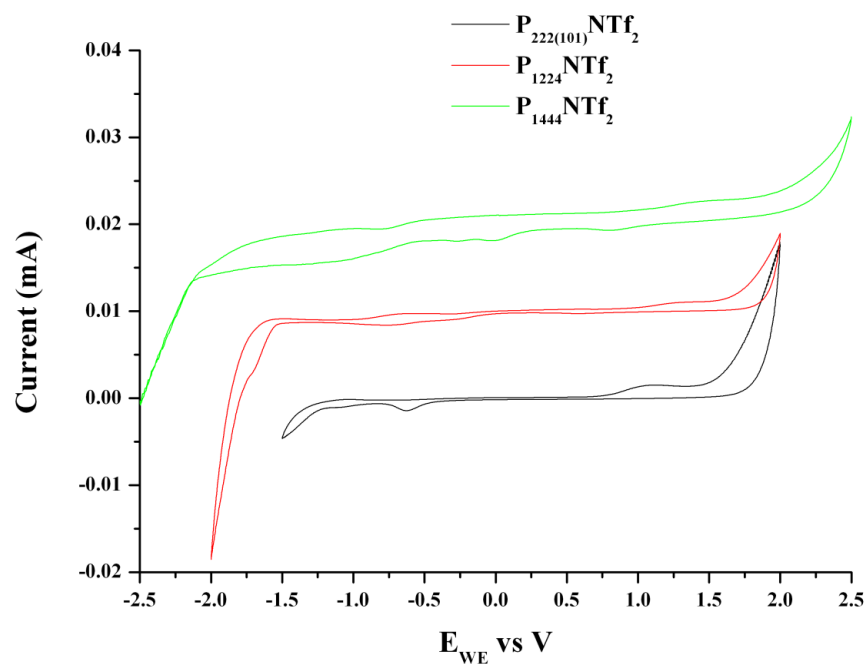


Figure A.23: CV of NTf_2^- anion ionic liquid series

A.4 UV spectroscopy and ATR-FTIR

A.4.1 UV spectroscopy

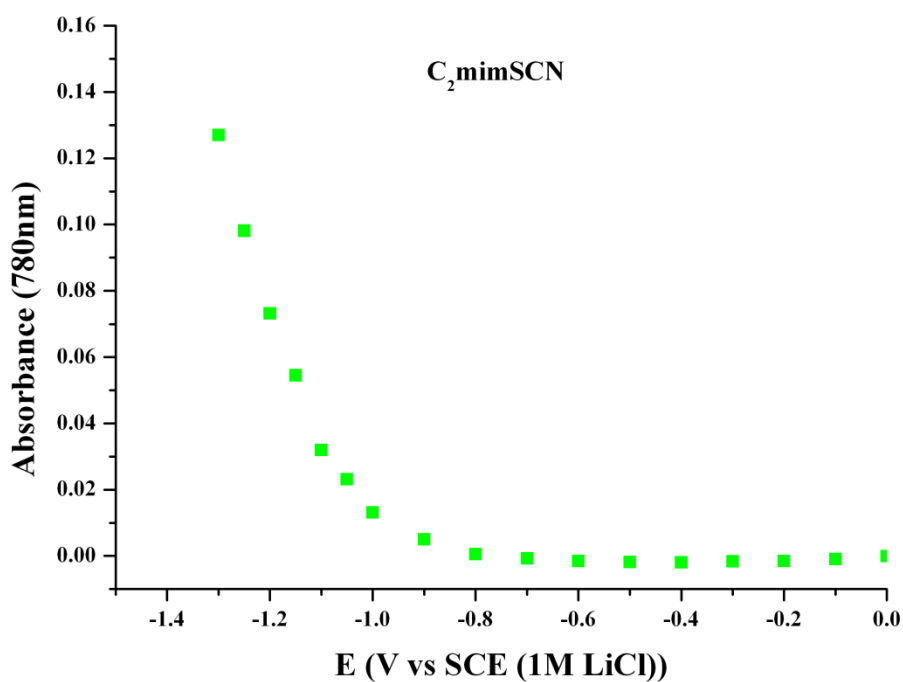


Figure A.24: Absorbance (780 nm) as a function of applied potential in C_2mimSCN

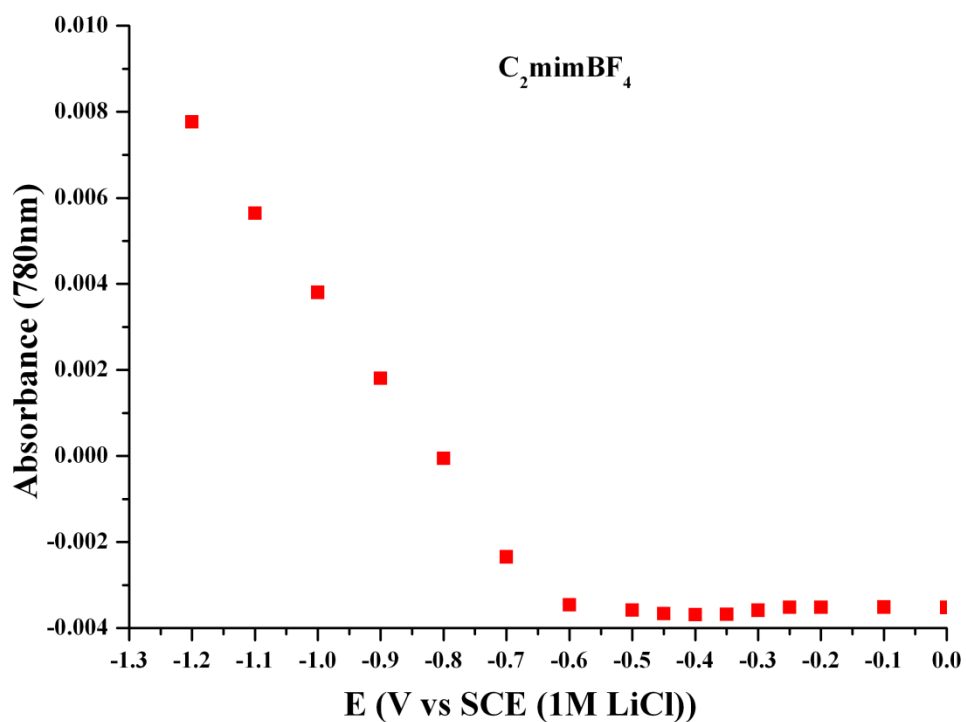


Figure A.25: Absorbance (780 nm) as a function of applied potential in C₂mimBF₄

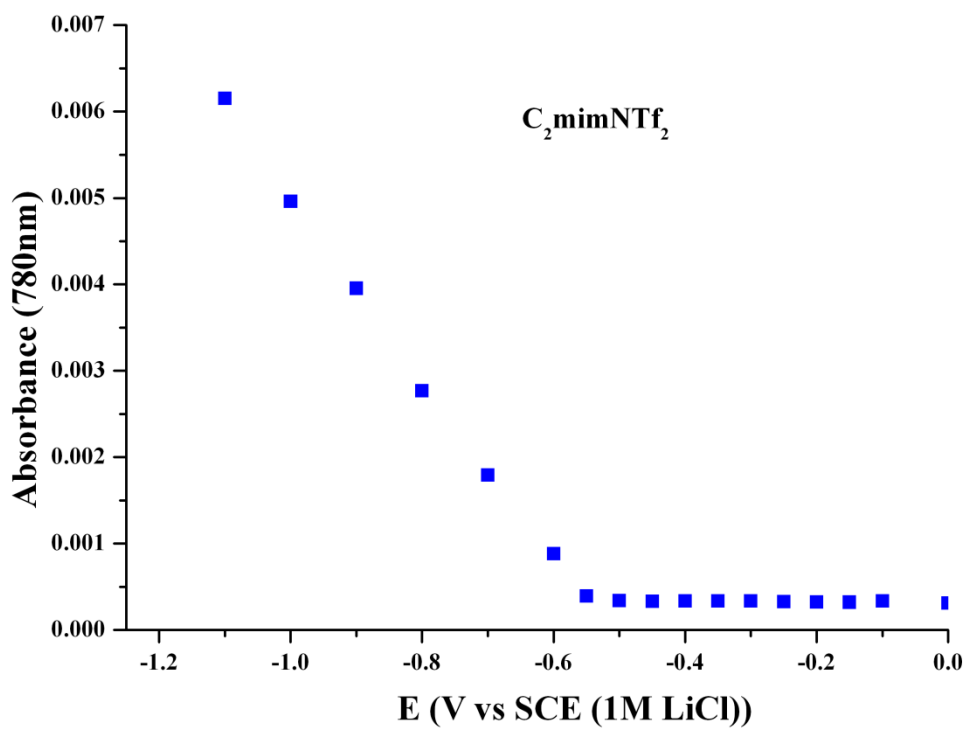


Figure A.26: Absorbance (780 nm) as a function of applied potential in C₂mimNTF₂

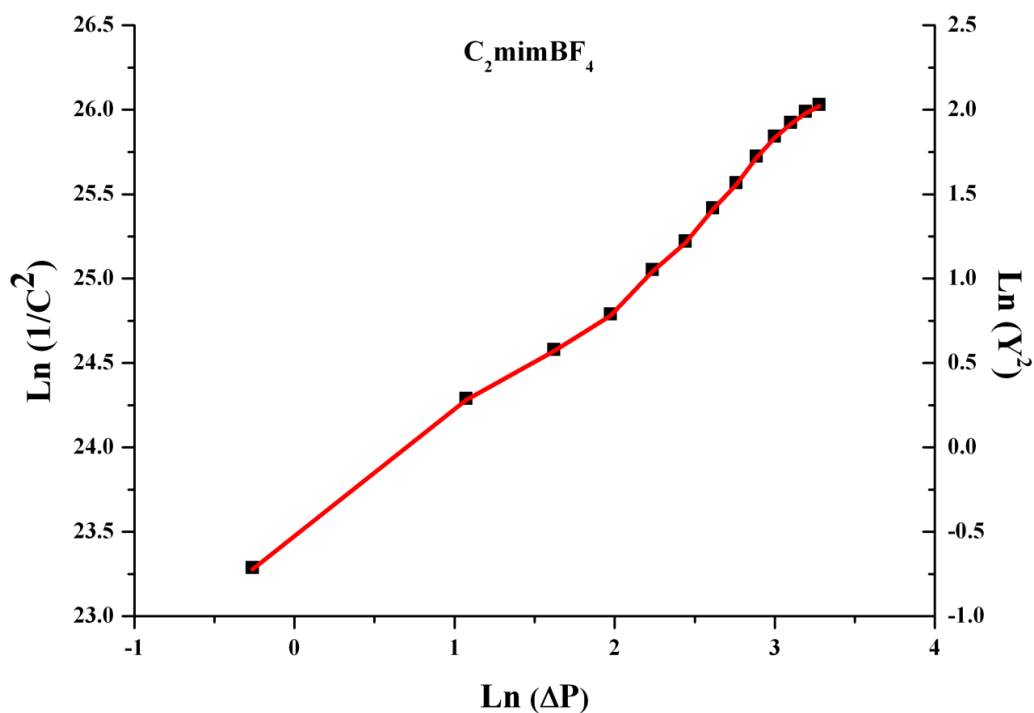


Figure A.27: Fitting of data for TiO_2 to the theoretical curve for $C_H/C_O = 0.5$

A.4.2 ATR-FTIR of untreated TiO_2 film and treated TiO_2 film

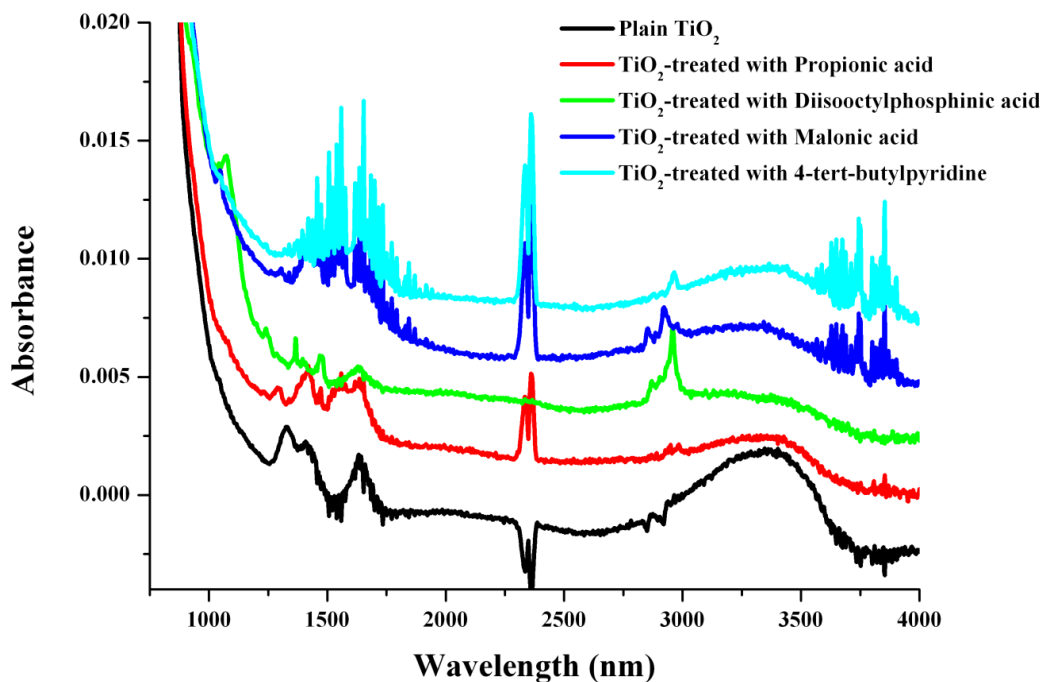


Figure A.28: ATR-FTIR of untreated TiO_2 film and treated TiO_2 film with propionic acid, diisooctylphosphinic acid, malonic acid and 4-tert-butylpyridine

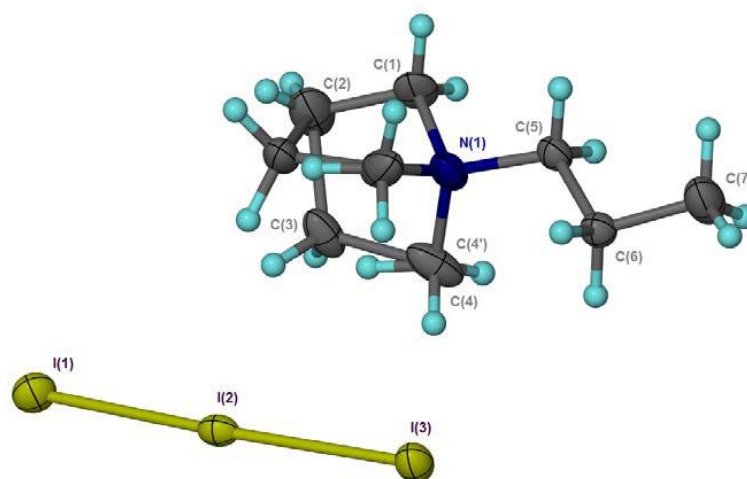
A.5 Crystal structure determination of the iodide and triiodide salt

In some ionic liquid electrolyte preparations, crystals of iodide and triiodide salts were formed overnight, thus leading to the solidification of the ionic liquids. The crystals obtained provide information about the packing behaviour and bond distance between the cations and anions. The crystals were determined by single crystal X-ray diffraction. The crystal structure of these compounds was structurally determined, and the figures and descriptions supplied, by Dr. Pamela Dean at Monash University.

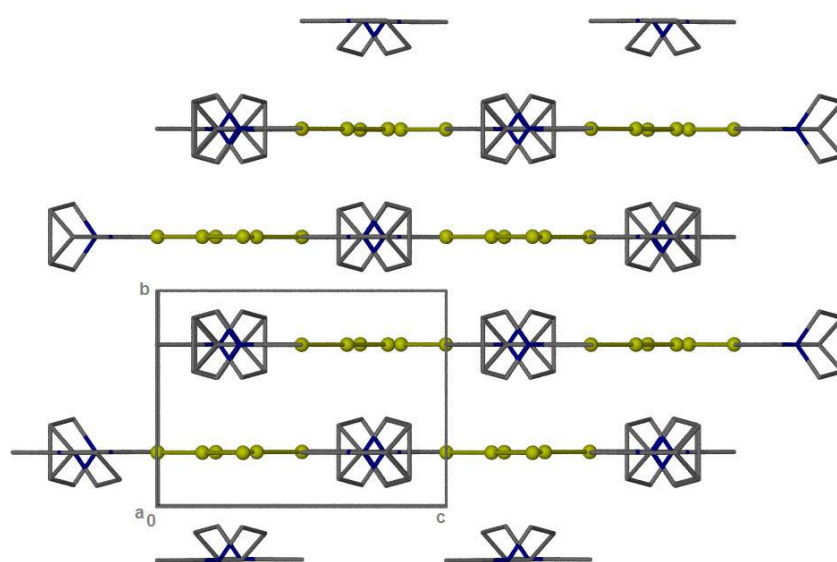
Crystal structure of 1-Propyl-1-methylpyrrolidinium Triiodide (C₃mpyrI₃)

X-ray-quality crystals of C₃mpyrI₃ were obtained overnight from an electrolyte mixture containing lithium iodide (0.0269 g, 0.201 mmol), iodine (0.0788 g, 0.310 mmol), 4-*tert*-butylpyridine (0.0781 g, 0.577 mmol), and 1-propyl-1-methylpyrrolidinium iodide (0.123 g, 0.482 mmol), which was made up to 1 mL with 1-propyl-1-methylpyrrolidinium bis(trifluoromethanesulfonyl)amide.

The structure of C₃mpyrI₃ (Figure A.29) was solved using direct methods and the refinement of the structure was obtained using full matrix least-squares refinement. The atoms I(1), I(2), I(3), N(1), C(1), C(2), C(5), C(6), and C(7) were found on a crystallographic mirror plane and the remaining carbon atoms, C(3) and C(4), were situated over two disordered positions. The site-occupancy factors (s.o.f.) of 0.5 each were assigned. The atoms C(4) and C(4') were restrained to occupy the same coordinates and have the same atomic displacement parameter and correspond to either one of the α ring carbon atoms or the methyl group carbon atom in each disorder component. Additionally, the C(3)–C(4) bond distance was restrained to a reasonable value. All non-hydrogen atoms were refined anisotropically. All the hydrogen atoms were placed in geometrically idealized positions and constrained to ride on their parent atoms with the C–H distances in the range 0.95–1.00 Å and $U_{\text{iso}}(\text{H})=1.2U_{\text{eq}}(\text{C})$. The highest remaining electron density peak ($1.02 \text{ e } \text{Å}^{-3}$) is located at a distance of 0.7 Å from I(1). C₃mpyrI₃ showed disorder that can either be in a twisted or half-chair conformation, and some atypical bond distances, for example C(4)–C(3) at 1.664(8) Å and C(3)–C(2) at 1.667(10) Å, which may be due to the disorder. The propyl chains adopt an energetically preferred *trans* zigzag conformation, with an N–C–C–C torsional angle of 180 °.



(a)



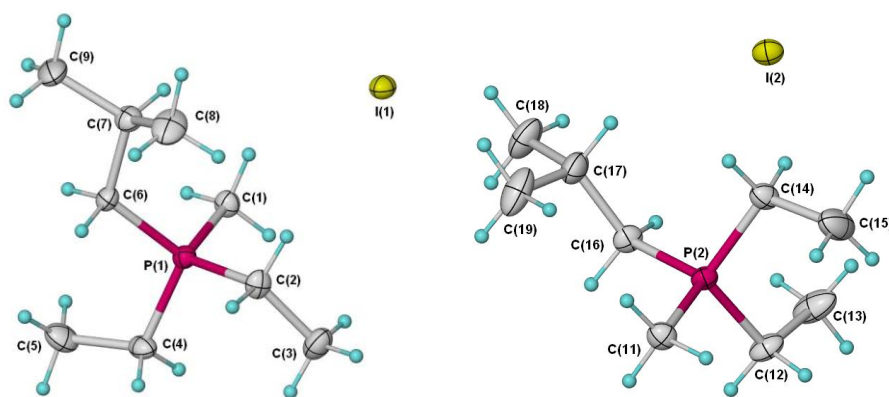
(b)

Figure A.29 (a) and (b) show the crystal structure of C_3mpyrI_3

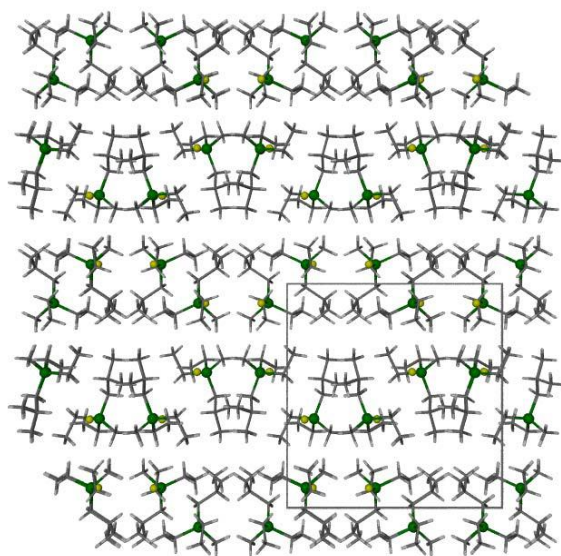
The unique component of C_3mpyrI_3 is shown with 50 % probability displacement ellipsoids (Figure A.29 (a)). The hydrogen atoms are shown as spheres of arbitrary size. The second part of the C_3mpyrI_3 ring is shown with symmetry equivalent atoms [symmetry code: $x, \frac{1}{2}-y, z$] to complete the ring, and both atoms of the disordered C(4)/(C4') are shown. Numbering of the hydrogen atoms of the disordered cation is omitted for clarity. The extended structure consists of layered motif of C_3mpyrI_3 (Figure A.29 (b)). Hydrogen atoms are omitted for clarity.

Crystal structure of diethylmethylisobutylphosphonium iodide ($P_{1224}I$)

X-ray crystals of $P_{1224}I$ (diethylmethylisobutylphosphonium iodide) were obtained overnight from an electrolyte mixture containing lithium iodide (0.0269 g, 0.201 mmol), iodine (0.0788 g, 0.310 mmol) and 4-tert-butylpyridine (0.0781 g, 0.577 mmol), which was made up to 1 ml with 65 volume % of 1-propyl-3-methylimidzaolium iodide and 35 volume % of diethylmethyl isobutylphosphonium bis(trifluoromethanesulfonyl)amide.



(a)



(b)

Figure A.30 (a) and (b) show the crystal structure of $P_{1224}I$

The asymmetric unit consists of two diethylmethylisobutylphosphonium cations and two iodide anions, all atoms of which sit on general positions (Figure A.30 (a)). $P_{1224}I$ crystallises in an orthorhombic lattice with eight pairs of ions occupying the unit cell. The phosphonium cation displays the usual bond lengths and angles seen for alkyl phosphonium cations. Both phosphoniums adopt a slightly disordered tetrahedral arrangement, with angles ranging from 107.0 to 112.71 ° for P(1) and 106.63 to 112.68 ° for P(2). The extended structure shows distinct layers of anion and cation clusters, which lie at 90 ° to all planes (Figure A.30 (b)). The closest P...I distance occurs between I(1)...P(1) with a distance of 4.246 Å. The closest I2 distance is 4.477 Å. Apart from the coulombic interaction, the most prevalent interaction is C—H...I close contacts, which link the cations and anions into a two dimensional sheet. As expected, several H—H interactions are also observed. No classical hydrogen bonding is seen.

Crystal structure of triethyl(methoxymethyl)phosphonium iodide ($P_{222(101)}I$)

X-ray crystals of $P_{222(101)}I$ were obtained overnight from an electrolyte mixture containing lithium iodide (0.045 g, 0.330 mmol), iodine (0.142 g, 0.559 mmol), N-methylbenzimidazole (0.176 g, 1.33 mmol), 1-ethyl-3-methylimidazolium iodide (0.955 g, 4.01 mmol), 1,3-dimethylimidazolium iodide (0.899 g, 4.01 mmol) and triethylmethoxymethylphosphonium bis(trifluoromethanesulfonyl)amide (2 g, 4.68 mmol).

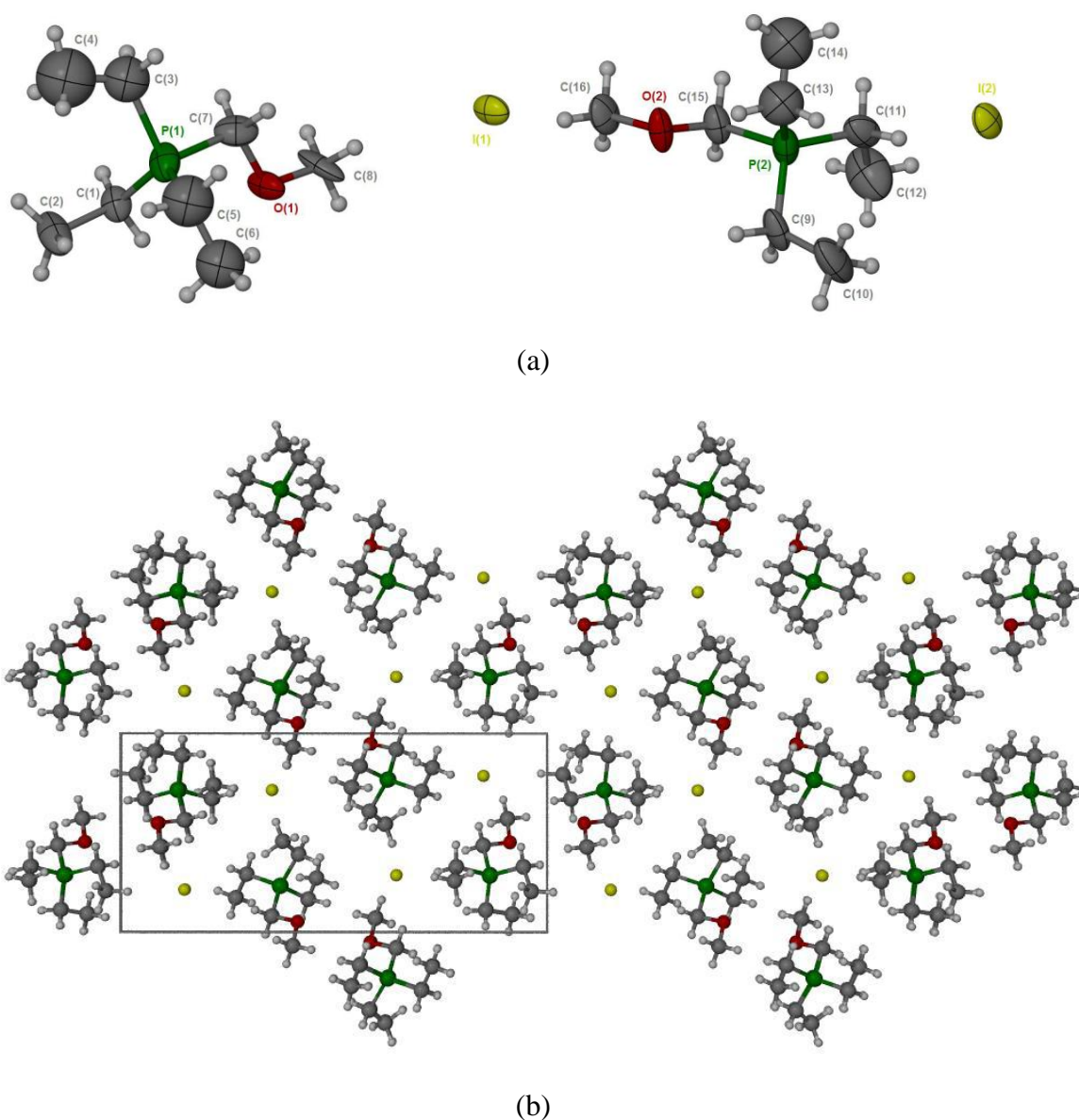


Figure A.31: (a) and (b) show the crystal structure of $P_{222(101)}I$

The asymmetric unit consists of two triethyl(methoxymethyl)phosphonium cations and two iodide anions, all atoms of which sit on general positions (Figure A.31 (a)). $P_{222(101)}I$

crystallises in a triclinic lattice, with four pairs of ions occupying the unit cell. The phosphonium cations display the usual bond lengths and angles seen for alkyl phosphonium cations, except for C(3)—C(4) 1.327 Å, P(1)—C(5) 1.715 Å and C(13)—C(14) 1.228 Å, which are shorter than usual. The atoms C(3), C(4), C(5), C(6), C(13) and C(14) were refined isotropically due to unusually large anisotropic factors. Both phosphonium adopt a slightly disordered tetrahedral arrangement, with angles ranging from 96.67 to 119.54 ° for P(1) and 103.73 to 111.90 ° for P(2). The extended structure show distinct layers of anions and cations, which lie at 45 ° to the bc plane (Figure A.31 (b)). The closest P...I distance occurs between I(2)...P(1), with a distance of 4.575 Å. The closest I(1)—P(2) distance is 4.702 Å. Apart from the coulombic interaction, the most prevalent interaction is C—H...I and C—H...O close contacts, which links the cations and anions into a three dimensional network. As expected, several H—H interactions are also seen. No classical hydrogen bonding is seen.

A.6 Electron Kinetic measurement

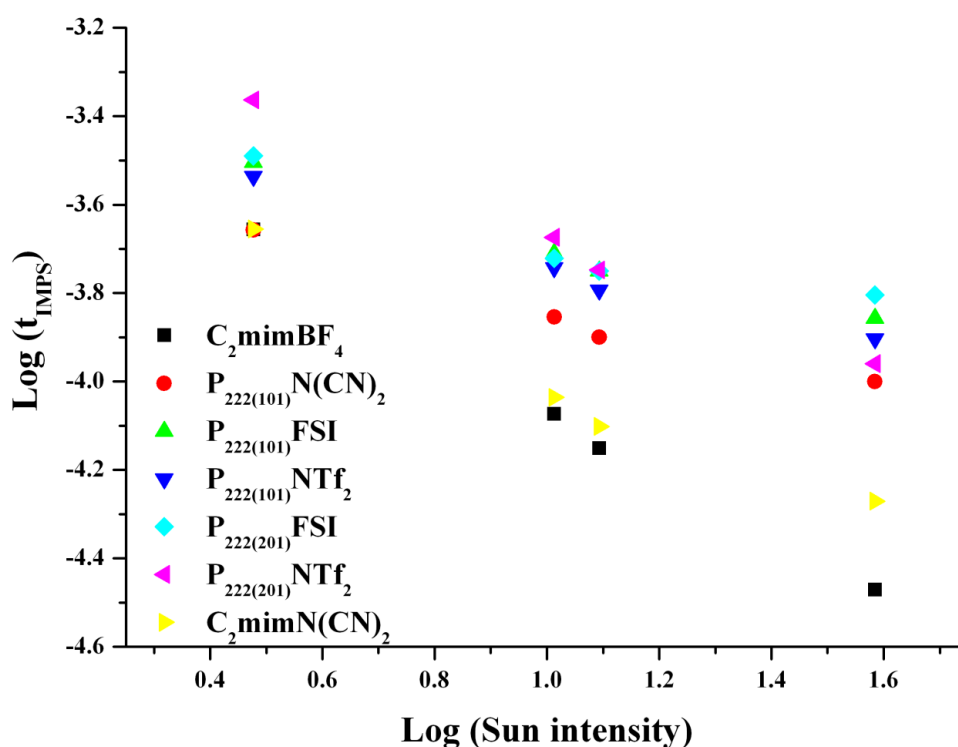


Figure A.32: IMPS measurements of THD1 devices with a range of ionic liquids

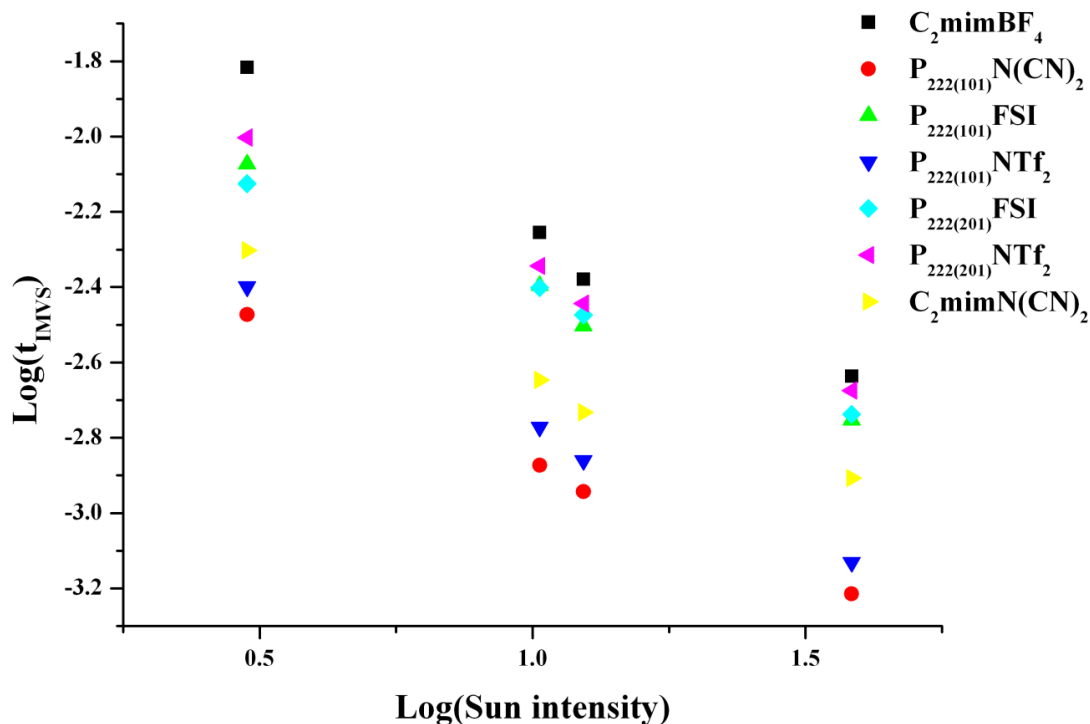


Figure A.33: IMVS measurements of THD1 devices with a range of ionic liquids

A.7 UV-Vis spectrum of the effect of chenodeoxycholic acid with porphyrin sensitisers

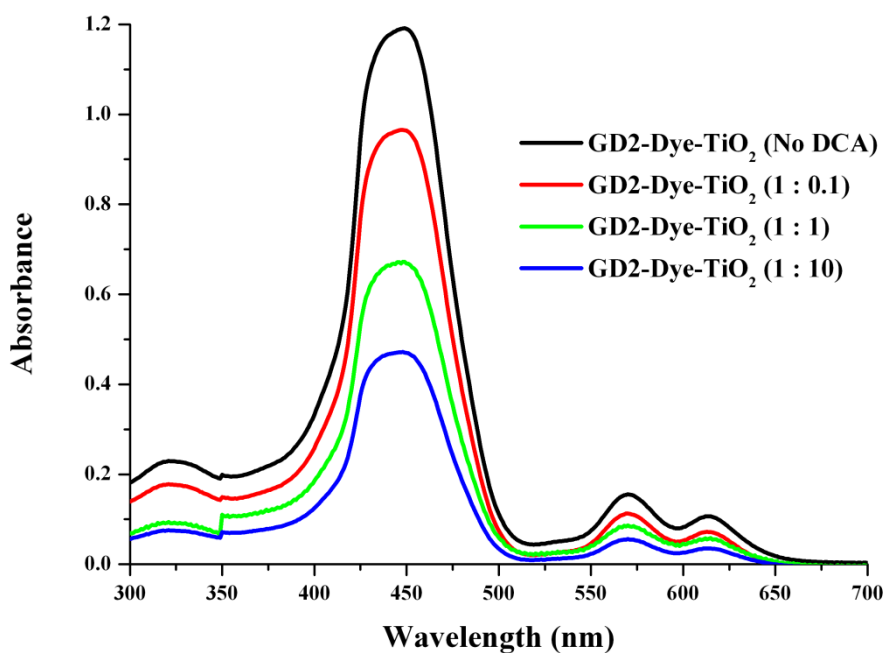


Figure A.34: Absorption spectrum of GD2 in presence of different concentration of DCA

A.8 Thermal analysis of neat pyrrolidinium ionic liquids

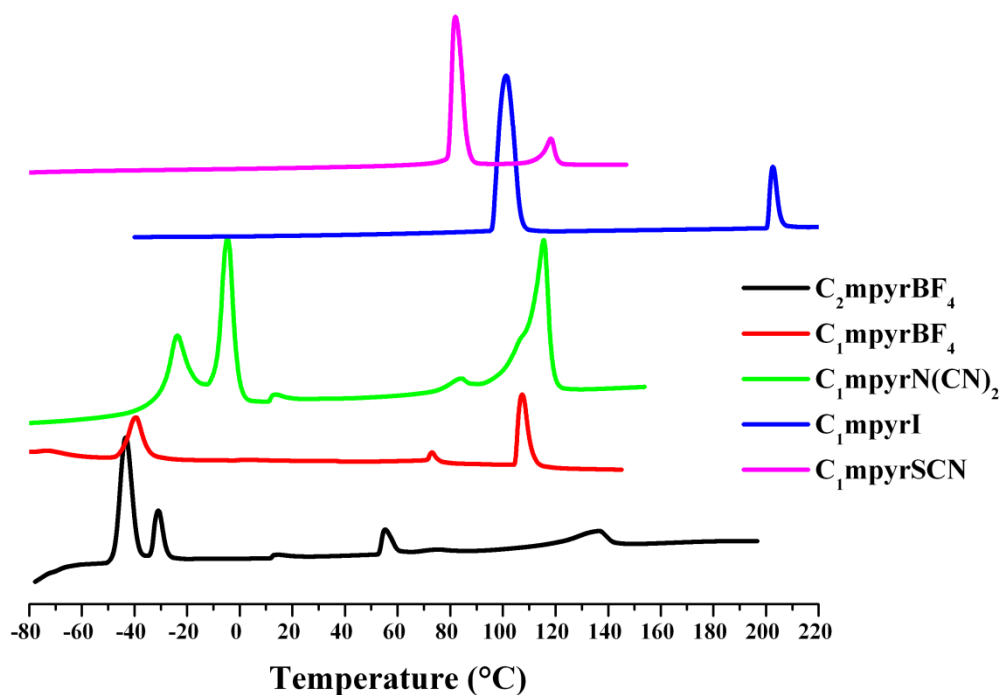


Figure A.35: DSC traces of a range of plastic crystals: $C_2\text{mpyrBF}_4$, $C_1\text{mpyrBF}_4$, $C_1\text{mpyrN(CN)}_2$, $C_1\text{mpyrI}$ and $C_1\text{mpyrSCN}$

A.9 Diagram of equivalent circuit for a symmetrical cell

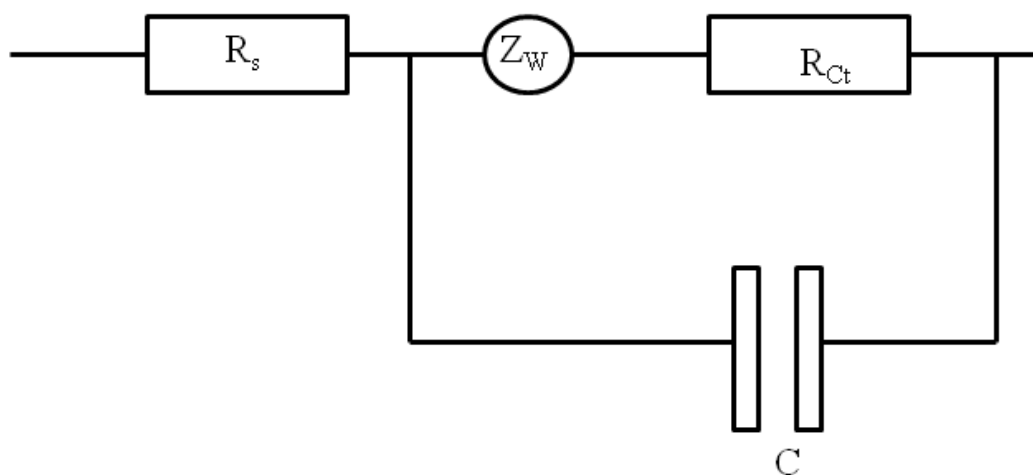


Figure A.36: Equivalent circuit for EIS, where R_s is series resistance, R_{ct} is the charge transfer resistance, C is the double layer capacitance and Z_W is the Warburg impedance

A.10 Publications

1. V. Armel, J. M. Pringle, M. Forsyth, D. R. MacFarlane, D. L. Officer and P. Wagner, "Ionic liquid electrolyte for porphyrin dye sensitised solar cells" *Chem. Commun.*, 2010, **46**, 3146-3148.
2. O. Winther-Jensen, V. Armel, M. Forsyth and D. R. MacFarlane, "In situ Photopolymerization of a Gel Ionic Liquid Electrolyte in the Presence of Iodine and Its Use in Dye Sensitized Solar Cells" *Macromol. Rapid Commun.*, 2010, **31**, 479-483.
3. J. M. Pringle, V. Armel and D. R. MacFarlane, "Electrodeposited PEDOT-on-plastic cathodes for dye sensitised solar cells" *Chem. Commun* 2010, **46**, 5367-5369.
4. J. M. Pringle, V. Armel, M. Forsyth and D. R. MacFarlane, "PEDOT-coated counter electrodes for dye sensitised solar cells" *Aust. J. Chem.*, 2009, **62**, 348-352.
5. R. Vijayaraghavan, M. Surianarayanan, V. Armel, D. R. MacFarlane and V. P. Sridhar, "Exothermic and thermal run away behaviour of some ionic liquids at elevated temperatures" *Chem. Commun.*, 2009, 6297-6299.
6. P. M. Dean, B. R. Clare, V. Armel, J. M. Pringle, C. M. Forsyth, M. Forsyth and D. MacFarlane, "Structural characterisation of novel ionic salts incorporating trihalide anions" *Aust. J. Chem.*, 2009, **62**, 334-340.

Conference contribution

1. Vanessa Armel, Tae-Hyuk Kwon, Maria Forsyth, Andrew Holmes and Douglas MacFarlane, "*Phosphonium based ionic liquids for organic dye sensitised solar cells*" 5th Annual International Electromaterials Science Symposium and 4th Australasian Symposium on Ionic Liquids February 2010. Presentation (Presentation prize awarded)
2. Vanessa Armel, Pawel Wagner, David L. Officer, Maria Forsyth and Douglas MacFarlane, "*Ionic material for porphyrin dye sensitised solar cells*" Conference on Ionic liquids-3 (COIL 3) June 2009. Poster presented.
3. Vanessa Armel, Maria Forsyth and Douglas MacFarlane, "*Ionic material as potential electrolytes for dye sensitised solar cells*" ACES Electromaterials Symposium, Wollongong, February 2009. Poster presented.